An Introduction to **Stellarators**

An Introduction to Stellarators

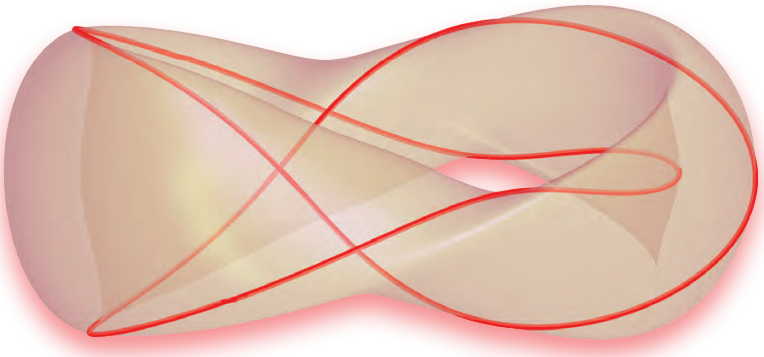

From Magnetic Fields to Symmetries and Optimization

Lise-Marie Imbert-Gérard
University of Arizona, Tucson, Arizona

Elizabeth J. Paul
Columbia University, New York, New York

Adelle M. Wright
University of Wisconsin - Madison, Madison, Wisconsin

siam

Society for Industrial and Applied Mathematics
Philadelphia

10 9 8 7 6 5 4 3 2 1

Publications Director	Kivmars H. Bowling
Executive Editor	Elizabeth Greenspan
Acquisitions Editor	Paula Callaghan
Developmental Editor	Rose Kolassiba
Managing Editor	Kelly Thomas
Production Editor	Lisa Briggeman
Copy Editor	Susan Fleshman
Production Manager	Rachel Ginder
Production Coordinator	Cally A. Shrader
Compositor	Cheryl Hufnagle
Graphic Designer	Doug Smock

Library of Congress Control Number 2024040172

Contents

List of Figures

List of Tables

List of Symbols and Acronyms

The most frequently used symbols and most common acronyms are summarized here. For a summary of various relevant vector calculus identities, we refer the reader to [137].

$\boldsymbol{B}$	Magnetic vector field
$\boldsymbol{A}$	Vector potential
$\boldsymbol{E}$	Electric vector field
$\boldsymbol{J}$	Current density
$\boldsymbol{r}$	Position vector
$\boldsymbol{R}$	Parameterization of $\mathbb{R}^3$ (function of 3 variables)
$\boldsymbol{q}$	Position for single-particle motion
$\boldsymbol{v}$	Velocity for single-particle motion
$\boldsymbol{p}$	Particle momentum
$\boldsymbol{q}_T$	Trajectory in physical space
$\dot{\boldsymbol{q}}$	Time derivative of $\boldsymbol{q}$
ρ	Mass density
p	Pressure
$\boldsymbol{u}$	Flow velocity
q	Particle charge
m	Particle mass
ψ_T	Normalized toroidal flux
ψ_P	Normalized poloidal flux
ι	Rotational transform
$\hat{\boldsymbol{b}}$	Unit vector in the direction of the magnetic field $\boldsymbol{B}/B$
$\hat{\boldsymbol{n}}$	Unit normal vector to a surface
$\hat{\boldsymbol{v}}$	Unit vector
Δ	Laplacian differential operator
Δf	Laplacian of a scalar function f (a scalar function)
$\Delta \boldsymbol{v}$	Laplacian of a vector field $\boldsymbol{v}$ (component-wise Laplacian)
∇	Gradient differential operator
∇f	Gradient of a scalar function f is a vector field
$\nabla \boldsymbol{v}$	Gradient of a vector field $\boldsymbol{v}$ is a tensor, written in index notation as $\partial_i v_j$
$\nabla\cdot$	Divergence differential operator
$\nabla \cdot \boldsymbol{v}$	Divergence of a vector field $\boldsymbol{v}$
$\nabla\times$	Curl differential operator
$\nabla \times \boldsymbol{v}$	Curl of a vector field $\boldsymbol{v}$
$\boldsymbol{v} \cdot \nabla$	$\boldsymbol{v}$-dot-grad operator
$(\boldsymbol{v} \cdot \nabla) f$	$\boldsymbol{v}$-dot-grad of a scalar function f (a scalar function)
$(\boldsymbol{v} \cdot \nabla) \boldsymbol{w}$	$\boldsymbol{v}$-dot-grad of a vector field $\boldsymbol{w}$ (component-wise)

MHD	Magnetohydrodynamics
ODE	Ordinary differential equation
PDE	Partial differential equation
MDE	Magnetic differential equation

Foreword

In August 2017, a group of applied mathematicians and plasma physicists gathered to discuss a collaboration proposal to the Simons Foundation on the topic of optimal design of stellarators. For the next six months, we met regularly, sometimes virtually and sometimes in person, to work on that proposal. Most applied mathematicians in the group came with some understanding of fluid mechanics and electromagnetics, but only the most general notions of what a stellarator is and how plasmas are modeled. On the other hand, the physicists knew that solving the tough challenges in stellarator design required deepening the mathematical foundations of the subject and learning cutting-edge numerical algorithms that could be applied. Six months of proposal writing also constituted an unintentional crash course, with the mathematicians often interrupting heated debates to ask about vocabulary or to request an explanation of the question at hand suitable for a five-year old. We (DB and ML) first met at those meetings, where we had frequent whispered conversations in which Matt answered many of David's questions about the physics, and David suggested algorithms that could be applied.

When this proposed Hidden Symmetries and Fusion Energy collaboration was funded, the months-long crash course gave way to years of the physicists and mathematicians in the group learning to communicate effectively about plasmas, fusion, optimization, PDEs, and many other topics. That meant not only understanding one another's vocabulary, but also understanding what questions interested who, and why those questions were the interesting ones. The book you are reading was first imagined during the early days of this collaboration, when we were all still learning how to talk to one another. Early drafts were an invaluable resource, both for ourselves and for bringing our colleagues up to speed. The authors are experienced in both applied mathematics and plasma physics and have been careful in their writing to appeal to both audiences.

Communication is as essential to successful scientific relationships as to any other relationship, and much of the success of the Simons Hidden Symmetries collaboration has been in the continued communication and cooperation among the mathematicians and physicists involved. We are leading the second phase of the collaboration now as an applied mathematician and a plasma physicist who have learned something about how to talk to each other about stellarators. We are thrilled to have this book, both for ourselves and as a way of teaching our students and colleagues about stellarators and about the many exciting mathematical problems related to their design and optimization.

David Bindel and Matt Landreman

Preface

This book project arose out of the collaboration on Hidden Symmetries and Fusion Energy[1] funded by the Simons Foundation, initially between 2018 and 2022 and then for a renewed period from 2022 to 2025. This collaboration was formed to foster interactions among experts in numerical optimization, dynamical systems, analysis of partial differential equations, and plasma physics in order to find stellarator configurations with hidden symmetries. Given the diverse backgrounds of the participants, establishing a common language was the first challenge to tackle. The original idea was to gather a collection of definitions of fundamental concepts relevant to stellarator design, in a form similar to a dictionary. However, due to the complexity of both the phenomena at play and the various models describing them, the need for a different format quickly became clear. The final result is closer to an introduction to mathematical modeling for stellarator design, and the end goal is twofold: making these topics accessible to a broader audience of scientists, and stimulating new contributions to the field of stellarator research.

In this book, we aim to present the basic theoretical building blocks to understand modeling of stellarator magnetic fields and some of the associated challenges, as well as the main stakes behind optimization for the design of stellarators, in a self-contained manner. As often as possible, the ideas are presented using equations and pictures and complemented with references to other relevant introductory material. The material is accessible to those who may not have a background in physics but are interested in applications of mathematical and computational tools to stellarator research. Readers are simply expected to have basic knowledge of classical physics, electromagnetism, partial differential equations, and calculus of variations, but prior knowledge of plasma physics is not required. We present the relevant models and their derivation when it is not too involved, and we particularly emphasize the assumptions underlying each derivation and each result.

In general, we aim to provide enough detail to cater to readers without any background while using language close enough to the plasma physics literature. In this way we hope that, on the one hand, the book will be accessible to a broad audience of scientists with an interest in stellarator design, including physicists, mathematicians, computer scientists, and engineers, and, on the other hand, it will equip this audience with sufficient knowledge in order to gain access to more advanced literature about recent developments in stellarator design.

More practically, after the introduction, the book is split into two parts. The first part gathers more general material regarding toroidal magnetic confinement, and the second part focuses on stellarators, from modeling aspects to design techniques. Essential material about Maxwell's equations and classical mechanics is gathered, respectively, in Chapters 2 and 3, while Appendices A and B provide a little more background on these topics. Several other chapters present mathematical tools and are placed where they become necessary to continue the reading. Chapters 5 and 9 introduce various types of coordinate systems, while Chapter 6 is dedicated to leveraging periodicity in the study of two fundamental equations.

[1] https://hiddensymmetries.princeton.edu/.

The first part of the book establishes a general introduction to the concept of a stellarator. Starting from Maxwell's equations, Chapter 4 provides the motivation behind the general concept of toroidal confinement. Next, Chapter 7 explains the fundamental difference between two competing types of toroidal magnetic confinement devices, the tokamak and the stellarator. Chapter 8 introduces the coupling between charged particles in a plasma and discusses electromagnetic fields under the form of the ideal MHD model.

The second part builds toward the description of mathematical models and numerical methods specifically dedicated to stellarator design. Chapter 10 highlights challenges inherent to the three-dimensional geometry of a stellarator, while Chapter 11 describes several common mathematical models for the stellarator magnetic field under different simplifying assumptions. Chapter 12 focuses on notions of symmetry and their consequences in terms of particle confinement. Finally, Chapter 13 presents the main concepts at play in stellarator optimization, and Chapter 14 provides an overview of more advanced topics on this subject.

Earlier versions of the material in this book were released over the past few years and have been used as teaching material both in the classroom and in more compact formats in summer schools. Newcomers to the field of stellarators, on either the theoretical side or the experimental side, have also reported their interest in these previous versions. In its final form, the book is suitable for teaching a class on stellarator design. The two parts can be considered separately from each other as well. For instance, a general introduction to concepts of magnetic confinement in toroidal geometry, with an emphasis on what distinguishes the tokamak and stellarator concepts, can be based on the first part, while a more advanced overview of optimization models and methods for stellarator design can be based on the second part.

Supplementary information about the figures in this book is available at this link: `https://bookstore.siam.org/ot202/bonus`.

Acknowledgments

This work was supported by the Simons Foundation (grant #560651, LMIG, AB, CH) and also by the Center for Scientific Computing and Mathematical Modeling from the University of Maryland.

The authors would like to thank particularly Stuart Hudson for his continuous support and encouragement over the years as the book project progressed and evolved. They would also like to thank the following colleagues for their valuable comments on the book: Craig Beidler, Daniel Bouche, Antoine Cerfon, Charles Dapogny, Bruno Després, William D'haeseleer, Nate Ferraro, Silke Glas, Jonathan Goodman, Per Helander, Sophia Henneberg, Rogerio Jorge, Matt Landreman, Joaquim Loizu, Nick McGreivy, Allan Reiman, Tonatiuh Sánchez Vizuet, Wrick Sengupta, Chris Smiet, Georg Stadler, Harold Weitzner, Yao Zhou, and Caoxiang Zhu.

Chapter 1
Introduction

Securing clean, safe, and abundant energy is a pressing global challenge. In order to avoid further climate change, humanity must adopt carbon-free energy sources on a large scale. While such sources exist, such as wind, solar, and nuclear fission energy, they also introduce additional complications: wind and solar energy are not widely dispatchable and are intermittent, while fission produces long-lived nuclear waste. As an alternative, harnessing fusion reactions holds promise for a clean, safe, and abundant energy source. Under the conditions necessary to achieve sustained fusion reactions, matter exists in a plasma state and can be confined by magnetic fields. While laboratory fusion has been possible since the 1930s, the challenge remains to reach the conditions for a self-sustaining reaction and harness the resulting energy.

Together, theoretical and experimental research in fusion energy has enabled significant progress toward achieving net energy production. There remain open questions for the design of the next generation of fusion devices. This book establishes the theoretical building blocks foundational to the design of a particular magnetic configuration, the stellarator.

This chapter briefly defines and discusses central ideas in plasma physics and magnetic confinement.

1.1 ▪ Plasma

Plasma is a state of matter. It is often called the fourth state of matter, in addition to solid, liquid, and gas. The characteristic behavior of each state of matter and the transition from solid to liquid, to gas, and finally to plasma, are determined by the kinetic energy of the molecules or atoms comprising the state.

Plasmas of relevance for magnetic confinement fusion are characterized by two defining features: partial or full ionization and collective behavior dominated by long-range electromagnetic forces.

- Ionization is the process of stripping electrons from atoms, resulting in some free electrons.[2] In a fully ionized gas, all of the electrons are stripped off all the atoms, and the resulting nuclei and electrons move independently rather than being bound together as atoms. In the plasma physics literature these nuclei are referred to as ions. This process

[2]Ionization can occur due to the collision of an atom with an electron or the absorption of a photon with sufficient energy, causing an electron to be removed from the atom. The inverse processes can also occur, as an atom and two electrons collide to form an atom and one electron, or an electron and ion can combine, releasing a photon. In equilibrium, these processes balance each other to determine the degree of ionization. A further discussion on ionization can be found in [91].

requires sufficiently large energy, quantified by the temperature, to overcome the Coulomb barrier, with the temperature being proportional to the averaged kinetic energy. If a gas is partially ionized, not all of the electrons are stripped off some of the atoms. The fraction of ionized atoms with respect to the total atom population depends on the temperature and density of the gas. At room temperature, the ionization fraction of a typical gas is negligibly small. In such a state, collisions with neutral particles are dominant. As the temperature increases, the ionization fraction can become large enough for collisions with neutral particles to be neglected. While neutrals may be present in some plasmas, plasmas of relevance for magnetic confinement fusion are characterized by a substantial ionized fraction. Since an ionized gas contains charged particles, a plasma interacts with electromagnetic fields.

- While collisions exist in both neutral gasses and plasmas, the collective behavior of neutral gas particles is determined solely by collisions. In a simple approximation, collisions for neutral particles are analogous to the exchange of energy and momentum experienced by billiard balls as they hit one another. This is considered a short-range interaction because the dynamics depend only on the properties of the colliding particles and not on those of other particles in the system. Since a charged particle produces a short-range electric field in its vicinity, this field only impacts the dynamics of nearby charged particles. A collision between charged particles refers to this short-range interaction governed by the fields. Charged particles are not in physical contact as they collide, unlike billiard ball collisions. In addition, charged particles also interact with macroscopic electromagnetic fields. Within the class of ionized gasses, weakly coupled plasmas are characterized by the dominance of collective, long-range interactions over collisions. In some plasmas, known as strongly coupled plasmas, short-range interactions become significant compared to long-range interactions. Since the collision frequency increases with the particle number density, an ionized gas must be sufficiently diffuse to be considered a weakly coupled plasma.

Plasmas are dielectric, in that they tend to shield out electrostatic potentials. The Debye length, λ_D, is the characteristic length scale over which other mobile charges damp the electric field produced by a charge. In a plasma with species indexed by s the Debye length is defined by

$$\lambda_D = \left(\sum_s \frac{n_s q_s^2}{\epsilon_0 T_s} \right)^{-1/2}, \tag{1.1}$$

where n_s is the number density, q_s is the charge, T_s is the temperature, and ϵ_0 is the vacuum permittivity. See, for example, Chapter 1 in [44]. In a plasma, the Debye length is typically much smaller than other length scales of the system, such as the major or minor radius of the torus. Many plasmas are quasineutral, meaning that the plasma appears neutral on length scales larger than the Debye length. On length scales smaller than λ_D, there may be a local nonneutrality, while on longer length scales, the plasma is neutral. Quasineutrality is characterized by

$$\sum_s n_s q_s = 0. \tag{1.2}$$

The plasmas of interest in this book are quasineutral.

Plasmas are ubiquitous in space and astrophysical environments. For example, the ionosphere, an upper layer in Earth's atmosphere, is partially ionized, and this plasma plays a critical role in shielding the planet from potentially harmful radiation from the sun. More generally, plasmas surround other astronomical bodies, such as other planets and pulsars. On the other hand,

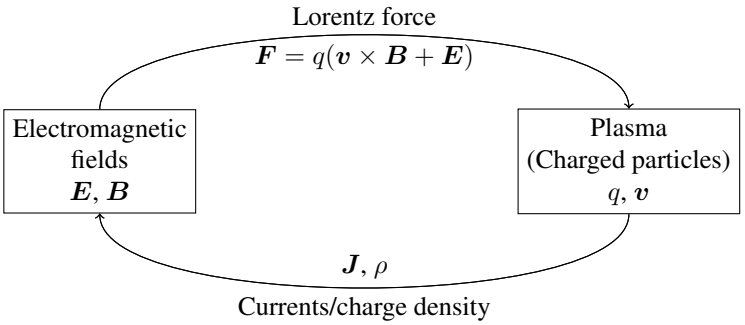

Figure 1.1*: Diagram of the coupling between fields (left box) and particles (right box). The electric and magnetic fields, $\boldsymbol{E}$ and $\boldsymbol{B}$, produce a Lorentz force $\boldsymbol{F}$ acting on particles with charge q and velocity $\boldsymbol{v}$. This, in turn, produces a current $\boldsymbol{J}$ and density ρ acting on the electric and magnetic fields, $\boldsymbol{E}$ and $\boldsymbol{B}$, through Maxwell's equations.*

on Earth, naturally occurring plasmas are not especially common but can be found in lightning and auroras. However, laboratory-created plasmas are widely used in many industrial processing applications [196], such as the deposition of thin layers of metal on surfaces as in solar panels or watches or for processing of materials, including the etching of superconductors. In medicine, plasma is used to treat specific cells [163]. Plasmas are also used in electric spacecraft propulsion [194].

The general setting of plasma modeling is represented in Figure 1.1, illustrating the coupling between electromagnetic fields and charged particle motion. In the presence of electromagnetic fields, charged particles move due to the Lorentz force. In turn, the electromagnetic fields are modified due to the presence and movement of charged particles. Thus, the motion of charged particles in fields is a highly coupled problem. Plasma physics studies the phenomena emerging from this complex system.

1.2 ▪ Fusion reactions and power source

Stars, including the sun, are giant balls of plasma bound by large gravitational forces. Stars are fueled by nuclear fusion reactions, which occur when two atomic nuclei combine to form new atomic nuclei and other products. The energy released by nuclear fusion reactions is due to the strong attractive force that binds nuclei together. The nuclear fusion process leads to a slight decrease in mass, resulting in the release of energy according to Einstein's famous $E = mc^2$ equation, where E is the energy released, m is the mass, and c is the physical constant defining the speed of light. Therefore, during a nuclear fusion reaction, the difference in mass m between the reactants and the products determines the change in energy, E.

The Coulomb force makes charges with equal signs repel and charges with opposite signs attract. For two particles to undergo a fusion reaction, they must be brought close enough, on the scale length of protons and neutrons, for the strong force to act. For particles with equal sign charges, this requires overcoming the repulsive Coulomb force, acting over much larger length scales. There are two basic ingredients for fusion reactions:

- sufficient energy, quantified by the temperature, to overcome the Coulomb barrier between the nuclei;
- sufficient density of nuclei to increase the frequency of collisions and potential fusion reactions.

At such density and temperature, matter is in a plasma state. The nuclei also need to be confined to the same vicinity for a sufficiently long period in order for a substantial number of fusion reactions to take place.

In the sun and other stars, the strong gravitational field confines a high-temperature plasma, yielding fusion reactions that power the star. Due to the large mass required, gravitational fields are impractical for laboratory confinement of plasmas. In order to realize fusion on Earth, other confinement techniques must be employed. The extreme temperatures and pressures required to achieve terrestrial fusion will rapidly damage any material. Therefore, the plasma must be well-separated from material surfaces. Any laboratory confinement device must be able to thermally insulate the hot plasma from the cooler material surfaces. The leading techniques for terrestrial confinement are inertial, involving the compression and heating of small targets using lasers [330], and magnetic, using strong magnetic fields. This book focuses on magnetic confinement, specifically, the stellarator concept.

There are several fusion reactions occurring in the sun, where the core temperature and density are approximately 15 million degrees Celsius and 1.4×10^{18} particles per cubic meter. The most energetically favorable reaction for terrestrial fusion, distinct from the dominant fusion reaction in the sun, is the fusion of deuterium, ${}^2_1\mathrm{D}$, and tritium, ${}^3_1\mathrm{T}$, to produce helium, ${}^4_2\mathrm{He}$, and an energetic neutron, n^0. This reaction, known as the D-T reaction, can be represented as

$$ {}^2_1\mathrm{D} + {}^3_1\mathrm{T} \longrightarrow {}^4_2\mathrm{He}\ (3.5\ \mathrm{MeV})\ + \mathrm{n}^0\ (14.1\ \mathrm{MeV}). \tag{1.3} $$

Under certain simplifying assumptions, the probability of a fusion reaction between a deuterium atom and a tritium atom depends on their energy. This probability peaks at an energy of 100 keV,[3] corresponding to about 1 billion degrees Celsius. A substantial number of D-T reactions occur at 10 keV, about 100 million degrees Celsius or about 10 times the temperature of the sun's core. This temperature has been achieved in several magnetic confinement facilities, where D-T reactions have been observed.

Nuclear fusion is one of the most energetic reactions known in nature. The D-T reaction produces 3.4×10^8 MJ of energy for every kg of fuel, in comparison with the combustion of gasoline producing 40 MJ. Fusion as a power source produces no greenhouse gasses and requires fuel that is either readily available or can be produced through known pathways: deuterium is found abundantly in Earth's oceans, and tritium can be produced with irradiation of lithium[4] by an energetic neutron. There are now schemes proposed to produce tritium as a byproduct of fusion reactions, for instance see Section 5.5 in [75]. Compared with wind and solar, fusion energy could provide a baseload source since it does not suffer from intermittency.

For comparison, nuclear fission and nuclear fusion yield similar energy per kilogram of fuel. However, nuclear fusion has several advantages over nuclear fission. While the D-T fusion reaction produces an energetic neutron, which can cause material structures in the plasma vessel to become radioactive, their half-life is only around 10 years. In contrast, the half-lives of fission byproducts can be over 10^4 years. For this reason, fusion energy eliminates challenges associated with long-lived radioactive waste. Unlike plutonium and uranium, which are the fuels of fission power, the fuels required for fusion power are not readily weaponized. Fission depends on a chain reaction since the byproducts of the fission reaction spawn more fission reactions. This can potentially lead to exponential growth in the energy produced. On the other hand, fusion power is inherently safe since it does not rely on a chain reaction.

In conclusion, harnessing the fusion mechanism as a power source on Earth would yield numerous benefits to society.

[3] The plasma temperature is typically measured in units of energy. If measured in Kelvin, we multiply by Boltzmann's constant $k_B = 1.38 \times 10^{-23}$J/K.

[4] Limited lithium resources may present a challenge to fusion energy.

1.3 ▪ Magnetic confinement for fusion

The interaction of charged particles constituting a plasma with magnetic fields can be exploited to confine plasmas. This is the principle of magnetic confinement. In this context, the geometry of the magnetic field is critical to achieve confinement. The following two notions are fundamental. Magnetic field lines refer to the streamlines of the magnetic field, and flux surfaces or magnetic surfaces refer to surfaces that are tangent to the magnetic field at all points.

The basis for toroidal magnetic confinement devices will be introduced in Chapter 7. The stellarator and the tokamak are toroidal magnetic confinement devices involving an externally imposed magnetic field. The total confining magnetic field in such devices is the sum of a field produced by currents within the plasma and by external currents due to electromagnetic coils. While other classes of devices exist, they will not be described in detail here.

Regardless of the method, the ultimate goal of all fusion power devices is to produce more energy than what is required to initiate the reactions. The D-T fusion reaction (1.3) results in a helium nucleus, or alpha particle, and a neutron. The neutron, being charge-neutral, is not confined by the magnetic fields and can leave the device. On the other hand, the alpha particle may be confined by the magnetic fields and can deposit its energy in the bulk plasma fuel through collisions. Initially, external heating is supplied to achieve the conditions required for the reaction. The ratio of the power produced by fusion reactions to the external power deposited into the plasma defines the quantity Q. The scientific break-even point corresponds to $Q = 1$. When the energy provided by the alpha particles is enough to heat the plasma and maintain the fusion conditions, the reaction becomes self-sustaining. This is referred to as ignition and occurs when $Q \to \infty$.

To reformulate, the goal of fusion energy research is to achieve ignition. Magnetic confinement fusion research has a long history and continues to be an active area of research today. The first laboratory magnetic confinement fusion device, known as a Z-pinch [20], was built in the late 1940s, and many have been built around the world since. As of 2024, the magnetic confinement device that has produced the most fusion energy is the Joint European Torus (JET), a tokamak that set the record in 2021 with 21.7 MJ produced [229]. JET holds the current record for net energy gain on a magnetic confinement device with $Q = 0.6$ [87], set in 1997. Initiated in 1988, the ITER project is one of the largest multinational scientific collaborations and involves 35 countries. The experimental device is currently under construction in France and aims to demonstrate the scientific viability of fusion power by reaching $Q > 10$ [149].

In order to reach ignition, the loss of energy due to deconfinement must be balanced by the energy produced by fusion. Heat naturally leaks from a hot plasma due to thermal conduction. The time scale of energy loss from the plasma is measured by the energy confinement time, τ_E. As mentioned in Section 1.2, sufficient density and temperature are required for the fusion reaction to occur. A simple figure of merit for fusion performance is the triple product, quantifying the distance from ignition. Given the particle density n in m^{-3}, the temperature T in keV, and the energy confinement time τ_E in seconds, the triple product is simply defined by $nT\tau_E$. For a plasma in thermal equilibrium, the condition for ignition is given by a lower bound on the triple product, called the Lawson criterion [190]:

$$nT\tau_E > 3 \times 10^{21}\ \mathrm{m}^{-3}\mathrm{keVs}.$$

While magnetic confinement experiments can reach the conditions necessary for fusion, the Lawson criterion has not been met in any magnetic confinement experiments as of 2024. However, some have come close [311]. The current record is held by the Tokamak Fusion Test Reactor (TFTR) at $7.9 \times 10^{20}\ \mathrm{m}^{-3}\mathrm{keVs}$ [108].

A more complete overview of magnetic confinement for fusion can be found in Chapter 1 in [304] or Chapter 6 in [75].

1.4 ▪ Plasma modeling

Modeling physical processes in a plasma is complex because each particle is coupled to every other particle through the electromagnetic fields, as illustrated in Figure 1.1. While a set of equations describing the motion of all individual particles coupled to Maxwell's equations provides a complete picture of how a coupled system evolves, it is hopeless to solve these equations in practice for any physical system of interest. Simplified approximate models are, therefore, helpful to glean physical understanding and for computational tractability. The choice of approximation depends on the problem at hand or the physical regime of interest, leading to a hierarchy of plasma physics models. Various models exist for magnetic confinement fusion plasmas. These can be organized into three overarching categories:

1. The *particle-based approach* studies the motion of particles in physical space in the presence of electromagnetic fields. The feedback of particles on the electromagnetic fields or collisions between particles can be included or neglected.

   Given electric and magnetic fields, single-particle motion refers to the study of the motion of particles while neglecting its feedback on the fields. Here, a trajectory, or orbit, refers to the particle motion evolving in time. Such approaches can provide a first approximation of the confinement properties of a given strong magnetic field.

2. The *kinetic approach* studies the evolution of the distribution of particles in velocity and position space rather than tracking the motion of individual particles. Particles can interact with each other through collisions and can be coupled to electromagnetic fields. An introduction can be found in Chapters 3–5 in [226] or Chapters 4–5 in [110].

3. The *fluid approach* studies the plasma as one or several fluids representing each species. Each fluid is described by fields in physical space rather than a distribution of all particles in velocity and position space. These fields include, for example, the density, pressure, and fluid flow velocity.

   Fluid models can be derived from kinetic models by averaging with respect to the velocity and closing the system of equations thanks to additional approximations. The resulting description in physical space has a reduced dimensionality compared to the velocity and position in phase space. Details of the derivation can be found in [165, 43].

In this setting, multiple characteristic length scales and time scales are separated by orders of magnitude. Table 1.1 provides a few characteristic length and time scales in magnetic confinement fusion plasmas. The Debye length, defined in (1.1), measures the characteristic decay length of the electrostatic potential of a charged particle. In the presence of a magnetic field, charged particles exhibit helical orbits around magnetic field lines with a characteristic radius called the gyroradius and a characteristic frequency called the gyrofrequency, as will be discussed in Section 4.1. Charged particles collide with one another with a characteristic frequency called the collision frequency [137]. As discussed in Section 1.3, the energy confinement time measures the time scale over which energy is lost from the hot plasma. A toroidal device's minor radius is a length scale characteristic of the overall size of the device.

The separation of scales motivates the development of a hierarchy of models of various complexity, obtained from asymptotic reductions based on the smallness of various physical parameters. As an example, the Debye length (1.1), λ_D, is much smaller than typical length scales for fusion devices, so the plasma can be assumed to be quasineutral.

In this book, scale separation simplifies the single-particle and fluid approaches. Single-particle approaches can be simplified following properties of the magnetic field. In magnetic confinement devices, the strong external magnetic field results in an ion gyrofrequency, Ω_i, that is much larger than other frequencies of interest. Consequently, the particle motion can be averaged

Table 1.1*: This table shows the typical length and time scales for several stellarator experiments: Wendelstein* 7*-AS (W7-AS), the Large Helical Device (LHD), and Wendelstein* 7*-X (W7-X). Due to the large range of scales, it is intractable to study phenomena involving all of these scales simultaneously.*

Name	Parameter	W7-AS [207]	LHD [161]	W7-X [283]
Electron Debye length	$\lambda_{D,e}$ [m]	3×10^{-5}	2×10^{-5}	9×10^{-5}
Ion gyroradius	ρ_i [m]	2×10^{-3}	3×10^{-3}	2×10^{-3}
Device minor radius	a [m]	0.20	0.60	0.50
Ion gyrofrequency	Ω_i [s^{-1}]	9×10^{7}	1×10^{8}	2×10^{8}
Collision frequency*	ν_{ee} [s^{-1}]	1×10^{5}	2×10^{5}	4×10^{3}
Energy confinement time	τ_E [s]	0.5	0.33	0.1

*Collision frequency refers to electron-electron collision frequency.

over the fast gyrofrequency to obtain simpler guiding center models, as will be done in Section 4.2. Fluid approaches can be simplified by leveraging properties of the temperature and density, as well as the magnetic field. A strong external magnetic field results in a small gyroradius compared to other characteristic scales. If the temperature is not too large and the density is sufficiently large, the collision frequency is large compared to other characteristic scales. These scale separations provide a simplified single-fluid model known as ideal magnetohydrodynamics (MHD), that will be introduced in Chapter 8. In practice, the collision frequency does not satisfy this ordering under tokamak and stellarator reactor conditions. Nonetheless, ideal MHD has been empirically demonstrated to be a valuable model for some fusion applications.

There is a wealth of interesting open problems related to the mathematical properties and numerical approximations for magnetic confinement plasma modeling.

1.5 ▪ Stellarator design

The concept of confinement is paramount for fusion devices in general, particularly toroidal devices such as tokamaks and stellarators. When designing a magnetic confinement device, maximizing the energy confinement time is an effective strategy for improving fusion performance by increasing the triple product introduced in Section 1.3. One of the methods to achieve this is by carefully designing the magnetic field.

The cross-section of tokamaks is constant the long way around the torus, a property referred to as axisymmetry, whereas the cross-sections of stellarators can vary significantly. Consequently, tokamak and stellarator concepts have different objectives for the design of the total magnetic field. Due to the symmetry of tokamaks, a substantial magnetic field driven by the plasma current is necessary and sufficient for confinement, as will be discussed in Sections 7.1 and 7.2. As a trade-off, the large plasma current can drive instabilities that can cause confinement loss. On the other hand, stellarators rely mostly on externally driven fields, so the risk of large plasma instabilities is reduced. However, as a trade-off, confinement is no longer guaranteed due to symmetry-breaking. Nonetheless, the freedom in the choice of the external field is leveraged to improve the confinement in a stellarator. Although the cross-sections of stellarators are not symmetric, stellarators can leverage hidden symmetries of the magnetic field to achieve confinement properties similar to those of tokamaks; such symmetries are the focus of Chapter 12. In switching from symmetric to nonsymmetric devices, an increasing modeling complexity is introduced as the dimensionality of the physical space moves from two to three dimensions.

Even though the first stellarator experiments predated the first tokamak, the tokamak concept soon took precedence in the 1960s, as early stellarators had poor confinement properties.

With the increase in available computing power since the 1980s, modern stellarators have been carefully designed using numerical optimization techniques.

In this book, stellarator design refers to the search for a desired external magnetic field and the magnets producing this field. In order to maximize the confinement time, it is natural to seek a stable equilibrium magnetic field. Stellarator design then requires optimization of the external field and magnets to obtain equilibria with desirable properties, such as enhanced confinement, stability, and hidden symmetries. This book aims to build the theoretical foundations for stellarator design.

1.6 ▪ Outline

This book is organized into two parts. Part I covers theoretical foundations and critical concepts for magnetic confinement. These are applied in Part II to stellarator design and optimization.

Chapters 2 and 3 summarize essential background material, while more details are provided in the appendices. Appendix A presents the set of equations that govern the evolution of electromagnetic fields, namely Maxwell's equations, under various sets of assumptions. Chapter 2 provides a comparison of the corresponding models. Chapter 3 reviews the equations of motion that describe the trajectories of charged particles in given electromagnetic fields. More details on this material are provided in Appendix B, particularly the relation between these equations of motion and the variational principles associated with the Lagrangian and Hamiltonian functionals.

Throughout the rest of the book, increasingly complex models are leveraged to study desirable properties of the fields.

For simplicity, the discussion starts with neglecting the coupling between the plasma and electromagnetic fields. Chapter 4 addresses particle confinement in a steady background magnetic field. This will motivate the desire for magnetic fields lying on nested toroidal surfaces.

Chapter 5 introduces convenient coordinate systems to describe toroidal confinement devices. Chapter 6 presents essential tools to leverage periodicity in the study of some differential equations. In Chapter 7, these ideas are applied to discuss concepts related to magnetic confinement and motivate the stellarator concept.

In Chapter 8, the particles and electromagnetic fields are coupled by modeling the plasma as a single fluid using the ideal MHD equations under simplifying assumptions valid for magnetic confinement fusion. Chapter 9 leverages the assumption of MHD equilibrium to define coordinate systems aligned with the magnetic field. Chapter 10 highlights challenges associated with the ideal MHD model in stellarators, and several approaches for modeling three-dimensional (3D) equilibrium fields are discussed in Chapter 11. These models provide the equations governing the time-independent fields from which the particle trajectories and other physical quantities of interest can be computed.

Chapter 12 introduces several notions of symmetry in stellarator design concepts and their consequences on confinement properties. These symmetries can be approximately realized in a configuration via optimization of the equilibrium magnetic field and magnet shapes using techniques described in Chapter 13. Chapter 14 concludes with an overview of several current research problems in stellarator optimization.

Chapters 5 and 9, respectively on nonorthogonal coordinate systems and magnetic coordinate systems, are provided for a self-contained presentation. They appear only when they become necessary to carry on the main discussion. Readers familiar with these topics can skip the corresponding chapters as they are limited to standard material.

The chapters on 3D equilibrium fields, symmetry, and optimization are the most important as they are fundamental to understanding stellarators. The rest of the book is constructed to enable discussion of these three central topics.

Part I

Electromagnetic fields and particle motion

Chapter 2

Minimal reminder on Maxwell's equations

Maxwell's equations are partial differential equations (PDEs) describing the time and spatial dependence of electric and magnetic fields given the charge and current density, ρ and $\boldsymbol{J}$. Since this theory is central to the study of plasmas, Appendix A briefly summarizes essential concepts. We aim to provide a brief overview of the relevant models for stellarator design, but their justification is beyond the scope of this book. The details of electromagnetic theory can be found in standard texts such as [150]. The fundamental equations are highlighted in Table 2.1.

In Chapter 4, we will discuss the trajectories of particles in static electromagnetic fields without considering the feedback of ρ and $\boldsymbol{J}$ on the fields. In Chapter 8, a more realistic model will include the coupling as follows: the Lorentz force describes how the electric and magnetic fields act on charged particle motion, while Maxwell's equations describe how electric and magnetic fields evolve in the presence of charge density ρ and current $\boldsymbol{J}$.

In the remainder of the book, we will use the SI system of units. Maxwell's equations are sometimes presented in Gaussian units, with corresponding rescaled physical constants. For a comparison between the SI and Gaussian systems, see [137].

Table 2.1: Summary of Maxwell's equations under several hypotheses of interest for stellarator design.

	Maxwell	Electrostatics	Magnetostatics	Vacuum fields
Hyp.		$\partial \boldsymbol{E}/\partial t = 0$ $\partial \boldsymbol{B}/\partial t = 0$	$\partial \boldsymbol{E}/\partial t = 0$ $\partial \boldsymbol{B}/\partial t = 0$	$\partial \boldsymbol{E}/\partial t = 0$ $\partial \boldsymbol{B}/\partial t = 0$ $\boldsymbol{J} = 0$ in Ω_{vac}
PDE model	$\nabla \cdot \boldsymbol{E} = \frac{\rho}{\epsilon_0}$ $\nabla \times \boldsymbol{B} = \mu_0 \boldsymbol{J} + \frac{1}{c^2}\frac{\partial \boldsymbol{E}}{\partial t}$ $\nabla \times \boldsymbol{E} = -\frac{\partial \boldsymbol{B}}{\partial t}$ $\nabla \cdot \boldsymbol{B} = 0$	$\nabla \cdot \boldsymbol{E} = \frac{\rho}{\epsilon_0}$ $\nabla \times \boldsymbol{E} = 0$	$\nabla \times \boldsymbol{B} = \mu_0 \boldsymbol{J}$ $\nabla \cdot \boldsymbol{B} = 0$	$\nabla \times \boldsymbol{B} = 0$ in Ω_{vac} $\nabla \cdot \boldsymbol{B} = 0$ in Ω_{vac}
Model $\Leftrightarrow$		$\boldsymbol{E} = -\nabla \Phi$ $\Delta \Phi = -\frac{\rho}{\epsilon_0}$	$\boldsymbol{B}(\boldsymbol{r}) = \frac{\mu_0}{4\pi} \times$ $\int_{\mathbb{R}^3} \frac{\boldsymbol{J}(\boldsymbol{r}') \times (\boldsymbol{r} - \boldsymbol{r}')}{\lvert \boldsymbol{r} - \boldsymbol{r}' \rvert^3} \, d^3 r'$	$\boldsymbol{B}(\boldsymbol{r}) = \frac{\mu_0}{4\pi} \times$ $\int_{\mathbb{R}^3 \setminus \Omega_{\text{vac}}} \frac{\boldsymbol{J}(\boldsymbol{r}') \times (\boldsymbol{r} - \boldsymbol{r}')}{\lvert \boldsymbol{r} - \boldsymbol{r}' \rvert^3} \, d^3 r'$ $\Leftrightarrow \begin{cases} \boldsymbol{B} = \nabla \Phi_B & \text{in } \Omega_{\text{vac}} \\ \Delta \Phi_B = 0 \end{cases}$
Given	$\boldsymbol{J}, \rho$	ρ	$\boldsymbol{J}$	$\boldsymbol{J}$ outside of Ω_{vac}

Chapter 3

Minimal reminder on classical mechanics for charged particle motion

Classical mechanics provides the equations of motion for bodies, such as charged particles, subject to given forces. Since the motion of charged particles is central to the description of plasmas, Appendix B briefly summarizes essential concepts.

We briefly review concepts from classical mechanics related to three equivalent formulations to study the evolution of a mechanical system. Newton's approach relies on balancing forces acting on a particle and the rate of change of its momentum. In contrast, variational approaches rely on the principle of least action. Instead of focusing on forces, variational methods focus on other physical quantities, such as kinetic and potential energy. They facilitate the identification of conserved quantities associated with symmetries and are well-suited to arbitrary choices of coordinates, while these can be cumbersome for a Newtonian formulation. However, nonconservative forces, such as frictional forces, are more easily represented in the Newtonian approach than in the Lagrangian or Hamiltonian approaches. For further reading on classical mechanics see [157, 293, 90].

The Lagrangian approach will enable us to more efficiently derive the guiding center model under the assumption of large magnetic field strength in Section 4.2, as scalar functions are more straightforward to manipulate than a set of ordinary differential equations (ODEs). The Hamiltonian approach will allow us to describe the concepts of integrability and perturbations away from integrability in Section 10.2. These concepts are also applied to the description of a single charged particle motion in electromagnetic fields, exploited later in Chapter 4, as well as in Chapter 10 to focus on magnetic field lines. In this context, various coordinate systems exploiting the geometry of the magnetic field will be key to expressing several problems compactly. Hence, variational approaches will prove particularly useful.

We now summarize the Newtonian, Lagrangian, Hamiltonian, and phase-space Lagrangian frameworks in Tables 3.1, 3.2, 3.3, and 3.4, respectively. In this context, it is important to note that the trajectories are functions of time t that satisfy the equations of motion, and they will always be denoted with a subscript T to distinguish them from the independent variables of the Lagrangian or Hamiltonian. For example, $\boldsymbol{q}_T$ refers to a trajectory as opposed to the independent variable $\boldsymbol{q}$.

Table 3.1*: Summary of the Newtonian framework for classical mechanics. The equations of motion, unknown quantities, and given quantities are provided along with the form of the force for charged particle motion. Newton's law is an equation for the trajectory of a particle, $\boldsymbol{q}_T$, as a function of time t. Further details are available in Appendix* B.1.

Equations of motion	$m\ddot{\boldsymbol{q}}_T(t) = \boldsymbol{F}\left(\boldsymbol{q}_T(t), \dot{\boldsymbol{q}}_T(t), t\right)$
Unknowns	$\boldsymbol{q}_T$
Given	m, $\boldsymbol{F}$
Charged particle	$\boldsymbol{F}(\boldsymbol{q}, \dot{\boldsymbol{q}}, t) = q\left(\dot{\boldsymbol{q}} \times \boldsymbol{B}(\boldsymbol{q}, t) + \boldsymbol{E}(\boldsymbol{q}, t)\right)$

Table 3.2*: Summary of the Lagrangian framework for classical mechanics. The equations of motion, unknown quantities, and given quantities are provided along with the form of the Lagrangian for charged particle motion. The unknown in the equations of motion is the trajectory of a particle, $\boldsymbol{q}_T$, as a function of time t. Further details are available in Appendix* B.2.

Equations of motion	$\dfrac{d}{dt}\left(\dfrac{\partial L\left(\boldsymbol{q}_T(t), \dot{\boldsymbol{q}}_T(t), t\right)}{\partial \dot{\boldsymbol{q}}}\right) = \dfrac{\partial L(\boldsymbol{q}_T(t), \dot{\boldsymbol{q}}_T(t), t)}{\partial \boldsymbol{q}}$
Unknowns	$\boldsymbol{q}_T$
Given	$L(\boldsymbol{q}, \dot{\boldsymbol{q}}, t)$
Charged particle	$L(\boldsymbol{q}, \dot{\boldsymbol{q}}, t) = \dfrac{m\lvert\dot{\boldsymbol{q}}\rvert^2}{2} + q\left(\boldsymbol{A}(\boldsymbol{q}, t) \cdot \dot{\boldsymbol{q}} - \Phi(\boldsymbol{q}, t)\right)$

Table 3.3*: Summary of the Hamiltonian framework for classical mechanics. The equations of motion, unknown quantities, and given quantities are provided along with the form of the Hamiltonian for charged particle motion. The unknowns in the equations of motion are $\mathbf{q}_T$ and $\mathbf{p}_T$ describing the trajectory of a particle as a function of time t. Further details are available in Appendix* B.3.

Equations of motion	$\dot{\boldsymbol{q}}_T(t) = \dfrac{\partial H(\boldsymbol{q}_T(t), \boldsymbol{p}_T(t), t)}{\partial \boldsymbol{p}}$ $\dot{\boldsymbol{p}}_T(t) = -\dfrac{\partial H(\boldsymbol{q}_T(t), \boldsymbol{p}_T(t), t)}{\partial \boldsymbol{q}}$
Unknowns	$\boldsymbol{q}_T$, $\boldsymbol{p}_T$
Given	$H(\boldsymbol{q}, \boldsymbol{p}, t)$
Charged particle	$H(\boldsymbol{q}, \boldsymbol{p}, t) = \dfrac{m\lvert\boldsymbol{p} - q\boldsymbol{A}\left(\boldsymbol{q}, t\right)\rvert^2}{2} + q\Phi(\boldsymbol{q}, t)$

Table 3.4*: Summary of the phase-space Lagrangian framework for classical mechanics. The equations of motion, unknown quantities, and given quantities are provided along with the form of the phase-space Lagrangian for charged particle motion. The unknowns in the equations of motion are* $\mathbf{q}_T$ *and* $\mathbf{p}_T$ *describing the trajectory of a particle as a function of time* t*. Further details are available in Appendix* B.4*.*

Equations of motion	$\frac{d}{dt}\left(\frac{\partial L_{\text{ph}}\left(\boldsymbol{q}_T(t), \dot{\boldsymbol{q}}_T(t), \boldsymbol{p}_T(t), \dot{\boldsymbol{p}}_T(t), t\right)}{\partial \dot{\boldsymbol{q}}}\right) = \frac{\partial L_{\text{ph}}(\boldsymbol{q}_T(t), \dot{\boldsymbol{q}}_T(t), \boldsymbol{p}_T(t), \dot{\boldsymbol{p}}_T(t), t)}{\partial \boldsymbol{q}}$ $\frac{d}{dt}\left(\frac{\partial L_{\text{ph}}\left(\boldsymbol{q}_T(t), \dot{\boldsymbol{q}}_T(t), \boldsymbol{p}_T(t), \dot{\boldsymbol{p}}_T(t), t\right)}{\partial \dot{\boldsymbol{p}}}\right) = \frac{\partial L_{\text{ph}}(\boldsymbol{q}_T(t), \dot{\boldsymbol{q}}_T(t), \boldsymbol{p}_T(t), \dot{\boldsymbol{p}}_T(t), t)}{\partial \boldsymbol{p}}$
Unknowns	$\boldsymbol{q}_T, \boldsymbol{p}_T$
Given	$L_{\text{ph}}(\boldsymbol{q}_T(t), \dot{\boldsymbol{q}}_T(t), \boldsymbol{p}_T(t), \dot{\boldsymbol{p}}_T(t), t)$
Charged particle	$L(\boldsymbol{q}, \dot{\boldsymbol{q}}, \boldsymbol{p}, \dot{\boldsymbol{p}}, t) = \boldsymbol{p} \cdot \dot{\boldsymbol{q}} - \frac{\lvert \boldsymbol{p} - q\boldsymbol{A}(\boldsymbol{q}, t)\rvert^2}{2m} - q\Phi(\boldsymbol{q}, t)$

Chapter 4

Single-particle motion in static electromagnetic fields

In the context of magnetic confinement fusion, charged particles in the plasma and the electromagnetic fields are intrinsically coupled. However, in typical experimental conditions of interest for stellarator design, a strong external magnetic field is imposed to confine particles. In comparison, the effect of the particles on the electromagnetic fields is sufficiently small to justify neglecting the coupling in a first approximation, in order to gain basic intuition about particle motion. This is the basis for single-particle motion models. These models neglect the coupling between fields and particles and consider instead given stationary electromagnetic fields, while the influence of the particle motion on the fields is not accounted for. In this setting, the Lorentz force produced by the magnetic field acts on the particle. A particle then follows complex orbits defined as solutions of the equations of classical mechanics introduced in Chapter 3, and there is a natural distinction between the motion along magnetic field lines and in the direction perpendicular to the field lines, often referred to as the motion across magnetic field lines.

Section 4.1 considers the equations of motion in a simple setting: a straight, uniform magnetic field. Here solutions can be computed explicitly. The motion perpendicular to the field lines is periodic with a period proportional to the magnetic field magnitude, while the motion along the field direction is not affected by the field strength. If the magnitude and direction of the field are not constant, the equations are not as simple, and so solutions are not known explicitly in general. Yet, since the Lorentz force remains perpendicular to the field, particle dynamics will still exhibit distinct properties in the parallel and perpendicular directions. Moreover, under the assumption of a strong magnetic field, there is a natural separation between the time scale of the motion along field lines in comparison to the fast periodic motion across field lines, called the gyromotion. This powerful concept, central in the field of magnetic confinement fusion, leads to an important tool, namely the notion of gyroaverage, to describe the motion averaged with respect to the perpendicular periodic motion. Section 4.2 discusses the corresponding reduction of the Lagrangian. Consequences of this model on the description of charged particle trajectories are discussed in Section 4.3. Finally, Section 4.4 introduces the basic ideas of toroidal magnetic fields, referring to magnetic fields lying in a toroidal domain, and their advantages for confinement.

Beyond single-particle motion, the coupling between fields and particles will be introduced in Chapter 8 in a fundamental model for the steady-state plasma and fields. This model is central to optimization techniques for stellarator design.

4.1 ▪ Motion in a uniform magnetic field

The concept of magnetic confinement can be illustrated by studying the trajectory of a particle in a strong, uniform magnetic field, in the absence of an electric field. We will use the orthonormal coordinate system $(\hat{\boldsymbol{e}}_1, \hat{\boldsymbol{e}}_2, \hat{\boldsymbol{e}}_3)$ such that $\hat{\boldsymbol{e}}_1 \times \hat{\boldsymbol{e}}_2 = \hat{\boldsymbol{e}}_3$ and assume that the first vector is aligned with the magnetic field, so that $\boldsymbol{B} = B\hat{\boldsymbol{e}}_1$.

We consider the motion of a particle of mass m and charge q, denoting by $\boldsymbol{q}$ its position. The Lorentz force (B.2) on the particle is given by $\boldsymbol{F}(\boldsymbol{q}, \dot{\boldsymbol{q}}, t) = qB\,(\dot{\boldsymbol{q}} \times \hat{\boldsymbol{e}}_1)$. According to (B.1), the resulting particle trajectory, $\boldsymbol{q}_T : \mathbb{R} \to \mathbb{R}^3$ parameterized by t, obeys equations of motion, expressed here as a first order system of two equations rather than a single second order equation

$$\begin{cases} \dfrac{d\boldsymbol{q}_T(t)}{dt} = \boldsymbol{v}_T(t), \\ m\dfrac{d\boldsymbol{v}_T(t)}{dt} = qB\,(\boldsymbol{v}_T(t) \times \hat{\boldsymbol{e}}_1), \end{cases} \tag{4.1}$$

where the first-order derivative of $\boldsymbol{q}_T$ is the velocity and the first-order derivative of $\boldsymbol{v}_T$ is the acceleration. If the initial velocity is expressed as $\boldsymbol{v}_{\text{init}} = v_\parallel \hat{\boldsymbol{e}}_1 + v_\perp\,(\cos(\varphi_{\text{init}})\hat{\boldsymbol{e}}_2 - \sin(\varphi_{\text{init}})\hat{\boldsymbol{e}}_3)$, the trajectory is given by

$$\boldsymbol{v}_T(t) = v_\parallel \hat{\boldsymbol{e}}_1 + v_\perp\left(\cos\left(\Omega t + \varphi_{\text{init}}\right)\hat{\boldsymbol{e}}_2 - \sin\left(\Omega t + \varphi_{\text{init}}\right)\hat{\boldsymbol{e}}_3\right),$$

where $\Omega := qB/m$ defines the gyrofrequency. Hence the trajectory will spiral about the magnetic field in a helical orbit. For an initial position $\boldsymbol{q}_{\text{init}} = (x_{\text{init}}, y_{\text{init}}, z_{\text{init}})$, the particle position is given by

$$\begin{aligned} \boldsymbol{q}_T(t) = (x_{\text{init}} + v_\parallel t)\hat{\boldsymbol{e}}_1 &+ \left(y_{\text{init}} - \frac{v_\perp}{\Omega}\sin(\varphi_{\text{init}}) + \frac{v_\perp}{\Omega}\sin\left(\Omega t + \varphi_{\text{init}}\right)\right)\hat{\boldsymbol{e}}_2 \\ &+ \left(z_{\text{init}} - \frac{v_\perp}{\Omega}\cos(\varphi_{\text{init}}) + \frac{v_\perp}{\Omega}\cos\left(\Omega t + \varphi_{\text{init}}\right)\right)\hat{\boldsymbol{e}}_3. \end{aligned} \tag{4.2}$$

Hence the motion in the direction of the magnetic field is constant, while the perpendicular motion is periodic with a frequency given by Ω. The sign of Ω is the sign of the particle's charge, q. Hence positive ions of mass m_i and charge q_i will rotate clockwise in the $\hat{\boldsymbol{e}}_2$-$\hat{\boldsymbol{e}}_3$ plane, at the frequency $\Omega_i = q_i B/m_i$, while electrons of mass m_e will rotate counterclockwise, at the frequency $\Omega_e = -eB/m_e$. Moreover, because Ω is inversely proportional to the mass, electrons rotate much more quickly than ions, with $\Omega_e = -\left(m_i e/(m_e q_i)\right)\Omega_i$, where the mass ratio scales as $m_i/m_e \approx 10^3$ and the charge ratio scales as $e/q_i \approx 1$.

When considering time scales $t \gg \Omega^{-1}$ for either species, it is useful to separate the motion in the direction of the magnetic field, also described as along field lines, from the periodic motion in the plane perpendicular to the magnetic field, called the gyromotion. Starting from the expression for the position (4.2), we will separate out the periodic and nonperiodic components to study this gyromotion. We denote by $\boldsymbol{\rho}_T$ the component of the particle position that is periodic in time, known as the gyroposition, and given by

$$\boldsymbol{\rho}_T(t) = \frac{v_\perp}{\Omega}\left(\cos(\Omega t + \varphi_{\text{init}})\hat{\boldsymbol{e}}_3 + \sin(\Omega t + \varphi_{\text{init}})\hat{\boldsymbol{e}}_2\right). \tag{4.3}$$

The nonperiodic term is then $(\boldsymbol{R}_G)_T(t) = \boldsymbol{q}_T(t) - \boldsymbol{\rho}_T(t)$:

$$(\boldsymbol{R}_G)_T = \left(x_{\text{init}} + v_\parallel t\right)\hat{\boldsymbol{e}}_1 + \left(y_{\text{init}} - \frac{v_\perp}{\Omega}\sin(\varphi_{\text{init}})\right)\hat{\boldsymbol{e}}_2 + \left(z_{\text{init}} - \frac{v_\perp}{\Omega}\cos(\varphi_{\text{init}})\right)\hat{\boldsymbol{e}}_3. \tag{4.4}$$

The quantity $|\boldsymbol{\rho}|$ is often referred to as the gyroradius. The component $\boldsymbol{\rho}$ is represented in Figure 4.1. The quantity $\boldsymbol{R}_G$ is referred to as the guiding center position as it is the center about

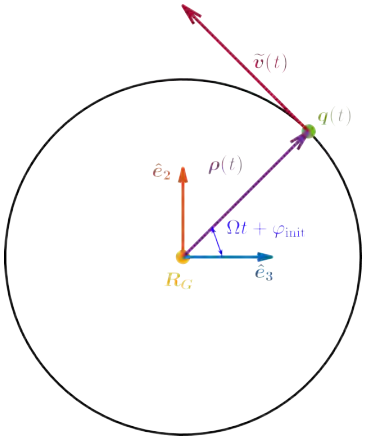

Figure 4.1*: The motion in the plane perpendicular to the magnetic field is described by the orthonormal* $\hat{\boldsymbol{e}}_2$*-*$\hat{\boldsymbol{e}}_3$ *basis. The direction of the magnetic field,* $\hat{\boldsymbol{e}}_1$*, points into the page. The perpendicular component* $\widetilde{\boldsymbol{v}} = \boldsymbol{v} - (\boldsymbol{v}\cdot\hat{\boldsymbol{e}}_1)\hat{\boldsymbol{e}}_1$ *describes the periodic velocity in the perpendicular plane. The particle position is decomposed into periodic and nonperiodic pieces as* $\boldsymbol{q} = \boldsymbol{R}_G + \boldsymbol{\rho}$*, where* $\boldsymbol{\rho}$ *is the gyroposition and* $\boldsymbol{R}_G$ *is the guiding center position.*

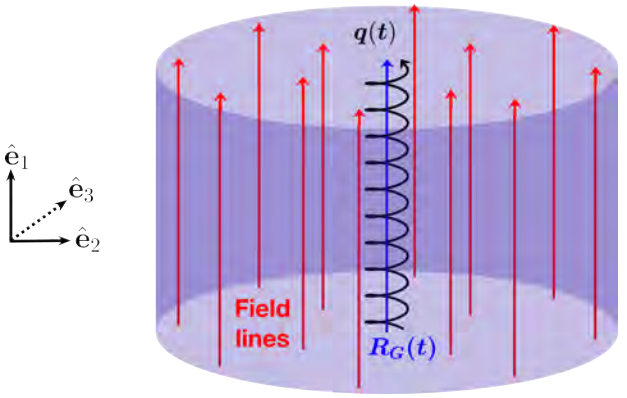

Figure 4.2*: In a straight, uniform magnetic field, charged particles exhibit fast helical motion about field lines (red). Each charged particle is confined in the direction perpendicular to the magnetic field but is free to move in the direction parallel to the magnetic field. The guiding center trajectory (blue) describes the averaged particle's motion along field lines, while the gyromotion (black) describes the position.*

which the particle is said to gyrate. In this setting, the guiding center moves purely along the field line lying at the center of the helical motion, as illustrated in Figure 4.2.

In summary, in a straight, uniform field, the distance between the particle and its guiding center is constant, while the motion of the guiding center is purely along a field line. In this way, the particle is confined in the direction perpendicular to the magnetic field, but its motion is not constrained in the direction parallel to the magnetic field. From a practical point of view, we can only produce an approximately straight uniform magnetic field, for instance with a solenoid. A solenoid is a cylindrical coil with several turns that generates a set of approximately straight field lines in a given volume of space, as illustrated in Figure 4.3. In such a device, a particle would stay away from the solenoid coils but could escape out the ends. An additional confining

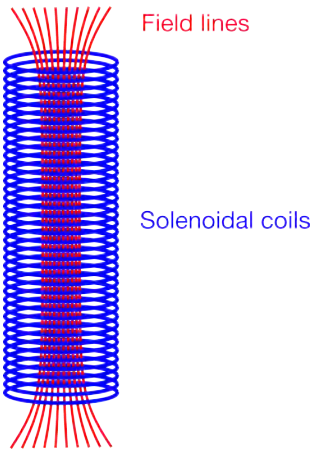

Figure 4.3*: A solenoid is used to produce an approximately straight, uniform magnetic field.*

mechanism is needed to avoid losses of particles along the field lines. Two confinement concepts have been developed to this avail: the mirror force, discussed in Section 4.3, and toroidal confinement, discussed in Section 4.4.

As $|\boldsymbol{\rho}| = v_\perp/\Omega$ is typically much smaller than most length scales of interest for the discussions of magnetic confinement devices in this book, which are discussed in Section 1.4, the particle motion is described by the guiding center motion to a good approximation. In Section 4.2 we will use this assumption to explore the trajectories of particles in the presence of more general electromagnetic fields.

4.2 ▪ Gyroaveraged Lagrangian

In this section we consider in the 3D case, $N = 3$, the motion of charged particles of mass m and charge q in general—not necessarily straight and uniform—static electric and magnetic fields within the Lagrangian framework. As in the case of a straight uniform magnetic field, there is a natural separation of time scales between the rapid gyration in the perpendicular plane and the slower motion of the guiding center under the assumption that the magnetic field is strong. By applying knowledge of the length and time scales involved, a simplified Lagrangian for the guiding center motion, (4.21), can be derived as follows.

1. Starting from the phase-space Lagrangian for single-particle motion in static electric and magnetic fields, (4.5), a coordinate transform is performed from the phase-space coordinates $(\boldsymbol{q}, \dot{\boldsymbol{q}}, \boldsymbol{p}, \dot{\boldsymbol{p}})$ to velocity-based coordinates $(\boldsymbol{q}, \dot{\boldsymbol{q}}, \boldsymbol{v}, \dot{\boldsymbol{v}})$, (4.6).

2. Under suitable assumptions, a small parameter, ϵ, is defined as the ratio of the gyroradius to the typical length scales of the system (4.9).

3. An additional coordinate transformation is defined, (4.10)–(4.11), from the particle position, $\boldsymbol{q}$, to the guiding center position, $\boldsymbol{R}_G$, and the gyroposition, $\boldsymbol{\rho}$. The particle velocity $\boldsymbol{v}$ is also transformed, (4.13), to the guiding center parallel velocity $v_\parallel$ in addition to the rotation velocity of the gyroposition.

4. A new Lagrangian is obtained by retaining only the terms in the Lagrangian of the leading-order $\mathcal{O}(\epsilon^0)$ and performing an average over the fast gyromotion using the operation defined in (4.15).

Further discussion of the gyroaveraged Lagrangian can be found in [197], Chapter 6 of [120], and [288].

4.2.1 ▪ Phase-space Lagrangian in velocity coordinates

While other sources work within the Newtonian framework and average the Lorentz force in order to obtain the guiding center motion, working within the Lagrangian framework is beneficial as it provides additional insight into the conserved quantities of the system. In particular, we use the phase-space Lagrangian framework because it allows for more freedom in the coordinate transformation. We will first express the phase-space Lagrangian in velocity variables rather than momentum variables in order to more effectively apply the previous assumptions on the guiding center motion. We will use the general phase-space Lagrangian for charged particle motion (B.26) (see Appendix B.4.2), additionally assuming static fields, namely

$$L_{\text{ph}}(\boldsymbol{q}, \dot{\boldsymbol{q}}, \boldsymbol{p}, \dot{\boldsymbol{p}}) = \boldsymbol{p} \cdot \dot{\boldsymbol{q}} - \frac{|\boldsymbol{p} - q\boldsymbol{A}(\boldsymbol{q})|^2}{2m} - q\Phi(\boldsymbol{q}). \tag{4.5}$$

To leverage the assumption of fast gyromotion, it is convenient to use coordinates that depend only on the characteristic length and time scales. Since this is not a feature of the canonical momentum, we will transform to a coordinate system based on the velocity rather than the canonical momentum. In phase-space coordinates, $(\boldsymbol{q}, \dot{\boldsymbol{q}}, \boldsymbol{p}, \dot{\boldsymbol{p}})$, the coordinate $\dot{\boldsymbol{q}}$ is the velocity. We define the quantity $\boldsymbol{v}$ by

$$\boldsymbol{v}(\boldsymbol{q}, \dot{\boldsymbol{q}}, \boldsymbol{p}, \dot{\boldsymbol{p}}) = \frac{\boldsymbol{p} - q\boldsymbol{A}(\boldsymbol{q})}{m}.$$

As a consequence, using the canonical momentum introduced in (B.15) (see Appendix B.3.3) and evaluated along any trajectory $(\boldsymbol{q}_T, \boldsymbol{p}_T) : \mathbb{R} \to \mathbb{R}^6$, namely

$$\boldsymbol{p}_T(t) = m\dot{\boldsymbol{q}}_T(t) + q\boldsymbol{A}(\boldsymbol{q}_T(t)),$$

we then have $\dot{\boldsymbol{q}}_T(t) = \boldsymbol{v}(\boldsymbol{q}_T(t), \dot{\boldsymbol{q}}_T(t), \boldsymbol{p}_T(t), \dot{\boldsymbol{p}}_T(t))$. Hence this quantity $\boldsymbol{v}$ indeed defines the velocity along a trajectory. Rather than defining $\boldsymbol{v} = \dot{\boldsymbol{q}}$, the previous definition is convenient for obtaining a formula for $\dot{\boldsymbol{v}}$ as a function of $(\boldsymbol{q}, \dot{\boldsymbol{q}}, \boldsymbol{p}, \dot{\boldsymbol{p}})$. We therefore propose a coordinate transformation [197] from the phase-space coordinates $(\boldsymbol{q}, \dot{\boldsymbol{q}}, \boldsymbol{p}, \dot{\boldsymbol{p}})$ to $(\boldsymbol{q}, \dot{\boldsymbol{q}}, \boldsymbol{v}, \dot{\boldsymbol{v}})$ defined by

$$\begin{cases} \boldsymbol{q}(\boldsymbol{q}, \dot{\boldsymbol{q}}, \boldsymbol{p}, \dot{\boldsymbol{p}}) = \boldsymbol{q}, \\ \dot{\boldsymbol{q}}(\boldsymbol{q}, \dot{\boldsymbol{q}}, \boldsymbol{p}, \dot{\boldsymbol{p}}) = \dot{\boldsymbol{q}}, \\ \boldsymbol{v}(\boldsymbol{q}, \dot{\boldsymbol{q}}, \boldsymbol{p}, \dot{\boldsymbol{p}}) = \dfrac{\boldsymbol{p} - q\boldsymbol{A}(\boldsymbol{q})}{m}, \\ \dot{\boldsymbol{v}}(\boldsymbol{q}, \dot{\boldsymbol{q}}, \boldsymbol{p}, \dot{\boldsymbol{p}}) = \dfrac{\dot{\boldsymbol{p}} - q\left(\dot{\boldsymbol{q}} \cdot \nabla\right)\boldsymbol{A}(\boldsymbol{q})}{m}. \end{cases} \tag{4.6}$$

Here, ∇ indicates derivatives with respect to $\boldsymbol{q}$. The Jacobian of the transformation is $1/m^2$, so this coordinate system is always defined. We denote by $\overline{L}_{\text{ph}}$ the phase-space Lagrangian in this modified coordinate system, namely

$$\overline{L}_{\text{ph}}(\boldsymbol{q}, \dot{\boldsymbol{q}}, \boldsymbol{v}, \dot{\boldsymbol{v}}) = (m\boldsymbol{v} + q\boldsymbol{A}(\boldsymbol{q})) \cdot \dot{\boldsymbol{q}} - \frac{m|\boldsymbol{v}|^2}{2} - q\Phi(\boldsymbol{q}). \tag{4.7}$$

Note that even though $\dot{\boldsymbol{q}}$ and $\boldsymbol{v}$ are equal along trajectories, in the new coordinate system they are treated as independent variables.

4.2.2 ▪ Guiding center assumptions

In this context, we will apply several scaling assumptions in order to further reduce the Lagrangian, following intuition of the characteristic features of trajectories in a uniform magnetic field. We define various length and time scales that characterize slow and fast motion, whose ratio defines a characteristic ordering parameter ϵ. For the fast gyration, Ω^{-1}, with the gyrofrequency $\Omega = qB/m$,[5] is the characteristic time scale; $v_\perp$ is the characteristic velocity, referring to the magnitude of the projection of $\boldsymbol{v}$ onto the plane perpendicular to the magnetic field; and $\rho = v_\perp/\Omega$ is the characteristic length scale of the fast gyration. For the comparatively slow guiding center motion, $v_t = \sqrt{2T/m}$ is the characteristic velocity of thermal particles with temperature T; L_B is the characteristic length scale of the system, defined as the gradient-scale length through $L_B^{-1} \sim |\nabla B|/B$; and $\omega_B \sim v_t/L_B$ is the characteristic frequency of thermal motion parallel to the field lines. Next, all physical quantities can be compared in magnitude to L_B and ω_B.

The following assumptions, based on orders of magnitude presented in Table 1.1, will be leveraged to considerably simplify the modified Lagrangian (4.7).

- The gyroradius is small compared with typical length scales of the system, implying
$$\rho/L_B \ll 1.$$
- The gyrofrequency is much larger than other frequencies of the system, implying[6]
$$\omega_B \ll \Omega_i \ll \Omega_e. \tag{4.8}$$

Based on these assumptions, we will perform an asymptotic expansion with respect to the small parameter
$$\epsilon \sim \frac{\rho}{L_B} \sim \frac{\omega_B}{\Omega} \ll 1. \tag{4.9}$$
For the sake of simplicity, it is assumed that the two small parameters ρ/L_B and ω_B/Ω are comparable to each other.

Under these assumptions, we expect the motion to be the sum of a fast gyromotion and a comparatively slow guiding center motion. This is the motivation for the coordinate transformation in Section 4.2.3. We furthermore assume the following.

- The electrostatic energy, $q\Phi$, is not too large compared to the thermal energy, T,[7]
$$\frac{q\Phi}{T} \sim 1.$$
- The velocity is approximately isotropic in the directions parallel and perpendicular to the magnetic field, with the velocity magnitude $v = \sqrt{v_\perp^2 + v_\parallel^2}$ satisfying
$$v \sim v_\parallel \sim v_\perp.$$
- The velocity scales as the thermal velocity,
$$v \sim v_t.$$

These assumptions will form the basis for comparing the relative magnitude of each term in the Lagrangian.

[5] Here Ω will be used without any subscript to refer to either the electron or ion gyrofrequency, depending on the values of q and m, as the assumed scaling (4.8) holds for both species.

[6] As a reminder, the ion and electron gyrofrequencies are related by $\Omega_e = -(m_i e/(m_e q_i))\,\Omega_i$, so $\Omega_i \ll \Omega_e$: ions rotate considerably more slowly than electrons.

[7] This implies that the guiding center motion across field lines is small with respect to the thermal velocity, v_t.

4.2.3 ▪ Guiding center coordinates

In Section 4.1, where a uniform magnetic field was assumed, the guiding center motion along field lines and the gyromotion in the perpendicular plane were conveniently described by appropriate coordinates. We now extend this approach to a nonuniform magnetic field by introducing a coordinate transformation that allows us to separate the guiding center motion and the gyromotion. We anticipate that the leading-order guiding center motion with respect to the small parameter ϵ will be described by the same equations of motion as those for a straight uniform magnetic field.

We consider particle motion in a field $\boldsymbol{B}(\boldsymbol{q}) = B(\boldsymbol{q})\hat{\boldsymbol{e}}_1(\boldsymbol{q})$ that is no longer assumed to be straight and uniform. Here $\hat{\boldsymbol{e}}_1(\boldsymbol{q}) = \hat{\boldsymbol{b}}(\boldsymbol{q})$ is a local unit vector in the direction of the magnetic field at $\boldsymbol{q}$. The unit vectors $\hat{\boldsymbol{e}}_2(\boldsymbol{q})$ and $\hat{\boldsymbol{e}}_3(\boldsymbol{q})$ form a basis of the plane perpendicular to $\boldsymbol{B}(\boldsymbol{q})$. At each point in $\boldsymbol{q} \in \mathbb{R}^3$, $(\hat{\boldsymbol{e}}_1, \hat{\boldsymbol{e}}_2, \hat{\boldsymbol{e}}_3)$ forms a local orthonormal basis, independent of the motion. However, unlike in Section 4.1, this basis depends on space as the magnetic field is not uniform. The unit vectors $\hat{\boldsymbol{e}}_2$ and $\hat{\boldsymbol{e}}_3$ span the plane perpendicular to the magnetic field. There could be several ways of defining such unit vectors. For example, in a curved magnetic field, $\hat{\boldsymbol{e}}_2$ could be chosen to coincide with the unit vector in the direction of the magnetic field curvature, $\boldsymbol{\kappa} = \left(\hat{\boldsymbol{b}} \cdot \nabla\right)\hat{\boldsymbol{b}}$, such that $\hat{\boldsymbol{e}}_2 = \boldsymbol{\kappa}/\left|\boldsymbol{\kappa}\right|$, and $\hat{\boldsymbol{e}}_3 = \hat{\boldsymbol{e}}_1 \times \hat{\boldsymbol{e}}_2$.

We then define a coordinate transformation from $(\boldsymbol{q}, \dot{\boldsymbol{q}}, \boldsymbol{v}, \dot{\boldsymbol{v}})$ to $(\boldsymbol{R}_G, \dot{\boldsymbol{R}}_G, \rho, \dot{\rho}, \varphi, \dot{\varphi}, v_\parallel, \dot{v}_\parallel)$, where $\boldsymbol{R}_G$ is the guiding center position, ρ is the gyroradius, $v_\parallel$ is the parallel velocity, and φ is the gyroangle. Initially, we have the vector position $\boldsymbol{r}$ and vector velocity $\boldsymbol{v}$ with their time derivatives, and we end up with a vector position $\boldsymbol{R}_G$ and three scalars related to the velocity $(\rho, \varphi, v_\parallel)$ along with their time derivatives. As we will see in Section 4.3.1, $v_\parallel$ will correspond with the parallel guiding center velocity along a trajectory. There are other possible choices of guiding center coordinates [109].

Motivated by the analysis in Section 4.1, we decompose the position vector, $\boldsymbol{q}$, into

$$\boldsymbol{q}(\boldsymbol{R}_G, \rho, \varphi) = \boldsymbol{R}_G + \boldsymbol{\rho}(\rho, \varphi, \boldsymbol{R}_G) \tag{4.10}$$

with

$$\boldsymbol{\rho}(\rho, \varphi, \boldsymbol{R}_G) = \rho\left(\sin(\varphi)\hat{\boldsymbol{e}}_2(\boldsymbol{R}_G) + \cos(\varphi)\hat{\boldsymbol{e}}_3(\boldsymbol{R}_G)\right). \tag{4.11}$$

Here, the gyroposition vector $\boldsymbol{\rho}$ accounts for the periodic gyromotion in the perpendicular plane. The scale of the gyromotion is assumed to be much smaller than the scale of the guiding center motion, $\rho/|\boldsymbol{R}_G| \ll 1$. Furthermore, the unit vectors are defined with respect to the magnetic field evaluated at the guiding center position. Similarly, the coordinate transformation for $\dot{\boldsymbol{q}}$ is decomposed into

$$\dot{\boldsymbol{q}}(\boldsymbol{R}_G, \dot{\boldsymbol{R}}_G, \rho, \dot{\rho}, \varphi, \dot{\varphi}) = \dot{\boldsymbol{R}}_G + \dot{\boldsymbol{\rho}}(\boldsymbol{R}_G, \dot{\boldsymbol{R}}_G, \rho, \dot{\rho}, \varphi, \dot{\varphi}),$$

where

$$\begin{aligned}\dot{\boldsymbol{\rho}}(\boldsymbol{R}_G, \dot{\boldsymbol{R}}_G, \rho, \dot{\rho}, \varphi, \dot{\varphi}) = {}& \dot{\rho}\left(\sin(\varphi)\hat{\boldsymbol{e}}_2(\boldsymbol{R}_G) + \cos(\varphi)\hat{\boldsymbol{e}}_3(\boldsymbol{R}_G)\right) \\ &+ \rho\dot{\varphi}\left(\cos(\varphi)\hat{\boldsymbol{e}}_2(\boldsymbol{R}_G) - \sin(\varphi)\hat{\boldsymbol{e}}_3(\boldsymbol{R}_G)\right) \\ &+ \rho\left(\sin(\varphi)\left(\dot{\boldsymbol{R}}_G \cdot \nabla\right)\hat{\boldsymbol{e}}_2(\boldsymbol{R}_G) + \cos(\varphi)\left(\dot{\boldsymbol{R}}_G \cdot \nabla\right)\hat{\boldsymbol{e}}_3(\boldsymbol{R}_G)\right).\end{aligned}$$

The above can be written in the compact form, namely

$$\begin{aligned}\dot{\boldsymbol{\rho}}(\boldsymbol{R}_G, \dot{\boldsymbol{R}}_G, \rho, \dot{\rho}, \varphi, \dot{\varphi}) = {}& \frac{\dot{\rho}}{\rho}\boldsymbol{\rho}(\boldsymbol{R}_G, \rho, \varphi) + \dot{\varphi}\left(\boldsymbol{\rho}(\boldsymbol{R}_G, \rho, \varphi) \times \hat{\boldsymbol{b}}(\boldsymbol{R}_G)\right) \\ &+ \left(\dot{\boldsymbol{R}}_G \cdot \nabla\right)\boldsymbol{\rho}(\boldsymbol{R}_G, \rho, \varphi).\end{aligned} \tag{4.12}$$

Here the operator ∇ denotes the gradient with respect to $\boldsymbol{R}_G$ only, corresponding for the small parameter ϵ to the leading order term of the full gradient. We decompose the velocity vector into

$$\boldsymbol{v}(\boldsymbol{R}_G, \rho, \varphi, \dot{\varphi}, v_\parallel) = v_\parallel \hat{\boldsymbol{b}}(\boldsymbol{R}_G) + \dot{\varphi}\left(\boldsymbol{\rho}(\boldsymbol{R}_G, \rho, \varphi) \times \hat{\boldsymbol{b}}(\boldsymbol{R}_G)\right). \tag{4.13}$$

Here the first term describes the parallel motion along field lines while the second term describes the gyration about field lines. Because $\dot{\boldsymbol{v}}$ does not appear in the Lagrangian, we will not define it here.

We define the Lagrangian $\widetilde{L}$ in the new coordinates by

$$\begin{aligned}\widetilde{L}(\boldsymbol{R}_G, \dot{\boldsymbol{R}}_G, \rho, \dot{\rho}, \varphi, \dot{\varphi}, v_\parallel, \dot{v}_\parallel) \\ = \left[m\boldsymbol{v}(\boldsymbol{R}_G, \rho, \varphi, \dot{\varphi}, v_\parallel) + q\boldsymbol{A}\left(\boldsymbol{q}(\boldsymbol{R}_G, \rho, \varphi)\right)\right] \cdot \dot{\boldsymbol{q}}(\boldsymbol{R}_G, \dot{\boldsymbol{R}}_G, \rho, \dot{\rho}, \varphi, \dot{\varphi}) \\ - \frac{m\left|\boldsymbol{v}(\boldsymbol{R}_G, \rho, \varphi, \dot{\varphi}, v_\parallel)\right|^2}{2} - q\Phi\left(\boldsymbol{q}(\boldsymbol{R}_G, \rho, \varphi)\right).\end{aligned} \tag{4.14}$$

Terms in the Lagrangian involving $\boldsymbol{\rho}$ (4.11) will be periodic in φ, while there is no such periodicity with respect to $\dot{\varphi}$. Next, we will introduce the operation of averaging over this periodic motion.

4.2.4 ▪ Ordering and gyroaveraging the Lagrangian

The previous Lagrangian (4.14) can now be simplified with the following operations:

- retaining only the leading-order terms, under the assumption (4.9), by neglecting all $\mathcal{O}(\epsilon)$ terms in the asymptotic expansion; [8]
- averaging the Lagrangian over the fast gyromotion under the assumption (4.8) by performing the gyroaveraging operation defined as

$$\langle F \rangle_\varphi = \frac{1}{2\pi}\int_0^{2\pi} F(\varphi)\, d\varphi, \tag{4.15}$$

where F is any scalar or vector quantity. The Lagrangian is periodic with respect to φ, as exhibited by its dependence on $\boldsymbol{\rho}$ (4.11). Therefore, the gyroaveraging operation is defined with respect to φ and not $\dot{\varphi}$. Performing the gyroaverage removes the fast variations of phenomena at high frequencies $\omega \sim \dot{\varphi}$ from the system to study phenomena that occur on a slower time scale. Neglecting high-order terms provides a simpler model to study the leading-order guiding center drifts. Next, for clarity, these operations will be performed successively on each term in $\widetilde{L}$.

A few general comments will be helpful in this task. We will consider how the phase-space variables will scale along a trajectory with respect to the characteristic length and time scales, using assumptions defined in Section 4.2.2.

- Since L_B represents a macroscopic length scale, the guiding center position will scale as

$$\boldsymbol{R}_G \sim L_B.$$

[8] In any asymptotic expansion, it would be standard to consider separately the lowest-order $\mathcal{O}(\epsilon^{-1})$ terms and the $\mathcal{O}(\epsilon^0)$ terms. In this case, the lowest-order Euler–Lagrange equations do not provide enough information in order to determine the motion, and the corresponding lowest-order Lagrangian is said to be singular. However, when both the $\mathcal{O}(\epsilon^{-1})$ and $\mathcal{O}(\epsilon^0)$ terms are retained, the resulting Euler–Lagrange equations provide an equation of motion for each of the phase-space variables [38].

Table 4.1*: Scaling of phase-space guiding center coordinates with respect to the characteristic length and time scales.*

Coordinate	$\boldsymbol{R}_G$	ρ	$\dot{\boldsymbol{R}}_G$	$\dot{\rho}$	$\dot{\varphi}$
Scales like	L_B	ϵL_B	$\omega_B L_B$	$\epsilon\omega_B L_B$	ω_B/ϵ

- Given (4.9), then

$$\rho \sim \epsilon L_B. \tag{4.16}$$

- Since the gyroangle increases rapidly with time, no assumption on the magnitude of φ will be made. Instead, we will average over this angle.
- The guiding center motion is slow in comparison to the fast gyromotion, so

$$\dot{\boldsymbol{R}}_G \sim v_t \sim \omega_B L_B.$$

- Given that $\rho \sim v_\perp/\Omega \sim v_t/\Omega$, the time derivative of the gyroradius will scale as

$$\dot{\rho} \sim \rho\dot{\Omega}/\Omega \sim \rho\dot{B}/B \sim \rho\omega_B \sim \epsilon\omega_B L_B,$$

  since $\Omega = qB/m$ is the gyrofrequency.
- Given intuition from trajectories in a straight magnetic field, then

$$\dot{\varphi} \sim \Omega \sim \omega_B/\epsilon. \tag{4.17}$$

These scalings are summarized in Table 4.1.

Remark 4.1. *We emphasize that L_B quantifies the gradient length scale of all quantities that depend on the guiding center position. For example, for a quantity $a(\boldsymbol{R}_G)$ its gradient scales as $\nabla a(\boldsymbol{R}_G) \sim a(\boldsymbol{R}_G)/L_B$. As a consequence, the time dependence along a trajectory of quantities depending on the guiding center position can be estimated as*

$$\dot{a}(\boldsymbol{R}_G) \sim \dot{\boldsymbol{R}}_G \cdot \nabla a(\boldsymbol{R}_G) \sim v_t a(\boldsymbol{R}_G)/L_B \sim \omega_B a(\boldsymbol{R}_G).$$

First, we consider $\dot{\boldsymbol{\rho}}$ defined in (4.12). Given (4.16), the first term in (4.12) scales as $\omega_B\rho$. The third term has the same scaling as the first one, since the $(\hat{\boldsymbol{e}}_1, \hat{\boldsymbol{e}}_2, \hat{\boldsymbol{e}}_3)$ basis depends on $\boldsymbol{R}_G$, so from Remark 4.1, $\left(\dot{\boldsymbol{R}}_G \cdot \nabla\right)\hat{\boldsymbol{e}}_{2,3}(\boldsymbol{R}_G) \sim \dot{\hat{\boldsymbol{e}}}_{2,3}(\boldsymbol{R}_G) \sim \omega_B$. On the other hand, the second term scales as $\epsilon^{-1}\omega_B\rho \sim \mathcal{O}(\epsilon^0)$ since $\dot{\varphi} \sim \epsilon^{-1}\omega_B$ according to (4.17). Therefore,

$$\dot{\boldsymbol{\rho}}\Big(\boldsymbol{R}_G, \dot{\boldsymbol{R}}_G, \rho, \dot{\rho}, \varphi, \dot{\varphi}\Big) = \dot{\varphi}\left(\boldsymbol{\rho}(\boldsymbol{R}_G, \rho, \varphi) \times \hat{\boldsymbol{b}}(\boldsymbol{R}_G)\right) + \mathcal{O}(\epsilon). \tag{4.18}$$

Then the vector and scalar potentials, initially introduced as functions of $\boldsymbol{q}$, must instead be expressed in terms of $\boldsymbol{R}_G$ and $\boldsymbol{\rho}$. Under the assumption that the scale of the gyromotion is much smaller than the scale of the guiding center motion, $\rho/|\boldsymbol{R}_G| \ll 1$, then

$$\begin{cases} \boldsymbol{A}(\boldsymbol{q}) = \boldsymbol{A}(\boldsymbol{R}_G) + (\boldsymbol{\rho}\cdot\nabla)\,\boldsymbol{A}(\boldsymbol{R}_G) + \mathcal{O}(\epsilon^2), \\ \Phi(\boldsymbol{q}) = \Phi(\boldsymbol{R}_G) + (\boldsymbol{\rho}\cdot\nabla)\,\Phi(\boldsymbol{R}_G) + \mathcal{O}(\epsilon^2). \end{cases} \tag{4.19}$$

We also note that the gyroaverage of any term that is linear in $\boldsymbol{\rho}$ will vanish since

$$\langle \boldsymbol{\rho} \rangle_\varphi = 0. \tag{4.20}$$

According to (4.18), the first term in $\widetilde{L}$ can be written as

$$\begin{aligned} &m\boldsymbol{v}\Big(\boldsymbol{R}_G, \rho, \varphi, \dot{\varphi}, v_\parallel\Big) \cdot \dot{\boldsymbol{q}}\Big(\boldsymbol{R}_G, \dot{\boldsymbol{R}}_G, \rho, \dot{\rho}, \varphi, \dot{\varphi}\Big) \\ &= m\left(v_\parallel \hat{\boldsymbol{b}}(\boldsymbol{R}_G) + \dot{\varphi}\left(\boldsymbol{\rho}(\boldsymbol{R}_G, \rho, \varphi) \times \hat{\boldsymbol{b}}(\boldsymbol{R}_G)\right)\right) \cdot \left(\dot{\boldsymbol{R}}_G + \dot{\varphi}\left(\boldsymbol{\rho}(\boldsymbol{R}_G, \rho, \varphi) \times \hat{\boldsymbol{b}}(\boldsymbol{R}_G)\right)\right) \\ &\qquad + \mathcal{O}(\epsilon). \end{aligned}$$

Then, using (4.20) to simplify, the gyroaverage of the previous equation gives

$$\Big\langle m\boldsymbol{v}(\boldsymbol{R}_G, \rho, \varphi, \dot{\varphi}, v_\parallel) \cdot \dot{\boldsymbol{q}}\Big(\boldsymbol{R}_G, \dot{\boldsymbol{R}}_G, \rho, \dot{\rho}, \varphi, \dot{\varphi}\Big)\Big\rangle_\varphi = m\left(v_\parallel \hat{\boldsymbol{b}}(\boldsymbol{R}_G) \cdot \dot{\boldsymbol{R}}_G + \dot{\varphi}^2\rho^2\right).$$

According to (4.18) and (4.19), the second term in $\widetilde{L}$ is

$$\begin{aligned} q\boldsymbol{A}\left(\boldsymbol{q}(\boldsymbol{R}_G, \rho, \varphi)\right) \cdot \dot{\boldsymbol{q}}\Big(\boldsymbol{R}_G, \dot{\boldsymbol{R}}_G, \rho, \dot{\rho}, \varphi, \dot{\varphi}\Big) &= q\boldsymbol{A}(\boldsymbol{R}_G) \cdot \Bigg[\dot{\boldsymbol{R}}_G + \frac{\dot{\rho}}{\rho}\boldsymbol{\rho}(\boldsymbol{R}_G, \rho, \varphi) \\ &\quad + \dot{\varphi}\left(\boldsymbol{\rho}(\boldsymbol{R}_G, \rho, \varphi) \times \hat{\boldsymbol{b}}(\boldsymbol{R}_G)\right) + \left(\dot{\boldsymbol{R}}_G \cdot \nabla\right)\boldsymbol{\rho}(\boldsymbol{R}_G, \rho, \varphi)\Bigg] \\ &\quad + q\left(\boldsymbol{\rho} \cdot \nabla\right)\boldsymbol{A}(\boldsymbol{R}_G) \cdot \left(\dot{\boldsymbol{R}}_G + \dot{\varphi}\left(\boldsymbol{\rho}(\boldsymbol{R}_G, \rho, \varphi) \times \hat{\boldsymbol{b}}(\boldsymbol{R}_G)\right)\right) + \mathcal{O}(\epsilon). \end{aligned}$$

Then by gyroaveraging with (4.20),

$$\begin{aligned} &\Big\langle q\boldsymbol{A}\left(\boldsymbol{q}(\boldsymbol{R}_G, \rho, \varphi)\right) \cdot \dot{\boldsymbol{q}}\Big(\boldsymbol{R}_G, \dot{\boldsymbol{R}}_G, \rho, \dot{\rho}, \varphi, \dot{\varphi}\Big)\Big\rangle_\varphi \\ &= \frac{q\dot{\varphi}\rho^2}{2}\left(-\left[\left(\hat{\boldsymbol{e}}_2(\boldsymbol{R}_G) \cdot \nabla\right)\boldsymbol{A}(\boldsymbol{R}_G)\right] \cdot \hat{\boldsymbol{e}}_3(\boldsymbol{R}_G) + \left[\left(\hat{\boldsymbol{e}}_3(\boldsymbol{R}_G) \cdot \nabla\right)\boldsymbol{A}(\boldsymbol{R}_G)\right] \cdot \hat{\boldsymbol{e}}_2(\boldsymbol{R}_G)\right) + \mathcal{O}(\epsilon). \end{aligned}$$

Using the vector identity $\boldsymbol{A} \times (\nabla \times \boldsymbol{B}) = (\nabla \boldsymbol{B}) \cdot \boldsymbol{A} - (\boldsymbol{A} \cdot \nabla)\boldsymbol{B}$, we obtain the vector identity $-\left[(\hat{\boldsymbol{e}}_2 \cdot \nabla)\boldsymbol{A}\right] \cdot \hat{\boldsymbol{e}}_3 + \left[(\hat{\boldsymbol{e}}_3 \cdot \nabla)\boldsymbol{A}\right] \cdot \hat{\boldsymbol{e}}_2 = \hat{\boldsymbol{e}}_3 \cdot (\hat{\boldsymbol{e}}_2 \times (\nabla \times \boldsymbol{A}))$. We refer the reader to the NRL Plasma Formulary for many useful vector identities [137]. Since $\hat{\boldsymbol{e}}_3 \times \hat{\boldsymbol{e}}_2 = -\hat{\boldsymbol{b}}$ and $\nabla \times \boldsymbol{A} = \boldsymbol{B}$, then

$$\Big\langle q\boldsymbol{A}\left(\boldsymbol{q}(\boldsymbol{R}_G, \rho, \varphi)\right) \cdot \dot{\boldsymbol{q}}\Big(\boldsymbol{R}_G, \dot{\boldsymbol{R}}_G, \rho, \dot{\rho}, \varphi, \dot{\varphi}\Big)\Big\rangle_\varphi = q\boldsymbol{A}(\boldsymbol{R}_G) \cdot \dot{\boldsymbol{R}}_G - \frac{q\dot{\varphi}\rho^2 B(\boldsymbol{R}_G)}{2}.$$

The third term is

$$-m\frac{|\boldsymbol{v}\Big(\boldsymbol{R}_G, \rho, \varphi, \dot{\varphi}, v_\parallel\Big)|^2}{2} = -\frac{mv_\parallel^2}{2} - \frac{m\rho^2\dot{\varphi}^2}{2}.$$

This term does not depend on the gyroangle and so is unchanged under the gyroaverage.

According to (4.19), the final term is

$$-q\Phi(\boldsymbol{q}) = -q\Phi(\boldsymbol{R}_G) + \mathcal{O}(\epsilon),$$

and it is also independent of the gyroangle.

As a conclusion, we define the gyroaveraged Lagrangian, denoted by $\mathcal{L}$, as

$$\begin{aligned}&\mathcal{L}\Big(\boldsymbol{R}_G, \dot{\boldsymbol{R}}_G, \rho, \dot{\rho}, \varphi, \dot{\varphi}, v_\parallel, \dot{v}_\parallel\Big)\\&= \Big(m v_\parallel \hat{\boldsymbol{b}}\left(\boldsymbol{R}_G\right) + q\boldsymbol{A}(\boldsymbol{R}_G)\Big)\cdot \dot{\boldsymbol{R}}_G - \frac{m v_\parallel^2}{2} + \frac{\rho^2\left(m\dot{\varphi}^2 - q\dot{\varphi}B(\boldsymbol{R}_G)\right)}{2} - q\Phi(\boldsymbol{R}_G). \quad (4.21)\end{aligned}$$

By construction, this gyroaveraged Lagrangian no longer depends on φ, even though it still depends on $\dot{\varphi}$. We will use this simplified Lagrangian to study guiding center motion.

4.3 ▪ Euler–Lagrange equations for the gyroaveraged motion

The gyroaveraged Lagrangian (4.21) describes the dynamics of the guiding center $\boldsymbol{R}_G$ in addition to the gyromotion variables, ρ and φ, and the parallel velocity, $v_\parallel$, in a time-independent magnetic field. We will evaluate the Euler–Lagrange equations associated to the minimization of $\mathcal{L}$, and perform further analysis of the conserved quantities and dynamics for guiding center motion, respectively, in Sections 4.3.1–4.3.2 and Sections 4.3.3–4.3.6. The results will lead to important concepts such as particle trapping and evidence the guiding center drift across field lines. This will motivate the concept of toroidal magnetic confinement, introduced in Section 4.4.

4.3.1 ▪ Euler–Lagrange equations for auxiliary variables

Together with several further simplifications, a coordinate transformation from position $\boldsymbol{q}$ and velocity $\boldsymbol{v}$ and their derivatives to the guiding center position $\boldsymbol{R}_G$, gyroradius ρ, gyroangle φ, and parallel velocity $v_\parallel$ and their derivatives was performed in Section 4.2.3 to obtain a gyroaveraged Lagrangian. In order to isolate the guiding center motion, the auxiliary variables, ρ and φ, describing the gyromotion, as well as $v_\parallel$, can be eliminated by studying the associated Euler–Lagrange equations.

First, thanks to the Euler–Lagrange equation for ρ, we can identify the gyrofrequency as follows. The gyroaveraged Lagrangian (4.21) is independent of $\dot{\rho}$, $\partial\mathcal{L}/\partial\dot{\rho} = 0$. Hence, along any trajectory $\boldsymbol{Q}_T = ((\boldsymbol{R}_G)_T, \rho_T, \varphi_T, (v_\parallel)_T) : \mathbb{R} \to \mathbb{R}^6$, the Euler–Lagrange equation corresponding to the gyroradius shows that

$$\frac{\partial\mathcal{L}\Big(\boldsymbol{Q}_T(t), \dot{\boldsymbol{Q}}_T(t)\Big)}{\partial\rho} = \frac{d}{dt}\left(\frac{\partial\mathcal{L}\Big(\boldsymbol{Q}_T(t), \dot{\boldsymbol{Q}}_T(t)\Big)}{\partial\dot{\rho}}\right) \Rightarrow \frac{\partial\mathcal{L}\Big(\boldsymbol{Q}_T(t), \dot{\boldsymbol{Q}}_T(t)\Big)}{\partial\rho} = 0.$$

Computing the partial derivative of the gyroaveraged Lagrangian (4.21), this implies

$$\dot{\varphi}_T(t) = \frac{qB((\boldsymbol{R}_G)_T(t))}{m}. \quad (4.22)$$

Hence $\dot{\varphi}$ corresponds to the gyrofrequency Ω found in Section 4.1 but for a space-dependent magnetic field $B(\boldsymbol{R}_G)$. By analogy, we define the gyrofrequency as a function of the guiding center position, namely

$$\Omega(\boldsymbol{R}_G) = \frac{qB(\boldsymbol{R}_G)}{m}. \quad (4.23)$$

In the literature, the gyrofrequency is expressed more compactly as $\Omega = qB/m$.

Second, thanks to the Euler–Lagrange equation for φ, we can identify a conserved quantity associated with the nearly periodic gyromotion, consistent with the assumption $\epsilon \ll 1$. The gyroaveraged Lagrangian (4.21) is independent of φ, $\partial\mathcal{L}/\partial\varphi = 0$. Hence, along any trajectory $\boldsymbol{Q}_T : \mathbb{R} \to \mathbb{R}^6$, the Euler–Lagrange equation corresponding to the gyroangle shows that

$$\frac{\partial\mathcal{L}\Big(\boldsymbol{Q}_T(t), \dot{\boldsymbol{Q}}_T(t)\Big)}{\partial\varphi} = \frac{d}{dt}\left(\frac{\partial\mathcal{L}\Big(\boldsymbol{Q}_T(t), \dot{\boldsymbol{Q}}_T(t)\Big)}{\partial\dot{\varphi}}\right)$$
$$\Rightarrow \frac{d}{dt}\left(m\rho_T(t)^2\dot{\varphi}_T(t) - \frac{\rho_T(t)^2 qB((\boldsymbol{R}_G)_T(t))}{2}\right) = 0.$$

This implies the conservation of the quantity $2m\rho^2\dot{\varphi} - \rho^2 qB(\boldsymbol{R}_G)$ along any trajectory. This can also be expressed in terms of the gyrofrequency as $m\rho^2\Omega(\boldsymbol{R}_G)$, along guiding center trajectories. Any multiple of this quantity is conserved along trajectories, but the one that is most often used in the literature is defined in terms of the perpendicular velocity, $v_\perp(\rho, \boldsymbol{R}_G) := \rho\Omega(\boldsymbol{R}_G)$, as

$$\mu = \frac{mv_\perp^2(\rho, \boldsymbol{R}_G)}{2B(\boldsymbol{R}_G)} \tag{4.24}$$

and is often referred to as the magnetic moment. This quantity can be interpreted as follows. The gyromotion in the perpendicular plane produces a current loop of radius ρ, and the magnitude of the associated magnetic dipole moment is μ. The magnetic moment plays a key role in the dynamics of guiding center motion. In the literature, the magnetic moment is expressed more compactly as $\mu = mv_\perp^2/(2B)$. Here $v_\perp$ is the perpendicular velocity associated with the gyromotion, as opposed to the velocity $(\dot{\boldsymbol{R}}_G)_\perp$ associated with the perpendicular guiding center motion.

Remark 4.2. *In classical mechanics, if a system exhibits separation of time scales between a fast periodic motion and a slower variation of underlying physical quantities of interest, then there exists an adiabatic invariant, defined as an approximately conserved quantity associated with nearly periodic motion. This can be proved by asymptotic expansion using the separation of time scales and averaging over the fast time scale* [90]. *The fast gyromotion of a single particle in a given magnetic field provides nearly periodic motion, and the assumption $\epsilon \ll 1$ ensures that the magnetic field varies slowly with respect to this time scale. Hence the existence of an adiabatic invariant is guaranteed.*

The magnetic moment μ is an example of an adiabatic invariant. Here the magnetic moment is exactly conserved for the approximate gyroaveraged Lagrangian, but it would only be approximately conserved for the original Lagrangian.

Last, thanks to the Euler–Lagrange equation for the parallel velocity $v_\parallel$, we obtain a constraint in terms of guiding center variables. Using (4.21), we evaluate the Euler–Lagrange equation corresponding to the parallel velocity. Along any trajectory $\boldsymbol{Q}_T : \mathbb{R} \to \mathbb{R}^6$ it reads

$$\frac{d}{dt}\left[\frac{\partial\mathcal{L}\Big(\boldsymbol{Q}_T(t), \dot{\boldsymbol{Q}}_T(t)\Big)}{\partial\dot{v}_\parallel}\right] = \frac{\partial\mathcal{L}\Big(\boldsymbol{Q}_T(t), \dot{\boldsymbol{Q}}_T(t)\Big)}{\partial v_\parallel}$$
$$= 0 \Rightarrow \big(v_\parallel\big)_T(t) = \hat{\boldsymbol{b}}((\boldsymbol{R}_G)_T(t)) \cdot (\dot{\boldsymbol{R}}_G)_T(t). \tag{4.25}$$

This fits with the intuition that $v_\parallel$ is the velocity of the guiding center along the magnetic field.

Remark 4.3. *We will soon see that there is a component of $\dot{\boldsymbol{R}}_G$ across field lines, but it will be smaller than $v_\parallel$ by a factor scaling like ϵ. Therefore, to lowest order, the guiding center motion follows field lines.*

The next goal is to leverage (4.22), (4.23), (4.24), and (4.25) in order to isolate the guiding center motion from (4.21), describing the trajectories of $\boldsymbol{R}_G$.

4.3.2 ▪ Energy conservation

Under the assumption of time independence of the electric and magnetic fields discussed in the introduction of Section 4.2, $\partial\Phi/\partial t = 0$ and $\partial \boldsymbol{A}/\partial t = 0$, the Lagrangian (4.21) does not depend explicitly on time, $\partial\mathcal{L}/\partial t = 0$. This will now result in conservation of energy for the guiding center motion.

Indeed, the total time derivative of $\mathcal{L}$ along a trajectory $\boldsymbol{Q}_T : \mathbb{R} \to \mathbb{R}^6$ can be expressed as

$$\begin{aligned}\frac{d\mathcal{L}\Big(\boldsymbol{Q}_T(t),\dot{\boldsymbol{Q}}_T(t)\Big)}{dt} &= (\dot{\boldsymbol{R}}_G)_T(t)\cdot\frac{\partial\mathcal{L}\Big(\boldsymbol{Q}_T(t),\dot{\boldsymbol{Q}}_T(t)\Big)}{\partial \boldsymbol{R}_G} + \dot\rho_T(t)\frac{\partial\mathcal{L}\Big(\boldsymbol{Q}_T(t),\dot{\boldsymbol{Q}}_T(t)\Big)}{\partial\rho}\\ &+\dot\varphi_T(t)\frac{\partial\mathcal{L}\Big(\boldsymbol{Q}_T(t),\dot{\boldsymbol{Q}}_T(t)\Big)}{\partial\varphi} + \big(\dot v_\parallel\big)_T(t)\frac{\partial\mathcal{L}\Big(\boldsymbol{Q}_T(t),\dot{\boldsymbol{Q}}_T(t)\Big)}{\partial v_\parallel} + (\ddot{\boldsymbol{R}}_G)_T(t)\cdot\frac{\partial\mathcal{L}\Big(\boldsymbol{Q}_T(t),\dot{\boldsymbol{Q}}_T(t)\Big)}{\partial\dot{\boldsymbol{R}}_G}\\ &+\ddot\rho_T(t)\frac{\partial\mathcal{L}\Big(\boldsymbol{Q}_T(t),\dot{\boldsymbol{Q}}_T(t)\Big)}{\partial\dot\rho} + \ddot\varphi_T(t)\frac{\partial\mathcal{L}\Big(\boldsymbol{Q}_T(t),\dot{\boldsymbol{Q}}_T(t)\Big)}{\partial\dot\varphi} + \big(\ddot v_\parallel\big)_T(t)\frac{\partial\mathcal{L}\Big(\boldsymbol{Q}_T(t),\dot{\boldsymbol{Q}}_T(t)\Big)}{\partial\dot v_\parallel}.\end{aligned}$$

Applying the Euler–Lagrange equations for $\boldsymbol{R}_G$, ρ, φ, and $v_\parallel$, we obtain

$$\begin{aligned}\frac{d\mathcal{L}\Big(\boldsymbol{Q}_T(t),\dot{\boldsymbol{Q}}_T(t)\Big)}{dt} = \frac{d}{dt}\Bigg((\dot{\boldsymbol{R}}_G)_T(t)\cdot\frac{\partial\mathcal{L}\Big(\boldsymbol{Q}_T(t),\dot{\boldsymbol{Q}}_T(t)\Big)}{\partial\dot{\boldsymbol{R}}_G} + \dot\rho_T(t)\frac{\partial\mathcal{L}\Big(\boldsymbol{Q}_T(t),\dot{\boldsymbol{Q}}_T(t)\Big)}{\partial\dot\rho}\\ + \dot\varphi_T(t)\frac{\partial\mathcal{L}\Big(\boldsymbol{Q}_T(t),\dot{\boldsymbol{Q}}_T(t)\Big)}{\partial\dot\varphi} + \big(\dot v_\parallel\big)_T(t)\frac{\partial\mathcal{L}\Big(\boldsymbol{Q}_T(t),\dot{\boldsymbol{Q}}_T(t)\Big)}{\partial\dot v_\parallel}\Bigg).\end{aligned} \tag{4.26}$$

Along a trajectory $\boldsymbol{Q}_T : \mathbb{R} \to \mathbb{R}^6$, the energy for the guiding center motion is then defined as

$$\begin{aligned}E(t) := \dot{\boldsymbol{R}}_G\cdot\frac{\partial\mathcal{L}\Big(\boldsymbol{Q}_T(t),\dot{\boldsymbol{Q}}_T(t)\Big)}{\partial\dot{\boldsymbol{R}}_G} + \dot\rho\frac{\partial\mathcal{L}\Big(\boldsymbol{Q}_T(t),\dot{\boldsymbol{Q}}_T(t)\Big)}{\partial\dot\rho} + \dot\varphi\frac{\partial\mathcal{L}\Big(\boldsymbol{Q}_T(t),\dot{\boldsymbol{Q}}_T(t)\Big)}{\partial\dot\varphi}\\ + \dot v_\parallel\frac{\partial\mathcal{L}\Big(\boldsymbol{Q}_T(t),\dot{\boldsymbol{Q}}_T(t)\Big)}{\partial\dot v_\parallel} - \mathcal{L}\Big(\boldsymbol{Q}_T(t),\dot{\boldsymbol{Q}}_T(t)\Big),\end{aligned} \tag{4.27}$$

so that according to (4.26), the time derivative of the energy vanishes

$$\frac{dE(t)}{dt} = 0,$$

so along a trajectory the energy E is constant in time. Thanks to the definition of the Lagrangian (4.21), the magnetic moment (4.24), and parallel velocity (4.25), along a trajectory the energy can be reformulated after elementary calculations as

$$E = \frac{m\left(v_\parallel\right)_T^2(t)}{2} + \mu B((\boldsymbol{R}_G)_T(t)) + q\Phi. \tag{4.28}$$

In the literature, this is expressed more compactly as

$$E = \frac{mv_\parallel^2}{2} + \mu B + q\Phi.$$

The conserved quantity E represents the total energy of a guiding center: the first two terms in (4.28) account for the kinetic energy, the energy due to the motion, while the last term accounts for the potential energy, the energy due to the fields.

Since E is conserved along a trajectory, it will be used below without any mention of argument, and considered as a prescribed parameter depending only on the initial conditions.

4.3.3 ▪ Particle trapping

Energy and magnetic moment conservation will have an important consequence on the guiding center motion: particles may be trapped in regions with low magnetic field strength. To explain this, for simplicity, here Φ is assumed to be constant in some region of space. The reader can refer to Section 12.2 for justification.

The parallel velocity along a trajectory $\boldsymbol{Q}_T : \mathbb{R} \to \mathbb{R}^6$ can be rewritten from the expression for the energy invariant (4.28) under the form

$$\left(v_\parallel\right)_T^2(t) = \frac{2\left[E - q\Phi - \mu B\left((\boldsymbol{R}_G)_T(t)\right)\right]}{m}.$$

Since $v_\parallel$ represents the velocity along a trajectory, it must be real-valued, and therefore $v_\parallel^2$ must be nonnegative. The sign of $v_\parallel^2$ depends on the comparison between the constant $(E - q\Phi)/\mu$ and the variable quantity $B(\boldsymbol{R}_G)$. Moreover, defining $B_{\text{crit}} := (E - q\Phi))/\mu$, then $v_\parallel^2$ vanishes at points where $B(\boldsymbol{R}_G) = B_{\text{crit}}$. The quantity $v_\parallel$ may or may not change sign depending on the value of B_{crit}: either particles continuously move in the same direction along field lines, or particles bounce between points of B_{crit}.

Given $\boldsymbol{B}$ and Φ defining a physical system, the values of the energy E and adiabatic invariant μ, respectively defined in (4.27) and (4.24), depend on the trajectory in phase space. From this point of view, the constraint $v_\parallel^2 \geq 0$ implies that trajectories cannot exist in regions of phase space where $B(\mathbf{R}_G) > (E - q\Phi)/\mu$. Along an individual trajectory, the values of the invariants (E, μ) are fixed, uniquely defining B_{crit}. At any time t along the trajectory, necessarily $B(\boldsymbol{R}_G)_T(t) \leq B_{\text{crit}}$. Therefore the trajectory cannot access regions where $B(\boldsymbol{R}_G)_T(t) > B_{\text{crit}}$.

The conservation of E and μ along individual trajectories leads to the result that trajectories cannot access regions with sufficiently large magnetic field. This effect is known as mirroring, as a trajectory will be reflected away from high field regions. While these trajectories refer to the guiding center motion, particles exhibit a fast gyromotion about the guiding center trajectories. Two types of particle motion are then defined according to the associated guiding center.

- Trapped particles have a guiding center trajectory such that $v_\parallel$ changes sign for values of $\mathbf{R}_G$ such that $B(\mathbf{R}_G) = B_{\text{crit}}$. These particles have sufficiently large values of the ratio μ/E and become trapped in regions of low field strength.

- Passing particles have a guiding center trajectory such that $v_\parallel$ maintains a constant sign. These particles have sufficiently small values of μ/E and never mirror.

As noted in Remark 4.3, the motion of guiding centers, and therefore particles, approximately follows magnetic field lines. To lowest order in ϵ, trapped guiding centers mirror between points where $B(\mathbf{R}_G) = B_{\text{crit}}$ along field lines, while passing guiding centers continuously move along field lines in the same direction.

Particle trapping is an important concept for confinement. One of the earliest magnetic confinement devices, known as the mirror machine, relies on a magnetic field that varies along one direction with a large value of the field strength on the two ends of the device. In this way, a large population of particles are reflected and remain confined. Trapped and passing particles tend to have very different confinement properties in magnetic confinement devices due to their distinct trajectories. In particular, a major challenge of designing a stellarator is confining trapped particles, as will be discussed in Section 12.2. Additional discussion on particle trapping can be found in Section 8.9 of [75].

4.3.4 ▪ Equation of motion for the guiding center

As a reminder from Section 4.1, in a uniform and straight magnetic field, guiding center motion exhibits a constant velocity along field lines. The following sections will show that guiding centers have an additional slow drift across field lines in the presence of, on the one hand, a nonuniform magnetic field and, on the other hand, curvature in the field.

We will obtain the guiding center trajectories $\mathbf{Q}_T : \mathbb{R} \to \mathbb{R}^6$ by considering the Euler–Lagrange equation for the guiding center position, namely

$$\frac{d}{dt}\left(\frac{\partial \mathcal{L}\Big(\boldsymbol{Q}_T(t), \dot{\boldsymbol{Q}}_T(t)\Big)}{\partial \dot{\boldsymbol{R}}_G}\right) = \frac{\partial \mathcal{L}\Big(\boldsymbol{Q}_T(t), \dot{\boldsymbol{Q}}_T(t)\Big)}{\partial \boldsymbol{R}_G},$$

using the guiding center Lagrangian expression (4.21) together with the definition of μ (4.24), and ∇ indicates $\partial/\partial \boldsymbol{R}_G$. The equation reads

$$\begin{aligned}\frac{d}{dt}\Big(m\left(v_\parallel\right)_T(t)\hat{\boldsymbol{b}}\left((\boldsymbol{R}_G)_T(t)\right) + q\boldsymbol{A}\left((\boldsymbol{R}_G)_T(t)\right)\Big) &= mv_\parallel \nabla\Big((\dot{\boldsymbol{R}}_G)_T(t)\cdot\hat{\boldsymbol{b}}\left((\boldsymbol{R}_G)_T(t)\right)\Big)\\ &+ q\nabla\Big((\dot{\boldsymbol{R}}_G)_T(t)\cdot\boldsymbol{A}\left((\boldsymbol{R}_G)_T(t)\right)\Big) - \left[\mu\nabla B + q\nabla\Phi\right]\left((\boldsymbol{R}_G)_T(t)\right).\end{aligned}$$

The time-derivative operator on the left-hand side can be written as

$$d/dt = \dot{\boldsymbol{R}}_G\cdot\nabla + \dot{v}_\parallel\partial/\partial v_\parallel,$$

as $\boldsymbol{R}_G$ and $v_\parallel$ are the only phase-space variables appearing in the expression. Using the vector identity $\nabla(\boldsymbol{a}\cdot\boldsymbol{b}) = \boldsymbol{a}\times(\nabla\times\boldsymbol{b}) + \boldsymbol{b}\times(\nabla\times\boldsymbol{a}) + (\boldsymbol{a}\cdot\nabla)\boldsymbol{b} + (\boldsymbol{b}\cdot\nabla)\boldsymbol{a}$ as well as the definitions of the electric and magnetic fields in terms of the vector and scalar potentials $\boldsymbol{E} = -\nabla\Phi$ and $\boldsymbol{B} = \nabla\times\boldsymbol{A}$ from (B.5), we obtain

$$\begin{aligned}m\dot{\left(v_\parallel\right)}_T(t)\hat{\boldsymbol{b}}\left((\boldsymbol{R}_G)_T(t)\right) = (\dot{\boldsymbol{R}}_G)_T(t)\times\Big(m\left(v_\parallel\right)_T(t)\nabla\times\hat{\boldsymbol{b}}\left((\boldsymbol{R}_G)_T(t)\right) + q\boldsymbol{B}\left((\boldsymbol{R}_G)_T(t)\right)\Big)\\ - \left[\mu\nabla B - q\boldsymbol{E}\right]\left((\boldsymbol{R}_G)_T(t)\right).\end{aligned} \tag{4.29}$$

In the literature, this is commonly written more compactly as

$$m\dot{v}_\parallel\hat{\boldsymbol{b}} = \dot{\boldsymbol{R}}_G\times\Big(mv_\parallel\nabla\times\hat{\boldsymbol{b}} + q\boldsymbol{B}\Big) - \mu\nabla B + q\boldsymbol{E}.$$

The resulting dynamics in the parallel and perpendicular directions are now obtained.

4.3.5 ▪ Parallel guiding center motion

By taking the dot product of (4.29) with $\hat{\boldsymbol{b}}$, the parallel guiding center acceleration is obtained as

$$\dot{\left(v_\parallel\right)}_T(t) \;=\; \left(v_\parallel\right)_T(t)(\dot{\boldsymbol{R}}_G)_T(t)\cdot\boldsymbol{\kappa}\left((\boldsymbol{R}_G)_T(t)\right) - \frac{1}{m}\Big[\mu\hat{\boldsymbol{b}}\cdot\nabla B - q\boldsymbol{E}\cdot\hat{\boldsymbol{b}}\Big]\left((\boldsymbol{R}_G)_T(t)\right),$$

where $\boldsymbol{\kappa} = \left(\hat{\boldsymbol{b}} \cdot \nabla\right)\hat{\boldsymbol{b}} = \left(\nabla \times \hat{\boldsymbol{b}}\right) \times \hat{\boldsymbol{b}}$ is the curvature of magnetic field lines. This is expressed more compactly in the literature as

$$\dot{v}_\parallel = v_\parallel \dot{\boldsymbol{R}}_G \cdot \boldsymbol{\kappa} - \frac{\mu}{m}\hat{\boldsymbol{b}} \cdot \nabla B + \frac{q}{m}\boldsymbol{E} \cdot \hat{\boldsymbol{b}}.$$

A discussion of the scaling of the different terms follows.

- The first term is smaller than the next two by a factor of ϵ according to the assumption (4.9). It can be interpreted as a small parallel drift due to the field inhomogeneity.
- The second term expresses the fact that particles are repelled from regions of large field strength, as discussed in Section 4.3.3.
- The third term accounts for acceleration in regions where the electric field is parallel to the magnetic field.

4.3.6 ▪ Perpendicular guiding center motion

We now take the cross product of (4.29) with $\hat{\boldsymbol{b}}$, combined with the parallel velocity expression (4.25), to obtain the following expression for the guiding center acceleration:

$$\begin{aligned}(\dot{\boldsymbol{R}_G})_T(t) = \Bigg[\left(v_\parallel\right)_T(t) \left(\boldsymbol{B}\left((\boldsymbol{R}_G)_T(t)\right) + \frac{m\left(v_\parallel\right)_T(t)}{q} \nabla \times \hat{\boldsymbol{b}}\left((\boldsymbol{R}_G)_T(t)\right)\right) \\ + \left[\frac{\mu}{q}\hat{\boldsymbol{b}} \times \nabla B + \boldsymbol{E} \times \hat{\boldsymbol{b}}\right]\left((\boldsymbol{R}_G)_T(t)\right)\Bigg] \\ \left(B\left((\boldsymbol{R}_G)_T(t)\right) + \frac{m\left(v_\parallel\right)_T(t)}{q}\left[\hat{\boldsymbol{b}} \cdot \left(\nabla \times \hat{\boldsymbol{b}}\right)\right]\left((\boldsymbol{R}_G)_T(t)\right)\right)^{-1}.\end{aligned}$$

Under the assumption (4.9), we note that $mv_\parallel \nabla \times \hat{\boldsymbol{b}}/q$ is smaller than $\boldsymbol{B}$ by a factor of ϵ. Therefore, the second term in the numerator is smaller than the first by a factor of ϵ, and similarly for the second term in the denominator compared with the first. We now focus on the component of the velocity that is perpendicular to the magnetic field, $(\dot{\boldsymbol{R}_G})_\perp = \hat{\boldsymbol{b}} \times \left(\dot{\boldsymbol{R}}_G \times \hat{\boldsymbol{b}}\right)$. Therefore, to lowest order in ϵ,

$$\begin{aligned}\left((\dot{\boldsymbol{R}_G})_T(t)\right)_\perp = \left(v_\parallel\right)_T^2(t)\left[\frac{\hat{\boldsymbol{b}} \times \boldsymbol{\kappa}}{\Omega}\right]\left((\boldsymbol{R}_G)_T(t)\right) \\ + \left[\frac{\mu}{q}\frac{\hat{\boldsymbol{b}} \times \nabla B}{B} + \frac{\boldsymbol{E} \times \boldsymbol{B}}{B^2}\right]\left((\boldsymbol{R}_G)_T(t)\right). \quad (4.30)\end{aligned}$$

This is expressed more compactly as

$$\left(\dot{\boldsymbol{R}}_G\right)_\perp = v_\parallel^2 \frac{\hat{\boldsymbol{b}} \times \boldsymbol{\kappa}}{\Omega} + \frac{\mu}{q}\frac{\hat{\boldsymbol{b}} \times \nabla B}{B} + \frac{\boldsymbol{E} \times \boldsymbol{B}}{B^2}.$$

The right-hand side has three separate terms.

- The first term is known as the curvature drift, denoted $\boldsymbol{v}_\kappa$, resulting from the centrifugal force experienced by a particle moving along curved field lines. It depends on the mass, field strength, and charge through Ω. The sign of this drift is different for ions and electrons as the species gyrate in opposite directions.

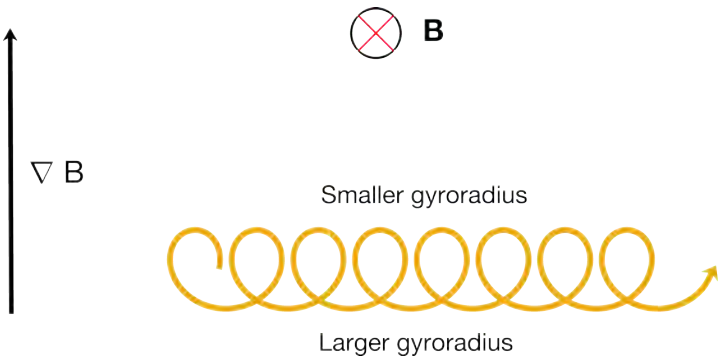

Figure 4.4*: Illustration of a particle orbit in a magnetic field pointing into the page with a gradient in the field strength pointing up. The trajectory of an ion is shown, with all motion projected into the plane perpendicular to* $\boldsymbol{B}$*. The ion will gyrate counterclockwise, with a smaller gyroradius in the region of stronger field. This results in what is called a grad-*B *drift to the right.*

- The second term is the grad-B drift, denoted by $\boldsymbol{v}_{\nabla B}$. This drift also depends on the field strength and charge. A physical picture of the grad-B drift can be found in Figure 4.4.
- The third term is the $\boldsymbol{E} \times \boldsymbol{B}$ drift, denoted by $\boldsymbol{v}_E$. This drift does not depend on the charge or mass, so it is the same for all species.

Further discussion of guiding center drifts can be found in Chapter 2 of [226], Section 2.4 of [110], Chapter 8 of [75], and Chapter 6 of [120].

4.4 ▪ Introduction to toroidal confinement

We focus here on the impact of magnetic field-line geometry on confinement. Although the magnetic field can be defined everywhere in space, in the context of magnetic confinement the goal is to confine a plasma within a bounded volume.

As described in Section 4.1, in a straight magnetic field a particle will gyrate about field lines. When the field is curved, that is, when its direction varies in space, or when its magnitude varies in space, particles will exhibit a drift across field lines in addition to their motion along field lines, as described in Section 4.3.

The structure of the magnetic field also affects collective properties such as the temperature of the plasma. As particles are approximately free to move in the direction parallel to the field, the temperature tends to reach an equilibrium rapidly along field lines [120].

In this section, we will use both the single-particle context and collective properties to discuss a magnetic field structure that is a central consideration for confinement in toroidal devices: the existence of nested toroidal flux surfaces.

4.4.1 ▪ Magnetic field lines and flux surfaces

In Section 4.1 we found that in a straight, uniform magnetic field, particles are confined in the direction perpendicular to the magnetic field lines. From the equations of motion (4.1), there is no confining force if the magnetic field vanishes. Moreover the radius of the gyromotion in the perpendicular direction scales inversely with the field strength, as expressed in (4.3). In order to take advantage of this perpendicular confinement, we will make the assumption that the magnetic field strength does not vanish within the confinement volume.

On the other hand, in a straight, uniform magnetic field, particles are not confined in the direction parallel to the magnetic field lines. In order to avoid losses of particles along straight field lines that leave the confinement volume, a different field-line structure is required. For particles to be confined within a bounded volume, a natural idea is to bend a set of straight field lines into a bounded volume. That is, field lines do not enter or exit through the boundary of this volume; therefore the field must be tangent to this boundary.

We can now comment on the possible topology of the boundary of the confinement volume. The simplest topology of a bounded volume is that of a sphere. The Hopf–Poincaré theorem [36] states that a nonvanishing, continuous 3D vector field cannot be tangent to a topologically spherical surface. However, a nonvanishing vector field can be tangent to surfaces with other topologies, the simplest being a torus. As we make the assumption that the magnetic field is nowhere vanishing, the boundary of the confinement volume cannot be a topologically spherical surface. However, it is possible for the boundary to be a toroidal surface. We will now assume that the confinement volume is toroidal. Depending on further assumptions on the model, this confinement volume can either be considered as a user-defined input, or be obtained by postprocessing an output.

Additional motivation for toroidal geometry arises from considerations of the collective properties of the particles. Since the temperature tends to reach an equilibrium rapidly along field lines [120], toroidal magnetic confinement devices avoid field lines that connect the plasma core to the cooler edge of the plasma. In this way, they maintain a hot plasma core that is not in contact with the material walls. If field lines from the plasma core do not intersect material surfaces, they must remain within a confined volume.

Within a bounded volume, each magnetic field line can exhibit different behaviors. If there exists a surface to which a magnetic field line is everywhere tangential, then the corresponding field line will lie on that surface instead of filling the plasma volume. Alternatively, if no such surface exists, the magnetic field line can instead fill a volume and is then known as a chaotic field line. Because temperature equilibrates rapidly along field lines [120], volume-filling field lines are not desirable as temperature would then become constant throughout the volume. Instead, to confine a hot plasma within a much colder material wall, it is necessary to maintain a temperature gradient between the core and the edge of the plasma. If there exists any region within the confinement domain where the field lines are volume-filling, the temperature is approximately constant. Therefore, to maximize the temperature gradient, it is desirable for the entire confinement volume to be filled with magnetic surfaces. Such surfaces are referred to as continuously nested surfaces. According to the previous discussion on the Hopf–Poincaré theorem, these surfaces cannot be spherical but can be toroidal.

The presence of toroidal magnetic surfaces in the volume is important for effectively confining a plasma. These considerations are the starting point for the concept of toroidal confinement. If all of these surfaces are nested around a single closed field line, the latter is called a magnetic axis. We denote this as the primary magnetic axis. Typically, the primary magnetic axis closes after one toroidal transit. In between two surfaces nested about the primary magnetic axis, it is possible to have a secondary magnetic axis. This secondary axis often does not close after one toroidal transit. A secondary set of surfaces can be nested about this secondary axis, forming what is called an island structure. Similar to chaotic regions, temperature is equilibrated rapidly within magnetic island chains [74]. Ideally, it is desirable for the magnetic field to lie on continuously nested toroidal surfaces with a single magnetic axis. This of course cannot be the case in the entire space, but such continuously nested toroidal flux surfaces can occupy a certain volume.

In perfect axisymmetry, continuously nested closed flux surfaces are guaranteed within the confinement domain if there is a nonzero toroidal current in the plasma. This statement will be justified in Sections 10.1–10.2 by demonstrating that the magnetic field-line flow can be described by a Hamiltonian system possessing a conserved quantity under the assumption of

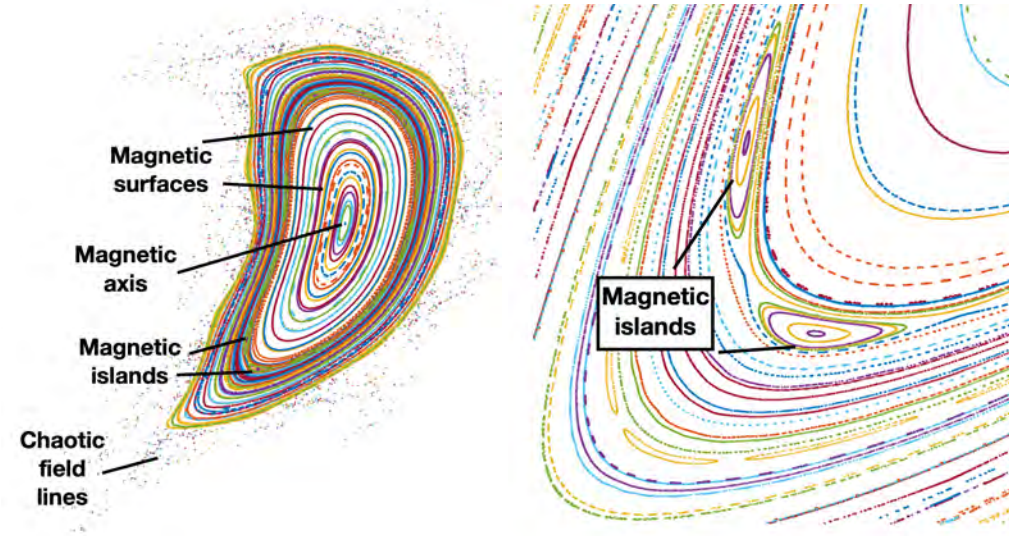

Figure 4.5*: Poincaré plot of a surface S. To produce it, field lines are followed, and each time they hit S, a point is marked on the plot with colors indicating a given field line. The magnetic field is generated by the coils of the NCSX stellarator* [322]*. Within the confinement region there are sets of magnetic surfaces as well as magnetic islands and chaotic field lines.*

axisymmetry. However, in 3D geometry, such as in a stellarator or a tokamak with 3D perturbations, field lines may become chaotic or may form islands in addition to forming nested flux surfaces in some regions of space, as can be seen in Figure 4.5.

Remark 4.4. *In order to maintain a temperature gradient across the confinement volume, continuously nested toroidal surfaces are beneficial. Many models leveraged in the context of stellarator design rely on the assumption of continuously nested toroidal surfaces, even though this assumption is not always valid in three dimensions. This is naturally also the case within this book, and in this context these surfaces will always be assumed to be smooth. In particular, it will allow for the introduction of coordinate systems adapted to the flux surfaces and to the periodicity inherent to toroidal geometries, as presented in Section* 5.5*. Thanks to these coordinate systems, periodicity can be used to formulate simpler mathematical models, as illustrated in Chapter* 6*.*

A common way to visualize the structure of a given toroidal magnetic field $\boldsymbol{B}$ is through a Poincaré plot. In a toroidal geometry, a toroidal angle refers to an angle measuring rotation about the main axis of the torus.[9] The setting for a Poincaré plot is a 2D plane, representing a given surface S, at constant toroidal angle. The intersection of the magnetic axis with S is a single point, and the intersection of the toroidally nested flux surfaces with S are closed curves nested around that point. The intersection of island structures with S appears as a secondary set of closed curves in between two primary closed curves. The plot is produced by following a set of field lines through many full toroidal rotations around the device and placing a point wherever a line passes through S. This process gradually fills out the closed curves as one follows field lines lying on surfaces. For chaotic field lines, the Poincaré plot displays a set of points that do

[9]One example of a toroidal angle is the angle from cylindrical coordinates when the main axis of the torus is chosen as the main axis for the cylindrical coordinates.

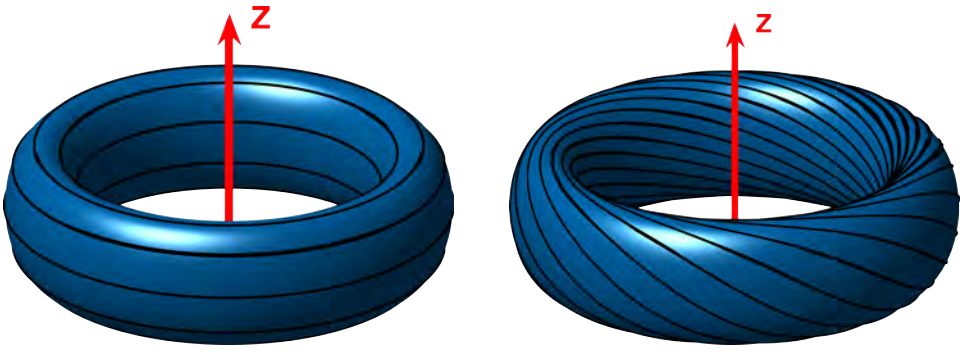

(a) (b)

Figure 4.6*: A purely toroidal field* (a) *cannot provide confinement due to the guiding center drifts. Therefore, we are interested in a magnetic field with both toroidal and poloidal components such that field lines twist to cover magnetic surfaces* (b).

not fill out curves. Refer to Figure 4.5 for a Poincaré plot of the magnetic field produced by the NCSX coils [322].

4.4.2 ▪ Poloidal component of the field

Toroidal magnetic fields are desirable for confinement and are naturally described using the canonical cylindrical coordinates (R, ϕ, Z).[10] In a toroidal region, a purely toroidal field only has a toroidal component, denoted B_ϕ, so that $\boldsymbol{B} = B_\phi \hat{\boldsymbol{\phi}}$, and its field lines are toroidally closed, each one of them forming a circle around the Z axis, as illustrated in Figure 4.6a. One could imagine generating such a set of toroidally closed field lines by bending a long solenoid to join its two open ends. Nearly toroidal field lines can be generated thanks to several individual circular coils placed along a common circular axis, as illustrated in Figure 4.7. Further considerations of such a toroidal system will now show that they do not lead to particle confinement. Instead, there is a need for the field to wrap around the flux surfaces, as illustrated in Figure 4.6. In other terms, the field will have both a component pointing the long way around the torus, referred to as the toroidal component, as well as a component pointing the short way around the torus, referred to as a poloidal component.

We study the field produced by such a coil configuration represented in Figure 4.7 with no other sources of current. The $\hat{\boldsymbol{Z}}$ vertical axis is the main axis of the configuration, each plane circular coil lies in a vertical plane including this axis, and they all lie on an axisymmetric torus. For the sake of the argument we will assume that the resulting magnetic field is purely toroidal and perfectly axisymmetric, meaning that $\boldsymbol{B} = B_\phi \hat{\boldsymbol{\phi}}$ and B_ϕ is independent of the angle ϕ. We will find that the magnitude of the toroidal field, B_ϕ, generated by the coils is a nonconstant function of the position. The field is stronger inside the toroidal shape, closer to the $\hat{\boldsymbol{Z}}$ axis of symmetry, and decreases as a function of the major radius R. This can be seen by computing the current passing through a particular circular surface S, lying in any horizontal plane whose boundary is a circle with radius R included between the major and minor radius of the torus shape supporting the coils and with height Z included between the highest and lowest points of this torus shape. Hence the boundary of the surface, ∂S, links through all of the coils as shown in Figure 4.7. Given a current density $\boldsymbol{J}$ supported by the coils and the normal $\hat{\boldsymbol{n}}$ to S, the resulting

[10] The cylindrical coordinates are uniquely defined only up to translations and rotations.

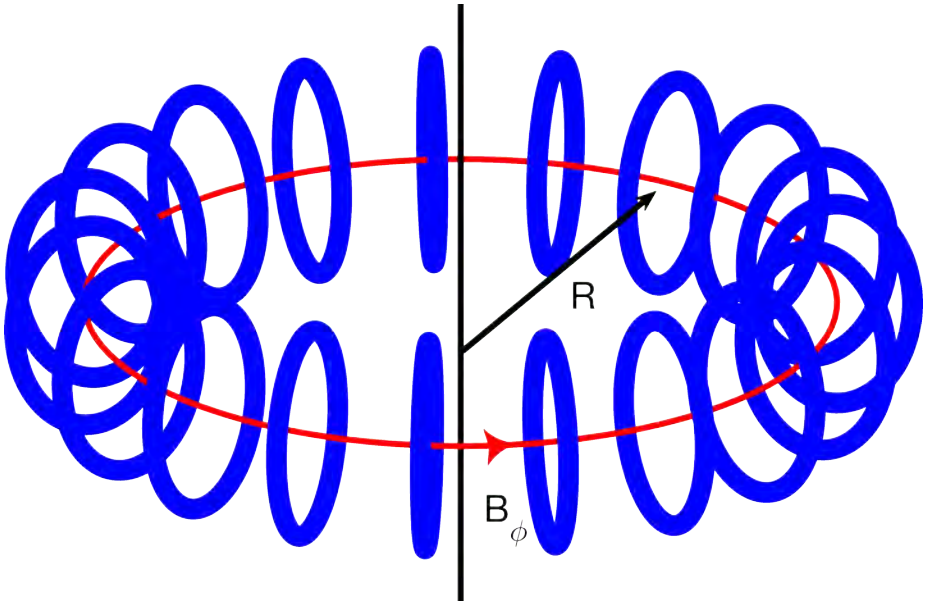

Figure 4.7: In a toroidal vacuum magnetic field, the magnitude of the toroidal field varies as $B_\phi \propto 1/R$ where R is the major radius, as can be seen by performing a line integral along the toroidal loop (red) enclosing coil current I, including contributions from the electromagnetic coils (blue).

current through S is then defined as

$$I = \int_S \boldsymbol{J}(\boldsymbol{r}) \cdot \hat{\boldsymbol{n}}(\boldsymbol{r})\, d^2 r.$$

Since the loop ∂S goes through the electromagnetic coils and there is no other source of current, the total current enclosed by the loop is the sum of the currents in each coil, independently of the radius R and height Z. On the other hand, the current can also be expressed in terms of the toroidal field, B_ϕ. This component is independent of the toroidal angle by axisymmetry and therefore is constant along the line integral. Indeed, from Ampère's law (A.7) we find

$$I = \frac{1}{\mu_0} \oint_{\partial S} \boldsymbol{B}(\boldsymbol{r}) \cdot d\boldsymbol{l}(\boldsymbol{r}).$$

Using ϕ to parameterize the line integral such that $\boldsymbol{B}(\boldsymbol{r}) \cdot d\boldsymbol{l}(\boldsymbol{r}) = RB_\phi(R, Z)d\phi$ we then get

$$I = \frac{2\pi R B_\phi(R, Z)}{\mu_0}.$$

As a result, for this configuration, the toroidal field strength is actually independent of Z and varies as $B_\phi(R) \propto 1/R$. The field inside the toroidal surface bounded by the coils is then

$$\boldsymbol{B}(R, \phi) = \frac{\mu_0 I}{2\pi R} \hat{\boldsymbol{\phi}}(\phi).$$

As discussed in Section 4.1, in a straight, uniform field, particles exhibit gyromotion about field lines. If the magnetic field is nonuniform or curved or if an electric field is introduced, a

particle will drift off of a field line on average, as discussed in Section 4.3. It is impossible to have good confinement in a purely toroidal and perfectly axisymmetric field, for which $\boldsymbol{B} = B_\phi \hat{\boldsymbol{\phi}}$ and B_ϕ depends only on R as described above, because of the following two drift phenomena.

- In the presence of a magnetic field $\boldsymbol{B}$ with a nonzero gradient of the field strength B, guiding centers drift off field lines at the velocity $\boldsymbol{v}_{\nabla B}$, introduced as the second term in (4.30), namely
$$\boldsymbol{v}_{\nabla B} = \frac{v_\perp^2}{2\Omega} \frac{\boldsymbol{B} \times \nabla B}{B^2},$$
where the gyrofrequency is $\Omega = qB/m$ and $v_\perp$ is the magnitude of the velocity perpendicular to the magnetic field. Since $\boldsymbol{B} \propto \hat{\boldsymbol{\phi}}$ and $\nabla B \propto \hat{\boldsymbol{R}}$, on average a particle will drift in the $\hat{\boldsymbol{\phi}} \times \hat{\boldsymbol{R}} = -\hat{\boldsymbol{Z}}$ vertical direction, either up or down depending on the sign of its charge q. According to similar arguments, the curvature drift $\boldsymbol{v}_\kappa$ also points in the positive or negative vertical direction depending on the sign of the charge. We will use the term magnetic drifts to denote both the grad-B and curvature drifts.

- As ions and electrons move in opposite directions, an electric field will appear in the vertical direction as a result of the separation of charges. This results in an additional $\boldsymbol{E} \times \boldsymbol{B}$ drift, namely
$$\boldsymbol{v}_E = \frac{\boldsymbol{E} \times \boldsymbol{B}}{B^2}.$$
Since $\boldsymbol{E} \propto \hat{\boldsymbol{Z}}$ and $\boldsymbol{B} \propto \hat{\boldsymbol{\phi}}$, this drift is in the radial direction. As the sign of the $\boldsymbol{E} \times \boldsymbol{B}$ drift is independent of the charge, both species will drift together radially out of the device.

As a consequence, a purely toroidal field cannot provide sufficient confinement.

Thanks to a poloidal magnetic field component, pointing the short way around the torus, these losses can be avoided. As we will discuss in Section 10.1, the existence of a poloidal magnetic field in axisymmetry ensures the existence of nested, toroidal magnetic surfaces. Consider field lines that twist to lie on a toroidal surface, having both a poloidal component and toroidal component, as represented in Figure 4.6b. As particles move along field lines, they will move above and below the $Z = 0$ plane. Consider a particle with a magnetic drift in the $\hat{\boldsymbol{Z}}$ direction starting from a given magnetic surface. When the particle is above the $Z = 0$ plane, it will have a magnetic drift in the $\hat{\boldsymbol{Z}}$ direction away from that surface, and when it is below the $Z = 0$ plane it will drift in the $\hat{\boldsymbol{Z}}$ direction back toward that surface. In this way, along a trajectory the net drift averages to zero, so a charged particle stays confined to its initial magnetic surface on average.

As described in [101], an analogy can be made with the motion of honey on a rotating honey dipper held horizontally. As gravity always pulls the fluid down, the honey will fall off the dipper if it is stationary. However, if the dipper is rotated, the honey will fall away from the dipper while it is on the bottom half and toward the dipper while it is on the upper half of the dipper. In this way, on average the honey will remain confined. In the same way, the twisting of the magnetic field lines allows particles to remain close to a given magnetic surface.

A poloidal magnetic field component is used for confinement in tokamaks and stellarators. While the existence of a poloidal field component guarantees confinement in a tokamak, in a stellarator additional constraints on the magnetic field are required to generally confine particle orbits. These will be discussed respectively in Section 7.2 and Chapter 12.

Chapter 5
Coordinate systems

Modeling toroidally confined plasmas requires the description of fields and other physical quantities in a toroidal domain. While many generic coordinate systems exist to describe physical domains, coordinate systems specifically adapted to given geometries are often more efficient tools for simplifying the geometric representation from the theoretical and computational points of view. This is particularly relevant in toroidal geometry, referring abstractly to a domain in $\mathbb{R}^3$ delimited by a genus one surface.

More specifically, in the context of toroidal confinement, for a given static magnetic field under specific assumptions beyond the toroidal geometry, coordinates can be adapted to the shape of the magnetic field itself.

- In general, toroidal coordinates rely on two periodic angle-like variables. A considerable benefit of such coordinates is that convenient simplifications follow from the associated periodicity of physical quantities, allowing, for instance, to leverage Fourier series techniques. This will be illustrated in Chapter 6.
- Under the fundamental assumption of continuously nested flux surfaces, described in Section 4.4, a radius-like coordinate can be defined from the toroidal flux surfaces. Physical processes occurring within a given flux surface are typically distinct in their space scales and time scales from those across surfaces. Many physical quantities, such as the temperature, can be assumed to be constant on flux surfaces, so a function of a single variable can model them.

A detailed introduction to these so-called flux coordinates for toroidal systems is provided in [55].

A brief discussion of the domain of interest for PDE models in toroidal confinement devices is presented in Section 5.2. A reminder of the canonical cylindrical coordinate system, often used to describe toroidal systems, is proposed in Section 5.3. A discussion of nonorthogonal coordinates, routinely arising in the description of magnetic geometries, is presented in Section 5.4. Section 5.5 discusses magnetic fields and toroidal magnetic surfaces as a motivation. Section 5.5.1 focuses on flux surfaces and how they are labeled. These surfaces form the basis for flux coordinate systems, described in Section 5.5.2.

5.1 ▪ A general comment on notation

While physical laws are inherently independent of coordinate systems, choosing an appropriate coordinate system can drastically simplify how they are expressed.

To describe a domain of interest in physical space, denoted $D_r \subset \mathbb{R}^3$, it is standard to denote by $\boldsymbol{r} \in D_r$ the position in space and to use a coordinate system to parameterize D_r. The relation existing between any coordinate system $\left(x^1, x^2, x^3\right)$, defined on a domain $D_c \subset \mathbb{R}^3$, and the position vector $\boldsymbol{r}$ can be expressed by

$$\boldsymbol{r} = \boldsymbol{R}\left(x^1, x^2, x^3\right),$$

where $\boldsymbol{R}$ is a bijection between D_c and D_r. Equivalently, this relation can be expressed as

$$\left(x^1, x^2, x^3\right) = (\boldsymbol{R})^{-1}(\boldsymbol{r}),$$

where $(\boldsymbol{R})^{-1}$ denotes the inverse of $\boldsymbol{R}$.

Any function on the domain of interest, either scalar-valued or vector-valued, can be expressed as a function of the position $\boldsymbol{r}$ or as a function of the coordinates $\left(x^1, x^2, x^3\right)$. For example, any quantity can be expressed as either a function f_r defined on D_r or a function f_c defined on D_c, related as follows:

$$\forall \left(x^1, x^2, x^3\right) \in D_c,\ f_c\left(x^1, x^2, x^3\right) = f_r\left(\boldsymbol{R}(x^1, x^2, x^3)\right). \tag{5.1}$$

It is standard practice to use a single symbol to refer to either of these two functions. For instance, $\boldsymbol{B}$ may refer to the magnetic field as a function of position or a function of a particular set of coordinates. However, it is crucial to consider the relation between the two functions in practical calculations. For example, any partial derivative of f_c will necessarily involve the application of the chain rule to the right-hand side of (5.1).

5.2 ▪ Domain of interest for toroidal confinement

In toroidal confinement, the goal is to achieve particle confinement through a carefully chosen magnetic field. The existence of continuously nested magnetic surfaces, discussed in Remark 4.4, is often assumed in at least some part of space as discussed in Section 4.4. Since magnetic confinement aims to confine a plasma within a given volume in $\mathbb{R}^3$, the domain of interest is naturally bounded.

The domain of interest is a toroidal volume, even if the boundary is not necessarily one of the nested flux surfaces. For simplicity, we assume that a straight axis passes through the torus hole but does not intersect this volume. In some discussions, while remaining a bounded toroidal volume, the domain of interest will also include regions without continuously nested toroidal flux surfaces.

Most of this book focuses on the confinement properties of the magnetic field in such a bounded toroidal volume. Outside of this bounded volume, magnets or coils must provide an external magnetic field. In the context of the theoretical study of properties of partial differential equations or their solutions, the boundary of this domain is assumed to be given. For some design problems, the domain boundary is unknown and approximated through optimization techniques. In other contexts, electromagnetic coils and the magnetic field generated by these coils may be given, and the boundary of the domain of interest, defined as the last closed flux surface of the field, is unknown. In Chapter 13, we will discuss some aspects of coil design. Some modeling problems account for other experimental components outside the confinement region, though this is beyond the scope of this book.

5.3 ▪ Canonical cylindrical coordinates

The classical cylindrical coordinates, denoted $(R, \phi, Z) \in \mathbb{R}^+ \times [0, 2\pi) \times \mathbb{R}$, can naturally describe toroidal geometry, as illustrated in Figure 5.1. Given a reference axis $\hat{\boldsymbol{Z}}$ and a reference

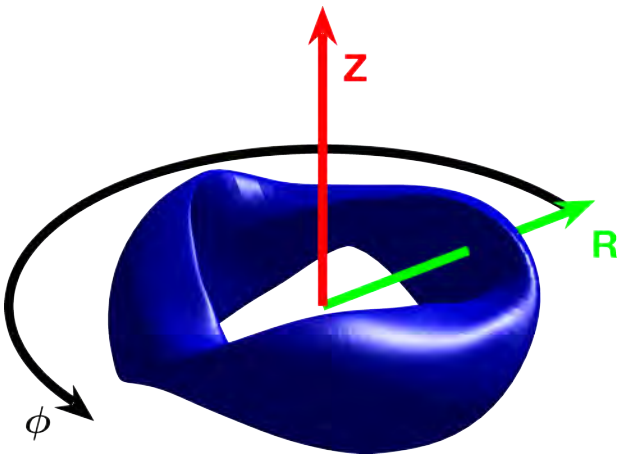

Figure 5.1*: The standard cylindrical coordinate system: R measures the distance to the $\hat{\boldsymbol{Z}}$ axis, and ϕ is the standard angle of the cylindrical coordinate system such that $\hat{\boldsymbol{R}} \times \hat{\boldsymbol{\phi}} = \hat{\boldsymbol{Z}}$.*

plane perpendicular to $\hat{\boldsymbol{Z}}$, the plane can be parameterized by Cartesian coordinates X and Y, with the unit vectors $(\hat{\boldsymbol{X}}, \hat{\boldsymbol{Y}}) = (\nabla X, \nabla Y)$ such that $\hat{\boldsymbol{X}} \times \hat{\boldsymbol{Y}} = \hat{\boldsymbol{Z}}$. The Cartesian coordinates are related to the cylindrical coordinates through $X = R\cos\phi$ and $Y = R\sin\phi$. The major radius then measures the distance from the $\hat{\boldsymbol{Z}}$ axis, while ϕ is an angle measured in the x-y plane. The unit vectors for the cylindrical coordinates can be expressed in terms of the gradients of the corresponding coordinates as $\hat{\boldsymbol{R}} = \nabla R$, $\hat{\boldsymbol{\phi}} = R\nabla\phi$, and $\hat{\boldsymbol{Z}} = \nabla Z$. A poloidal plane is defined as a half-plane at constant ϕ, so that $(\hat{\boldsymbol{R}}, \hat{\boldsymbol{Z}})$ is an orthonormal basis of the poloidal plane, while $\hat{\boldsymbol{\phi}}$ is orthogonal to the poloidal plane.

Cylindrical coordinates have a singularity at $R = 0$, along the $\hat{\boldsymbol{Z}}$ axis, as ϕ is discontinuous across the axis. However, since we assume that there exists a straight axis passing through the torus hole but not intersecting the domain of interest, we can choose this as the $\hat{\boldsymbol{Z}}$ axis. Then, the singularity of cylindrical coordinates is outside the domain of interest, so this singularity does not come into play in the context of this book.

Using cylindrical coordinates in the context of axisymmetric geometries is generally convenient, as ϕ is a symmetry direction. Note that these coordinates can be used independently of the magnetic field geometry for nonsymmetric systems. In contrast, coordinate systems depending on the magnetic field geometry may have the advantage of simplifying the expression of quantities of interest. However, it is important to remember that additional assumptions on the magnetic field geometry, such as flux coordinates, will restrict the existence of such coordinate systems. In particular, cylindrical coordinates can describe systems without continuously nested surfaces, while flux coordinates can only describe regions with continuously nested surfaces.

Section 4.6.1 of [55] discusses the cylindrical coordinate system.

5.4 ▪ Nonorthogonal coordinates

An orthogonal coordinate system $\left(x^1, x^2, x^3\right)$ is a system satisfying $\nabla x^i \cdot \nabla x^j = 0$ for $i \neq j$, and all other coordinate systems are nonorthogonal. The interested reader can refer to [56] for a complete presentation of Riemannian geometry including the material covered in this section.

While the classical cylindrical coordinates introduced in the previous section form an orthogonal system, a general coordinate system $\left(x^1, x^2, x^3\right)$ may not be orthogonal. One such example, particularly useful to stellarators, is a general flux coordinate system previously introduced in Section 5.5.2.

Remark 5.1. *Considering a coordinate system* $\left(x^1, x^2, x^3\right)$*, two local bases can be defined at any point* $\boldsymbol{R}\left(x^1, x^2, x^3\right) \in \mathbb{R}^3$*:*

- *the contravariant basis* $(\nabla x^1, \nabla x^2, \nabla x^3)$*, that is, the basis of the gradients of the coordinates;*
- *the covariant basis* $\left(\partial \boldsymbol{R}/\partial x^1, \partial \boldsymbol{R}/\partial x^2, \partial \boldsymbol{R}/\partial x^3\right)$*, that is, the basis of the partial derivatives of the position vector.*

As discussed in Section 5.1*, these vectors may refer to functions of position or functions of a particular set of coordinates. However, because of their definition, we distinguish between the two bases. Since the gradient operator is defined independently of any coordinate system and acts on functions depending on the position* $\boldsymbol{r}$*, it is more common to express the contravariant basis vectors as functions of the position,* $\nabla x^i(\boldsymbol{r})$*. On the other hand, since the covariant basis vectors are computed from partial derivatives with respect to coordinates, it is more common to express the covariant basis vectors as functions of the coordinates,* $\partial \boldsymbol{R}\left(x^1, x^2, x^3\right)/\partial x^i$*.*

We now turn to the so-called dual properties of the two bases. The contravariant basis vectors ∇x^i are perpendicular to isosurfaces of the coordinate x^i, while the covariant basis vectors $\partial \boldsymbol{R}/\partial x^i$ are tangent to isosurfaces of the coordinates x^j and x^k. We can make the following comments at any point in the domain of interest.

- The covariant basis vector $\partial \boldsymbol{R}/\partial x^i$ points in the direction in which only x^i changes, as illustrated in Figure 5.2. Since x^j and x^k are constant in the direction of the covariant basis vector $\partial \boldsymbol{R}/\partial x^i$, it follows that $\nabla x^j \cdot \partial \boldsymbol{R}/\partial x^i = 0$ for $i \neq j$.
- Consider the differential change in x^i associated with a change in position, $d\boldsymbol{r}$, namely $dx^i = d\boldsymbol{r} \cdot \nabla x^i$. According to the chain rule, $d\boldsymbol{r} = \sum_{j=1}^{3} \partial \boldsymbol{R}/\partial x^j dx^j$. According to the previous bullet point, this then implies that $\nabla x^i \cdot \partial \boldsymbol{R}/\partial x^i = 1$.

This can be summarized as a fundamental property: the covariant and contravariant bases are said to be dual or reciprocal. That is, at any point where the coordinate system is defined,

$$\boxed{\nabla x^i\Big(\boldsymbol{R}\left(x^1, x^2, x^3\right)\Big) \cdot \frac{\partial \boldsymbol{R}\left(x^1, x^2, x^3\right)}{\partial x^j} = \delta_{i,j} \text{ for all indices } i, j \in \{1, 2, 3\}.} \tag{5.2}$$

As a consequence of this duality, for (i, j, k) being either $(1, 2, 3)$ or one of its cyclic permutations, the basis vectors are related by the following expressions:

$$\begin{cases} \dfrac{\partial \boldsymbol{R}\left(x^1, x^2, x^3\right)}{\partial x^k} = \dfrac{\nabla x^i\Big(\boldsymbol{R}\left(x^1, x^2, x^3\right)\Big) \times \nabla x^j\Big(\boldsymbol{R}\left(x^1, x^2, x^3\right)\Big)}{\Big(\nabla x^i\Big(\boldsymbol{R}\left(x^1, x^2, x^3\right)\Big) \times \nabla x^j\Big(\boldsymbol{R}\left(x^1, x^2, x^3\right)\Big)\Big) \cdot \nabla x^k\Big(\boldsymbol{R}\left(x^1, x^2, x^3\right)\Big)}, \\ \nabla x^k\Big(\boldsymbol{R}\left(x^1, x^2, x^3\right)\Big) = \dfrac{\dfrac{\partial \boldsymbol{R}\left(x^1, x^2, x^3\right)}{\partial x^i} \times \dfrac{\partial \boldsymbol{R}\left(x^1, x^2, x^3\right)}{\partial x^j}}{\left(\dfrac{\partial \boldsymbol{R}\left(x^1, x^2, x^3\right)}{\partial x^i} \times \dfrac{\partial \boldsymbol{R}\left(x^1, x^2, x^3\right)}{\partial x^j}\right) \cdot \dfrac{\partial \boldsymbol{R}\left(x^1, x^2, x^3\right)}{\partial x^k}}. \end{cases} \tag{5.3}$$

In general, these two bases are not orthogonal. However, some coordinate systems, such as Cartesian or cylindrical coordinates, are orthogonal at any point $\boldsymbol{r} \in \mathbb{R}^3$. Note that the contravariant and covariant bases can only be orthogonal simultaneously. In particular, it is a direct

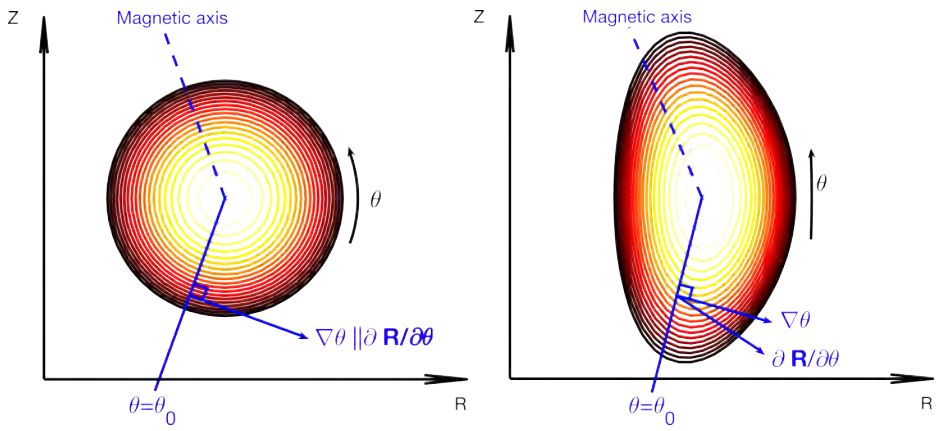

Figure 5.2: Comparison of orthogonal (left) and nonorthogonal (right) flux coordinate systems (r, θ, ϕ) in a plane of constant ϕ. In this plane, the (R, Z) axes of cylindrical coordinates are represented for convenience. Curves of constant coordinate r for orthogonal and nonorthogonal coordinates are shown with the color gradient indicating the change in r. In an orthogonal system (left), the covariant and contravariant basis vectors for a given coordinate are parallel. In contrast, in a nonorthogonal system (right), covariant and contravariant basis vectors are no longer parallel.

consequence of (5.3) that the orthogonality of the contravariant basis implies the orthogonality of the covariant basis.

As a consequence of (5.3), in an orthogonal coordinate system, each coordinate's covariant and contravariant basis vectors are parallel. In other words, ∇x^i is parallel to $\partial \boldsymbol{R}/\partial x^i$ for all $i \in \{1, 2, 3\}$. Indeed, in an orthogonal coordinate system, at any point $\left(y^1, y^2, y^3\right) \in \mathbb{R}^3$ any two surfaces of constant coordinates, for example the surfaces of constant x^i and constant x^j for $i \neq j$, respectively $\{\left(x^1, x^2, x^3\right) \in \mathbb{R}^3, x^i = y^i\}$ and $\{\left(x^1, x^2, x^3\right) \in \mathbb{R}^3, x^j = y^j\}$, have orthogonal tangent planes along their intersection. By contrast, in a nonorthogonal coordinate system, covariant and contravariant basis vectors are not necessarily parallel, and surfaces of constant coordinates do not necessarily have orthogonal tangent planes, as illustrated in Figure 5.2.

The Jacobian, required to evaluate integrals, can be defined for a general coordinate system in terms of covariant basis vectors as

$$\sqrt{g}\left(x^1, x^2, x^3\right) = \left(\frac{\partial \boldsymbol{R}\left(x^1, x^2, x^3\right)}{\partial x^1} \times \frac{\partial \boldsymbol{R}\left(x^1, x^2, x^3\right)}{\partial x^2}\right) \cdot \frac{\partial \boldsymbol{R}\left(x^1, x^2, x^3\right)}{\partial x^3} \tag{5.4}$$

or, equivalently, in terms of contravariant basis vectors as

$$\sqrt{g}\Big(\boldsymbol{R}\left(x^1, x^2, x^3\right)\Big) = \frac{1}{\left(\nabla x^1\Big(\boldsymbol{R}\left(x^1, x^2, x^3\right)\Big) \times \nabla x^2\Big(\boldsymbol{R}\left(x^1, x^2, x^3\right)\Big)\right) \cdot \nabla x^3\Big(\boldsymbol{R}\left(x^1, x^2, x^3\right)\Big)}. \tag{5.5}$$

These two formulas illustrate that, as discussed in Remark 5.1, the Jacobian can refer to either a function of position or a function of coordinates. In practice, depending on the formula under consideration, either option can be more convenient.

A coordinate system is well-defined if and only if these sets of three either covariant or contravariant vectors form a basis of $\mathbb{R}^3$ at any point of the domain. It is then clear that the coordinate system is well-defined if and only if the denominator of the Jacobian is nonzero in (5.5) and, equivalently, if and only if the Jacobian is nonzero in (5.4).

These bases are particularly useful for describing vector fields: any vector field can be expressed in terms of its components in either the covariant or contravariant bases. While the vector field can be defined independently of any coordinate system, the definition of its components depends on the choice of basis and, therefore, on the choice of a coordinate system. As a result, it is standard to write the components as functions of the coordinates rather than functions of position. A vector field $\boldsymbol{A}$ can be expressed in the contravariant basis at any point $\boldsymbol{r} = \boldsymbol{R}\left(x^1, x^2, x^3\right)$ as

$$\boldsymbol{A}\Big(\boldsymbol{R}\left(x^1, x^2, x^3\right)\Big) = \sum_{i=1}^{3} A_i\left(x^1, x^2, x^3\right) \nabla x^i\Big(\boldsymbol{R}\left(x^1, x^2, x^3\right)\Big). \tag{5.6}$$

In order to find an explicit expression for the covariant components A_i of the field, for any k from 1 to 3, consider the inner product of the previous identity with the kth covariant basis vector

$$\boldsymbol{A}\Big(\boldsymbol{R}\left(x^1, x^2, x^3\right)\Big) \cdot \frac{\partial \boldsymbol{R}\left(x^1, x^2, x^3\right)}{\partial x^k} = \sum_{i=1}^{3} A_i\left(x^1, x^2, x^3\right) \nabla x^i\Big(\boldsymbol{R}\left(x^1, x^2, x^3\right)\Big) \cdot \frac{\partial \boldsymbol{R}\left(x^1, x^2, x^3\right)}{\partial x^k}.$$

According to the duality relation between the two bases (5.2), this yields

$$A_k\left(x^1, x^2, x^3\right) = \boldsymbol{A}\Big(\boldsymbol{R}\left(x^1, x^2, x^3\right)\Big) \cdot \frac{\partial \boldsymbol{R}\left(x^1, x^2, x^3\right)}{\partial x^k} \quad \forall k \in \{1, 2, 3\}.$$

These A_k are the covariant components of the given vector field $\boldsymbol{A}$. Correspondingly, the expression (5.6) is called the covariant form of the vector field $\boldsymbol{A}$. Similarly, a vector field $\boldsymbol{A}$ can be expressed in the covariant basis at any point $\boldsymbol{r} = \boldsymbol{R}\left(x^1, x^2, x^3\right)$ under the form

$$\boldsymbol{A}\Big(\boldsymbol{R}\left(x^1, x^2, x^3\right)\Big) = \sum_{i=1}^{3} A^i\left(x^1, x^2, x^3\right) \frac{\partial \boldsymbol{R}\left(x^1, x^2, x^3\right)}{\partial x^i}. \tag{5.7}$$

In order to find an explicit expression for the components A^i of the field, for any k from 1 to 3, consider the inner product of the previous identity with the kth contravariant basis vector

$$\boldsymbol{A}\Big(\boldsymbol{R}\left(x^1, x^2, x^3\right)\Big) \cdot \Big[\nabla x^k\Big]\Big(\boldsymbol{R}\left(x^1, x^2, x^3\right)\Big) = \sum_{i=1}^{3} A^i\left(x^1, x^2, x^3\right) \frac{\partial \boldsymbol{R}\left(x^1, x^2, x^3\right)}{\partial x^i} \cdot \Big[\nabla x^k\Big]\Big(\boldsymbol{R}\left(x^1, x^2, x^3\right)\Big).$$

According to the duality relation between the two bases (5.2), this yields

$$A^k\left(x^1, x^2, x^3\right) = \boldsymbol{A}\Big(\boldsymbol{R}\left(x^1, x^2, x^3\right)\Big) \cdot \Big[\nabla x^k\Big]\Big(\boldsymbol{R}\left(x^1, x^2, x^3\right)\Big) \quad \forall k \in \{1, 2, 3\}.$$

These components A^k are the contravariant components of the given vector field $\boldsymbol{A}$. Correspondingly, the expression (5.7) is called the contravariant form of the vector field $\boldsymbol{A}$.

A further discussion of nonorthogonal coordinates can be found in Chapter 2 of [55]. We gather in Table 5.1 some of the basic formulas for integrating and differentiating in such coordinates for later reference.

Table 5.1*: Summary of formulas used to describe the geometry of a nonorthogonal coordinate system* $\left(x^1, x^2, x^3\right)$*. The triplet of indices* (i, j, k) *is a circular permutation of* $\{1, 2, 3\}$*,* $\boldsymbol{A}$ *denotes a differentiable vector field, and* q *denotes a differentiable scalar function.*

Covariant form	$\boldsymbol{A} = \sum_{i=1}^{3} A_i \nabla x^i$ with $A_i = \boldsymbol{A} \cdot \partial \boldsymbol{R} / \partial x^i$
Contravariant form	$\boldsymbol{A} = \sum_{i=1}^{3} A^i \dfrac{\partial \boldsymbol{R}}{\partial x^i}$ with $A^i = \boldsymbol{A} \cdot \nabla x^i$
Jacobian $\sqrt{g}$	$\left(\dfrac{\partial \boldsymbol{R}}{\partial x^1} \times \dfrac{\partial \boldsymbol{R}}{\partial x^2}\right) \cdot \dfrac{\partial \boldsymbol{R}}{\partial x^3} = \dfrac{1}{(\nabla x^1 \times \nabla x^2) \cdot \nabla x^3}$
Relation between basis vectors	$\dfrac{\partial \boldsymbol{R}}{\partial x^k} = \sqrt{g}\left(\nabla x^i \times \nabla x^j\right)$
Relation between basis vectors	$\nabla x^k = \sqrt{g}^{-1}\left(\dfrac{\partial \boldsymbol{R}}{\partial x^i} \times \dfrac{\partial \boldsymbol{R}}{\partial x^j}\right)$
Differential volume	$d^3 r = \lvert\sqrt{g}\rvert dx^1 dx^2 dx^3$
Differential surface area (constant x^k)	$d^2 r = \lvert\sqrt{g}\rvert \lvert\nabla x^k\rvert dx^i dx^j$ $= \left\lvert \dfrac{\partial \boldsymbol{R}}{\partial x^i} \times \dfrac{\partial \boldsymbol{R}}{\partial x^j} \right\rvert dx^i dx^j$
Differential length (constant x^j, x^k)	$d\ell = \left\lvert \dfrac{\partial \boldsymbol{R}}{\partial x^i} \right\rvert dx^i = \lvert\sqrt{g}\rvert \lvert\nabla x^j \times \nabla x^k\rvert dx^i$
Unit normal vector (constant x^k)	$\hat{\boldsymbol{n}} = \left(\dfrac{\partial \boldsymbol{R}}{\partial x^i} \times \dfrac{\partial \boldsymbol{R}}{\partial x^j}\right) \left\lvert \dfrac{\partial \boldsymbol{R}}{\partial x^i} \times \dfrac{\partial \boldsymbol{R}}{\partial x^j} \right\rvert^{-1}$
Divergence of a vector field	$\nabla \cdot \boldsymbol{A} = \sum_{i=1}^{3} \dfrac{1}{\sqrt{g}} \dfrac{\partial}{\partial x^i}\left(\sqrt{g} A^i\right)$
Curl of a vector field	$\nabla \times \boldsymbol{A} = \sum_{k=1}^{3} \dfrac{1}{\sqrt{g}} \left(\dfrac{\partial A_j}{\partial x^i} - \dfrac{\partial A_i}{\partial x^j}\right) \dfrac{\partial \boldsymbol{R}}{\partial x^k}$
Gradient of a scalar function	$\nabla q = \sum_{i=1}^{3} \dfrac{\partial q}{\partial x^i} \nabla x^i$
Differential path	$d\boldsymbol{r} = \sum_{i=1}^{3} \dfrac{\partial \boldsymbol{R}}{\partial x^i} dx^i$

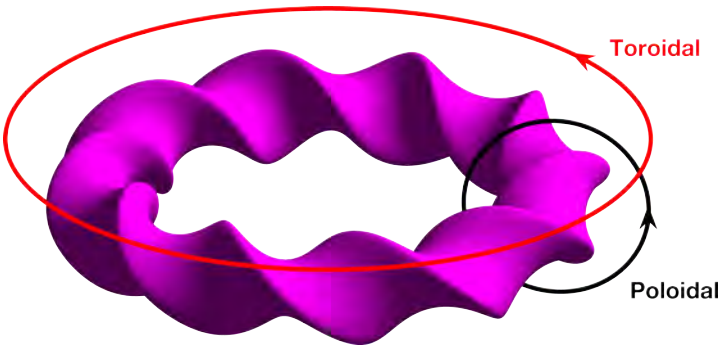

Figure 5.3*: The position in a toroidal system is often described by two angles. A poloidal angle increases from* 0 *to* 2π *on any closed poloidal loop about the magnetic axis, the short way around the torus. One such poloidal loop is represented in black. A toroidal angle increases from* 0 *to* 2π *on any closed toroidal loop about the major axis of the coordinate system, the long way around the torus. One such toroidal loop is represented in red.*

5.5 ▪ A magnetic field–dependent coordinate system

As the domain of interest is a toroidal volume, defining a toroidal coordinate system is useful. This refers to a coordinate system with one radius-like coordinate, s, and two angle-like coordinates parameterizing each surface of constant s. In any toroidal coordinate system, the term toroidal angle refers to the direction the long way around the torus, while the term poloidal refers to the direction the short way around the torus. Choosing a toroidal angle that increases by 2π upon a toroidal loop and a poloidal angle that increases by 2π upon a poloidal loop is standard. Other choices are also possible, such as choosing angles that increase by 1 upon a loop. The coordinate curves are defined by fixing the surface label s and either the toroidal or the poloidal coordinate. These coordinate curves close respectively poloidally or toroidally after a period of 2π. A brief description of toroidal geometry can be found in Figure 5.3.

In the context of toroidal confinement, under the fundamental assumption that the magnetic field has continuously nested flux surfaces throughout the domain of interest, discussed in Remark 4.4, we will define here particular toroidal coordinate systems depending on the magnetic field. In the context of stellarator modeling, flux coordinates depend on a given magnetic field, while in the context of stellarator design the magnetic field is unknown. Hence it is crucial to keep in mind that a flux coordinate system can be defined abstractly even though the magnetic field may be unknown.

As a side note, we mention that in principle, defining a local set of flux coordinates within a magnetic island is possible. However, it is impossible to define a single set of valid flux coordinates throughout the whole domain when continuously nested flux surfaces do not exist in a whole domain of interest, for instance, because of the existence of magnetic islands.

5.5.1 ▪ Flux surface labels

Under the fundamental assumption that the magnetic field has continuously nested flux surfaces throughout the domain of interest, discussed in Remark 4.4, certain physical quantities may be constant on flux surfaces. We will refer to such quantities as flux functions. For example, in practice, particles are mostly confined to flux surfaces; therefore, in some models, the temperature, density, and pressure are approximately flux functions.

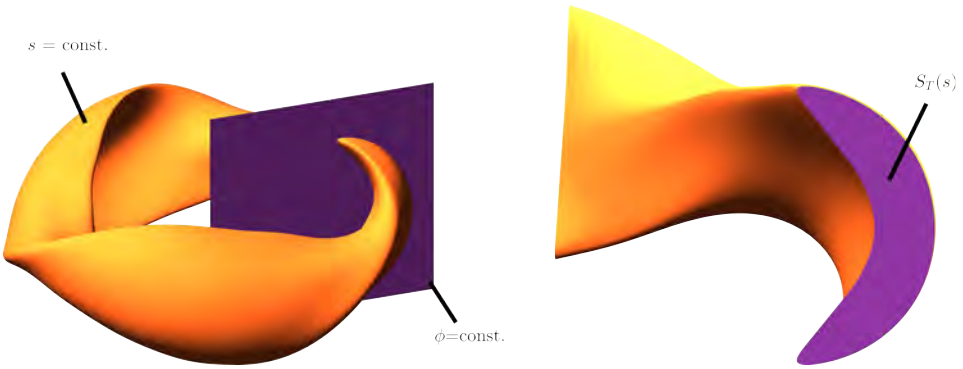

Figure 5.4*: The toroidal flux, $\Psi_T(s,\phi)$, is the magnetic flux through a surface at constant ϕ bounded by the surface labeled by s. This flux is independent of ϕ.*

Under this assumption, there is a unique magnetic axis within the domain of interest. Then a flux surface label, generally denoted by s, is a smooth one-to-one real-valued function defined on the set of flux surfaces and changes monotonically with the distance to the magnetic axis, either increasing or decreasing. In the stellarator literature, it is often assumed to vanish on the magnetic axis. A value of s can uniquely label each flux surface, so a flux surface label is, in particular, a flux function. We will introduce the two most natural examples of standard flux labels: the poloidal and toroidal fluxes.

Let ϕ be a value of the toroidal angle, s be a value of the flux surface label, and $S_T(s,\phi)$ be the section of the bounded volume delimited by the flux surface s in the poloidal surface ϕ, as illustrated in Figure 5.4. The toroidal flux, Ψ_T, of a given flux surface with flux label s, is the flux of magnetic field through $S_T(s,\phi)$. It can be expressed as

$$\Psi_T(s,\phi) = \int_{S_T(s,\phi)} \boldsymbol{B}(\boldsymbol{r}) \cdot \hat{\boldsymbol{n}}(\boldsymbol{r})\, d^2r, \tag{5.8}$$

where $\hat{\boldsymbol{n}}(\boldsymbol{r})$ is an oriented unit normal to the surface $S_T(s,\phi)$ at $\boldsymbol{r}$, and d^2r is the surface area element. Since any constant s surface is a magnetic flux surface, the magnetic field is tangent to these surfaces, in other words, $\boldsymbol{B}(\boldsymbol{r}) \cdot \hat{\boldsymbol{n}}(\boldsymbol{r}) = 0$ along these surfaces. Moreover, there are no sources or sinks of magnetic field since $\nabla \cdot \boldsymbol{B} = 0$. Therefore, for a given s, the flux Ψ_T is independent of ϕ. Indeed, we can integrate the divergence-free condition over a closed volume bounded by the constant s, $\phi = \phi_1$, and $\phi = \phi_2$ surfaces. Using the divergence theorem, the divergence-free condition implies that the total flux through the boundary must vanish. Since the constant s surface is a flux surface, the flux through each end must be equal in magnitude, or $\Psi_T(s,\phi_1) = \Psi_T(s,\phi_2)$.

Let θ be a poloidal angle. Similarly, the poloidal flux of a given flux surface, s, is the flux of the magnetic field through a surface at constant θ bounded between the magnetic axis and the constant s surface, denoted $S_P(s,\theta)$, as illustrated in Figure 5.5. It can be expressed as

$$\Psi_P(s,\theta) = \int_{S_P(s,\theta)} \boldsymbol{B}(\boldsymbol{r}) \cdot \hat{\boldsymbol{n}}(\boldsymbol{r})\, d^2r, \tag{5.9}$$

where $\hat{\boldsymbol{n}}(\boldsymbol{r})$ is an oriented unit normal to the surface S_P at $\boldsymbol{r}$. Again, since any constant s surface is a magnetic flux surface, then the magnetic field is tangent to these surfaces, in other words, $\boldsymbol{B}(\boldsymbol{r}) \cdot \hat{\boldsymbol{n}}(\boldsymbol{r}) = 0$ along these surfaces. Moreover, there are no sources or sinks of magnetic field since $\nabla \cdot \boldsymbol{B} = 0$. Therefore, following an argument similar to that for the toroidal flux, for a given s, the flux Ψ_P is independent of θ.

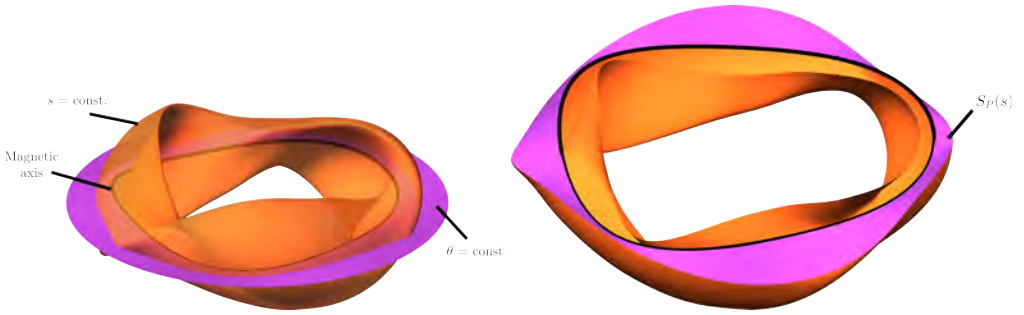

Figure 5.5: The poloidal flux, $\Psi_P(s,\theta)$, is the magnetic flux through a ribbon-like surface (pink) at constant θ bounded by the surface labeled by s (orange) and the magnetic axis (black). This flux is independent of θ.

Further discussion of flux functions can be found in Chapter 4 of [55].

5.5.2 ▪ Flux coordinates

Under the fundamental assumption that the magnetic field has continuously nested flux surfaces throughout the domain of interest, discussed in Remark 4.4, toroidal coordinate systems can be constructed using a flux label as the radius-like coordinate. These are known as flux coordinate systems. For a fixed value of the flux label, the other two coordinates describe the position on the corresponding flux surface. Here, as an illustration, we describe the particular choice of poloidal and toroidal angles.

Under this assumption, any toroidal domain of interest can be described by flux coordinates $(s,\theta,\phi) \in \mathbb{R}^+ \times [0,2\pi) \times [0,2\pi)$, where ϕ is a toroidal angle, θ is a poloidal angle, and s is a flux surface label. The label s is assumed to vanish on the magnetic axis and must be bounded. If the boundary of the domain of interest is a flux surface, then there is a fixed flux label value $s_0 > 0$ such that the boundary is the flux surface labeled by $s = s_0$. If not, the upper bound for s can depend on the angles. An example of nested toroidal surfaces with circular cross-sections is illustrated in Figure 5.7. It is important to underline that flux coordinate systems have a singularity at $s = 0$, along the magnetic axis, as θ is discontinuous across the axis in any toroidal plane, for constant ϕ, as illustrated in Figure 5.6.

Using any flux coordinates, the toroidal flux is expressed as

$$\Psi_T(s) = \int_0^s \int_0^{2\pi} \frac{\boldsymbol{B}\cdot\nabla\phi}{\nabla s\cdot\nabla\theta\times\nabla\phi}\left(\boldsymbol{R}(s',\theta,\phi_0)\right)\, d\theta ds', \tag{5.10}$$

where $\nabla\phi/|\nabla\phi|$ is a unit normal to the surface, the integral is taken over a surface S_T at constant ϕ_0 parameterized by $\{\boldsymbol{R}(s',\theta,\phi_0), s' \in [0,s], \theta \in [0,2\pi)\}$, and $|\nabla\phi|(\nabla s\cdot\nabla\theta\times\nabla\phi)^{-1}d\theta ds'$ is the surface area element. As $\boldsymbol{B}$ is tangent to the flux surface, the definition of the toroidal flux is independent of the choice of a surface S_T in the integral (5.10): the surface S_T can be any surface parameterized by $\boldsymbol{R}(s',\theta,\phi_0(s',\theta)), s' \in [0,s], \theta \in [0,2\pi)$, whose boundary is a closed poloidal curve. While flux coordinates can be used with any flux label, we will use the toroidal flux function $\psi = \Psi_T/(2\pi)$ as the flux surface label in this text. In a torus with circular cross-section surfaces centered about the same axis, as illustrated in Figure 5.7, a flux label is the minor radius, measuring the distance to the magnetic axis within a poloidal plane. Other examples of flux functions are described in Section 5.5.1. Similarly, several choices of the toroidal and poloidal angles can be made, as discussed in Chapter 9.

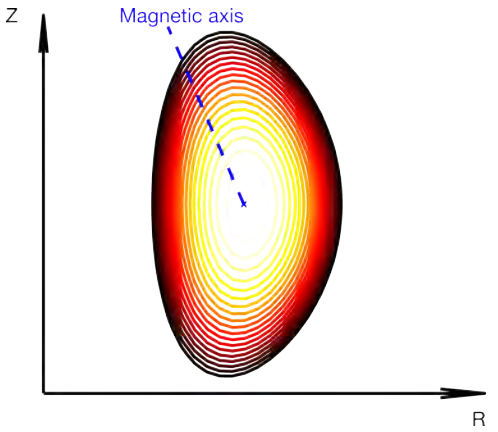

Figure 5.6: Poloidal angle θ and level curves of the flux label $\psi = \Psi_T/(2\pi)$ in a poloidal half-plane defined by a value of ϕ, with the color gradient indicating the change in ψ. In the poloidal plane, the magnetic axis is the point enclosed by all the flux surfaces.

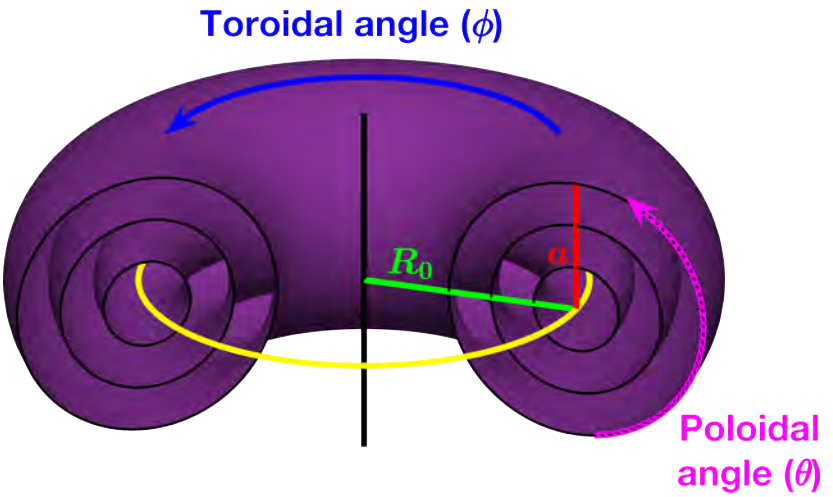

Figure 5.7: A flux coordinate system in a circular cross-section torus with circular cross-section surfaces centered about the same axis. Poloidal and toroidal angles describe the location on a flux surface. In this case, the magnetic axis (yellow) is the line enclosed by all nested surfaces and is a circle. The major radius, R_0, is the radius of this circle. A given point's minor radius, a, is the distance between the point and the magnetic axis within a poloidal plane defined by constant ϕ. Coordinates similar to (a, θ, ϕ) can be constructed for nonaxisymmetric systems, where a is a flux surface label.

For further reference, the poloidal flux is

$$\Psi_P(s) = \int_0^s \int_0^{2\pi} \frac{\boldsymbol{B} \cdot \nabla\theta}{\nabla s \cdot (\nabla\theta \times \nabla\phi)} \left(\boldsymbol{R}(s', \theta_0, \phi)\right) \, d\phi ds', \tag{5.11}$$

where $\nabla\theta/|\nabla\theta|$ is a unit normal, the integral is taken over a surface S_P at constant θ_0 parameterized by $\{\boldsymbol{R}(s', \theta_0, \phi), s' \in [0, s], \phi \in [0, 2\pi)\}$, and $|\nabla\theta|(\nabla s \cdot (\nabla\theta \times \nabla\phi))^{-1} d\phi ds'$ is the

surface area element. Similarly, the definition of the poloidal flux is independent of the choice of a surface S_P in the integral (5.11): the surface S_P can be any surface parameterized by $\boldsymbol{R}(s', \theta_0(s', \phi), \phi), s' \in [0, s], \phi \in [0, 2\pi)$, whose boundary is a closed toroidal curve.

Remark 5.2. *In the tokamak community, the poloidal flux function $\psi_P = \Psi_P/(2\pi)$ is commonly used, as discussed in Section* 7.1.

Remark 5.3. *We can relate the scale of these fluxes to the components of the magnetic field under the assumption of a torus with a circular toroidal cross-section with major radius R_0 and minor radius a. Given the toroidal magnetic field $B_T = \boldsymbol{B} \cdot \nabla\phi/|\nabla\phi|$, the toroidal flux scales as $\Psi_T \approx \pi a^2 B_T$. Likewise, if the poloidal magnetic field is $B_P = \boldsymbol{B} \cdot \nabla\theta/|\nabla\theta|$, then the poloidal flux scales as $\Psi_P \approx 2\pi R_0 a B_P$. In practice, B_T and B_P are not constant, but this provides a valid order of magnitude approximation.*

As flux coordinates are generally nonorthogonal, which was introduced in Section 5.4, the magnetic field can be expressed in its covariant form,

$$\begin{aligned}\boldsymbol{B}(\psi, \theta, \phi) = B_\psi(\psi, \theta, \phi)\nabla\psi(\boldsymbol{R}(\psi, \theta, \phi)) + B_\theta(\psi, \theta, \phi)\nabla\theta(\boldsymbol{R}(\psi, \theta, \phi)) \\ + B_\phi(\psi, \theta, \phi)\nabla\phi(\boldsymbol{R}(\psi, \theta, \phi)),\end{aligned}$$

and its contravariant form,

$$\boldsymbol{B}(\psi, \theta, \phi) = B^\theta(\psi, \theta, \phi)\frac{\partial \boldsymbol{R}(\psi, \theta, \phi)}{\partial\theta} + B^\phi(\psi, \theta, \phi)\frac{\partial \boldsymbol{R}(\psi, \theta, \phi)}{\partial\phi}.$$

This is the first example of simplification coming from the use of flux coordinates: the radial contravariant component of the magnetic field vanishes following the assumption that $\boldsymbol{B}\cdot\nabla\psi = 0$ and the dual property of the two bases. Note that it is not sufficient to fully describe the magnetic field by either the covariant or contravariant components, as the geometry of the flux surfaces must also be provided to define the basis vectors.

Chapter 6
Toroidal periodicity and differential equations

The physical motivation for toroidal geometry was introduced in Chapter 4, and there is a natural notion of periodicity in such geometries. Vector field–dependent toroidal coordinates, with two periodic angle-like variables, were then introduced in Chapter 5 under the fundamental assumption of continuously nested flux surfaces of the vector field, discussed in Remark 4.4. In this context, toroidal periodicity refers to the associated periodicity of physical quantities with respect to the two angles, either in two dimensions along a fixed flux surface or in three dimensions.

This chapter illustrates how to take advantage of this toroidal periodicity to derive useful expressions for the solutions to two particular differential equations that will play an essential role on several occasions in the rest of the book. These examples evidence the relevance of flux coordinates to obtain simplified formulations and, therefore, the importance of the assumption of continuously nested magnetic surfaces introduced in Remark 4.4.

The first example considers an equation often derived from a divergence-free condition. While this condition is standard in many applications of electromagnetism and fluid dynamics, the periodic setting will provide a convenient general expression of the two initial unknowns in terms of a single new unknown. The second example considers an equation describing transport along the field lines of a given magnetic field. The periodic setting will give rise to a necessary condition on the equation's right-hand side for the existence of solutions. The Fourier series solution will then be studied, including its standard form presented in the plasma physics literature. Further comments on field lines and periodicity will also be formulated.

6.1 ▪ Divergence-free-like equation

The first equation of interest may be derived, in appropriate coordinates, in two different ways: either from a divergence-free condition or to express that one component of the curl of a vector field vanishes. The unknowns are two functions, usually two components of a vector field denoted by F_1, F_2. They are assumed to be smooth, and the equation reads

$$\frac{\partial F_1}{\partial x^1} + \frac{\partial F_2}{\partial x^2} = 0 \tag{6.1}$$

in a coordinate system $\left(x^0, x^1, x^2\right)$. We will first comment on the PDE itself and then comment on periodicity aspects.

Finding the components F_1, F_2 satisfying this condition is not a well-posed problem, as many pairs of solutions exist. Nonetheless, the condition can be leveraged to express a simplified relationship between the two unknowns in terms of a single function, as follows. We will see

that there exists a function v such that

$$\begin{cases} F_1 = \dfrac{\partial v}{\partial x^2}, \\ F_2 = -\dfrac{\partial v}{\partial x^1}. \end{cases} \tag{6.2}$$

This function v can be referred to as a stream function and can be used to recast the vector field in terms of only one function of three variables. Moreover, assuming that the functions F_1 and F_2 are periodic with respect to $\left(x^1, x^2\right)$, this function v will be the sum of a periodic term and linear terms with respect to x^1 and x^2.

This equation will come into play in the context of magnetic coordinates in Chapter 9 to study the magnetic field both under its contravariant form in Section 9.1.1 and under its covariant form in Section 9.1.2. The variable x^0 will then be a flux label, while the variables x^1, x^2 will be poloidal and toroidal angles, so the field will then be periodic with respect to the two angles. In Sections 7.1, 10.3.4, and 13.4.4, the divergence condition arises in a 2D setting, where no variable x^0 exists, so the functions depending only on x^0 are constant.

6.1.1 ▪ Existence

Given two functions F_1 and F_2 satisfying (6.1), we now prove the existence of a function v satisfying (6.2). On the one hand, it is clear that, given any function f of two variables, any function

$$v\left(x^0, x^1, x^2\right) := f\left(x^0, x^1\right) + \int_0^{x^2} F_1\left(x^0, x^1, \widetilde{x}^2\right)\, d\widetilde{x}^2$$

necessarily satisfies

$$\frac{\partial v\left(x^0, x^1, x^2\right)}{\partial x^2} = F_1\left(x^0, x^1, x^2\right).$$

On the other hand, any such function v also satisfies

$$\begin{aligned} \frac{\partial v\left(x^0, x^1, x^2\right)}{\partial x^1} &= \frac{\partial f\left(x^0, x^1\right)}{\partial x^1} + \int_0^{x^2} \frac{\partial F_1\left(x^0, x^1, \widetilde{x}^2\right)}{\partial x^1}\, d\widetilde{x}^2 \\ &= \frac{\partial f\left(x^0, x^1\right)}{\partial x^1} - \int_0^{x^2} \frac{\partial F_2\left(x^0, x^1, \widetilde{x}^2\right)}{\partial \widetilde{x}^2}\, d\widetilde{x}^2 \text{ from (6.1)} \\ &= \frac{\partial f\left(x^0, x^1\right)}{\partial x^1} - F_2\left(x^0, x^1, x^2\right) + F_2\left(x^0, x^1, 0\right). \end{aligned}$$

In particular, if we choose $f\left(x^0, x^1\right) := C\left(x^0\right) - \int_0^{x^1} F_2\left(x^0, \widetilde{x}^1, 0\right)\, d\widetilde{x}^1$ for any function C of one variable, then the corresponding function

$$v\left(x^0, x^1, x^2\right) := C\left(x^0\right) - \int_0^{x^1} F_2\left(x^0, \widetilde{x}^1, 0\right)\, d\widetilde{x}^1 + \int_0^{x^2} F_1\left(x^0, x^1, \widetilde{x}^2\right)\, d\widetilde{x}^2$$

satisfies the desired property (6.2) under the assumption (6.1). There is no unique function v satisfying this property since it is not affected by the choice of the function $C(x^0)$.

6.1.2 ▪ Periodic setting

In toroidal geometry, the functions F_1 and F_2 might be periodic with respect to $\left(x^1, x^2\right)$. We will now see that periodicity provides more details about the function v, as discussed in [55].

If F_1 and F_2 are assumed to be 2π-periodic with respect to the two variables $\left(x^1, x^2\right)$, then the derivatives of v satisfying (6.2) must be periodic as well. However, v itself is not necessarily periodic. Instead, v can be decomposed into the sum of a periodic term and a nonperiodic term, with the latter term's derivatives being periodic. In other words, there exists a function v_p periodic in $\left(x^1, x^2\right)$, and two functions f_1, f_2 of the variable x^0, such that

$$v\left(x^0, x^1, x^2\right) = f_1\left(x^0\right) x^1 + f_2\left(x^0\right) x^2 + v_p\left(x^0, x^1, x^2\right),$$

satisfies (6.1)–(6.2).

The following statement summarizes the previous discussion:

> If periodic functions F_1, F_2 satisfy $\dfrac{\partial F_1}{\partial x^1} + \dfrac{\partial F_2}{\partial x^2} = 0$,
> there exists v_p periodic in $\left(x^1, x^2\right)$ and f_1, f_2 functions of x^0 such that
> v defined by $v\left(x^0, x^1, x^2\right) = f_1\left(x^0\right) x^1 + f_2\left(x^0\right) x^2 + v_p\left(x^0, x^1, x^2\right)$
> satisfies $F_1 = \dfrac{\partial v}{\partial x^2}$ and $F_2 = -\dfrac{\partial v}{\partial x^1}$.

In this context, v satisfies

$$\begin{cases} \dfrac{\partial v}{\partial x^1}\left(x^0, x^1, x^2\right) = f_1\left(x^0\right) + \dfrac{\partial v_p}{\partial x^1}\left(x^0, x^1, x^2\right), \\ \dfrac{\partial v}{\partial x^2}\left(x^0, x^1, x^2\right) = f_2\left(x^0\right) + \dfrac{\partial v_p}{\partial x^2}\left(x^0, x^1, x^2\right). \end{cases}$$

This indeed implies that

$$\frac{\partial}{\partial x^1}\left(\frac{\partial v}{\partial x^2}\right) + \frac{\partial}{\partial x^2}\left(-\frac{\partial v}{\partial x^1}\right) = 0$$

for any functions f_1, f_2, and independently of adding any function of x^0 to v_p. Hence, neither of the functions f_1, f_2 nor v_p is unique.

6.2 ▪ Magnetic differential equation

The second equation of interest is a formulation of the so-called magnetic differential equation (MDE). The prototype of this equation was introduced in [170]. For given field $\boldsymbol{B}$ and scalar function F, it has the general form

$$\boldsymbol{B} \cdot \nabla u = F, \tag{6.3}$$

where u is the unknown. We assume the existence of closed flux surfaces and focus here on the interpretation of this equation expressed in some appropriate flux coordinates. For clarity, we will first ignore the radius-like variable and focus on a 2D periodic domain $(0, 2\pi)^2$.

Using a particular choice of flux coordinates[11] $\left(\psi, x^1, x^2\right)$, a simple rescaling of (6.3), multiplying by the Jacobian $\sqrt{g}$, simplifies the problem at hand. Considering a periodic function f of two variables, equal to $\sqrt{g}F$, and a real number $\iota \neq 0$,[12] the problem is the following:

$$\begin{aligned} &\text{Find a periodic function } u \text{ such that} \\ &\iota \frac{\partial u}{\partial x^1} + \frac{\partial u}{\partial x^2} = f. \end{aligned} \tag{6.4}$$

[11] These appropriate coordinates are the so-called magnetic coordinates introduced in Chapter 9.

[12] This real number is the so-called rotational transform introduced in Section 7.3.

The solution is not unique since, given any solution u, the sum of u and any constant defines another solution. Beyond the nonuniqueness, the differential operator has fundamental properties related to magnetic field lines in the periodic setting that will be central to the upcoming discussion.

The MDE will come into play in the context of 3D equilibrium fields in Sections 10.2.3 and 10.3.1. It also comes into play in the context of Boozer coordinates in Section 9.2.3, although it will be derived differently there.

6.2.1 ▪ Periodic setting

There is a necessary condition for the existence of periodic solutions to problem (6.4), and this section is dedicated to proving this condition. However, it is not always a sufficient condition: while it is sufficient for ι irrational, it is not sufficient if ι is rational. These conditions are related to the fundamental properties of the differential operator, as we will now see.

For any periodic function u, the average with respect to $\left(x^1, x^2\right)$ equals zero, namely

$$\int_{(0,2\pi)^2} \iota \frac{\partial u\left(x^1, x^2\right)}{\partial x^1} + \frac{\partial u\left(x^1, x^2\right)}{\partial x^2}\, dx^1 dx^2 = 0.$$

Therefore, for a solution to problem (6.4) to exist, it is necessary for the average of the right-hand side f with respect to $\left(x^1, x^2\right)$ to vanish. A necessary condition for the existence of periodic solutions is then

$$\int_0^{2\pi} \int_0^{2\pi} f\left(x^1, x^2\right)\, dx^1 dx^2 = 0. \tag{6.5}$$

The differential operator $\iota\partial/\partial x^1 + \partial/\partial x^2$ has another important property. Along any parameterized curve $s \mapsto \left(x_P^1(s), x_P^2(s)\right)$ in the x^1-x^2 plane, consider any function u of two variables evaluated along the curve as the function $s \mapsto u\left(x_P^1(s), x_P^2(s)\right)$. Then, the derivative of this function is

$$\frac{d}{ds}\left[u\left(x_P^1(s), x_P^2(s)\right)\right] = {x_P^1}'(s) \frac{\partial u\left(x_P^1(s), x_P^2(s)\right)}{\partial x^1} + {x_P^2}'(s) \frac{\partial u\left(x_P^1(s), x_P^2(s)\right)}{\partial x^2}.$$

So, if the curve is such that

$$\begin{cases} {x_P^1}'(s) = \iota, \\ {x_P^2}'(s) = 1, \end{cases} \tag{6.6}$$

then any function u satisfies

$$\frac{d}{ds}\left[u\left(x_P^1(s), x_P^2(s)\right)\right] = \iota \frac{\partial u\left(x_P^1(s), x_P^2(s)\right)}{\partial x^1} + \frac{\partial u\left(x_P^1(s), x_P^2(s)\right)}{\partial x^2}. \tag{6.7}$$

In particular, along any curve satisfying (6.6), any solution u to problem (6.4) satisfies

$$\frac{d}{ds}\left[u\left(x_P^1(s), x_P^2(s)\right)\right] = f\left(x_P^1(s), x_P^2(s)\right). \tag{6.8}$$

In other words, along each of the parallel straight lines $s \mapsto \left(x_P^1(s), x_P^2(s)\right)$ satisfying (6.6), the governing equation reduces to an ordinary differential equation, namely

$$y'(s) = f\left(x_P^1(s), x_P^2(s)\right)$$

for the unknown $y(s) := u\left(x_P^1(s), x_P^2(s)\right)$. Such curves are called characteristics in the theory of hyperbolic partial differential equations [70].

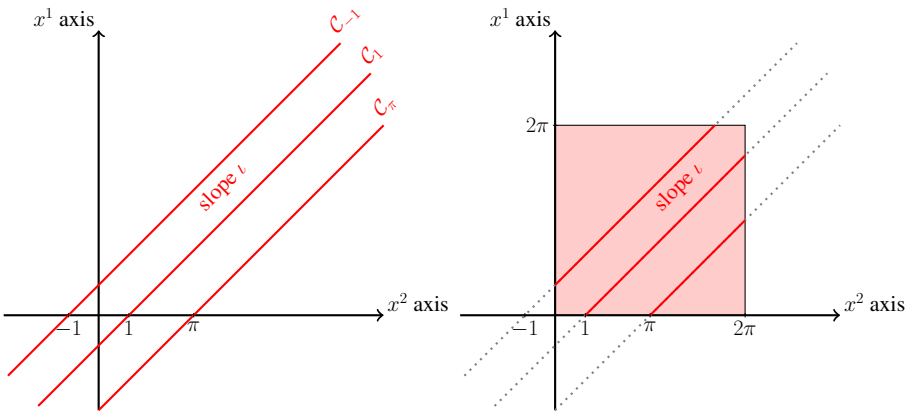

Figure 6.1*: Three characteristic curves, $\mathcal{C}_\sigma$, represented in the x^2-x^1 plane for $\sigma \in \{1, -1, \pi\}$. Comparison of the nonperiodic (left) and periodic (right) settings. The periodic domain $(0, 2\pi)^2$ is represented in light red.*

For the differential operator $\iota\partial/\partial x^1 + \partial/\partial x^2$, characteristics are lines of slope ι in the x^2-x^1 plane. They can be labeled by a parameter $\sigma = x^2 - x^1/\iota$.[13] The characteristic $\mathcal{C}_\sigma$ passing through the point $(0, \sigma)$ can be explicitly described as

$$\begin{cases} x^1_\sigma(s) = \iota s, \\ x^2_\sigma(s) = s + \sigma. \end{cases}$$

This is illustrated in Figure 6.1. Here σ represents the value of x^2 when $x^1 = 0$. In the nonperiodic setting, they are infinite lines. In the periodic setting, the definition has to be interpreted modulo 2π, and two situations can occur according to whether the parameter ι is rational or not. Figure 6.2 illustrates both the periodic setting and the nonperiodic setting. More precisely,

- if ι is irrational, then the characteristics are also infinite periodic lines;
- if ι is rational, then the characteristics are closed curves.

Indeed, in the rational case, ι being represented by the irreducible fraction $\iota = N/D$,[14] for some N and D in $\mathbb{N}$, each characteristic $\mathcal{C}_\sigma$ wraps around the periodic domain since

$$\begin{cases} x^1_\sigma(s) = \iota s \bmod 2\pi, \\ x^2_\sigma(s) = s + \sigma \bmod 2\pi. \end{cases}$$

Starting at $s = 0$ from the point $\big(x^1_\sigma(0), x^2_\sigma(0)\big) = (0, \sigma)$, each characteristic wraps around the domain N times in the x^1 direction and D times in the x^2 direction before it closes onto itself, as $s_D = 2\pi D$ is the smallest nonzero value of s along the characteristic such that

$$\begin{cases} x^1_\sigma(s_D) = 0 \bmod 2\pi, \\ x^2_\sigma(s_D) = \sigma \bmod 2\pi. \end{cases}$$

[13] There is no unique choice of a field-line label, as any real multiple of this label also defines a label. For instance, $\alpha = x^1 - \iota x^2$ will be used in Section 6.2.4.

[14] In stellarators and tokamaks, the values of ι do not change sign within the confinement domain. Consequently, we assume that the toroidal coordinate system is oriented so that $\iota > 0$.

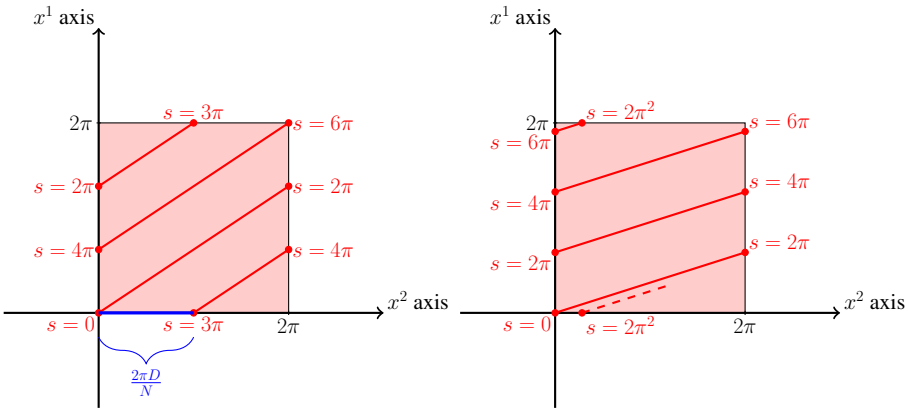

Figure 6.2: The characteristic $\mathcal{C}_0$ represented in the x^2-x^1 plane for $\iota = 2/3$ (left) and $\iota = 1/\pi$ (right). In the rational case, the characteristic is closed and parameterized by $s \in (0, s_D)$. The interval of characteristic label, $(0, 2\pi D/N \bmod 2\pi)$, is represented in blue along the x^2 axis. In the irrational case, since the characteristic is infinite, only the part corresponding to $s \in (0, s_D)$ is represented, while the dashed line represents a part corresponding to $s \geq s_D$. The periodic domain $(0, 2\pi)^2$ is represented in light red, and the values of the parameter $s \in (0, s_D)$ are indicated where the characteristic reaches a boundary of the periodic domain.

Moreover, in this case, the characteristics can be labeled by $\sigma \in (0, 2\pi D/N \bmod 2\pi)$. Then, from the property (6.7) of the differential operator, for any periodic function u, it is straightforward to verify that along any characteristics $\mathcal{C}_\sigma$, u satisfies

$$\int_0^{2\pi D} \left(\iota \frac{\partial u\left(x_\sigma^1(s), x_\sigma^2(s)\right)}{\partial x^1} + \frac{\partial u\left(x_\sigma^1(s), x_\sigma^2(s)\right)}{\partial x^2} \right) ds = 0.$$

So, a necessary condition for the existence of a solution to (6.8) along a characteristic is

$$\int_0^{2\pi D} f\left(x_\sigma^1(s), x_\sigma^2(s)\right) ds = 0.$$

Therefore, for the existence of a solution to problem (6.4) for ι rational, the integral of the right-hand side must vanish along each closed characteristic, that is,

$$\forall \sigma \in (0, 2\pi D/N \bmod 2\pi), \quad \int_0^{2\pi D} f(\iota s, s + \sigma)\, ds = 0. \tag{6.9}$$

In the irrational case, however, since the characteristics are not closed, periodicity does not require any condition along characteristics.

Moreover, in the rational case, any function f satisfying (6.9) on each characteristic necessarily satisfies the average condition (6.5). To prove this, we leverage the change of variables $\left(x^1, x^2\right) = (\iota s, s + \sigma)$, between the sets $\{(s, \sigma) \in (0, 2\pi D) \times (0, 2\pi D/N \bmod 2\pi)\}$ and $\{\left(x^1, x^2\right) \in (0, 2\pi)^2\}$. Note that this change of variables is well-defined since the corresponding Jacobian, ι, is constant and, therefore, different from zero on the entire domain. As a matter of fact, given any function f, the change of variable yields directly

$$\int_0^{2\pi} \int_0^{2\pi} f\left(x^1, x^2\right) dx^1 dx^2 = \iota \int_0^{2\pi/N} \left(\int_0^{2\pi D} f(\iota s, s + \sigma)\, ds \right) d\sigma.$$

This proves the claim.

In conclusion, we have found a necessary condition for the existence of periodic solutions to problem (6.4). In order to study solutions to this problem, we will assume that this condition is satisfied. Hence, for further reference, we define the following assumption:

$$\begin{cases} \displaystyle\int_0^{2\pi D} f(\iota s, s+\sigma)\, ds = 0 \ \forall \sigma \in (0, 2\pi/N) & \text{if } \iota \in \mathbb{Q}, \iota = \frac{N}{D} \text{ (irreducible fraction)}, \\ \displaystyle\int_0^{2\pi}\int_0^{2\pi} f\left(x^1, x^2\right)\, dx^1 dx^2 = 0 & \text{if } \iota \in \mathbb{R}\backslash\mathbb{Q}. \end{cases} \tag{6.10}$$

Beyond this chapter, this assumption will be examined in the given context of various applications, specifically regarding physical interpretation.

6.2.2 ▪ Fourier series solution

Taking advantage of the periodic setting, an integrable solution can be sought in the form of a Fourier series. To do so, we assume that the right-hand side f is integrable and that its Fourier series can be integrated term by term. The unknown u is integrable, and its Fourier series can be differentiated term by term.

First, in the Fourier series context, we interpret assumption (6.10) for the right-hand side f. We write the Fourier expansion of the doubly periodic right-hand side f as

$$f\left(x^1, x^2\right) = \sum_{(m,n)\in\mathbb{Z}^2} b_{m,n} e^{i(mx^1 - nx^2)},$$

with complex Fourier coefficients $\{b_{m,n}\}_{(m,n)\in\mathbb{Z}^2}$. Since f is assumed to be integrable, the Fourier series converges. In this context, assumption (6.10) can naturally be interpreted in terms of Fourier coefficients $b_{m,n}$ of f. As a matter of fact, for ι both rational and irrational, the assumption can be expressed by leveraging term-by-term integration:

- for ι irrational,

$$\int_0^{2\pi}\int_0^{2\pi} f\left(x^1, x^2\right)\, dx^1 dx^2 = \sum_{(m,n)\in\mathbb{Z}^2} b_{m,n} \left(\underbrace{\int_0^{2\pi} e^{imx^1}\, dx^1}_{=2\pi\delta(m)}\right)\left(\underbrace{\int_0^{2\pi} e^{-inx^2}\, dx^2}_{=2\pi\delta(n)}\right),$$

- while for $\iota = \frac{N}{D}$ (irreducible fraction) and any $\sigma \in \left(0, \frac{2\pi D}{N} \bmod 2\pi\right)$,

$$\int_0^{2\pi D} f(\iota s, s+\sigma)\, ds \quad = \sum_{(m,n)\in\mathbb{Z}^2} b_{m,n} \left(\underbrace{\int_0^{2\pi D} e^{i(m\iota - n)s}\, ds}_{2\pi D\delta(n-\iota m)}\right) e^{-in\sigma},$$

where δ is the Dirac-δ function. Therefore, in the Fourier setting, assumption (6.10) is equivalent to

$$\begin{cases} b_{m,n} = 0 \ \forall (m,n) \in \mathbb{Z}^2 \text{ such that } m\iota = n & \text{if } \iota \in \mathbb{Q}, \\ b_{0,0} = 0 & \text{if } \iota \in \mathbb{R}\backslash\mathbb{Q}. \end{cases}$$

This can be equivalently stated, independently of whether ι is rational or not, as the following assumption:

$$\boxed{b_{m,n} = 0 \ \forall (m,n) \in \mathbb{Z}^2 \text{ such that } m\iota = n.} \tag{6.11}$$

We then seek the solution u as a Fourier series

$$u\left(x^1, x^2\right) = \mathcal{K} + \sum_{(m,n)\in\mathbb{Z}^2\backslash\{(0,0)\}} a_{m,n} e^{i\left(mx^1 - nx^2\right)}.$$

Since the solution is assumed to be differentiable term by term, formally

$$\iota \frac{\partial u\left(x^1, x^2\right)}{\partial x^1} + \frac{\partial u\left(x^1, x^2\right)}{\partial x^2} = \sum_{(m,n)\in\mathbb{Z}^2\backslash\{(0,0)\}} i(\iota m - n) a_{m,n} e^{i\left(mx^1 - nx^2\right)}.$$

Hence, for such a u to satisfy the governing equation, the necessary conditions are

$$b_{0,0} = 0,$$

$$\forall (m,n) \in \mathbb{Z}^2\backslash\{(0,0)\},\ a_{m,n} i(\iota m - n) = b_{m,n}. \tag{6.12}$$

For convenience we will denote by $\mathcal{S}_0$ the set of indices $(m,n) \in \mathbb{Z}^2$ such that m and n are not both zero and $\iota m - n = 0$, so $\mathcal{S}_0 = \{(m,n) \in \mathbb{Z}^2\backslash\{(0,0)\}$ such that $n/m = \iota\}$. For any $(m,n) \in \mathcal{S}_0$, (6.12) reduces to a condition on the right-hand side of the governing equation, namely $b_{m,n} = 0$. Here, again, two situations can occur depending on the value of ι.

- When ι is irrational, $\mathcal{S}_0$ is empty, and the only condition on the right-hand side is $b_{0,0} = 0$.
- When ι is rational, $\mathcal{S}_0$ is not empty, and (6.12) implies for all $(m,n) \in \mathcal{S}_0$ the condition $b_{m,n} = 0$ in addition to the condition $b_{0,0} = 0$.

These two situations are unsurprising: they are precisely summarized by assumption (6.11). Correspondingly, depending on the value of ι, two situations can occur in terms of the solution u.

- When ι is irrational, under the necessary condition $b_{0,0} = 0$ on the right-hand side, (6.12) uniquely defines the set of coefficients with indices in $\mathbb{Z}^2\backslash\{(0,0)\}$,

  $$a_{m,n} = \frac{i b_{m,n}}{n - \iota m} \forall (m,n) \in \mathbb{Z}^2\backslash\{(0,0)\},$$

  while the constant coefficient $\mathcal{K}$ is free.
- When ι is rational, under the necessary conditions $b_{m,n} = 0$ for all $(m,n) \in \{(0,0)\} \cup \mathcal{S}_0$, (6.12) uniquely defines the set of coefficients with indices in $\mathbb{Z}^2\backslash\{(0,0)\}$ that are not in $\mathcal{S}_0$,

  $$a_{m,n} = \frac{i b_{m,n}}{n - \iota m} \forall (m,n) \in \mathbb{Z}^2 \text{ with } \iota m \neq n,$$

  while the coefficients $\{a_{m,n}, (m,n) \in \mathcal{S}_0\}$ as well as $\mathcal{K}$ are free.

There is at least one free parameter in any case, namely $\mathcal{K}$, and free parameters reflect the fact that the solution is not unique. Here, the solution is never unique, as was already mentioned just after the statement of the governing equation (6.4).

In both cases, formally, under assumption (6.11) on the right-hand side, the general Fourier solution u is usually written in the magnetic confinement literature in terms of free parameters $\mathcal{K}$ and Δ_{mn} as

$$u\left(x^1, x^2\right) = \mathcal{K} + \sum_{(m,n)\in\mathbb{Z}^2\backslash\{(0,0)\}} \left(\frac{i}{n - \iota m} b_{m,n} + \Delta_{m,n} \delta(n - \iota m) \right) e^{i\left(mx^1 - nx^2\right)}, \tag{6.13}$$

and the $\Delta_{m,n}$ terms only play a role in the rational case. This expression can be confusing as the denominator $n - \iota m$ vanishes for infinitely many indices $(m, n) \in \mathbb{Z}^2 \backslash \{(0, 0)\}$; however, it is implicit that for these indices the numerator $b_{m,n}$ is assumed to be zero and the corresponding term in the sum is considered to be zero. A more rigorous formulation would read

$$u\left(x^1, x^2\right) = \mathcal{K} + \sum_{(m,n)\in\mathbb{Z}^2, n\neq\iota m} \frac{i}{n - \iota m} b_{m,n} e^{i\left(mx^1 - nx^2\right)} + \sum_{(m,n)\in\mathcal{S}_0} \Delta_{m,n} e^{i\left(mx^1 - nx^2\right)}. \tag{6.14}$$

It is crucial to understand that these last two formulas are only formal. In order to prove convergence and justify the term-by-term differentiation, thereby proving the existence of a solution, one has to study properties of the right-hand side f's Fourier coefficients, $b_{m,n}$, as well as the set of free parameters uniquely defining the Fourier solution, namely

$$\{\mathcal{K}\} \cup \{\Delta_{m,n}, (m, n) \in \mathbb{Z}^2, \iota = n/m\}. \tag{6.15}$$

Remark 6.1. *Approximation properties of real numbers by rational numbers come into play in this context: given any real number ι, the quantity $n - \iota m$ gets arbitrarily small for infinitely many indices $(m, n) \in \mathbb{Z}^2$. This is related to Hurwitz's theorem, stating that for all $\iota \in \mathbb{R}\backslash\mathbb{Q}$, there exist infinitely many $n/m \in \mathbb{Q}$ such that $|\iota - n/m| \leq 1/\left(\sqrt{5}m^2\right)$.*

In the perturbation theory of classical mechanics, the so-called problem of small divisors is concerned with the fact that this quantity $n - \iota m$ appears in the denominator of a series. More can be found about this in [164, 316].

In terms of convergence of the Fourier solution, in the first series in (6.14) *there is a competition between the numerator $b_{m,n}$ and the denominator $n - \iota m$. The convergence of this series depends not only on properties of the right-hand side f's Fourier coefficients but also on the value of ι.*

In terms of numerical computation of the Fourier solution, only finite sums—corresponding to truncated series—can be computed. While the quantity $m\iota - n$ gets arbitrarily small in the series terms, it can be small in truncated sums. This can be a source of accumulated error when performing divisions by these small denominators in finite precision arithmetic. In particular, if ι is irrational and well approximated by n/m with small values of $|m|$, $|n|$, this can affect the accuracy of numerical solutions [12]. *Such fractions are referred to as low-order rationals in the literature.*

6.2.3 ▪ An interpretation of the free parameters

In the rational case, the free parameters (6.15) in the formal Fourier solution (6.13) can then be interpreted formally in the context of characteristics. This is the topic of this section, and it will be done by comparing, along a characteristic, the solutions obtained from the method of characteristics and the Fourier method, respectively.

As already mentioned, along any characteristic curve $\mathcal{C}_\sigma$, the governing equation reduces to an ordinary differential equation. More precisely, this ordinary differential equation for the unknown y_σ, defined earlier as the unknown u along the characteristic, or $y_\sigma(s) := u\left(x^1_\sigma(s), x^2_\sigma(s)\right)$, reads

$$\frac{dy_\sigma(s)}{ds} = f(\iota s, s + \sigma).$$

The method of characteristics considers values of the solution u separately along each characteristic as a solution to this ordinary differential equation. Unlike the Fourier method, this

method does not require any assumption of integrability of the solution u across characteristics. Along a characteristic $\mathcal{C}_\sigma$, the general form of solution—with respect to the reference point $\big(x^1_\sigma(0), x^2_\sigma(0)\big) = (0, \sigma)$—reads

$$y_\sigma(s) = y_\sigma(0) + \int_0^s f\big(\iota\tilde{s}, \tilde{s} + \sigma\big)\, d\tilde{s}. \tag{6.16}$$

Under assumption (6.9) on the right-hand side f, the solution along each characteristic is unique for any given initial condition $y_\sigma(0)$, and this solution has $\mathcal{C}^1$ regularity with respect to s if f is continuous along the characteristic. Here assumption (6.9) ensures that y_σ is $2\pi D$ periodic. However, the solution is not necessarily continuous across characteristics, and the periodic setting of the two-dimensional problem will now lead to further considerations.

As discussed in Section 6.2.1, the domain can be described in terms of a set of closed characteristics. Each point in the periodic domain lies on a unique characteristic. In this case, in order to uniquely define a solution to (6.4) at each point $\big(x^1, x^2\big)$ in the periodic domain, it is then sufficient to define uniquely a solution (6.16) on each characteristic by providing one initial condition per closed characteristic, namely, the value of $y_\sigma(0)$. Providing one value per characteristic corresponds to providing a function of the characteristic label σ, hereafter denoted h. Then, even though there is no unique solution to (6.4), there is a unique solution to (6.4) satisfying the condition $u(0, \sigma) = h(\sigma)$. In other words, under assumption (6.9) on the right-hand side f, given ι represented by the irreducible fraction $\iota = N/D$, for some N and D in $\mathbb{N}$, and given any function $h : (0, 2\pi D/N \bmod 2\pi) \to \mathbb{C}$, the following problem has a unique solution:

$$\begin{aligned} &\text{Find a periodic function } u \text{ such that} \\ &\iota\frac{\partial u}{\partial x^1} + \frac{\partial u}{\partial x^2} = f \text{ on } (0, 2\pi)^2, \\ &u(0, \sigma) = h(\sigma)\ \forall \sigma \in (0, 2\pi D/N \bmod 2\pi). \end{aligned} \tag{6.17}$$

This solution is given along each characteristic $\mathcal{C}_\sigma$ by

$$\forall s \in (0, 2\pi D),\ u\left(x^1_\sigma(s), x^2_\sigma(s)\right) = h(\sigma) + \int_0^s f\big(\iota\tilde{s}, \tilde{s} + \sigma\big)\, d\tilde{s}. \tag{6.18}$$

Remark 6.2. *The value of the solution u at a given point $(b, a) \in (0, 2\pi)^2$ can be obtained as follows. First, compute the label $\sigma_{(a,b)}$ of the characteristic passing through the point, using the formula $\sigma_{(a,b)} = a - b/\iota \bmod 2\pi/N$. In the x^2-x^1 plane represented in Figure* 6.3*, this corresponds to tracing back, starting from (a, b), the periodic line of slope ι until it intersects the horizontal axis, precisely at the point $\big(\sigma_{(a,b)}, 0\big)$ in the x^2-x^1 plane. Second, find the value of $s_{(a,b)} \in (0, 2\pi D)$ such that $\big(x^1_{\sigma_{(a,b)}}\big(s_{(a,b)}\big), x^2_{\sigma_{(a,b)}}\big(s_{(a,b)}\big)\big) = (b, a)$, using the formula $s = b/\iota$. In Figure* 6.3 *this corresponds to the distance between the points $(a - b/\iota, 0)$ and $(a, 0)$ in the x^2-x^1 plane. Finally, the value of the solution u at the given point (a, b) in the x^2-x^1 plane can be obtained as $u\big(x^1_{\sigma_{(a,b)}}\big(s_{(a,b)}\big), x^2_{\sigma_{(a,b)}}\big(s_{(a,b)}\big)\big)$ from* (6.18)*.*

Here, there is no smoothness restriction on the initial condition h. The solution u is smooth along each characteristic but not necessarily across characteristics, depending on the smoothness of h and f. For comparison with (6.18), we can then evaluate the Fourier solution u in (6.13) at any point $\big(x^1_\sigma(s), x^2_\sigma(s)\big)$ along a characteristic $\mathcal{C}_\sigma$, namely evaluate $u\left(x^1_\sigma(s), x^2_\sigma(s)\right)$, and identify two terms: on the one hand, the f-dependent term is

$$\sum_{(m,n)\in\mathbb{Z}^2, n\neq\iota m} \frac{i}{n - \iota m} b_{m,n} e^{i\left(m x^1_\sigma(s) - n x^2_\sigma(s)\right)} = \int_0^s f\big(\iota\tilde{s}, \tilde{s} + \sigma\big)\, d\tilde{s}; \tag{6.19}$$

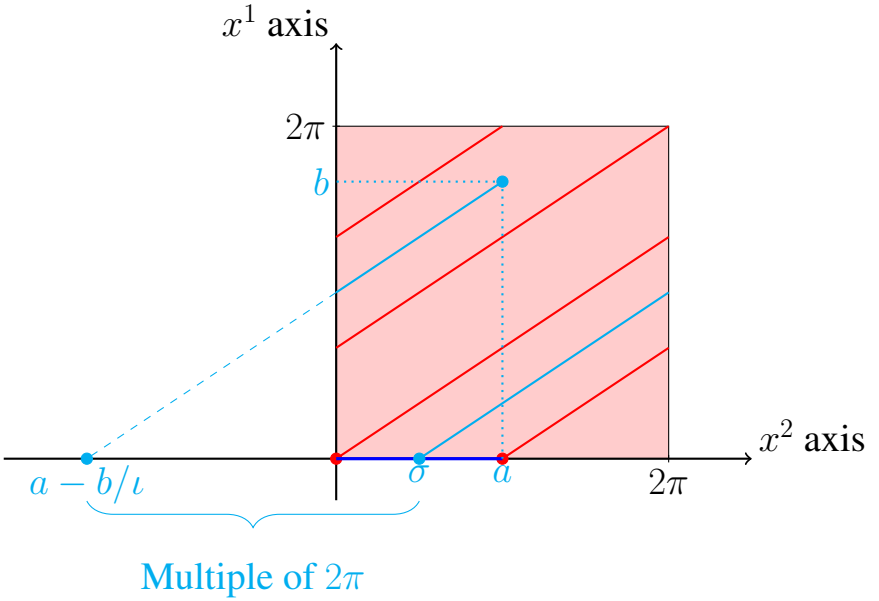

Figure 6.3: The closed characteristic $\mathcal{C}_0$ is represented in red in the x^2-x^1 plane, for $\iota = 2/3$ as in the left panel of Figure 6.2. The interval of the characteristic label, $(0, 2\pi D/N \text{ mod } 2\pi)$, is represented in blue along the x^2 axis. A given point $(a, b) \in (0, 2\pi)^2$ and the characteristic $\mathcal{C}_\sigma$ going through this point, labeled by $\sigma = a - b/\iota \text{ mod } 2\pi$, are represented in cyan.

on the other hand, the f-independent term is

$$\begin{aligned}&\mathcal{K} + \sum_{(m,n)\in\mathbb{Z}^2\setminus\{(0,0)\}} \Delta_{m,n}\delta(n-\iota m)e^{i\left(mx^1_\sigma(s)-nx^2_\sigma(s)\right)}\\ &= \mathcal{K} + \sum_{(m,n)\in\mathbb{Z}^2\setminus\{(0,0)\}} \Delta_{m,n}\delta(n-\iota m)e^{i(s(\iota m-n)-n\sigma)}.\end{aligned}$$

Remark 6.3. *The set of indices $\mathcal{T} = \mathcal{S}_0 \cup \{(0,0)\}$, that is, $\mathcal{T} = \{(m,n) \in \mathbb{Z}^2, n - \iota m\}$, plays an important role here. Indeed, in the previous sum, any term corresponding to a pair $(m,n) \notin \mathcal{T}$ is zero because then $\delta(n-\iota m) = 0$. The set $\mathcal{T}$ can be expressed differently for convenience, thanks to the following statements. For any $(m,n) \in \mathcal{T}$, $n/m = N/D$ and, equivalently, $nD = mN$. Hence, since D and N have no other common divisors than 1, n is divisible by N, and m is divisible by D. So, the quantity $n/N = m/D$ is a unique integer. Conversely, for any integer p, the pair (pD, pN) belongs to $\mathcal{T}$.*

As a consequence we can write $\mathcal{T} = \{(pD, pN), p \in \mathbb{Z}\}$. This can then be leveraged to conveniently rewrite the f-independent term above.

The f-independent term can then be written as

$$\begin{aligned}&\mathcal{K} + \sum_{(m,n)\in\mathbb{Z}^2\setminus\{(0,0)\}} \Delta_{m,n}\delta(n-\iota m)e^{-in\sigma}\\ &= \sum_{p\in\mathbb{Z}} c_p e^{-ipN\sigma} \text{ with } c_0 = \mathcal{K}, \text{ and } \forall p \in \mathbb{Z}\setminus\{0\}\ c_p := \Delta_{pD,pN}.\end{aligned}$$

This term is independent of s, so it is constant along $\mathcal{C}_\sigma$. In particular, it is equal to its value for $s = 0$, that is to $u\left(x^1_\sigma(0), x^2_\sigma(0)\right) = u(0,\sigma)$, because the f-dependent term (6.19) is equal to 0

for $s = 0$. Moreover, according to the initial condition in (6.17), the value of this sum over p is also equal to $h(\sigma)$.

Beyond an individual characteristic, it is natural to turn to the set of all characteristics. The set of characteristics is described by $\sigma \in (0, 2\pi D/N \bmod 2\pi)$. The f-independent term in the Fourier solution, namely

$$\forall \sigma \in (0, 2\pi D/N \bmod 2\pi), \sum_{p\in\mathbb{Z}} c_p e^{-ipN\sigma} = h(\sigma),$$

is uniquely defined by the free parameters $c_0 = \mathcal{K}$ and $c_p = \Delta_{pD,pN}$ for $p \neq 0$. In other words, the set of free parameters $\{c_p, p \in \mathbb{Z}\}$ is precisely the set of degrees of freedom that uniquely defines the right-hand side h of the initial condition in (6.17) as a Fourier series.

The conclusion then stems from the fact that the set of free parameters defined in (6.15), namely $\{\mathcal{K}\} \cup \{\Delta_{m,n}, (m,n) \in \mathcal{T}\backslash\{(0,0)\}\}$, is equal to the set $\{c_p, p \in \mathbb{Z}\}$: the free parameters that uniquely define the formal Fourier solution (6.13) are precisely the parameters required to uniquely define an integrable function h and, therefore, uniquely define a solution with the method of characteristics.

Table 6.1 summarizes the general form of the solution to the magnetic differential equation on a 2D periodic domain.

6.2.4 ▪ 3D setting and singularities

While the previous discussion in this section is limited to the 2D setting, the problem of interest is usually derived in the 3D setting. Here, parts of the previous material are interpreted in the 3D setting. For a particular flux coordinate system $\left(\psi, x^1, x^2\right)$, with ι being a nonvanishing function of ψ, the problem of interest reads as follows:

$$\begin{aligned} &\text{Find a function } u \text{ periodic with respect to } \left(x^1, x^2\right) \text{ such that} \\ &\iota(\psi)\frac{\partial u\left(\psi, x^1, x^2\right)}{\partial x_1} + \frac{\partial u\left(\psi, x^1, x^2\right)}{\partial x^2} = f\left(\psi, x^1, x^2\right). \end{aligned} \tag{6.20}$$

In this context, a Fourier solution can be sought, with coefficients depending on the variable ψ, writing the Fourier expansion of the doubly periodic right-hand side f as

$$f\left(\psi, x^1, x^2\right) = \sum_{(m,n)\in\mathbb{Z}^2} b_{m,n}(\psi) e^{i\left(mx^1 - nx^2\right)},$$

where the Fourier coefficients $b_{m,n}$ are complex-valued functions of ψ. Then, under the assumption

$$\boxed{b_{m,n}(\psi) = 0 \; \forall (m,n) \in \mathbb{Z}^2 \text{ such that } m\iota(\psi) = n, \; \forall \psi,} \tag{6.21}$$

including $b_{0,0}(\psi) = 0$ for all ψ independently of the value of $\iota(\psi)$, formally, the general Fourier solution reads

$$\begin{aligned} u\Big(\boldsymbol{R}\left(\psi, x^1, x^2\right)\Big) &= \mathcal{K}(\psi) + \sum_{(m,n)\in\mathbb{Z}^2\backslash\{(0,0)\}} \Delta_{m,n}(\psi)\delta(n - \iota(\psi)m) e^{i\left(mx^1 - nx^2\right)} \\ &+ \sum_{(m,n)\in\mathbb{Z}^2, n\neq\iota(\psi)m} \frac{i}{n - \iota(\psi)m} b_{m,n}(\psi) e^{i\left(mx^1 - nx^2\right)}. \end{aligned} \tag{6.22}$$

In the 2D setting, the free parameters are constants. By contrast, the free parameters depend on ψ in the 3D setting.

Table 6.1: Formal Fourier series solution of the MDE $\iota\partial u/\partial x^1 + \partial u/\partial x^2 = f$ on a two-dimensional periodic domain, comparing the rational case, $\iota = N/D$ (irreducible fraction), and irrational case. The assumptions on the right-hand side (R.H.S.) f are necessary conditions for the existence of a solution. Here $\mathcal{S}_0$ is defined by $\mathcal{S}_0 = \{(m,n) \in \mathbb{Z}^2 \backslash (0,0)$ such that $m\iota = n\}$, and it defines the summation index set.

	$\iota = \dfrac{N}{D}$ rational	ι irrational
R.H.S.	$f\left(x^1, x^2\right) = \displaystyle\sum_{(m,n)\in\mathcal{S}} b_{m,n} e^{i\left(mx^1 - nx^2\right)}$	
Assumption	$\displaystyle\int_0^{2\pi D} f(\iota s, s+\sigma)\, ds = 0 \;\; \forall \sigma \in \left[0, \frac{2\pi}{N}\right)$ $\Leftrightarrow b_{m,n} = 0 \; \forall (m,n) \in \mathbb{Z}^2$ s.t. $n = \iota m$	$\displaystyle\int_0^{2\pi}\int_0^{2\pi} f\left(x^1, x^2\right)\, dx^1 dx^2 = 0$ $\Leftrightarrow b_{0,0} = 0$
Parameters	$\mathcal{K}, \left\{\Delta_{m,n}, (m,n) \in \mathbb{Z}^2 \backslash \{(0,0)\}, \iota = \dfrac{n}{m}\right\}$	$\mathcal{K}$
Solution	$u\left(x^1, x^2\right)$ $= \mathcal{K} + \displaystyle\sum_{(m,n)\in\mathcal{S}_0} \Delta_{m,n} e^{i\left(mx^1 - nx^2\right)}$ $+ \displaystyle\sum_{(m,n)\in\mathbb{Z}^2,\, n\neq\iota m} \frac{ib_{m,n}}{n - \iota m} e^{i\left(mx^1 - nx^2\right)}$	$u\left(x^1, x^2\right)$ $= \mathcal{K}$ $+ \displaystyle\sum_{(m,n)\in\mathbb{Z}^2\backslash\{(0,0)\}} \frac{ib_{m,n}}{n - \iota m} e^{i\left(mx^1 - nx^2\right)}$

Remark 6.4. *Again, it is crucial to understand that* (6.22) *is only formal. On the one hand, in the* 2*D context, the convergence properties of this series for each value of* ψ *still depend on convergence properties of the Fourier series of* $\left(x^1, x^2\right) \mapsto f\left(\psi, x^1, x^2\right)$*, as well as on the free set of parameters depending on* ψ $\{\Delta_{m,n}(\psi), (m,n) \in \mathbb{Z}^2 \backslash \{(0,0)\}, \iota(\psi) = n/m\}$*, as discussed in Section* 6.2.2*. On the other hand, in the* 3*D context, the smoothness of the solution depends on some properties of the whole function* f *and the free set of functions*

$$\{\psi \mapsto \Delta_{m.n}(\psi), (m,n) \in \mathbb{Z}^2 \backslash \{(0,0)\}, \iota(\psi) = n/m\}.$$

This formal Fourier series solution expression is said to have two so-called singularities. These singularities are related to the questions of the existence and uniqueness of a solution to the 3D problem (6.20).

1. The first sum term in (6.22) is said in the literature to contain a so-called delta-function singularity, referring to the fact that this term can be nonzero only at rational values of $\iota(\psi)$ because of the δ-function. It corresponds to the fact that on rational flux surfaces, besides being defined up to $\mathcal{K}(\psi)$, the solution is also defined up to the parameters

$$\{\Delta_{m,n}(\psi) \ \ \forall (m,n) \in \mathbb{Z}^2 \backslash \{(0,0)\} \text{ such that } m\iota(\psi) = n\}.$$

   For each given value of $\iota(\psi)$, this set is empty in the irrational case, whereas it is an infinite set of free parameters in the rational case.

2. The second sum term in (6.22) is said in the literature to contain a singularity of type $1/x$, referring to the division by the quantity $x = \iota(\psi) - n/m$, as it vanishes for every ψ and $(m,n) \in \mathbb{Z}^2$ such that $\iota(\psi) = n/m$. It corresponds to the fact that the solution does not exist for some doubly periodic right-hand sides, as illustrated by the necessary condition for the existence of solutions (6.21). Moreover, this quantity x also gets arbitrarily small for values of (m,n) as $\{n/m, (m,n) \in \mathbb{Z}^2\}$ includes arbitrarily accurate rational approximations of any real value $\iota(\psi)$. This is a concern from the series convergence point of view and the numerical approximation point of view, as discussed in Remark 6.1. To avoid confusion, it is important to remember that these ψ and $(m,n) \in \mathbb{Z}^2$ such that $\iota(\psi) = n/m$ are not included in the summation term in (6.22): there is no division by zero.

However, these two so-called singularities have different physical interpretations. These will be discussed further in Section 10.3.

In particular flux coordinates, known as magnetic coordinates that will be used to derive the magnetic differential equation, characteristics and magnetic field lines coincide. In this context, for the physical interpretation of 3D quantities, it is standard to consider averages over a flux surface instead of the integrals over the periodic domain introduced in Section 6.2.1, that is, for any physical quantity A, the quantity

$$\langle A \rangle_\psi := \frac{\displaystyle\int_0^{2\pi}\int_0^{2\pi} (A\sqrt{g})\Big(\boldsymbol{R}\left(\psi, x^1, x^2\right)\Big)\, dx^1 dx^2}{\displaystyle\int_0^{2\pi}\int_0^{2\pi} \sqrt{g}\Big(\boldsymbol{R}\left(\psi, x^1, x^2\right)\Big)\, dx^1 dx^2} \tag{6.23}$$

$$\text{rather than} \int_0^{2\pi}\int_0^{2\pi} \widetilde{A}\Big(\boldsymbol{R}\left(\psi, x^1, x^2\right)\Big)\, dx^1 dx^2,$$

where $\widetilde{A} = \sqrt{g}A$, and $\sqrt{g} = \left(\nabla\psi \cdot \nabla x^1 \times \nabla x^2\right)^{-1}$ is the Jacobian for a flux coordinate system $\left(\psi, x^1, x^2\right)$ as described in Section 5.5.2. For further reference, we call this operation $\langle\cdot\rangle_\psi$ a

flux-surface average. For a given surface labeled by ψ, it is then clear that these two integrals are simply multiples of each other. So, they vanish simultaneously. Hence, in the 3D setting, the necessary condition for the existence of doubly periodic solutions is

$$\begin{aligned}&\int_0^{2\pi}\int_0^{2\pi} f\Big(\boldsymbol{R}\left(\psi, x^1, x^2\right)\Big)\, dx^1 dx^2 = 0 \ \ \forall \psi,\\ &\Leftrightarrow \langle F\rangle_\psi = 0 \ \ \forall \psi,\end{aligned}$$

where $f = \sqrt{g}F$. Similarly, when ι is rational, it is standard to consider integrals over closed field lines in a different set of coordinates. We consider a coordinate system (ψ, α, l), with the field-line label $\alpha := x^1 - \iota x^2$ and the length along the field line l, so that in particular $\partial \boldsymbol{R}/\partial l = \boldsymbol{B}/B$, as well as the change of coordinates $\left(\psi, x^1, x^2\right) = \left(\psi, x_L^1(\alpha, l), x_L^2(\alpha, l)\right)$. Further details on this coordinate system, including its nonvanishing Jacobian, can be found in Section 9.3. Then the magnetic differential equation divided by B reads $\partial \boldsymbol{R}/\partial l \cdot \nabla u = F/B$ or, equivalently in the (ψ, α, l) coordinate system,

$$\frac{\partial}{\partial l}\Big[u\left(\psi, x_L^1(\alpha, l), x_L^2(\alpha, l)\right)\Big] = \frac{F}{B}\left(\psi, x_L^1(\alpha, l), x_L^2(\alpha, l)\right).$$

So, on any given closed field line $\mathcal{C}_\alpha$ lying on a flux surface labeled by $\psi = \psi_0$ and of length $L(\alpha)$, we have

$$\int_0^{L(\alpha)} \frac{\partial}{\partial l}\Big[u\left(\psi, x_L^1(\alpha, l), x_L^2(\alpha, l)\right)\Big]\, dl = 0,$$

and the condition of existence of periodic solutions along the field line reads

$$\begin{aligned}&\int_0^{L(\alpha)} \frac{F}{B}\left(\psi, x_L^1(\alpha, l), x_L^2(\alpha, l)\right)\, dl = 0\\ &\text{rather than } \int_0^{2\pi D} f\left(\psi_0, x_\sigma^1(s), x_\sigma^2(s)\right)\, ds = 0,\end{aligned}$$

where for the record $f = \sqrt{g}F$. Furthermore, since $|\partial \boldsymbol{R}/\partial l| = 1$, the differential length along any field line $\mathcal{C}$ is $d\ell = dl$, so for any function A, we have

$$\int_0^{L(\alpha)} A\left(\psi, x_L^1(\alpha, l), x_L^2(\alpha, l)\right)\, dl = \oint_{\mathcal{C}} A\, d\ell.$$

Hence, in the 3D setting, the necessary condition for the existence of periodic solutions along closed field lines is

$$\begin{aligned}&\int_0^{2\pi D} (\sqrt{g}F)(\psi, \iota s, s+\sigma)\, ds = 0 \ \ \forall \sigma \in \left(0, \frac{2\pi D}{N} \bmod 2\pi\right), \ \forall \psi,\\ &\Leftrightarrow \oint_{\mathcal{C}} \frac{F}{B}\, d\ell = 0 \text{ for all closed field lines } \mathcal{C} \text{ on all surfaces } \psi.\end{aligned}$$

Chapter 7
Toroidal magnetic confinement

As mentioned, the concept of confinement is paramount for magnetic confinement devices. We can now discuss the confinement of particles in toroidal magnetic configurations. This section focuses on two leading approaches: the tokamak and the stellarator. In Section 7.1, we propose a formal definition of axisymmetry, the fundamental property of the tokamak. In Section 7.2, we will see that axisymmetry leads to the approximate conservation of the flux label along trajectories, hence providing approximate particle confinement. Section 7.3 focuses on a concept central to toroidal confinement, as it quantifies the poloidal twist of magnetic lines described in Section 4.4.2: the rotational transform. Since this twist of the field lines is necessary for particle confinement in toroidal geometry, examining the mechanisms that generate the twist is crucial. In the literature, this is described as producing a rotational transform. The two subsections illustrate how it can be produced, respectively, with and without the assumption of axisymmetry. We will find that confinement in axisymmetry is associated with a major challenge: the necessity of a current within the confinement region. By contrast, without the assumption of axisymmetry, this current is not necessary; instead, a nonaxisymmetric geometry can produce rotational transform. This is the fundamental difference between the tokamak and stellarator concepts. Some advantages and challenges of these two concepts are then discussed in Section 7.4.

A detailed computation of the rotational transform on the axis will be presented in Section 11.2. Section 12.1 will revisit particle confinement without axisymmetry.

7.1 ▪ Continuous symmetry and axisymmetry

In a given coordinate system $\left(x^1, x^2, x^3\right)$, a continuous symmetry of a scalar field refers to the independence with respect to a given coordinate. More explicitly, continuous symmetry of a scalar field $f\left(x^1, x^2, x^3\right)$ with respect to x^i is defined as

$$\frac{\partial f\left(x^1, x^2, x^3\right)}{\partial x^i} = 0.$$

In a Cartesian coordinate system, such a continuous symmetry would amount to a translational invariance. In contrast, in the cylindrical coordinate system, introduced in Section 5.3, if x^i is the angle, then this amounts to a rotational invariance.

Axisymmetry of a scalar field is an invariance with respect to rotation about an axis and is an example of a continuous symmetry. In cylindrical coordinates (R, ϕ, Z), it is the symmetry with

respect to the azimuthal toroidal angle, ϕ, so axisymmetry of a scalar field f is defined by

$$\frac{\partial f(R,\phi,Z)}{\partial \phi} = 0.$$

Considering a vector field $\boldsymbol{F}$ as

$$\boldsymbol{F}(R,\phi,Z) = F_R(R,\phi,Z)\hat{\boldsymbol{R}}(\phi) + F_\phi(R,\phi,Z)\hat{\boldsymbol{\phi}}(\phi) + F_Z(R,\phi,Z)\hat{\boldsymbol{Z}},$$

axisymmetry of $\boldsymbol{F}$ is then defined by

$$\frac{\partial F_R(R,\phi,Z)}{\partial \phi} = 0,\ \frac{\partial F_\phi(R,\phi,Z)}{\partial \phi} = 0,\ \frac{\partial F_Z(R,\phi,Z)}{\partial \phi} = 0.$$

This implies that the magnitude of an axisymmetric vector field $\boldsymbol{F}$, namely $F = |\boldsymbol{F}|$, is itself axisymmetric.

We now obtain a simplified form for the magnetic field under the assumption of axisymmetry and toroidal magnetic surfaces. Moreover, we will show that an axisymmetric vector potential can be chosen under the same assumptions.

For an axisymmetric field $\boldsymbol{B}$, the condition $\nabla \cdot \boldsymbol{B} = 0$ can be expressed using the classical formula for the divergence in cylindrical coordinates as

$$\frac{1}{R}\frac{\partial (RB_R(R,Z))}{\partial R} + \frac{\partial B_Z(R,Z)}{\partial Z} = 0$$

or, equivalently, $\partial(RB_R)/\partial R + \partial(RB_Z)/\partial Z = 0$.

Remark 7.1. *The previous equation is of the form* (6.1)*. Considering the flux coordinates* (R,Z) *as well as* $F_1 = RB_R$ *and* $F_2 = RB_Z$*, we can thus apply the results discussed in Section* 6.1.

According to Remark 7.1, we can express B_R and B_Z in terms of a stream function, χ, as

$$\begin{cases} B_R(R,Z) = -\dfrac{1}{R}\dfrac{\partial \chi(R,Z)}{\partial Z}, \\ B_Z(R,Z) = \dfrac{1}{R}\dfrac{\partial \chi(R,Z)}{\partial R}. \end{cases}$$

Hence the poloidal component of the field, defined as $\boldsymbol{B}_P := B_R\hat{\boldsymbol{R}} + B_Z\hat{\boldsymbol{Z}}$, can be expressed as

$$\boldsymbol{B}_P(R,\phi,Z) = \frac{1}{R}\nabla\chi(R,Z) \times \hat{\boldsymbol{\phi}}(\phi).$$

The axisymmetric field also has an axisymmetric toroidal component, B_ϕ, even if it does not appear in the divergence-free condition. Thus, we can write the total field as

$$\boldsymbol{B}(R,\phi,Z) = \frac{1}{R}\nabla\chi(R,Z) \times \hat{\boldsymbol{\phi}}(\phi) + B_\phi(R,Z)\hat{\boldsymbol{\phi}}(\phi).$$

As a result, $\boldsymbol{B} \cdot \nabla\chi = 0$. We assume that χ is differentiable, so the level sets of χ form surfaces, except at critical points where $\nabla\chi = 0$. These critical points may be isolated or may form critical lines or surfaces, but we are not interested in purely toroidal fields such that $\nabla\chi = 0$ in a volume, as was explained in Section 4.4.2. As we are interested in toroidal confinement, we will assume that these isosurfaces of χ are toroidal. In this case, χ is a flux function, and by axisymmetry, the magnetic axis lies in a constant-Z plane.

We will show that the stream function χ is related to the normalized poloidal flux defined in Remark 5.2 by $\psi_P = \Psi_P/(2\pi)$. To compute the flux of a given surface $\chi = \chi_0$, we choose a surface S_P to lie on the $Z = Z_0$ plane, on which the magnetic axis lies. The surface S_P is an annulus bounded by the magnetic axis and a given magnetic surface, labeled by ψ_P. It is the area bounded between the magnetic axis, R_a, and R_0, the largest value of the major radius corresponding to the intersection of S_P and the isosurface $\chi = \chi_0$. Then on S_P the unit normal is $\hat{\boldsymbol{n}} = \hat{\boldsymbol{Z}}$, and under the assumption of axisymmetry, the differential area element is expressed by $d^2r = 2\pi R dR$. So, the flux is

$$\psi_P = \frac{1}{2\pi}\int_{S_P} \boldsymbol{B}(\boldsymbol{r}) \cdot \hat{\boldsymbol{n}}(\boldsymbol{r})\, d^2r.$$

Since $\hat{\phi} = R\nabla\phi$ and $\boldsymbol{B}\cdot\hat{\boldsymbol{n}} = (\nabla\chi \times \nabla\phi)\cdot\hat{\boldsymbol{Z}}$, then $\boldsymbol{B}\cdot\hat{\boldsymbol{n}} = (1/R)\partial\chi(R,Z)/\partial R$, and the flux can be expressed as

$$\begin{aligned}\psi_P &= \int_{R_a}^{R_0} \frac{\partial\chi(R,Z_0)}{\partial R}\, dR \\ &= \chi_0 - \chi(R_a, Z_0).\end{aligned}$$

Since the quantity $\chi(R_a, Z_0)$ is independent of the surface considered, the difference between the stream function and the poloidal flux is constant. As the stream function can be shifted by a constant without changing the field, we are then free to write the magnetic field as

$$\boldsymbol{B}(R,\phi,Z) = \frac{1}{R}\nabla\psi_P(R,Z)\times\hat{\boldsymbol{\phi}}(\phi) + B_\phi(R,Z)\hat{\boldsymbol{\phi}}(\phi). \tag{7.1}$$

This simplified form for the magnetic field under the assumption of axisymmetry will become useful in Sections 7.3 and 8.4. Since the gradient reads $\nabla = \hat{\boldsymbol{R}}\partial/\partial R + \hat{\boldsymbol{\phi}}/R\partial/\partial\phi + \hat{\boldsymbol{Z}}\partial/\partial Z$ in cylindrical coordinates, it can also be conveniently rewritten as

$$\boldsymbol{B}(R,\phi,Z) = \nabla\times\left(\frac{\psi_P(R,Z)}{R}\hat{\boldsymbol{\phi}}(\phi) + \int_0^Z B_\phi\big(R,Z'\big)\, dZ'\,\hat{\boldsymbol{R}}(\phi)\right).$$

Then defining

$$A_R(R,Z) = \int_0^Z B_\phi\big(R,Z'\big)\, dZ'$$

and

$$\boldsymbol{A}(R,\phi,Z) = \frac{\psi_P(R,Z)}{R}\hat{\boldsymbol{\phi}}(\phi) + A_R(R,Z)\hat{\boldsymbol{R}}(\phi), \tag{7.2}$$

this shows that $\boldsymbol{B} = \nabla\times\boldsymbol{A}$. This proves that for any axisymmetric divergence-free field, $\boldsymbol{B}$, with toroidal flux surfaces, there exists an axisymmetric vector potential $\boldsymbol{A}$.

We will consider several other implications of axisymmetry in Sections 7.2 and 7.3. Under the assumption of axisymmetry, there are only two nontrivial spatial variables, as the system is assumed to be independent of the toroidal angle. Axisymmetric configurations are then said to be 2D. Some magnetic confinement devices, such as tokamaks, are designed to have magnetic fields close to axisymmetry, according to the above definition. Without this assumption, a physical system is said to be 3D. In particular, stellarator devices are inherently 3D configurations.

7.2 ▪ Particle confinement in axisymmetry

This section demonstrates that axisymmetry is desirable because it guarantees momentum conservation, in turn guaranteeing the confinement of particles in the absence of collisions to leading order. The starting point will be the Lagrangian for the motion of a single particle with mass m and charge q in a magnetic field $\boldsymbol{B}$.

We assume that the magnetic field is divergence-free. Hence, as described in Appendix B.2, the field can be expressed in terms of a vector potential $\boldsymbol{A}$ as $\boldsymbol{B} = \nabla \times \boldsymbol{A}$. We also assume that the field $\boldsymbol{B}$ is time-independent and axisymmetric.

We express the vector potential in the cylindrical coordinate system, (R,ϕ,Z) introduced in Section 5.3 as $\boldsymbol{A} = A_R\hat{\boldsymbol{R}} + A_\phi\hat{\boldsymbol{\phi}} + A_Z\hat{\boldsymbol{Z}}$. Axisymmetry of $\boldsymbol{B}$ implies that $\boldsymbol{A}$ can be chosen to be axisymmetric, as described in Section 7.1. Under the assumption of time independence, we then express the Lagrangian for the particle motion (B.6) in the cylindrical coordinate system,

$$L(R,\phi,Z,\dot{R},\dot{\phi},\dot{Z}) = \frac{m}{2}\left(\dot{R}^2 + R^2\dot{\phi}^2 + \dot{Z}^2\right) + q\left(A_R(R,\phi,Z)\dot{R} + A_\phi(R,\phi,Z)R\dot{\phi} + A_Z(R,\phi,Z)\dot{Z}\right).$$

Under the assumption of axisymmetry, the Lagrangian becomes independent of ϕ. So ϕ is an ignorable coordinate as defined in Appendix B.2.2. Thus, L has a continuous symmetry with respect to ϕ. Next, we study the corresponding conserved quantity.

Along a trajectory, $(R_T,\phi_T,Z_T) : \mathbb{R} \to (\mathbb{R}^N)^3$, the corresponding Euler–Lagrange equation for the toroidal angle is

$$\frac{d}{dt}\left(\frac{\partial L(R_T(t),\phi_T(t),Z_T(t),\dot{R}_T(t),\dot{\phi}_T(t),\dot{Z}_T(t))}{\partial\dot{\phi}}\right) = 0.$$

Hence the so-called toroidal canonical momentum, defined as

$$p_\phi(R,\phi,Z,\dot{R},\dot{\phi},\dot{Z}) := \frac{\partial L(R,\phi,Z,\dot{R},\dot{\phi},\dot{Z})}{\partial\dot{\phi}},$$

is a constant of motion since along a trajectory

$$\frac{d}{dt}[p_\phi\left(R_T(t),\phi_T(t),Z_T(t)\right)] = 0.$$

Remark 7.2. *This is an example of Noether's theorem* [90]*: any continuous symmetry, in this case, toroidal rotational symmetry, implies a conserved quantity, in this case, p_ϕ.*

To gain additional insight into this quantity, we will now estimate the size of each term in

$$p_\phi(R,\phi,Z,\dot{R},\dot{\phi},\dot{Z}) = mR^2\dot{\phi} + qA_\phi(R,Z)R.$$

As can be seen in (7.2), the poloidal flux is $\psi_P = RA_\phi$. As discussed in Remark 5.3, in a torus with major radius R_0, minor radius a, and poloidal field magnitude $B_P := |\boldsymbol{B}_P|$, the poloidal flux scales as $\psi_P \approx R_0 a B_P$.

We can also approximate $R\dot{\phi} \approx v_t$, where $v_t = \sqrt{2T/m}$ is the thermal velocity. Moreover, under the large aspect ratio assumption, namely $a/R_0 \ll 1$, then $R \approx R_0$.[15] So, we find the ratio of the two terms in p_ϕ to be

$$\frac{mR^2\dot{\phi}}{q\psi_P} \approx \frac{mv_t}{qB_P a} \approx \frac{\rho B}{aB_P},$$

[15]Remember that $R \in [R_0 - a, R_0 + a]$ in the toroidal domain of interest.

where $\rho = v_t m/(qB)$ is the gyroradius introduced in Section 4.2. As can be seen in Table 1.1, $\rho/a \ll 1$ in typical toroidal confinement experiments. Therefore, if the poloidal field strength is of comparable size to the total field strength, this ratio $\epsilon_P := \rho B/(aB_P) \ll 1$. So we can make the approximation $p_\phi \approx q\psi_P$.

As p_ϕ is then approximately constant on a flux surface meaning a particle on an initial magnetic surface ψ_P^0 will be confined within a small distance $\Delta\psi_P \approx \epsilon_P \psi_P^0$ from the initial surface. As ϵ_P scales inversely with respect to B_P, this is another way to understand the need for a strong poloidal magnetic field for confinement in a tokamak as discussed in Section 4.4.2. More details on confinement in axisymmetry can be found in [197] and Chapter 7 of [120].

In 3D geometry without axisymmetry, this result does not apply, so much more care must be taken to achieve good confinement. However, a so-called hidden symmetry can be exploited to obtain similar confinement properties in a stellarator, as will be explored in Section 12.1.

7.3 ▪ Rotational transform

As described in Section 4.4.2, a poloidal component for the magnetic field is required for confinement, resulting in twisted field lines rather than a purely toroidal field lying in a plane. This twist in the field lines is quantified by the rotational transform, ι, indicating the number of poloidal turns of a field line around the magnetic axis for each toroidal turn around the $\hat{\boldsymbol{Z}}$ axis. In the tokamak literature, the safety factor $q = 1/\iota$ is often used rather than the rotational transform.

For any given field line, the rotational transform can be defined in terms of the change in poloidal angle, $(\Delta\theta)_k$, after the kth toroidal turn following a field line around the toroidal domain,

$$\iota = \lim_{n\to\infty} \frac{\sum_{k=1}^{n} (\Delta\theta)_k}{2\pi n}.$$

This definition of the rotational transform holds even if flux surfaces do not exist since it relies on a field line's poloidal and toroidal rotations with respect to a field line that closes after one toroidal transit. This closed field line is the magnetic axis in the presence of continuously nested flux surfaces. Since magnetic field lines cannot cross one another, the rotational transform ι is the same for all field lines on a given surface. If continuously nested flux surfaces exist, then the rotational transform can be defined in terms of the toroidal and poloidal fluxes, (5.8)–(5.9), as

$$\iota(\psi) = \frac{d\psi_P(\psi)}{d\psi}. \tag{7.3}$$

Here $\psi = \Psi_T/(2\pi)$ and $\psi_P = \Psi_P/(2\pi)$ are the rescaled toroidal and poloidal fluxes. According to this definition, the rotational transform is another example of a flux function.

The link between the rotational transform (7.3) and the poloidal component of the field can be evidenced as follows. Given the expression for the poloidal flux ψ_P (5.11), we can evaluate the rotational transform as defined above in a flux coordinate system (ψ, θ, ϕ), namely

$$\iota(\psi) = \frac{1}{2\pi} \int_0^{2\pi} \frac{\boldsymbol{B}\cdot\nabla\theta}{\nabla\psi\cdot\nabla\theta\times\nabla\phi} \left(\boldsymbol{R}(\psi,\theta_0,\phi)\right) d\phi,$$

where the integration is performed at fixed poloidal angle $\theta = \theta_0$, and the Jacobian $\nabla\psi\cdot\nabla\theta\times\nabla\phi$ cannot vanish for a well-defined flux coordinate system. Therefore, it is clear that $\iota(\psi)$ can be nonzero only for magnetic fields with a nonzero poloidal component, $\boldsymbol{B}\cdot\nabla\theta \neq 0$.

On a given surface, the rotational transform (7.3) quantifies the twist of field lines around the surface. When the rotational transform is rational, $\iota = n/m$ for $m \in \mathbb{Z}\backslash\{0\}$ and $n \in \mathbb{Z}$, a

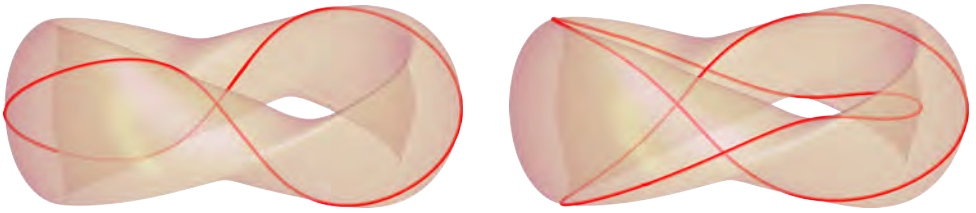

(a) $\iota = 2$ (b) $\iota = 3/2$

Figure 7.1: Two examples of field lines on a toroidal surface. An $\iota = 2$ field line (left) makes two poloidal turns for each toroidal turn, while an $\iota = 3/2$ field line (right) makes three poloidal turns for two toroidal turns. As both are rational field lines, they close on themselves after a finite number of toroidal turns.

field line closes on itself after n toroidal turns, having completed m poloidal turns. Therefore, a single field line does not cover the entire surface, as illustrated in Figure 7.1. Flux surfaces with rational values of ι are known as rational surfaces. When ι is irrational, a given field line comes arbitrarily close to every point on what is called an irrational surface.

Now, the mechanisms for producing rotational transform to generate the twist of field lines as they wrap around flux surfaces, will be explored both with and without the assumption of axisymmetry.

- In the context of axisymmetry, as described below in Section 7.3.1, a relation between the rotational transform and the toroidal current can be derived. As a result, rotational transform can be produced by driving a toroidal plasma current.

- Without the assumption of axisymmetry, the previous argument does not hold; instead, as described below in Section 7.3.2, the rotational transform can be related to geometric properties of the magnetic axis, based on a near-magnetic-axis model. By contrast, in this context, rotational transform can be produced by the nonplanarity of the magnetic axis and nonaxisymmetry of the magnetic surfaces.

This introduces the fundamental difference between the tokamak and stellarator concepts that is later discussed in Section 7.4.

7.3.1 ▪ Producing rotational transform with axisymmetry

The most straightforward way to produce rotational transform is with a toroidal plasma current, creating a poloidal magnetic field from Ampère's law (A.7). As we will now see, this is the only possibility under the assumption of axisymmetry. This discussion assumes the existence of closed, nested flux surfaces.

The starting point is the expression for the magnetic field in terms of the poloidal flux in cylindrical coordinates (7.1) with $\hat{\phi} = R\nabla\phi$, repeated here for the reader's convenience:

$$\boldsymbol{B}(R,\phi,Z) = \nabla\psi_P(R,Z) \times \nabla\phi + B_\phi(R,Z)\hat{\boldsymbol{\phi}}. \tag{7.4}$$

We now consider the implications of the above expression on the toroidal current. In order to define the toroidal current, consider a flux coordinate system (ψ,θ,ϕ) and a closed curve lying on a flux surface at a constant toroidal angle, $C_T(\psi,\phi) := \{(\psi,\theta,\phi), \theta \in [0,2\pi)\}$, as well as the surface enclosed by this curve, denoted by $S_T(\psi,\phi) := \{(\widetilde{\psi},\theta,\phi), \widetilde{\psi} \leq \psi, \theta \in [0,2\pi)\}$ and

shown in Figure 5.4. The toroidal current through a surface $S_T(\psi,\phi)$ is the surface integral

$$I_T(\psi,\phi) = \int_{S_T(\psi,\phi)} \boldsymbol{J}(\boldsymbol{r})\cdot\hat{\boldsymbol{n}}(\boldsymbol{r})\,d^2r.$$

It can be expressed using Ampère's law (A.7) as the line integral

$$I_T(\psi,\phi) = \frac{1}{\mu_0}\oint_{\partial S_T(\psi,\phi)} \boldsymbol{B}(\boldsymbol{r})\cdot d\boldsymbol{l}(\boldsymbol{r}).$$

Since

$$d\boldsymbol{l} = \frac{\partial \boldsymbol{R}}{\partial\theta}d\theta$$

along the curve $\partial S_T(\psi,\phi)$, then from the expression of $\boldsymbol{B}$ in (7.4), together with the dual relations (5.3), the integrand of the line integral reads

$$\boldsymbol{B}\cdot\frac{\partial\boldsymbol{R}}{\partial\theta} = \nabla\psi_P\times\nabla\phi\cdot\frac{\partial\boldsymbol{R}}{\partial\theta}.$$

Because $\partial\boldsymbol{R}/\partial\theta = \nabla\phi\times\nabla\psi/(\nabla\psi\times\nabla\theta\cdot\nabla\phi)$ and $\nabla\psi_P = \iota\nabla\psi$, it yields

$$\boldsymbol{B}\cdot\frac{\partial\boldsymbol{R}}{\partial\theta} = -\frac{\iota|\nabla\psi\times\nabla\phi|^2}{(\nabla\psi\times\nabla\theta\cdot\nabla\phi)}.$$

Therefore, this integrand is sign-definite and cannot vanish for a well-defined flux coordinate system with $\iota(\psi)\neq 0$. Hence, under these conditions, the toroidal current I_T is nonzero. Furthermore, in order to produce rotational transform in an axisymmetric system with flux surfaces, a toroidal current is necessary. Thus, axisymmetric devices require current in the confinement region. This mechanism forms the basis for confinement in a tokamak, as discussed in Section 7.4.1.

7.3.2 ▪ Producing rotational transform without axisymmetry

If axisymmetry is broken, the magnetic field cannot be written as (7.4), and the argument in the previous section no longer holds. As we will see, rotational transform does not necessarily require plasma current in the absence of axisymmetry. Instead, a classic result of Mercier [210, 116] demonstrates the mechanisms generating rotational transform on the magnetic axis from 3D fields.

The result of Mercier relies, under the assumption of continuously nested toroidal flux surfaces discussed in Remark 4.4, on an asymptotic expansion with respect to the distance from the magnetic axis. While the complete proof of this result is postponed to Section 11.2 to avoid long technical details, the resulting closed form of the approximate rotational transform on the magnetic axis is introduced here for the sake of argument.

We will use a Frenet–Serret coordinate system to discuss this result, later proved in Section 11.2. We define orthonormal unit vectors, the unit tangent vector $\hat{\boldsymbol{e}}_1^P$ in the direction of the magnetic field, the unit normal vector $\hat{\boldsymbol{e}}_2^P$ in the direction of the magnetic curvature $\boldsymbol{\kappa}$, and a vector $\hat{\boldsymbol{e}}_3^P$ orthogonal to the two previous ones, at any point $P\in\mathbb{R}^3$, as follows:

$$\begin{cases} \hat{\boldsymbol{e}}_1^P = \hat{\boldsymbol{b}}(P), \\ \hat{\boldsymbol{e}}_2^P = \dfrac{\boldsymbol{\kappa}(P)}{|\boldsymbol{\kappa}(P)|} \text{ with } \boldsymbol{\kappa}(P) = \Big(\hat{\boldsymbol{b}}(P)\cdot\nabla\Big)\hat{\boldsymbol{b}}(P), \\ \hat{\boldsymbol{e}}_3^P = \hat{\boldsymbol{e}}_1^P\times\hat{\boldsymbol{e}}_2^P, \end{cases} \tag{7.5}$$

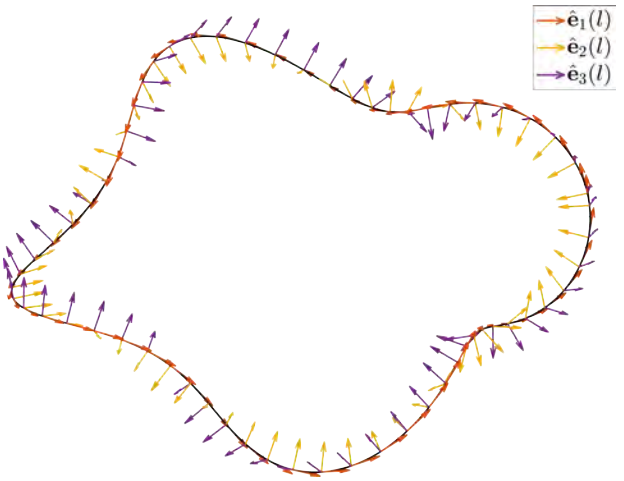

Figure 7.2: The magnetic axis of the TJ-II stellarator (black) with the orthonormal Frenet–Serret unit vectors.

where $\hat{\boldsymbol{b}}$ is the direction of the magnetic field. The magnetic axis can be defined by a line $\boldsymbol{r}_0(l)$, where l is the arclength, a parameter measuring the distance along the curve. Along the magnetic axis, the Frenet–Serret basis can be parameterized by l, and it will be written $(\hat{\boldsymbol{e}}_1(l), \hat{\boldsymbol{e}}_2(l), \hat{\boldsymbol{e}}_3(l))$. The basis vectors $\hat{\boldsymbol{e}}_2$ and $\hat{\boldsymbol{e}}_3$ define a plane perpendicular to the magnetic axis. The Frenet–Serret unit vectors on the magnetic axis of the Spanish stellarator TJ-II are shown in Figure 7.2.

As a result of the detailed calculation presented in Section 11.2, we find that the cross-sections of the flux surfaces in the $\hat{\boldsymbol{e}}_2$-$\hat{\boldsymbol{e}}_3$ plane form ellipses. The calculation is discussed using four key parameters, illustrated in Figure 7.3.

- The torsion $\tau(l)$ of the magnetic axis is defined by $\tau(l) = -\hat{\boldsymbol{e}}_3'(l) \cdot \hat{\boldsymbol{e}}_2(l)$, and it satisfies $\hat{\boldsymbol{e}}_3'(l) = -\tau(l)\hat{\boldsymbol{e}}_2(l)$. The torsion of a planar curve vanishes at all points, and τ can be considered a measure of the nonplanarity of the magnetic axis.
- The ellipticity parameter, $\eta(l)$, relates the major axis, a, and the minor axis, b, of the ellipse through $b = e^{-\eta(l)}a$. Thus, large values of $\eta(l)$ indicate more pronounced ellipticity.
- The angle of the major axis of the ellipse with respect to $\hat{\boldsymbol{e}}_2$ is denoted by $\delta(l)$. Thus, large values of $\delta'(l)$ indicate an ellipse rotating rapidly with respect to the normal direction.
- The number of net poloidal rotations of the curvature vector is denoted by the integer m. Thus, large values of m indicate that the Frenet–Serret frame is making more net rotations.

The expression for the rotational transform $\iota(\psi)$ on the magnetic axis, $\psi = 0$, of length L in terms of these parameters is

$$\iota(0) = \frac{1}{2\pi}\left(-2\pi m - \delta(L) + \delta(0) + \int_0^L \frac{\delta'(l) - \tau(l)}{\cosh(\eta(l))}\, dl\right).$$

In order to have a nonzero rotational transform in the absence of plasma current, a nonzero value of either $\delta'(l)$ or $\tau(l)$ is required. These mechanisms imply the breaking of toroidal symmetry as defined in Section 7.1, through either a nonplanar magnetic axis or magnetic surfaces with twisting ellipticity. These mechanisms form the basis for confinement in a stellarator, as discussed in Section 7.4.2.

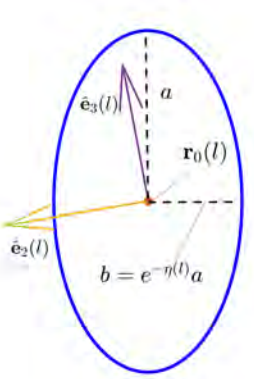

Figure 7.3: Plane perpendicular to the magnetic axis at a point $\mathbf{r}_0(l)$. The unit vectors $\hat{\mathbf{e}}_2(l)$ and $\hat{\mathbf{e}}_3(l)$ defined through (7.5) form a basis of the plane. The magnetic surfaces near the axis are elliptical with major axis a and minor axis b.

7.4 ▪ Toroidal confinement devices

Toroidal magnetic confinement devices rely on rotational transform for confinement. In order to produce the required rotational transform, the axisymmetric tokamak, described in Section 7.4.1, relies on plasma current while the stellarator, described in Section 7.4.2, relies on the shaping of the magnetic field.

7.4.1 ▪ Tokamak

A tokamak is one example of a toroidal confinement device with genus one topology. The magnetic field of a tokamak is designed under the assumption of axisymmetry according to the definition provided in Section 7.1. Thus, many physical scalar quantities are independent of the toroidal angle, ϕ. In practice, these scalar quantities are not exactly independent of the toroidal angle because the magnetic field is not precisely axisymmetric. This symmetry-breaking can be introduced unintentionally, for example, due to misaligned coils, or deliberately to control the plasma's stability [71]. However, this approximation is often sufficient because the field is close enough to axisymmetry.

As shown in Section 7.2, a poloidal magnetic field is necessary for confinement in axisymmetry. Moreover, as shown in Section 7.3, toroidal plasma current is required to produce this poloidal component. While there is some self-generated plasma current,[16] it is insufficient for confinement, so it needs to be driven externally. Often, this is done with a transformer through electromagnetic induction. An electric field is induced in the plasma by varying the current through a central transformer coil, as illustrated in Figure 7.4. As the current through the transformer coil cannot be increased or decreased indefinitely, this cannot be used as a steady-state approach. Driving current in a tokamak reactor requires a significant amount of energy, as described for instance in Chapter 3 of [304], reducing its efficiency. Many dangerous plasma instabilities are also driven by plasma current. The result of these instabilities is a sudden loss of confinement of the plasma, called a disruption.

Although the need for current has some disadvantages, the tokamak configuration is advantageous because of its simple geometry. The toroidal symmetry ensures that the collisionless particle orbits are confined in the presence of a strong poloidal magnetic field, as discussed in

[16] A self-generated plasma current refers to a current generated by the plasma as opposed to an externally imposed current.

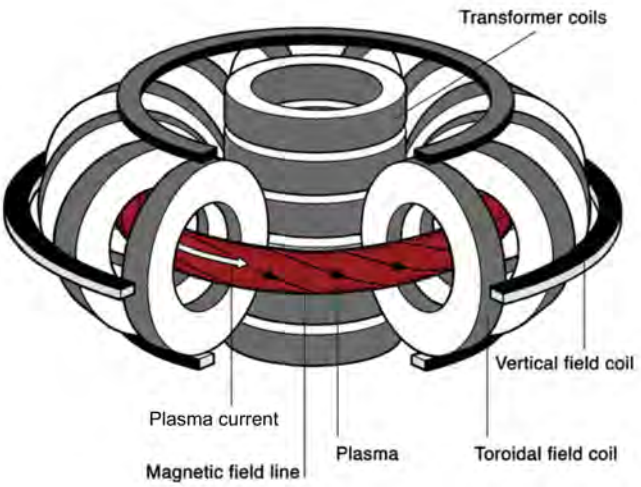

Figure 7.4*: The poloidal magnetic field of a tokamak is produced by toroidal plasma current. This plasma current is in turn driven inductively by transformer coils. The toroidal field is produced by electromagnetic coils modeled as planar curves. Figure reproduced from* [206]*. Reprinted with permission from the Max Planck Institute for Plasma Physics. Tokamak.* `http://www.ipp.mpg.de/14869/tokamak`*,* 2018*. Accessed:* 2018-10-04*.*

Section 7.2. The toroidal field coils of a tokamak are planar curves that are relatively easy to construct in contrast with those of a stellarator, as illustrated in Figure 7.4.

7.4.2 ▪ Stellarator

While a stellarator is also a toroidal confinement device with genus one topology, unlike a tokamak, it is designed to be far from axisymmetry according to the definitions in Section 7.1. Due to its lack of axisymmetry, plasma current is not required to produce a poloidal magnetic field component. Instead, stellarators use torsion and ellipticity to produce rotational transform through symmetry-breaking as discussed in Section 7.3. These mechanisms require shaping the magnetic field. This idea was the basis for the first stellarator designed by Spitzer [270], featuring a magnetic axis shaped as a figure eight to produce torsion of the magnetic axis.

A significant advantage of the stellarator over the tokamak as a power plant concept is that it does not require an external current drive, limiting technical challenges and costs associated with driving current. Although stellarators generally do not have externally driven current, a small amount of self-driven current arises due to the averaged motion of ions and electrons. Due to the small plasma current, stellarators tend to be more stable than tokamaks in regard to current-driven instabilities. Moreover, stellarators do not need an inductive electric field, so they can be run in a steady state.

As stellarator coils have to produce a carefully shaped magnetic field to have a sufficient poloidal field, they tend to be much more complex than tokamak coils, as illustrated in Figure 7.5. Furthermore, due to their lack of axisymmetry, stellarators do not enjoy automatic magnetic field integrability, discussed briefly in Section 7.1 and explored in more detail in Chapter 10. Moreover, automatic approximate particle confinement is no longer guaranteed in three dimensions as it is for axisymmetry, as discussed in Section 7.2. This motivates the search for 3D magnetic fields with more general symmetries, introduced in Chapter 12, and the numerical optimization of the magnetic field and coils as discussed in Chapter 13.

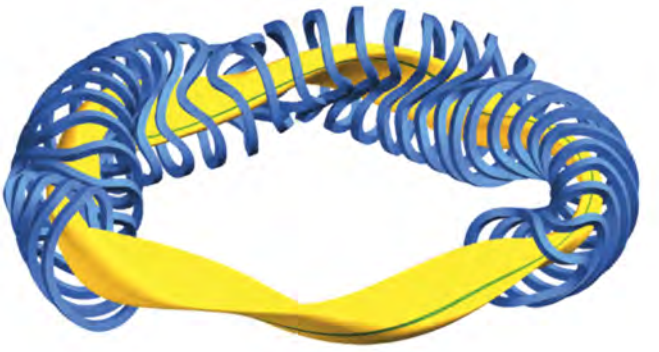

Figure 7.5*: A stellarator confines charged particles with magnetic fields without continuous toroidal symmetry. The coils of the Wendelstein* 7*-X device are shown along with the outer magnetic surface (yellow) and a field line (blue). The rather complicated electromagnetic coils produce the twisting of the field line around the surface. Figure reproduced from* [205]*. Reprinted with permission from the Max Planck Institute for Plasma Physics. Magnetic coils and plasma from Wendelstein* 7*-X.* `https://www.ipp.mpg.de/2523775/konzeptentwicklung`*,* 2018*. Accessed:* 2018-10-04.

Chapter 8

Coupling of particles and electromagnetic fields: Ideal magnetohydrodynamics

While a plasma, made of charged particles, is intrinsically coupled to electromagnetic fields, considering the single-particle motion in given fields as in Chapter 4 leads to the notion of toroidal confinement. In order to further investigate the concept of a stellarator as presented in Chapter 7, it is now natural to introduce models coupling plasma and electromagnetic fields. Ideal MHD models, central to this chapter, are fundamental models for the design of stellarators.

Magnetohydrodynamics refers to a hierarchy of fluid models of a plasma relevant for describing the large-scale, global behavior of the confinement and vacuum regions of fusion plasmas, as described in Appendix A.3 and Section 5.2. They couple Maxwell's equations with a fluid model for the particles. They describe the plasma by a mass density ρ, the center of mass fluid velocity $\boldsymbol{u}$, species-summed pressure p, and current density $\boldsymbol{J}$. Different MHD models describe different physical regimes, corresponding to assumptions on the length and time scales of interest, as introduced in Section 1.4. For example, some models include the effects of resistivity, viscosity, and perpendicular heat diffusion. In this chapter, we focus on the relatively simple ideal MHD model, assuming instead that the plasma is perfectly conducting and ignoring the effect of viscosity. A more detailed discussion of other MHD models is presented in Chapters 10 and 11.

The ideal MHD equations will be discussed in Section 8.1. An important consequence of the ideal MHD model is the preservation of the topology of magnetic surfaces as they move with the plasma flow. This is known as flux freezing and is discussed in Section 8.2. For applications associated with magnetic confinement, it is important to understand the limit of ideal MHD when the fluid flow and time dependence vanish, resulting in the ideal MHD equilibrium equations. These are discussed in Section 8.3. The ideal MHD equilibrium equations are significantly simplified under the fundamental assumption of the existence of continuously nested toroidal magnetic surfaces discussed in Remark 4.4. In particular, this assumption allows for the use of flux coordinates, with two periodic coordinates providing mathematical simplification as illustrated in Chapter 6. As we have seen in Chapter 7, continuously nested toroidal surfaces are guaranteed in axisymmetry. The Grad–Shafranov equation, resulting from the ideal MHD equilibrium equations in axisymmetry, is presented in Section 8.4.

While continuously nested surfaces do not always exist in three dimensions, we can still seek a class of simplified solutions assuming continuously nested surfaces. This simplifies the mathematical model and, in turn, reduces computational complexity. However, in three dimensions, this simplification can lead to challenges associated with the behavior of solutions when $\nabla p \neq 0$ on these surfaces, which is further discussed in Chapter 10.

8.1 ▪ Ideal MHD

The ideal MHD equations can be obtained from kinetic or fluid models under certain assumptions.

- The collision frequency is sufficiently large so the electron and ion temperatures are equilibrated.
- The gyroradius is small compared to length scales of interest.
- The system is nonrelativistic, so that the displacement current, $\partial \boldsymbol{E}/\partial t$, can be dropped from Ampère's law, as discussed in Remark A.3.
- Frequencies faster than the electron plasma frequency, the characteristic frequency of oscillations of the charge density [44], $\omega_{pe} = \sqrt{n_e e^2/(\mu_0 m_e)}$, are not included. Here n_e and m_e are the electron number density and mass, respectively.
- The plasma is assumed to be perfectly conducting so its resistivity is negligible.

The details of how the ideal MHD model is obtained under these assumptions are explained more thoroughly in many references [226, 76, 89].

These assumptions have the following consequences.

- Since the displacement current is dropped from Ampère's law, MHD does not include light waves.
- As this is a fluid model, it does not account for velocity space effects such as particle trapping.
- As high frequencies and small wavelengths are neglected, MHD describes the macroscopic, low-frequency behavior of plasmas.
- An important result of the assumption of a perfectly conducting plasma is the frozen-in theorem, stating that the magnetic field is frozen into the fluid and must move with it. This will be discussed in Section 8.2.

Conditions for the validity of ideal MHD are described in more detail in Chapter 2 of [76].

We now outline the equations satisfied by the fluid mass density ρ, current density $\boldsymbol{J}$, and flow velocity $\boldsymbol{u}$ in the ideal MHD model. The continuity equation ensures mass conservation,

$$\frac{\partial \rho}{\partial t} + \nabla \cdot (\rho \boldsymbol{u}) = 0. \tag{8.1}$$

Momentum density obeys a similar conservation equation,

$$\rho \left(\frac{\partial}{\partial t} + \boldsymbol{u} \cdot \nabla \right) \boldsymbol{u} = \boldsymbol{J} \times \boldsymbol{B} - \nabla p. \tag{8.2}$$

The ideal energy conservation equation is

$$\left(\frac{\partial}{\partial t} + \boldsymbol{u} \cdot \nabla \right) p + \gamma p \nabla \cdot \boldsymbol{u} = 0 \tag{8.3}$$

and, when combined with (8.1), yields the entropy conservation equation,

$$\left(\frac{\partial}{\partial t} + \boldsymbol{u} \cdot \nabla \right) \left(\frac{p}{\rho^\gamma} \right) = 0. \tag{8.4}$$

Here γ is the ratio of specific heats where $\gamma = 5/3$ for a monatomic gas.

The electric and magnetic fields, $\boldsymbol{E}$ and $\boldsymbol{B}$, obey Maxwell's equations, presented in Chapter 2, under the nonrelativistic limit,

$$\begin{cases} \nabla \times \boldsymbol{B} = \mu_0 \boldsymbol{J}, \\ \nabla \times \boldsymbol{E} = -\dfrac{\partial \boldsymbol{B}}{\partial t}, \\ \nabla \cdot \boldsymbol{B} = 0. \end{cases} \tag{8.5}$$

The assumption of a perfectly conducting plasma can be stated as

$$\boldsymbol{E} + \boldsymbol{u} \times \boldsymbol{B} = 0. \tag{8.6}$$

Since the electric field in a frame moving with velocity $\boldsymbol{u}$ is given by $\boldsymbol{E} + \boldsymbol{u} \times \boldsymbol{B}$, assuming $|\boldsymbol{u}|$ is much smaller than the speed of light c, the above states that the electric field in the frame of reference moving with the plasma is zero. Thus, the plasma is perfectly conducting.

Since the electric field $\boldsymbol{E}$ and current $\boldsymbol{J}$ can be expressed explicitly as

$$\begin{aligned} \boldsymbol{E} &= -\boldsymbol{u} \times \boldsymbol{B}, \\ \boldsymbol{J} &= \frac{1}{\mu_0} \nabla \times \boldsymbol{B}, \end{aligned}$$

they can be substituted from the other equations to obtain a PDE system for the unknowns ρ, $\boldsymbol{u}$, p, and $\boldsymbol{B}$,

$$\begin{cases} \dfrac{\partial \rho}{\partial t} + \nabla \cdot (\rho \boldsymbol{u}) = 0, \\ \rho \left(\dfrac{\partial}{\partial t} + \boldsymbol{u} \cdot \nabla \right) \boldsymbol{u} = \dfrac{(\nabla \times \boldsymbol{B}) \times \boldsymbol{B}}{\mu_0} - \nabla p, \\ \left(\dfrac{\partial}{\partial t} + \boldsymbol{u} \cdot \nabla \right) p + \gamma p \nabla \cdot \boldsymbol{u} = 0, \\ \dfrac{\partial \boldsymbol{B}}{\partial t} = \nabla \times (\boldsymbol{u} \times \boldsymbol{B}), \\ \nabla \cdot \boldsymbol{B} = 0. \end{cases} \tag{8.7}$$

8.2 ▪ Flux freezing

An important consequence of the ideal MHD equations is Alfvén's flux freezing theorem. This theorem relies on the equation

$$\frac{\partial \boldsymbol{B}}{\partial t} = \nabla \times (\boldsymbol{u} \times \boldsymbol{B}). \tag{8.8}$$

The theorem states that the magnetic flux through an open surface moving with an ideal MHD plasma does not change in time. Stated another way, magnetic field lines move with an ideal MHD plasma. We will first discuss how this theorem follows from (8.8). We will then introduce an important consequence for stellarator design: ideal MHD does not allow changes in the topology of magnetic surfaces as they move with the plasma flow. This informs the choice of model for practical stellarator design, discussed in detail in Chapters 10 and 11.

8.2.1 ▪ Flux through a surface and conservation

In this section, we define the concept of magnetic flux through a surface and prove that it is conserved when the surface is carried by the plasma flow under ideal MHD evolution.

Given a time-independent magnetic field $\boldsymbol{B}$ and any fixed surface S, the magnetic flux through S is defined by

$$\Phi_S = \int_S \boldsymbol{B}(\boldsymbol{r}) \cdot \hat{\boldsymbol{n}}(\boldsymbol{r})\, d^2r.$$

Similarly, given a time-dependent magnetic field $\boldsymbol{B}(\boldsymbol{r}, t)$ and any surface $S(t)$ evolving in time, at any time t the magnetic flux through $S(t)$ is defined by

$$\Phi_{S(t)}(t) = \int_{S(t)} \boldsymbol{B}(\boldsymbol{r}, t) \cdot \hat{\boldsymbol{n}}(\boldsymbol{r}, t)\, d^2r.$$

In the context of any fluid moving with velocity $\boldsymbol{u}$, we introduce the concept of moving with the flow. Trajectories are solutions to the differential equation $\dot{\boldsymbol{x}}(t) = \boldsymbol{u}(\boldsymbol{x}(t), t)$, and $\boldsymbol{x}(t)$ is the trajectory emerging from $\boldsymbol{x}(0)$. A set of points moving with the flow is defined by

- an initial set of points $\mathcal{S}_0$, and
- at any time t, the set of points $\boldsymbol{x}(t)$ satisfying the initial condition $\boldsymbol{x}(0) \in \mathcal{S}_0$ and the differential equation $\dot{\boldsymbol{x}}(t) = \boldsymbol{u}(\boldsymbol{x}(t), t)$.

At a given time t, the set of points is denoted $\mathcal{S}(t)$. For example, this set can define a surface or a volume moving with the flow.

In a plasma described by ρ, $\boldsymbol{u}$, $\boldsymbol{B}$, and p satisfying the ideal MHD model (8.7), consider the magnetic flux through an open surface $\mathcal{S}(t)$ moving with the plasma flow, $\Phi_{\mathcal{S}(t)}$. We will now determine the time derivative of $\Phi_{\mathcal{S}(t)}$ as it moves with the plasma. This time derivative includes contributions from the time derivative of the magnetic field, namely $\partial \boldsymbol{B}/\partial t + (\boldsymbol{u} \cdot \nabla)\boldsymbol{B}$, as well as the time derivative of the unit normal vector and surface area element,

$$\frac{d\Phi_{\mathcal{S}(t)}(t)}{dt} = \int_{\mathcal{S}(t)} \left(\frac{\partial \boldsymbol{B}(\boldsymbol{r}, t)}{\partial t} + (\boldsymbol{u}(\boldsymbol{r}, t) \cdot \nabla)\, \boldsymbol{B}(\boldsymbol{r}, t) \right) \cdot \hat{\boldsymbol{n}}(\boldsymbol{r})\, d^2r + \int_{\mathcal{S}(t)} \boldsymbol{B}(\boldsymbol{r}, t) \cdot \frac{d\left[\hat{\boldsymbol{n}}(\boldsymbol{r}) d^2r(\boldsymbol{r})\right]}{dt}.$$

To compute the time derivative of $\hat{\boldsymbol{n}}(\boldsymbol{r})d^2r(\boldsymbol{r})$, we evaluate $\boldsymbol{r}$ at a point $\boldsymbol{x}(t) \in \mathcal{S}(t)$ moving with the plasma flow. According to [298, 89], we use the formula

$$\frac{d\left[\hat{\boldsymbol{n}}(\boldsymbol{r}) d^2r(\boldsymbol{r})\right]}{dt} = \left[-\nabla \boldsymbol{u}(\boldsymbol{r}, t) \cdot \hat{\boldsymbol{n}}(\boldsymbol{r}, t) + \nabla \cdot \boldsymbol{u}(\boldsymbol{r}, t) \hat{\boldsymbol{n}}(\boldsymbol{r}, t)\right]\, d^2r(\boldsymbol{r}(t), t),$$

along with (8.8), to obtain

$$\frac{d\Phi_{\mathcal{S}(t)}(t)}{dt} = \int_{\mathcal{S}(t)} \Big[\nabla \times (\boldsymbol{u}(\boldsymbol{r}, t) \times \boldsymbol{B}(\boldsymbol{r}, t)) + (\boldsymbol{u}(\boldsymbol{r}, t) \cdot \nabla)\, \boldsymbol{B}(\boldsymbol{r}, t) - (\boldsymbol{B}(\boldsymbol{r}, t) \cdot \nabla)\, \boldsymbol{u}(\boldsymbol{r}, t) + (\nabla \cdot \boldsymbol{u}(\boldsymbol{r}, t)) \boldsymbol{B}(\boldsymbol{r}, t) \Big] \cdot \hat{\boldsymbol{n}}(\boldsymbol{r})\, d^2r.$$

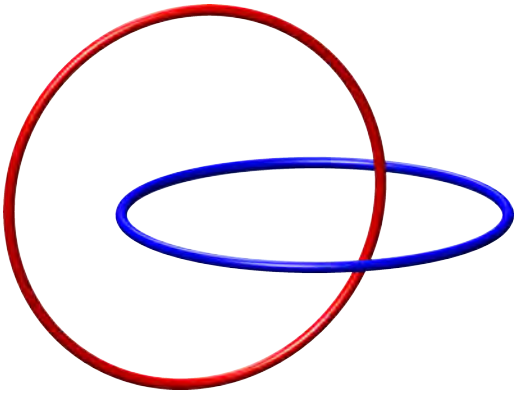

Figure 8.1*: Two closed magnetic field lines are linked with each other. This linking of field lines is preserved under ideal MHD.*

Using the vector identity $\nabla \times (\boldsymbol{A} \times \boldsymbol{B}) = \boldsymbol{A}(\nabla \cdot \boldsymbol{B}) - \boldsymbol{B}(\nabla \cdot \boldsymbol{A}) + (\boldsymbol{B} \cdot \nabla)\,\boldsymbol{A} - (\boldsymbol{A} \cdot \nabla)\,\boldsymbol{B}$, we then conclude that

$$\frac{d\Phi_{S(t)}(t)}{dt} = 0.$$

The so-called flux freezing theorem states that the magnetic flux is conserved through any surface moving with the plasma under ideal MHD evolution.

8.2.2 ▪ Implications for the magnetic field topology

The flux freezing theorem can be interpreted in terms of the magnetic field dynamics: it precludes changes in the magnetic field topology. The magnetic field topology refers to structures formed by magnetic field lines, including the topology of magnetic surfaces when they exist and the linking (or interlacing) of a field line with other field lines or with itself. This severely limits the dynamics that ideal MHD models can describe.

The flux through any surface moving with the ideal MHD flow is constant according to the discussion in Section 8.2.1. This has several implications:

- if we consider an initial magnetic field that contains a magnetic surface, this will remain a magnetic surface as the field evolves;
- the topology of a given magnetic surface cannot change; for instance, the number of holes in the surface cannot change in time;
- if the magnetic field contains continuously nested flux surfaces, this topology will be preserved, and magnetic islands cannot form;
- a magnetic field without continuously nested magnetic surfaces cannot evolve to a state with continuously nested magnetic surfaces under the ideal MHD model.

Furthermore, flux freezing can be shown to preserve the number of times magnetic field lines link with each other [76], and Figure 8.1 illustrates the notion of link. In this sense, the magnetic field topology is said to be preserved under ideal MHD. These considerations will be discussed in the application to 3D equilibrium models in Chapters 10 and 11.

8.3 ▪ Ideal MHD equilibrium

We now consider the ideal MHD equations under the assumption of static equilibrium, corresponding to the MHD system (8.7) together with $\boldsymbol{u} = 0$ and time independence of all the fields at play. The characteristic velocities associated with ideal MHD are the Alfvén speed, $v_A = B/\sqrt{\mu_0 \rho}$, and the sound speed, $c_s = \sqrt{\gamma p/\rho}$. When the magnitude of the flow speed $|\boldsymbol{u}|$ is small in comparison to these speeds, $|\boldsymbol{u}| \ll v_A$ and $|\boldsymbol{u}| \ll c_s$, then a static model is appropriate [76]. Considering a characteristic length scale L associated with a physical system, such as the major or minor radius of a torus, we can deduce a characteristic time scale associated with ideal MHD dynamics, $t_A \sim L/v_A$ and $t_s \sim L/c_s$. An equilibrium model is appropriate considering time scales $t \gg t_A$ and $t \gg t_s$. These assumptions are often relevant when considering the transport time scales of fusion plasmas, as discussed in Section 1.4. The conservation of momentum density (8.2) shows that the plasma pressure gradient balances electromagnetic forces,

$$\boldsymbol{J} \times \boldsymbol{B} = \nabla p. \tag{8.9}$$

The equilibrium fields must also satisfy the divergence-free condition and Ampère's law. As a summary, the ideal MHD equilibrium equations read

$$\begin{cases} \boldsymbol{J} \times \boldsymbol{B} &= \nabla p, \\ \nabla \times \boldsymbol{B} &= \mu_0 \boldsymbol{J}, \\ \nabla \cdot \boldsymbol{B} &= 0. \end{cases} \tag{8.10}$$

For magnetic confinement fusion, this nonlinear system of PDEs is often solved in a toroidal domain Ω. The interested reader can refer to [33] for a result of existence for solutions to (8.10) on a toroidal domain with the flux surface boundary condition, namely $\boldsymbol{B} \cdot \hat{\boldsymbol{n}} = 0$, for certain pressure profiles, and to [47] for the construction of solutions on a smooth bounded domain with the same boundary condition and adding a small driving force.

The force balance condition (8.9) is often considered under the assumption that the pressure depends only on a flux surface label, $p(\psi)$, the notion introduced in Section 5.5.1. Then the force balance equation (8.9) implies that $\boldsymbol{J} \cdot \nabla \psi = 0$, so that streamlines of the current density and magnetic field lie on surfaces of constant ψ.

The resulting equations in axisymmetry are described next in Section 8.4, and further details about computing 3D MHD equilibria will be discussed in Chapters 10 and 11. Even in the study of a steady-state solution, applying equilibrium models is sometimes challenging. There are alternative methods for numerically approximating equilibria that consider instead long-time solutions to time-dependent models, as described in Section 10.4.3.

8.4 ▪ MHD equilibrium in a tokamak: Grad–Shafranov

We now consider the MHD equilibrium equations under the assumption of axisymmetry as introduced in Section 7.4.1. The derivation involves a simplified form for the magnetic field in axisymmetry and a subsequent formulation of the current density. Both will then be combined to evaluate the force balance condition. We will find that this reduces (8.10) to a 2D, nonlinear PDE known as the Grad–Shafranov equation.

We begin with a convenient expression for the magnetic field in terms of the poloidal flux function ψ_P, discussed in Section 7.3.1, in the cylindrical coordinate system (R, ϕ, Z). For convenience, (7.4) is repeated here:

$$\boldsymbol{B}(R, \phi, Z) = \nabla \psi_P(R, Z) \times \nabla \phi + B_\phi(R, Z) \hat{\boldsymbol{\phi}}.$$

This can be rewritten as

$$\boldsymbol{B}(R,\phi,Z) = \frac{1}{R}\nabla\psi_P(R,Z)\times\hat{\boldsymbol{\phi}} + RB_\phi(R,Z)\nabla\phi,$$

since $\nabla\phi = \hat{\boldsymbol{\phi}}/R$. To simplify the above expression for the magnetic field, defining $F := RB_\phi$ is standard. Because this function is related to the integrated poloidal current, $I_P(\psi_P)$, defined in Section 9.1.2, through $F(\psi_P) = \mu_0 I_P(\psi_P)/(2\pi)$, we note that $F(\psi_P)$ is a flux function. Therefore, the magnetic field reads

$$\boldsymbol{B}(R,\phi,Z) = \frac{1}{R}\nabla\psi_P(R,Z)\times\hat{\boldsymbol{\phi}} + F(\psi_P)\nabla\phi.$$

Then the current can be expressed using Ampère's law $\nabla\times\boldsymbol{B} = \mu_0\boldsymbol{J}$,

$$\mu_0\boldsymbol{J} = \nabla\times\left(\frac{\nabla\psi_P}{R^2}\times\left(R\hat{\boldsymbol{\phi}}\right)\right) + \nabla F(\psi_P)\times\nabla\phi.$$

Applying the vector identity $\nabla\times(\boldsymbol{A}\times\boldsymbol{B}) = (\nabla\cdot\boldsymbol{B})\boldsymbol{A} - (\nabla\cdot\boldsymbol{A})\boldsymbol{B} + (\boldsymbol{B}\cdot\nabla)\boldsymbol{A} - (\boldsymbol{A}\cdot\nabla)\boldsymbol{B}$, we obtain

$$\mu_0\boldsymbol{J} = \nabla\cdot\left(R\hat{\boldsymbol{\phi}}\right)\frac{\nabla\psi_P}{R^2} - \nabla\cdot\left(\frac{\nabla\psi_P}{R^2}\right)R\hat{\boldsymbol{\phi}} + (R\hat{\boldsymbol{\phi}}\cdot\nabla)\left(\frac{\nabla\psi_P}{R^2}\right) - \left(\frac{\nabla\psi_P}{R^2}\cdot\nabla\right)\left(R\hat{\boldsymbol{\phi}}\right) + \nabla F(\psi_P)\times\nabla\phi. \quad (8.11)$$

Several simplifications follow from the properties of the cylindrical coordinate system.

- Since $\nabla\cdot\left(R\hat{\boldsymbol{\phi}}\right) = R\nabla\cdot\hat{\boldsymbol{\phi}} + \hat{\boldsymbol{\phi}}\cdot\nabla R$ while in cylindrical coordinates $\hat{\boldsymbol{\phi}}\cdot\nabla R = 0$ and $\nabla\cdot\hat{\boldsymbol{\phi}} = 0$, then $\nabla\cdot\left(R\hat{\boldsymbol{\phi}}\right)$ vanishes. Therefore, the first term vanishes.
- In cylindrical coordinates the gradient reads $\nabla = \hat{\boldsymbol{R}}\partial/\partial R + \hat{\boldsymbol{\phi}}/R\partial/\partial\phi + \hat{\boldsymbol{Z}}\partial/\partial Z$, and so $\nabla\psi_P(R,Z) = \hat{\boldsymbol{R}}\partial\psi_P(R,Z)/\partial R + \hat{\boldsymbol{Z}}\partial\psi_P(R,Z)/\partial Z$.
  - Because $(\hat{\boldsymbol{R}},\hat{\boldsymbol{\phi}},\hat{\boldsymbol{Z}})$ is orthonormal, the differential operator $\nabla\psi_P(R,Z)\cdot\nabla$ is equal to $(\partial\psi_P(R,Z)/\partial R)\partial/\partial R + (\partial\psi_P(R,Z)/\partial Z)\partial/\partial Z$. Moreover, since $\partial\hat{\boldsymbol{\phi}}/\partial R = 0$ and $\partial\hat{\boldsymbol{\phi}}/\partial Z = 0$, we find $\nabla\psi_P\cdot\nabla(R\hat{\boldsymbol{\phi}}) = (\partial\psi_P(R,Z)/\partial R)\,\hat{\boldsymbol{\phi}}$.
  - Furthermore, because $\hat{\boldsymbol{\phi}}\cdot\nabla = 1/R\partial/\partial\phi$, then

    $$(R\hat{\boldsymbol{\phi}}\cdot\nabla)\left(\frac{\nabla\psi_P}{R^2}\right) = \frac{1}{R^2}\frac{\partial}{\partial\phi}\left(\hat{\boldsymbol{R}}\frac{\partial\psi_P(R,Z)}{\partial R} + \hat{\boldsymbol{Z}}\frac{\partial\psi_P(R,Z)}{\partial Z}\right).$$

    But $\partial\hat{\boldsymbol{R}}/\partial\phi = \hat{\boldsymbol{\phi}}$ and $\partial\hat{\boldsymbol{Z}}/\partial\phi = 0$, so $(R\hat{\boldsymbol{\phi}}\cdot\nabla)\left(\nabla\psi_P/R^2\right) = \hat{\boldsymbol{\phi}}/R^2\partial\psi_P(R,Z)/\partial R$. Therefore, the third and fourth terms on the right-hand side of (8.11) vanish.

This yields a simplified expression for the current density, namely

$$\mu_0\boldsymbol{J} = -R\nabla\cdot\left(\frac{\nabla\psi_P}{R^2}\right)\hat{\boldsymbol{\phi}} + \nabla F(\psi_P)\times\nabla\phi.$$

As a result, in a tokamak, the vector unknowns, $\boldsymbol{B}$ and $\boldsymbol{J}$, can be expressed in terms of the scalar unknown $\psi_P(R,Z)$, namely

$$\begin{cases} \boldsymbol{B} = \frac{1}{R}\nabla\psi_P(R,Z)\times\hat{\boldsymbol{\phi}} + F(\psi_P)\nabla\phi, \\ \boldsymbol{J} = \frac{1}{\mu_0}\left(-R\nabla\cdot\left(\frac{\nabla\psi_P}{R^2}\right)\hat{\boldsymbol{\phi}} + \nabla F(\psi_P)\times\nabla\phi\right). \end{cases} \quad (8.12)$$

Given this form for $\boldsymbol{B}$ and $\boldsymbol{J}$, the force balance equation $\boldsymbol{J} \times \boldsymbol{B} = \nabla p$ reads

$$\frac{1}{\mu_0}\left[-\nabla\psi_P(R,Z)\nabla\cdot\left(\frac{\nabla\psi_P(R,Z)}{R^2}\right) - \frac{F\left(\psi_P(R,Z)\right)\nabla F\left(\psi_P(R,Z)\right)}{R^2}\right] = \nabla p\left(\psi_P(R,Z)\right).$$

Since the left- and right-hand sides of this expression are proportional to $\nabla\psi_P$, it is sufficient to enforce the projection of force balance along $\partial\boldsymbol{R}/\partial\psi_P$. After multiplying through by $(R^2\mu_0)$, this results in the Grad–Shafranov equation, namely

$$R^2\nabla\cdot\left(\frac{\nabla\psi_P(R,Z)}{R^2}\right) = -\mu_0 R^2 p'(\psi_P(R,Z)) - F(\psi_P(R,Z))F'(\psi_P(R,Z)). \tag{8.13}$$

This is a nonlinear elliptic equation for the unknown $\psi_P(R,Z)$ while the pressure profile p and the poloidal current function $F = \mu_0 I_P/(2\pi)$ are given. In the literature, the notation $\Delta^*\psi_P = R^2\nabla\cdot\left(R^{-2}\nabla\psi_P\right)$ is often used.

The Grad–Shafranov equation (8.13) is solved in a smooth bounded domain Ω in the R-Z plane, together with the boundary condition $\psi_P = \psi_{P0}$ on $\partial\Omega$ for a fixed value ψ_{P0}. Prescribing this constant Dirichlet boundary condition ensures that the boundary of Ω is a constant-flux curve.

Once ψ_P is determined in Ω, the magnetic field is known from (8.12) in the axisymmetric toroidal domain defined by the rotation of Ω about the symmetry axis. The boundary of the 3D domain is the flux surface of label ψ_{P0}. The field is axisymmetric by construction. The shape of the flux surfaces in $\mathbb{R}^3$ is determined by the rotation of $\psi_P(R,Z)$ about the symmetry axis. In conclusion, given the shape of the outer boundary and specified pressure and current profiles, the Grad–Shafranov solution provides the shape of the inner flux surfaces.

More details about the Grad–Shafranov equation can be found in Chapter 7 of [120] and Chapter 6 of [76]. For a discussion of computational methods for the Grad–Shafranov equation, refer to Chapter 4 of [151]. In some special cases, the 3D MHD equilibrium equations can be formulated using a Grad–Shafranov equation [34]. However, general 3D MHD equilibrium models are more complex and will be discussed in Chapter 11.

8.5 ▪ Summary

Under various sets of hypotheses, the ideal MHD equations can be reduced to simpler models. Common reduced models are gathered in Table 8.1.

Table 8.1*: Summary of the ideal MHD equations under several hypotheses, emphasizing the set of unknowns as opposed to quantities that can be eliminated from the system.*

	Ideal MHD	MHD equilibrium	Grad–Shafranov
Hyp.	$\partial \boldsymbol{E}/\partial t = 0$ Low frequency/long wavelength 3D	$\boldsymbol{u} = 0$ $\partial/\partial t = 0$ 3D	MHD equilibrium $\partial/\partial \phi = 0$ 2D (R,Z)
PDE model	$\dfrac{\partial \rho}{\partial t} + \nabla \cdot (\rho \boldsymbol{u}) = 0$ $\rho \left(\dfrac{\partial}{\partial t} + \boldsymbol{u} \cdot \nabla \right) \boldsymbol{u} = \boldsymbol{J} \times \boldsymbol{B} - \nabla p$ $\left(\dfrac{\partial}{\partial t} + \boldsymbol{u} \cdot \nabla \right) p + \gamma p \nabla \cdot \boldsymbol{u} = 0$ $\dfrac{\partial \boldsymbol{B}}{\partial t} = -\nabla \times \boldsymbol{E}$ $\nabla \cdot \boldsymbol{B} = 0$ $\boldsymbol{E} + \boldsymbol{u} \times \boldsymbol{B} = 0$ $\nabla \times \boldsymbol{B} = \mu_0 \boldsymbol{J}$	$\boldsymbol{J} \times \boldsymbol{B} = \nabla p$ $\nabla \cdot \boldsymbol{B} = 0$ $\nabla \times \boldsymbol{B} = \mu_0 \boldsymbol{J}$	Given $F(\psi_P)$ and $p(\psi_P)$, $R^2 \nabla \cdot \left(\dfrac{\nabla \psi_P}{R^2} \right) = -\mu_0 R^2 p'(\psi_P) - F(\psi_P) F'(\psi_P)$
Unkn.	ρ, $\boldsymbol{u}$, p, $\boldsymbol{B}$	$\boldsymbol{B}$, p	$\psi_P(R, Z)$
With	$\boldsymbol{E}$ function of $\boldsymbol{B}$, $\boldsymbol{u}$ $\boldsymbol{J}$ function of $\boldsymbol{B}$	$\boldsymbol{J}$ function of $\boldsymbol{B}$	$\boldsymbol{B} = \nabla \psi_P \times \nabla \phi + F(\psi_P) \nabla \phi$ $\boldsymbol{J} = \dfrac{1}{\mu_0} \left(- R \nabla \cdot \left(\dfrac{\nabla \psi_P}{R^2} \right) \hat{\boldsymbol{\phi}} + \nabla F(\psi_P) \times \nabla \phi \right)$

Part II

Toward stellarator design

Chapter 9
Magnetic coordinates

Beyond the introductory material presented in Part I to study magnetic confinement in toroidal geometry, further properties of magnetic fields can be leveraged to develop more specific theoretical tools in order to simplify the formulation of many mathematical questions.

Under the fundamental assumption that the given vector field $\boldsymbol{B}$ has continuously nested toroidal flux surfaces throughout the domain of interest, toroidal coordinate systems using a flux label as the radius-like coordinate were introduced in Section 5.5.2 under the name of flux coordinates. Under the additional assumption that the vector field $\boldsymbol{B}$ is divergence-free, a particular kind of flux coordinates, called magnetic coordinates, is introduced here as a convenient tool to simplify the expression of the magnetic field and of other quantities of interest. With poloidal angle and toroidal angle respectively denoted ϑ and φ, the fundamental property of magnetic coordinates is that the ratio B^ϑ / B^φ of the contravariant components of the magnetic field is a constant on each magnetic surface. This implies that, given a value of the rotational transform ι determining a given magnetic surface, field lines appear straight when represented in the φ-ϑ plane, with a slope given by ι. This is an important example of the impact of the choice coordinate system and how drastically it simplifies the description of magnetic field lines, from 3D curves to straight lines.

This chapter is organized as follows. Magnetic coordinates are constructed from general flux coordinates in Section 9.1.1. Their definition leads to the desired contravariant form and the defining property. The covariant form is simplified under the assumption of MHD equilibrium in Section 9.1.2. A special form of magnetic coordinates, called Boozer coordinates, is introduced in Section 9.2. A related coordinate system, the field-line following coordinates, is introduced in Section 9.3. Further simplifications of the expression in these field-line following coordinates for differential and integral operators along field lines are derived. Section 9.4 presents a summary of covariant and contravariant forms of the magnetic field comparing formulas in the three types of coordinate systems: magnetic coordinates, Boozer coordinates, and field-line following coordinates.

In the following chapters, these coordinate systems will be exploited to describe several challenges arising when studying nonaxisymmetric magnetic equilibria in Chapter 10 and to present various models of MHD equilibrium both with and without the assumption of continuously nested toroidal flux surfaces in Chapter 11. These coordinates systems are also key to introducing various types of symmetries that can be leveraged to obtain confinement properties. This will be done in Chapters 12 and 13.

9.1 ▪ Magnetic coordinates

Given a magnetic field $\boldsymbol{B}$ with continuously nested toroidal flux surfaces, magnetic coordinates are constructed from a general flux coordinate system (ψ, θ, ϕ) where θ is any poloidal angle, ϕ is any toroidal angle, and $\psi = \Psi_T/2\pi$ is the toroidal flux label, introduced in Section 5.5.1. Their derivation relies on the divergence-free assumption, $\nabla \cdot \boldsymbol{B} = 0$, leveraged to simplify the contravariant form of the field in Section 9.1.1. The covariant form can be further simplified under the assumption $\boldsymbol{J} \cdot \nabla\psi = 0$ as discussed in Section 9.1.2.

9.1.1 ▪ Contravariant form

Since $\boldsymbol{B} \cdot \nabla\psi = 0$, as in any flux coordinate system, the radial contravariant component of the field is zero, and therefore the magnetic field can be written as

$$\boldsymbol{B} = B^\theta \frac{\partial \boldsymbol{R}}{\partial \theta} + B^\phi \frac{\partial \boldsymbol{R}}{\partial \phi},$$

(B^θ, B^ϕ) being the toroidal and poloidal contravariant components. The divergence-free condition $\nabla \cdot \boldsymbol{B} = 0$ is then equivalent to

$$0 = \frac{1}{\sqrt{g}} \left(\frac{\partial (B^\theta \sqrt{g})}{\partial \theta} + \frac{\partial (B^\phi \sqrt{g})}{\partial \phi} \right), \tag{9.1}$$

where $\sqrt{g} = (\nabla\psi \times \nabla\theta \cdot \nabla\phi)^{-1}$.

Remark 9.1. *Equation* (9.1) *is of the form* (6.1)*. Considering the flux coordinates* (ψ, θ, ϕ) *as well as the functions* $F_1 = -B^\theta\sqrt{g}$ *and* $F_2 = -B^\phi\sqrt{g}$*, we can thus apply the results discussed in Section* 6.1.

According to Remark 9.1, for a divergence-free magnetic field expressed in flux coordinates (ψ, θ, ϕ), there exist one function λ periodic in (θ, ϕ) and two functions j, h of one variable satisfying the following relations for $\alpha(\psi, \theta, \phi) := j(\psi)\theta + h(\psi)\phi + \lambda(\psi, \theta, \phi)$:

$$\begin{cases} B^\theta \sqrt{g} = -\dfrac{\partial \alpha}{\partial \phi}, \\ B^\phi \sqrt{g} = \dfrac{\partial \alpha}{\partial \theta}, \end{cases} \quad \text{implying that } \boldsymbol{B} = \frac{1}{\sqrt{g}} \left(\frac{\partial \alpha}{\partial \theta} \frac{\partial \boldsymbol{R}}{\partial \phi} - \frac{\partial \alpha}{\partial \phi} \frac{\partial \boldsymbol{R}}{\partial \theta} \right). \tag{9.2}$$

As a consequence, leveraging the relations between basis vectors, summarized in Table 5.1, we get

$$\boldsymbol{B} = \nabla\psi \times \left(\frac{\partial \alpha}{\partial \theta} \nabla\theta + \frac{\partial \alpha}{\partial \phi} \nabla\phi \right).$$

This immediately yields a more compact expression for the magnetic field:

$$\boldsymbol{B} = \nabla\psi \times \nabla\alpha. \tag{9.3}$$

Hence, the definition of α leads to the magnetic field expression:

$$\boldsymbol{B}(\boldsymbol{R}(\psi, \theta, \phi)) = [\nabla\psi](\psi, \theta, \phi) \times \Big(j(\psi)[\nabla\theta](\psi, \theta, \phi) + h(\psi)[\nabla\phi](\psi, \theta, \phi) + [\nabla\lambda](\psi, \theta, \phi) \Big).$$

So j and h are related to the toroidal and poloidal contravariant components of the field, and we can now relate them to the toroidal and poloidal fluxes introduced in Chapter 5. Indeed, thanks

to the expression of the fluxes in flux coordinates, (5.10) and (5.11), we have

$$\begin{aligned}\Psi_T(\psi) &= \int_0^{\psi}\int_0^{2\pi} \left[\sqrt{g}\boldsymbol{B}\cdot\nabla\phi\right]\left(\boldsymbol{R}\Big(\widetilde{\psi},\theta,\phi_0\Big)\right) d\theta d\widetilde{\psi} \\ &= \int_0^{\psi}\int_0^{2\pi} \frac{\partial\alpha\left(\widetilde{\psi},\theta,\phi_0\right)}{\partial\theta}\, d\theta d\widetilde{\psi} \\ &= \int_0^{\psi}\int_0^{2\pi} j\Big(\widetilde{\psi}\Big)\, d\theta d\widetilde{\psi} \text{ as } \lambda \text{ is periodic} \\ &= 2\pi\int_0^{\psi} j\Big(\widetilde{\psi}\Big)\, d\widetilde{\psi},\end{aligned}$$

and similarly

$$\begin{aligned}\Psi_P(\psi) &= \int_0^{\psi}\int_0^{2\pi} \left[\sqrt{g}\boldsymbol{B}\cdot\nabla\theta\right]\left(\boldsymbol{R}(\widetilde{\psi},\theta_0,\phi)\right) d\phi d\widetilde{\psi} \\ &= \int_0^{\psi}\int_0^{2\pi} -\frac{\partial\alpha\left(\widetilde{\psi},\theta_0,\phi\right)}{\partial\phi}\, d\phi d\widetilde{\psi} \\ &= \int_0^{\psi}\int_0^{2\pi} -h\Big(\widetilde{\psi}\Big)\, d\phi d\widetilde{\psi} \text{ as } \lambda \text{ is periodic} \\ &= 2\pi\int_0^{\psi} -h\Big(\widetilde{\psi}\Big)\, d\widetilde{\psi}.\end{aligned}$$

Since, by choice of the flux label and definition of the rotational transform (7.3), we know that

$$\Psi_T(\psi) = 2\pi\psi \text{ and } \iota(\psi) = \psi_P'(\psi),$$

this shows that

$$j(\psi) = 1 \text{ and } h(\psi) = -\iota(\psi).$$

To summarize, in terms of the magnetic field, we obtain

$$\boldsymbol{B}\big(\boldsymbol{R}(\psi,\theta,\phi)\big) = \left[\nabla\psi\times\nabla\left(\theta+\lambda-\iota\nabla\phi\right)\right]\big(\boldsymbol{R}(\psi,\theta,\phi)\big). \tag{9.4}$$

Hence at any point $\boldsymbol{R}(\psi,\vartheta,\varphi)$ we have

$$\begin{aligned}\boldsymbol{B}\cdot\nabla\phi &= \big(\nabla\psi\times\nabla\left(\theta+\lambda\right)\big)\cdot\nabla\phi, \\ \boldsymbol{B}\cdot\nabla\left(\theta+\lambda\right) &= \iota\big(\nabla\psi\times\nabla\left(\theta+\lambda\right)\big)\cdot\nabla\phi.\end{aligned}$$

Therefore, at any point $\boldsymbol{R}(\psi,\vartheta,\varphi)$, $\big(\nabla\psi\times\nabla\left(\theta+\lambda\right)\big)\cdot\nabla\phi = 0$ if and only if $\boldsymbol{B}=0$, as this is equivalent to both contravariant components vanishing. Since the field never vanishes, as discussed in Section 4.4.1, this guarantees that $\big(\nabla\psi\times\nabla\big(\theta+\lambda\big)\big)\cdot\nabla\phi\neq 0$ everywhere.

As a result, with $\vartheta := \theta+\lambda$ and $\varphi := \phi$, then (ψ,ϑ,φ) defines a coordinate system called a magnetic coordinate system. Following this definition, (9.4) gives the contravariant expression of the field in these magnetic coordinates as

$$\boldsymbol{B}\big(\boldsymbol{R}(\psi,\theta,\phi)\big) = \left[\nabla\psi\times\nabla\vartheta\right]\big(\boldsymbol{R}(\psi,\theta,\phi)\big) - \iota(\psi)\left[\nabla\psi\times\nabla\varphi\right]\big(\boldsymbol{R}(\psi,\theta,\phi)\big), \tag{9.5}$$

or equivalently,

$$\boldsymbol{B}\big(\boldsymbol{R}(\psi,\theta,\phi)\big) = \sqrt{g}^{-1}\big(\boldsymbol{R}(\psi,\theta,\phi)\big)\left(\iota(\psi)\frac{\partial\boldsymbol{R}(\psi,\vartheta,\varphi)}{\partial\vartheta} + \frac{\partial\boldsymbol{R}(\psi,\vartheta,\varphi)}{\partial\varphi}\right). \tag{9.6}$$

In a more compact way

$$\boldsymbol{B} = \nabla\psi \times \nabla\vartheta - \iota\nabla\psi \times \nabla\varphi \Leftrightarrow \boldsymbol{B} = \sqrt{g}^{-1}\left(\iota\frac{\partial \boldsymbol{R}}{\partial\vartheta} + \frac{\partial \boldsymbol{R}}{\partial\varphi}\right).$$

Noting that $\boldsymbol{B}\cdot\nabla\varphi = \nabla\psi\times\nabla\vartheta\cdot\nabla\varphi$, also equal to $\sqrt{g}^{-1}$, this quantity never vanishes as pointed out earlier. At any point $\boldsymbol{R}(\psi,\vartheta,\varphi)$, we then see that

$$\left[\frac{\boldsymbol{B}\cdot\nabla\vartheta}{\boldsymbol{B}\cdot\nabla\varphi}\right]\big(\boldsymbol{R}(\psi,\theta,\phi)\big) \text{ is constant on a flux surface and equal to } \iota(\psi). \tag{9.7}$$

Since $\boldsymbol{B}\cdot\nabla\varphi \neq 0$ everywhere, the trajectories of magnetic field lines can be parameterized by the toroidal angle, φ. While ψ is constant along magnetic field lines, the poloidal angle of a field line will vary with the toroidal angle. Any field line can then be described by one value of the flux label, ψ_l, and a function of the toroidal angle $\vartheta_l(\varphi)$. Physical quantities are 2π periodic with respect to φ at fixed (ψ,ϑ), but a field-line trajectory does not necessarily close after a change in φ of 2π. Therefore, the trajectory in φ may be defined for a range longer than 2π.

Along a field line, the chain rule reads

$$\frac{d\boldsymbol{R}(\psi_l,\vartheta_l(\varphi),\varphi)}{d\varphi} = \frac{\partial\boldsymbol{R}(\psi_l,\vartheta_l(\varphi),\varphi)}{\partial\vartheta}\frac{d\vartheta_l(\varphi)}{d\varphi} + \frac{\partial\boldsymbol{R}(\psi_l,\vartheta_l(\varphi),\varphi)}{\partial\varphi}.$$

By definition, $d\boldsymbol{R}/d\varphi(\psi_l,\vartheta_l(\varphi),\varphi)$ is proportional to $\boldsymbol{B}$ since it follows the path of a field line. We can therefore write $d\boldsymbol{R}/d\varphi(\psi_l,\vartheta_l(\varphi),\varphi) = A(\psi_l,\vartheta_l(\varphi),\varphi)\boldsymbol{B}(\psi_l,\vartheta_l(\varphi),\varphi)$ for some proportionality factor A. By dotting $\nabla\varphi$ into both sides of the above expression and applying the duality of the basis vectors, we determine $A = (\boldsymbol{B}\cdot\nabla\varphi)^{-1}$. By dotting $\nabla\vartheta$ in the above expression and applying the definition for A, we determine the trajectory in the ϑ-φ plane,

$$\frac{d\vartheta_l(\varphi)}{d\varphi} = \frac{[\boldsymbol{B}\cdot\nabla\vartheta]\,(\psi_l,\vartheta_l(\varphi),\varphi)}{[\boldsymbol{B}\cdot\nabla\varphi]\,(\psi_l,\vartheta_l(\varphi),\varphi)}.$$

According to (9.7), this implies that

$$\frac{d\vartheta_l(\varphi)}{d\varphi} = \iota(\psi_l).$$

This is the defining property of magnetic coordinates:

On a flux surface ψ, field lines are straight in magnetic coordinates (ϑ,φ).

Magnetic coordinates have many applications in both analytic and numerical calculations. For example, the computation of ideal MHD equilibrium fields can be formulated as a variational problem for the magnetic coordinates $\psi(\boldsymbol{r})$ and $\lambda(\boldsymbol{r})$, as will be done in Section 11.1.1. Magnetic coordinates will be used for several calculations, such as in discussions of guiding center confinement with omnigeneity and quasisymmetry in Sections 12.2 and 12.1.1.

Several choices of magnetic coordinates exist. We will discuss a particular choice of magnetic coordinates, known as Boozer coordinates, in Section 9.2.

9.1.2 ▪ Covariant form

The magnetic field can also be written in the covariant form in magnetic coordinates (ψ,ϑ,φ):

$$\boldsymbol{B} = B_\psi\nabla\psi + B_\vartheta\nabla\vartheta + B_\varphi\nabla\varphi.$$

Here we obtain expressions for the covariant components (B_ψ, B_ϑ,B_φ) given the currents linking the plasma in the absence of radial current, $\boldsymbol{J}\cdot\nabla\psi = 0$ or equivalently $\nabla\times\boldsymbol{B}\cdot\nabla\psi = 0$. Under this assumption, we can then reformulate the covariant expression of the magnetic field, thanks to convenient properties of B_ϑ, B_φ, and B_ψ. More generally, the analysis in this section applies not just to magnetic coordinates but to any flux coordinate system, only requiring the absence of radial current.

Even though the vanishing of radial current, $\boldsymbol{J}\cdot\nabla\psi = 0$, is not required to construct magnetic coordinates, it will simplify the covariant representation. The assumption of vanishing radial current arises, for example, under the MHD equilibrium equations. Indeed, by combining Ampère's law with the ideal MHD force balance, we get

$$\begin{cases} \nabla\times\boldsymbol{B} = \mu_0\boldsymbol{J}, \\ \boldsymbol{J}\times\boldsymbol{B} = \nabla p, \\ p \text{ function of only } \psi, \end{cases} \Rightarrow \nabla\times\boldsymbol{B}\cdot\nabla\psi = 0. \tag{9.8}$$

We now evaluate the radial current. From Table 5.1, the curl of $\boldsymbol{B}$ in magnetic coordinates is expressed in the covariant basis in terms of the field's covariant components as

$$\sqrt{g}\nabla\times\boldsymbol{B} = \left(\frac{\partial B_\vartheta}{\partial\psi} - \frac{\partial B_\psi}{\partial\vartheta}\right)\frac{\partial\boldsymbol{R}}{\partial\varphi} + \left(\frac{\partial B_\psi}{\partial\varphi} - \frac{\partial B_\varphi}{\partial\psi}\right)\frac{\partial\boldsymbol{R}}{\partial\vartheta} + \left(\frac{\partial B_\varphi}{\partial\vartheta} - \frac{\partial B_\vartheta}{\partial\varphi}\right)\frac{\partial\boldsymbol{R}}{\partial\psi},$$

and the duality of the covariant and contravariant bases then yields

$$\sqrt{g}\nabla\times\boldsymbol{B}\cdot\nabla\psi = \frac{\partial B_\varphi}{\partial\vartheta} - \frac{\partial B_\vartheta}{\partial\varphi}.$$

Thus we obtain

$$\frac{\partial B_\varphi}{\partial\vartheta} - \frac{\partial B_\vartheta}{\partial\varphi} = 0. \tag{9.9}$$

Remark 9.2. *Equation* (9.9) *is of the form* (6.1)*. Considering the magnetic coordinates* (ψ,ϑ,φ) *as well as* $F_1 = B_\varphi$ *and* $F_2 = -B_\vartheta$ *we can thus apply the results discussed in Section* 6.1.

According to Remark 9.2, there exist one function H periodic in (ϑ,φ) and two functions I, G of one variable, defining $\overline{H}(\psi,\theta,\phi) := I(\psi)\vartheta + G(\psi)\varphi + H(\psi,\vartheta,\varphi)$, such that the covariant components of $\boldsymbol{B}$ expressed in magnetic coordinates (ψ,ϑ,φ) satisfy

$$\begin{cases} B_\vartheta(\psi,\vartheta,\varphi) = \dfrac{\partial\overline{H}(\psi,\vartheta,\varphi)}{\partial\vartheta}, \\ B_\varphi(\psi,\vartheta,\varphi) = \dfrac{\partial\overline{H}(\psi,\vartheta,\varphi)}{\partial\varphi}. \end{cases} \tag{9.10}$$

We can now relate the functions I and G to the integrated toroidal and poloidal currents.

In order to define the toroidal current, consider a closed curve lying on a flux surface at a constant toroidal angle, $C_T(\psi,\varphi) := \{(\psi,\vartheta,\varphi), \vartheta\in[0,2\pi)\}$, as well as the surface enclosed by this curve, denoted by $S_T(\psi,\varphi) := \left\{\left(\widetilde{\psi},\vartheta,\varphi\right), \widetilde{\psi}\le\psi, \vartheta\in[0,2\pi)\right\}$ and shown in Figure 9.1. The toroidal current is then defined as

$$I_T(\psi,\varphi) = \int_{S_T(\psi,\varphi)} \boldsymbol{J}(\boldsymbol{r})\cdot\hat{\boldsymbol{n}}(\boldsymbol{r})\,d^2r, \tag{9.11}$$

where $\hat{\boldsymbol{n}}$ is a unit normal vector to the surface $S_T(\psi,\varphi)$, pointing in the same direction for all $\boldsymbol{r}\in S_T(\psi,\varphi)$. The above integral only includes contributions to the toroidal current from the

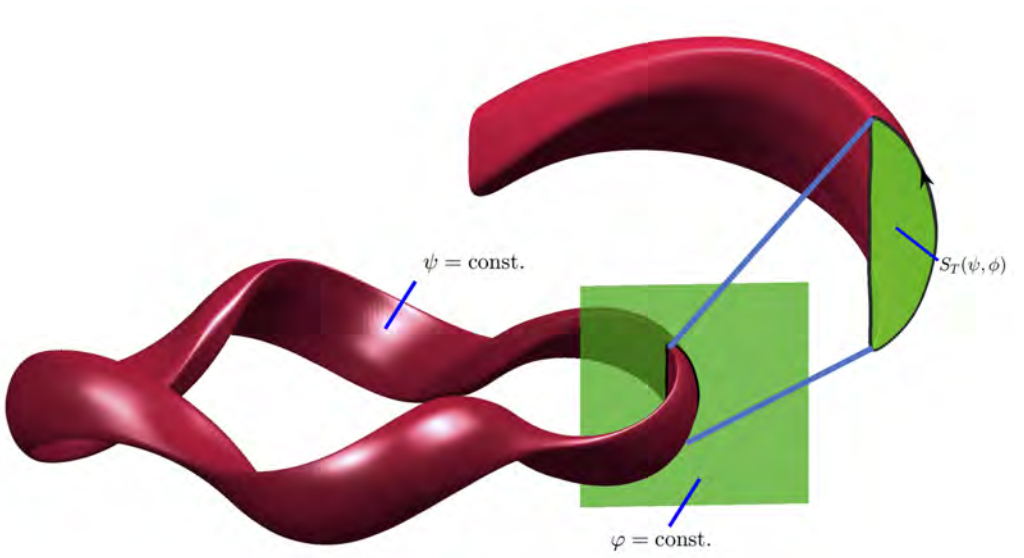

Figure 9.1*: The integration curve at constant φ and ψ. The black curve encloses a surface $S_T(\psi, \varphi)$ within the green surface. The toroidal current is integrated over $S_T(\psi, \varphi)$.*

plasma current. But Ampère's law reads $\mu_0 \boldsymbol{J} = \nabla \times \boldsymbol{B}$, hence by Stokes' theorem

$$\begin{aligned}\mu_0 I_T(\psi,\varphi) &= \oint_{C_T(\psi,\varphi)} \boldsymbol{B}(\boldsymbol{r}) \cdot d\boldsymbol{l}(\boldsymbol{r}) \qquad \text{with } d\boldsymbol{l} = (\partial \boldsymbol{R}/\partial\vartheta)\, d\vartheta \\ &= \int_0^{2\pi} B_\vartheta(\psi,\vartheta,\varphi)\, d\vartheta \qquad \text{since } B_\vartheta = \boldsymbol{B} \cdot \frac{\partial \boldsymbol{R}}{\partial \vartheta}.\end{aligned}$$

As a consequence,

$$\begin{aligned}\frac{\partial I_T(\psi,\varphi)}{\partial \varphi} &= \frac{1}{\mu_0}\int_0^{2\pi} \frac{\partial B_\vartheta(\psi,\vartheta,\varphi)}{\partial \varphi}\, d\vartheta \\ &= \frac{1}{\mu_0}\int_0^{2\pi} \frac{\partial B_\varphi(\psi,\vartheta,\varphi)}{\partial \vartheta}\, d\vartheta \qquad \text{from (9.9)} \\ &= 0 \qquad\qquad\qquad\qquad\qquad\qquad\quad \text{by periodicity of } B_\varphi.\end{aligned}$$

Thus, the toroidal current is a flux function, $I_T(\psi)$. And beyond this remark,

$$\begin{aligned}\mu_0 I_T(\psi) &= \int_0^{2\pi} \left(I(\psi) + \frac{\partial H(\psi,\vartheta,\varphi)}{\partial \vartheta} \right) d\vartheta \qquad \text{from (9.10)} \\ &= 2\pi I(\psi) \qquad\qquad\qquad\qquad\qquad\quad \text{by periodicity of } H.\end{aligned}$$

So finally, we have identified

$$I(\psi) = \frac{\mu_0}{2\pi} I_T(\psi).$$

Similarly, in order to define the poloidal current, consider a closed curve lying on a flux surface at a constant poloidal angle, $C_P(\psi,\vartheta) := \{(\psi,\vartheta,\varphi), \varphi \in [0,2\pi)\}$, as well as the surface enclosed by this curve, denoted by $S_P(\psi,\vartheta) := \left\{ \left(\widetilde{\psi},\vartheta,\varphi\right), \widetilde{\psi} \le \psi, \varphi \in [0,2\pi) \right\}$ and shown in in Figure 9.2. The poloidal current is then defined as

$$I_P(\psi,\vartheta) = \int_{S_P(\psi,\vartheta)} \boldsymbol{J}(\boldsymbol{r}) \cdot \hat{\boldsymbol{n}}(\boldsymbol{r})\, d^2 r.$$

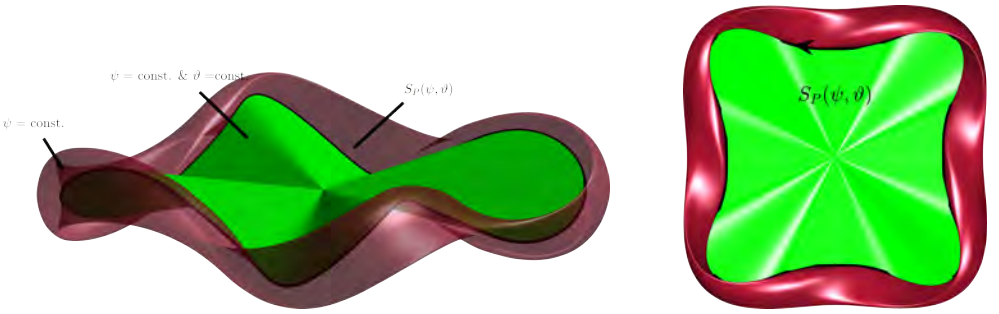

(a) (b)

Figure 9.2: The integration curve at constant ϑ and ψ. The black curve encloses the green surface $S_P(\psi,\vartheta)$ through which the poloidal current is integrated.

Depending on $S_P(\psi,\vartheta)$, the above integral includes contributions to the poloidal current from outside the constant ψ surface, including both the plasma current and any external currents, such as electromagnetic coils. But again, Ampère's law combined with Stokes' theorem gives

$$\begin{aligned}\mu_0 I_P(\psi,\vartheta) &= \oint_{C_P(\psi)} \boldsymbol{B}(\boldsymbol{r})\cdot d\boldsymbol{l}(\boldsymbol{r}) \quad \text{with } d\boldsymbol{l} = \frac{\partial \boldsymbol{R}}{\partial\varphi}\,d\varphi \\ &= \int_0^{2\pi} B_\varphi(\psi,\vartheta,\varphi)\,d\varphi \quad \text{since } B_\varphi = \boldsymbol{B}\cdot\frac{\partial \boldsymbol{R}}{\partial\varphi}.\end{aligned}$$

As a consequence,

$$\begin{aligned}\frac{\partial I_P(\psi,\vartheta)}{\partial\vartheta} &= \frac{1}{\mu_0}\int_0^{2\pi}\frac{\partial B_\varphi(\psi,\vartheta,\varphi)}{\partial\vartheta}\,d\varphi \\ &= \frac{1}{\mu_0}\int_0^{2\pi}\frac{\partial B_\vartheta(\psi,\vartheta,\varphi)}{\partial\varphi}\,d\varphi \quad \text{from (9.9)} \\ &= 0 \qquad\qquad\qquad\qquad\qquad\quad \text{by periodicity of } B_\vartheta,\end{aligned}$$

thus, the poloidal current is also a flux function, $I_P(\psi)$. And moreover,

$$\begin{aligned}\mu_0 I_P(\psi) &= \int_0^{2\pi}\left(G(\psi)+\frac{\partial H(\psi,\vartheta,\varphi)}{\partial\varphi}\right)d\varphi \quad \text{from (9.10)} \\ &= 2\pi G(\psi) \qquad\qquad\qquad\qquad\quad \text{by periodicity of } H.\end{aligned}$$

So finally we have identified

$$G(\psi) = \frac{\mu_0}{2\pi} I_P(\psi).$$

Furthermore, returning to the covariant form of the magnetic field, define the function $\overline{K}$ as

$$\overline{K}(\psi,\vartheta,\varphi) := B_\psi(\psi,\vartheta,\varphi) - \frac{\partial H(\psi,\vartheta,\varphi)}{\partial\psi}.$$

Then, given a function H satisfying (9.10), the covariant form of an equilibrium magnetic field in magnetic coordinates can be expressed as

$$\begin{cases} \boldsymbol{B} = I\nabla\vartheta + G\nabla\varphi + \overline{K}\nabla\psi + \nabla H \\ \text{with } I(\psi) = \dfrac{\mu_0}{2\pi} I_T(\psi) \text{ and } G(\psi) = \dfrac{\mu_0}{2\pi} I_P(\psi). \end{cases} \tag{9.12}$$

Additional details regarding magnetic coordinates can be found in Chapter 6 of [55] and Section 2 of [116].

9.2 ▪ Boozer coordinates

Boozer coordinates are a specific kind of magnetic coordinates. As magnetic coordinates, they are defined given a magnetic field $\boldsymbol{B}$ under the assumption of the existence of flux surfaces introduced in Remark 4.4. Moreover, they rely on the assumptions that the magnetic field is divergence-free and that the radial current vanishes, $\nabla \times \boldsymbol{B} \cdot \nabla\psi = 0$. We remark that a generalization of Boozer coordinates has been developed that does not require vanishing radial current [255].

Boozer coordinates are constructed such that the magnetic field has a simple form when expanded in the covariant form. This specific choice of magnetic coordinates is especially useful for some applications, as discussed in Section 12.1. The angles ϑ_B and φ_B are chosen such that the magnetic field can be written in the following way:

$$\begin{aligned}\boldsymbol{B}\big(\boldsymbol{R}(\psi,\vartheta_B,\varphi_B)\big) = I(\psi)[\nabla\vartheta_B]\big(\boldsymbol{R}(\psi,\vartheta_B,\varphi_B)\big) + G(\psi)[\nabla\varphi_B]\big(\boldsymbol{R}(\psi,\vartheta_B,\varphi_B)\big)\\ + K(\psi,\vartheta_B,\varphi_B)[\nabla\psi]\big(\boldsymbol{R}(\psi,\vartheta_B,\varphi_B)\big).\end{aligned} \tag{9.13}$$

More compactly, this is expressed in the literature as

$$\boldsymbol{B}(\psi,\vartheta_B,\varphi_B) = I(\psi)\nabla\vartheta_B + G(\psi)\nabla\varphi_B + K(\psi,\vartheta_B,\varphi_B)\nabla\psi.$$

Compared with the general covariant form for magnetic coordinates of equilibrium fields (9.12), it shows that the Boozer angles must be chosen such that H vanishes.

As a result, in Boozer coordinates, the poloidal and toroidal covariant components of the magnetic field, $B_{\vartheta_B} = I$ and $B_{\varphi_B} = G$, are constant on any flux surface, as they depend only on the flux label ψ. Furthermore, they can be related to the net toroidal and poloidal currents as in (9.12). The only covariant component that is not constant on a flux surface is the radial component $B_\psi = K$. It will be studied hereafter and expressed explicitly in terms of the field strength. Boozer coordinates will then become natural tools to study symmetries in the field strength and leverage their benefits in terms of particle confinement, in particular leading to the notion of quasisymmetry, introduced later in Section 12.1.

9.2.1 ▪ Justification

In order to find such a coordinate system, we can start from a magnetic field in the covariant form (9.12) in any magnetic coordinate system (ψ,ϑ,φ). To define new coordinates $\left(\psi,\widetilde{\vartheta},\widetilde{\varphi}\right)$ while preserving the magnetic coordinate property, we define the new angles $\widetilde{\vartheta}$ and $\widetilde{\varphi}$ as

$$\begin{cases}\widetilde{\vartheta} = \vartheta + \iota(\psi)\gamma(\psi,\vartheta,\varphi),\\ \widetilde{\varphi} = \varphi + \gamma(\psi,\vartheta,\varphi),\end{cases} \quad \text{for some function } \gamma \text{ to be determined.}$$

In fact, this guarantees that the new coordinates satisfy $\vartheta - \iota(\psi)\varphi = \widetilde{\vartheta} - \iota(\psi)\widetilde{\varphi}$. Since

$$\begin{cases}\nabla\widetilde{\vartheta} = \nabla\vartheta + \nabla\big(\iota\gamma\big),\\ \nabla\widetilde{\varphi} = \nabla\varphi + \nabla\big(\gamma\big),\end{cases}$$

while $I\nabla(\iota\gamma) + G\nabla\gamma = \nabla\big(I\iota\gamma + G\gamma\big) - \big(I'\iota\gamma + G'\gamma\big)\nabla\psi$, we can express the magnetic field $\boldsymbol{B}$ in the new contravariant basis $\big(\nabla\psi,\nabla\widetilde{\vartheta},\nabla\widetilde{\varphi}\big)$ as

$$I\nabla\vartheta + G\nabla\varphi + \overline{K}\nabla\psi + \nabla H = I\nabla\widetilde{\vartheta} + G\nabla\widetilde{\varphi} + \overline{K}\nabla\psi + \nabla H + \big(I'\iota\gamma + G'\gamma\big)\nabla\psi - \nabla\big(I\iota\gamma + G\gamma\big).$$

Hence, with the particular choice

$$\gamma\left(\psi,\vartheta,\varphi\right) = \frac{H\left(\psi,\vartheta,\varphi\right)}{I(\psi)\iota(\psi) + G(\psi)},$$

we can express the field in the desired form (9.13) with $K = \overline{K} + (I'\iota + G')\gamma$. With this choice of transformation, we will denote $\vartheta_B = \vartheta + \iota(\psi)\gamma(\psi,\vartheta,\varphi)$ and $\varphi_B = \varphi + \gamma(\psi,\vartheta,\varphi)$.

Remark 9.3. *In a stellarator, $G(\psi) \gg I(\psi)$ since a large toroidal current is not required while $\iota(\psi) \sim 1$. Therefore, the denominator $I(\psi)\iota(\psi) + G(\psi)$ is typically nonvanishing for conditions of interest, and the coordinate transformation is well-defined.*

9.2.2 ▪ Properties

The definition of Boozer coordinates leads to a simplified expression of the Jacobian. Since Boozer coordinates are a particular choice of magnetic coordinates, we can leverage both the covariant form of the field expressed in Boozer coordinates (9.13) and the contravariant form of the field expressed in any magnetic coordinate system (9.6), namely

$$\begin{cases} \boldsymbol{B}\big(\boldsymbol{R}(\psi,\vartheta_B,\varphi_B)\big) = \sqrt{g}^{-1}\big(\boldsymbol{R}(\psi,\vartheta_B,\varphi_B)\big)\left(\iota(\psi)\dfrac{\partial \boldsymbol{R}(\psi,\vartheta_B,\varphi_B)}{\partial \vartheta_B} + \dfrac{\partial \boldsymbol{R}(\psi,\vartheta_B,\varphi_B)}{\partial \varphi_B}\right), \\ \boldsymbol{B}\big(\boldsymbol{R}(\psi,\vartheta_B,\varphi_B)\big) = I(\psi)\left[\nabla\vartheta_B\right](\psi,\vartheta_B,\varphi_B) + G(\psi)\left[\nabla\varphi_B\right](\psi,\vartheta_B,\varphi_B) \\ \qquad\qquad + K(\psi,\vartheta_B,\varphi_B)\left[\nabla\psi\right](\psi,\vartheta_B,\varphi_B). \end{cases}$$

Taking their dot product results in a new expression for $\sqrt{g} = (\nabla\psi \times \nabla\vartheta_B \cdot \nabla\varphi_B)^{-1}$, the Jacobian, as follows:

$$\sqrt{g}\big(\boldsymbol{R}(\psi,\vartheta_B,\varphi_B)\big) = \frac{G(\psi) + \iota(\psi)I(\psi)}{B^2\big(\boldsymbol{R}(\psi,\vartheta_B,\varphi_B)\big)}. \tag{9.14}$$

This expression of the Jacobian now depends on the magnetic field strength and three flux functions: the integrated poloidal current, the integrated toroidal current, and the rotational transform. Furthermore, variations of the Jacobian on a surface are only due to the field strength. Thus, in both the covariant and contravariant representations, all components of the magnetic field can be described by five scalar quantities: $I(\psi)$, $G(\psi)$, $\iota(\psi)$, $K(\psi,\vartheta_B,\varphi_B)$, and $B\big(\boldsymbol{R}(\psi,\vartheta_B,\varphi_B)\big)$. Furthermore, we will see in Section 9.2.3 that the covariant component K is related to B.

Remark 9.4. *In a given coordinate system, knowing either the covariant or the contravariant components of a vector field is sufficient to define a vector field. By opposition, if the field is unknown and a magnetic coordinate system is used, then knowing either the covariant or the contravariant components of a vector field is not sufficient to define a vector field because the definition of the basis vectors depends on the definition of the field. For instance, in Boozer coordinates, explicit formulas for $I(\psi)$, $G(\psi)$, $\iota(\psi)$, and $K(\psi,\vartheta_B,\varphi_B)$ are not sufficient to determine the field $\boldsymbol{B}$.*

For convenience, according to Table 5.1, the covariant components of the field, namely

$$\begin{cases} B_\psi(\psi,\vartheta_B,\varphi_B) = K(\psi,\vartheta_B,\varphi_B), \\ B_{\vartheta_B}(\psi,\vartheta_B,\varphi_B) = I(\psi), \\ B_{\varphi_B}(\psi,\vartheta_B,\varphi_B) = G(\psi), \end{cases}$$

then provide the following expression for the curl in Boozer coordinates:

$$\begin{aligned} &\nabla \times \boldsymbol{B}\big(\boldsymbol{R}(\psi,\vartheta_B,\varphi_B)\big) \\ &\quad = \frac{1}{\sqrt{g}\big(\boldsymbol{R}(\psi,\vartheta_B,\varphi_B)\big)}\left[\left(I'(\psi) - \frac{\partial K(\psi,\vartheta_B,\varphi_B)}{\partial \vartheta_B}\right)\frac{\partial \boldsymbol{R}(\psi,\vartheta_B,\varphi_B)}{\partial \varphi_B}\right. \\ &\qquad\qquad \left. + \left(\frac{\partial K(\psi,\vartheta_B,\varphi_B)}{\partial \varphi_B} - G'(\psi)\right)\frac{\partial \boldsymbol{R}(\psi,\vartheta_B,\varphi_B)}{\partial \vartheta_B}\right]. \end{aligned} \tag{9.15}$$

Boozer coordinates are especially useful for stellarators, as quasisymmetric magnetic fields are important for confinement and precisely defined in terms of Boozer coordinates. Boozer coordinates simplify the expression for the guiding center Lagrangian, enabling the formulation of quasisymmetry as discussed in Section 12.1.1. The simple covariant form of the magnetic field in Boozer coordinates is also used for numerical and analytical calculations, such as neoclassical transport [224, 187]. In practice, Boozer coordinates are constructed to study quasisymmetry and simplify numerical calculations.

Boozer coordinates are discussed in Section 6.6 of [55] and Section 2.5 of [116].

9.2.3 ▪ Radial covariant component

The Jacobian in Boozer coordinates expressed in (9.14) is determined from the field strength, $B\big(\boldsymbol{R}(\psi,\vartheta_B,\varphi_B)\big)$, as well as the net poloidal and toroidal currents, $G(\psi)$ and $I(\psi)$, and the rotational transform $\iota(\psi)$. Given these quantities, we will obtain here an expression for the radial covariant component, $K(\psi,\vartheta_B,\varphi_B)$, by applying the MHD equilibrium force balance condition (9.8).

Assuming Ampère's law combined with the ideal MHD force balance with pressure only depending on the flux label, $p(\psi)$, the magnetic field satisfies

$$(\nabla\times\boldsymbol{B})\times\boldsymbol{B}=\mu_0 p'(\psi)\nabla\psi.$$

The contravariant form of the field together with the curl expressed in (9.15) then gives

$$\begin{aligned}\frac{1}{\sqrt{g}\big(\boldsymbol{R}(\psi,\vartheta_B,\varphi_B)\big)^2}\Bigg(&\left(I'(\psi)-\frac{\partial K(\psi,\vartheta_B,\varphi_B)}{\partial\vartheta_B}\right)\frac{\partial\boldsymbol{R}(\psi,\vartheta_B,\varphi_B)}{\partial\varphi_B}\\&+\left(\frac{\partial K(\psi,\vartheta_B,\varphi_B)}{\partial\varphi_B}-G'(\psi)\right)\frac{\partial\boldsymbol{R}(\psi,\vartheta_B,\varphi_B)}{\partial\vartheta_B}\Bigg)\\&\times\left(\frac{\partial\boldsymbol{R}(\psi,\vartheta_B,\varphi_B)}{\partial\varphi_B}+\iota(\psi)\frac{\partial\boldsymbol{R}(\psi,\vartheta_B,\varphi_B)}{\partial\vartheta_B}\right)\\&=\mu_0 p'(\psi)\,[\nabla\psi]\,(\psi,\vartheta_B,\varphi_B).\end{aligned}$$

Taking the dot product with $\partial\boldsymbol{R}/\partial\psi$ and using the duality of the basis vectors, we get the following equation for the radial covariant component K:

$$\begin{aligned}\iota(\psi)\frac{\partial K(\psi,\vartheta_B,\varphi_B)}{\partial\vartheta_B}+\frac{\partial K(\psi,\vartheta_B,\varphi_B)}{\partial\varphi_B}\\=\sqrt{g}\big(\boldsymbol{R}(\psi,\vartheta_B,\varphi_B)\big)\mu_0 p'(\psi)+G'(\psi)+\iota(\psi)I'(\psi).\end{aligned}\tag{9.16}$$

Remark 9.5. *The partial differential equation* (9.16) *is a magnetic differential equation of the form* (6.4)*. Considering the Boozer coordinates* $(\psi,\vartheta_B,\varphi_B)$ *as well as the right-hand side* $f(\psi,\vartheta_B,\varphi_B)=\sqrt{g}\big(\boldsymbol{R}(\psi,\vartheta_B,\varphi_B)\big)\mu_0 p'(\psi)+G'(\psi)+\iota(\psi)I'(\psi)$ *we can thus apply the results discussed in Section* 6.2*.*

According to Remark 9.5, let us first comment on the Fourier representation of the right-hand side. Since the right-hand side f depends on the two angles (ϑ_B,φ_B) only via the Jacobian, namely $\sqrt{g}\big(\boldsymbol{R}(\psi,\vartheta_B,\varphi_B)\big)=(G(\psi)+\iota(\psi)I(\psi))/B^2\big(\boldsymbol{R}(\psi,\vartheta_B,\varphi_B)\big)$, we focus on B^{-2}. As B is bounded away from zero (see Section 4.4.2) and doubly periodic, we write the doubly

periodic function B^{-2} as

$$B^{-2}\big(\boldsymbol{R}(\psi,\vartheta_B,\varphi_B)\big) = B_0^{-2}(\psi) + \sum_{m,n,(m,n)\neq(0,0)} b_{m,n}(\psi) e^{i(m\vartheta_B - n\varphi_B)} \tag{9.17}$$

with $B_0^{-2}(\psi) := (2\pi)^{-2}\int_0^{2\pi}\int_0^{2\pi} B^{-2}\big(\boldsymbol{R}(\psi,\vartheta_B,\varphi_B)\big)\, d\vartheta_B d\varphi_B$ and the other Fourier coefficients $\{b_{m,n}(\psi)\}_{(m,n)\in\mathbb{Z}^2,(m,n)\neq(0,0)}$. The necessary condition for the existence of doubly periodic solutions to (9.16), namely $\int_0^{2\pi}\int_0^{2\pi} f(\psi,x_1,x_2)\, dx_1 dx_2 = 0$, is then equivalent to

$$\frac{G(\psi)+\iota(\psi)I(\psi)}{B_0^2(\psi)}\mu_0 p'(\psi) + G'(\psi) + \iota(\psi)I'(\psi) = 0.$$

Hence, under this condition, the right-hand side reads

$$f(\psi,\vartheta_B,\varphi_B) = \big(G(\psi)+\iota(\psi)I(\psi)\big)\mu_0 p'(\psi) \sum_{(m,n)\in\mathbb{Z}^2\setminus\{(0,0)\}} b_{m,n}(\psi) e^{i(m\vartheta_B - n\varphi_B)} \ \ \forall\psi.$$

Because $G(\psi)+\iota(\psi)I(\psi)$ is nonvanishing according to Remark 9.3, the condition of existence for periodic solutions along closed field lines when ι is rational reads

$$p'(\psi) b_{m,n}(\psi) = 0 \ \forall (m,n)\in\mathbb{Z}^2 \text{ such that } \iota = \frac{n}{m} \ \ \forall\psi.$$

Under these two conditions, formally, the general Fourier solution then reads

$$\begin{aligned} K(\psi,\vartheta_B,\varphi_B) = \mathcal{K}(\psi) &+ \sum_{(m,n)\in\mathbb{Z}^2\setminus\{(0,0)\}} \Delta_{m,n}(\psi)\delta(n-\iota(\psi)m) e^{i(m\vartheta_B - n\varphi_B)} \\ &+ \sum_{(m,n)\in\mathbb{Z}^2, m\neq\iota(\psi)n} \frac{i\big(G(\psi)+\iota(\psi)I(\psi)\big)\mu_0 p'(\psi)}{n-\iota(\psi)m} b_{m,n}(\psi) e^{i(m\vartheta_B - n\varphi_B)}, \end{aligned}$$

where $\mathcal{K}(\psi)$ and $\{\Delta_{m,n}(\psi), (m,n)\in\mathbb{Z}^2\setminus\{(0,0)\}, \iota(\psi) = n/m\}$ are free functions. The solution exhibits the so-called Dirac-δ function and $1/x$ singularities mentioned in Section 6.2.4 and will be discussed further in Section 10.3.

This expression summarizes how the radial covariant component K depends on the field strength B. As a consequence, all components of the magnetic field in the covariant representation can be described by four scalar quantities: $I(\psi)$, $G(\psi)$, $\iota(\psi)$, and $B\big(\boldsymbol{R}(\psi,\vartheta_B,\varphi_B)\big)$. This will highlight the critical role of the magnetic field strength B and will be central to symmetry discussions in Section 12.1.

9.3 ▪ Field-line following coordinates

The concept of flux coordinates relies on the assumption of continuously nested toroidal surfaces in the region of interest. For a given magnetic field $\boldsymbol{B}$, flux coordinates consist of one radius-like coordinate, labeling surfaces between the magnetic axis and the outermost surface, and two periodic angles, describing poloidal and toroidal cross-sections, respectively. The concept of magnetic coordinates relies on the further assumption of a divergence-free field; magnetic coordinates are flux coordinates with angles defined to guarantee that the ratio between the contravariant components of the field remains constant on each flux surface. The concept of field-line following coordinates relies on one coordinate labeling field lines, denoted α, and one coordinate measuring the length along individual field lines, l; field-line following coordinates are flux coordinates but not magnetic coordinates.

Starting from magnetic coordinates, they will now be defined to simplify differential and integral operators along field lines. However, the coordinate curves obtained by fixing the surface label ψ and either α or l do not necessarily close in the poloidal or toroidal directions. Hence α and l are not poloidal and toroidal angles; therefore, the system (ψ, α, l) does not define a magnetic coordinate system. A field-line following coordinate system is sometimes called a Clebsch coordinate system in the literature [116, 55].

Given any magnetic coordinate system $(\psi, \vartheta, \varphi)$, a field-line following coordinate system (ψ, α, l) is defined by

- the same flux label ψ,
- the field-line label defined by $\alpha = \vartheta - \iota(\psi)\varphi$,
- the length along a field line l, implicitly defined by $\frac{\partial \boldsymbol{R}(\psi,\alpha,l)}{\partial l} = \hat{\boldsymbol{b}}(\psi, \alpha, l)$ or equivalently

$$\boldsymbol{B}\big(\boldsymbol{R}(\psi, \vartheta_B, \varphi_B)\big) = B\big(\boldsymbol{R}(\psi, \vartheta_B, \varphi_B)\big)\frac{\partial \boldsymbol{R}(\psi, \alpha, l)}{\partial l}, \tag{9.18}$$

where $\hat{\boldsymbol{b}} := \boldsymbol{B}/B$ is the unit vector aligned with the magnetic field. Next, we obtain simplified forms for both the contravariant and covariant components of the field and the Jacobian of the new coordinate system.

Given the contravariant components of the magnetic field as expressed in magnetic coordinates in (9.5), namely

$$\boldsymbol{B}\big(\boldsymbol{R}(\psi, \vartheta_B, \varphi_B)\big) = [\nabla\psi \times \nabla\vartheta]\,\big(\boldsymbol{R}(\psi, \vartheta_B, \varphi_B)\big) - \iota(\psi)\,[\nabla\psi \times \nabla\varphi]\,\big(\boldsymbol{R}(\psi, \vartheta_B, \varphi_B)\big),$$

the simplified contravariant form in field-line following coordinates reads

$$\boldsymbol{B}\big(\boldsymbol{R}(\psi, \vartheta_B, \varphi_B)\big) = [\nabla\psi \times \nabla\alpha]\,\big(\boldsymbol{R}(\psi, \vartheta_B, \varphi_B)\big). \tag{9.19}$$

Remark 9.6. *Consequently, $\boldsymbol{B} \cdot \nabla\alpha = 0$, so α is constant along a magnetic field line. This justifies the name field-line label. Therefore, this system shares a fundamental property with magnetic coordinates: field lines are straight in the α-l plane since the coordinate α is constant along field lines.*

The covariant form for the magnetic field is defined as

$$\begin{aligned}\boldsymbol{B}\big(\boldsymbol{R}(\psi, \vartheta_B, \varphi_B)\big) = {} & B_\psi(\psi, \alpha, l)\,[\nabla\psi]\,\big(\boldsymbol{R}(\psi, \vartheta_B, \varphi_B)\big) \\ & + B_\alpha(\psi, \alpha, l)\,[\nabla\alpha]\,\big(\boldsymbol{R}(\psi, \vartheta_B, \varphi_B)\big) + B_l(\psi, \alpha, l)\,[\nabla l]\,\big(\boldsymbol{R}(\psi, \vartheta_B, \varphi_B)\big).\end{aligned}$$

The inner product of this expression with $\hat{\boldsymbol{b}} = \partial\boldsymbol{R}/\partial l$ shows that $B_l = B$ thanks to the duality of the covariant and contravariant bases. The other two components, B_ψ and B_α, do not have similarly simple formulas but can be obtained from the dual relations as $B_\psi = \hat{\boldsymbol{b}} \cdot \nabla\alpha \times \nabla l$ and $B_\alpha = \hat{\boldsymbol{b}} \cdot \nabla l \times \nabla\psi$.

The Jacobian is defined by

$$\sqrt{g}\big(\boldsymbol{R}(\psi, \vartheta_B, \varphi_B)\big) = \frac{1}{[\nabla\psi \times \nabla\alpha \cdot \nabla l]\,\big(\boldsymbol{R}(\psi, \vartheta_B, \varphi_B)\big)}.$$

Since combining (9.19) with (9.18) one gets

$$[\nabla\psi \times \nabla\alpha \cdot \nabla l]\,\big(\boldsymbol{R}(\psi, \vartheta_B, \varphi_B)\big) = B\big(\boldsymbol{R}(\psi, \vartheta_B, \varphi_B)\big)\frac{\partial \boldsymbol{R}(\psi, \alpha, l)}{\partial l} \cdot [\nabla l]\,\big(\boldsymbol{R}(\psi, \vartheta_B, \varphi_B)\big),$$

and, thanks to the duality of the basis vectors (see Table 5.1) the Jacobian can be written

$$\sqrt{g}\big(\boldsymbol{R}(\psi,\vartheta_B,\varphi_B)\big) = \frac{1}{B\big(\boldsymbol{R}(\psi,\vartheta_B,\varphi_B)\big)}.$$

Remark 9.7. *In order to specify a point on a magnetic surface, ψ, one must define a closed curve that is not parallel to field lines, $\mathcal{C}_\psi$, on which $l = 0$. For example, one natural choice is the intersection of the magnetic surface and a constant φ surface. The initial position along C_ψ defines the field-line label, α. The length l is then measured from $l = 0$ until a given field line returns to $\mathcal{C}_\psi$ at some length $L(\psi,\alpha)$. The position on the surface is then specified with $\alpha \in [0, 2\pi)$ and $l \in [0, L(\psi,\alpha))$. While physical quantities are periodic with respect to α, they are not necessarily periodic with respect to $L(\psi,\alpha)$ unless field lines close.*

The differential operator $\hat{\boldsymbol{b}} \cdot \nabla$ also has a simpler expression in the new coordinates. Since the gradient is defined as

$$\nabla = \nabla\psi\frac{\partial}{\partial\psi} + \nabla\alpha\frac{\partial}{\partial\alpha} + \nabla l\frac{\partial}{\partial l}$$

then, according to (9.18), the operator can be written as

$$\hat{\boldsymbol{b}} \cdot \nabla = \frac{\partial \boldsymbol{R}}{\partial l} \cdot \nabla\psi\frac{\partial}{\partial\psi} + \frac{\partial \boldsymbol{R}}{\partial l} \cdot \nabla\alpha\frac{\partial}{\partial\alpha} + \frac{\partial \boldsymbol{R}}{\partial l} \cdot \nabla l\frac{\partial}{\partial l}.$$

Finally, by duality of the bases, this yields

$$\hat{\boldsymbol{b}} \cdot \nabla = \frac{\partial}{\partial l}.$$

In summary, the (ψ,α,l) coordinate system builds upon magnetic coordinate systems to simplify expressions for differential and integral operators along field lines. As in the case of Boozer coordinates, the Jacobian takes a simple form and is related to the magnetic field strength. While one of the covariant components of the field can be obtained explicitly in terms of the field strength, the other two components require additional geometric quantities.

9.4 ▪ Summary

Table 9.1 summarizes the important properties of magnetic, Boozer, and field-line following coordinate systems.

Table 9.1: Summary of important properties of magnetic, Boozer, and field-line following coordinates.

	Magnetic coordinates	Boozer coordinates	Field-line following coordinates
Assumptions	$\nabla \cdot \boldsymbol{B} = 0$	$\nabla \cdot \boldsymbol{B} = 0$ $\boldsymbol{J} \cdot \nabla\psi = 0$	$\nabla \cdot \boldsymbol{B} = 0$
Contravariant form	$\boldsymbol{B} = \nabla\psi \times \nabla\vartheta - \iota(\psi)\nabla\psi \times \nabla\varphi$	$\boldsymbol{B} = \nabla\psi \times \nabla\vartheta_B - \iota(\psi)\nabla\psi \times \nabla\varphi_B$	$\boldsymbol{B} = \nabla\psi \times \nabla\alpha$
Covariant form	$\boldsymbol{B} = B_\vartheta(\psi,\vartheta,\varphi)\nabla\vartheta + B_\varphi(\psi,\vartheta,\varphi)\nabla\varphi$ $+B_\psi(\psi,\vartheta,\varphi)\nabla\psi$	$\boldsymbol{B} = I(\psi)\nabla\vartheta_B + G(\psi)\nabla\varphi_B$ $+\, K(\psi,\vartheta_B,\varphi_B)\nabla\psi$ $G(\psi) = \mu_0 I_P(\psi)/2\pi$ $I(\psi) = \mu_0 I_T(\psi)/2\pi$	$\boldsymbol{B} = \Big(\hat{\boldsymbol{b}}\cdot\nabla\alpha\times\nabla l\Big)\nabla\psi$ $+\Big(\hat{\boldsymbol{b}}\cdot\nabla l\times\nabla\psi\Big)\nabla\alpha + B\nabla l$
Jacobian $\sqrt{g}$	$\dfrac{B_\varphi(\psi,\vartheta,\varphi) + \iota(\psi)B_\vartheta(\psi,\vartheta,\varphi)}{B^2(\psi,\vartheta,\varphi)}$	$\dfrac{G(\psi) + \iota(\psi)I(\psi)}{B^2(\psi,\vartheta_B,\varphi_B)}$	$\dfrac{1}{B(\psi,\alpha,l)}$

Chapter 10
Challenges associated with 3D equilibrium fields

In toroidal magnetic confinement, an axisymmetric setting is often referred to as a 2D setting, because quantities that are independent of the toroidal angle can be studied as a function of only two variables in a poloidal plane. A tokamak is then referred to as a 2D configuration. By contrast, a nonaxisymmetric setting is referred to as a 3D setting. A stellarator is referred to as a 3D configuration. These two types of toroidal magnetic configurations have many different sets of advantages and drawbacks in terms of confinement. In particular, unlike in a 2D setting, 3D magnetic fields are no longer guaranteed to have continuously nested flux surfaces. This result is the central point of this chapter and is particularly important for toroidal devices since closed nested surfaces are crucial for confinement.

The equations of motion describing field-line trajectories in a toroidal magnetic field can be cast as a Hamiltonian system. In this context, in Sections 10.1 and 10.2, we highlight the relationship between the existence of surfaces in 2D and 3D on the one hand and the concept of integrability of Hamiltonian systems on the other hand. Using this concept, the existence of flux surfaces arises as a fundamental consequence of the Hamiltonian nature of the system under the assumption of axisymmetry. As we will see, in 3D systems compared to 2D systems, the loss of a continuous symmetry with respect to the toroidal angle results in a corresponding loss of a conserved quantity. This has important implications for confinement, as the existence of continuously nested flux surfaces is no longer guaranteed.

The existence or otherwise of continuously nested flux surfaces in 3D magnetic fields is a property of the field-line Hamiltonian and independent of any additionally imposed physical model, such as ideal MHD. Even though their existence is not guaranteed in 3D without axisymmetry, we examine in Section 10.3 the consequences of the assumption of the existence of nested flux surfaces, introduced in Remark 4.4, on the ideal MHD equilibrium current. This will lead to further considerations on the assumption of flux surfaces and the equilibrium model:

- additional assumptions can guarantee the existence of a solution for a problem related to this current in an MHD equilibrium in Section 10.3.2;

- the possible nonexistence of this solution motivates the consideration of different models, either without the assumption of surfaces in Section 10.3.4 or beyond ideal MHD models in Section 10.4.

The following chapters will present tools to study confinement for the design of 3D configurations. Various models of equilibrium magnetic fields will be presented in Chapter 11, while symmetries and their consequences will be discussed in Chapter 12.

10.1 ▪ From existence to nonexistence of magnetic surfaces

In axisymmetric geometry, we will find that the equations describing the position of field lines possess a conserved quantity, implying that the field lines lie on surfaces. When axisymmetry is broken, however, the conserved quantity may be lost, leading to the possibility of nonexistence of surfaces. In the following sections, we will describe how this conserved quantity arises due to a variational principle for field-line flow analogous to the variational principle arising in Hamiltonian mechanics.

10.1.1 ▪ Analysis of the vector potential

While in Section 5.5.2 and Chapter 9, the assumption of magnetic surfaces was leveraged to introduce convenient coordinate systems, these surfaces do not exist for a general 3D field. Here, we will introduce a new coordinate system without the assumption of surfaces to show that axisymmetry yields the existence of magnetic surfaces. We will leverage this coordinate system in Sections 10.1.2 and 10.1.3 to further study the structure of magnetic field lines without the assumption of surfaces.

Consider a coordinate system (r, θ, ϕ), where r labels nested toroidal surfaces, not necessarily flux surfaces, and (θ, ϕ) are poloidal and toroidal angles on these surfaces. The vector potential is not uniquely defined since adding a curl-free field, the gradient of any scalar function, does not affect the value of $\boldsymbol{B} = \nabla \times \boldsymbol{A}$. As mentioned previously in Remark A.1, the standard to choose $\boldsymbol{A}$ is called the gauge. Any vector potential $\boldsymbol{A}$ can be expressed in the contravariant basis in terms of its covariant components (A_θ, A_ϕ, A_r), but it can equivalently be written in terms of three functions (ψ_1, ψ_2, g) as

$$\boldsymbol{A} = \psi_1 \nabla\theta - \psi_2 \nabla\phi + \nabla g,$$

where $A_r = \partial g/\partial r$, $A_\theta = \psi_1 + \partial g/\partial\theta$, and $A_\phi = -\psi_2 + \partial g/\partial\phi$. This form for the vector potential is convenient since the radial component of the vector potential is expressed in terms of the gradient of a scalar function, the last term in the above expression. We then choose a gauge in which the vector potential satisfies

$$\boldsymbol{A} = \psi_1 \nabla\theta - \psi_2 \nabla\phi, \tag{10.1}$$

and the corresponding magnetic field is

$$\boldsymbol{B} = \nabla\psi_1 \times \nabla\theta - \nabla\psi_2 \times \nabla\phi. \tag{10.2}$$

Here surfaces of constant ψ_1 do not necessarily overlap with those of constant ψ_2, and neither ψ_1 nor ψ_2 needs to coincide with magnetic fluxes. In comparison, the contravariant form (9.5) of the magnetic field in magnetic coordinates can be written as

$$\boldsymbol{B} = \nabla\psi \times \nabla\vartheta - \nabla\psi_P \times \nabla\varphi,$$

where the toroidal flux is $2\pi\psi$ and the poloidal flux is $\Psi_P = 2\pi\psi_P$, while $\psi_P'(\psi) = \iota(\psi)$. For this reason, the notation ψ_T, ψ_P rather than ψ_1, ψ_2 is sometimes used in the literature even without the assumption of surfaces [24].

If we assume that the toroidal magnetic field does not vanish within a volume, $\boldsymbol{B} \cdot \nabla\phi \neq 0$ or equivalently $\nabla\psi_1 \times \nabla\theta \cdot \nabla\phi \neq 0$, then (ψ_1, θ, ϕ) defines a coordinate system within this volume. As discussed earlier, this is a natural assumption in the context of toroidal magnetic confinement since the toroidal component of the field is crucial to confinement considerations. We can then express the vector potential (10.1) in this coordinate system under its covariant form as

$$\boldsymbol{A}\big(\boldsymbol{R}(\psi_1, \theta, \phi)\big) = \psi_1 \left[\nabla\theta\right]\big(\boldsymbol{R}(\psi_1, \theta, \phi)\big) - \psi_2(\psi_1, \theta, \phi)\left[\nabla\phi\right]\big(\boldsymbol{R}(\psi_1, \theta, \phi)\big), \tag{10.3}$$

with or without the assumption of magnetic surfaces. We can now consider the axisymmetric case, where ϕ is a cylindrical toroidal angle introduced in Section 5.3 and $\partial\psi_2/\partial\phi = 0$. As

$$\boldsymbol{B}\cdot\nabla\psi_2 = \frac{\partial\psi_2}{\partial\phi}\nabla\psi_1\times\nabla\theta\cdot\nabla\phi,$$

then as a consequence $\boldsymbol{B}\cdot\nabla\psi_2 = 0$. Since ψ_2 is differentiable, the level sets of ψ_2 form surfaces, except at critical points where $\nabla\psi_2 = 0$. These critical points may be isolated or may form critical lines or surfaces, but we are not interested in purely toroidal fields such that $\nabla\psi_2 = 0$ in a volume, as discussed in Section 4.4.2. Thus, we can conclude that axisymmetry implies the existence of magnetic surfaces, yet their topology is not determined at this point. As we will see next, breaking the toroidal symmetry may lead to the loss of magnetic surfaces.

The (ψ_1, θ, ϕ) coordinate system will be central to the discussion of a variational principle for field-line flow and its relationship with Hamiltonian dynamics in the next section. This will allow for exploring the existence of magnetic surfaces, or integrability, in more general fields in Section 10.2.

10.1.2 ▪ Variational principle for field-line flow

We begin by showing that field lines obey equations of motion derived from a variational principle analogous to Hamilton's principle in classical mechanics. Given a magnetic field $\boldsymbol{B}$, the equations of motion describing the position of a field line, $\boldsymbol{R}_T$, as a function of the distance along a field line, l, is given by

$$\frac{d\boldsymbol{R}_T(l)}{dl} = \hat{\boldsymbol{b}}\big(\boldsymbol{R}_T(l)\big), \tag{10.4}$$

where $\hat{\boldsymbol{b}} := \boldsymbol{B}/B$. We consider the vector potential $\boldsymbol{A}$ for the divergence-free magnetic field $\boldsymbol{B}$, related by (A.5). We also consider two fixed values of the parameter l, denoted l_1 and l_2, together with the associated functional:

$$W[\boldsymbol{R}_T] := \int_{l_1}^{l_2} \boldsymbol{A}\big(\boldsymbol{R}_T(l)\big)\cdot\frac{d\boldsymbol{R}_T(l)}{dl}\,dl. \tag{10.5}$$

The first variation of $W[\boldsymbol{R}_T]$ reads

$$\begin{aligned}\delta W[\boldsymbol{R}_T;\delta\boldsymbol{R}_T] &= \int_{l_1}^{l_2}\left(\boldsymbol{A}\big(\delta\boldsymbol{R}_T(l)\big)\cdot\frac{d\boldsymbol{R}_T(l)}{dl} + \boldsymbol{A}\big(\boldsymbol{R}_T(l)\big)\cdot\frac{d\delta\boldsymbol{R}_T(l)}{dl}\right)dl\\ &= \int_{l_1}^{l_2}\delta\boldsymbol{R}_T(l)\cdot\left(\nabla\boldsymbol{A}\big(\boldsymbol{R}_T(l)\big)\cdot\frac{d\boldsymbol{R}_T(l)}{dl} - \left(\frac{d\boldsymbol{R}_T(l)}{dl}\cdot\nabla\right)\boldsymbol{A}\big(\boldsymbol{R}_T(l)\big)\right)dl,\end{aligned}$$

obtained by integration by parts using the boundary condition $\boldsymbol{A}\cdot\delta\boldsymbol{R}_T = 0$ at the fixed endpoints of the trajectory, namely $\boldsymbol{R}_T(l_1)$ and $\boldsymbol{R}_T(l_2)$. At a stationary point, $\delta W[\boldsymbol{r};\delta\boldsymbol{r}]$ must vanish for any $\delta\boldsymbol{R}(l)$; thus, the quantity in parentheses on the second line of the above expression must vanish. According to the vector identity $(\nabla\times\boldsymbol{a})\times\boldsymbol{b} = (\boldsymbol{b}\cdot\nabla)\,\boldsymbol{a} - (\nabla\boldsymbol{a})\cdot\boldsymbol{b}$ for any smooth vector fields $\boldsymbol{a}$ and $\boldsymbol{b}$, we obtain the condition

$$\Big(\nabla\times\boldsymbol{A}\big(\boldsymbol{R}_T(l)\big)\Big)\times\frac{d\boldsymbol{R}_T(l)}{dl} = 0,$$

implying that $d\boldsymbol{R}_T/dl$ is parallel to $\hat{\boldsymbol{b}}$ since $\boldsymbol{B} = \nabla \times \boldsymbol{A}$. Furthermore, $d\boldsymbol{R}_T(l)/dl$ is a unit vector by definition. Thus, we recover the equations of motion describing a field line (10.4).

10.1.3 ▪ Relation to Hamiltonian dynamics

In Section 10.1.1, analyzing the vector potential in toroidal coordinates showed that axisymmetry implies the existence of surfaces under the assumption that $\boldsymbol{B} \cdot \nabla\theta \neq 0$ and $\boldsymbol{B} \cdot \nabla\phi \neq 0$. This property is a consequence of the Hamiltonian nature of field-line flow, as will be shown by considering the equations of field-line flow as a Hamiltonian system. The connection between Hamiltonian mechanics and the variational principle for field-line flow is explicitly shown by casting the latter as a Hamiltonian system.

The functional W defined in (10.5) can then conveniently be expressed thanks to toroidal coordinates (ψ_1, θ, ϕ), by focusing on the integrand as follows. First, since $\boldsymbol{B} \cdot \nabla\phi \neq 0$, field lines can be parameterized by ϕ as $\boldsymbol{R}_T : \phi \in \mathbb{R} \mapsto (\psi_{1T}(\phi), \theta_T(\phi), \phi) \in \mathbb{R}^3$. Therefore, in particular,

$$\frac{d\boldsymbol{R}_T(\phi)}{d\phi} = \frac{\partial \boldsymbol{R}(\psi_{1T}(\phi), \theta_T(\phi), \phi}{\partial \psi_1} \frac{d\psi_{1T}(\phi)}{d\phi} + \frac{\partial \boldsymbol{R}(\psi_{1T}(\phi), \theta_T(\phi), \phi}{\partial \theta} \frac{d\theta_T(\phi)}{d\phi} + \frac{\partial \boldsymbol{R}(\psi_{1T}(\phi), \theta_T(\phi), \phi}{\partial \phi}.$$

Hence, with the expression of the vector potential (10.3), along a trajectory, the integrand in (10.5) can be expressed as

$$\boldsymbol{A}\big(\boldsymbol{R}_T(\phi)\big) \cdot \frac{d\boldsymbol{R}_T(\phi)}{d\phi} = \psi_{1T}(\phi) \frac{d\theta_T(\phi)}{d\phi} - \psi_2\Big(\psi_{1T}(\phi), \theta_T(\phi), \phi\Big).$$

Given two fixed values of the parameter ϕ, denoted ϕ_1 and ϕ_2, the functional W can then be expressed as

$$W[\psi_{1T}, \theta_T] = \int_{\phi_1}^{\phi_2} \left(\psi_{1T}(\phi) \frac{d\theta_T(\phi)}{d\phi} - \psi_2\Big(\psi_{1T}(\phi), \theta_T(\phi), \phi\Big) \right) d\phi. \tag{10.6}$$

This is analogous to the functional that appears in the variational principle for Hamiltonian mechanics (B.10), where (θ, ψ_1, ϕ) correspond to $(\boldsymbol{q}, \boldsymbol{p}, t)$, and ψ_2 corresponds to the Hamiltonian H. The field-line flow setting is a 1- or 1.5-dimensional Hamiltonian system, depending on whether axisymmetry is imposed.

The resulting Euler–Lagrange equations are given by

$$\begin{cases} \dfrac{d\theta_T(\phi)}{d\phi} = \dfrac{\partial \psi_2(\theta(\phi), \psi_1(\phi), \phi)}{\partial \psi_1}, \\ \dfrac{d\psi_{1T}(\phi)}{d\phi} = -\dfrac{\partial \psi_2(\theta(\phi), \psi_1(\phi), \phi)}{\partial \theta}. \end{cases} \tag{10.7}$$

Thus, by analogy with Hamilton's equations (B.11), if the system is axisymmetric, or equivalently if ψ_2 does not depend explicitly on ϕ, then ψ_2 is a constant of the motion,

$$\frac{d\psi_2(\theta_T(\phi), \psi_{1T}(\phi), \phi)}{d\phi} = 0. \tag{10.8}$$

Since an axisymmetric field-line flow can be described as a 1-dimensional Hamiltonian system from (10.7), the fact that the Hamiltonian ψ_2 is constant along a trajectory, as seen in (10.8), is sufficient to show that the system is integrable. Thus, magnetic field lines are confined to lie on invariant tori, namely the surfaces of constant ψ_2 in phase space, that correspond to toroidal magnetic surfaces in physical space. This is analogous to a time-independent Hamiltonian system, yielding energy conservation (B.12).

In nonaxisymmetric systems, integrability of the field-line flow is no longer guaranteed as the Hamiltonian is not a constant of the motion. Further discussion of the Hamiltonian nature of field-line flow can be found in many references [39, 21, 68, 116].

10.2 ▪ Integrability of Hamiltonian systems and existence of flux surfaces

Since the behavior of magnetic field lines can be described by a Hamiltonian system, we now apply techniques from Hamiltonian dynamics to illustrate the fundamental challenges associated with nonaxisymmetric magnetic fields, specifically the nonexistence of flux surfaces. The integrability of the field-line Hamiltonian system gives rise to the existence of flux surfaces. In Section 10.2.1, we introduce the Hamilton–Jacobi method to find solutions of integrable Hamiltonian systems. If a solution to the Hamilton–Jacobi equation exists, it can be leveraged to solve the trajectories of the Hamiltonian system. This will be illustrated in Section 10.2.2 for the case of action-angle coordinates. In Section 10.2.3, we consider the existence of solutions to the Hamilton–Jacobi equation in a more general setting by constructing formal solutions using a series expansion with respect to the distance from integrability. In general, however, a solution of the Hamilton–Jacobi equation is not guaranteed to exist. We show that a convergent series solution cannot be constructed in general. This highlights the critical challenges in maintaining magnetic surfaces in a 3D magnetic field as one moves away from axisymmetry. In Section 10.2.4, we discuss the KAM theorem, describing the conditions under which surfaces may persist in the presence of a perturbation away from integrability.

As the following discussion generally applies to 1- and 1.5-dimensional Hamiltonian systems, we primarily use notation consistent with the dynamical systems literature throughout the section. The canonical coordinates are denoted (q, p, t) with $H(q, p, t)$ the Hamiltonian and the action-angle coordinates (Q, P, t), except for the specific example of the action-angle transformation for the field-line flow Hamiltonian considered at the end of Section 10.2.2. For clarity, a correspondence between conventional variables of Hamiltonian mechanics and the Hamiltonian for field-line flow is summarized in Table 10.1.

10.2.1 ▪ Hamilton–Jacobi method

Given the desirable properties of integrable systems, we now describe a method to identify a constant of motion by seeking a new coordinate system where the Hamiltonian is independent of one coordinate. Such a coordinate is referred to as ignorable. This method is called the Hamilton–Jacobi method. It yields a PDE formulation of the integrability problem: a system is integrable if the corresponding Hamilton–Jacobi equation has a solution. We are interested in the 1-dimensional field-line flow Hamiltonian, so we consider only 1-dimensional autonomous and 1.5-dimensional nonautonomous Hamiltonian systems. As a reminder, in the 1-dimensional autonomous case, because of the existence of one constant of motion, the system satisfies the definition of integrability. However, the subsequent discussion regarding nonintegrability can be generalized to higher-dimensional systems.

The Hamilton–Jacobi method [164, 217, 90] relies on particular coordinate transformations, so-called canonical transformations, to seek ignorable coordinates. A canonical transformation is a diffeomorphism, $(q, p) \in \mathbb{R}^2 \mapsto \big(Q(q, p), P(q, p)\big) \in \mathbb{R}^2$, preserving the Poisson bracket in the following sense. For any functions (f, g) defined on the phase space, we define functions $(\widetilde{f}, \widetilde{g})$ such that $\widetilde{f}\big(Q(q, p), P(q, p)\big) = f(q, p)$ and $\widetilde{g}\big(Q(q, p), P(q, p)\big) = g(q, p)$ for all (p, q) in phase space. The Poisson bracket, defined in Section B.3, is then said to be preserved by the canonical transformation if $\{f(q, p), g(q, p)\} = \{\widetilde{f}\big(Q(q, p), P(q, p)\big), \widetilde{g}\big(Q(q, p), P(q, p)\big)\}$ for all (p, q)

Table 10.1*: Correspondence between a generic Hamiltonian and the field-line flow Hamiltonian. For consistency with the general Hamiltonian dynamics literature, we use* (q, p, t) *coordinates, except where we consider the specific example of the Hamiltonian for field-line flow, in which case we use* (θ, ψ_1, ϕ)*. The notation dof refers to the degree of freedom.*

	Generic (1- or 1.5-dof)	Field-line flow
Canonical coordinates	q p	θ ψ_1
Time-like coordinate	t	ϕ
Hamiltonian	$H(p, q, t)$	$\psi_2(\theta, \psi_1, \phi)$
Action-angle coordinates	P $Q_T(t) = Q_0 + \omega_T t$	$\psi = \Psi_T/2\pi$ $Q_T(\phi) = Q_0 + \iota(\psi)\phi$
Frequency	ω_T	$\iota(\psi)$
Hamiltonian in action-angle coordinates	$K(P)$	$\psi_P(\psi)$

in phase space. In particular, both the mapping and its inverse are smooth and differentiable, and it defines a coordinate transformation between (p, q) and (P, Q). The goal is to describe the motion in a simplified form thanks to an appropriate coordinate system transformation. For example, in Section 10.2.3, we will seek a coordinate transformation where the new Hamiltonian is the zero function.

In this method, given a Hamiltonian system, the coordinate transformation is defined indirectly via a generating function, which is the unknown. It is assumed that the generating function, $S : \mathbb{R} \times \mathbb{R} \times \mathbb{R} \to \mathbb{R}$ defined as a function of (q, P, t), is such that the coordinate transformation $(q, p) \mapsto \big(Q(q, p), P(q, p)\big)$ can be explicitly defined by the following relation:

$$\begin{cases} p = \dfrac{\partial S(q, P, t)}{\partial q}, \\ Q = \dfrac{\partial S(q, P, t)}{\partial P}, \end{cases} \quad \forall (p, q, P, Q, t) \in \mathbb{R}^5. \tag{10.9}$$

In the literature, for instance in Chapter 9 of [90], there are four basic canonical generating functions. The function S satisfying (10.9) is referred to as a generating function of the second kind. It is standard to choose the second kind for the Hamilton–Jacobi method. The goal is then to find S to obtain a desired simplified Hamiltonian in the transformed coordinate system (Q, P). As we will justify below, this can be expressed as finding S such that

$$H\left(q, \frac{\partial S(q, P, t)}{\partial q}, t\right) + \frac{\partial S(q, P, t)}{\partial t} = K\left(\frac{\partial S(q, P, t)}{\partial P}, P, t\right), \tag{10.10}$$

where H is the original Hamiltonian and K is the new Hamiltonian in the transformed coordinates. This is called the nonlinear Hamilton–Jacobi equation in S, a first-order PDE. The goal is to find an S, a function of three independent variables, namely q, P, and t, satisfying (10.10).

The Hamilton–Jacobi equation arises to preserve the Hamiltonian structure when changing coordinates via a generating function of the second kind. This means that in the new coordinates,

the equations of motion are given by Hamilton's equations with the new Hamiltonian K. In order to justify this, given the Hamiltonian H in terms of the original coordinates (q, p), let us assume the existence of a function S satisfying (10.9). Then the total derivative of S along a trajectory, $(q_T, p_T) : \mathbb{R} \to \mathbb{R} \times \mathbb{R}$ or $(Q_T, P_T) : \mathbb{R} \to \mathbb{R} \times \mathbb{R}$ in the transformed coordinates, is given by

$$\frac{dS(q_T(t), P_T(t), t)}{dt} = p_T(t)\frac{dq_T(t)}{dt} + Q_T(t)\frac{dP_T(t)}{dt} + \frac{\partial S(q_T(t), P_T(t), t)}{\partial t}.$$

We will now use the above expression to simplify the variational functional introduced in (10.6). Analysis of the variational functional will then lead to Hamilton's equations in the new coordinates. Indeed, by defining a function K, a function of the transformed coordinates (Q, P) and time t, as

$$K(Q, P, t) := H(q(Q, P), p(Q, P), t) + \frac{\partial S(q(Q, P), P, t)}{\partial t},$$

we can express the integrand along a trajectory $(q_T, p_T) : \mathbb{R} \to \mathbb{R} \times \mathbb{R}$ in terms of the new coordinates as

$$\begin{aligned} &p_T(t)\frac{dq_T(t)}{dt} - H(q_T(t), p_T(t), t) \\ &= -Q_T(t)\frac{dP_T(t)}{dt} - K(Q_T(t), P_T(t), t) + \frac{dS\Big(q\big(Q_T(t), P_T(t)\big), P_T(t), t\Big)}{dt}, \end{aligned}$$

where $(Q_T, P_T) : \mathbb{R} \to \mathbb{R} \times \mathbb{R}$ is the trajectory in the new coordinates. Hence, compared to the variational functional introduced to derive Hamilton's equations (10.6), namely

$$\mathcal{W}[q_T, p_T] := \int_{t_{\text{init}}}^{t_{\text{final}}} \left(p_T(t)\frac{dq_T(t)}{dt} - H(q_T(t), p_T(t), t) \right) dt,$$

we define the variational functional in the new coordinates by

$$\begin{aligned} &\widetilde{\mathcal{W}}[Q_T, P_T] \\ &:= \int_{t_{\text{init}}}^{t_{\text{final}}} \left(-Q_T(t)\frac{dP_T(t)}{dt} - K(Q_T(t), P_T(t), t) + \frac{dS\Big(q\big(Q_T(t), P_T(t)\big), P_T(t), t\Big)}{dt} \right) dt, \end{aligned}$$

which is equivalent to

$$\begin{aligned} \widetilde{\mathcal{W}}[Q_T, P_T] = \int_{t_{\text{init}}}^{t_{\text{final}}} &\left(P_T(t)\frac{dQ_T(t)}{dt} - K(Q_T(t), P_T(t), t) \right) dt \\ &+ \Big[S\Big(q\big(Q_T(t), P_T(t)\big), P_T(t), t\Big) - P_T(t)Q_T(t) \Big]_{t_{\text{init}}}^{t_{\text{final}}}. \end{aligned}$$

So Hamilton's equations of motion in the transformed coordinates, corresponding to stationary points of $\widetilde{\mathcal{W}}$ for fixed initial and final points of the trajectory, are

$$\frac{dQ_T(t)}{dt} = \frac{\partial K(Q_T(t), P_T(t), t)}{\partial P}, \tag{10.11a}$$

$$\frac{dP_T(t)}{dt} = -\frac{\partial K(Q_T(t), P_T(t), t)}{\partial Q}. \tag{10.11b}$$

The boundary terms in the definition of $\widetilde{\mathcal{W}}$ do not contribute to the equations of motion given that trajectories are such that Q_T and P_T are fixed at the boundaries. We can see that the equations of motion in the (q, p) coordinates are analogous to the equations of motion in the (Q, P) coordinates when replacing H by K. Thus, the Hamiltonian structure is said to be preserved.

Thanks to the Hamilton–Jacobi method, we can study the equations of motion in a convenient set of coordinates instead of the original ones. An appropriate change of coordinates can evidence specific properties of a physical system, such as integrability, even though it may not be apparent in the original coordinate system. To investigate if a system has a desired property, we can choose a particular form of K. If the new Hamiltonian system clearly possesses the desired property, then the existence of a solution to the Hamilton–Jacobi equation guarantees that the physical system possesses the desired property.

Since we seek a transformation to an integrable system, then from (10.11b) we can, for example, choose the new Hamiltonian to be independent of Q and t such that P is a constant of the motion,

$$H\left(q, \frac{\partial S(q, P, t)}{\partial q}, t\right) + \frac{\partial S(q, P, t)}{\partial t} = K(P). \tag{10.12}$$

Suppose a generating function $S(q, P, t)$ can be found as a solution to this equation. In that case, the system is integrable since K is autonomous and one conserved quantity exists, namely P.

Even if a system is known to be integrable, the Hamilton–Jacobi method may yield a coordinate system that greatly simplifies the motion. This will be demonstrated in Section 10.2.2 with the construction of action-angle coordinates. More generally, obtaining solutions to the Hamilton–Jacobi equation may be difficult, as discussed in Section 10.2.3 by applying a perturbation series solution. Moreover, a solution is not guaranteed to exist.

10.2.2 ▪ Action-angle coordinates

We now consider a particular setting to solve the Hamilton–Jacobi equation (10.12). We assume an autonomous system exhibiting periodic motion: either p is periodic in q or both p and q are periodic in time with the same frequency. The Hamilton–Jacobi method provides convenient coordinates to describe such systems, known as action-angle coordinates. The trajectories in these coordinates are particularly simple, as we assume the following: the momentum P is a constant in time, the position Q grows linearly in time, and the latter can be interpreted as an angle. Because the trajectories are so simple, this coordinate system will be well-suited to study perturbations about integrable systems in Section 10.2.3.

We consider a 1D autonomous Hamiltonian system, with the Hamiltonian $H(q, p)$. As a reminder, in this case, H is a constant of the motion. Here, we will start from assumptions on the transformed trajectories and describe the associated properties of the new Hamiltonian. We then focus on simplifying the Hamilton–Jacobi equation through a judicious explicit choice for this new Hamiltonian. More precisely, we seek a canonical coordinate transformation of a particular form to simplify motion.

- We choose the new momentum P such that it is only a function of H, $P = f(H(q, p))$. Since H is a constant of the motion, along any trajectory $(Q_T, P_T) : \mathbb{R} \to \mathbb{R} \times \mathbb{R}$, this yields

$$\frac{dP_T(t)}{dt} = 0. \tag{10.13}$$

  We also assume that the relation between H and P can be inverted so that we can express the constant of motion H as a function of P only, $H(q, p) = E(P(q, p))$.

- We further assume that the new position coordinate increases linearly in time, so along any trajectory $(Q_T, P_T) : \mathbb{R} \to \mathbb{R} \times \mathbb{R}$,

$$\frac{dQ_T(t)}{dt} = \omega_T \tag{10.14}$$

  for some given frequency ω_T constant along each trajectory. Furthermore, we assume that Q can be interpreted as an angle-like quantity. Thus, we expect many physical quantities to be periodic in Q.

This has consequences on the form of the new Hamiltonian K.

- From the first assumption (10.13) and the second equation of motion (10.11b) we conclude that the new Hamiltonian is independent of Q.
- From the second assumption (10.14) and the first equation of motion (10.11a) we conclude that $\partial K(Q, P, t)/\partial P$ is independent of time.

Therefore, under these assumptions, we can express the new Hamiltonian in the general form $K(Q, P, t) = F_P(P) + F_t(t)$ for some general functions F_P and F_t. We note from the equations of motion (10.11) that adding a function of only time, F_t, does not change the trajectories. Thus, we can choose $F_t(t) = 0$. Hence, to satisfy the desired properties of the equations of motion, we can choose the new Hamiltonian K to be only a function of P. In other words, the Hamiltonian is chosen to remain autonomous under the transformation. Under these assumptions the Hamilton–Jacobi equation (10.10) then takes the form

$$\frac{\partial S(q, P, t)}{\partial t} = K(P) - E(P).$$

We are free to make the further simplifying assumption that $K(P) = E(P)$. While this assumption does not simplify the trajectories, it will simplify the Hamilton–Jacobi equation for S. In particular, assuming $K(P) = E(P)$, the generating function must be independent of time.

To summarize, under the assumptions on the new trajectories, (10.13) and (10.14), we choose to define the new Hamiltonian as $K(P) = E(P)$ so that the Hamilton–Jacobi equation boils down to

$$\frac{\partial S(q, P, t)}{\partial t} = 0. \tag{10.15}$$

We will denote this time-independent generating function by $W(q, P)$.

Rather than solving explicitly (10.15) for S or W, we now derive a coordinate transformation to the action-angle coordinates (Q, P), valid for any generating function $S(q, P, t) = W(q, P)$. In order to find an expression for Q in terms of the independent variables (q, P), we start from the second generating relation from (10.9),

$$Q(q, P) = \frac{\partial W(q, P)}{\partial P},$$

and integrate the first generating relation between an arbitrary initial point q_0 and q to obtain an expression for W:

$$W(q, P) = \int_{q_0}^{q} p\big(q', P\big)\, dq'.$$

Combining the two, we get

$$Q(q, P) = \frac{\partial}{\partial P} \int_{q_0}^{q} p\big(q', P\big)\, dq'.$$

We now seek a form for Q such that it can be interpreted as an angle-like quantity. To do so, we consider the change in this new coordinate, ΔQ, over one period of the motion:

$$\Delta Q := \oint \frac{\partial Q(q,P)}{\partial q}\, dq, \text{ that satisfies } \Delta Q = \frac{\partial}{\partial P}\left(\oint p(q,P)\, dq\right).$$

We require this change in the new coordinate, ΔQ, to be 2π:

$$\Delta Q = 2\pi.$$

So far, P has been assumed to be only a function of H. We can now specify the definition of P to ensure that the above equality holds. Therefore, assuming that the definition of the Hamiltonian, $H(p,q)$, can be inverted to express p explicitly as a function of q and H, we define the new momentum, often called the action variable, as an integral over one period of the motion by

$$P(H) = \frac{1}{2\pi}\oint p(q,H)\, dq. \tag{10.16}$$

The integral is performed along one period of the motion, beginning at coordinate q_0 until the trajectory returns to q_0. It is clear from this definition that P is a constant of the motion as expected since the integral is over q while H is constant along trajectories.

Even when the trajectories p_T and q_T are known, performing a coordinate transform can still be helpful if the motion is simplified in action-angle coordinates. In this case, the integral definition for P can be computed along a trajectory (p_T, q_T) for a single period of the motion so that

$$P = \frac{1}{2\pi}\oint p_T(t)\frac{dq_T(t)}{dt}\, dt.$$

Remark 10.1. *We will now apply the action-angle coordinate transformation to the field-line flow system under the assumption of axisymmetry. The field-line flow Hamiltonian system is integrable under the assumption of axisymmetry, as it is a* 1*-degree-of-freedom autonomous system with one constant of the motion, namely* ψ_2 *as was shown in* (10.8)*. Furthermore, we assume that the momentum,* ψ_1*, is periodic in the coordinate* θ*. Thus, a transformation into action-angle coordinates exists for this system. Using the mapping to the field-line flow system given in Table* 10.1*, the action integral* (10.16) *for the field-line flow Hamiltonian system is given by*

$$P(\psi_2) = \frac{1}{2\pi}\int_0^{2\pi} \psi_1(\theta,\psi_2)\, d\theta.$$

The integration is performed at constant ψ_2 *along a closed poloidal loop. Moreover, since* $\psi_1 = \boldsymbol{A}\cdot\partial\boldsymbol{R}/\partial\theta$ *from* (10.3)*, we can rewrite the integral as* $P = 1/(2\pi)\oint \boldsymbol{A}(\boldsymbol{r})\cdot d\boldsymbol{r}$*. Upon application of Stokes' theorem,* P *is related to the magnetic flux through* S_T*, a surface enclosed by the isosurface of* ψ_2 *at constant toroidal angle, as illustrated in Figure* 5.5*,*

$$P = \frac{1}{2\pi}\int_{S_T} \boldsymbol{B}\cdot\hat{\boldsymbol{n}}\, d^2r,$$

where $\hat{\boldsymbol{n}}$ *is a unit normal vector to* S_T*. Therefore* $P = (1/2\pi)\Psi_T = \psi$*, the toroidal flux function introduced in* (5.8)*. By a similar argument, the new Hamiltonian is* $K(P) = (1/2\pi)\Psi_P = \psi_P$*, the poloidal flux function introduced in* (5.9)*.*

From (10.11a)*, the angle coordinate then satisfies*

$$\frac{dQ_T(\phi)}{d\phi} = \frac{d\psi_P(\psi)}{d\psi}.$$

Recalling from (7.3) *that* $\iota(\psi) = \psi_P'(\psi)$*, the frequency in the action-angle coordinates is the rotational transform. As a consequence, the new coordinate increases linearly with the toroidal angle,*

$$Q_T(\phi) = Q_0 + \iota(\psi)\phi,$$

where Q_0 *is an arbitrary initial condition. Therefore, the new angle coordinate can be interpreted as the poloidal angle in magnetic coordinates described in Chapter* 9*, as the quantity* $(Q - \iota\phi)$ *is constant along a field line.*

10.2.3 ▪ Perturbations about integrability

Without axisymmetry, magnetic field lines are described by a 1.5-degree-of-freedom Hamiltonian. As such, it is not generally integrable, and the existence of continuously nested flux surfaces is no longer guaranteed. To illustrate the challenges associated with maintaining integrability, we consider the effect of a perturbation about a 1-degree-of-freedom autonomous Hamiltonian, H_0. We show that preserving integrability requires additional conditions to be imposed on the Hamiltonian. This highlights the difficulty of constructing 3D integrable magnetic fields, even very close to axisymmetry.

We express the perturbed Hamiltonian, H, as a series with respect to some small parameter ϵ. We then seek conditions under which we can reveal the integrability of H by computing the generating function, S, from the Hamilton–Jacobi equation (10.12) order by order in ϵ. In this general approach, the existence of a solution for S at each order, together with the convergence of the resulting series, would show that H is integrable. We refer to [164, 73], Chapter 12 in [90], and Chapter 2 in [195] for further details on the perturbation series approach. Here, we limit the discussion to first-order terms for simplicity.

We begin with an integrable 1-degree-of-freedom Hamiltonian for which a canonical transformation exists to the action-angle coordinates (Q_0, P_0), with the transformed integrable Hamiltonian $H_0(P_0)$. Our interest lies in determining the integrability of the perturbed Hamiltonian, $H(Q_0, P_0, t)$, by seeking a particular canonical transformation from (Q_0, P_0) to (Q, P) that guarantees integrability of H. As a reminder, two independent constants of the motion are required for integrability since $H(P_0, Q_0, t)$ is a 1.5-degree-of-freedom Hamiltonian, as opposed to a single constant required for the unperturbed 1-degree-of-freedom Hamiltonian. Table 10.2 summarizes the correspondence between these two cases. Here, we will start from an assumption on the periodicity of the motion in addition to assumptions on the two desired constants of motion, motivated by properties of the integrable Hamiltonian H_0.

- The motion is assumed to be periodic with respect to Q_0 and time.
- The new momentum, P, is assumed to be a constant of motion.
- The new coordinate, Q, is assumed to be a constant of motion.

This has an important consequence on the new Hamiltonian K from Hamilton's equation (10.11).

- The new Hamiltonian K is independent of both P and Q.

Moreover, as already mentioned, adding any function of only time to the new Hamiltonian does not affect the equations of motion. To satisfy the desired properties of the equations of motion,

Table 10.2*: Summary of notation for unperturbed and perturbed Hamiltonian systems. The notation dof refers to degree of freedom.*

	Unperturbed Hamiltonian	Perturbed Hamiltonian
Number of dofs	1-dof	1.5-dof
Original Hamiltonian	$H_0(P_0)$	$H(Q_0, P_0, t)$
Transformed coordinates	(Q, P)	(Q, P)
Transformed Hamiltonian	K_0	K

we are free to choose the new Hamiltonian to be constant, and for simplicity, we choose $K = 0$. Under these assumptions, in what follows, we will first consider the coordinate transformation for the unperturbed case to use it as a starting point in the perturbed case later.

In the unperturbed case, thanks to the integrability of H_0, we can construct explicitly a coordinate transformation from (Q_0, P_0) to (Q, P) in which the transformed Hamiltonian is as simple as in the desired perturbed case, namely $K_0 = 0$. As a reminder, in this case, along any trajectories (Q_{0T}, P_{0T}), we have $dQ_{0T}(t)/dt = \omega_0(P_{0T})$ and $dP_{0T}(t)/dt = 0$ with the frequency $\omega_0(P_0) = dH_0(P_0)/dP_0$. Indeed, the associated Hamilton–Jacobi equation then takes the form

$$H_0\left(\frac{\partial S_0(Q_0, \mathsf{P}, t)}{\partial Q_0}\right) + \frac{\partial S_0(Q_0, \mathsf{P}, t)}{\partial t} = 0$$

for the generating function $S_0(Q_0, \mathsf{P}, t)$, and an explicit solution can be written under the form $S_0(Q_0, \mathsf{P}, t) = -H_0(\mathsf{P})t + Q_0\mathsf{P}$. This coordinate transformation then gives

$$\begin{cases} \mathsf{Q}(Q_0, \mathsf{P}, t) = \dfrac{\partial S_0(Q_0, \mathsf{P}, t)}{\partial \mathsf{P}}, \\ P_0(Q_0, \mathsf{P}, t) = \dfrac{\partial S_0(Q_0, \mathsf{P}, t)}{\partial Q_0}. \end{cases}$$

Therefore, the coordinate transform can then be expressed explicitly as

$$\begin{cases} \mathsf{Q} = Q_0 - H_0'(P_0)t, \\ \mathsf{P} = P_0. \end{cases} \tag{10.17}$$

As desired, P is a constant of the motion since P_0 is one. Moreover, along any trajectory, defined in the new coordinates as $(\mathsf{Q}_T, \mathsf{P}_T)$ and the original coordinates as (Q_{0T}, P_{0T}), we have from Hamilton's equations of motion in the original coordinates

$$\frac{d\mathsf{Q}_T(t)}{dt} = \frac{dQ_{0T}(t)}{dt} - H_0'(P_{0T}),$$

and therefore

$$\frac{d\mathsf{Q}_T(t)}{dt} = 0.$$

Hence, Q is another constant of motion. Although we obtained two constants of the motion, Q and P, we remark that they are not in involution, as the Poisson bracket $\{\mathsf{Q}, \mathsf{P}\}_{Q_0, P_0} = 1$. This implies that the two quantities are not independent.

We now turn to transforming the perturbed Hamiltonian $H(P_0, Q_0, t)$ into the new coordinates (Q, P). The corresponding Hamilton–Jacobi equation reads

$$H\left(Q_0, \frac{\partial S(Q_0, P, t)}{\partial Q_0}, t\right) + \frac{\partial S(Q_0, P, t)}{\partial t} = 0 \tag{10.18}$$

for the generating function $S(Q_0, P, t)$. Our goal is to obtain conditions under which this Hamiltonian system is integrable. Thus, using a perturbation series approach, (10.18) can be solved order by order. Here, we only consider terms up to linear order. Assuming that the perturbed Hamiltonian, $H(Q_0, P_0, t)$, can be expressed as a series about $H_0(P_0)$,

$$H(Q_0, P_0, t) = H_0(P_0) + \sum_{i=1}^{\infty} \epsilon^i H_i(Q_0, P_0, t), \tag{10.19}$$

for some $\epsilon \ll 1$, we seek a generating function, $S(Q_0, P, t)$ as a series about $S_0(Q_0, P, t)$,

$$S(Q_0, P, t) = S_0(Q_0, P, t) + \sum_{i=1}^{\infty} \epsilon^i S_i(Q_0, P, t). \tag{10.20}$$

At each order in ϵ, the $\mathcal{O}(\epsilon^n)$ terms of (10.18) provide equations for the corresponding S_n. In this section, we will not consider the convergence properties of (10.20). However, we note that if for all $i \geq 1$, there exists S_i satisfying (10.18) at the corresponding order with respect to ϵ, and if the resulting series for $S(Q_0, P, t)$ converges, then the desired canonical coordinate transformation exists. If the corresponding new coordinates (Q, P) are independent, then the Hamiltonian $H(Q_0, P_0, t)$ is integrable. If (10.20) does not formally converge but there exists an S_i satisfying (10.18) for all $0 \leq i \leq N$ where N is some integer and the corresponding (Q, P) are independent, then we may say $H(Q_0, P_0, t)$ is integrable up to some order N. Note that H is integrable to at least zeroth order by assumption.

The $\mathcal{O}(\epsilon)$ terms provide an equation for S_1 given S_0, H_0, and H_1:

$$\frac{dH_0(P_0)}{dP_0}\frac{\partial S_1(Q_0, P, t)}{\partial Q_0} + \frac{\partial S_1(Q_0, P, t)}{\partial t} = -H_1\left(Q_0, \frac{\partial S_0(Q_0, P, t)}{\partial Q_0}, t\right),$$

where the first term has been Taylor expanded around $\partial S_0(Q_0, P, t)/\partial Q_0$. Moreover the unperturbed frequency is $\omega_0(P_0) = dH_0(P_0)/dP_0$ and from (10.17) we have $P_0 = P + \mathcal{O}(\epsilon)$. Then $\omega_0(P_0) = \omega_0(P) + \mathcal{O}(\epsilon)$. Hence the $\mathcal{O}(\epsilon)$ terms from (10.18) reduce to

$$\omega_0(P)\frac{\partial S_1(Q_0, P, t)}{\partial Q_0} + \frac{\partial S_1(Q_0, P, t)}{\partial t} = -H_1\left(Q_0, P, t\right). \tag{10.21}$$

As a reminder, constructing action-angle coordinates relies on the assumption of periodic motion. We have assumed that periodicity is preserved by the perturbation such that, at each order, the Hamiltonian and generating function are periodic in Q_0 and in time.

Remark 10.2. *The partial differential equation* (10.21) *is a magnetic differential equation of the form* (6.4)*. We can thus apply the results discussed in Section* 6.2*, considering the coordinates* (P, Q_0, t) *as well as the right-hand side* $\widetilde{F}(P, Q_0, t) = -H_1\left(Q_0, P, t\right)$.

According to Remark 10.2, let us first comment on the right-hand side's Fourier representation. Since $\widetilde{F}$ is doubly periodic, we write it as

$$H_1\left(Q_0, P, t\right) = \sum_{m,n} H_1^{m,n}(P) e^{i(mQ_0 - nt)}.$$

The necessary condition of existence for periodic solutions to (10.21) reads

$$H_1^{m,n}(P) = 0 \; \forall (m,n) \in \mathbb{Z}^2 \text{ such that } m\omega_0(P) = n, \; \forall P. \tag{10.22}$$

Then, formally, the general Fourier solution reads

$$S_1(Q_0,P,t) = \overline{S}_1(P) + \sum_{(m,n)\in\mathbb{Z}^2\setminus\{(0,0)\}} \Delta_{m,n}(P)\delta(\omega_0(P)m - n)e^{i(mQ_0-nt)} + \sum_{(m,n)\in\mathbb{Z}^2, n\neq\omega_0(P)m} \frac{iH_1^{m,n}(P)}{m\omega_0(P)-n} e^{i(mQ_0-nt)}.$$

This expression summarizes how the first-order generating function term S_1 depends on the first-order Hamiltonian term H_1 and the zeroth-order generating function term S_0 and Hamiltonian term H_0. In addition to exhibiting the Dirac-δ function singularity, the quantity $(m\omega_0(P) - n)$ appears in the denominator. As mentioned in Section 6.2.4, while there is no division by zero, terms in the denominator can get arbitrarily small, meaning that the series may not converge. Consequently,

- the nonuniqueness of the solution is reflected by the free parameters $\Delta_{m,n}$ and $\overline{S}_1$,
- a necessary condition for the existence of a solution is that $H_1^{m,n}(P) = 0$ for all pairs $(m,n) \in \mathbb{Z}^2$ such that $m\omega_0(P) = n$; moreover, the series can only converge under additional conditions on the Fourier coefficients $H_1^{m,n}$.

In particular, as discussed in Remark 6.1, the existence of the solution requires additional constraints on H_1 in the neighborhood of rational values of the rotational frequency, $\omega_0(P) = n/m$ for $n,\ m \neq 0$.

Even at first order in the perturbation amplitude, we obtain a restriction on the perturbed Hamiltonian for the desired canonical coordinate transformation to exist. In other words, even if a perturbation from integrability is arbitrarily small, it is not guaranteed to preserve integrability. Similarly, to obtain integrability at higher orders of ϵ would require additional constraints on the properties of H.

The preceding results illustrate that integrability is especially fragile in the neighborhood of rational values of the unperturbed frequency, $\omega_0(P)$. In other words, the persistence of integrability is particularly sensitive to the properties of $H_1^{m,n}$ for n/m close to $\omega_0(P)$. In the field-line flow Hamiltonian context, recall that $\omega_0(P)$ corresponds to the rotational transform according to Table 10.1. As the integrability of the magnetic field indicates the existence of flux surfaces, we conclude that flux surfaces in the neighborhood of rational surfaces may not exist unless additional constraints are placed on the magnetic field. We explore this notion of fragility in more detail in the following section.

10.2.4 ▪ Persistence of some flux surfaces: KAM theory

In Section 10.2.3, we evidence the difficulty in maintaining integrability, even if the Hamiltonian, $H(Q_0,P_0,t)$, remains close to an integrable Hamiltonian, $H_0(P_0)$. This difficulty is heightened near rational values of the unperturbed frequency, $\omega_0(P_0)$, where additional constraints must be satisfied to ensure the existence of a solution to the Hamilton–Jacobi problem. In the unperturbed system, trajectories are confined to invariant tori, forming surfaces of constant P_0 that foliate phase space. In the perturbed system, some or all of these surfaces may be destroyed due to loss of integrability.

Nonetheless, some invariant surfaces may persist in a perturbed system under appropriate conditions. In this section, we briefly describe the persistence of some surfaces in the perturbed system, following the results of Kolmogorov [160], Arnold [7], and Moser [218], known as the KAM theorem. We will describe the theorem's result here, but we refer the interested reader to several other sources [248, 195] for the details of the proof.

The proof of the KAM theorem relies on a more sophisticated perturbation approach than that presented in Section 10.2.3, allowing one to overcome the problem of small divisors for certain initial conditions. For this reason, in this section, we do not express the perturbed Hamiltonian as a series in a small parameter ϵ as in (10.19). Instead, we consider a perturbed Hamiltonian, H, close to an integrable one, H_0, and given by

$$H(Q_0, P_0, t) = H_0(P_0) + \delta H_1(Q_0, P_0, t),$$

where δ is some parameter. Here $H_0(P_0)$ defines the unperturbed Hamiltonian in action-angle coordinates exhibiting periodic motion, as described in Section 10.2.2. Suppose the perturbed Hamiltonian, H, is integrable and the periodicity of the motion is preserved. In that case, the perturbed Hamiltonian can similarly be expressed in action-angle coordinates (Q, P) as $K(P)$ for some canonical momentum P, a constant of the motion. If they exist, such momenta form invariant tori foliating phase space, and each surface of constant P has an associated frequency, $\omega(P)$.

While such a global action-angle transformation is not always possible, some invariant surfaces may persist at finite and nonzero perturbation amplitude δ. An invariant surface, P_0, of the unperturbed Hamiltonian, with associated frequency $\omega_0(P_0)$, is said to persist if it can be deformed continuously with respect to δ into an invariant surface P_δ of the perturbed system for a frequency $\omega_\delta(P_\delta)$.

The KAM theorem states that a given invariant surface persists under the following conditions.

- Perturbations are sufficiently small, $\delta \ll 1$.
- The unperturbed frequency $\omega_0(P_0)$ satisfies the Diophantine condition,

$$\exists (c, k) \in \mathbb{R}^+ \times \mathbb{N}, k \geq 2, \text{ s.t. } \forall (m, n) \in \mathbb{Z}^* \times \mathbb{Z}, \left| \omega_0(P_0) - \frac{n}{m} \right| \geq \frac{c}{m^k}. \tag{10.23}$$

  Here, c is a scalar that depends on the magnitude of the perturbation. This condition excludes regions surrounding each rational value of the frequency $\omega_0(P_0) = n/m$. For the magnetic field-line flow context, where $\omega_0(P_0)$ is ι, the condition (10.23) means that the rotational transform must be sufficiently irrational.

- The frequencies of the unperturbed Hamiltonian are nondegenerate,

$$|\omega_0'(P_0)| > 0, \tag{10.24}$$

  implying that there does not exist multiple unperturbed periodic orbits with the same frequency. In the context of field-line flow, this means that the magnetic shear, $\iota'(\psi)$, cannot vanish at any point. As there are applications in which this assumption cannot be made, for example, stellarators sometimes are designed to have small magnetic shear, a similar theory has been developed for degenerate systems [50, 217].

An important result of measure theory is that the set of frequencies satisfying the Diophantine condition (10.23) is of nonzero measure in $\mathbb{R}$, in the sense of Lebesgue. The KAM theorem implies that for a Hamiltonian system sufficiently close to integrability satisfying (10.24), a set of tori of the unperturbed Hamiltonian system with nonzero Lebesgue measure in phase space

Table 10.3*: Summary of notation for the field-line flow Hamiltonian* (10.25)*.*

	Canonical Hamiltonian	Field-line flow Hamiltonian
Perturbed Hamiltonian	$H(Q_0, P_0, t) = H_0(P_0)$ $+\delta H_1(Q_0, P_0, t)$	$\psi_2(\psi_1, \theta, \phi)$
Unperturbed Hamiltonian	$H_0(P_0)$	$\psi_1^2/2$
Perturbation	$\delta H_1(Q_0, P_0, t)$	$\psi_2(\psi_1, \theta, \phi) - \psi_1^2/2$
Frequency	ω_0	ψ_1

survives. In the context of field-line flow, this means that a nonzero volume of flux surfaces can persist, even in the presence of perturbations away from axisymmetry.

While the KAM theorem states conditions guaranteeing the persistence of invariant surfaces, other invariant surfaces may break up as the perturbation from integrability, δ, increases. When this happens, the trajectories no longer lie on nested tori and may exhibit different types of behavior, as introduced in Section 4.4.1.

- The trajectories may fill an area on a Poincaré plot; they are then known as chaotic, sometimes called stochastic or irregular.
- The trajectories may lie on surfaces with a different topology, forming so-called island structures.
- The trajectories may lie on so-called cantori, or partial barriers, that are partially destroyed invariant tori forming surfaces that are not closed but instead have holes possibly crossed by some trajectories.

Remark 10.3. *We will now illustrate the KAM theorem by considering a model magnetic field. As a reminder, the correspondence between the field-line flow and canonical Hamiltonian variables is found in Table* 10.1*. In an orthonormal coordinate system* (ψ_1, θ, ϕ) *with* θ *and* ϕ *assumed to be* 2π*-periodic, we consider the field*

$$\begin{cases} \boldsymbol{B}\big(\boldsymbol{R}(\psi_1, \theta, \phi)\big) = \nabla\psi_1 \times \nabla\theta - \nabla\psi_2(\psi_1, \theta, \phi) \times \nabla\phi, \\ \psi_2(\psi_1, \theta, \phi) = \dfrac{\psi_1^2}{2} + \delta\psi_1(\psi_1 - 1)\big[\cos(4\theta - \phi) + \cos(4\theta - 2\phi) + \cos(4\theta - 3\phi)\big]. \end{cases} \tag{10.25}$$

As seen in Section 10.1.1*,* $\psi_2(\psi_1, \theta, \phi)$ *is the Hamiltonian for the magnetic field-line flow. When* $\delta = 0$*, the corresponding Hamiltonian system is integrable, as the Hamiltonian becomes time-independent, so* ϕ*-independent in this context.*

We can make a correspondence between $\psi_2(\psi_1, \theta, \phi)$ *and the perturbed Hamiltonian* (10.19) *analyzed in Section* 10.2.3*. Here* $H_0(P_0)$ *is analogous to* $\psi_1^2/2$*, and* $H_1(Q_0, P_0, t)$ *is analogous to the remaining terms in* $\psi_2(\psi_1, \theta, \phi)$*. In particular, the unperturbed Hamiltonian,* $\psi_1^2/2$*, is in action-angle form, with canonical frequency given by* $d\left(\psi_1^2/2\right)/d\psi_1 = \psi_1$*, analogous to* ω_0*. This is summarized in Table* 10.3*. Recalling the necessary condition for integrability at* $\mathcal{O}(\epsilon)$ (10.22)*, we note that this condition will not be satisfied when the perturbed Hamiltonian has Fourier harmonics,* (n, m)*, such that* $m\psi_1 - n = 0$ *for the unperturbed frequency* ψ_1*. Here this occurs when* $\psi_1 = 1/4,\ 1/2$*, and* $3/4$*. According to the perturbation series approach discussion*

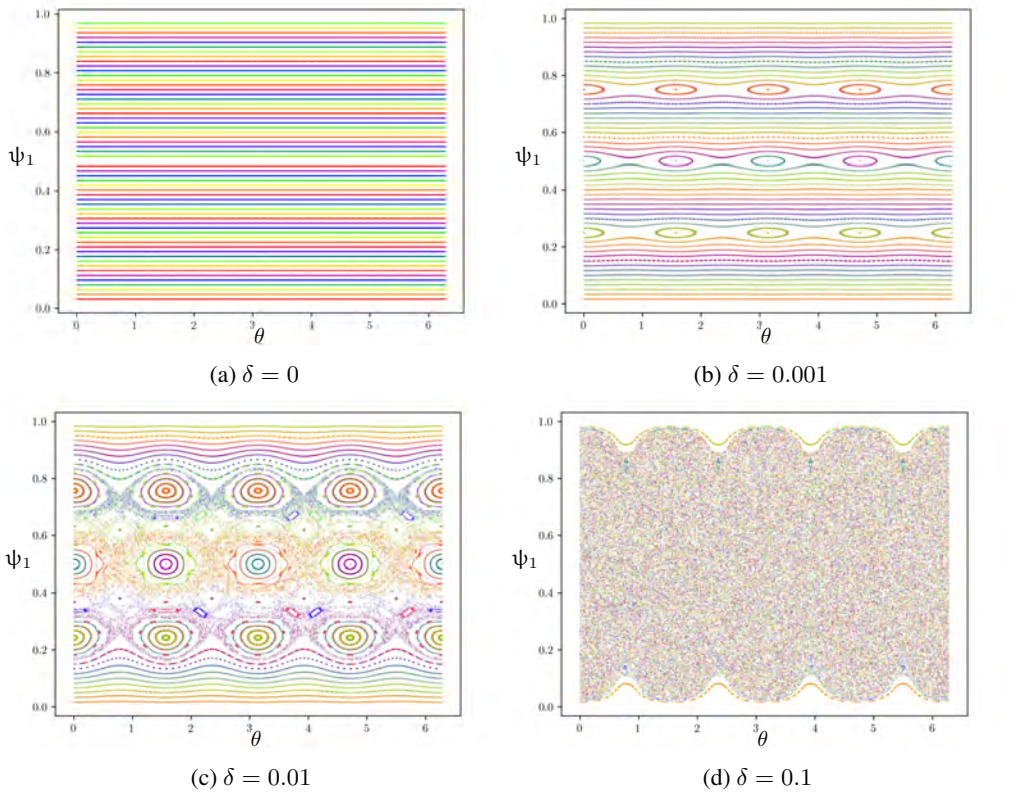

(a) $\delta = 0$ (b) $\delta = 0.001$

(c) $\delta = 0.01$ (d) $\delta = 0.1$

Figure 10.1*: Poincaré plots are shown for the model magnetic field* (10.25) *with several values of* δ*.*

in Section 10.2.3*, integrability will be most fragile near these surfaces. Indeed, this is illustrated in Figure* 10.1*. As* δ *is increased from* 0 *to* $\delta = 0.001$*, islands begin to form near these surfaces. These island chains then overlap as* δ *is further increased to* 0.01*, resulting in secondary island chains and a chaotic layer. However, we note that some surfaces persist at moderate* δ*. For larger perturbation amplitude,* $\delta = 0.1$*, almost all surfaces are destroyed, and the trajectories become chaotic.*

An important practical consequence of these results is that confinement is not entirely destroyed upon an infinitesimal deviation away from axisymmetry, which necessarily occurs in all real tokamak and stellarator devices. In closing, we note that the existence of some flux surfaces, as shown above, is distinct from the existence of continuously nested flux surfaces, as occurs in axisymmetric magnetic fields. This behavior results from the Hamiltonian nature of the flow of static magnetic field lines. It is thus independent of the choice of physical model used to describe the plasma itself. In modeling plasmas, it is therefore important to note the compatibility of the magnetic field's imposed properties with the model's assumptions. Next, we discuss some implications in the context of 3D MHD equilibria.

10.3 ▪ Singularities and surface currents in 3D ideal MHD

As we saw in Section 10.2, the existence or otherwise of magnetic surfaces in 3D is a direct consequence of the Hamiltonian nature of the field-line flow system. In general, 3D magnetic

fields may not be integrable. Nonetheless, as described in Section 4.4, flux surfaces guarantee good confinement properties. Consequently, we are typically interested in configurations with at least a region with good flux surfaces. Therefore, we consider the impact of this assumption on the ideal MHD equilibrium model in Section 10.3.1. Then, in Sections 10.3.2 and 10.3.3, we find that, under this assumption,

- additional requirements on the smoothness of the pressure profile or the magnetic geometry guarantee the existence of a solution;
- sheet currents may form on rational surfaces.

In the literature, the current is said to exhibit a $1/x$ singularity and a delta-function (or δ-function) singularity, both introduced in Section 6.2.4. As a reminder, there is no division by zero. Instead, the $1/x$ singularity refers to terms in the denominator of the form $\iota(\psi) - n/m$ that can become arbitrarily small and lead to nonconvergence.

As an alternative to imposing additional assumptions on the pressure or magnetic geometry, we discuss the consequence of relaxing the assumption of continuously nested flux surfaces in Section 10.3.4. When continuously nested flux surfaces are not assumed, magnetic islands or regions of chaotic magnetic field lines can exist in the plasma volume. These more general ideal MHD equilibrium solutions exhibit different properties and may not suffer from the previous singularities.

10.3.1 ▪ Parallel current density

We consider an ideal equilibrium field $\boldsymbol{B}$ with closed nested flux surfaces and pressure constant on each flux surface. The goal here is to emphasize that these assumptions are insufficient to guarantee physical solutions for the current. We derive from the ideal MHD equilibrium model an equation for the parallel current density, the so-called magnetic differential equation (MDE) introduced in Section 6.2, and interpret the singularities of the Fourier solutions in terms of the current. Analysis of the MDE highlights the challenges of obtaining 3D equilibrium solutions due to the integral constraints that arise at rational surfaces. The existence of solutions will then be closely related to current singularities and surface currents associated with rational surfaces in the 3D setting.

The current $\boldsymbol{J}$ can be decomposed into its parallel and perpendicular components under the form $\boldsymbol{J} = J_\parallel \boldsymbol{B}/B + \boldsymbol{J}_\perp$. The perpendicular current $\boldsymbol{J}_\perp$ can be evaluated from the equilibrium force balance $\boldsymbol{J} \times \boldsymbol{B} = \nabla p$ in terms of the magnetic field and the pressure profile as

$$\boldsymbol{J}_\perp = \frac{\boldsymbol{B} \times \nabla p}{B^2}.$$

To determine the parallel current $J_\parallel$, we use the fact that Ampère's law $\nabla \times \boldsymbol{B} = \mu_0 \boldsymbol{J}$ implies that $\nabla \cdot \boldsymbol{J} = 0$, giving

$$\boldsymbol{B} \cdot \nabla \left(\frac{J_\parallel}{B} \right) = -\nabla \cdot \boldsymbol{J}_\perp.$$

Hence, for a given pressure profile p and a given field $\boldsymbol{B}$, the parallel current satisfies the equation

$$\boldsymbol{B} \cdot \nabla \left(\frac{J_\parallel}{B} \right) = -\nabla \cdot \left(\frac{\boldsymbol{B} \times \nabla p}{B^2} \right). \tag{10.26}$$

Remark 10.4. *The partial differential equation* (10.26) *is a magnetic differential equation of the form* (6.3). *Considering any magnetic coordinate system* $(\psi, \vartheta, \varphi)$ *as well as the right-hand side* $F = -\nabla \cdot \left(\boldsymbol{B} \times \nabla p / B^2 \right)$ *we can thus apply the results discussed in Section* 6.2.

According to Remark 10.4, let us comment first on the right-hand side. The necessary condition of existence for doubly periodic solutions to (10.26) is $\langle F \rangle_\psi = 0$ for all ψ. Here, the right-hand side is the divergence of a vector field. Using Table 5.1, for any field $\boldsymbol{A}$, the flux-surface average of its divergence, namely

$$\begin{aligned}
&\langle \nabla \cdot \boldsymbol{A} \rangle_\psi \\
&= \frac{\displaystyle\int_0^{2\pi}\int_0^{2\pi} \left[\sqrt{g}\nabla\cdot\boldsymbol{A}\right](\psi,\vartheta,\varphi)\, d\vartheta d\varphi}{\displaystyle\int_0^{2\pi}\int_0^{2\pi} \sqrt{g}(\psi,\vartheta,\varphi)\, d\vartheta d\varphi} \\
&= \frac{\displaystyle\int_0^{2\pi}\int_0^{2\pi} \left[\frac{\partial}{\partial\psi}\left(\sqrt{g}\boldsymbol{A}\cdot\nabla\psi\right) + \frac{\partial}{\partial\vartheta}\left(\sqrt{g}\boldsymbol{A}\cdot\nabla\vartheta\right) + \frac{\partial}{\partial\varphi}\left(\sqrt{g}\boldsymbol{A}\cdot\nabla\varphi\right)\right](\psi,\vartheta,\varphi)\, d\vartheta d\varphi}{\displaystyle\int_0^{2\pi}\int_0^{2\pi} \sqrt{g}(\psi,\vartheta,\varphi)\, d\vartheta d\varphi},
\end{aligned}$$

always simplifies by periodicity with respect to (ϑ, φ) into

$$\langle \nabla \cdot \boldsymbol{A} \rangle_\psi = \frac{\displaystyle\int_0^{2\pi}\int_0^{2\pi} \left[\frac{\partial}{\partial\psi}\left(\sqrt{g}\boldsymbol{A}\cdot\nabla\psi\right)\right](\psi,\vartheta,\varphi)\, d\vartheta d\varphi}{\displaystyle\int_0^{2\pi}\int_0^{2\pi} \sqrt{g}(\psi,\vartheta,\varphi)\, d\vartheta d\varphi}.$$

Furthermore, because the pressure p depends only on the flux label ψ, the vector field defined by $(\boldsymbol{B}\times\nabla p)/B^2 = \left(p'(\psi)/B^2\right)\boldsymbol{B}\times\nabla\psi$ happens to be tangent to any flux surface. As a result, the flux-surface average of $F = -\nabla\cdot\left(\boldsymbol{B}\times\nabla p/B^2\right)$ is always zero, without any additional assumption on $\boldsymbol{B}$ and p.

Then, in the rational case, the necessary condition for the existence of periodic solutions to (10.26) along closed field lines is $\oint_{\mathcal{C}} F/B\, d\ell = 0$ for all closed field lines $\mathcal{C}$ and all surfaces ψ. Here, to compute the line integral of F/B, we express F in the coordinate system (ψ, α, l) introduced in Section 9.3 as

$$F(\psi,\alpha,l) = -p'(\psi)B(\psi,\alpha,l)\left[\frac{\partial}{\partial l}\left(\frac{\boldsymbol{B}\times\nabla\psi\cdot\nabla l}{B^3}\right) + \frac{\partial}{\partial\alpha}\left(\frac{\boldsymbol{B}\times\nabla\psi\cdot\nabla\alpha}{B^3}\right)\right](\psi,\alpha,l). \tag{10.27}$$

In obtaining the above expression, we have applied the expression for the divergence in nonorthogonal coordinates; see Table 5.1.

As a consequence, along a given closed field line $\mathcal{C}$ of length L_C, we have

$$\int_0^{L_c} \frac{F(\psi,\alpha,l)}{B(\psi,\alpha,l)}\, dl = -p'(\psi)\frac{\partial}{\partial\alpha}\left(\int_0^{L_c}\frac{dl}{B(\psi,\alpha,l)}\right),$$

since the contribution to the integral from the first term in (10.27) vanishes due to the assumption of periodicity in l and that $\boldsymbol{B}\times\nabla\psi\cdot\nabla\alpha = B^2$. As a result, the necessary condition of existence for periodic solutions along closed field lines can be expressed as

$$p'(\psi)\frac{\partial}{\partial\alpha}\left(\int_0^{L_C}\frac{dl}{B(\psi,\alpha,l)}\right) = 0. \tag{10.28}$$

To summarize this discussion on the right-hand side F of (10.26), the necessary condition for the existence of doubly periodic solutions is automatically satisfied by F in the irrational case, but not in the rational case.

Since in magnetic coordinates we have $\boldsymbol{B}\cdot\nabla\varphi = \sqrt{g}^{-1}$ and $\boldsymbol{B}\cdot\nabla\vartheta = \sqrt{g}^{-1}\iota(\psi)$, the magnetic differential equation (10.26) can be written equivalently as

$$\iota(\psi)\frac{\partial}{\partial\vartheta}\left(\frac{J_\parallel}{B}\right) + \frac{\partial}{\partial\varphi}\left(\frac{J_\parallel}{B}\right) = -\sqrt{g}\nabla\cdot\left(\frac{\boldsymbol{B}\times\nabla p}{B^2}\right)$$

with the right-hand side $\widetilde{F} := \sqrt{g}F$. Then, under assumption (10.28), the Fourier representation of the right-hand side reads

$$\widetilde{F}(\psi,\vartheta,\varphi) = \sum_{(m,n)\in\mathbb{Z}^2\setminus\{(0,0)\}} b_{m,n}(\psi)e^{i(m\vartheta-n\varphi)} \;\; \forall\psi,$$

where the Fourier coefficients satisfy

$$b_{m,n}(\psi) = 0 \;\forall(m,n)\in\mathbb{Z}^2\setminus\{(0,0)\} \text{ such that } \iota = \frac{n}{m},\; \forall\psi, \tag{10.29}$$

while $b_{(0,0)}(\psi) = 0$ since the flux-surface average (6.23) of F, and equivalently the average of $\widetilde{F}$, is always zero. Then, formally, the general Fourier solution reads

$$\begin{aligned}\left(\frac{J_\parallel}{B}\right)(\psi,\vartheta,\varphi) = \;& \mathcal{K}(\psi) + \sum_{(m,n)\in\mathbb{Z}^2\setminus\{(0,0)\}} \Delta_{m,n}(\psi)\delta(\iota(\psi)m-n)e^{i(m\vartheta-n\varphi)} \\ & + \sum_{(m,n)\in\mathbb{Z}^2, m\neq\iota(\psi)n} \frac{i}{n-\iota(\psi)m} b_{m,n}(\psi)e^{i(m\vartheta-n\varphi)}.\end{aligned} \tag{10.30}$$

This expression summarizes how the parallel current depends on the field strength B and the pressure p, assuming that the two series converge. As a reminder, the convergence of the second term depends exclusively on properties of the $b_{m,n}(\psi)$, these coefficients depending on the field $\boldsymbol{B}$ and pressure p. In contrast, the convergence of the first term depends on the free parameters $\Delta_{m,n}(\psi)$. Those are not determined by the MDE itself but could be determined from the full ideal MHD equilibrium equations, taking the curl of $\boldsymbol{B}$ to compute $\boldsymbol{J}$ throughout the volume.

The Pfirsch–Schlüter current refers to the contribution to the parallel current from the two summation terms. These have different physical interpretations.

- The so-called δ-function term, the first sum in (10.30), corresponds to localization of the current density, $\boldsymbol{J}$, to 2D surfaces, namely the set of rational flux surfaces. These localized current densities are referred to as current sheets. The amplitude of this localized current density is not determined by the MDE (10.26) itself.
- The so-called $1/x$ term, the second sum in (10.30), is not localized to rational surfaces and is entirely determined by the right-hand side of the MDE. As a result, it depends on the pressure gradient and is sometimes referred to as the pressure gradient–driven current.

The following two sections present a physical interpretation of the integral constraint and the δ-function term.

Remark 10.5. *As mentioned in Section* 6.2.4*, the literature refers to the* $1/x$ *singularity, meaning the division by the quantity* $x = \iota(\psi) - n/m$*, as it vanishes for every* ψ *and* $(m,n)\in\mathbb{Z}^2$ *such that* $\iota(\psi) = n/m$[17] *as well as the* δ*-function singularity. See, for example, Section* 2.11 *in* [116] *for a discussion of these current singularities.*

[17] As a reminder, these ψ and $(m,n)\in\mathbb{Z}^2$ such that $\iota(\psi) = n/m$ are not included in the summation term in (10.30): there is no division by zero.

Recent analysis and numerical calculations have explored the nature of the current singularities in the Hahm–Kulsrud–Taylor problem described in Section 10.3.4*, consisting of a mirror-symmetric* 2*D Cartesian geometry with an* $\iota = 0$ *rational surface on the midplane. In* [136]*, the authors describe a singularity of the current scaling as* $1/\iota(\psi)$ *near the rational surface under particular hypotheses. Due to the compression of flux surfaces near the rational surfaces, their solution for the current scales as* $1/\sqrt{x}$ *where* x *measures distance from the rational surface. Note that the current density does not satisfy the integral constraints yet exhibits an integrable singularity.*

10.3.2 ▪ Satisfying the integral constraints at rational surfaces

We have just seen that the solution for the parallel current does not exist unless integral constraints on the right-hand side, $F = -\nabla \cdot (\boldsymbol{B} \times \nabla p)/B^2$, of the MDE (10.26) are satisfied on rational surfaces, namely (10.28). As a reminder, a rational surface refers to a flux surface labeled ψ such that the value of the rotational transform $\iota(\psi)$ is rational. We now consider sufficient conditions for these constraints to be satisfied.

The necessary conditions of existence for periodic solutions are expressed in (10.28) along each given closed field line $\mathcal{C}$ of length L_C as

$$p'(\psi)\frac{\partial}{\partial \alpha}\left(\int_0^{L_C} \frac{dl}{B(\psi,\alpha,l)}\right) = 0. \tag{10.31}$$

Since this condition is expressed as a product, there are two natural approaches to guarantee that this constraint is satisfied: either by an assumption on the pressure profile or the magnetic field geometry.

- One is to assume that the pressure gradient vanishes on all rational surfaces.
  - This is, for instance, true under the assumption that $p'(\psi) = 0$ throughout the entire plasma volume. The corresponding pressure profile is constant. However, this case is of limited interest for many practical applications since a fusion device must support significant pressure gradients.
  - More generally, this can also be true under the assumption that $p'(\psi) = 0$ except at a finite number of irrational surfaces. The pressure profile is piecewise constant with a finite number of jumps, referred to as a stepped pressure profile as discussed in Section 11.5. This allows for a pressure difference between the core and edge of a fusion device.
  - A yet more general assumption would be $p'(\psi) = 0$ on all rational surfaces but with no restriction at any irrational surface so that the pressure gradient could be discontinuous almost everywhere. The corresponding pressure profile would then be fractal. This assumption was proposed by Grad [93] and was more recently studied in [166].
- The other one is to assume that the magnetic field $\boldsymbol{B}$ on each rational surface satisfies

$$\frac{\partial}{\partial \alpha}\left(\int_0^{L_C} \frac{dl}{B(\psi,\alpha,l)}\right) = 0.$$

  The simplest way to do so is by avoiding rational surfaces.
  - This is possible if $\iota'(\psi) = 0$ throughout the plasma volume, and ι is a constant irrational value. However, this constraint may be overly restrictive.

- More generally, rational values of the rotational transform can be avoided under the assumption that $\iota'(\psi) = 0$ and ι is a constant irrational value, except for a finite number of jumps. The magnetic surfaces on which such jumps occur must support a current sheet. Such a configuration is referred to as having a stepped rotational transform [201, 141].

As described in Section 8.3, the ideal MHD equilibrium equations are typically solved with a prescribed plasma boundary and profiles of the rotational transform and pressure. An ideal MHD equilibrium solution may not exist for a given 3D plasma boundary. However, in principle, obtaining an equilibrium that satisfies the integral constraints may be possible by carefully choosing the plasma boundary.

- A technique to construct $\boldsymbol{B}$ approximately satisfying the condition was proposed in [300, 321, 301]. The technique assumes the rotational transform remains close to a rational value, implying low magnetic shear. The magnetic field is represented as a series expansion. The constraint $\partial/\partial\alpha(\oint 1/B \; d\ell) = 0$ is enforced at each order in the expansion by tuning the magnetic geometry. However, the series expansion is not convergent in general.
- A particular equilibrium solution has been computed to all orders [302], assuming all field lines are closed.

The first approach requires that the pressure profiles are either constant or not smooth, but this is often not realistic. On the other hand, the second approach potentially allows for pressure profiles, and this may be considered more relevant as $p'(\psi)$ can be continuous. However, the class of admissible equilibrium boundary shapes may be reduced compared to the construction of equilibria where the pressure gradient is constrained without assumption on the field.

These additional assumptions on the geometry of the domain or pressure profile are sufficient to guarantee the existence of solutions to the MDE (10.26). These assumptions may not always be desirable, as they further restrict the class of allowable equilibria.

From the point of view of computing approximate solutions, given $\boldsymbol{B}$ as an approximate numerical solution of the ideal MHD equations, it is not guaranteed that the approximate right-hand side $\tilde{F}$ of the MDE satisfies the integral constraint (10.28). Consequently, there is no solution to the MDE in this case. Nevertheless, the parallel current can be evaluated directly by applying Ampère's law to the approximate equilibrium magnetic field instead of solving the MDE.

On the other hand, it is not necessary to satisfy the integral constraint if alternatives to the ideal MHD model with continuously nested surfaces are considered. This can include relaxing the assumption of continuously nested surfaces or including nonideal effects. In Section 10.3.4, we will explore the impact of relaxing the assumption of continuously nested surfaces in a simple model. Several models without the assumption of surfaces are discussed in Sections 11.3, 11.4, and 11.5. Section 10.4 discusses nonideal MHD models and their application to approximating equilibrium fields.

10.3.3 ▪ Delta-function singularities

After integration, the δ-function singularity of (10.30) can be a nonzero and finite term localized to rational surfaces and known as a current sheet. Current sheets may be interpreted as idealizations of highly spatially localized currents in the limit of infinite conductivity. The behavior of such localized currents near rational surfaces has been investigated numerically by 3D ideal MHD equilibrium codes [200, 192, 214]. In these three references, the current density was computed from an ideal MHD equilibrium numerical solution. In certain limits, the resulting

densities display a localization in a region close to a 2D surface. This is consistent with the δ-function current expected from the MDE solution under the assumption of continuously nested flux surfaces.

- In [200], it is assumed that a finite number of nested closed flux surfaces exist, as opposed to the continuously nested flux surfaces as discussed previously. Section 11.5 will present more details on the corresponding equilibrium model. The jump in the tangential component of the field is computed across a volume bounded by two closed flux surfaces and is related to a current sheet on a surface in Section 10.3.4. The authors then study the behavior of this jump in the limit as the toroidal flux between the two closed flux surfaces approaches zero.
- In [192, 214], it is assumed that flux surfaces are continuously nested. The current density is evaluated from derivatives of the equilibrium magnetic field. More details on the corresponding equilibrium model will be presented in Section 11.1.2. A single harmonic (n, m) of the current density (10.30) can be examined to reveal a δ-function-like behavior at a single surface where $\iota(\psi) = n/m$. In both articles, the authors study the behavior of such a mode as the resolution in the radial direction is refined.

Current sheets imply a discontinuity of the tangential magnetic field, as shown in Appendix C. However, in many physical systems of interest, such a discontinuity will not arise. If we seek solutions with a smooth tangential magnetic field, it is natural to consider modifying the assumptions. In what follows, we will describe two ways to do so. In Section 10.3.4, we consider a simplified ideal MHD equilibrium problem in the neighborhood of a rational surface. We will find that magnetic islands can open up on the rational surface if the assumption of continuously nested flux surfaces is relaxed. In Section 10.4, we will describe models that extend beyond ideal MHD equilibrium and include important physical effects such as resistivity.

10.3.4 ▪ Islands and surface currents in a simplified model

As we have seen in previous sections, so-called current singularities can arise at rational surfaces, and we want to gain further insight into the nature of these singularities in ideal MHD equilibria. This section aims to showcase a family of magnetic fields, close to each other and not necessarily smooth, focusing on their behavior on a given rational surface. Rather than attacking the full 3D problem, we consider a simplified 2D setting containing some key features, allowing us to isolate a single rational surface. Imposing smoothness of the magnetic field will lead to an island chain on the rational surface. Imposing that the rational surface remains a flux surface and allowing for nonsmoothness then leads to a surface current instead of an island chain at that rational surface.

The so-called Hahm–Kulsrud–Taylor [98] model refers to an equilibrium magnetic field with continuously nested surfaces in 2D slab geometry[18] with oppositely directed magnetic fields about a symmetry plane. By applying a perturbation to the boundary of the domain, this model is widely used to study a range of reconnection phenomena involving the formation of current sheets and magnetic islands [329], and the plasmoid instability, a secondary instability of current sheets with applications in fusion, space, and astrophysical plasmas [46]. We will leverage this method to compute a perturbed ideal MHD equilibrium exhibiting islands and current sheets, focusing on the first-order term in a series expansion. Specifically, we will focus on the behavior of the solution on the symmetry plane that is also a rational surface with $\iota = 0$ in the unperturbed domain. The computational details will be presented in Appendix D for clarity.

We consider the ideal MHD equilibrium model. The divergence-free condition is $\nabla \cdot \boldsymbol{B} = 0$ and the force balance condition (8.9) reads $\nabla p = \boldsymbol{J} \times \boldsymbol{B}$. Taking the curl of (8.9) and using

[18] A 2D slab geometry refers to a 3D problem such that physical quantities are independent of one Cartesian coordinate.

Ampère's law $\nabla \times \boldsymbol{B} = \mu_0 \boldsymbol{J}$ to eliminate $\boldsymbol{J} = (\nabla \times \boldsymbol{B})/\mu_0$, we can recast (8.9) in a form that is independent of the pressure, p, and given by

$$\nabla \times \left(\left(\nabla \times \boldsymbol{B} \right) \times \boldsymbol{B} \right) = 0. \tag{10.32}$$

The pressure p was eliminated here, but it can be reconstructed from the field $\boldsymbol{B}$. We do not constrain the pressure to be a flux function. Instead, we will build a family of solutions to a boundary value problem for the magnetic field governed by (10.32).

Consider a physical system in $\mathbb{R}^3$ described by Cartesian coordinates (x, y, z), where x acts as a radial coordinate, while y and z are angle-like coordinates. All physical quantities are assumed to be 2π-periodic with respect to the y coordinate and independent of the z coordinate. Thinking of z as the toroidal angle, the latter corresponds to assuming axisymmetry. Moreover, to simplify the problem further, we assume that the z component of the field is a constant B_T. While a will represent a reference length of the problem, the parameter $\delta > 0$ will stand for the amplitude of the perturbation.

As a consequence of the assumption of axisymmetry, magnetic surfaces are guaranteed in the solution. However, because the poloidal field vanishes when $\iota = 0$, the assumptions described in Section 10.1 are no longer satisfied. For this reason, magnetic surfaces exist but do not all close with the same topology and can possibly exhibit island structure.

The original procedure presented in [98] uses the parameter δ and focuses on small perturbations in the regime $\delta \ll a$. However, δ has units of length and is therefore scale dependent. In the following discussion, we perform a perturbation series analysis with respect to the dimensionless small parameter $\mathrm{d} = \delta/a$ in the regime $\mathrm{d} \ll 1$, following a more recent version of the analysis presented in [51].

For a fixed integer k and fixed value $a > \delta$ with $x_{\pm \mathrm{d}}(y) = \pm a(1 - \mathrm{d}\cos(ky))$, we will consider 2D domains defined by

$$\Omega_{\mathrm{d}} = \{(x, y), y \in (0, 2\pi), x \in (x_{-\mathrm{d}}, x_{+\mathrm{d}})\}.$$

Both the reference domain, for $\mathrm{d} = 0$, and the perturbed domain, for $1 > \mathrm{d} > 0$, are shown in the y-x plane in Figure 10.2. We will also refer to the half-domain:

$$\Omega_{\mathrm{d}}^{+} := \Omega_{\mathrm{d}} \cap \{(x, y) \in \mathbb{R}^2, x > 0\}.$$

Because of periodicity with respect to y, we define the boundaries as

$$\Gamma_{\mathrm{d}}^{+} = \{(x_{+\mathrm{d}}(y), y)\,, y \in (0, 2\pi)\}\,,\ \Gamma_{\mathrm{d}}^{-} = \{(x_{-\mathrm{d}}(y), y)\,, y \in (0, 2\pi)\}\,,$$

$$\Gamma_{\mathrm{d}} = \Gamma_{\mathrm{d}}^{+} \cup \Gamma_{\mathrm{d}}^{-}.$$

The general boundary value problem for $\boldsymbol{B}$ can now be stated as follows:

$$\begin{cases} \nabla \times ((\nabla \times \boldsymbol{B}) \times \boldsymbol{B}) = 0 & \text{in } \Omega_{\mathrm{d}}, \\ \nabla \cdot \boldsymbol{B} = 0 & \text{in } \Omega_{\mathrm{d}}, \\ \boldsymbol{B} \cdot \hat{\boldsymbol{n}} = 0 & \text{on } \Gamma_{\mathrm{d}}. \end{cases} \tag{10.33}$$

We focus on building a family of solutions under the following assumptions.

1. The field $\boldsymbol{B}$ has a z component that is constant in space for all $\mathrm{d} \geq 0$.
2. The field $\boldsymbol{B}$ is independent of z.

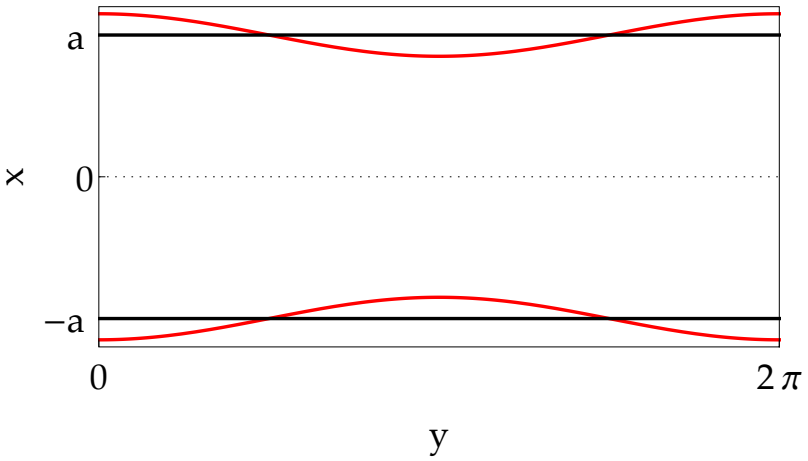

Figure 10.2*: The reference,* $\mathrm{d} = 0$*, and perturbed,* $\mathrm{d} > 0$*, domains in the* y*-*x *plane are shown. The black and red lines correspond to* $x = \pm a$ *and* $x_{\pm \mathrm{d}}(y)$*, respectively.*

3. We are going to focus on $\boldsymbol{B}$ up to linear order in d, and consider a reference solution independent of y.
4. The solutions satisfy a reflection symmetry property across $x = 0$ that allows the BVP to be reduced to a problem on the half-domain Ω_{d}^{+}.

We can leverage these assumptions as follows.

i. The amplitude of the z component of the magnetic field will be denoted B_T.

ii. The field $\boldsymbol{B}$ and its divergence can be written $\boldsymbol{B}(x,y) = B_x(x,y)\hat{\boldsymbol{x}} + B_y(x,y)\hat{\boldsymbol{y}} + B_T\hat{\boldsymbol{z}}$ and $\nabla \cdot \boldsymbol{B} = \partial B_x/\partial x + \partial B_y/\partial y$. So, as a consequence of the divergence condition in (10.33), we get

$$\frac{\partial B_x(x,y)}{\partial x} + \frac{\partial B_y(x,y)}{\partial y} = 0.$$

Remark 10.6. *The previous equation is of the form* (6.1)*. Considering the coordinates* (x,y) *as well as* $F_1 = -B_x$ *and* $F_2 = -B_y$*, we can thus apply the results discussed in Section* 6.1*, more precisely, the existence result discussed in* 6.1.1.

According to Remark 10.6, for the field components there exists one function ψ of (x,y) satisfying

$$\begin{cases} B_x(x,y) &= -\dfrac{\partial \psi(x,y)}{\partial y}, \\ B_y(x,y) &= \dfrac{\partial \psi(x,y)}{\partial x}. \end{cases} \tag{10.34}$$

As a result, given a constant B_T, the magnetic field is entirely defined by the scalar function ψ since it can be expressed as

$$\boldsymbol{B}(x,y) = B_T\hat{\boldsymbol{z}} + \hat{\boldsymbol{z}} \times \nabla\psi(x,y). \tag{10.35}$$

iii. In general, it is possible to recast the boundary value problem (10.33) as a boundary value problem for ψ on Ω_{d}. However, we will focus on ψ and $\boldsymbol{B}$ up to linear order in d.

To that avail, we expand the function $\psi(x, y)$ as a perturbation series with respect to d, focusing on the zeroth and first-order terms,

$$\psi(x, y) = \psi_0(x) + \mathrm{d}\psi_1(x, y) + \mathcal{O}\left(\mathrm{d}^2\right), \tag{10.36}$$

and similarly for the magnetic field:

$$\boldsymbol{B}(x, y) = \boldsymbol{B}_0(x, y) + \mathrm{d}\boldsymbol{B}_1(x, y) + \mathcal{O}\left(\mathrm{d}^2\right). \tag{10.37}$$

The relation (10.35) between $\boldsymbol{B}$ and ψ naturally leads to relations between their corresponding terms in the previous expansions. Under the assumption that the perturbed magnetic field retains a constant out-of-plane component equal to B_T, the reference magnetic field $\boldsymbol{B}_0$ is related to the reference ψ_0 as follows:

$$\boldsymbol{B}_0 = B_T\hat{\boldsymbol{z}} + \hat{\boldsymbol{z}} \times \nabla\psi_0(x), \tag{10.38}$$

while the perturbed magnetic field is related to ψ_1 as follows:

$$\boldsymbol{B}_1 = \hat{\boldsymbol{z}} \times \nabla\psi_1(x, y). \tag{10.39}$$

iv. We impose reflection symmetry, meaning that $\psi(-x, y) = \psi(x, y)$. Consequently, we seek ψ_1 in Ω_{d}^+ rather than the full Ω_{d}. As we will see, depending on the value of a parameter denoted $\Psi^k(0)$, the resulting solution is not necessarily differentiable across $x = 0$, so it will not be a strong solution.[19]

In this context, we can first construct a reference $\boldsymbol{B}_0$ satisfying the original equilibrium boundary value problem (10.33), thanks to an appropriate choice of ψ_0. We can then show that the general boundary value problem (10.33) for $\boldsymbol{B}_1$—thanks to the derivation of a modified boundary condition for ψ_1—reduces to a boundary value problem for ψ_1 on the reference domain, Ω_0, instead of the perturbed domain Ω_{d}. Finally, we can construct a family of solutions for ψ_1 that leads to different properties of the resulting solution $\boldsymbol{B}$, defined up to order $\mathcal{O}(\mathrm{d})$. For clarity, this procedure is presented in detail in Appendix D.

As described in Appendix D, given parameters a, B_0, k, and d, we can construct solutions for ψ on the half-domain Ω_0^+ to $\mathcal{O}(\mathrm{d}^0)$ (see (D.7) for reference),

$$\psi_0(x) = \frac{B_0 x^2}{2a},$$

and $\mathcal{O}(\mathrm{d}^1)$ (see (D.13) for reference),

$$\psi_1(x, y) = \left(\Psi^k(0)\cosh(kx) + \frac{aB_0 - \Psi^k(0)\cosh(ka)}{\sinh(ka)}\sinh(kx)\right)\cos(ky).$$

Given these solutions ψ_0 and ψ_1, we obtain a family of first-order approximations of ψ parameterized by the value of $\Psi^k(0)$ and defined on the full domain Ω_0 by

$$\psi(x, y) = \frac{B_0}{2a}x^2 + \mathrm{d}\left(\Psi^k(0)\left(\cosh(kx) - \frac{\sinh(k|x|)}{\tanh(ka)}\right) + aB_0\frac{\sinh(k|x|)}{\sinh(ka)}\right)\cos(ky), \tag{10.40}$$

where the absolute value guarantees the reflection symmetry $\psi(-x, y) = \psi(x, y)$. As a remark, imposing reflection symmetry can yield a nondifferentiable solution along the $x = 0$ plane. As

[19] In this case, it will still be a solution but in a weaker sense (more precisely as a distribution).

noted earlier, the corresponding field is a weak solution of the PDE problem (10.33), a solution in the sense of distributions.

Considering the family of first-order approximate fields $\boldsymbol{B}(x,y) = B_T\hat{\boldsymbol{z}} + \hat{\boldsymbol{z}} \times \nabla\psi(x,y)$ obtained from ψ (10.40), we now emphasize the relation between the parameter $\Psi^k(0)$ and properties of the corresponding equilibrium along the symmetry plane.

On the one hand, consider the amount of magnetic flux (per unit length in z) crossing the symmetry plane. It is defined between $y = 0$ and $y = Y$ and along the surface at $x = 0$ by

$$\int_0^Y \boldsymbol{B}(0,y)\cdot\hat{\boldsymbol{x}}\,dy = \int_0^Y B_x(0,y)\,dy.$$

Thus since

$$\int_0^Y \boldsymbol{B}(0,y)\cdot\hat{\boldsymbol{x}}\,dy = \psi(0,0) - \psi(0,Y),$$

so

$$\int_0^Y \boldsymbol{B}(0,y)\cdot\hat{\boldsymbol{x}}\,dy = \mathrm{d}\Psi^k(0)(1-\cos(kY)). \tag{10.41}$$

Hence, $\Psi^k(0)$ is proportional to the flux crossing the $x = 0$ axis.

On the other hand, consider the current density $\boldsymbol{K}$ along the symmetry plane, as described in Appendix C, defined in terms of the field jump across the symmetry plane by

$$\boldsymbol{K}(0,y) = \mu_0^{-1}\hat{\boldsymbol{n}} \times [\![\boldsymbol{B}]\!]_{x=0}(y).$$

Since B_z is constant while along the symmetry plane $\hat{\boldsymbol{n}} = \hat{\boldsymbol{x}}$, then the current density can be expressed as

$$\boldsymbol{K}(0,y) = \mu_0^{-1}[\![B_y]\!]_{x=0}\hat{\boldsymbol{z}}(y).$$

The jump in B_y across the axis $x = 0$ can be expressed at a point y in terms of ψ as

$$[\![B_y]\!]_{x=0}(y) = \left.\frac{\partial\psi(x,y)}{\partial x}\right|_{x\to 0^+} - \left.\frac{\partial\psi(x,y)}{\partial x}\right|_{x\to 0^-}. \tag{10.42}$$

Due to reflection symmetry, the function $\psi(x,y)$ may not be differentiable at $x = 0$. Therefore, in order to evaluate the jump in $\partial\psi/\partial x$, we compute the one-sided derivatives by taking the limits $x \to 0^+$ and $x \to 0^-$ as follows:

$$\begin{cases} \left.\dfrac{\partial\psi(x,y)}{\partial x}\right|_{x\to 0^+} = \mathrm{d}k\left(-\dfrac{\Psi^k(0)}{\tanh(ka)} + \dfrac{aB_0}{\sinh(ka)}\right)\cos(ky), \\ \left.\dfrac{\partial\psi(x,y)}{\partial x}\right|_{x\to 0^-} = \mathrm{d}k\left(\dfrac{\Psi^k(0)}{\tanh(ka)} - \dfrac{aB_0}{\sinh(ka)}\right)\cos(ky); \end{cases}$$

therefore, the jump can be expressed as

$$[\![B_y]\!]_{x=0}(y) = \frac{2k\mathrm{d}\cos(ky)}{\sinh(ka)}\left[aB_0 - \Psi^k(0)\cosh(ka)\right]. \tag{10.43}$$

The current density along $x = 0$ can finally be expressed as

$$\boldsymbol{K}(0,y) = \mu_0^{-1}\frac{2k\mathrm{d}\cos(ky)}{\sinh(ka)}\left[aB_0 - \Psi^k(0)\cosh(ka)\right]\hat{\boldsymbol{z}}. \tag{10.44}$$

There are two particular values of interest for the parameter $\Psi^k(0)$. One is $\Psi^k(0) = 0$, for which the flux (10.41) is always zero, so the corresponding field has a flux surface lying on the

axis $x = 0$ while there is a current supported on this surface according to (10.44). Note that for $\Psi^k(0) \neq 0$, the solution is not constant along the $x = 0$ plane. Hence, this plane is not a level set. The other one is $\Psi^k(0) = aB_0/\cosh(ka)$, for which the field jump (10.43) is always zero, so the symmetry plane does not support a surface current and it is not a flux surface according to (10.41).

We now consider the topology of the level sets of ψ for these two approximate solutions in the domain Ω_0, where we say that the boundaries $x = \pm a$ are closed in y and z by periodicity. In this context, magnetic islands correspond to regions where the level sets of ψ are closed but with a different topology than the boundaries. The centers of magnetic islands, called O points, correspond to isolated local minima and maxima of ψ, while the points that separate magnetic islands, called X points, correspond to saddle points or their nonsmooth counterparts as illustrated in Figure D.3. If there are no X or O points in the domain, then all of the level sets of ψ have the same topology as the boundaries. Given the expression (10.40) for ψ, the existence of local extrema and saddle points can be determined as detailed in Appendix D. The properties of the function ψ depend on the parameters d, k, and a. In particular, since the Hahm–Kulsrud–Taylor model is derived in the $\mathrm{d} \ll 1$ regime, according to Appendix D we will assume $\mathrm{d} < \sinh(ka)/(k^2a^2\sinh(kx_L))$ and $\mathrm{d} < \cosh(ka)/(k^2a^2)$ where x_L is the unique solution of $kx_L = 1/\tanh(kx_L)$. We now summarize the important results:

- In the nonsmooth case, corresponding to $\Psi^k(0) = 0$, there are two sets of stationary points, $(\pm x_1, y_S)$ and $(\pm x_2, y_S)$ for any y_S satisfying $ky_S = \pi[2\pi]$, where the values x_1 and x_2 are the two positive solutions of $\sinh(ka)/(\mathrm{d}ka^2)x_{1,2} = \cosh(kx_{1,2})$ with $0 < x_1 < x_2$. The points $(\pm x_1, y_S)$ are isolated local minima while $(\pm x_2, y_S)$ are saddle points. These stationary points will appear in the domain Ω_0 if $x_{1,2} \in (0, a)$. Since when d goes to 0 then x_1 goes to 0 while x_2 goes to infinity (see Figure D.1 for reference), in the limit $\mathrm{d} \ll 1$ then $x_1 < a$ while $x_2 > a$. Hence, for d small enough, this gives rise to sets of magnetic islands off of the $x = 0$ plane[20] if $x_1 < a$, while the $x = 0$ plane remains a magnetic surface.

- In the smooth case, corresponding to $\Psi^k(0) = aB_0/\cosh(ka)$, there are two sets of saddle points away from the $x = 0$ plane, $(\pm x_S, y_S)$ for any y_S satisfying $ky_S = \pi[2\pi]$ and x_S is the unique positive solution of $\cosh(ka)/(\mathrm{d}ka^2)x_S = \sinh(kx_S)$. On the $x = 0$ plane, there are sets of saddle points for all y_M such that $ky_M = 0[2\pi]$ and local minima for all y_m such that $ky_m = \pi[2\pi]$. Since when d goes to 0 then x_S goes to infinity (see Figure D.5 for reference), in the limit $\mathrm{d} \ll 1$ then $x_S > a$. Hence, for d small enough, this gives rise to magnetic islands on the $x = 0$ plane with no X points away from the $x = 0$ plane.

An illustration of these different topological structures arising in the solutions for $\Psi^k(0) = 0$ and $\Psi^k(0) = aB_0/\cosh(ka)$ is displayed in Figure 10.3.

To summarize, we have used a linearized perturbed ideal MHD equilibrium model without assuming continuously nested flux surfaces. We have seen that rational surfaces can support different structures depending on whether the rational surface is assumed to remain a flux surface. If the rational surface remains a flux surface, then a current sheet is supported on the rational surface in the model considered. This is analogous to the δ-function singularity discussed in previous sections under the assumption that continuously nested surfaces remain. If the rational surface does not remain a flux surface, then magnetic islands open up along the rational surface.

[20] These islands off of the $x = 0$ plane are referred to in the literature as residual islands [25] or shielded-half-islands [53], and from Appendix D we know that their O points get closer to the $x = 0$ plane as d goes to zero. It was shown [25] that nonlinear terms, that are neglected in the linear method considered in this section, yield a contribution to the total current density that prevents the existence of residual islands. As a result, continuously nested flux surfaces are present near $x = 0$ when $\mathrm{d} > 0$. Therefore, these islands' appearance is interpreted as an artifact of the linear model.

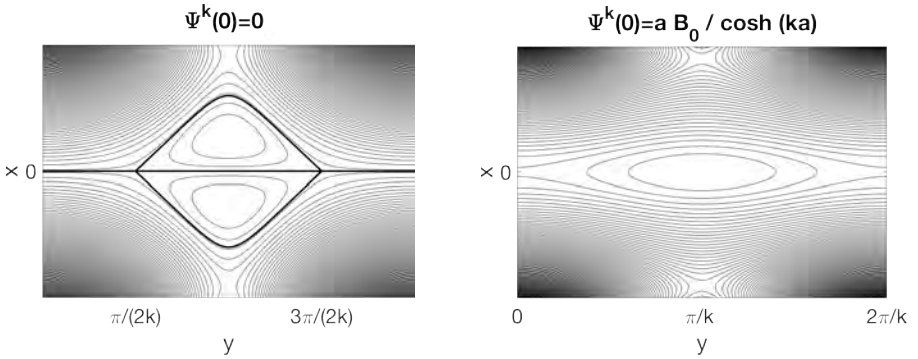

Figure 10.3*: Solutions of* (10.40) *in the* y*-*x *plane for* $\Psi^k(0) = 0$ *for* $\delta = 0.6$ *(left) and for* $\Psi^k(0) = aB_0/\cosh(ka)$ *for* $\delta = 0.3$ *(right), with* $B_0 = 1$*,* $a = 1$*, and* $k = 1$*.*

In terms of the parameter $\Psi^k(0)$ defining the family of solutions, this corresponds to $\Psi^k(0) = 0$ and $\Psi^k(0) \neq 0$, respectively.

In this section, by relaxing the assumption of continuously nested surfaces, we could exhibit equilibria with different behavior near a rational surface, namely a flux surface or an island chain. In the next section, we relax other assumptions of the ideal MHD model and illustrate how these may impact 3D magnetic fields.

10.4 ▪ Beyond ideal MHD equilibria

So far, in this chapter, we have considered magnetic fields under the ideal MHD equilibrium model. As a reminder, ideal MHD equilibria correspond with the steady state, $\partial/\partial t = 0$, and static, $\boldsymbol{u} = 0$, limit of the ideal MHD evolution equations, (8.1)–(8.6). Several limitations of the ideal MHD equilibrium model have been discussed previously.

- The current density may exhibit localization near rational surfaces, behavior that may be challenging to approximate numerically, as described in Section 10.3.3.
- The ideal MHD equilibrium equation for the parallel current density generally does not have a solution unless constraints are placed on the pressure profile or geometry, as described in Section 10.3.2.
- Topological changes observed in experimental fusion plasmas, known to significantly impact transport and confinement [314, 244], cannot arise in ideal MHD because of the flux freezing constraint, as described in Section 8.2.

It is then natural to consider models beyond ideal MHD, including time dependence and nonideal effects. In this section, we will introduce other time-evolution models that include additional physical effects and discuss the implications for 3D magnetic fields. Specifically, in Section 10.4.1, we will consider the addition of resistivity, relaxing the frozen-in flux constraint. In Section 10.4.2, we will discuss viscosity, allowing for diffusion of momentum, and perpendicular heat diffusion, allowing for diffusion of pressure. In Section 10.4.3, we discuss the application of time-evolution models for approximating equilibria.

10.4.1 ▪ Resistive MHD models

The ideal MHD model assumes an ideally conducting plasma and is often used in stellarator optimization to model the steady-state plasma and magnetic field. However, in practice, fusion

plasmas are not ideally conducting because there is a small amount of friction due to collisions between electrons and ions. This effect, briefly mentioned in Section 8.1, is known as resistivity and can be described by kinetic models. Reduced models describing kinetic effects can also be introduced into fluid models as illustrated in [43]. We present the equations of the so-called resistive MHD models and discuss the consequences on the flux freezing constraint. This will highlight why resistivity is an important extension of ideal MHD to model processes involving changes in the magnetic field topology.

Without resistivity, solutions of the ideal MHD model may become unbounded after a finite time interval [324, 111, 309]. Furthermore, as discussed in Section 10.3, solutions to the ideal MHD model can have δ-function behavior near rational surfaces. Some regularizing effects of resistivity on solutions of the ideal MHD time-evolution model are studied in [189].

Compared to ideal MHD, in Ohm's law (8.6), resistivity is modeled by the addition of a right-hand side proportional to a scalar quantity η, hence replacing the latter by

$$\boldsymbol{E} + \boldsymbol{u} \times \boldsymbol{B} = \eta \boldsymbol{J}. \tag{10.45}$$

Resistivity, $\eta \geq 0$, characterizes the resistance of a material to the flow of charged particles, also called current. In plasmas, several effects can contribute to the overall plasma resistivity. Collisions between electrons and ions are one important source of resistivity. For instance, the so-called Spitzer model [271] accounts for this collisional effect and leads to the scaling $\eta \propto T_e^{-3/2}$ where T_e is the electron temperature. For simplicity, the discussion in this section is limited to a simple model where η is constant with respect to space and time.

As a reminder, flux freezing arises due to the ideal induction equation (8.8) for $\boldsymbol{B}$, namely

$$\frac{\partial \boldsymbol{B}}{\partial t} = \nabla \times (\boldsymbol{u} \times \boldsymbol{B}).$$

To illustrate how the flux freezing constraint is affected by resistivity, we will now derive the corresponding resistive induction equation. Combining on the one hand (10.45) with Faraday's law, $\nabla \times \boldsymbol{E} = -\partial \boldsymbol{B}/\partial t$, and on the other hand Ampère's law $\nabla \times \boldsymbol{B} = \mu_0 \boldsymbol{J}$ together with the vector identity $\nabla \times (\nabla \times \boldsymbol{B}) = \nabla(\nabla \cdot \boldsymbol{B}) - \Delta \boldsymbol{B}$ yields the desired resistive induction equation:

$$\frac{\partial \boldsymbol{B}}{\partial t} = \nabla \times (\boldsymbol{u} \times \boldsymbol{B}) + \frac{\eta}{\mu_0} \Delta \boldsymbol{B}. \tag{10.46}$$

Hence, the resistive induction equation has an additional diffusion-like term on the right-hand side compared to ideal MHD. This additional term depends only on $\boldsymbol{B}$, but not on $\boldsymbol{u}$. As a result, the magnetic field lines still diffuse without any flow.

As described in Section 8.2, the change in the magnetic flux through a surface S is

$$\frac{d\Phi_S(t)}{dt} = \frac{\eta}{\mu_0} \int_{S(t)} \hat{\boldsymbol{n}}(\boldsymbol{r}, t) \cdot (\Delta \boldsymbol{B}(\boldsymbol{r}, t)) \, d^2 r,$$

while in the ideal MHD model $d\Phi_S/dt = 0$. Thus, flux freezing generally does not hold in the resistive MHD model. Since flux freezing need not hold everywhere, nonzero resistivity allows for changes in the topology of magnetic field lines and the formation of magnetic islands via magnetic reconnection.

Compared to ideal MHD, in the energy conservation equation (8.3), resistivity is modeled by a source of electromagnetic heating, so the equation becomes

$$\frac{1}{\gamma - 1} \left[\left(\frac{\partial}{\partial t} + \boldsymbol{u} \cdot \nabla \right) p + \gamma p \nabla \cdot \boldsymbol{u} \right] = \boldsymbol{J} \cdot (\boldsymbol{E} + \boldsymbol{u} \times \boldsymbol{B}).$$

As a reminder from Section 8.1, γ is the ratio of specific heats. According to the resistive Ohm's law (10.45), the right-hand side reduces to

$$\frac{1}{\gamma-1}\left[\left(\frac{\partial}{\partial t}+\boldsymbol{u}\cdot\nabla\right)p+\gamma p\nabla\cdot\boldsymbol{u}\right]=\eta J^2. \tag{10.47}$$

In Section 10.4.2, we will see that (10.47) can also be modified to include effects due to viscous dissipation and thermal conduction.

Remark 10.7. *As in Section* 8.1*, combining* (10.47) *with the continuity equation* (8.1) *leads to a modified entropy equation:*

$$\frac{\rho^\gamma}{\gamma-1}\left(\frac{\partial}{\partial t}+\boldsymbol{u}\cdot\nabla\right)\left(\frac{p}{\rho^\gamma}\right)=\eta J^2.$$

Assuming $\eta\neq 0$, on inspection of (10.47) it appears that a static equilibrium, $\partial/\partial t=0$ and $\boldsymbol{u}=0$, implies that $J=0$. Since we are generally interested in equilibria with a current $J\neq 0$, an additional source term is introduced for the pressure, S_P, into (10.47):

$$\frac{1}{\gamma-1}\left[\left(\frac{\partial}{\partial t}+\boldsymbol{u}\cdot\nabla\right)p+\gamma p\nabla\cdot\boldsymbol{u}\right]=\eta J^2+S_P. \tag{10.48}$$

If $\eta J^2>0$ in (10.47), this term leads to an increase in energy due to electromagnetic heating. In a steady state, since $0=\eta J^2+S_P$, the pressure source term must be negative, $S_P<0$, and thus actually acts as a sink. Therefore, S_P is often chosen to be negative in order to reach a steady state with nonzero current.

Remark 10.8. *As will be discussed in Section* 10.4.3*, computing equilibria is an important application of time-dependent MHD models for stellarators. Computing resistive equilibria with current motivated the introduction of the source S_P. In practice, other source terms can also be included to model additional effects.*

To summarize, a time-dependent resistive MHD model with a constant η is obtained by combining the resistive Ohm's law (10.45) and the modified energy conservation equation (10.47) with (8.1), (8.2), and (8.5):

$$\begin{cases} \dfrac{\partial\rho}{\partial t}+\nabla\cdot(\rho\boldsymbol{u})=0, \\ \rho\left(\dfrac{\partial}{\partial t}+\boldsymbol{u}\cdot\nabla\right)\boldsymbol{u}=\dfrac{(\nabla\times\boldsymbol{B})\times\boldsymbol{B}}{\mu_0}-\nabla p, \\ \dfrac{1}{\gamma-1}\left[\left(\dfrac{\partial}{\partial t}+\boldsymbol{u}\cdot\nabla\right)p+\gamma p\nabla\cdot\boldsymbol{u}\right]=\dfrac{\eta}{\mu_0^2}|\nabla\times\boldsymbol{B}|^2+S_P, \\ \dfrac{\partial\boldsymbol{B}}{\partial t}=\nabla\times(\boldsymbol{u}\times\boldsymbol{B})+\dfrac{\eta}{\mu_0}\Delta\boldsymbol{B}, \\ \nabla\cdot\boldsymbol{B}=0. \end{cases} \tag{10.49}$$

As in (10.46), the resistive Ohm's law (10.45) has been used to eliminate the electric field, $\boldsymbol{E}$, in Faraday's law. Moreover, the current $\boldsymbol{J}$ was also eliminated as it can be expressed explicitly as $\boldsymbol{J}=\frac{1}{\mu_0}\nabla\times\boldsymbol{B}$.

In general, the numerical solution of (10.49) is very challenging and the subject of active research. In Section 10.4.3, we will discuss briefly some general considerations for computing approximate equilibrium solutions of resistive MHD models.

10.4.2 ▪ Other diffusion effects: Momentum and pressure

As discussed in Section 10.4.1, even though kinetic models describe the details of collisions between electrons and ions, the effect can still be captured in MHD models by a diffusive term for the current density. Similarly, collisions between other particle species can produce additional diffusion effects, including momentum and pressure. Like resistivity, the details of the collisional dynamics can be described by kinetic models. The relationship to fluid models is derived in [43].

From the ideal MHD force balance, $\boldsymbol{J} \times \boldsymbol{B} = \nabla p$, it follows that $\boldsymbol{B} \cdot \nabla p = 0$. Hence, the pressure is constant along magnetic field lines. In a region of chaotic magnetic field lines, where a given magnetic field may fill the volume, the ideal MHD model implies that the pressure must also be constant in these regions. In practice, however, nonzero diffusion of heat along field lines can lead to pressure gradients in chaotic regions, as has been confirmed experimentally in the W7-AS [323, 251] and LHD [259, 287, 285] stellarators. Thus, nonideal effects are required to model these regions more accurately. This section discusses some of these effects, such as viscosity, anisotropic pressure, and heat diffusivity.

Collisions between particles moving in a plasma can result in the transfer of momentum. This produces an effect called viscosity that can inhibit flows. Since momentum is proportional to mass and $m_i \gg m_e$, in the absence of neutrals, collisions between ions are a dominant source of viscosity. A reduced model for viscosity can be introduced into the MHD model by replacing the momentum balance equation by

$$\rho \left(\frac{\partial}{\partial t} + \boldsymbol{u} \cdot \nabla \right) \boldsymbol{u} = \boldsymbol{J} \times \boldsymbol{B} - \nabla p + \mu \Delta \boldsymbol{u}. \tag{10.50}$$

The constant μ is referred to as a viscosity coefficient and the term $\mu \Delta \boldsymbol{u}$ acts like a diffusive term for the fluid flow providing a simple model for diffusion of momentum. Since the model depends only on the flow $\boldsymbol{u}$ and not on the field $\boldsymbol{B}$, unlike resistivity, other equations in the MHD model are unchanged.

Remark 10.9. *The momentum balance equation* (10.50) *can be derived by simplification of a more general pressure term. The total force acting on a fluid element is then denoted by* $\nabla \cdot \overleftrightarrow{\boldsymbol{p}}$ [76, 135] *where* $\overleftrightarrow{\boldsymbol{p}}$ *is a symmetric* 3×3 *matrix also known as a stress tensor. The stress tensor can be decomposed into*

$$\overleftrightarrow{\boldsymbol{p}}(\boldsymbol{r}) = p(\boldsymbol{r}) \overleftrightarrow{\boldsymbol{I}} + \overleftrightarrow{\boldsymbol{\Pi}}(\boldsymbol{r}).$$

Here $p(\boldsymbol{r})$ *is the scalar pressure already considered in the discussion so far and* $\overleftrightarrow{\boldsymbol{I}}$ *is the identity tensor. The terms in the so-called viscous stress tensor* $\overleftrightarrow{\boldsymbol{\Pi}}(\boldsymbol{r})$ *are derived from kinetic descriptions, including various collisional processes, and depend on the collisionality of the plasma under consideration. Under certain assumptions,* $\nabla \cdot \overleftrightarrow{\boldsymbol{\Pi}} \approx -\mu \Delta \boldsymbol{u}$*. More on this can be found in* [43, 28].

The entropy equation (10.48) can be further modified to include diffusion of pressure by adding a thermal conductivity term,

$$\frac{1}{\gamma - 1} \left[\left(\frac{\partial}{\partial t} + \boldsymbol{u} \cdot \nabla \right) p + \gamma p \nabla \cdot \boldsymbol{u} \right] = \eta J^2 + S_P + \nabla \cdot \left(\rho \overleftrightarrow{\boldsymbol{\kappa}} \cdot \nabla \left(\frac{p}{\rho} \right) \right), \tag{10.51}$$

where $\overleftrightarrow{\boldsymbol{\kappa}}$ is a thermal conductivity tensor. By setting ρ to be constant and choosing $\overleftrightarrow{\boldsymbol{\kappa}}$ to be diagonal, with parallel and perpendicular thermal conductivity coefficients, $\kappa_\parallel$ and $\kappa_\perp$, we arrive

at a simple model for anisotropic pressure diffusion where

$$\nabla \cdot \left(\rho \overleftrightarrow{\boldsymbol{\kappa}} \cdot \nabla \left(\frac{p}{\rho} \right) \right) = \nabla \cdot \left(\kappa_{\parallel} \nabla_{\parallel} p + \kappa_{\perp} \nabla_{\perp} p \right).$$

The parallel and perpendicular gradients are defined as $\nabla_{\parallel} = \hat{\boldsymbol{b}}\left(\hat{\boldsymbol{b}} \cdot \nabla\right)$ and $\nabla_{\perp} = \nabla - \hat{\boldsymbol{b}}\left(\hat{\boldsymbol{b}} \cdot \nabla\right)$. This model for anisotropic pressure diffusion has been used to study the stochastic field regions [143], as it allows for temperature equilibration both parallel and perpendicular to the magnetic field.

Incorporating (10.50) and (10.51) into (10.49) provides a generalized MHD model including nonideal effects associated with resistivity, viscosity, and thermal transport, given by

$$\begin{cases} \dfrac{\partial \rho}{\partial t} + \nabla \cdot (\rho \boldsymbol{u}) = 0, \\ \rho \left(\dfrac{\partial}{\partial t} + \boldsymbol{u} \cdot \nabla \right) \boldsymbol{u} = \dfrac{(\nabla \times \boldsymbol{B}) \times \boldsymbol{B}}{\mu_0} - \nabla p + \mu \Delta \boldsymbol{u}, \\ \dfrac{1}{\gamma - 1} \left[\left(\dfrac{\partial}{\partial t} + \boldsymbol{u} \cdot \nabla \right) p + \gamma p \nabla \cdot \boldsymbol{u} \right] = \dfrac{\eta}{\mu_0^2} |\nabla \times \boldsymbol{B}|^2 + S_P + \nabla \cdot \left(\rho \overleftrightarrow{\boldsymbol{\kappa}} \cdot \nabla \left(\dfrac{p}{\rho} \right) \right), \\ \dfrac{\partial \boldsymbol{B}}{\partial t} = \nabla \times (\boldsymbol{u} \times \boldsymbol{B}) + \dfrac{\eta}{\mu_0} \Delta \boldsymbol{B}, \\ \nabla \cdot \boldsymbol{B} = 0. \end{cases} \tag{10.52}$$

In practice, the values of the diffusion coefficients, including η, μ, $\kappa_{\parallel}$, and $\kappa_{\perp}$, can be both physically and numerically motivated. They can, for example, be informed by empirical measurements or selected to aid numerical stability.

Solving nonideal MHD models in stellarator geometry presents an additional challenge because of the strongly shaped, nonaxisymmetric computational domain. Tools that address these challenges have only been developed relatively recently. Examples of nonideal MHD initial-value codes with some stellarator modeling capability include M3D-C1 [152], NIMROD [269], JOREK [48], M3D [282], MIPS [291], and HINT2 [287]. The HINT2 model will be discussed in greater detail in Section 11.3.

10.4.3 ▪ Numerical approximation of equilibria

In general, obtaining exact analytic solutions for stellarator equilibria is impossible, but numerical methods can be used to compute approximate equilibria. In order to overcome the challenges associated with ideal MHD equilibria, we will discuss briefly some general considerations for computing approximate equilibrium solutions as quasi-steady-state solutions to time-dependent nonideal MHD models.

Given a time-dependent model, the corresponding equilibrium model is defined by setting the time-derivative terms to zero. An equilibrium or steady-state solution can be defined as the solution to the equilibrium model. There may or may not be a relationship between the long-time behavior of a time-dependent solution and an equilibrium solution. Depending on the initial conditions, the solutions of a nonlinear time-dependent model can exhibit several types of behavior.

1. After some time, the solution reaches a steady state, and all quantities become independent of time.

2. The solution converges with time to an equilibrium. In the long term, it may evolve slowly compared to some time scales of interest. This defines a quasi-steady state.

3. The solution does not reach either a steady state or a quasi-steady state; for example, it may become unbounded or exhibit cyclic behavior.

Suppose, for some initial condition, the solution converges to a steady state or reaches a quasi-steady state. In that case, this can be the basis for a numerical method to approximate the corresponding equilibrium by computing numerically an approximate solution to the initial-value problem for a long time. Since the topology of the magnetic field is not prescribed by the topology of the initial condition, this approach can be advantageous to approximate stellarator equilibria without continuously nested flux surfaces.

On the other hand, the question of convergence to a steady-state solution for a given initial condition remains an open question. Besides, computing long-term solutions to a time-dependent problem is considerably more costly than directly computing solutions to an equilibrium problem, particularly if the solution converges slowly toward a steady state. From the numerical point of view, it is also difficult to distinguish between steady-state and quasi-steady-state solutions. Furthermore, sensitivity to the initial condition may complicate the numerical approximation of solutions to nonlinear models.

Several reduced models incorporating some features of the nonideal MHD evolution but with accelerated convergence properties have been proposed. This includes the so-called relaxation methods that form the basis for 3D MHD equilibrium codes such as HINT and HINT2 [286]. These are discussed in Section 11.3. An iterative method allowing pressure transport along field lines is the basis for the PIES code [250] and is discussed in Section 11.3.

Chapter 11

Models of 3D ideal MHD equilibrium magnetic fields

To model stellarators and many other physical phenomena, equilibrium solutions and their stability properties are often studied to assess steady-state behavior. In stellarators, achieving a steady state is desirable for confining energy. In principle, the particles and the fields are coupled. Due to the separation of scales in magnetic confinement devices, it is often a good approximation to model the large-scale behavior with ideal MHD models as introduced in Section 8.3. While other models exist, the MHD equilibrium model has been shown to be relatively reliable for fusion plasmas with strong magnetic fields. See, for instance, Chapter 2 of [76]. Ideal MHD equilibrium provides a relatively simple set of equations and is computationally tractable. For this reason, ideal MHD is often applied to study the global behavior of toroidal plasmas, including both the plasma and the vacuum region surrounding the plasma.

While ideal MHD models the equilibrium balance between the plasma and magnetic field the impact of the equilibrium field on the plasma dynamics is also of interest. Therefore, once a time-independent magnetic field is obtained, other models can be leveraged to assess properties of the field, such as stability, transport, and particle trajectories, as described in Chapter 4.

We will consider several levels of approximation. Pressure gradients and currents in the plasma can be included, as in Sections 11.1.2 and 11.3. An important subset of ideal MHD models is the force-free model, presented in Section 11.4, where all currents are parallel to the magnetic field while the pressure is constant throughout the domain of interest. MRxMHD extends the force-free model, introduced in Section 11.5, allowing for annular regions, each with a force-free magnetic field. In the vacuum model, presented in Section 11.6, currents and pressure gradients are not included in the equilibrium model. Thus, some models include the feedback of the plasma on the magnetic field. However, the vacuum model does not.

There is also a distinction between models based on the assumption of surfaces. As discussed in Chapter 10, the existence of continuously nested toroidal flux surfaces cannot generally be assumed in 3D. However, models based on this assumption are often applied because of their computational efficiency. These are discussed in Sections 11.1.1 and 11.1.2. In Section 11.2, the existence of 3D equilibrium solutions with magnetic surfaces is demonstrated by considering an asymptotic expansion of the ideal MHD equations near the magnetic axis. An alternative model assumes the existence of only some surfaces in Section 11.5. Others rely on the existence of only one surface, serving as the boundary of the computational domain in Sections 11.4 and 11.6. Models not assuming the existence of any surfaces are presented in Sections 11.3 and 11.6. We will discuss the benefits and related challenges of the various 3D equilibrium models in the context of different applications. Section 11.7 presents a summary of the PDE models introduced in this chapter and proposes an analogy with a fluid mechanics model.

11.1 ▪ Equilibria with assumption of surfaces

In the context of axisymmetry, the ideal MHD force balance equations result in the Grad–Shafranov equation, introduced in Section 8.4, a PDE for the poloidal flux function ψ_P given the boundary of the toroidal domain and two flux functions, $F(\psi_P)$ and $p(\psi_P)$. The field is then defined in terms of ψ_P. Although continuously nested flux surfaces do not always exist in 3D fields, imposing this assumption provides a numerically tractable boundary value problem. Moreover, as discussed in Remark 4.4, this assumption is relevant because such surfaces exhibit favorable confinement properties. The assumption should ultimately be checked with other methods described in the following sections, which do not assume the existence of surfaces.

In analogy with the Grad–Shafranov problem, for 3D systems, it is common to consider ideal MHD force balance solutions, namely $\boldsymbol{B}$ satisfying

$$\begin{cases} (\nabla \times \boldsymbol{B}) \times \boldsymbol{B} = \mu_0 \nabla p(\psi) & \text{in } \Omega, \\ \nabla \cdot \boldsymbol{B} = 0 & \text{in } \Omega, \\ \boldsymbol{B} \cdot \hat{\boldsymbol{n}} = 0 & \text{on } \partial\Omega, \end{cases} \tag{11.1}$$

with prescribed pressure $p(\psi)$, rotational transform $\iota(\psi)$, domain boundary $\partial\Omega$, and toroidal flux function on the boundary $\psi(\partial\Omega)$.

11.1.1 ▪ Variational principle for equilibria

This section focuses on the variational principle for MHD equilibria with surfaces. This follows from the intuition that the plasma will tend toward a state that minimizes the energy. Equilibria will then be found via variational calculus techniques to minimize the plasma energy, subject to constraints. These constraints include the existence of a set of closed, nested flux surfaces. However, this is not to say that the variational principle provides any information on the evolution to an equilibrium state. The idea of finding ideal MHD equilibria via energy minimization was first studied in the 1950s [170], but remains widely used today for numerical approximation of equilibria.

The goal here is to show that finding solutions to (11.1) is equivalent to finding stationary points of W defined by

$$W[\boldsymbol{B}, p] = \int_\Omega \left(\frac{B^2(\boldsymbol{r})}{2\mu_0} - p(\boldsymbol{r}) \right) d^3 r, \tag{11.2}$$

with respect to perturbations of $\boldsymbol{B}$ and p, subject to several constraints:

1. there exists a set of flux surfaces such that $\boldsymbol{B} \cdot \nabla\psi = 0$, labeled by a toroidal flux label ψ;
2. $\nabla \cdot \boldsymbol{B} = 0$;
3. the pressure as a function of flux is fixed $\delta p(\psi) = 0$;
4. the rotational transform as a function of flux is fixed, $\delta\iota(\psi) = 0$;
5. the total toroidal flux enclosed by the toroidal domain is fixed, $\delta\psi = 0$ on $\partial\Omega$.

Constraints 1 and 4 correspond to constraints of ideal MHD and preclude changes to the magnetic field topology, as discussed in Section 8.2. Constraints 3 and 4 arise from the assumption that $p(\psi)$ and $\iota(\psi)$ are prescribed in (11.1). Constraint 5 corresponds to the assumption that the plasma is surrounded by a perfectly conducting boundary such that the magnetic field lines must lie tangent to this surface. This constraint also ensures that the prescribed $\psi(\partial\Omega)$ is fixed and $\partial\Omega$

remains a flux function according to (11.1). Although we assume that flux surfaces exist, their shapes are unknown and will be determined from the variational principle. We now see that the constraints on the variational principle ensure that the second and third ideal MHD conditions in (11.1) are satisfied and the prescribed quantities are held fixed. The force balance condition, the first expression in (11.1), is satisfied by stationary points of the energy functional. This will now be shown by directly evaluating the linear perturbation to the energy functional thanks to an expression for the perturbed magnetic field subject to the above constraints.

First, the field $\boldsymbol{B}$ is expressed in a flux coordinate system (ψ, θ, ϕ), with the toroidal flux function $\psi = \Psi_T/2\pi$, to obtain a convenient expression for the perturbation subject to the desired constraints. As a reminder, the field is unknown. Therefore, the position of surfaces of constant ψ is also unknown, while θ and ϕ are the poloidal and toroidal angles that are given functions of space, assumed to be fixed. As shown in equation (9.4), the magnetic field in a toroidal system under constraints 1 and 2 can generally be expressed as

$$\boldsymbol{B}\big(\boldsymbol{R}(\psi,\theta,\phi)\big) = \left[\nabla\psi \times \nabla\left(\theta - \iota\phi + \lambda\right)\right]\big(\boldsymbol{R}(\psi,\theta,\phi)\big).$$

Therefore, we will consider variations of the functions $\{\lambda(\boldsymbol{r}), \psi(\boldsymbol{r})\}$ rather than $\boldsymbol{B}(\boldsymbol{r})$, as the angles $\{\theta(\boldsymbol{r}), \phi(\boldsymbol{r})\}$ and the rotational transform $\iota(\psi)$ are given.

The linear perturbation to the magnetic field can then be expressed as

$$\begin{aligned}\delta\boldsymbol{B}[\lambda(\boldsymbol{r}),\psi(\boldsymbol{r});\delta\lambda(\boldsymbol{r}),\delta\psi(\boldsymbol{r})] = \nabla\delta\psi(\boldsymbol{r}) \times \nabla\left[\theta(\boldsymbol{r}) - \iota\big(\psi(\boldsymbol{r})\big)\phi(\boldsymbol{r}) + \lambda(\boldsymbol{r})\right] \\ + \nabla\psi(\boldsymbol{r}) \times \nabla\left[-\iota'\big(\psi(\boldsymbol{r})\big)\delta\psi(\boldsymbol{r})\phi(\boldsymbol{r}) + \delta\lambda(\boldsymbol{r})\right].\end{aligned}$$

Moreover, constraint 3 is enforced by expressing the perturbation to the pressure at a given position in terms of the perturbation to the flux label,

$$\delta p(\boldsymbol{r}) = p'\big(\psi(\boldsymbol{r})\big)\delta\psi(\boldsymbol{r}).$$

The first variation of W with respect to λ is

$$\delta W[\lambda,\psi;\delta\lambda] = \int_\Omega \frac{\boldsymbol{B}\times\nabla\psi\cdot\nabla\delta\lambda}{\mu_0}\,d^3r,$$

and using integration by parts, it can be written as

$$\delta W[\lambda,\psi;\delta\lambda] = -\int_\Omega \delta\lambda\frac{(\nabla\times\boldsymbol{B})\cdot\nabla\psi}{\mu_0}\,d^3r,$$

noting that if $\partial\Omega$ is a flux surface, the boundary term vanishes. Thus, a condition satisfied by stationary points of W reads

$$(\nabla\times\boldsymbol{B})\cdot\nabla\psi = 0. \tag{11.3}$$

We now consider the first variation of W with respect to ψ,

$$\delta W[\lambda,\psi;\delta\psi] = \int_\Omega \left(\frac{\boldsymbol{B}\cdot(\nabla\delta\psi\times\nabla(\theta-\iota\phi+\lambda)+\nabla\psi\times\nabla\left[-\iota'\phi\delta\psi\right])}{\mu_0} - p'\delta\psi\right)d^3r,$$

where both ι and p are considered functions of ψ, and $'$ indicates derivatives with respect to ψ. Using integration by parts, noting that the boundary terms will vanish as $\delta\psi = 0$ on $\partial\Omega$, it can be written

$$\delta W[\lambda,\psi;\delta\psi] = \int_\Omega \delta\psi\left(\frac{\nabla\times\boldsymbol{B}\cdot\nabla(\theta-\iota\phi+\lambda)+\iota'\phi\nabla\times\boldsymbol{B}\cdot\nabla\psi}{\mu_0} - p'\right)d^3r.$$

The second term in the above expression will vanish from (11.3), so we have the condition

$$\frac{1}{\mu_0}\nabla \times \boldsymbol{B} \cdot \nabla(\theta - \iota\phi + \lambda) - p' = 0.$$

Because $(\nabla \times \boldsymbol{B}) \times \boldsymbol{B} = \nabla\psi\left((\nabla \times \boldsymbol{B}) \cdot \nabla\left(\theta - \iota\phi + \lambda\right)\right)$ due to (11.3), this yields

$$\frac{(\nabla \times \boldsymbol{B}) \times \boldsymbol{B}}{\mu_0} \cdot \frac{\partial \boldsymbol{R}}{\partial \psi} - p' = 0. \tag{11.4}$$

Together, conditions (11.3) and (11.4) correspond to the $\boldsymbol{B} \times \nabla\psi$ and $\partial\boldsymbol{R}/\partial\psi$ components of the force balance condition, respectively. The $\boldsymbol{B}$ component of force balance is satisfied from the assumption $\boldsymbol{B} \cdot \nabla\psi = 0$. As a result, any stationary point of W satisfies the three vector components of (11.1). Therefore, finding stationary points of W with respect to λ and ψ is equivalent to finding solutions of (11.1) under the above assumptions.

This implies that an equilibrium magnetic field can be obtained efficiently from a variational method if the assumption of constraints 1–5 is applicable. Applications for 3D MHD calculations will be discussed in the following section.

The discussion in this section is similar to that in [170] and [116]. A discussion of numerical applications of energy principles for MHD equilibria is given in Section 4.5 of [151].

11.1.2 ▪ Computational approach

Under the assumption of continuously nested flux surfaces, equilibrium fields on a given domain Ω can be sought by applying the previous variational approach, for instance, via a gradient-descent method. This is the basis for the NSTAB [79] and VMEC [132, 129] codes. The DESC code solves the same system without a variational approach [66].

For this approach, several quantities need to be supplied.

- The pressure $p(\psi)$ is a given function depending only on the flux surface label. The profile may have a simple functional form, such as a spline or power series, and can be chosen to be consistent with experimental data.

- The rotational transform $\iota(\psi)$ is a second given function depending only on the flux surface label. Alternatively, the toroidal current enclosed by a flux surface, $I_T(\psi)$, can be given instead. In this case, the variational approach can be applied iteratively with different $\iota(\psi)$ profiles until the desired toroidal current profile is matched. In both cases, these profiles can similarly be chosen to be consistent with experimental measurements. The current profile can be chosen to be consistent with kinetic calculations.

- The boundary of the domain must be supplied, often using a Fourier series, as displayed in (13.11). The value of the toroidal flux (5.10) on $\partial\Omega$, Ψ_T, is also specified, setting the overall scale of the magnetic field.

The above approach is referred to as fixed-boundary since the plasma boundary is prescribed and coincides with the boundary of the computational domain.

There is an alternative approach known as free-boundary, considering the location of electromagnetic coils and their currents to be instead prescribed within the computational domain, and the plasma boundary is computed self-consistently. The region outside the plasma domain within the computational domain is called the vacuum region. We then seek a plasma boundary $\partial\Omega$ for which the total field in the vacuum region, $\boldsymbol{B}_V$, satisfies two conditions: the total pressure should be continuous across the boundary between the vacuum and plasma region, $\left(p + B^2/2\mu_0\right)|_{\partial\Omega} = \left(B_V^2/2\mu_0\right)|_{\partial\Omega}$, while the boundary should define a flux surface,

$\boldsymbol{B}_V \cdot \hat{\boldsymbol{n}}|_{\partial\Omega} = 0$. The assumption of continuity of total pressure arises from imposing force balance at the boundary. This method is implemented via the following iterative process.

1. Choose the coil currents and positions, the total toroidal flux, and two flux functions, $p(\psi)$ and either $\iota(\psi)$ or $I_T(\psi)$.
2. Choose an initial guess for the plasma boundary $\partial\Omega$.
3. Given the the plasma boundary $\partial\Omega$, follow steps (a) to (e):
   (a) The magnetic field $\boldsymbol{B}$ is determined in Ω using the fixed-boundary equilibrium approach as described above.
   (b) From the solution $\boldsymbol{B}$, the total pressure at the inside of the plasma boundary is evaluated as $\left(p + B^2/2\mu_0\right)|_{\partial\Omega}$, and the plasma current is evaluated inside Ω as $\boldsymbol{J} = \nabla \times \boldsymbol{B}/\mu_0$.
   (c) The vacuum magnetic field outside Ω, denoted $\boldsymbol{B}_V$, satisfying the boundary condition $\boldsymbol{B}_V \cdot \hat{\boldsymbol{n}}|_{\partial\Omega} = 0$, can be represented using a scalar potential as $\boldsymbol{B}_V = \nabla\Phi$. Laplace's equation, $\Delta\Phi = 0$, is then solved outside Ω, with the Neumann boundary condition, $\hat{\boldsymbol{n}} \cdot \nabla\Phi|_{\partial\Omega} = 0$. The net coil currents and plasma currents are used to solve for Φ as described in Section 11.6.
   (d) From the solution $\boldsymbol{B}_V$, the total pressure on the outside of the plasma boundary is evaluated as $\left(B_V^2/2\mu_0\right)|_{\partial\Omega}$.
   (e) While $\left(p + B^2/2\mu_0\right)|_{\partial\Omega} \neq \left(B_V^2/2\mu_0\right)|_{\partial\Omega}$, update the boundary $\partial\Omega$ of the plasma domain and repeat step 3.

This method is used in the free-boundary VMEC code [129].

11.2 ▪ A near-axis approach with the assumption of surfaces

Some of the challenges associated with 3D MHD equilibria can be circumvented by restricting our attention to a localized region near the magnetic axis. A near-axis approach to construct such local equilibria is presented here using a vacuum magnetic field model for simplicity, although it has been extended to a more general ideal MHD model [210]. The approach relies on an asymptotic expansion with respect to the distance from the axis under the assumption of continuously nested toroidal flux surfaces introduced in Remark 4.4. Unlike the numerical approximation of equilibrium solutions, the near-axis expansion approach provides closed-form expressions for quantities of interest, yielding further insight into the connection between geometry and confinement properties. As an illustration, we will obtain expressions for the geometry of the magnetic surfaces and the corresponding rotational transform on the magnetic axis. Section 11.2.1 defines a local coordinate system and the asymptotic expansion to obtain an approximate vacuum magnetic field model. Section 11.2.2 focuses on the flux label and the shape of corresponding flux surfaces. Section 11.2.3 focuses on the field-line label and the properties of the corresponding rotational transform.

11.2.1 ▪ From the axis to a nearby equilibrium model

The starting point is a simple closed curve defining the magnetic axis. A local coordinate system is first defined starting from this curve. The equations for a vacuum magnetic field with surfaces are then expressed in this coordinate system. An asymptotic expansion with respect to the distance from the axis is applied, and the resulting equations are solved to obtain the magnetic field near the axis to a desired order.

The magnetic axis $\boldsymbol{R}_0$ is parameterized by the length, l. The corresponding Frenet–Serret orthonormal basis introduced in Section 7.3 is denoted by $(\hat{\boldsymbol{e}}_1(l), \hat{\boldsymbol{e}}_2(l), \hat{\boldsymbol{e}}_3(l))$. As a reminder, the unit vector $\hat{\boldsymbol{e}}_1(l) = \boldsymbol{R}_0'(l)$ is tangent to the magnetic field, the curvature $\boldsymbol{\kappa}(l) = \boldsymbol{R}_0''(l)$, $\hat{\boldsymbol{e}}_2(l) = \boldsymbol{\kappa}(l)/|\boldsymbol{\kappa}(l)|$ is a unit vector in the curvature direction, and $\hat{\boldsymbol{e}}_3(l) = \hat{\boldsymbol{e}}_1(l) \times \hat{\boldsymbol{e}}_2(l)$. We then define polar coordinates in the $\hat{\boldsymbol{e}}_2$-$\hat{\boldsymbol{e}}_3$ plane, namely $(\rho, \vartheta) \in \mathbb{R}^+ \times [0, 2\pi)$. The parameterized position can then be expressed as

$$\boldsymbol{R}(\rho, \vartheta, l) = \boldsymbol{R}_0(l) + \rho \cos(\vartheta) \hat{\boldsymbol{e}}_2(l) + \rho \sin(\vartheta) \hat{\boldsymbol{e}}_3(l). \tag{11.5}$$

In order to construct an orthogonal coordinate system, we define the angle $\omega = \vartheta + \int_0^l \tau(l')\, dl'$, where $\tau(l) = -\hat{\boldsymbol{e}}_3'(l) \cdot \hat{\boldsymbol{e}}_2(l)$ is the torsion of the magnetic axis introduced in Section 7.3.2. In the orthogonal coordinate system (ρ, ω, l) the Jacobian is given by

$$\sqrt{g}(\rho, \omega, l) = \rho \left(1 - \kappa(l) \rho \cos\left(\omega - \int_0^l \tau(l')\, dl'\right)\right), \tag{11.6}$$

where $\kappa(l) = |\boldsymbol{\kappa}(l)|$ is the magnitude of the curvature. For convenience, the geometric factor is then defined near the curve as $h(\rho, \omega, l) = 1 - \kappa(l)\rho \cos\left(\omega - \int_0^l \tau(l')\, dl'\right)$, so that $\sqrt{g} = \rho h$.

We seek a vacuum field solution, introduced in Section A.3, near the curve $\boldsymbol{R}_0$, so $\boldsymbol{B}$ is both divergence- and curl-free. From the curl-free condition, we can represent the field by a scalar potential, $\boldsymbol{B}(\boldsymbol{r}) = \nabla \Phi(\boldsymbol{r})$. From the divergence-free condition, the potential must satisfy Laplace's equation, following Section A.3, $\Delta \Phi(\boldsymbol{r}) = 0$. Since continuously nested flux surfaces are assumed to exist, the magnetic field can be described in terms of field-line following coordinates by a toroidal flux label ψ and a function labeling field lines, α, satisfying

$$\nabla \Phi(\boldsymbol{r}) = \nabla \psi(\boldsymbol{r}) \times \nabla \alpha(\boldsymbol{r}), \tag{11.7}$$

as described in Section 9.3. In order to build the vacuum magnetic field, we now seek the unknown scalar functions Φ, ψ, and α. There is no unique solution to this problem for two reasons: (1) each unknown can be defined up to an additive constant without altering (11.7), and (2) the right-hand side being bilinear in (ψ, α), each of these two unknowns can be multiplied respectively by a constant and its inverse without altering the equation. This second point will be addressed through the constant μ defined below by imposing that $\psi(\boldsymbol{r})$ be the toroidal flux label. The functions $\Phi(\boldsymbol{r})$ and $\alpha(\boldsymbol{r})$ need not be periodic functions of l and ω, while $\psi(\boldsymbol{r})$ must be periodic as it is related to the magnetic flux.

Expressed in the orthogonal coordinate system (ρ, ω, l), (11.7) is equivalent to the following set of equations for ψ, α and Φ:

$$\begin{cases} \dfrac{1}{\rho h}\left(\dfrac{\partial \psi}{\partial \rho}\dfrac{\partial \alpha}{\partial \omega} - \dfrac{\partial \psi}{\partial \omega}\dfrac{\partial \alpha}{\partial \rho}\right) = \dfrac{\partial \Phi}{\partial l}, \\ \dfrac{1}{\rho h}\left(\dfrac{\partial \psi}{\partial \omega}\dfrac{\partial \alpha}{\partial l} - \dfrac{\partial \alpha}{\partial \omega}\dfrac{\partial \psi}{\partial l}\right) = \dfrac{\partial \Phi}{\partial \rho}, \\ \dfrac{1}{h}\left(\dfrac{\partial \psi}{\partial l}\dfrac{\partial \alpha}{\partial \rho} - \dfrac{\partial \alpha}{\partial l}\dfrac{\partial \psi}{\partial \rho}\right) = \dfrac{1}{\rho}\dfrac{\partial \Phi}{\partial \omega}, \end{cases} \tag{11.8}$$

where as a reminder $h = \sqrt{g}/\rho$ is a known function of (ρ, ω, l). Moreover, Laplace's equation for Φ is expressed as

$$\frac{1}{h\rho}\frac{\partial}{\partial \rho}\left(h\rho \frac{\partial \Phi}{\partial \rho}\right) + \frac{1}{h\rho^2}\frac{\partial}{\partial \omega}\left(h \frac{\partial \Phi}{\partial \omega}\right) + \frac{1}{h}\frac{\partial}{\partial l}\left(h \frac{\partial \Phi}{\partial l}\right) = 0. \tag{11.9}$$

Rather than search for a general solution to (11.8)–(11.9) for ψ, α, and Φ, this approach focuses on a local solution near the magnetic axis, thanks to the following asymptotic series expansions in $\rho/L \ll 1$ where L is the length of the magnetic axis:

$$\begin{cases} \Phi(\rho,\omega,l) = \Phi_0(\omega,l) + \Phi_1(\omega,l)\rho + \Phi_2(\omega,l)\rho^2 + \mathcal{O}(\rho^3), \\ \psi(\rho,\omega,l) = \psi_2(\omega,l)\rho^2 + \mathcal{O}(\rho^3), \\ \alpha(\rho,\omega,l) = \alpha_0(\omega,l) + \alpha_1(\omega,l)\rho + \mathcal{O}(\rho^2), \end{cases} \tag{11.10}$$

where $\psi_0 = 0$ as the magnetic flux vanishes on the magnetic axis, and $\psi_1 = 0$ from analyticity assumptions [156]. As a remark, the definition of the geometric quantity h directly reads as an expansion $h_0 + h_1(l,\omega)\rho$ with respect to ρ where $h_0 = 1$.

The next goal is to understand the properties of the lowest-order flux function, ψ_2, and lowest-order field-line label, α_0. We will, therefore, focus on the lowest orders of (11.8) that involve these two quantities, namely

$$\begin{cases} \dfrac{\partial \alpha_0}{\partial l} = -\dfrac{\partial \Phi_2}{\partial \omega}\dfrac{1}{2\psi_2}, \\ \dfrac{\partial \alpha_0}{\partial \omega} = \dfrac{\partial \Phi_0}{\partial l}\dfrac{1}{2\psi_2}. \end{cases} \tag{11.11}$$

Because these are coupled to Φ_0 and Φ_2, we will also consider the lowest-order terms in (11.8) involving Φ_0, namely

$$\frac{\partial \Phi_0}{\partial \omega} = 0, \tag{11.12}$$

as well as the lowest-order terms in (11.9) involving Φ_0 and Φ_2, namely

$$4\Phi_2 + \frac{\partial^2 \Phi_2}{\partial \omega^2} + \frac{\partial h_1}{\partial \omega}\frac{\partial \Phi_1}{\partial \omega} + \frac{\partial^2 \Phi_0}{\partial l^2} = 0. \tag{11.13}$$

Since Φ_0 and Φ_2 are coupled to Φ_1, we determine Φ_1 from the lowest-order terms in (11.8) involving Φ_1, yielding

$$\Phi_1 = 0. \tag{11.14}$$

Given a curve $\boldsymbol{R}_0$, and any functions Φ_0 and Φ_2 satisfying (11.12) and (11.13), then the vector field defined by $\nabla(\rho^2\psi_2) \times \nabla\alpha_0$ associated to functions α_0 and ψ_2 satisfying (11.11) has the following properties:

- it is divergence-free,
- it exhibits continuously nested flux surfaces defined as the level sets of ψ_2,
- it is consistent with the assumption of a vacuum field.

In Sections 11.2.2 and 11.2.3, we will discuss solutions for ψ_2 and α_0, respectively, in order to interpret the geometry of the flux surfaces and the relationship between this geometry and the rotational transform.

11.2.2 ▪ Flux surfaces

Since it is ψ_2 that defines the lowest-order flux surface shapes for the vector field $\nabla(\rho^2\psi_2)\times\nabla\alpha_0$, the goal is to obtain a PDE satisfied by $\psi_2(\omega,l)$, find a class of solutions, and comment on the

corresponding shape of flux surfaces. From (11.11), since partial derivatives commute, we obtain the following PDE for $1/\psi_2$:

$$\frac{\partial}{\partial\omega}\left(\frac{\partial\Phi_2}{\partial\omega}\frac{1}{\psi_2}\right)+\frac{\partial}{\partial l}\left(\frac{\partial\Phi_0}{\partial l}\frac{1}{\psi_2}\right)=0. \tag{11.15}$$

To obtain an equation on ψ_2 alone we then turn to Φ_2 and Φ_0.

Remark 11.1. *The lowest-order magnetic field, defined by $\boldsymbol{B}_0 = \nabla\Phi_0$, coincides with the magnetic field on the magnetic axis $\boldsymbol{R}_0$. In particular, along the magnetic axis, the magnetic field is tangent to the curve: $\boldsymbol{B}_0 = B_0\boldsymbol{R}_0'$, where the amplitude of the field is $B_0 = \sqrt{\boldsymbol{B}_0\cdot\boldsymbol{B}_0}$. Moreover, l is the length along the curve, so this amplitude can also be expressed along the curve as $B_0 = \boldsymbol{B}_0\cdot\boldsymbol{R}_0'$ because $\boldsymbol{R}_0'$ is a unit vector.*

On the one hand, Φ_0 satisfies (11.12). This implies that Φ_0 is an unknown function of l only: $\Phi_0(l)$. Moreover, according to the previous remark, the lowest-order magnetic field satisfies $\boldsymbol{B}_0 = \Phi_0'\nabla l$. So since by duality $\boldsymbol{R}_0'\cdot\nabla l = 1$ then the function Φ_0 is related to the magnetic field strength on the axis as $B_0(l) = \Phi_0'(l)$. On the other hand, thanks to (11.14), Φ_2 satisfies (11.13) now written as

$$4\Phi_2+\frac{\partial^2\Phi_2}{\partial\omega^2}+\Phi_0''=0. \tag{11.16}$$

Using the method of variation of constants, the general solution could be sought in the form of the sum of two products: a product of $\cos(\omega)$ by a function of ω and l, and a product of $\sin(\omega)$ by another function of ω and l. Without loss of generality, any function of l only can be added simultaneously to the argument ω in the cosine and sine functions. Since the polar angle in the $\hat{\boldsymbol{e}}_2$-$\hat{\boldsymbol{e}}_3$ plane, defined as $\vartheta = \omega - \int_0^l \tau(l')\,dl'$, is of particular interest for the interpretation of the solutions in the following discussion, the general solution for Φ_2 can be expressed in terms of Φ_0 as

$$\Phi_2(\omega,l) = -\frac{\Phi_0''(l)}{4}+C_c(l)\cos(2u(\omega,l))+C_s(l)\sin(2u(\omega,l)), \tag{11.17}$$

where $u(\omega,l) = \omega - \int_0^l \tau(l')\,dl' + \delta(l)$ and $\delta(l)$, $C_c(l)$, and $C_s(l)$ are integration constants with respect to ω. Here $\delta(l) = u(\omega,l)-\vartheta$ can be interpreted as an angle with respect to the curvature vector.

A linear PDE for ψ_2 can now be obtained. Combining (11.15) with (11.16) gives

$$\frac{\partial\Phi_2}{\partial\omega}\frac{\partial\psi_2}{\partial\omega}+\Phi_0'\frac{\partial\psi_2}{\partial l}+4\Phi_2\psi_2=0.$$

It can be verified [155] that the set of functions

$$\psi_2(\omega,l) = \Phi_0'(l)\mu\left(e^{\eta(l)}\cos^2 u(\omega,l)+e^{-\eta(l)}\sin^2 u(\omega,l)\right), \tag{11.18}$$

depending on constants of integration $\eta(l)$ and μ,[21] satisfies the previous differential equation if C_s and C_c satisfy

$$\begin{cases} C_c(l) &= -\dfrac{\Phi_0'(l)\eta'(l)}{4}, \\ C_s(l) &= \dfrac{\Phi_0'(l)(\delta'(l)-\tau(l))}{2}\tanh(\eta(l)). \end{cases}$$

[21] By specifying that ψ is a toroidal flux label, the constant μ can be shown to be 1/2. We will keep the following expressions in terms of general μ.

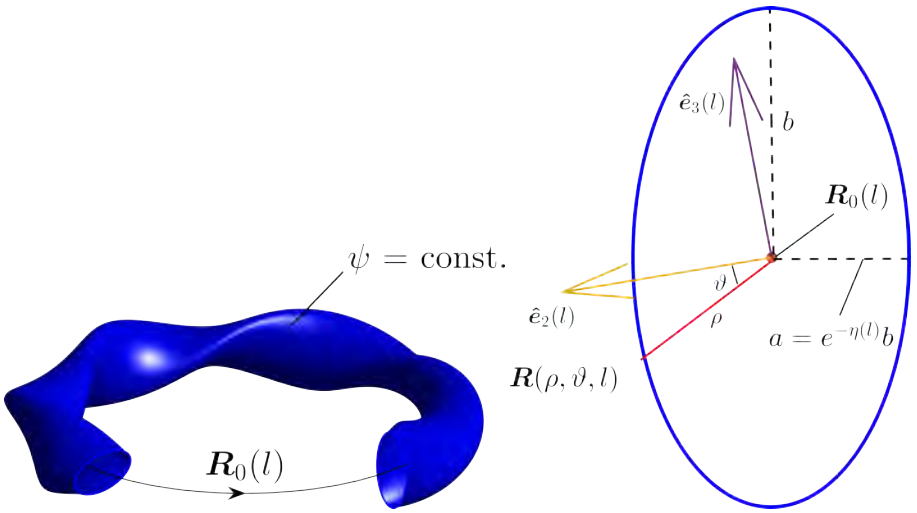

Figure 11.1*: We consider a surface of constant ψ near the magnetic axis, $\boldsymbol{R}_0(l)$* (a)*. The cross-section of such a surface in the plane spanned by $\hat{\boldsymbol{e}}_1(l)$ and $\hat{\boldsymbol{e}}_2(l)$ is shown in* (b)*. A point in this plane is given in the (ρ, ϑ, l) coordinate system by* (11.5)*. Near the axis, the magnetic surfaces take the form of an ellipse with major axis a and minor axis b.*

In a neighborhood of the curve $\boldsymbol{R}_0$, given any two functions Φ_0 and η of l, any constant μ, and any function α_0, the field $\nabla(\rho^2\psi_2) \times \nabla\alpha_0$ exhibits continuously nested toroidal flux surfaces, defined by the level sets of the flux label $\psi_2(\rho, \omega, l) = \rho^2\psi_2(\omega, l)$.

The geometry of these flux surfaces can then be interpreted from (11.18). Defining the quantities

$$\begin{cases} a(l) &= \dfrac{e^{-\eta(l)/2}}{\sqrt{\mu\Phi_0'(l)}}, \\ b(l) &= \dfrac{e^{\eta(l)/2}}{\sqrt{\mu\Phi_0'(l)}}, \end{cases}$$

the expression for the flux label ψ_2 now reads

$$\psi_2(\rho, \omega, l) = \frac{\rho^2 \cos^2(u(\omega, l))}{a^2(l)} + \frac{\rho^2 \sin^2(u(\omega, l))}{b^2(l)}.$$

This formula now provides an interpretation of the shape of flux surfaces in a neighborhood of the curve since fixing a value of ψ_2 defines a particular magnetic surface, while l is a toroidal angle. Indeed, at fixed ψ_2, for each value of l the previous expression defines an ellipse, in the l-dependent $\hat{\boldsymbol{e}}_2$-$\hat{\boldsymbol{e}}_3$ plane, parameterized by ρ and the angle u measured with respect to the semiminor axis of the ellipse. The semiminor and semimajor axes are defined by $a(l)\sqrt{\psi_2}$ and $b(l)\sqrt{\psi_2}$, respectively. The eccentricity of the ellipse is given by $e = \sqrt{1 - e^{-2\eta(l)}}$, with larger values of e indicating stronger elongation of the ellipse.

As the angle with respect to the semiminor axis is given by $u = \vartheta + \delta(l)$ and ϑ denotes an angle in the poloidal plane with respect to the curvature vector, $\delta(l)$ can be interpreted as the angle between the major axis of the ellipse and the curvature vector. The coordinate system is shown in Figure 11.1.

Remark 11.2. *Three free functions arise in the expression for ψ_2, namely $\eta(l)$, $\Phi_0(l)$, and $\delta(l)$. As shown by the formulas for the semiminor axis, the semimajor axis, and eccentricity, the choice of these free functions impacts the shape of the flux surfaces.*

11.2.3 ▪ Rotational transform

As discussed in Section 4.4.2, the rotational transform is essential for toroidal confinement. We will compute the rotational transform of the field $\nabla(\rho^2\psi_2) \times \nabla\alpha_0$ on the magnetic axis. This will evidence the dependence of the rotational transform on the geometry of the magnetic axis and flux surface. Notably, the class of approximate equilibrium solutions studied in this section will be shown to allow for nonzero rotational transform, highlighting the potential for stellarators to generate rotational transform without plasma current. The goal is to obtain a PDE involving $\alpha_0(\omega, l)$ and find a class of solutions to comment on the associated rotational transform.

Combining the first equation of (11.11) with the expressions (11.17) for Φ_2 and (11.18) for ψ_2 obtained in the previous section yields a simple differential equation for α_0,

$$\frac{\partial\alpha_0}{\partial l} = -\frac{2\left(\delta'(l) - \tau(l)\right)\cos\left(2u(\omega,l)\right)\tanh(\eta(l)) + \eta'(l)\sin\left(2u(\omega,l)\right)}{4\mu\left(e^{\eta(l)}\cos^2(u(\omega,l)) + e^{-\eta(l)}\sin^2(u(\omega,l))\right)}.$$

This is equivalent to a more convenient formulation:

$$\frac{\partial\alpha_0}{\partial l} = \frac{1}{2\mu}\left(\frac{\partial}{\partial l}\left[\arctan\left(e^{-\eta(l)}\tan u(\omega,l)\right)\right] - \frac{\delta'(l) - \tau(l)}{\cosh(\eta(l))}\right).$$

Then α_0 can be expressed depending on a constant of integration $\overline{\alpha}$ as

$$\alpha_0(\omega,l) = \overline{\alpha} + \frac{1}{2\mu}\arctan\left(e^{-\eta(l)}\tan u(\omega,l)\right) - \frac{1}{2\mu}\int_0^l \frac{\delta'(l') - \tau(l')}{\cosh(\eta(l'))}\,dl'. \tag{11.19}$$

Following the discussion in Chapter 9, recall that the field-line label for a given magnetic field can be expressed conveniently in terms of the rotational transform using a general flux coordinate system. In order to study the rotational transform, we now introduce a convenient flux coordinate system for the field $\nabla(\rho^2\psi_2) \times \nabla\alpha_0$. Since α_0 is independent of ρ, it is equivalently independent of flux in a flux coordinate system. Hence, the flux label can be chosen arbitrarily. The toroidal angle is chosen to be the normalized length along the axis, $\zeta = 2\pi l/L$. A poloidal angle can then be defined starting from ϑ, the polar angle in the $\hat{\boldsymbol{e}}_2$-$\hat{\boldsymbol{e}}_3$ plane. Due to the rotation of the curvature vector, a 2π period in ϑ can generally correspond with m toroidal transits in addition to one poloidal transit for some integer m. The poloidal angle is defined as a shift to ϑ such that it is a purely poloidal angle, $\overline{\vartheta} = \vartheta - m2\pi l/L$. In terms of the initial angles (ω, l), $\overline{\vartheta}(\omega,l) = \omega - \int_0^l \tau(l')\,dl' - m2\pi l/L$.

Since α_0 is independent of the flux label ψ, the discussion in Chapter 9 leads to the field-line label expressed in the poloidal and toroidal angles as

$$\alpha_0\Big(\omega\Big(\overline{\vartheta},l\Big),l\Big) = \overline{\vartheta} - \iota_0\frac{2\pi l}{L} + \lambda\Big(\overline{\vartheta},l\Big),$$

where λ is a periodic function of the two angles, and the rotational transform ι_0 is independent of ψ. Thanks to periodicity with respect to toroidal angle l, the rotational transform then satisfies

$$\iota_0 = \frac{\alpha_0\Big(\omega\Big(\overline{\vartheta},0\Big),0\Big) - \alpha_0\Big(\omega\Big(\overline{\vartheta},L\Big),L\Big)}{2\pi}$$

for any value of $\overline{\vartheta}$. Evaluating this expression with the α_0 solution (11.19) in the coordinate system $(\overline{\vartheta}, l)$, we obtain

$$\iota_0 = \frac{1}{4\pi\mu}\left(-2\pi m - \delta(L) + \delta(0) + \int_0^L \frac{\delta'(l) - \tau(l)}{\cosh(\eta(l))}\, dl\right).$$

As a consequence, for the field $\nabla(\rho^2\psi_2) \times \nabla\alpha_0$ defined from the magnetic axis $\boldsymbol{R}_0$, rotational transform can be produced near the axis due to the following geometric features:

- torsion $\tau(l)$ of the magnetic axis,
- rotating ellipticity $\delta'(l)$ of the flux surfaces,
- and rotation of the curvature vector, m.

In other words, if the magnetic axis is nonplanar or the flux surfaces are ellipses that twist as one moves toroidally, there may be a nonzero rotational transform. A stellarator's magnetic axis can be chosen so that ι_0 is sufficiently large to provide confinement.

In conclusion, we have constructed approximate 3D equilibrium solutions with magnetic surfaces valid locally in a neighborhood of the magnetic axis with a possibly nonzero rotational transform. This classic result of Mercier [210] is also discussed in [267, 116, 156]. While this section has focused on solutions of the vacuum equations, similar techniques can be applied in the presence of current and pressure gradients. Understanding 3D equilibria with near-axis expansions continues to be an active area of research [81, 185, 186], and near-axis solutions have been shown to be consistent with 3D numerical equilibrium calculations of quasisymmetric configurations [176]. These solutions can be used in stellarator optimization, as will be discussed further in Chapter 14. Details about the domain of validity of the near-axis expansion can be found in [178].

11.3 ▪ Equilibria without the assumption of surfaces

Remark 4.4 motivates the interest for continuously nested flux surfaces. As discussed in Section 10.2, in general 3D geometry, continuously nested toroidal flux surfaces are not guaranteed to exist. In this section, we discuss models for computing equilibrium solutions allowing for a pressure gradient, $\nabla p \neq 0$, without the assumption that magnetic surfaces exist and are continuously nested toroidal surfaces. Other approaches for computing 3D equilibria without the assumption of surfaces, but with additional assumptions on the pressure profile, are described in Sections 11.4, 11.5, and 11.6.

As a reminder, the force balance condition (8.9) implies that $\boldsymbol{B} \cdot \nabla p = 0$ and $\boldsymbol{J} \cdot \nabla p = 0$ so that pressure is constant both along field lines and along streamlines of the current density. While models assuming surfaces can satisfy this condition by enforcing that pressure is a given flux function, the pressure cannot be imposed in the absence of surfaces as it will not generally satisfy these conditions. Several numerical approaches for finding solutions without continuously nested toroidal flux surfaces have been developed. In this section, three particular iterative approaches will be discussed.

The approach employed by the PIES code [250] is to provide a pressure distribution p as well as an initial guess for $\boldsymbol{B}$ in Ω such that $\boldsymbol{B} \cdot \nabla p = 0$. For example, the initial field could be computed with the variational approach introduced in Section 11.1. The ideal MHD equilibrium equations (8.10) are then solved iteratively for the field and the current as follows.

- Given a field $\boldsymbol{B}$, the updated current is computed in two steps.
  - The current density perpendicular to the magnetic field is known from the force balance $\boldsymbol{J} \times \boldsymbol{B} = \nabla p$,
$$\boldsymbol{J}_\perp = \frac{1}{B}\hat{\boldsymbol{b}} \times \nabla p.$$
  - The parallel current can be computed by enforcing that $\nabla \cdot \boldsymbol{J} = 0$, a direct consequence of $\nabla \times \boldsymbol{B} = \mu_0 \boldsymbol{J}$,
$$\boldsymbol{B} \cdot \nabla \left(\frac{J_\parallel}{B} \right) = -\nabla \cdot \left(\frac{1}{B}\hat{\boldsymbol{b}} \cdot \nabla p \right).$$
- Given $\boldsymbol{J} = \boldsymbol{J}_\perp + J_\parallel \hat{\boldsymbol{b}}$, the updated magnetic field can be determined from $\nabla \times \boldsymbol{B} = \mu_0 \boldsymbol{J}$.

This iteration continues until a convergence criterion is met. Several approaches can be used to numerically solve the magnetic differential equation for $J_\parallel$. In regions of good flux surfaces, magnetic coordinates can be leveraged similarly to the analysis in Section 10.3. A statistical averaging approach can be employed in regions of chaotic fields, as described in [169]. As discussed in Section 6.2, solutions to the MDE may not always exist and can give rise to nonsmooth behavior. Methods of correction of the source function [138] and resonance broadening theory [251] have been proposed to enable the solubility of the MDE.

The HINT [106] and HINT2 [286] codes use a procedure that involves iterating on the magnetic field and pressure, starting from an initial guess for each. The field and the pressure are then computed iteratively as follows.

- Given magnetic field $\boldsymbol{B}$, the updated pressure p is determined iteratively, starting from an initial guess, to satisfy approximately $\boldsymbol{B} \cdot \nabla p = 0$ within a prescribed tolerance.
- Given a pressure p, the updated $\boldsymbol{B}$ is determined from a time-dependent model,
$$\begin{cases} \rho \dfrac{\partial \boldsymbol{u}}{\partial t} &= -\nabla p + \dfrac{(\nabla \times \boldsymbol{B}) \times \boldsymbol{B}}{\mu_0}, \\ \dfrac{\partial \boldsymbol{B}}{\partial t} &= \nabla \times \left(\boldsymbol{u} \times \boldsymbol{B} - \frac{\eta}{\mu_0} \nabla \times \boldsymbol{B} \right), \end{cases}$$
  where the density ρ is constant and fixed.

This iteration continues until a convergence criterion is met. The solution is then interpreted as an equilibrium state. The HINT and HINT2 model neglects the nonlinear term $(\boldsymbol{u} \cdot \nabla)\, \boldsymbol{u}$ of the momentum equation in the resistive MHD model (10.49) discussed in Section 10.4.1.

The SIESTA code [130] uses a variational method similar to that described in Section 11.1.1. An ideal MHD equilibrium is initially computed. Then, its pressure is used as an initial guess, and the initial guess for the magnetic field is the sum of the ideal MHD equilibrium field plus a small resonant magnetic perturbation. The goal of the following iterative process is to solve the force balance system, $\boldsymbol{J} \times \boldsymbol{B} - \nabla p = 0$, without assuming the existence of nested surfaces.

- A physics-based preconditioner is used to obtain a descent direction of the energy functional defined in Section 11.1.1. The pressure and magnetic field are updated according to the descent direction.
- The magnetic field is allowed to resistively relax for several iterations following:
$$\frac{\partial \boldsymbol{B}}{\partial t} = \frac{\eta}{\mu_0} \Delta \boldsymbol{B}.$$

The iterations associated with reducing the ideal force balance error and resistive relaxation are interlaced to allow the magnetic surfaces to break up while approximately satisfying ideal MHD force balance. The resistivity parameter η is generally chosen to be larger than physical values to accelerate the convergence.

11.4 ▪ Force-free fields

The force-free equilibrium model is another equilibrium model without the assumption of continuously nested flux surfaces. In this model, the pressure force ∇p is neglected: $\boldsymbol{J} \times \boldsymbol{B} = 0$. Consequently, the plasma current is parallel to the magnetic field everywhere. In this section, we discuss the question of the existence and uniqueness of solutions, as well as a variational method for computing such states.

As a remark, the force-free model is consistent with the assumption of a nonintegrable magnetic field. If a given field line comes arbitrarily close to every point within a domain Ω, then from $\boldsymbol{J} \times \boldsymbol{B} = \nabla p$, we conclude that pressure must be constant within Ω. Therefore, the magnetic field is force-free. Force-free fields have been used to model stellarator equilibria under certain conditions, for example in [2].

Combining $\boldsymbol{J} \times \boldsymbol{B} = 0$ and $\nabla \times \boldsymbol{B} = \mu_0 \boldsymbol{J}$ gives $(\nabla \times \boldsymbol{B}) \times \boldsymbol{B} = 0$. This implies that the equilibrium field satisfies for some scalar function λ

$$\nabla \times \boldsymbol{B} = \lambda \boldsymbol{B}. \tag{11.20}$$

A force-free magnetic field is a solution to this equation, and the overall scale factor of a solution is not determined from (11.20). While λ refers to any scalar function, it is related to the corresponding current $\boldsymbol{J} = \nabla \times \boldsymbol{B}/\mu_0$ since

$$\lambda = \frac{\mu_0}{B^2} \boldsymbol{J} \cdot \boldsymbol{B}.$$

So, more precisely, λ is proportional to the parallel current density. Because the current is parallel to the magnetic field, this can be restated in terms of the current magnitude J as

$$\lambda = \pm \frac{\mu_0}{B} J.$$

Remark 11.3. *Combining* $\nabla \cdot \boldsymbol{B} = 0$ *and* (11.20) *implies that*

$$\boldsymbol{B} \cdot \nabla \lambda = 0.$$

In other words, λ *is constant along field lines. When* λ *is taken to be a constant to satisfy the above, the corresponding model is called the linear force-free model. We will make this assumption throughout this discussion. This assumption is physically motivated, for example, for modeling a chaotic magnetic field in which gradients of* λ *cannot be supported.*

The existence and uniqueness of solutions to (11.20) has been shown for toroidal domains and toroidal annuli under specific assumptions [167]. Related comments are summarized below.

- Consider a toroidal domain Ω. The boundary of the domain is a flux surface under the following condition:
$$\boldsymbol{B} \cdot \hat{\boldsymbol{n}} = 0 \qquad \text{on } \partial\Omega. \tag{11.21}$$
Moreover, the toroidal flux enclosed by Ω can be specified to determine the overall scale of $\boldsymbol{B}$. Given a fixed constant Ψ_T and a surface at constant poloidal angle bounded by $\partial\Omega$,

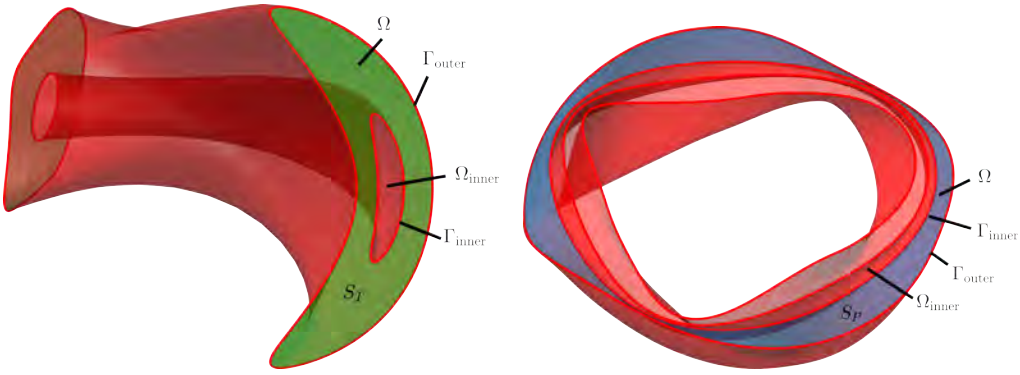

Figure 11.2*: A force-free equilibrium can be computed in an annular region* Ω *bounded by toroidal surfaces* Γ_{outer} *and* Γ_{inner} *given the flux of magnetic field through a surface at constant toroidal angle,* S_T*, represented in green in* (a)*, and the flux through a surface at constant poloidal angle,* S_P*, represented in blue in* (b)*, bounded by* Γ_{inner} *and* Γ_{outer}*.*

denoted S_T, the corresponding assumption reads

$$\int_{S_T} \boldsymbol{B} \cdot \hat{\boldsymbol{n}}\, d^2r = \Psi_T. \tag{11.22}$$

If the constant λ is fixed, the force-free equation (11.20) in Ω together with a boundary condition (11.21) as well as the flux condition (11.22) has a unique solution.

- Consider a toroidal annulus Ω defined as $\Omega_{\text{outer}} \backslash \Omega_{\text{inner}}$, where Ω_{outer} and Ω_{inner} are toroidal volumes such that $\Omega_{\text{inner}} \subset \Omega_{\text{outer}}$, as represented in Figure 11.2. These volumes are limited by two toroidal surfaces, Γ_{outer} and Γ_{inner}, so that $\partial\Omega = \Gamma_{\text{outer}} \cup \Gamma_{\text{inner}}$. Consider two surfaces bounded by Γ_{outer} and Γ_{inner}, one at constant poloidal angle, denoted S_T, and one at constant toroidal angle, denoted S_P. Given fixed constants $\Psi_T(\Gamma_{\text{outer}})$ and $\Psi_T(\Gamma_{\text{inner}})$, the toroidal flux and poloidal flux enclosed by Ω can be specified as

$$\begin{cases} \displaystyle\int_{S_T} \boldsymbol{B} \cdot \hat{\boldsymbol{n}}\, d^2r &= \Psi_T(\Gamma_{\text{outer}}) - \Psi_T(\Gamma_{\text{inner}}), \\ \displaystyle\int_{S_P} \boldsymbol{B} \cdot \hat{\boldsymbol{n}}\, d^2r &= \Psi_P(\Gamma_{\text{outer}}) - \Psi_P(\Gamma_{\text{inner}}). \end{cases} \tag{11.23}$$

If the constant λ is fixed, the force-free equation (11.20) in Ω together with the boundary condition (11.21) on the entire boundary and the flux constraints (11.23) has a unique solution.

Alternatively, the magnetic helicity can be prescribed instead of λ, as will be done in the next paragraph. Given a magnetic field $\boldsymbol{B}$ and its vector potential $\boldsymbol{A}$, the magnetic helicity is defined by

$$K = \int_\Omega \boldsymbol{A} \cdot \boldsymbol{B}\, d^3r. \tag{11.24}$$

If K is prescribed, then λ is sought together with $\boldsymbol{B}$ to satisfy the above condition. Rather analogously to helicity in fluid dynamics, K is a measure of the knottedness of magnetic field

lines, as discussed further in [16]. Although K depends explicitly on $\boldsymbol{A}$, if $\partial\Omega$ is a flux surface such that $\boldsymbol{B}\cdot\hat{\boldsymbol{n}}|_{\partial\Omega} = 0$, then K is independent of the choice of gauge, a notion introduced in Section A.1. The helicity K can be interpreted as the Gauss linking number [15], a notion relevant in fields such as knot theory, algebraic topology, and differential geometry.

As in Section 11.1.1, force-free equilibria in a toroidal domain can be found by minimizing an energy functional. Consider the functional W defined by

$$W[\boldsymbol{A}] = \int_\Omega \frac{(\nabla\times\boldsymbol{A})\cdot(\nabla\times\boldsymbol{A})}{2\mu_0}\, d^3r,$$

subject to the following constraints:

1. the total magnetic helicity (11.24) is given and constant;
2. the boundary of the domain, $\partial\Omega$, is a magnetic surface such that $\boldsymbol{B}\cdot\hat{\boldsymbol{n}}|_{\partial\Omega} = 0$;
3. the boundary of the domain is fixed such that the perturbation to the magnetic field satisfies $\delta\boldsymbol{B}\cdot\hat{\boldsymbol{n}}|_{\partial\Omega} = 0$;
4. the toroidal magnetic flux through Ω is fixed,

$$\int_{S_T} \boldsymbol{B}\cdot\hat{\boldsymbol{n}}\, d^2r = \Psi_T \qquad \text{on } \partial\Omega.$$

This leads to the result that the perturbation to the vector potential satisfies $\delta\boldsymbol{A}\times\hat{\boldsymbol{n}} = 0$ on $\partial\Omega$.[22]

Imposing constraint 1 with a Lagrange multiplier α and computing the first variation in W with respect to $\boldsymbol{A}$ yields

$$\delta W[\boldsymbol{A};\delta\boldsymbol{A}] = \int_\Omega \left(\frac{(\nabla\times\boldsymbol{A})\cdot(\nabla\times\delta\boldsymbol{A})}{\mu_0} - \alpha\left(\boldsymbol{A}\cdot(\nabla\times\delta\boldsymbol{A}) - \delta\boldsymbol{A}\cdot(\nabla\times\boldsymbol{A})\right)\right) d^3r.$$

Integrating by parts, we obtain

$$\delta W[\boldsymbol{A};\delta\boldsymbol{A}] = \int_\Omega \delta\boldsymbol{A}\cdot\left(\frac{\nabla\times(\nabla\times\boldsymbol{A})}{\mu_0} - 2\alpha\nabla\times\boldsymbol{A}\right) d^3r + \int_{\partial\Omega} \delta\boldsymbol{A}\times\hat{\boldsymbol{n}}\cdot\left(\alpha\boldsymbol{A} - \frac{\nabla\times\boldsymbol{A}}{\mu_0}\right) d^2r.$$

The surface term vanishes under constraint 4, hence

$$\delta W[\boldsymbol{A};\delta\boldsymbol{A}] = \int_\Omega \delta\boldsymbol{A}\cdot\left(\frac{\nabla\times(\nabla\times\boldsymbol{A})}{\mu_0} - 2\alpha\nabla\times\boldsymbol{A}\right) d^3r. \tag{11.26}$$

Thus for any stationary point $\boldsymbol{A}$ of W the corresponding field $\boldsymbol{B} = \nabla\times\boldsymbol{A}$ indeed satisfies (11.20) with $\lambda = 2\alpha/\mu_0$. The existence of a variational principle can form the basis for efficient numerical approximation of a force-free field.

[22] This can be seen by noting that the perturbed magnetic field can be written in magnetic coordinates as

$$\delta\boldsymbol{B} = \nabla\delta\psi\times\nabla\alpha + \nabla\psi\times\nabla\delta\alpha = \nabla\times\left(\delta\psi\nabla\alpha - \delta\alpha\nabla\psi\right), \tag{11.25}$$

where $\alpha = \vartheta - \iota\varphi$ is the field-line label and $\delta\psi = 0$ on $\delta\Omega$ from constraint 4. Thus, the perturbed vector potential can be taken to be $\delta\boldsymbol{A} = -\delta\alpha\nabla\psi$ on $\partial\Omega$.

While the variational principle presented in Section 11.1.1 requires that the local topology of the magnetic field is fixed during variations, only the global helicity is fixed when performing variations of (11.26). This model allows for islands or chaotic field regions to form as the energy is minimized.

The extension of this model to describe multiple force-free regions is presented in the following section. The Boundary Integral Equation Solver for Taylor states (BIEST) code [204] relies on a force-free field model in a fixed stellarator geometry and can approximate fields in a single-region domain and a multiple-region domain. In both cases, the Stepped Pressure Equilibrium Code (SPEC) [140] can also be used to compute force-free magnetic fields.

11.5 ▪ Multiregion stepped pressure equilibrium

The multiregion relaxed MHD (MRxMHD) equilibrium model [134, 54] generalizes the single-volume force-free state by allowing discontinuous, or stepped, pressure profiles and thus permitting the pressure to vary throughout the plasma volume. The domain is partitioned into nested toroidal annuli volumes in which the plasma is force-free and p is constant. These volumes are separated by interfaces that accommodate jumps in p. The geometry of the interfaces is not known *a priori* and must satisfy a specified set of jump and flux conditions described below. Note that these interface conditions are similar to those used in immiscible fluid models or capillary interface models where the interfaces between phases or fluids are unknown.[23]

Consider a toroidal domain, Ω, in which p and λ are piecewise constant. The domain is partitioned into m nested toroidal subregions Ω_i for all i from 1 to m. The innermost volume, Ω_1, is a genus one torus, while the other volumes, Ω_i for $i \geq 2$, are genus two tori. For each i from 2 to m, Ω_i is bounded by two nonintersecting toroidal surfaces, Γ_{i-1} and Γ_i. The innermost volume Ω_1 is bounded by a single toroidal surface, Γ_1, while the outermost boundary is the domain boundary, $\Gamma_m = \partial\Omega$. The discontinuities of p and λ occur at the surfaces, Γ_i.

The components of the model are described below.

- The parameters $\{\lambda_i\}_{1\leq i\leq m}$ define the λ profile as $\lambda = \lambda_i$ in Ω_i for all i from 1 to m, while the magnetic field $\boldsymbol{B} = \boldsymbol{B}_i$ in Ω_i for all i from 1 to m satisfies

$$\nabla \times \boldsymbol{B}_i = \lambda_i \boldsymbol{B}_i \text{ in } \Omega_i. \tag{11.27}$$

- The parameters $\{p_i\}_{1\leq i\leq m}$ define the stepped pressure profile as $p = p_i$ in Ω_i for all i from 1 to m, while the total pressure balance, including the plasma pressure p and the magnetic pressure $B^2/(2\mu_0)$ at the interfaces, is expressed as

$$[\![p + B^2/2\mu_0]\!]_{\Gamma_i} = 0 \ \ \forall i \text{ between 1 and } m-1. \tag{11.28}$$

- The flux surface conditions hold at the interfaces

$$\boldsymbol{B}\cdot\hat{\boldsymbol{n}} = 0 \text{ on } \Gamma_i \ \ \forall i \text{ between 1 and } m.$$

- The parameters $\{\Psi_T^i, \Psi_P^i\}_{2\leq i\leq m}$ define the toroidal and poloidal fluxes across each annular subdomain

$$\begin{cases} \displaystyle\int_{S_{T_i}} \boldsymbol{B}\cdot\hat{\boldsymbol{n}}\, d^2r = \Psi_T^i \ \ \forall i \text{ between 2 and } m, \\ \displaystyle\int_{S_{P_i}} \boldsymbol{B}\cdot\hat{\boldsymbol{n}}\, d^2r = \Psi_P^i \ \ \forall i \text{ between 2 and } m. \end{cases} \tag{11.29}$$

[23] A discussion of a flux condition on an artificial boundary within the domain to ensure well-posedness for a Navier–Stokes problem is presented in [124], while [125] addresses numerical aspects of a flow through an aperture in an infinite wall, and [145, 294] discuss a jump condition modeling force balance at an unknown interface.

Here S_{T_i} is a surface at constant toroidal angle bounded by surfaces Γ_i and Γ_{i-1}, and S_{P_i} is a surface at constant poloidal angle bounded by surfaces Γ_i and Γ_{i-1}.

- The parameter Ψ_T^1 defines the toroidal flux across the innermost toroidal domain Ω_1

$$\int_{S_{T_1}} \boldsymbol{B} \cdot \hat{\boldsymbol{n}}\, d^2r = \Psi_T^1, \tag{11.30}$$

where S_{T_1} is a surface at constant toroidal angle bounded by Γ_1.

In summary, given $\{\lambda_i, p_i, \Psi_T^i\}_{1\le i\le m}$ and $\{\Psi_P^i\}_{2\le i\le m}$, the force-free field equations (11.27) can be solved, subject to the constraints (11.28)–(11.30), to determine the position of free surfaces $\{\Gamma_i\}_{1\le i\le m}$ and value of the magnetic field $\boldsymbol{B}_i$ in $\cup_{1\le i\le m}\Omega_i$. In place of $\{\lambda_i\}_{1\le i\le m}$, the total helicity in each Ω_i may be prescribed and, in place of $\psi_T^1 \cup \{\Psi_T^i, \Psi_P^i\}_{2\le i\le m}$, the value of the rotational transform on each $\Gamma_i^{-,+}$ for $1 \le i \le m$ may be fixed.

An important characteristic of the model is that Γ_i, referred to as ideal interfaces, are magnetic surfaces. Between these ideal interfaces, the topology of the magnetic field is not constrained. This way, the model allows for islands and chaotic regions while allowing for a pressure differential across the volume thanks to pressure jumps at the interfaces.

This model is the basis for the Stepped Pressure Equilibrium Code (SPEC) [140]. This code solves for the magnetic field, iterating on the position of the interfaces until the constraints are satisfied.

11.6 ▪ Vacuum fields

Vacuum fields are an important subset of force-free magnetic fields corresponding to $\lambda = 0$ and do not assume continuously nested toroidal surfaces. As described in Section A.3, the vacuum model for magnetic fields can be used if there is no current in a given domain, $\boldsymbol{J} = 0$. For the vacuum approximation to be valid, an additional assumption of vanishing pressure gradients must be made since $\boldsymbol{J} \times \boldsymbol{B} = 0$. Even if these assumptions are not valid within the confinement region, the vacuum model can describe the region outside the confinement region. Under the vacuum assumption, $\boldsymbol{B}$ is curl-free from $\nabla \times \boldsymbol{B} = \mu_0 \boldsymbol{J}$, so it can be written in terms of a scalar potential, $\boldsymbol{B} = \nabla \Phi_B$. The scalar potential Φ_B must satisfy Laplace's equation, $\Delta \Phi_B = 0$. In a toroidal domain, additional constraints on the functional form of Φ_B and boundary condition are necessary to ensure that Ω is current-free.

Consider Laplace's equation in a toroidal domain, Ω, assuming general toroidal and poloidal angles θ and ζ, and a radial coordinate, r, that is not necessarily a flux label. In general, as $\boldsymbol{B} = \nabla \Phi_B$ must be periodic in θ and ζ, the scalar potential can be separated into periodic and nonperiodic pieces,

$$\Phi_B(r, \theta, \zeta) = \widetilde{\Phi}_B(r, \theta, \zeta) + A(r)\zeta + C(r)\theta, \tag{11.31}$$

where $\widetilde{\Phi}_B$ is periodic in θ and ζ.

The constraints placed on the functions $A(r)$ and $C(r)$ by the vacuum field assumption will now be discussed. Because there is no current inside Ω, the current enclosed by a poloidal loop about the torus vanishes. Hence Ampère's law $\nabla \times \boldsymbol{B} = \mu_0 \boldsymbol{J}$, using a loop at constant ϕ on the boundary of the toroidal domain, $\partial\Omega$, gives

$$\oint_{\zeta=\text{const.}} \boldsymbol{B} \cdot d\boldsymbol{l} = 0. \tag{11.32}$$

Using $d\boldsymbol{l} = (\partial \boldsymbol{R}/\partial\theta)\, d\theta$ this implies that $C(r) = 0$ everywhere in Ω. Similarly, the function $A(r)$ can be determined by considering a loop at constant θ on $\partial\Omega$,

$$\oint_{\theta=\text{const.}} \boldsymbol{B} \cdot d\boldsymbol{l} = \mu_0 I_P. \tag{11.33}$$

Using $d\boldsymbol{l} = (\partial \boldsymbol{R}/\partial\zeta)\, d\zeta$, this implies that $A(r) = \mu_0 I_P/2\pi$. As there is no current in Ω, I_P is the total coil current linking the plasma poloidally, and therefore $A(r)$ is a constant. The integrals in (11.32) and (11.33) are described in Section 9.1.2.

The boundary condition for Φ_B on $\partial\Omega$ is determined by specifying $\boldsymbol{B}\cdot\hat{\boldsymbol{n}}$ on $\partial\Omega$,

$$\hat{\boldsymbol{n}} \cdot \nabla\widetilde{\Phi}_B = \boldsymbol{B}\cdot\hat{\boldsymbol{n}} - \frac{\mu_0 I_P}{2\pi}\hat{\boldsymbol{n}}\cdot\nabla\zeta \qquad \text{on } \partial\Omega.$$

If $\partial\Omega$ is a magnetic surface, then $\boldsymbol{B}\cdot\hat{\boldsymbol{n}} = 0$.

To summarize, a field $\boldsymbol{B}(r,\theta,\zeta) = \nabla(\widetilde{\Phi}_B(r,\theta,\zeta) + \mu_0 I_P/2\pi\zeta)$ is a vacuum field in a toroidal domain Ω if $\widetilde{\Phi}_B$ satisfies Laplace's equation

$$\Delta\widetilde{\Phi}_B(r,\theta,\zeta) = -\frac{\mu_0 I_P}{2\pi}\Delta(\zeta) \qquad \text{in } \Omega$$

subject to this Neumann boundary condition on $\partial\Omega$. The system can be solved using a Green's function method, as in the NESTOR code [212].

Alternatively, the fields in a vacuum region can also be computed using the Biot–Savart law (A.9) applied to sources of current outside the vacuum region. Thus, the magnetic field can be determined if the currents in electromagnetic coils are provided.

11.7 ▪ Summary and analogy with steady Euler flow

Table 11.1 summarizes the models that describe equilibrium stellarator magnetic fields in a toroidal domain Ω with an associated boundary condition.

As an example of the connection between plasma and fluid dynamics, the MHD equilibrium equations share many similarities with the steady Euler flow equations. Over the years, this has facilitated the exchange of ideas between the fluid dynamics and plasma physics communities. Examples include [215, 113, 33].

The steady, $\partial/\partial t = 0$, incompressible Euler equations with constant density, ρ_0, are equations for the flow velocity $\boldsymbol{u}$ and pressure P. They can be written

$$\begin{cases} (\boldsymbol{u}\cdot\nabla)\,\boldsymbol{u} = -\nabla\left(\dfrac{P}{\rho_0}\right) \\ \nabla\cdot\boldsymbol{u} = 0. \end{cases} \quad\Leftrightarrow\quad \begin{cases} (\nabla\times\boldsymbol{u})\times\boldsymbol{u} = -\nabla\left(\dfrac{P}{\rho_0} + \dfrac{u^2}{2}\right) \\ \nabla\cdot\boldsymbol{u} = 0. \end{cases}$$

Conservation of momentum density is expressed by the first equations, while the second equation expresses incompressibility of the flow. The vorticity is defined as $\boldsymbol{\omega} = \nabla\times\boldsymbol{u}$. Beltrami flows describe states where the vorticity is parallel to $\boldsymbol{u}$ and are analogous to force-free fields. Flows with vanishing vorticity can be expressed in terms of a potential and are analogous to vacuum fields. The comparison is presented in Table 11.2.

Table 11.1*: Summary of MHD equilibrium models.*

	MHD equilibrium (surfaces assumed)	Force-free fields	Vacuum fields
Hyp.	$\boldsymbol{J} \times \boldsymbol{B} \neq 0$ $\nabla p \neq 0$	$\boldsymbol{J} \times \boldsymbol{B} = 0$ $\nabla p = 0$ and $\lambda = \text{const.}$	$\boldsymbol{J} = 0$ $\nabla p = 0$
PDE model	$\boldsymbol{J} \times \boldsymbol{B} = \nabla p$ $\nabla \cdot \boldsymbol{B} = 0$ $\mu_0 \boldsymbol{J} = \nabla \times \boldsymbol{B}$	$\nabla \times \boldsymbol{B} = \lambda \boldsymbol{B}$ $\mu_0 \boldsymbol{J} = \nabla \times \boldsymbol{B}$	$\Delta \widetilde{\Phi}_B = 0$
Given	$p(\psi)$, $\iota(\psi)$, Ψ_T	λ, Ψ_T	I_P
Unkn.	$\boldsymbol{B}$	$\boldsymbol{B}$	$\widetilde{\Phi}_B$
With	$\boldsymbol{J}$ function of $\boldsymbol{B}$	$\boldsymbol{J}$ function of $\boldsymbol{B}$	$\boldsymbol{B} = \nabla\left(\widetilde{\Phi}_B + (\mu_0 I_P/2\pi)\,\zeta\right)$
BC	$\boldsymbol{B} \cdot \hat{\boldsymbol{n}} = 0$	$\boldsymbol{B} \cdot \hat{\boldsymbol{n}} = 0$	$\hat{\boldsymbol{n}} \cdot \nabla \widetilde{\Phi}_B + (\mu_0 I_P/2\pi)\,\hat{\boldsymbol{n}} \cdot \nabla \zeta = \boldsymbol{B} \cdot \hat{\boldsymbol{n}}$

Table 11.2*: A comparison of the steady Euler models with the MHD equilibrium models.*

Hyp.	Steady Euler models	MHD equilibrium models
	$(\nabla \times \boldsymbol{u}) \times \boldsymbol{u} = -\nabla\left(\dfrac{P}{\rho_0} + \dfrac{u^2}{2}\right)$ $\nabla \cdot \boldsymbol{u} = 0$	$(\nabla \times \boldsymbol{B}) \times \boldsymbol{B} = \mu_0 \nabla p$ $\nabla \cdot \boldsymbol{B} = 0$
Beltrami flows/fields (vorticity parallel to field)	$\nabla \times \boldsymbol{u} = \alpha \boldsymbol{u}$ $\nabla \cdot \boldsymbol{u} = 0$	$\nabla \times \boldsymbol{B} = \lambda \boldsymbol{B}$ $\nabla \cdot \boldsymbol{B} = 0$
Potential flows (zero vorticity)	$\boldsymbol{u} = \nabla \varphi$ $\Delta \varphi = 0$	$\boldsymbol{B} = \nabla \Phi_B$ $\Delta \Phi_B = 0$

Chapter 12

Symmetries in stellarators

The notion of symmetry has a long history in physics. Due to the strong connection between symmetries and conserved quantities, leveraging symmetries can provide new physical insight, as illustrated in Appendix B. For further examples, in toroidal magnetic confinement, axisymmetry implies conservation of the canonical angular momentum, as described in Section 7.2, and existence of magnetic surfaces, as in described Section 10.1.

The most natural type of symmetry in a toroidal geometry is axisymmetry. Although the stellarator is not axisymmetric, other types of symmetries of the magnetic field have been introduced to design stellarators with some improved properties. Such symmetries are referred to as hidden symmetries. In particular, symmetry concepts have been introduced in order to exploit properties of the equilibrium magnetic field to improve confinement properties.

In Section 12.1, an important symmetry guaranteeing confinement of guiding center trajectories, quasisymmetry, is discussed. In Section 12.2, a generalization of quasisymmetry known as omnigeneity is introduced. Other symmetries, such as N_P symmetry and stellarator symmetry, are used to simplify the geometric description of stellarators. In Section 12.3.1, a periodicity in the number of field periods, often referred to as N_P symmetry, is presented. In Section 12.3.2, a discrete reflection symmetry, known as stellarator symmetry, is described. While these two discrete symmetries may not result in improved confinement as quasisymmetry and omnigeneity do, they are present in almost all experimental stellarator configurations to date.

While each symmetry has an exact theoretical definition, it is important to keep in mind that perfect symmetry can never be achieved in practice. Indeed, on the one hand other physics considerations must be accounted for when designing the magnetic field, and on the other hand coils cannot be engineered to perfectly reproduce the desired field. Moreover, the theoretical models for stellarator design focus on the field and coils, but do not take into account any other parts of the device. Nonetheless, symmetries can be achieved up to a small level of tolerance, and the design of stellarator configurations with hidden symmetries is an active area of research. It is, for instance, the main focus of the *Hidden Symmetries and Fusion Energy* collaboration, an interdisciplinary collaboration funded by the Simons Foundation from 2018 to 2025.[24]

The next chapter will turn to optimization models and computational methods for stellarator design. In particular, hidden symmetries of the equilibrium field will be one of many engineering and physics objectives of interest for the optimization.

[24]The collaboration website can be found at https://hiddensymmetries.princeton.edu/.

12.1 ▪ Quasisymmetry

In the context of axisymmetry, independence of physical quantities with respect to the toroidal angle yields conservation of angular momentum, providing approximate particle confinement. The concept of quasisymmetry similarly allows for conservation of a canonical momentum due to a symmetry of the magnetic field strength when expressed in a specific coordinate system. This hidden symmetry provides a method for confinement of guiding center trajectories.

The notion of quasisymmetry [23, 232] is introduced in terms of Boozer coordinates, described in Section 9.2. It is defined as a symmetry of the field strength, B, with respect to a linear combination of Boozer angles, ϑ_B and φ_B. As a reminder, this definition then relies on the assumption that the magnetic field has continuously nested toroidal flux surfaces, discussed in Remark 4.4. A magnetic field $\boldsymbol{B}$ is quasisymmetric if there exists a change of coordinates $(\psi, \vartheta_B, \varphi_B) \to (\psi, \chi, \eta)$, where $\chi = M\vartheta_B - N\varphi_B$ and $\eta = M'\vartheta_B - N'\varphi_B$ with $M'N \neq MN'$, such that the magnetic field amplitude is independent of the coordinate η,

$$\frac{\partial}{\partial \eta}\Big[B\left(\boldsymbol{R}(\psi, \chi, \eta)\right)\Big] = 0. \tag{12.1}$$

The assumption $M'N \neq MN'$ is required for a well-defined Jacobian. Thus there exists a symmetry direction when the field strength is expressed in Boozer coordinates.

The term quasisymmetry refers to the fact that it is a property of the field strength B rather than the full vector field $\boldsymbol{B}$. By contrast, axisymmetry introduced in Section 7.1 refers to a symmetry of each of the vector components of the field.

Consequences of quasisymmetry on guiding center motion, in particular the associated conservation of canonical momentum, will be studied in Section 12.1.1. Different choices of the parameters (M, N, M', N') will define different types of quasisymmetry; some of them will be discussed in Section 12.1.2. Other definitions of quasisymmetry that do not require Boozer coordinates are discussed in Section 12.1.3.

12.1.1 ▪ Guiding center motion in quasisymmetry

We will study the consequences of this symmetry on guiding center motion. As a reminder from Section 7.2, if the Lagrangian is independent of one coordinate, this implies the existence of a conserved quantity. Our aim will be to compute this conserved quantity and discuss the implications. The analysis will be similar to that in Section 7.2, where axisymmetry was shown to provide angular momentum conservation for charged particle motion, yielding approximate confinement of the motion to flux surfaces under the assumption of a strong magnetic field.

Consider the guiding center motion for charged particles of mass m and charge q in static electric and magnetic fields within the Lagrangian framework presented in Section 4.2 under the following assumptions. The magnetic field has continuously nested flux surfaces, guaranteeing the existence of Boozer coordinates. It is quaisymmetric and satisfies $\boldsymbol{B} = \nabla \times \boldsymbol{A}$. The electric field satisfies $\boldsymbol{E} = -\nabla\Phi$. To simplify the discussion we will assume Φ is a flux function. In practice, this is a good approximation for stellarator configurations [116].

To investigate the impact of quasisymmetry on guiding center motion, we use the gyroaveraged Lagrangian (4.21) rewritten using the definition of the magnetic moment $\mu = m\rho^2\dot{\varphi}^2/(2B)$,

$$\begin{aligned}&\mathcal{L}(\boldsymbol{R}_G, \dot{\boldsymbol{R}}_G, \rho, \dot{\rho}, \varphi, \dot{\varphi}, v_\parallel, \dot{v}_\parallel)\\ &= \Big(q\boldsymbol{A}(\boldsymbol{R}_G) + mv_\parallel \hat{\boldsymbol{b}}\left(\boldsymbol{R}_G\right)\Big) \cdot \dot{\boldsymbol{R}}_G - \frac{mv_\parallel^2}{2} + \frac{\rho^2 m\dot{\varphi}^2}{2} + \mu\left(\boldsymbol{R}_G, \rho, \dot{\varphi}\right) B(\boldsymbol{R}_G) - q\Phi(\boldsymbol{R}_G).\end{aligned} \tag{12.2}$$

Here again $\boldsymbol{R}_G$ is the guiding center position, ρ is the gyroradius, φ is the gyroangle, and $v_\parallel$ is the parallel velocity. The Lagrangian will first be expressed in the linear combinations of Boozer coordinates defined above (ψ,χ,η) and then simplified under the assumption of quasisymmetry. As a reminder, the transformation from Boozer coordinates $(\psi, \vartheta_B, \varphi_B)$ to their linear combinations (ψ, χ, η) is given by

$$\begin{cases} \vartheta_B = \dfrac{N\eta - N'\chi}{M'N - MN'}, \\ \varphi_B = \dfrac{M\eta - M'\chi}{M'N - MN'}. \end{cases}$$

The change of coordinates from $(\boldsymbol{R}_G, \dot{\boldsymbol{R}}_G)$ to $(\psi, \dot{\psi}, \chi, \dot{\chi}, \eta, \dot{\eta})$ is defined by

$$\begin{cases} \boldsymbol{R}_G\left(\psi, \dot{\psi}, \chi, \dot{\chi}, \eta, \dot{\eta}\right) = \boldsymbol{R}(\psi, \chi, \eta), \\ \dot{\boldsymbol{R}}_G\left(\psi, \dot{\psi}, \chi, \dot{\chi}, \eta, \dot{\eta}\right) = \dot{\psi}\dfrac{\partial \boldsymbol{R}(\psi, \chi, \eta)}{\partial \psi} + \dot{\chi}\dfrac{\partial \boldsymbol{R}(\psi, \chi, \eta)}{\partial \chi} + \dot{\eta}\dfrac{\partial \boldsymbol{R}(\psi, \chi, \eta)}{\partial \eta}. \end{cases}$$

The first two terms in the Lagrangian can then be simplified as follows. The vector potential can be expressed in Boozer coordinates as

$$\boldsymbol{A}(\psi, \vartheta_B, \varphi_B) = \psi \nabla \vartheta_B - \psi_P(\psi) \nabla \varphi_B,$$

where $\psi_P = \Psi_P / 2\pi$ is the poloidal flux function such that $\psi_P'(\psi) = \iota(\psi)$. Note that upon application of a curl, we recover the Boozer contravariant form of $\boldsymbol{B}$ (9.6). Then

$$\left[\boldsymbol{A}(\boldsymbol{R}_G) \cdot \dot{\boldsymbol{R}}_G\right]\left(\psi, \dot{\psi}, \chi, \dot{\chi}, \eta, \dot{\eta}\right) = \frac{N\psi - M\psi_P(\psi)}{M'N - MN'}\dot{\eta} + \frac{M'\psi_P(\psi) - N'\psi}{M'N - MN'}\dot{\chi}.$$

Using the covariant form (9.13) of the field in Boozer coordinates $(\psi, \vartheta_B, \varphi_B)$ with $\hat{\boldsymbol{b}} = \boldsymbol{B}/B$, we obtain

$$\begin{aligned} &\left[\hat{\boldsymbol{b}}\left(\boldsymbol{R}_G\right) \cdot \dot{\boldsymbol{R}}_G\right]\left(\psi, \dot{\psi}, \chi, \dot{\chi}, \eta, \dot{\eta}\right) \\ &\qquad = \frac{\dot{\psi} K(\psi, \chi, \eta) + \dot{\chi}\left(-N' I(\psi) - M' G(\psi)\right) + \dot{\eta}\left(N I(\psi) + M G(\psi)\right)}{B(\psi, \chi, \eta)\left(M'N - MN'\right)}. \end{aligned}$$

Here K is the radial covariant component of the magnetic field. In Section 9.2.3 it was shown that if $\iota \notin \mathbb{Q}$,[25] then

$$K(\psi, \vartheta_B, \varphi_B) = \mathcal{K}(\psi) + i\mu_0 \frac{dp(\psi)}{d\psi} \sum_{m,n,mn\neq 0} \left(\frac{G(\psi) + \iota(\psi) I(\psi)}{n - \iota(\psi) m} b_{m,n}(\psi)\right) e^{i(m\vartheta_B - n\varphi_B)},$$

where $b_{m,n}$ are the Fourier harmonics of $1/B^2$. So if $B(\boldsymbol{R}(\psi, \vartheta_B, \varphi_B))$ varies on a surface only through $\chi = M\vartheta_B - N\varphi_B$, then so must K as $b_{m,n}$ vanishes for $m/n \neq M/N$. Therefore, K has the same symmetry properties as B in Boozer coordinates.

Defining $\boldsymbol{Q} = (\psi, \dot{\psi}, \chi, \dot{\chi}, \eta, \dot{\eta}, \varphi, \dot{\varphi}, v_\parallel, \dot{v}_\parallel)$, the gyroaveraged Lagrangian in Boozer coordinates then reads

$$\begin{aligned} \mathcal{L}(\boldsymbol{Q}) = m v_\parallel &\frac{\dot{\psi} K(\psi, \chi) + \dot{\chi}\left(-N' I(\psi) - M' G(\psi)\right) + \dot{\eta}\left(N I(\psi) + M G(\psi)\right)}{B(\psi, \chi)\left(M'N - MN'\right)} \\ &+ q\left(\frac{N\psi - M\psi_P(\psi)}{M'N - MN'}\dot{\eta} + \frac{M'\psi_P(\psi) - N'\psi}{M'N - MN'}\dot{\chi}\right) \\ &- \frac{m v_\parallel^2}{2} + \frac{\rho^2 m \dot{\varphi}^2}{2} + \mu\left(\psi, \chi, \rho, \dot{\varphi}\right) B(\psi, \chi) - q\Phi(\psi). \end{aligned}$$

[25] Even though this argument relies on $\iota \notin \mathbb{Q}$, the result is still true with closed field lines [67, 35].

This right-hand side being independent of η shows that $\mathcal{L}$ is independent of η. The Euler–Lagrange equation corresponding to η then implies that the canonical momentum, defined by $p_\eta(\boldsymbol{Q}) = \partial\mathcal{L}(\boldsymbol{Q})/\partial\dot{\eta}$, is conserved along trajectories: for any $\boldsymbol{Q}_T : \mathbb{R} \to \mathbb{R}^{10}$,

$$\frac{\partial\mathcal{L}(\boldsymbol{Q}_T(t))}{\partial\eta} = \frac{d}{dt}\left(\frac{\partial L\big(\boldsymbol{Q}_T(t)\big)}{\partial\dot{\eta}}\right) \Rightarrow \frac{dp_\eta\big(\boldsymbol{Q}_T(t)\big)}{dt} = 0. \tag{12.3}$$

This canonical momentum is explicitly given by

$$p_\eta(\boldsymbol{Q}) = \frac{1}{M'N - MN'}\left(\frac{mv_\parallel\big(NI(\psi) + MG(\psi)\big)}{B(\psi,\chi)} + q\big(N\psi - M\psi_P(\psi)\big)\right).$$

The conservation of p_η implies that particles remain confined to constant p_η surfaces in phase space. According to Appendix B.3.2, since guiding center motion defines a 2-degree-of-freedom Hamiltonian system, the existence of two conserved quantities, namely p_η and energy, implies integrability of the guiding center motion. Thus the guiding center trajectories are confined to invariant tori in phase space in a quasisymmetric system. We now consider the implications for confinement in physical space. As we did in Section 7.2, we will consider the relative size of each term in p_η under the assumption of a strong magnetic field, $\epsilon = \rho/L_B \ll 1$, where $\rho = mv_t/(qB)$ is the gyroradius and L_B is a typical length scale of the magnetic field, as introduced in Section 4.2.2.

- Here we will approximate $v_\parallel \sim v_t$ where v_t is the thermal velocity, as was assumed in Section 4.1.
- The scaling of the toroidal flux is assumed to be $\psi \sim r^2 B_T/2$, where r is an approximate scale of the minor radius and B_T is an approximate toroidal field strength. Assuming that $\iota \sim \mathcal{O}(\epsilon^0)$, the poloidal flux is assumed to scale as $\psi_P(\psi) \sim \iota\psi$ since $\psi_P'(\psi) = \iota$.
- In stellarators, the toroidal plasma current is much smaller than the poloidal current in the coils, so we can assume that $I(\psi) \ll G(\psi)$, as the covariant components are defined such that $G(\psi) = \mu_0 I_P(\psi)/2\pi$ and $I(\psi) = \mu_0 I_T(\psi)/2\pi$. Since most of the poloidal current flows through the coils, G is assumed independent of ψ. This assumption also leads to $G \sim RB_T$, where R is the approximate scale of the major radius.
- We assume that the approximate minor and major radii scale as $r \sim R \sim L_B$.

It then follows that the ratio of the two terms in p_η scales as

$$\frac{mv_\parallel\big(NI(\psi) + MG(\psi)\big)/B}{q\big(N\psi - M\psi_P(\psi)\big)} \sim \frac{v_t G}{\Omega r^2 G/(2R)} \sim \frac{\rho}{L_B} \sim \epsilon \ll 1,$$

where $\Omega = qB/m$ is the gyrofrequency.

Thus, we can approximate $p_\eta \sim q\big(N\psi - M\psi_P(\psi)\big)/(M'N - MN')$ to lowest order in ϵ. So the Euler–Lagrange equation (12.3) implies that, to lowest order in ϵ, along any trajectory $\psi_T : \mathbb{R} \to \mathbb{R}$,

$$\frac{d\psi_T(t)}{dt} \approx 0.$$

We can therefore conclude that guiding center orbits stay close to a flux surface under the assumption of a strong magnetic field, as they do in axisymmetry. In this way, guiding center motion exhibits good confinement properties under the assumption of quasisymmetry.

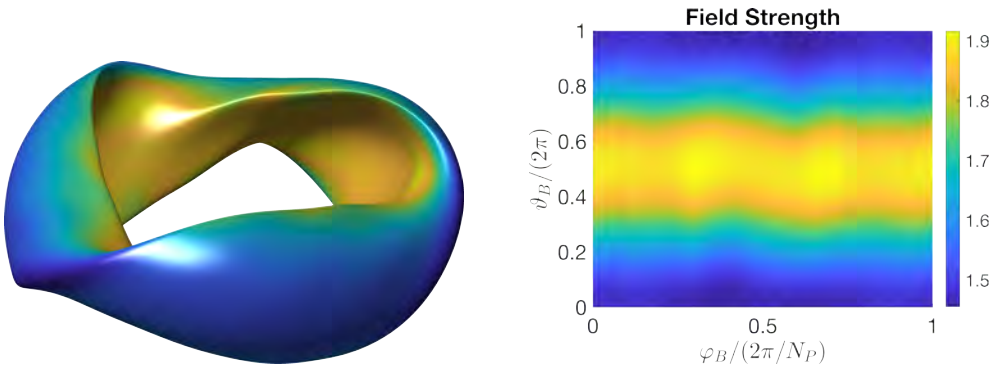

(a) (b)

Figure 12.1*:* (a) *The last magnetic surface of NCSX is shown with the color scale indicating field strength.* (b) *The field strength on the last magnetic surface is plotted as a function of the two Boozer angles. As NCSX is quasiaxisymmetric, B is nearly constant along lines of constant ϑ_B. This approximately quasiaxisymmetric equilibrium was obtained through numerical optimization techniques, presented in Chapter* 13.

12.1.2 ▪ Types of quasisymmetry

Quasisymmetry can be organized into three categories, depending on the values of M and N defining the coordinate $\chi = M\vartheta_B - N\varphi_B$.

Quasiaxisymmetry (QA) refers to the case $N = 0$. Thus contours of B close toroidally without wrapping poloidally around the flux surface as illustrated in Figure 12.1. Several other configurations have been designed to be close to QA, including Aries-CS [223], CFQS [264], ESTELL [61], QuASDEX [123], and MUSE [246]. The stellarator NCSX was designed to be approximately quasiaxisymmetric [322] and was partially constructed at the Princeton Plasma Physics Laboratory.

Quasipoloidal (QP) symmetry refers to the case $M = 0$ so that contours of B close poloidally without wrapping toroidally around the flux surface. Section 2.7 from [174] shows that this type of symmetry cannot be achieved in practice near the axis due to the requirement that the pressure gradient vanishes on the axis. However, away from the axis, it may be possible to get close to QP symmetry. The Quasi Poloidal Stellarator [279] is an example of a configuration designed for QP symmetry.

Quasihelical (QH) symmetry refers to the case $M \neq 0$ and $N \neq 0$. Thus contours of B close both toroidally and poloidally, or helically as illustrated in Figure 12.2. The Helically Symmetric Experiment (HSX) at the University of Wisconsin - Madison [5] is a quasihelically symmetric stellarator experiment. Several other QH configurations have also been designed [232, 171] but not constructed.

12.1.3 ▪ Other definitions

Several equivalent definitions of quasisymmetry are described in other references, for example, [116, 177]. One representation that does not rely upon a transformation to Boozer coordinates will be discussed in this section.

According to [121], a magnetic field $\boldsymbol{B}$ is quasisymmetric if there exists a flux function $F(\psi)$ such that

$$\boldsymbol{B} \times \nabla\psi \cdot \nabla B = F(\psi)\boldsymbol{B} \cdot \nabla B. \tag{12.4}$$

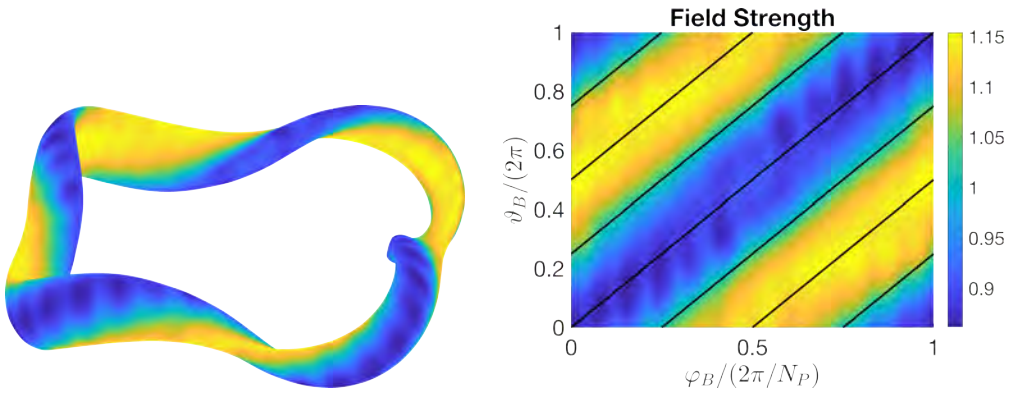

(a) (b)

Figure 12.2*:* (a) *The last magnetic surface of HSX is shown with the color scale indicating field strength.* (b) *The field strength on the last magnetic surface is plotted as a function of the two Boozer angles. As HSX is quasihelically symmetric, B is nearly constant along lines of constant $\vartheta_B - N_P\varphi_B$ (black), where N_P is the number of field periods as defined in Section* 12.3.1*. This approximately quasihelically symmetric equilibrium was obtained through numerical optimization techniques, presented in Chapter* 13*.*

This expression of quasisymmetry will be leveraged to study the motion of trapped particles in Section 12.2.

Using the contravariant representation of the magnetic field in Boozer coordinates to rewrite the right-hand side and the covariant representation to rewrite the left-hand side of (12.4), we can see that the definition of quasisymmetry presented in Section 12.1 implies (12.4) with

$$F(\psi) = \frac{NI(\psi) + MG(\psi)}{\iota(\psi)M - N} \tag{12.5}$$

for quasisymmetry with poloidal mode M and toroidal mode N.

The converse is also true: a magnetic field $\boldsymbol{B}$ satisfying (12.4) also satisfies (12.1). Indeed, expressing (12.4) in Boozer coordinates, for all $(\psi, \vartheta_B, \varphi_B) \in (a,b) \times (0,2\pi) \times (0,2\pi)$

$$\big(-F(\psi) - I(\psi)\big)\frac{\partial B(\psi,\vartheta_B,\varphi_B)}{\partial \varphi_B} + \big(G(\psi) - \iota(\psi)F(\psi)\big)\frac{\partial B(\psi,\vartheta_B,\varphi_B)}{\partial \vartheta_B} = 0 \tag{12.6}$$

and writing B in a Fourier series in the two angles,

$$B(\psi,\vartheta_B,\varphi_B) = \sum_{m,n} B_{m,n}(\psi) e^{i(m\vartheta_B - n\varphi_B)},$$

implies the following condition:

$$\forall (m,n) \in \mathbb{Z}^2, \forall \psi \in (a,b), \Big(\big(I(\psi) + F(\psi)\big)n + \big(G(\psi) - \iota(\psi)F(\psi)\big)m\Big) B_{m,n}(\psi) = 0.$$

In order to satisfy this condition, some $B_{m,n}(\psi)$ can be constantly equal to zero, but the corresponding terms would not contribute to the field $\boldsymbol{B}$. Other $B_{m,n}(\psi)$ can be nonzero at least for some interval $(c,d) \subset (a,b)$. Hence, in order to express explicitly the consequence of (12.6)

on the Fourier field $\boldsymbol{B}$, the goal is now to identify the pairs of indices (m, n) such that the condition

$$\forall \psi \in (c,d), \big(I(\psi) + F(\psi)\big)n + \big(G(\psi) - \iota(\psi)F(\psi)\big)m = 0 \tag{12.7}$$

is satisfied since only Fourier modes for these indices will contribute to the field.

The functions of ψ in this expression have an important property: the two functions $I + F$ and $G - \iota F$ of ψ cannot vanish simultaneously. For future reference, this can equivalently be expressed by

$$\forall \psi \in (a,b), \begin{cases} \text{either } I(\psi) + F(\psi) \neq 0, \\ \text{or } G(\psi) - \iota(\psi)F(\psi) \neq 0. \end{cases} \tag{12.8}$$

This important property can be proved by contradiction as follows. Assume that there exists a ψ_0 such that

$$\begin{cases} I(\psi_0) + F(\psi_0) = 0, \\ G(\psi_0) - \iota(\psi_0)F(\psi_0) = 0, \end{cases}$$

or equivalently

$$\begin{cases} F(\psi_0) = -I(\psi_0), \\ G(\psi_0) + \iota(\psi_0)I(\psi_0) = 0. \end{cases}$$

This is a contradiction since the Jacobian of the Boozer coordinate system can be expressed as $\sqrt{g} = (G(\psi) + \iota(\psi)I(\psi))/B^2$ and is not zero for all $\psi \in (a,b)$.

Two possible situations can then arise:

$$\text{(i) } \forall \psi \in (c,d), I(\psi) + F(\psi) = 0 \text{ or (ii) } \exists \psi_0 \in (c,d), I(\psi_0) + F(\psi_0) \neq 0.$$

(i) In the first situation, (12.7) is equivalent to

$$\forall \psi \in (c,d), (G(\psi) - \iota(\psi)F(\psi))\, m = 0.$$

Besides, (12.8) implies that

$$\forall \psi \in (c,d), G(\psi) + \iota(\psi)F(\psi) \neq 0,$$

and therefore $m = 0$.

Hence in situation (i), the field $\boldsymbol{B}$ has the form

$$B(\psi, \vartheta_B, \varphi_B) = \sum_n B_{0,n}(\psi) e^{-in\varphi_B},$$

it only depends on φ_B and hence it satisfies (12.1) for $\eta = \vartheta_B$, and this field satisfies (12.1) for $(M, N) = (0, 1)$.

(ii) In the second situation, by continuity there is a neighborhood $\mathcal{D}$ of ψ_0 such that

$$\forall \psi \in \mathcal{D}, I(\psi) + F(\psi) \neq 0.$$

Then (12.7) implies that

$$\forall \psi \in \mathcal{D}, m\frac{G(\psi) - \iota(\psi)F(\psi)}{I(\psi) + F(\psi)} = n.$$

This is equivalent to

$$\begin{cases} \text{either } m = 0, \text{ and so } n = 0, \\ \text{or } \forall \psi \in \mathcal{D}, \dfrac{G(\psi) - \iota(\psi)F(\psi)}{I(\psi) + F(\psi)} = \dfrac{n}{m}. \end{cases}$$

So the pairs of indices (m, n) satisfying (12.7) are either $(0, 0)$ or the pairs satisfying

$$\forall \psi \in \mathcal{D}, \frac{G(\psi) - \iota(\psi)F(\psi)}{I(\psi) + F(\psi)} = \frac{n}{m}.$$

This implies that the left-hand side is constant on $\mathcal{D}$ and that there exists a rational number $K = \frac{N_*}{M_*}$, with two coprime integers (N_*, M_*), such that $M_* n = N_* m$.
Hence in situation (ii), the field $\boldsymbol{B}$ has the form

$$B(\psi, \vartheta_B, \varphi_B) = \sum_{k \in \mathbb{Z}} B_{kM_*, kN_*}(\psi) e^{ik(M_* \vartheta_B - N_* \varphi_B)},$$

it only depends on $M_* \vartheta_B - N_* \varphi_B$, and hence it satisfies (12.1) for $\eta = M' \vartheta_B - N' \varphi_B$ as long as (M', N') are chosen so that $M_* N' \neq N_* M'$.

As announced, this proves that in either of the two possible situations the definition (12.1) is indeed verified by a field satisfying the definition (12.4).

12.2 ▪ Omnigeneity

As a reminder from Section 4.2, guiding center theory requires the assumption of a strong magnetic field. As discussed in the previous section, quasisymmetry implies the conservation of canonical momentum, yielding guiding center confinement under this assumption. However, quasisymmetry is not a necessary condition for confinement. We will discuss a generalization of quasisymmetry, known as omnigeneity, enabling the confinement of guiding center trajectories in a similar way but without involving conservation of a canonical momentum. As a reminder from Section 4.2, guiding center trajectories in a strong magnetic field tend to move along field lines. As discussed in Section 4.4, the motion is confined in the direction parallel to the field in the presence of continuously nested toroidal flux surfaces. In a toroidal magnetic field, the curvature and gradient of the field lead to components of the guiding center velocities perpendicular to the field. These are known as drifts and can generally lead to unconfined orbits. Omnigeneous magnetic fields guarantee a vanishing time-averaged magnetic drift of particle trajectories away from a given magnetic surface. In this way, particles stay confined to a given magnetic surface on average.

The definition of omnigeneity then requires a preliminary discussion about particle trajectories. We begin with a brief reminder of guiding center motion. We will then define the time-averaged magnetic drifts that form the basis for the definition of omnigeneity. These time-averaged drifts will then be related to a so-called parallel adiabatic invariant, an approximate conserved quantity in magnetic confinement devices as introduced in Remark 4.2, to demonstrate the connection between omnigeneity and a symmetry of this adiabatic invariant.

To define omnigeneity, we will analyze guiding center motion in a static magnetic field without a radial current, $(\nabla \times \boldsymbol{B}) \cdot \nabla \psi = 0$, and without an electric field. As discussed in Section 4.2, guiding center motion is obtained under the assumption that $\epsilon = \rho / L_B \ll 1$, where ρ is the gyroradius and L_B is a typical length scale of the magnetic field strength.

At $\mathcal{O}(\epsilon^0)$, the motion of guiding centers is simply along field lines. The magnetic moment $\mu = m v_\perp^2 / (2B)$ is conserved along a guiding center trajectory, where $v_\perp$ is the magnitude of the

velocity perpendicular to the magnetic field, introduced in Section 4.3.1. In addition, the energy of a particle, $E = mv_\parallel^2/2 + \mu B$, is conserved in time-independent fields, as described in Section 4.3.2. As a reminder, along a trajectory, the parallel velocity can be expressed in terms of E and μ,

$$v_\parallel = \pm\sqrt{\frac{2(E - \mu B\left(\boldsymbol{R}_G\right))}{m}}.$$

According to Section 4.3.3, this results in trapping of some particles in regions of low magnetic field strength, the parallel velocity can vanish at points where the field strength B reaches the critical value $B_{\text{crit}} := E/\mu$, a constant along a trajectory. Particles with B_{crit} value exceeding the maximum magnetic field strength in a given region are said to be passing particles, and otherwise they are said to be trapped particles. Defining $\sigma = \text{sign}(v_\parallel)$, $v_\parallel$ can also be written as a function of position and the constants of motion E and μ:

$$v_\parallel\left(\boldsymbol{R}_G, E, \mu, \sigma\right) = \sigma\sqrt{\frac{2(E - \mu B\left(\boldsymbol{R}_G\right))}{m}}. \tag{12.9}$$

For passing particles, σ is conserved along the trajectory, while for trapped particles σ flips along different segments of the trajectory.

At $\mathcal{O}(\epsilon)$, the drift (4.30) experienced by guiding center trajectories is repeated here for convenience. Along any guiding center trajectory, the drift velocity is given for $(\boldsymbol{R}_G)_T : \mathbb{R} \to \mathbb{R}^3$ by

$$\left((\dot{\boldsymbol{R}_G})_T(t)\right)_\perp = \left[\frac{v_\parallel^2 \hat{\boldsymbol{b}} \times \boldsymbol{\kappa}}{\Omega} + \frac{\mu \hat{\boldsymbol{b}} \times \nabla B}{qB}\right]\left((\boldsymbol{R}_G)_T(t)\right).$$

In this section, we will use the shorthand notation $\boldsymbol{V}_{\text{drift}}(t) = \left((\dot{\boldsymbol{R}_G})_T(t)\right)_\perp$ to denote the guiding center drift velocity along a trajectory. The component of the velocity corresponding to drifts away from magnetic surfaces, also called radial drift, is given by $\boldsymbol{V}_{\text{drift}} \cdot \nabla\psi$. Under the assumption that $\nabla \times \boldsymbol{B} \cdot \nabla\psi$ vanishes, then $\hat{\boldsymbol{b}} \times \boldsymbol{\kappa} \cdot \nabla\psi = \left(\hat{\boldsymbol{b}} \times \nabla B \cdot \nabla\psi\right)/B$. Hence the radial drift can be written as

$$\left[\boldsymbol{V}_{\text{drift}} \cdot \nabla\psi\right]\left((\boldsymbol{R}_G)_T(t)\right) = \left[\left(v_\parallel^2 + \frac{\mu B}{m}\right)\frac{\boldsymbol{B} \times \nabla B \cdot \nabla\psi}{B^2\Omega}\right]\left((\boldsymbol{R}_G)_T(t)\right). \tag{12.10}$$

Treating $v_\parallel$ as a function of position and using the identity $\nabla \cdot (\boldsymbol{B} \times \nabla\psi) = 0$, a consequence of $\nabla\psi \cdot (\nabla \times \boldsymbol{B}) = 0$, this expression can be further simplified as follows:

$$\left[\boldsymbol{V}_{\text{drift}} \cdot \nabla\psi\right]\left((\boldsymbol{R}_G)_T(t)\right) = \left[\frac{v_\parallel}{\Omega}\nabla \cdot \left(\frac{v_\parallel}{B}\boldsymbol{B} \times \nabla\psi\right)\right]\left((\boldsymbol{R}_G)_T(t)\right). \tag{12.11}$$

If $\boldsymbol{V}_{\text{drift}} \cdot \nabla\psi$ could vanish along all trajectories, then all particles would be confined to magnetic surfaces up to $\mathcal{O}(\epsilon)$. However, in practice obtaining a magnetic field such that this constraint is satisfied is very restrictive [49]. Yet under a weaker condition, particles could remain within a small distance of a given surface, still providing good confinement. Indeed, a less restrictive condition is to seek that particles remain close to a given surface, the distance being quantified by an averaging process. We define an approximate time average. Since the $\mathcal{O}(\epsilon^0)$ motion is along magnetic field lines, we can approximate the time along a trajectory by considering only the parallel motion. In order to introduce this time average, we now leverage the (ψ, α, l) coordinate system introduced in Section 9.3, where ψ is a flux label, α is a field-line label such

that $\boldsymbol{B} = \nabla\psi \times \nabla\alpha$, and l measures length along field lines. The corresponding Jacobian is $\sqrt{g} = 1/B$. The approximate differential time is then $dt = dl/v_\parallel$. During a portion of a trajectory when $\sigma = +1$, the change in l is positive while $v_\parallel > 0$. Therefore t increases along the trajectory. Similarly, when $\sigma = -1$, the change in l is negative while $v_\parallel < 0$, thus t increases. We conclude that $dt = d\ell/|v_\parallel|$ where $d\ell = \sigma dl$ measures length along a trajectory, and the time average operation is independent of σ.

Formally, the time average of a given quantity A is defined as

$$\langle A\rangle(\psi,\alpha,E,\mu) = \frac{\oint \dfrac{A(\psi,\alpha,l)\,dl}{v_\parallel(\psi,\alpha,l,E,\mu,\sigma)}}{\oint \dfrac{dl}{v_\parallel(\psi,\alpha,l,E,\mu,\sigma)}}.$$

The notation $\oint$ indicates integration along a time interval, depending on the trapping state and type of magnetic surface.

- In the case of trapped particles, this $\mathcal{O}(\epsilon^0)$ parallel motion is periodic in time, since particles move between points $l_\pm$ where $B(\psi,\alpha,l_\pm) = B_{\text{crit}}$. The time average can then be performed along the closed loop from l_- to l_+ and back to l_-:

$$\begin{aligned}\langle A\rangle(\psi,\alpha,E,\mu) &= \frac{\displaystyle\int_{l_-}^{l_+} \frac{A(\psi,\alpha,l)\,dl}{v_\parallel(\psi,\alpha,l,E,\mu,\sigma)} - \int_{l_+}^{l_-} \frac{A(\psi,\alpha,l)\,dl}{v_\parallel(\psi,\alpha,l,E,\mu,\sigma)}}{\displaystyle\int_{l_-}^{l_+} \frac{dl}{v_\parallel(\psi,\alpha,l,E,\mu,\sigma)} - \int_{l_+}^{l_-} \frac{dl}{v_\parallel(\psi,\alpha,l,E,\mu,\sigma)}} \\ &= \frac{\displaystyle\int_{l_-}^{l_+} \frac{A(\psi,\alpha,l)\,dl}{v_\parallel(\psi,\alpha,l,E,\mu,\sigma)}}{\displaystyle\int_{l_-}^{l_+} \frac{dl}{v_\parallel(\psi,\alpha,l,E,\mu,\sigma)}}.\end{aligned}$$

- For passing particles on a rational surface, the parallel motion is also periodic, and the time average can be performed along a closed field line.

- For passing particles on an irrational surface, the parallel motion is no longer periodic. In this case, the time average can be performed by integrating along a field line until it comes arbitrarily close to its starting point. In this case, as discussed in [55, 116], the time average then reads

$$\langle A\rangle(\psi,\alpha,E,\mu) = \frac{\displaystyle\int_0^{2\pi}\int_0^{L} \frac{A(\psi,\alpha,l)}{v_\parallel(\psi,\alpha,l,E,\mu,\sigma)}\,dl d\alpha}{\displaystyle\int_0^{2\pi}\int_0^{L} \frac{dl d\alpha}{v_\parallel(\psi,\alpha,l,E,\mu,\sigma)}}, \tag{12.12}$$

  where the l integral is taken along one toroidal loop from 0 to L.

The time interval associated with the average is then defined as

$$\tau(\psi,\alpha,E,\mu) = \oint \frac{dl}{v_\parallel(\psi,\alpha,l,E,\mu,\sigma)}.$$

In order to introduce the definition of omnigeneity, we now turn to evaluating the time average of the radial drift. Since $v_\parallel$ can be treated as a function of (ψ,α,l,E,μ), we will also treat the

radial drift as a function of position. Using the expression for the divergence from Table 5.1, the radial drift (12.11) is evaluated in the (ψ, α, l) coordinate system:

$$\left[\boldsymbol{V}_{\text{drift}} \cdot \nabla\psi\right](\psi, \alpha, l, E, \mu) = \left[\frac{m v_\parallel}{q}\left(\frac{\partial v_\parallel}{\partial \alpha} + \frac{\partial}{\partial l}\left[\frac{v_\parallel \hat{\boldsymbol{b}} \times \nabla\psi \cdot \nabla l}{B}\right]\right)\right](\psi, \alpha, l, E, \mu, \sigma)\,. \tag{12.13}$$

The averaging procedure applied to the radial drift then gives

$$\left\langle \boldsymbol{V}_{\text{drift}} \cdot \nabla\psi \right\rangle(\psi, \alpha, E, \mu) = \frac{\oint \left[\frac{m}{q}\left(\frac{\partial v_\parallel}{\partial \alpha} + \frac{\partial}{\partial l}\left[\frac{v_\parallel \hat{\boldsymbol{b}} \times \nabla\psi \cdot \nabla l}{B}\right]\right)\right](\psi, \alpha, l, E, \mu)\, dl}{\tau(\psi, \alpha, E, \mu)}.$$

In the above, since the integration is performed at constant α, the α derivative can be pulled out of the integral. Since the average is performed over a closed loop in l, the averaged radial drift simplifies to

$$\left\langle \boldsymbol{V}_{\text{drift}} \cdot \nabla\psi \right\rangle(\psi, \alpha, E, \mu) = \frac{m \frac{\partial}{\partial \alpha}\left(\oint v_\parallel(\psi, \alpha, l, E, \mu, \sigma)\, dl\right)}{q\tau(\psi, \alpha, E, \mu)}.$$

A condition to cancel the averaged radial drift then reads

$$\frac{\partial}{\partial \alpha}\left(\oint v_\parallel(\psi, \alpha, l, E, \mu, \sigma)\, dl\right) = 0. \tag{12.14}$$

Using the expression for $v_\parallel$ (12.9), this condition can be written equivalently as

$$\frac{\partial}{\partial \alpha}\left(\oint \sqrt{1 - \frac{B(\psi, \alpha, l)}{B_{\text{crit}}}}\, dl\right) = 0. \tag{12.15}$$

This shows that the condition only involves properties of the magnetic field, since the quantity B_{crit} is constant along a trajectory. If (12.15) is satisfied for all $1/B_{\text{crit}} \in [0, 1/B_{\text{min}}]$ where B_{min} is the minimum magnetic field strength in the confinement region, then the time-averaged radial drift for all guiding center trajectories will vanish. A magnetic field satisfying this property is said to be omnigeneous [99, 41].

In the case of passing particles on an irrational magnetic surface, since the time average (12.12) involves a periodic integral in α, the omnigeneity condition is automatically satisfied. Thus passing particles are well-confined if irrational magnetic surfaces exist. However, confinement of passing particles on rational surfaces [67] and trapped particles requires an additional restriction on the magnetic geometry. The search for omnigeneous magnetic fields, therefore, requires special attention to these cases.

We now highlight the connection between omnigeneity and symmetry properties. The quantity that appears in the omnigeneity condition (12.15), namely

$$J_\parallel(\psi, \alpha, E, \mu) = \oint v_\parallel(\psi, \alpha, l, E, \mu, \sigma)\, dl, \tag{12.16}$$

is called the parallel adiabatic invariant. As we will demonstrate, $J_\parallel$ is an approximately conserved quantity associated with periodic motion and is, therefore, an adiabatic invariant according to Remark 4.2.

With the definition (12.14), we remark that omnigeneity is equivalent to

$$\frac{\partial}{\partial \alpha}\left(J_{\|}(\psi,\alpha,E,\mu)\right)=0\ \forall(\psi,\alpha,E,\mu).$$

This shows that symmetry of $J_{\|}$ with respect to α implies time-averaged confinement. The parallel adiabatic invariant can next be interpreted as an approximate constant of the motion. Indeed, the averaged radial drift is related to the derivative of $J_{\|}$ through $\langle \boldsymbol{V}_{\text{drift}}\cdot\nabla\psi\rangle = m/(q\tau)\partial J_{\|}/\partial\alpha$. Besides, the in-surface magnetic drift $\langle \boldsymbol{V}_{\text{drift}}\cdot\nabla\alpha\rangle$ can be evaluated using a procedure similar to the one used to obtain the radial magnetic drift. The resulting averaged drift reads

$$\begin{cases} \langle \boldsymbol{V}_{\text{drift}}\cdot\nabla\psi\rangle(\psi,\alpha,E,\mu) &= \dfrac{m}{q\tau(\psi,\alpha,E,\mu)}\dfrac{\partial J_{\|}(\psi,\alpha,E,\mu)}{\partial\alpha}, \\ \langle \boldsymbol{V}_{\text{drift}}\cdot\nabla\alpha\rangle(\psi,\alpha,E,\mu) &= -\dfrac{m}{q\tau(\psi,\alpha,E,\mu)}\dfrac{\partial J_{\|}(\psi,\alpha,E,\mu)}{\partial\psi}. \end{cases} \tag{12.17}$$

Using the chain rule, the averaged change in $J_{\|}$ along a trajectory can then be stated as

$$\langle \boldsymbol{V}_{\text{drift}}\cdot\nabla\left(J_{\|}\right)\rangle(\psi,\alpha,E,\mu)=\left[\frac{\partial J_{\|}}{\partial\alpha}\langle \boldsymbol{V}_{\text{drift}}\cdot\nabla\alpha\rangle+\frac{\partial J_{\|}}{\partial\psi}\langle \boldsymbol{V}_{\text{drift}}\cdot\nabla\psi\rangle\right](\psi,\alpha,E,\mu)=0.$$

This implies that the drift orbits are approximately confined to surfaces of constant $J_{\|}$. Another way to state the omnigeneity condition is as follows: surfaces of constant $J_{\|}$ should align with surfaces of constant ψ.

Remark 12.1. *Quasisymmetry implies omnigeneity as follows. If a magnetic field satisfies* (12.4)*, then the radial drift* (12.10) *can be written as*

$$[\boldsymbol{V}_{\textit{drift}}\cdot\nabla\psi](\psi,\alpha,E,\mu)=\left[v_{\|}\frac{\partial}{\partial l}\left(\frac{v_{\|}}{\Omega}\right)F(\psi)\right](\psi,\alpha,E,\mu).$$

Since the time average operation involves a periodic integral over l normalized by $v_{\|}$, the averaged radial drift $\langle \boldsymbol{V}_{\textit{drift}}\cdot\nabla\psi\rangle = 0$. Therefore, quasisymmetric magnetic fields satisfy the omnigeneity property (12.14)*. However, omnigeneity includes a much wider class of magnetic fields than quasisymmetry. The relationship between quasisymmetry and omnigeneity is discussed in several references* [41, 40, 182]*. It can be shown that an infinitely differentiable omnigeneous magnetic field must be quasisymmetric* [41].

Construction of nearly omnigeneous magnetic fields has been demonstrated [241] based on equilibria near the magnetic axis introduced in Section 11.2. The Wendelstein 7-X stellarator is an example of an existing quasiomnigeneous configuration designed with numerical optimization techniques [95, 96].

12.3 ▪ Discrete symmetries

In addition to quasisymmetry or omnigeneity, stellarators can possess discrete symmetries. In contrast to a continuous symmetry, approximate particle confinement is not a consequence of discrete symmetries. Instead, discrete symmetries can be leveraged to simplify stellarator design. Invariance with respect to spatial translation, known as field period or N_P symmetry, is discussed in Section 12.3.1, while symmetry with respect to reflection about a specific plane, known as stellarator symmetry, is discussed in Section 12.3.2.

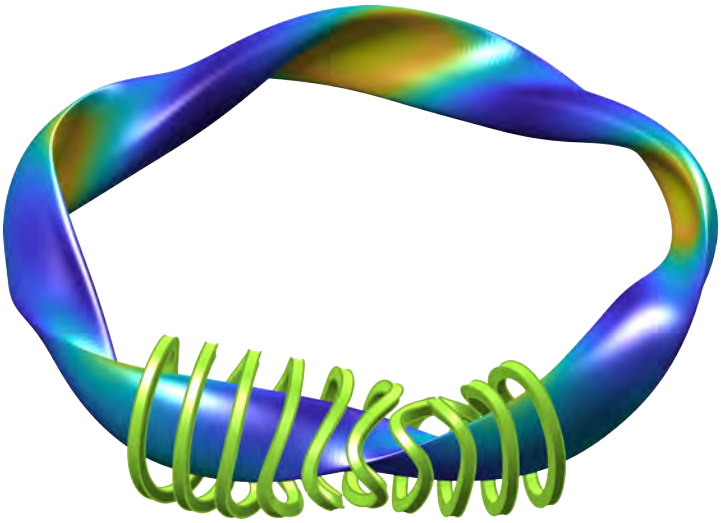

Figure 12.3*: The last closed magnetic surface of the W7-X configuration is shown with the color scale indicating the field strength. The electromagnetic coil shapes are shown for one field period of the device.*

12.3.1 ▪ Field period symmetry

A magnetic field $\boldsymbol{B}$ is said to possess field period symmetry, also known as N_P symmetry, if it satisfies

$$\begin{cases} \boldsymbol{B}(\psi, \theta, \zeta + 2\pi/N_P) = \boldsymbol{B}(\psi, \theta, \zeta), \\ \text{or } \boldsymbol{B}(R, \phi + 2\pi/N_P, Z) = \boldsymbol{B}(R, \phi, Z), \end{cases}$$

when expressed in either flux coordinates, introduced in Section 5.5.2, or cylindrical coordinates, introduced in Section 5.3. The constant N_P is a positive integer and can be referred to as the field periodicity. A given stellarator configuration is said to possess N_P symmetry if the equilibrium magnetic field $\boldsymbol{B}$ is N_P symmetric.

In an N_P symmetric configuration, many physical quantities are periodic with respect to N_P. This property can be leveraged to simplify both computational and practical problems. For example, the W7-X stellarator has five toroidal field periods, and as a result, the same coil shapes can be used for each field period. In Figure 12.3, a magnetic surface of W7-X is shown, with the color scale indicating the field strength. The electromagnetic coils are shown for one field period.

12.3.2 ▪ Stellarator symmetry

Stellarator symmetry refers to a discrete symmetry with respect to a specific reflection transformation. The assumption of stellarator symmetry has been made in the design of almost every stellarator configuration to date [186]. A detailed discussion of stellarator symmetry is given in [52].

A transformation $\mathcal{T}$ between vector fields can be defined as follows. If two vector fields $\boldsymbol{F}$ and $\boldsymbol{G}$ are such that $\boldsymbol{G} = \mathcal{T}(\boldsymbol{F})$, and can be expressed in cylindrical coordinates as

$$\begin{cases} \boldsymbol{F} = F_R \hat{\boldsymbol{R}} + F_\phi \hat{\boldsymbol{\phi}} + F_Z \hat{\boldsymbol{Z}}, \\ \boldsymbol{G} = G_R \hat{\boldsymbol{R}} + G_\phi \hat{\boldsymbol{\phi}} + G_Z \hat{\boldsymbol{Z}}, \end{cases}$$

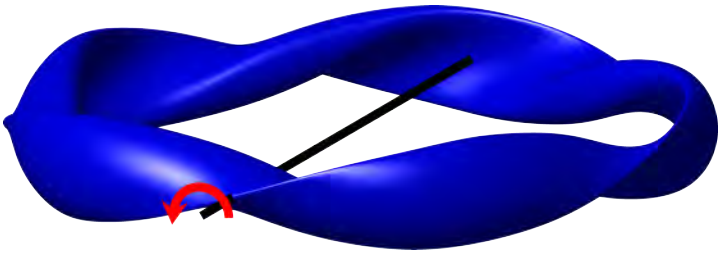

Figure 12.4*: Stellarator symmetry describes an inversion about the line* $Z = 0$, $\phi = 0$. *The last-closed surface of the stellarator symmetric W7-X configuration is shown.*

then $\boldsymbol{G}$ is defined by

$$\begin{cases} G_R(R,\phi,Z) = F_R(R,-\phi,-Z), \\ G_\phi(R,\phi,Z) = F_\phi(R,-\phi,-Z), \\ G_Z(R,\phi,Z) = F_Z(R,-\phi,-Z). \end{cases}$$

The transformation $\mathcal{T}$ is an inversion about the line $\phi = 0, Z = 0$, as illustrated in Figure 12.4. The term stellarator symmetry for a vector field $\boldsymbol{F}$ is the property defined by

$$\mathcal{T}[\boldsymbol{F}] = -F_R\hat{\boldsymbol{R}} + F_\phi\hat{\boldsymbol{\phi}} + F_Z\hat{\boldsymbol{Z}}. \tag{12.18}$$

A given stellarator configuration is said to possess stellarator symmetry if the equilibrium magnetic field $\boldsymbol{B}$ is stellarator symmetric.

It can be shown that if the magnetic field $\boldsymbol{B}$ exhibits this symmetry, then so does the current density $\boldsymbol{J}$ upon application of Ampère's law $\nabla \times \boldsymbol{B} = \mu_0 \boldsymbol{J}$ in cylindrical coordinates. Suppose that a vector field $\boldsymbol{F}$ possesses stellarator symmetry. This implies that the magnitude F of the vector field exhibits the following symmetry:

$$F(R,-\phi,-Z) = F(R,\phi,Z).$$

Thus the field strength B and magnitude of the current density J exhibit this property for a stellarator symmetric configuration.

In order to simplify the expression of some physical quantities of a stellarator symmetric field, stellarator symmetry can also be expressed in general flux coordinates (ψ,θ,ζ) introduced in Section 5.5.2, where ψ is a flux label, θ is a poloidal angle, and ζ is a toroidal angle. For a coordinate system preserving stellarator symmetry, the following property holds for the cylindrical coordinates (R,ϕ,Z):

$$\begin{cases} R(\psi,-\theta,-\zeta) = R(\psi,\theta,\zeta), \\ \phi(\psi,-\theta,-\zeta) = -\phi(\psi,\theta,\zeta), \\ Z(\psi,-\theta,-\zeta) = -Z(\psi,\theta,\zeta). \end{cases}$$

Therefore, if $\boldsymbol{G} = \mathcal{T}(\boldsymbol{F})$ where $\mathcal{T}$ is the transformation from the stellarator symmetry definition (12.18), then the cylindrical components of the fields expressed in terms of flux coordinates satisfy

$$\begin{cases} G_R(\psi,\theta,\zeta) = F_R(\psi,-\theta,-\zeta), \\ G_\phi(\psi,\theta,\zeta) = F_\phi(\psi,-\theta,-\zeta), \\ G_Z(\psi,\theta,\zeta) = F_Z(\psi,-\theta,-\zeta). \end{cases}$$

Hence, given (12.18), for a stellarator symmetric field $\boldsymbol{F}$, F_R is odd with respect to (θ, ζ) while F_Z and F_ϕ are even. Thus stellarator symmetry implies a definite parity of many physical quantities, and these quantities are even or odd with respect to (θ, ζ). Quantities with a definite parity can be expressed in terms of only a sine or cosine series rather than a general Fourier series. For example, in a stellarator symmetric field $\boldsymbol{B}$, the field strength B can be expressed with just a cosine series:

$$B(\psi, \theta, \zeta) = \sum_{m,n} B_{mn}(\psi) \cos(m\theta - n\zeta).$$

This illustrates how stellarator symmetry provides computational efficiency by reducing the number of degrees of freedom required to define a field.

Chapter 13
Optimization for stellarator design

As we have seen in Chapter 7, one advantage of stellarators compared to tokamaks is that they do not rely on a large plasma current to produce the necessary rotational transform. On the other hand, as described respectively in Sections 10.2 and 7.2, neither existence of magnetic surfaces nor single-particle confinement is guaranteed in 3D configurations as each is in axisymmetry. Instead, other desirable properties can be studied to guarantee favorable confinement capabilities. Stellarators are then carefully designed to satisfy approximately a set of desirable properties, and this is commonly formulated within an optimization framework. Optimization of tokamak magnetic fields is also possible [127]. However, because the number of degrees of freedom is reduced for 2D compared to 3D configurations, there is a smaller optimization landscape to leverage in order to improve confinement. Since confinement in stellarators is primarily provided by external fields, it may be easier to design and control the external fields to maintain good performance. On the other hand, since tokamaks rely on magnetic fields produced by the plasma for confinement, the performance becomes much more sensitive to changes in the plasma profiles. Consequently, this presents a challenge for optimizing tokamak performance as it requires controlling internal profiles. A similar situation arises for stellarator performance as the ratio of thermal to magnetic pressure, quantified by the parameter β discussed further in Section 13.1, increases. In this regime, the increased plasma pressure generally drives plasma current as discussed in Sections 10.3.1 and 13.1.1, and an increased fraction of the magnetic field is driven by the plasma current. However, even at higher β, the fraction of the magnetic field produced by the plasma current is smaller in stellarators than in tokamaks. Thus, stellarator performance may be less sensitive to changes in the plasma profiles. For these reasons, the field of numerical stellarator optimization is more developed than that of tokamak optimization.

In a stellarator device, magnets or coils must ultimately produce the desired magnetic field, and these must be manufactured and assembled. The concept of stellarator design refers to two aspects:

1. the magnetic field is designed based on equilibrium models,
2. coils are designed to generate this desired magnetic field.

In addition to the concept of confinement, central to the field design, some engineering and manufacturing considerations must also be accounted for in the coil design.

The stellarator design process can be performed with two different approaches. In the so-called two-stage approach, the field is designed first, and the coils are designed in the second step. By contrast, the field and coils are designed simultaneously in the so-called single-stage approach. Since the two-stage approach decouples the two aspects, it generally reduces the

computational cost of the problem. This advantage has made the two-stage approach more widely used. However, the second stage might result in complicated coil shapes [88, 153]. These might be impossible to construct and may also interfere with the maintenance and diagnostics of the experiment. Besides, tight tolerances on coil manufacturing and positioning are a significant driver of costs for the stellarator program. In this context, the one-stage approach provides additional flexibility, allowing for balance between engineering tolerances and deviation of physics objectives.

Stellarator design problems are commonly formulated in terms of numerical optimization: a function defining various physics or engineering objectives is minimized, possibly subject to additional constraints. Iterative optimization algorithms are then leveraged to approximate a solution to the numerical problem, either a local or a global minimum. This chapter will describe standard optimization considerations, techniques, and tools for stellarator design. Examples of desirable physical and engineering properties will be presented respectively in Sections 13.1 and 13.3. Then, based on models presented in Chapter 11, we will describe the two steps of stellarator design in the two-stage approach: optimization of the plasma boundary with the fixed-boundary approach in Section 13.2 and optimization of coil shapes in Section 13.4. Section 13.5 presents a few examples of optimized configurations to illustrate some successes and challenges.

13.1 ▪ Physics objectives for stellarator optimization

The primary goal of stellarator optimization is to achieve good plasma confinement. In the two-stage approach, confinement properties of a given equilibrium magnetic field are assessed independently of the coils.

The existence of magnetic surfaces within a large volume and confinement of single-particle trajectories are the most standard properties leveraged in stellarator design. It is important to remember that measures of these theoretical confinement properties, in practice, cannot be evaluated exactly but will be approximated from calculations of the equilibrium magnetic field. For example, symmetry properties discussed in Chapter 12 cannot be achieved exactly. However, sufficient guiding center confinement may still be achieved if these symmetry properties hold to a high enough precision.

In addition to symmetry, many other considerations, both physical and practical, can be taken into account in the optimization process. Often, proxy functions are used as simplified figures of merit for approximating the behavior of more complex physics objective functions. For example, measurements of quasisymmetry are a proxy for guiding center confinement. Defining proxy functions for stellarator optimization is an active field of research. We now outline important physics considerations and some corresponding proxy functions commonly leveraged in stellarator optimization.

13.1.1 ▪ Plasma current

The current resulting from plasma motion has an important impact on toroidal confinement devices. In a tokamak, plasma current is required for confinement, as discussed in Section 7.3.1. The plasma current in a tokamak is typically mostly externally driven, with some contribution from self-driven mechanisms. By contrast, externally driven plasma current is not required for confinement in a stellarator. Nonetheless, self-driven sources remain. In general, these self-driven sources of plasma current [116] arise from both MHD and kinetic effects. The parallel bootstrap current arises due to collisions between trapped and passing particles in the presence of density and temperature gradients. The parallel Pfirsch–Schlüter and perpendicular diamagnetic currents occur due to MHD equilibrium pressure gradients. The impact of the plasma current on some equilibrium properties and coil complexity can be considered in the design process.

The diamagnetic and Pfirsch–Schlüter currents arise from considerations of MHD force balance, $(\nabla \times \boldsymbol{B}) \times \boldsymbol{B} = \mu_0 \nabla p$, given $\boldsymbol{B}$ and p as a function of the flux label only, as mentioned in Section 10.3.1. The perpendicular diamagnetic current is evaluated from force balance as

$$\boldsymbol{J}_\perp = \frac{\boldsymbol{B} \times \nabla p}{B^2}.$$

This diamagnetic current generally arises in the presence of a pressure gradient. As for the parallel current, it satisfies the MDE resulting from $\nabla \cdot \boldsymbol{J} = 0$:

$$\boldsymbol{B} \cdot \nabla \left(\frac{J_\parallel}{B} \right) = -\nabla \cdot \boldsymbol{J}_\perp.$$

Since the MDE does not constrain the average value of the quantity on a magnetic surface $S(\psi)$, namely

$$\left\langle \frac{J_\parallel}{B} \right\rangle_{S(\psi)} = \frac{1}{4\pi^2} \int_0^{2\pi} \int_0^{2\pi} \frac{J_\parallel}{B} \, d\theta d\zeta,$$

this averaged parallel current is not set by MHD theory. The Pfirsch–Schlüter current refers to the component of the parallel current that is constrained by the MDE, namely

$$J_{\text{PS}} = J_\parallel - B \left\langle \frac{J_\parallel}{B} \right\rangle_{S(\psi)}. \tag{13.1}$$

Since the right-hand side of the MDE is proportional to the pressure gradient, the Pfirsch–Schlüter current is said to be pressure-driven. It can give rise to an outward shift of the magnetic axis, known as the Shafranov shift, potentially leading to a degradation of magnetic surfaces with increasing pressure [296] as described in Section 13.1.2. One approach to reducing the Pfirsch–Schlüter current is by minimizing the right-hand side of the MDE. This right-hand side is proportional to the geometric factor $\boldsymbol{B} \times \nabla B \cdot \nabla \psi$ and is related to the geodesic curvature, the component of the magnetic field curvature that is tangent to a flux surface. Hence, a design criterion for the W7-AS stellarator was minimizing the geodesic curvature, and experiments verified the resulting Shafranov shift [307].

Since the rotational transform impacts confinement properties in a device, it is important to emphasize the relation between current sources and the ι profile. As discussed in Section 7.3.1, in the lack of any contribution from the 3D field geometry, ι is proportional to the integrated toroidal current, defined in (9.11). It can be shown [116] that the Pfirsch–Schlüter current does not contribute toward the integrated toroidal current. On the other hand, the diamagnetic current can only contribute to the integrated toroidal current in the presence of nonzero $\langle J_\parallel / B \rangle_{S(\psi)}$. While neither the Pfirsch–Schlüter current nor the diamagnetic current directly impacts the rotational transform, they both can affect other equilibrium properties with increasing β, as described in Section 13.1.2.

While the average quantity $\left\langle J_\parallel / B \right\rangle_{S(\psi)}$ impacts the ι profile, it is not constrained by MHD yet can be determined from kinetic theory or current drive mechanisms. The bootstrap current is one important kinetic effect that can drive this averaged current. In the presence of density and temperature gradients, trapped guiding center orbits provide the bootstrap current, enhanced through collisions with passing particles. Since changes in the density and temperature profiles during device operation may modify the bootstrap current and, therefore, the ι profile, it may be desirable to minimize the bootstrap current. If the bootstrap current is reduced, the magnetic field structure becomes less sensitive to changes in β. Since the width of trapped-particle orbits drives this current source, considerations of characteristic orbit widths may inform the choice of stellarator class during the design process. For example, in quasisymmetric configurations

introduced in Section 12.1, the orbit width under the assumption of $I \ll G$ is proportional to $MG/(M\iota - N)$. The choice of quasisymmetry helicity defined through M and N has an impact on the bootstrap current as follows:

- For QP configurations, $M = 0$ and $N \neq 0$, the bootstrap current is small in magnitude and vanishes if $I = 0$.
- For QA configurations, $M \neq 0$ and $N = 0$, and the orbit width is inversely proportional to the rotational transform.
- For QH configurations, $M \neq 0$ and $N \neq 0$, the orbit width is inversely proportional to $M\iota - N$. For typical configurations, $N \gg M\iota$, and the orbit width is reduced in QH configurations compared to QA configurations. Therefore, QH configurations may be advantageous for their reduced bootstrap current.

We can also consider the impact of orbit width in omnigeneous configurations introduced in Section 12.2. While the orbit width in omnigeneous magnetic fields generally differs from the simple expression above, similar conclusions can be made with regard to the choice of helicity for the closure of the magnetic field contours. If the contours of the field strength of an omnigeneous magnetic field close poloidally, as they do in a QP configuration, the configuration is said to be quasi-isodynamic (QI). QI configurations may be advantageous for some design scenarios since they have vanishing bootstrap current [119]. Optimization for small bootstrap current may also be performed with proxy functions, such as a low-collisionality model [263] or other semi-analytic fits of kinetic calculations [181].

As an illustration, control of the edge rotational transform is vital for designs with an island divertor [84]. The divertor is the device used to remove heat and unwanted fusion products, such as helium, from the confinement region. It requires that material structures intersect a large island at a specific location. Thus, an uncontrolled shift in the rotational transform may lead to malfunction of such a divertor system. Furthermore, the rotational transform may shift to low-order rational values due to the bootstrap current. This effect may lead to the potential growth of magnetic islands, as described in Section 13.1.2, especially in low-shear devices. The Wendelstein 7-X (W7-X) configuration was designed for reduced bootstrap current [96] and is close to QI.

Despite these disadvantages of plasma current, significant bootstrap current may be desirable in some situations. For instance, the bootstrap current may provide a source of rotational transform in addition to the external coils; hence, the coil complexity may be reduced. In some situations, pressure-driven plasma current can also reduce the width of islands compared to those in a vacuum configuration [18]. For instance, the National Compact Stellarator eXperiment (NCSX) was designed to be quasiaxisymmetric with a significant fraction of rotational transform provided by the bootstrap current [131].

13.1.2 ▪ Equilibrium properties

One of the most fundamental objectives in designing a stellarator is obtaining a large volume of continuously nested magnetic flux surfaces. As explained in Chapter 10, rather than exhibiting continuously nested magnetic surfaces, a general 3D magnetic field contains islands and chaotic regions, and both may degrade confinement properties. Moreover, even while starting from an equilibrium without islands and chaotic regions, there is no guarantee that solutions to an MHD model will conserve the same magnetic field structure. Physics objectives for stellarator optimization can be based on quantifying certain equilibrium properties related to magnetic surfaces, islands, and chaotic regions, both in the equilibrium and its time evolution. The ability to obtain a large volume of nested surfaces can be related to two quantities. The first is the ratio

of the plasma pressure to the magnetic pressure, known as the plasma β. It is formally defined as $\beta := p/(B^2/(2\mu_0))$ and can be evaluated differently. For example, p and B can be evaluated at the magnetic axis, providing a local measure of β. Alternatively, p and B may be averaged over the entire plasma volume, providing a global measure of β. The second is the magnetic shear, defined as $\iota'(\psi)$.

High values for β are associated with two effects that can make achieving a large volume of nested surfaces challenging.

- Increasing plasma pressure produces an outward shift of the magnetic axis known as the Shafranov shift. At large values, when the shift becomes comparable to the minor radius, this effect leads to the break-up of flux surfaces [272, 116].
- As β is increased, the current produced by the plasma, such as the MHD-driven diamagnetic and Pfirsch–Schlüter currents and neoclassical-driven bootstrap currents, described in Section 13.1.1, can produce resonant magnetic perturbations that degrade magnetic surfaces [259, 142, 202].

For these reasons, an operating limit on β in stellarators often arises due to properties of the equilibrium. This is referred to as the equilibrium β limit.

The presence of magnetic islands is associated with two main effects impacting plasma performance in stellarators. On the one hand, magnetic islands may degrade performance since they lead to local flattening of the pressure profile [74]. On the other hand, nonlinear interactions between magnetic islands can also lead to the formation of chaotic magnetic fields [195], as illustrated in Figure 10.1. As illustrated in Section 10.3.4 for a simplified model, rational surfaces can be associated with δ-function current densities or magnetic islands, depending on whether continuously nested surfaces are assumed. To highlight the connection between magnetic islands and properties of the rotational transform, we consider here a time-independent magnetic field with continuously nested flux surfaces, expressed in magnetic coordinates $(\psi, \vartheta, \varphi)$. We then focus on a given rational surface, ψ_0, with $\iota(\psi_0) = N/M$. A resonant perturbation to the magnetic field can be applied, and its resonant radial component can be expressed in the magnetic coordinates of the unperturbed field as $\delta\boldsymbol{B} \cdot \nabla\psi = B^{\psi}_{m,n}(\psi) \exp\left(i(m\vartheta - n\varphi)\right)$, associated to a pair (m, n) satisfying $nM = mN$. In this framework [247, 193], the width of the corresponding magnetic island can be obtained as

$$w \propto \left(\frac{B^{\psi}_{m,n}(\psi_0)}{m\iota'(\psi_0)} \right)^{1/2}. \tag{13.2}$$

- Since island width goes like $1/\sqrt{m}$, resonant surfaces at low-order rationals, as defined in Remark 6.1, in the equilibrium are associated with the formation of large islands. Therefore, avoiding low-order rational surfaces can be an approach to obtaining and maintaining a large volume of nested surfaces. Since the rational numbers are dense within real numbers, a practical approach is to identify a specific set of low-order resonant values of ι and to choose a target value far from that set [231]. Hence, in this case, the magnetic shear is close to zero.
- By contrast, since island width goes like $1/\sqrt{\iota'(\psi)}$, magnetic shear can reduce island width. Therefore, an alternative approach is to target large magnetic shear. The function ι then varies significantly within the volume. While this results in ι crossing numerous low-order rational surfaces, the width of the corresponding islands is reduced due to large magnetic shear.

In practice, the magnetic island width [105] and other related figures of merit [142, 10] can be directly minimized for a set of rational surfaces in the optimization of stellarator coils.

13.1.3 ▪ Quasisymmetry and omnigeneity

As described in Chapter 12, certain symmetries of the magnetic field lead to approximate confinement of guiding center trajectories. Two strategies to achieve approximate guiding center confinement in an optimized configuration are to impose quasisymmetry or impose omnigeneity.

Quasisymmetry implies guiding center confinement [21] and neoclassical properties that are comparable to those of an equivalent tokamak [116], including the ability to rotate in the direction of quasisymmetry [121]. Quasisymmetry is typically targeted in optimization by minimizing the symmetry-breaking Fourier harmonics of the magnetic field strength. Writing B in a Fourier series in the two Boozer angles,

$$B(\psi, \vartheta_B, \varphi_B) = \sum_{m,n} B_{m,n}(\psi) e^{i(m\vartheta_B - n\varphi_B)},$$

a common objective function to achieve approximate quasisymmetry with helicity M and N is a function of ψ only defined as

$$f_{\text{QS},1}(\psi) = \frac{\sum_{mN \neq nM} B_{m,n}^2(\psi)}{B_{0,0}^2(\psi)}. \tag{13.3}$$

The alternative form of quasisymmetry described in Section 12.1.3 can also be used to define an objective function [184]:

$$f_{\text{QS},2}(\psi) = \left\langle \left(\frac{\boldsymbol{B} \times \nabla\psi \cdot \nabla B - F \boldsymbol{B} \cdot \nabla B}{B^2} \right)^2 \right\rangle_\psi, \tag{13.4}$$

where F defined through (12.5) is a function of ψ only and $\langle \cdot \rangle_\psi$ is the flux-surface average defined in (6.23).

An omnigeneous magnetic field does not allow any time-averaged drift of particles off magnetic surfaces. Omnigeneity can be targeted in optimization by computing properties of the parallel adiabatic invariant (12.16). If $J_\parallel$ is constant on a magnetic surface for all values of the particle energy and magnetic moment, then the collisionless trajectories will experience no net radial drift, or the magnetic field is omnigeneous [41]. Thus, several properties involving $J_\parallel$, such as its variation within a flux surface for all classes of particles,

$$f_{\text{QO}}(\psi, E) = \int_0^{\mu_{\max}} \int_0^{2\pi} \left(J_\parallel(\psi, \alpha, E, \mu) - \langle J_\parallel(\psi, \alpha, E, \mu) \rangle_\psi \right)^2 d\alpha d\mu, \tag{13.5}$$

have been targeted in stellarator optimization [274, 62]. Here a fixed value of E can be chosen while integration is performed for all μ since the geometric dependence of $J_\parallel$ only enters through $B_{\text{crit}} = E/\mu$ in (12.15). Alternatively, the magnetic field can be compared with models that are explicitly constructed to be omnigeneous [92, 154, 65], and the difference between the two can be minimized.

13.1.4 ▪ Neoclassical transport

Collisions between charged particles will generally enhance the transport due to guiding center drifts due to the unconfined particle motion. Known as neoclassical transport, this process is amplified in nonomnigeneous configurations. Neoclassical theory predicts the behavior of the bulk population of charged particles, described by a Maxwell–Boltzmann distribution to the

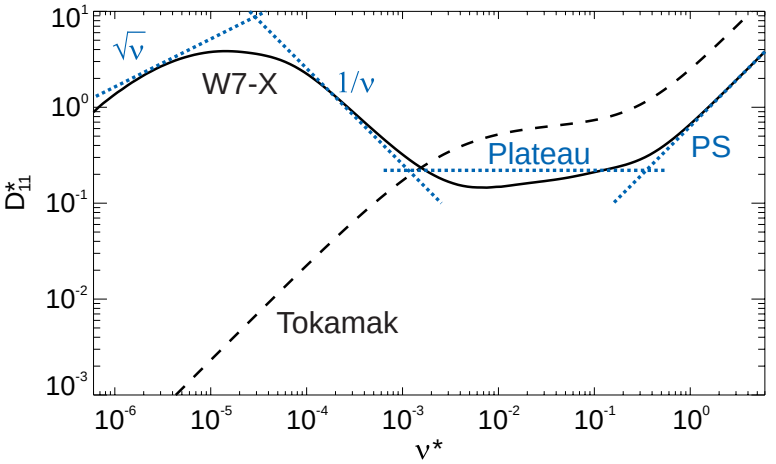

Figure 13.1*: The so-called neoclassical diffusion coefficient, D^*_{11}, as a function of the normalized collisionality, $\nu_* = \nu R/(\iota v)$, where ν is the collision frequency, ι is the rotational transform, v is the speed, and R is the major radius. The dashed and solid curves correspond respectively to a tokamak equilibrium field and to the W7-X equilibrium field. At higher collisionality, the stellarator and tokamak fields exhibit similar scaling of the diffusion coefficient with ν^*. At low collisionality, the axisymmetric field exhibits a regime in which $D^*_{11} \propto \nu$, while the stellarator exhibits $D^*_{11} \propto 1/\nu$. Thus, the neoclassical transport in a general 3D field can be especially deleterious at low collisionality. Figure reproduced from* [117]*. Used with permission of IOP Publishing, Ltd, from "Stellarator and tokamak plasmas: a comparison," P. Helander, C. D. Beidler, T. M. Bird, M. Drevlak, Y. Feng, R. Hatzky, F. Jenko, R. Kleiber, J. H. E. Proll, Yu. Turkin,* 54, 12, 2012*; permission conveyed through Copyright Clearance Center, Inc.*

lowest order. The Maxwell–Boltzmann distribution models a population of particles of mass m and temperature T in thermodynamic equilibrium

$$f(\boldsymbol{v}) = A \exp\left(-\frac{mv^2}{2T}\right) \tag{13.6}$$

for constant A.

In classical unoptimized stellarators, neoclassical transport is typically the dominant transport channel, as opposed to turbulent transport due to fluctuations. Stellarators experience enhanced neoclassical transport at low collisionality in comparison with tokamaks, as illustrated in Figure 13.1. Since neoclassical transport is reduced in quasisymmetric and omnigeneous magnetic fields, objective functions defined in Section 13.1.3 can be targeted to improve neoclassical confinement. Neoclassical transport is often computed with reduced models [322, 172]. As an example, the effective ripple [224, 236] quantifies the geometric dependence of transport in the low-collisionality $1/\nu$ regime:

$$\epsilon_{\text{eff}}^{3/2}(\psi) = \frac{\pi}{4\sqrt{2}V'(\psi)\epsilon_{\text{ref}}^2} \int_{1/B_{\max}}^{1/B_{\min}} \int_0^{2\pi} \sum_i \frac{\left(\dfrac{\partial K_i(\alpha,\lambda)}{\partial \alpha}\right)}{\lambda I_i(\alpha,\lambda)} \, d\lambda d\alpha. \tag{13.7}$$

Here $\lambda = \mu/E$ is the pitch angle, $B_{\min}$ and $B_{\max}$ are the minimum and maximum values of the field strength on a surface labeled by ψ, ϵ_{ref} is a reference aspect ratio, and $V(\psi)$ is the volume enclosed by the constant ψ surface. Summation is performed over trapping wells, and

this requires identifying all the points where the field magnitude B is equal to the critical value B_{crit} along a given field line. We have defined the integrals along a field line:

$$\begin{cases} I_i(\alpha,\lambda) &= \oint \dfrac{v_\parallel}{Bv}\, dl, \\ K_i(\alpha,\lambda) &= \oint \dfrac{v_\parallel^3}{Bv^3}\, dl. \end{cases}$$

A brief overview of neoclassical physics in stellarators can be found in Section 4 of [116]. A review of neoclassical optimization strategies is given in [221].

13.1.5 ▪ Energetic particles

Energetic particles are particles with much higher velocities than the typical velocity of the entire population. To be more precise, we can introduce the bulk population, consisting of particles approximately in thermodynamic equilibrium, described by a Maxwell–Boltzmann distribution (13.6). The typical velocity of the bulk can then be quantified using the thermal velocity of a Maxwellian distribution, $v_t = \sqrt{2T/m}$. In this context, energetic particles are then defined as particles with $v \gg v_t$.

Alpha particles, produced through a nuclear fusion reaction, as mentioned in Section 1.2, are an example of energetic particles. In order for the fusion reactions to be self-sustaining, alpha particles must be confined long enough to deposit their energy in the bulk population. Losses of energetic particles concentrated in a region of space can lead to damage of in-vessel experimental components and must be avoided.

The confinement of energetic particles can be studied by following single-particle trajectories in the presence of collisions with other charged particles [59, 209]. Collisional diffusion and deflection are minimal at energies near the birth energy of 3.5 MeV for a D-T reaction (Chapter 3 in [120]), so collisionless guiding center orbits are an informative metric of energetic particle confinement. If the collision frequency is small enough that energetic ions can complete their bounce or transit orbits, then the parallel adiabatic invariant (12.16) is an approximately conserved quantity along energetic particle trajectories. Thus, one method to improve energetic particle confinement under the collisionless approximation is by targeting omnigeneity or quasisymmetry as described in Section 13.1.3.

By optimizing equilibria to be close to quasisymmetry, it has been shown that excellent energetic particle confinement can be obtained [184, 181]. There is some evidence that targeting quasisymmetry near the half-radius may also improve energetic particle confinement [122]. Confinement can also be improved [60, 9] by targeting objective functions that quantify the net radial drift of certain classes of trapped particles [62, 225, 295]. As an example, a common function to quantify confinement [225, 295] is

$$\gamma_c(\psi,\alpha,E,\mu) = \frac{2}{\pi}\tan^{-1}\left(\frac{\langle \boldsymbol{V}_{\text{drift}}\cdot\nabla\psi\rangle\,(\psi,\alpha,E,\mu)}{\langle \boldsymbol{V}_{\text{drift}}\cdot\nabla\alpha\rangle\,(\psi,\alpha,E,\mu)}\right), \tag{13.8}$$

defined in terms of the average radial and in-surface drifts introduced in (12.17). Minimizing γ_c promotes the alignment of surfaces of constant $J_\parallel$ with magnetic surfaces.

13.1.6 ▪ Stability

Stability is a general property of equilibria in the context of dynamical systems. The robustness of an equilibrium to perturbations is referred to as stability. Stability is defined as follows in

terms of the time evolution of solutions starting from a perturbed state, defined as the sum of the equilibrium plus a small perturbation. For a stable equilibrium, any given perturbation away from equilibrium will decay in time. On the other hand, an unstable equilibrium is characterized by perturbations that grow in time.

The stability of magnetically confined fusion plasmas to macroscopic perturbations is well modeled by MHD theory, as for instance discussed in Chapter 2 of [75]. Starting from a perturbation of an MHD unstable equilibrium, the plasma might evolve toward a lower energy state. This process can result in significant expulsion of energy from the plasma and lowering confinement, potentially damaging device components. The maximum achievable plasma β can also be limited by MHD instabilities associated with pressure gradients and magnetic field curvature. This imposes constraints on the parameter space in which devices can be operated, also known as operating regimes.

Common proxies for reducing pressure-driven MHD instabilities include the Mercier criterion [211] and the magnetic well parameter [94],

$$f_W(\psi) = V''(\psi), \tag{13.9}$$

where $V(\psi)$ is the volume enclosed by the magnetic surface labeled by ψ and primes indicate derivatives.

These criteria have been widely applied in stellarator optimization [318, 260, 42, 123]. The magnetic shear, introduced in Section 13.1.2 in the context of equilibrium magnetic islands, can also be used to improve stability with respect to pressure-driven modes [114].

While linear MHD stability proxy functions are often used in design studies, there is some experimental evidence that stellarator configurations may be able to operate above the linear MHD stability β threshold [303]. Rather than restricting the operating regime, MHD instabilities can grow to relatively small amplitudes that slowly degrade the confinement. For example, the LHD has operated up to a volume-averaged β of 5% without any abrupt termination of the plasma due to large-scale MHD instabilities [259]. While the operating β may not always be determined by pressure-driven instabilities, it may be desirable to design a stellarator with an increased linear β limit to reduce transport caused by MHD modes.

In addition to pressure-driven modes, a class of MHD instabilities can be driven by plasma current. Since stellarators have a much smaller total current than tokamaks, they enjoy overall enhanced stability properties. However, as β increases, the bootstrap and Pfirsch–Schlüter currents described in Section 13.1.1 may increase in magnitude, and current-driven modes may become unstable. Thus, reducing these sources of self-driven current may enhance MHD stability.

13.1.7 ▪ Summary

In Table 13.1, we summarize common confinement objectives for stellarator optimization.

13.2 ▪ Fixed-boundary MHD optimization

Both the free-boundary approach and the fixed-boundary approach to computing an MHD equilibrium were introduced in Section 11.1.2. As a reminder, in the former, the computational domain includes not only the plasma volume but also a vacuum region surrounding the plasma, as well as the location of electromagnetic coils supporting prescribed currents. By contrast, in the fixed-boundary approach to compute an MHD equilibrium on a given domain Ω, the boundary $\partial\Omega$ of the computational domain is the plasma boundary. The latter is, therefore, the natural approach in the framework of two-stage stellarator optimization and is the topic of this section.

Table 13.1*: Summary of common stellarator equilibrium objectives.*

Physics parameter	*Equilibrium properties*	*Stability*	*Collisionless particle confinement*	*Neoclassical particle confinement*
Island width (13.2)	✓			
Shafranov shift	✓			
Magnetic shear	✓	✓		
Bootstrap current	✓	✓		
Pfirsch–Schlüter current (13.1)	✓	✓		
Geodesic curvature	✓	✓	✓	✓
Mercier criterion		✓		
Magnetic well (13.9)		✓		
Quasisymmetry (13.3), (13.4)			✓	✓
Omnigeneity (13.5), (13.8)			✓	✓
Effective ripple (13.7)				✓

The MHD equilibrium equations are repeated here for convenience:

$$\begin{cases} (\nabla \times \boldsymbol{B}) \times \boldsymbol{B} = \mu_0 \nabla p & \text{in } \Omega, \\ \nabla \cdot \boldsymbol{B} = 0 & \text{in } \Omega, \\ \boldsymbol{B} \cdot \hat{\boldsymbol{n}} = 0 & \text{on } \partial\Omega. \end{cases} \tag{13.10}$$

Solutions are computed assuming that a continuously nested set of magnetic surfaces exist, labeled by the toroidal flux $2\pi\psi$ as explained in Section 5.5.1. Magnetic coordinates $(\psi, \vartheta, \varphi)$ can then be used to describe the domain. The pressure, $p(\psi)$, and one other function of flux, such as the rotational transform $\iota(\psi)$ or enclosed toroidal current $I_T(\psi)$, are prescribed. Many models of 3D equilibria exist, as discussed in Chapter 11. However, this model has historically been the standard choice for fixed-boundary optimization using codes such as VMEC [132], NSTAB [79], BETA [11], or DESC [66]. This is partly for computational efficiency, as the variational principle introduced in Section 11.1.1 can be employed. The assumption, discussed in Remark 4.4, of continuously nested flux surfaces is also convenient as many physical quantities of interest are based on models with magnetic surfaces, such as the Boozer coordinate transformation introduced in Section 9.2.

In this context, the magnetic geometry throughout the volume Ω is determined by the shape of $\partial\Omega$. As many physical parameters depend on the magnetic geometry, it is thus reasonable to search for the optimal shape of $\partial\Omega$ with respect to a set of physics objectives. This is the fixed-boundary optimization approach, first introduced by Nührenburg and Zille [232].

The plasma boundary, $\partial\Omega$, is a toroidal surface and can be parameterized by a poloidal angle θ and toroidal angle ϕ. The toroidal angle is often chosen to coincide with the cylindrical angle ϕ. In cylindrical coordinates, the plasma boundary can be described by the radius $R(\theta, \phi)$ and the height $Z(\theta, \phi)$. These coordinates can be expressed in a Fourier series. In particular, under the assumption of stellarator symmetry introduced in Section 12.3.2, $R(\theta, \phi)$ is even in (θ, ϕ) while $Z(\theta, \phi)$ is odd in (θ, ϕ). Since they are also real-valued, they can then be expressed compactly

in terms of real Fourier series as

$$\begin{cases} R(\theta,\phi) = \displaystyle\sum_{(m,n)\in\mathcal{D}^R} R_{m,n}\cos(m\theta - n\phi), \\ Z(\theta,\phi) = \displaystyle\sum_{(m,n)\in\mathcal{D}^Z} Z_{m,n}\sin(m\theta - n\phi), \end{cases} \tag{13.11}$$

where, by a combination of the real-valued and parity properties of R and Z, $\mathcal{D}^Z \subset \mathbb{Z}^2$ is the set of (m,n) pairs such that $n > 0$ only for $m = 0$ otherwise $n \in \mathbb{Z}$ for $m \geq 0$, or more compactly $\mathcal{D}^Z := (\mathbb{N}\times\mathbb{Z}) \cup (\{0\}\times\mathbb{N})$, and $D^R = D^Z \cup (0,0)$. Equivalently we could choose $\tilde{\mathcal{D}}^Z := (\mathbb{Z}\times\mathbb{N}) \cup (\mathbb{N}\times\{0\})$; however, the previous choice is more common. So, the set of parameters

$$\left\{R_{m,n} \in \mathbb{R}, (m,n) \in \mathcal{D}^R\right\} \cup \left\{Z_{m,n} \in \mathbb{R}, (m,n) \in \mathcal{D}^Z\right\}$$

uniquely defines the shape of $\partial\Omega$. In practice, a finite number of these modes are retained. Assuming that the maximum poloidal and toroidal mode numbers are fixed and denoted respectively by M and N, the finite sets $\mathcal{D}^R_{M,N}$ and $\mathcal{D}^Z_{M,N}$ of indices are defined as

$$\begin{cases} \mathcal{D}^R_{M,N} := \{(m,n) \in D^R, m \leq M, |n| \leq N\}, \\ \mathcal{D}^Z_{M,N} := \{(m,n) \in D^Z, m \leq M, |n| \leq N\}. \end{cases}$$

The corresponding $2(2MN + M + N) + 1$ parameters

$$\left\{R_{m,n} \in \mathbb{R}, (m,n) \in \mathcal{D}^R_{M,N}\right\} \cup \left\{Z_{m,n} \in \mathbb{R}, (m,n) \in \mathcal{D}^Z_{M,N}\right\}$$

are the minimization variables for the fixed-boundary MHD optimization. This is simply one choice of parameterization for toroidal surfaces used in the widely used VMEC code. Another possible choice used in the NSATB code is the Garabedian representation [77, 80].

Given a plasma boundary, as well as two free functions of the flux, such as the pressure p and either the toroidal current enclosed by a flux surface I_T or the rotational transform ι, the problem is then to find an MHD equilibrium field $\boldsymbol{B}$ satisfying (13.10) on the corresponding domain. Under additional assumptions [139, 233], including assumptions on the pressure profile (see [134, 54] and the related Section 11.5), the problem can be well-posed, meaning that there exists a unique solution. In practice, an approximate solution can be computed thanks to a numerical method. Alternatively, the current can be considered an output of the equilibrium calculation, determined by self-consistent modeling of the bootstrap current, the parallel current predicted by neoclassical theory [131, 279, 181]. In this approach, the equilibrium is computed with an iterative method: (i) an MHD equilibrium is computed with a prescribed $I_T(\psi)$ according to (13.10), and (ii) the bootstrap current $I_T^{\text{boots}}(\psi)$ is computed from the resulting equilibrium field. If the two currents do not match, then $I_T(\psi)$ is updated to $I_T^{\text{boots}}(\psi)$ for the next iteration. The two steps are iterated until $I_T(\psi)$ and $I_T^{\text{boots}}(\psi)$ match.

Given an equilibrium field, the total objective function, usually denoted by χ^2, is commonly defined via contributions from various specific objectives. For quantities of interest defined by functions $f_i^{\text{equilibrium}}$ of the field and associated target values f_i^{target}, the total objective function can then be written as

$$\chi^2(\boldsymbol{B}) = \sum_i \frac{\left(f_i^{\text{target}} - f_i^{\text{equilibrium}}(\boldsymbol{B})\right)^2}{\sigma_i^2}, \tag{13.12}$$

where the σ_i's are scaling factors setting the relative importance of each of the contributions. Depending on the specific objectives, the total objective χ^2 can be evaluated, for instance, directly from the Fourier coefficients of $\boldsymbol{B}$ as in Section 13.1.2, or can require some postprocessing, such

as computing its magnitude or performing integration as in Section 13.1.4. While some possible choices of objectives were introduced in Section 13.1, choosing the physics objectives in order to define the total objective χ^2, including the functions $f_i^{\text{equilibrium}}$ as well as the target values f_i^{target}, is an active field of research.

If the boundary is described for fixed maximum poloidal and toroidal mode numbers, M and N, by a set of $2(2MN + M + N) + 1$ coefficients

$$\mathcal{S}_{N,M} := \left\{R_{m,n} \in \mathbb{R}, (m,n) \in \mathcal{D}^R_{M,N}\right\} \cup \left\{Z_{m,n} \in \mathbb{R}, (m,n) \in \mathcal{D}^Z_{M,N}\right\},$$

and if $\boldsymbol{B}_b$ denotes the MHD equilibrium defined by (13.10) on the corresponding domain, the fixed-boundary optimization problem can be expressed as

$$\min_{\mathcal{S}_{N,M}} \chi^2\Big(\boldsymbol{B}_b\left(\mathcal{S}_{N,M}\right)\Big).$$

The choice of optimization algorithm will determine how the optimization parameters are adjusted to arrive at a local or global minimum within a given tolerance. In practice, several optimization algorithms have been applied to the fixed-boundary approach [274, 222, 60], including gradient-free methods such as the Brent algorithm [31], particle swarm [234], and differential evolution [276], as well as gradient-based methods such as the Levenberg–Marquardt algorithm [216]. Historically, gradient-based methods for equilibrium optimization rely on finite-difference approximations of the gradient rather than analytic gradients. Recent advances in the numerical methods related to stellarator optimization will be further discussed in Chapter 14.

To summarize this fixed-boundary approach, the problem is to find an optimal toroidal surface representing the boundary of a plasma in an equilibrium model. The problem is defined in terms of the following.

- The objective function χ^2 is defined in terms of the functions $f_i^{\text{equilibrium}}$ and the values $\left\{f_i^{\text{target}}, \sigma_i\right\}_i$.
- Two flux functions, $p(\psi)$ and $I_T(\psi)$, are fixed to define a well-posed equilibrium problem, or $I_T(\psi)$ is iterated for consistency with bootstrap current calculations.

The complete optimization process can be described by the following iterative method.

1. (Initialization) Find an initial boundary shape $\partial\Omega^{\text{init}}$.
   (a) Compute the initial MHD equilibrium magnetic field in Ω from $\partial\Omega^{\text{init}}$.
   (b) Evaluate the objective χ^2 from the resulting magnetic field.
2. (Iteration) Until χ^2 satisfies a stopping criterion, repeat the following steps.
   (a) Adjust $\partial\Omega$ according to the optimization algorithm.
   (b) Compute the MHD equilibrium magnetic field in Ω from $\partial\Omega$.
   (c) Evaluate the objective χ^2 from the resulting magnetic field.

In practice, this process relies on two codes: an MHD equilibrium code to compute an approximate MHD equilibrium and an optimization code implementing the optimization algorithm. For example, equilibrium calculations are often performed in VMEC, DESC, or SPEC, and this scheme is implemented in various optimization codes, including STELLOPT [273], ROSE [60], SIMSOPT [183], and DESC [64]. Moreover, other physics codes can be used in order to evaluate equilibrium properties and objective functions.

The first demonstration of this approach by Nührenberg and Zille [232], leveraging the BETA equilibrium code, resulted in the Helias class of stellarators. The boundary was optimized to

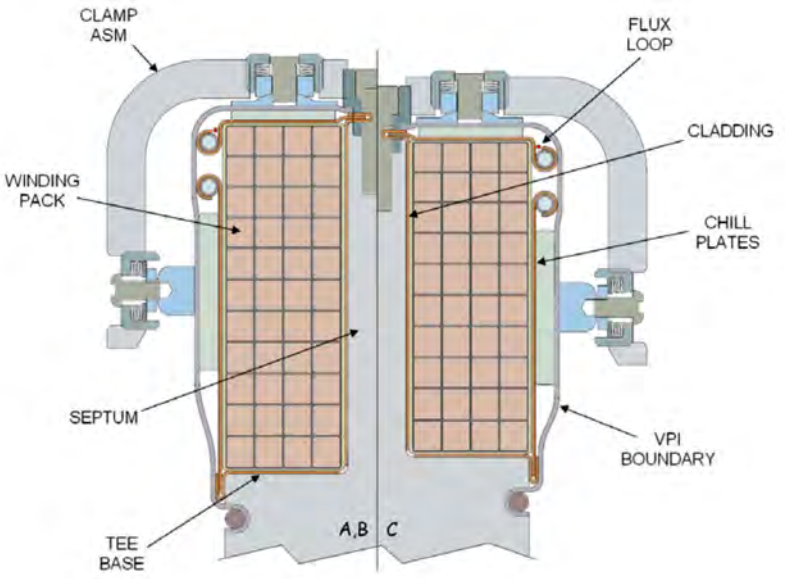

Figure 13.2*: A cross-section of a modular coil of the NCSX stellarator, displaying the conducting material that comprises the winding pack in addition to support and cooling structures. Figure reproduced from* [277]*. Reprinted from B. Stratton, A. Brooks, T. Brown, D. Johnson, G. Labik, E. Lazarus, N. Pomphrey, S. Raftopoulos, M. Zarnstorff; External magnetic diagnostics for the National Compact Stellarator Experiment. Rev. Sci. Instrum.* 1 *October* 2006*;* 77 (10)*:* 10*E*314*, with the permission of AIP Publishing.*

obtain a quasisymmetric magnetic field, in addition to considerations on the rotational transform, on the magnetic well, and on bootstrap current. The W7-X stellarator was later designed based on further optimization of one of the Helias configurations [13]. Several other examples will be given in Section 13.5.

In the two-stage approach, once the fixed-boundary optimization is complete, a set of electromagnetic coils consistent with $\partial\Omega$ are sought. This generally nontrivial task will be discussed next.

13.3 ▪ Engineering metrics for stellarator optimization

In a stellarator, the plasma shape and confinement properties depend strongly on the magnetic field produced by the coils and, thus, on the properties of the coils themselves. Historically, the construction and assembly of stellarator coils have been a significant driver of the cost of stellarator experiments [159, 252]. This makes coils and their properties a key consideration in modern stellarator optimization.

A critical engineering aspect is the manufacturability of a coil set, as coil shapes that are very complex are more difficult to build and install. The electromagnets providing the magnetic field in stellarators consist of several substructures, including several turns of conducting material, support structures, and cooling systems. For context, the winding pack of one NCSX modular coil is provided in Figure 13.2. The compatibility of stellarator coil shapes with the required winding pack structure must be accounted for in the optimization.

The coil shapes must also not interfere with other required device components. The region between the plasma boundary and the coils is needed to allow for several experimental

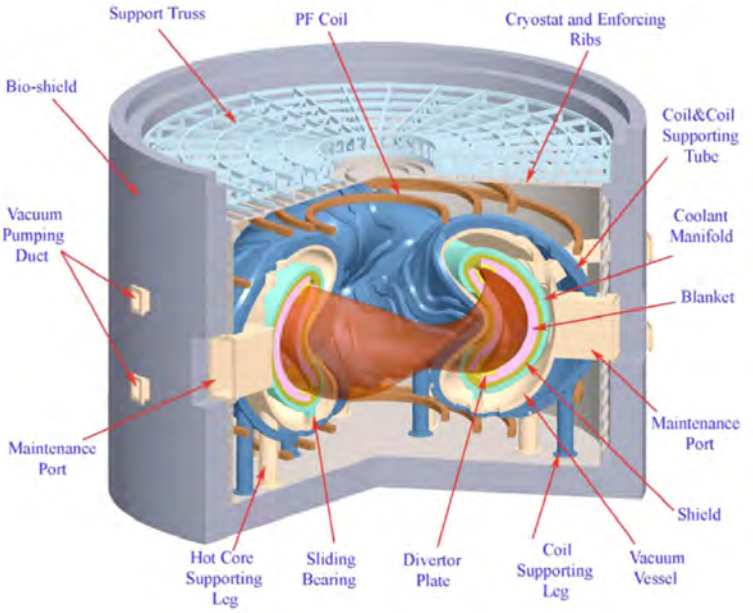

Figure 13.3*: A schematic of the ARIES-CS stellarator power plant concept. The modular coils lie on a supporting surface (blue). There must be sufficient space between coils to accommodate maintenance ports and vacuum pumping ducts. There must be sufficient space between the coils and the plasma (red) to allow for the blanket (pink), divertor plates (yellow), neutron shielding (dark yellow), coolant manifold (green), and vacuum vessel (beige). Figure reproduced from* [223]*. The ARIES-CS compact stellarator fusion power plant, Najmabadi, F., Raffray, A. R., Abdel-Khalik, S. I., Bromberg, L., Crosatti, L., El-Guebaly, L., . . . Zarnstorff, M., Fusion Science and Technology,* 54 (2008)*, pp.* 655–672*, reprinted by permission of Taylor & Francis Ltd.*

components, such as the first wall and vacuum vessel. In a reactor, a minimum coil-plasma distance is necessary to have sufficiently thick neutron shielding and blanket used for absorption of neutrons and tritium breeding [172]. Moreover, there should be sufficient width between coils to allow for diagnostic and maintenance ports. In Figure 13.3, a schematic diagram of the ARIES-CS stellarator power plant concept illustrates how stellarator coils must accommodate various structures in an experiment or reactor.

These engineering features can be quantified using several objective functions.

- *Coil length*: Long coils are costly since more conducting material is required.
- *Coil curvature*: There is a minimum value of the radius of curvature due to the cross-section of the winding pack. Tight bends may also reduce the integrity of conducting material.
- *Coil torsion*: Torsion, measuring the nonplanarity of the coil, may lead to strains on the conducting material.
- *Coil-coil spacing*: Sufficient space is needed for diagnostic and maintenance access.
- *Coil-plasma distance*: Sufficient room is needed for the vacuum vessel, first wall, and coil casing. In a reactor, additional room is needed for the blanket and neutron shielding.

The specific formulation of these objective functions under several coil models is discussed in Sections 13.4.4 and 13.4.5.

13.4 ▪ Coil optimization

In the two-stage optimization approach, electromagnetic coils are optimized as a second step, given a target outer boundary of the plasma, $\partial\Omega$, as well as the magnetic field due to the plasma current in Ω, both obtained from the first step. The confinement region then refers to the volume bounded by the plasma boundary. Coils are a set of electromagnets, or currents, intended to be placed outside of the confinement region in order to produce the desired confining magnetic field. It is important to keep in mind that this magnetic field, in practice, is numerically computed from an equilibrium model.

In order to produce the desired magnetic field, the primary goal is thus to find a set of currents, $\boldsymbol{J}^{\text{coil}}$, in the vacuum regions such that the corresponding total magnetic field—the sum of the magnetic field due to $\boldsymbol{J}^{\text{coil}}$, $\boldsymbol{B}^{\text{coil}}$, and a given magnetic field, $\boldsymbol{B}^{\text{plasma}}$, due to the plasma currents—is tangent to $\partial\Omega$:

$$\boldsymbol{B} \cdot \hat{\boldsymbol{n}}|_{\partial\Omega} = 0, \tag{13.13}$$

where $\hat{\boldsymbol{n}}$ denotes the exterior tangent on $\partial\Omega$. Sometimes coil optimization is instead performed given a prescribed normal field on a reference surface, but for simplicity, we will assume that $\partial\Omega$ is a magnetic surface. The following discussion would still hold if we replace (13.13) by a boundary condition imposing a nontrivial value of $\boldsymbol{B}\cdot\hat{\boldsymbol{n}}|_{\partial\Omega}$ on a reference surface. The magnetic field due to the coils can be computed from the Biot–Savart law (A.9), while the magnetic field due to the plasma current is an input for this step. We restrict our interest to a subset of coils, taking into account engineering-related constraints discussed in Section 13.3. We will assume that there is a distance $d_c > 0$ between the boundary of the plasma and the coils. We will also assume that the coils are contained in a bounded volume. These two assumptions are summarized by the definition of a volume Ω_c, including the support of the current $\boldsymbol{J}^{\text{coil}}$. Therefore the coil design problem can initially be expressed as follows: for a fixed plasma volume Ω, given $\boldsymbol{B}^{\text{plasma}}(\boldsymbol{r})$ on the plasma boundary $\partial\Omega$, find $\boldsymbol{J}^{\text{coil}}(\boldsymbol{r}')$ for all $\boldsymbol{r}' \in \Omega_c \subset \mathbb{R}^3\backslash\Omega$ such that

$$\boldsymbol{B}^{\text{plasma}}(\boldsymbol{r}) \cdot \hat{\boldsymbol{n}}(\boldsymbol{r}) = -\frac{\mu_0}{4\pi} \int_{\Omega_c} \frac{\boldsymbol{J}^{\text{coil}}(\boldsymbol{r}') \times (\boldsymbol{r} - \boldsymbol{r}') \cdot \hat{\boldsymbol{n}}(\boldsymbol{r})}{|\boldsymbol{r} - \boldsymbol{r}'|^3}\, d\boldsymbol{r}' \tag{13.14}$$

for all $\boldsymbol{r} \in \partial\Omega$.

Problems of the form (13.14) are generally ill-posed, as is discussed in Section 13.4.1. We then discuss several regularization methods for such problems in Section 13.4.2. The material in these two sections is independent of the following ones and is intended to provide a theoretical view of the mathematical problem expressed in (13.14).

Instead, a common approach is to formulate a coil design optimization problem as presented next in Section 13.4.3, combining an objective targeting the approximation of (13.14), together with an additional engineering objective. Further common assumptions imposed on the coils problem are discussed in the following sections, including assumptions on the support of the currents along with desirable properties of coils.

While the unknown $\boldsymbol{J}^{\text{coil}}$ was initially introduced with support in $\Omega_c \subset \mathbb{R}^3\backslash\Omega$, from the experimental point of view, the currents will be supported by coils. Such stellarator coils have an actual volume, referred to as their finite build, consisting of several layers, each with several turns of the conducting material. As a first approximation, the finite build of coils is often not taken into account during the design process: the support of the unknown function $\boldsymbol{J}^{\text{coil}}$ is limited to having no volume. There are two most common ways to model such coils: assuming that all currents in

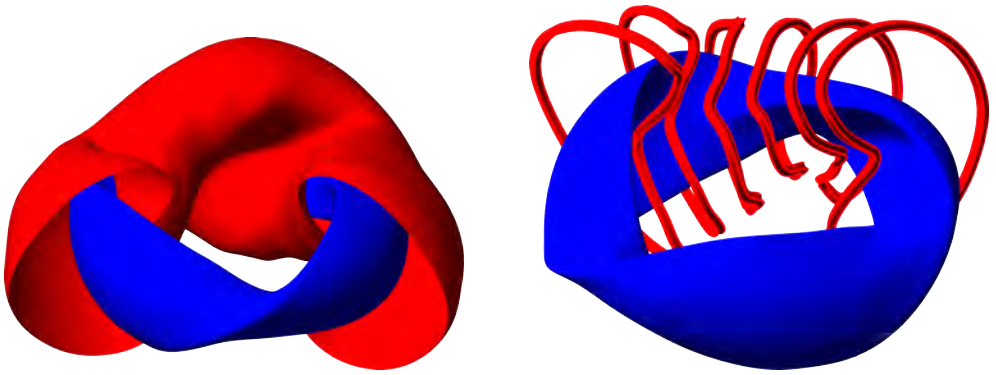

(a) (b)

Figure 13.4*:* (a) *The outer boundary of the NCSX LI*383 *equilibrium* [322] *is shown (blue) along with a winding surface (red) that is chosen to be uniformly offset from the plasma boundary.* (b) *Coils (red) computed from REGCOIL using the winding surface and target plasma boundary are shown for one period of the device.*

the region Ω_c are restricted to a toroidal surface, as discussed in Section 13.4.4, or assuming that the currents are restricted to a finite number of filamentary lines, as discussed in Section 13.4.5. In the latter case, the curves will define the shapes of the physical coils, while in the former case, the coil shapes will be chosen in a postprocessing step following some streamlines of the computed current. An illustration is provided in Figure 13.4.

13.4.1 ▪ Ill-posedness of first-kind integral equations

This section is dedicated to showing that the coil design problem is ill-posed in the following sense. In the mathematical community, a problem is said to be well-posed in the sense of Hadamard [97] if

1. it has a unique solution;

2. small changes in prescribed data result in small changes in the solution.

Otherwise, the problem is said to be ill-posed.

The integral problem (13.14) is in the form of a Fredholm integral equation of the first kind. Given functions K and g, such a problem has the general form

$$\text{Find } f \text{ such that } g(t) = \int K(t,s) f(s)\, ds. \tag{13.15}$$

The function K is called the kernel of the integral term. Each of the functions f and g can be defined in any dimension $d \in \mathbb{N}$, their domains of definition can be bounded or not, and they may be vector-valued. For instance, the integral problem (13.14) involves a vector-valued unknown $\boldsymbol{J}^{\text{coil}}$, the integral is taken over a 3D bounded set Ω_c, and the Green's function kernel is vector-valued. More details on the domain of definition of the unknown $\boldsymbol{J}^{\text{coil}}$ will be subject to discussion in the following sections. We will now infer that integral equations of the first kind are ill-posed in the following sense:

- there does not necessarily exist a solution for any given function g,

- in some cases, the solution is not unique,
- small changes in prescribed data g do not, in general, control the corresponding change in the solution f.

The theory of integral operators and integral equations has been widely developed in the literature. Standard applications include scattering theory and inverse problems [45] or linear flow problems [243]. The discussion in this section is based on [104, 168, 306]. Here, to present the mathematical challenges associated with Fredholm integral equations of the first kind, we will consider the following setting:

- two domains, $\Omega_1 \subset \mathbb{R}^{d_1}$ on which the equation holds, and the domain of integration $\Omega_2 \subset \mathbb{R}^{d_2}$, not necessarily bounded;
- two real Hilbert spaces, $\mathcal{H}_1 = L^2(\Omega_1, \mathbb{R}^{n_1})$ and $\mathcal{H}_2 = L^2(\Omega_2, \mathbb{R}^{n_2})$, the Lebesgue spaces of functions $G : \Omega_i \to \mathbb{R}^{n_i}$ such that $\int_{\Omega_i} G(t) \cdot G(t)\, dt < \infty$, equipped with the standard inner product

$$\langle G, H \rangle = \int_{\Omega_i} G(t) \cdot H(t)\, dt \quad \forall G, H \in \mathcal{H}_i \text{ for } i = 1, 2;$$

  these are also called spaces of measurable square-integrable functions, either scalar-valued if $n_i = 1$ or vector-valued if $n_i > 1$;
- square-integrable kernels $K : \Omega_1 \times \Omega_2 \to \mathbb{R}^{n_1 \times n_2}$ in the sense

$$\int \int_{\Omega_1 \times \Omega_2} \|K(t,s)\|^2_{\mathbb{R}^{n_1 \times n_2}}\, dtds < \infty,$$

  where $\|\cdot\|_{\mathbb{R}^{n_1 \times n_2}}$ is the matrix norm induced by the Euclidean vector norms, that is to say, $\|A\|_{\mathbb{R}^{n_1 \times n_2}} = \sup\{\|Ax\|_{\mathbb{R}^{n_1}} : x \in \mathbb{R}^{n_2}, \|x\|_{\mathbb{R}^{n_2}} = 1\}$.

For instance, for the integral problem (13.14), the data is prescribed on the surface defining the plasma boundary, $\Omega_1 = \partial\Omega \in \mathbb{R}^3$, so $d_1 = 3$, the volume outside of which the current vanishes is $\Omega_2 = \Omega_c \in \mathbb{R}^3$, so $d_2 = 3$, the data is scalar-valued, $n_1 = 1$, the unknown $\boldsymbol{J}^{\text{coil}}$ is vector-valued, $n_2 = 3$, and the kernel is square integrable as it is bounded on the bounded domain $\partial\Omega \times \Omega_c$.

For all the following arguments, we will consider K to be square integrable. Given $f \in \mathcal{H}_2$, the function defined on Ω_1 by

$$t \mapsto \int_{\Omega_2} K(t,s) f(s)\, ds$$

is an element of $\mathcal{H}_1$, since as K and f are both square integrable

$$\begin{aligned}&\int_{\Omega_1} \left(\int_{\Omega_2} K(t,s) f(s)\, ds \right) \cdot \left(\int_{\Omega_2} K(t,s) f(s)\, ds \right) dt \\ &\leq \int_{\Omega_1} \left(\int_{\Omega_2} \|K(t,s)\|^2_{\mathbb{R}^{n_1 \times n_2}}\, ds \right) \left(\int_{\Omega_2} f(s) \cdot f(s)\, ds \right) dt < \infty.\end{aligned}$$

Hence, we can define a linear operator $F_K : \mathcal{H}_2 \to \mathcal{H}_1$ as the mapping

$$f \mapsto \int_{\Omega_2} K(\cdot, s) f(s)\, ds. \tag{13.16}$$

The problem at stake can then be posed abstractly as

$$\begin{aligned}&\text{Assume } g \in \mathcal{H}_1 \text{ and } K \text{ are given.} \\ &\text{Find } f \in \mathcal{H}_2 \text{ such that } F_K[f] = g.\end{aligned} \tag{13.17}$$

Square-integrable kernels give rise to integral operators belonging to a class known as compact operators. Compact operators share many properties with operators in finite-dimensional spaces. However, due to the infinite dimensionality of the spaces involved, they are very sensitive to variations in problem data. In a metric space, a compact operator can be characterized by the fact that the image of any bounded sequence by the operator contains a converging subsequence. See, for instance, Chapter 22 in [191]. The key property leading to the ill-posedness of the integral problem (13.14) is that the associated operator F_K is compact.

The operator F_K has an adjoint operator, F_K^*, defined by

$$\langle F_K[G], H\rangle = \langle G, F_K^*[H]\rangle \quad \forall (G,H) \in \mathcal{H}_2 \times \mathcal{H}_1,$$

and this adjoint is also compact. The composition $F_K^* F_K$ is self-adjoint, since

$$\begin{aligned}\forall G, H \in \mathcal{H}_2,\ \langle F_K^* F_K[G], H\rangle &= \langle F_K[G], F_K[H]\rangle \\ &= \langle G, F_K^* F_K[H]\rangle.\end{aligned}$$

The set of eigenvalues of a self-adjoint operator is countable. For $F_K^* F_K$ they will be denoted $\{\alpha_i\}_{i\in\mathbb{N}}$, repeated according to their multiplicity, while the set of associated eigenfunctions $\{\varphi_i\}_{i\in\mathbb{N}}$ forms a basis of $\mathcal{H}_2$. It can be shown that $\{\alpha_i\}_{i\in\mathbb{N}}$ are nonnegative, and they form either a finite set or a countably infinite set with $\alpha_i \to 0$ [168]. Therefore, we can number the eigenvalues $\{\alpha_i\}$ in decreasing order such that $\alpha_1 \geq \alpha_2 \geq \cdots \geq 0$. We define N_F to be the largest integer such that $\alpha_{N_F} > 0$ and $\alpha_i = 0$ for all $i > N_F$ if there is a finite number of eigenvalues, or $N_F = \infty$ if there is a countable infinite set of eigenvalues.

The singular values of F_K are then defined as $\mu_i := \sqrt{\alpha_i}$ for i from 1 to N_F while the associated singular functions are defined for i from 1 to N_F by

$$\begin{cases} u_i = \varphi_i \in \mathcal{H}_2, \\ v_i = \dfrac{F_K[u_i]}{\mu_i} \in \mathcal{H}_1, \end{cases}$$

that satisfy, for i from 1 to N_F,

$$\begin{cases} F_K[u_i] = \mu_i v_i, \\ F_K^*[v_i] = \mu_i u_i. \end{cases} \tag{13.18}$$

Furthermore, from the orthonormality of the $\{\varphi_i\}$ basis, the singular functions satisfy the following orthonormality conditions:

$$\begin{cases} \langle u_i, u_j\rangle = \delta_{i,j}, \\ \langle v_i, v_j\rangle = \delta_{i,j}. \end{cases} \tag{13.19}$$

Finally, if $N_F < \infty$, we can conveniently set $\mu_i = 0$ for all $i > N_F$, define a basis of the null space of F_K by $\{u_i = \varphi_i, i > N_F\}$, and let $\{v_i, i > N_F\}$ be any orthonormal basis of $\mathcal{H}_1 \setminus \mathrm{Span}\{v_i, i \leq N_F\}$. As a result, independently of the value of N_F, the sets $\{u_i, i \in \mathbb{N}\}$ and $\{v_i, i \in \mathbb{N}\}$ form orthonormal bases of $\mathcal{H}_2$ and $\mathcal{H}_1$. Then (13.18) still holds for $\{u_i\}$ and $\{v_i\}$ with $i \in \mathbb{N}$, since for all $i > N_F$ we have

$$\begin{cases} F_K[u_i] = 0 = \mu_i v_i, \\ F_K^*[v_i] = \displaystyle\sum_{j=1}^{\infty} u_j \langle , F_K^*[v_i], u_j\rangle = \sum_{j=1}^{N_F} u_j \langle v_i, F_K[u_j]\rangle = \mu_i u_i. \end{cases}$$

From (13.18) and (13.19), the image of the operator F_K can then be described in terms of singular functions as

$$\begin{aligned}\forall f \in \mathcal{H}_2,\ F_K[f] &= \sum_{i=1}^{\infty} v_i \langle F_K[f], v_i\rangle \\ &= \sum_{i=1}^{\infty} v_i \mu_i \langle f, u_i\rangle,\end{aligned}$$

hence

$$\forall f \in \mathcal{H}_2,\ F_K[f] = \sum_{i=1}^{N_F} v_i \mu_i \langle f, u_i\rangle. \tag{13.20}$$

We can now turn back to the problem (13.17), now reformulated as follows. For a given square-integrable kernel K, there exists an associated singular value decomposition (SVD) of the corresponding compact integral operator F_K. The SVD provides singular values and functions $\{(\mu_j, u_j, v_j), j \in \mathbb{N}\}$. Any $g \in \mathcal{H}_1$ is uniquely defined by its coordinates in the $\{v_i\}_i$ basis,

$$g = \sum_{i=1}^{\infty} \langle v_i, g\rangle v_i,$$

so the problem reads as follows:

$$\begin{aligned}&\text{Assume } g = \sum_{i=1}^{\infty} \langle v_i, g\rangle v_i \in \mathcal{H}_1 \text{ is given.} \\ &\text{Find } f \in \mathcal{H}_2 \text{ such that } \sum_{i=1}^{N_F} v_i \mu_i \langle f, u_i\rangle = g.\end{aligned} \tag{13.21}$$

We first consider the case in which $N_F < +\infty$. In this case, problem (13.21) has no unique solution, as the linear operator (13.16) has a nontrivial null space. To demonstrate this, suppose that $\hat{f}(s)$ satisfies (13.21). Then for any $n > N_F$, $f := \hat{f} + u_n$ will also be a solution since u_n is in the null space of F_K. Thus, the problem is not well-posed.

In this case, the image of $\mathcal{H}_2$ by the operator F_K is included in $\mathcal{H}_1$, but here it is smaller than $\mathcal{H}_1$. Indeed, from (13.20) then $F_K[\mathcal{H}_2] = \text{Span}\{v_i, 1 \le i \le N_F\}$, so $F_K[\mathcal{H}_2] \neq \mathcal{H}_1$. As a result, although a solution may not exist for all functions g in $\mathcal{H}_1$, there exists a solution as long as g belongs to the image $F_K[\mathcal{H}_2]$,

$$g \in F_K[\mathcal{H}_2] \Leftrightarrow \langle v_i, g\rangle = 0 \ \ \forall i > N_F.$$

Under this condition, then g can be expressed in terms of v_i singular functions as

$$g = \sum_{i=1}^{N_F} \langle v_i, g\rangle v_i,$$

and one particular (nonunique) solution to (13.21) can be written as

$$f = \sum_{i=1}^{N_F} \frac{u_i \langle v_i, g\rangle}{\mu_i},$$

while any solution is given, for any set of coefficients $\{c_i \in \mathbb{R}, i \ge N_F + 1\}$, by

$$f = \sum_{i=1}^{N_F} \frac{u_i \langle v_i, g\rangle}{\mu_i} + \sum_{i=N_F+1}^{\infty} c_i \varphi_i(s).$$

We now consider the case $N_F = \infty$, so that $\mu_i > 0$ for all i with $\mu_i \to 0$ as $i \to \infty$. Then $g \in \mathcal{H}_1$ can be expressed in the singular function basis as

$$g = \sum_{i=1}^{\infty} \langle v_i, g \rangle v_i.$$

So, from (13.20), if a function $f \in \text{Span}\{u_i, i \in \mathbb{N}\}$ is a solution to (13.21), it necessarily reads

$$f = \sum_{i=1}^{\infty} \frac{\langle v_i, g \rangle}{\mu_i} u_i. \tag{13.22}$$

Note that since $\mu_i \to 0$ as $i \to \infty$, this shows that f is less smooth than g, and F_K is sometimes described as a smoothing operator. Thus, for a square-integrable solution to exist, we must have

$$\langle f, f \rangle < \infty \Leftrightarrow \sum_{i=1}^{\infty} \left(\frac{\langle v_i, g \rangle}{\mu_i} \right)^2 < \infty. \tag{13.23}$$

The above condition effectively sets a constraint on the allowable $g \in \mathcal{H}_1$ that can be prescribed such that (13.21) has a solution in $\mathcal{H}_2$. However, under this condition, the solution is unique. Note that the constraint on g is stronger than that required for square-integrability, namely

$$\langle g, g \rangle < \infty \Leftrightarrow \sum_{i=1}^{\infty} \langle v_i, g \rangle^2 < \infty,$$

since the $\mu_i \to 0$. Therefore, again the image $F_K[\mathcal{H}_2]$ is a subspace of $\mathcal{H}_1$ that is smaller than $\mathcal{H}_1$. Thus, the problem, as stated in (13.21), is ill-posed, as a solution does not exist unless additional constraints are placed on the prescribed data K and g.

We have now considered both cases of N_F finite and $N_F = +\infty$. In both cases, we find that the problem stated as (13.21) does not have a solution unless an additional constraint is placed on g. Thus, the general problem (13.17) is ill-posed, as a square-integrable solution does not exist for every $g \in \mathcal{H}_1$. In other words, the compact linear operator F_K defined on the infinite-dimensional Hilbert space $\mathcal{H}_2$ does not have a continuous inverse.

Next, suppose that we consider g such that (13.23) is satisfied and a square-integrable solution exists. Now, we consider the second condition for a well-posed problem by evaluating the result of perturbation in the prescribed data. Consider a perturbation of the data by $g \to g + \delta g$. For the coils problem, this could come from any numerical error in the computed normal magnetic field from the equilibrium. In particular, we consider a perturbation $\delta g = \Delta v_{i_0}$ for a scalar Δ and particular singular vector v_{i_0}. This will result in a perturbation of the solution by

$$\delta f = \frac{u_{i_0} \Delta}{\mu_{i_0}},$$

which follows from (13.22). The condition for square-integrability of δf now becomes

$$\sum_{i=1}^{\infty} \frac{\langle v_i, \delta g \rangle^2}{\mu_i^2} = \frac{\Delta^2}{\mu_{i_0}^2} < \infty.$$

The above condition does not hold for an arbitrary perturbation of the data, as the $\mu_i \to 0$ as $i \to \infty$, and a nonzero perturbation δg can be made in the direction v_{i_0} for $i_0 \to \infty$. Thus, the perturbation of the data may result in an arbitrarily large perturbation of the solution, and the problem is generally ill-posed. In this way, solving an integral equation of the first kind tends to amplify noise.

In general, a numerical approximation of a given equation may be viewed as the solution to the same equation with perturbed data, so the ill-posed nature of the problem has consequences for the numerical approximation of a solution. Despite the possible ill-posedness of the problem, there is considerable interest in methods for a stable numerical approximation of a solution when a solution exists. Computing a numerical approximation of the solution can be more or less challenging depending on further properties of the kernel K, and it is more challenging when the kernel is smooth [320]. In the particular case of (13.14), since the equation is evaluated at $\boldsymbol{r}$, away from the domain of integration Ω_c, the kernel is smooth, therefore the coil design problem is numerically challenging.

We will now turn to classical methods for the numerical treatment of integral equations of the first kind for a general kernel K that have been leveraged in the plasma physics literature.

13.4.2 ▪ Regularization

In order to be able to compute accurately and efficiently a numerical approximation to a solution of a challenging ill-posed problem, the problem can first be reformulated as a well-posed problem to be solved approximately by a numerical method. In the context of ill-posed problems, regularization methods refer to stable numerical methods to compute an approximate solution to the initial problem. Such methods usually rely on a modified well-posed problem, the so-called regularized problem. This one, unlike the original problem, is well-posed, so it can be solved thanks to a stable numerical method. This process introduces an error due to the approximation of the problem, and accuracy has to be balanced with stability. We limit our discussion here to two standard methods, truncated SVD and Tikhonov regularization, while more details can be found in [168].

The main results from this section can be summarized as follows. Given the singular vectors $\{v_i\}$ and $\{u_i\}$ and singular values $\{\mu_i\}$ of the integral operator F_K, for a parameter k, the truncated SVD problem reads as follows:

$$\begin{aligned} &\text{Given } g_k = \sum_{i=1}^{k} \langle v_i, g\rangle v_i \in \mathcal{H}_1, \\ &\text{find } f_k \in \mathcal{H}_2 \text{ such that } \sum_{i=1}^{k} v_i \mu_i \langle f_k, u_i\rangle = g_k. \end{aligned} \tag{13.24}$$

The Tikhonov regularized problem reads as follows:

$$\text{Find } W \in \mathcal{H}_2 \text{ such that } G_K[W] = F_K^*[g],$$

where the operator $G_K : \mathcal{H}_2 \to \mathcal{H}_2$ is defined as $G_K = F_K^* F_K + \lambda I$, I being the identity operator on $\mathcal{H}_2$ and $\lambda > 0$ is a parameter to be fixed. The Tikhonov problem can be equivalently formulated as the optimization problem,

$$\min_{W \in \mathcal{H}_2} \chi^2(W) \text{ where } \chi^2(W) := \langle g - F_K[W], g - F_K[W]\rangle + \lambda \langle W, W\rangle .$$

For both regularization methods,

- a unique, square-integrable solution exists;
- a square-integrable change to the data g yields a square-integrable change to the solution f;
- the regularization parameter, k or λ, balances the stability of the solution with the accuracy of the integral equation.

These statements are explained in the following.

The truncated SVD problem (13.24) naturally has a unique solution given by

$$f_k = \sum_{i=1}^{k} \frac{u_i \langle g, v_i \rangle}{\mu_i}. \tag{13.25}$$

By construction, f_k is square integrable as it is a finite sum: the effect of the small singular values as $i \to \infty$ are not retained in comparison with the solution of the ill-posed problem (13.22). The application of this truncation also improves the stability of the solution with respect to noise in the prescribed data. Indeed, consider a perturbation of the data $g \to g + \delta g$, resulting in a perturbation of the solution

$$\delta f_k = \sum_{i=1}^{k} \frac{u_i}{\mu_i} \langle \delta g, v_i \rangle. \tag{13.26}$$

Thanks to the truncation, the noise associated with large i is removed; thus, δf_k is square-integrable. If $\langle g, v_i \rangle / \mu_i$ decays sufficiently fast as $i \to \infty$, then f_k will yield a good approximation for f as $k \to \infty$. In this way, the regularized problem (13.24) is well-posed according to the definition presented in Section 13.4.1.

This then provides a natural approach to construct a numerical method to approximate a solution of (13.17) by solving numerically the well-posed regularized problem (13.24). It is, however, important to understand the role of the regularization parameter k. For the regularized solution (13.25), we can compute the residual $R[f_k] := g - F_K[f_k]$ for the initial problem,

$$R[f_k] = \sum_{i=k+1}^{\infty} v_i \langle v_i, g \rangle.$$

As the regularization parameter k goes to infinity, the residual $R[f_k]$ goes to zero since it contains fewer nonzero components, while the numerical stability decreases. Indeed, although δf_k will remain square integrable as long as k is finite, a given perturbation of the data, δg, in the direction of one of the singular vectors, v_i, will result in a larger perturbation of the solution as in (13.26) due to its multiplication by $1/\mu_i$. On the other hand, for $k \to 1$, the numerical stability increases while the residual $R[f_k] \to g$, so f_k is a poor approximation to the initial problem. As a consequence, the role of the regularization parameter k is to balance the accuracy and stability of the regularized problem.

As the mere definition of the regularized problem relies here on the singular values of the operator F_K, it is crucial to keep in mind that any numerical method relying on the truncated SVD regularization will require some approximation of these singular values. The truncated SVD technique has been applied to compute approximate solutions of (13.14) in several stellarator coil design codes [242, 180]. In these two references, both the right-hand side g and the unknown f are supported on toroidal surfaces. The problem is then naturally approximated in terms of truncated Fourier series, and the approximated truncated SVD is computed as the SVD of the discretized linear integral operator. The minimum approximated singular value retained in the SVD computation must be chosen carefully in order to improve numerical stability while maintaining accuracy. Another application of a similar truncated SVD technique to stellarator design can be found in [171].

A second common regularization method is Tikhonov regularization [290], introducing additional information about the nature of the solution in the regularized problem. The first-kind integral problem (13.17) can be formulated as an optimization problem by seeking W, that minimizes the residual $g - F_K[W]$. In the Tikhonov approach, one seeks to minimize the sum of the residual, $g - F_K[W]$, and a regularization term. The residual term is also called a penalty

term. The additional term can be chosen appropriately depending on the desired or expected features of the solution, the most classical choice being related to the norm of the solution. The corresponding regularized problem then reads

$$\min_{W\in\mathcal{H}_2} \chi^2(W) \text{ where } \chi^2(W) := \langle g - F_K[W], g - F_K[W]\rangle + \lambda \langle W, W\rangle,$$

where λ is a parameter to be fixed. We will now show that this regularized problem is well-posed for $\lambda > 0$. The above functional, χ^2, is strongly convex (see Chapter 3 in [27]) as its second variation with respect to W is positive definite,

$$\delta^2\chi^2(W;\delta W,\delta W) = 2\langle \delta W, (F_K^* F_K + \lambda)\,\delta W\rangle > 0 \quad \forall \delta W \in \mathcal{H}_2,$$

for any $\lambda > 0$, as $F_K^* F_K$ is a symmetric positive semidefinite operator. Thus, χ^2 has a unique global minimum. The functional reaches its minimum value at its unique stationary point W_m, defined by

$$\begin{aligned}
&\delta\chi^2(W_m;\delta W) = 0, \quad \forall \delta W \in \mathcal{H}_2,\\
&\Leftrightarrow 2\langle \delta W, F_K^*\,(F_K W_m - g) + \lambda W_m\rangle = 0, \quad \forall \delta W \in \mathcal{H}_2,\\
&\Leftrightarrow (F_K^* F_K + \lambda)\, W_m = F_K^*[g].
\end{aligned}$$

Solving the regularized problem is, therefore, equivalent to solving the following linear problem:

$$\text{Find } W \in \mathcal{H}_2 \text{ such that } G_K[W] = F_K^*[g], \tag{13.27}$$

where the operator $G_K : \mathcal{H}_2 \to \mathcal{H}_2$ is defined as $G_K = F_K^* F_K + \lambda I$, I being the identity operator on $\mathcal{H}_2$. Due to the strong convexity of χ^2, a unique solution to $G_K[W] = F_K^*[g]$ exists. Since it is equivalent to the regularized problem, then the regularized problem itself has a unique solution. As the equation is linear, uniqueness can also be proved as follows: the uniqueness of the solution is equivalent to the null space of the operator G_K being trivial. This can be proved for $\lambda > 0$. Indeed, for any W such that $G_K[W] = 0$, then $\langle G_K[W], W\rangle = 0$, hence $\lambda\langle W, W\rangle + \langle F_K[W], F_K[W]\rangle = 0$, implying that $W = 0$ if (and only if) $\lambda > 0$.

To underscore the benefit of Tikhonov regularization, we consider the eigenspectrum of G_K. We note that the eigenfunctions of $F_K^* F_K$, denoted by $\{\varphi_i\}_{i\in\mathbb{N}}$, will also be eigenfunctions of G_K with corresponding eigenvalues $\{\alpha_i + \lambda\}_{i\in\mathbb{N}}$, where $\{\alpha_i\}_{i\in\mathbb{N}}$ are the eigenvalues of $F_K^* F_K$. The image of the operator G_K can then be expressed in terms of its eigenspectrum as

$$\begin{aligned}
\forall W \in \mathcal{H}_2, \quad G_K[W] &= G_K\left[\sum_{i=1}^{\infty} \varphi_i \langle W, \varphi_i\rangle\right]\\
&= \sum_{i=1}^{\infty} G_K[\varphi_i]\langle W, \varphi_i\rangle\\
&= \sum_{i=1}^{\infty} (\alpha_i + \lambda)\varphi_i \langle W, \varphi_i\rangle.
\end{aligned}$$

Thanks to the properties of the singular functions (13.18), the quantity $F_K^*[g]$ can be expanded in the basis of the singular functions of F_K as

$$F_K^*[g] = \sum_{i=1}^{\infty} \langle u_i, F_K^*[g]\rangle u_i = \sum_{i=1}^{\infty} \langle F_K[u_i], g\rangle u_i = \sum_{i=1}^{\infty} \mu_i \langle v_i, g\rangle u_i.$$

This shows again that the problem (13.27) has a unique solution given by

$$W_m = \sum_{i=1}^{\infty} u_i \frac{\mu_i}{\mu_i^2 + \lambda} \langle v_i, g\rangle, \tag{13.28}$$

and it is the unique solution to the regularized problem. Indeed, we can easily verify that this function is square integrable for any $\lambda > 0$ and $g \in \mathcal{H}_1$, as

$$\langle W_m, W_m \rangle = \sum_{i=1}^{\infty} \frac{\mu_i^2}{(\mu_i^2 + \lambda)^2} \langle v_i, g \rangle^2 \leq \frac{1}{4\lambda} \sum_{i=1}^{\infty} \langle v_i, g \rangle^2 = \frac{1}{4\lambda} \langle g, g \rangle < \infty. \tag{13.29}$$

The above holds due to the inequality of arithmetic and geometric means, $x + y \geq 2\sqrt{xy}$ for all nonnegative x and y. We can now show that Tikhonov regularization improves the stability of the solution to perturbation of the data. Consider a perturbation $g \to g + \delta g$; from (13.28)–(13.29) it results in a perturbation of the solution given by

$$\delta W_m = \sum_{i=1}^{\infty} u_i \frac{\mu_i}{\mu_i^2 + \lambda} \langle v_i, \delta g \rangle \quad \text{with } \langle \delta W_m, \delta W_m \rangle \leq \frac{\langle \delta g, \delta g \rangle}{4\lambda}. \tag{13.30}$$

Thus, a square-integrable change in the prescribed data, δg, will result in a square-integrable change to the solution, δW_m, and the norm of the change in the solution is controlled by the norm of the change in the data. In this way, the regularized problem (13.27) is well-posed according to the definition presented in Section 13.4.1. The solution of the regularized problem now depends continuously on the prescribed data, g, for any $\lambda > 0$.

This provides another natural approach to construct a numerical method for approximate solutions of (13.17), by solving numerically the well-posed regularized problem (13.27). It is, however, important to understand the role of the regularization parameter λ. For the regularized solution (13.28), we can compute the residual $R[W_m] := g - F_K[W_m]$ for the initial problem,

$$R[W_m] = \sum_{i=1}^{\infty} \frac{\lambda}{\mu_i^2 + \lambda} \langle v_i, g \rangle v_i.$$

So for $\lambda \to \infty$, that is, for a large regularization term, the constant in the stability estimate (13.30) is $1/(4\lambda) \to 0$, while the residual $R[W_m] \to g$, so W_m is a poor approximation to the initial problem. Large values of λ are associated with low accuracy. In contrast, for $\lambda \to 0$, that is, for a small regularization term, the residual $R[W_m] \to 0$ independently of the data g, while the constant in the stability estimate (13.30) is $1/(4\lambda) \to \infty$, so the solution becomes more sensitive to noise in the data. Small values of λ are associated with poor stability. As a consequence, again, the role of the regularization parameter λ is to balance the accuracy and stability of the regularized problem.

To summarize, the first regularization method relies on a well-posed finite-dimensional problem while the second method relies on a well-posed optimization problem in infinite dimensions. Following this discussion on integral equations of the first kind, including their ill-posedness and methods for regularization, we return to the practical formulation of the coil design problem. The construction of an approximated solution to the first-kind integral equation (13.14) combined with other constraints via the numerical treatment of optimization problems will be addressed next after additional assumptions guided by practical considerations lead to a simplified problem.

13.4.3 ▪ Overview of the coil design problem

The ill-posedness of the integral equation (13.14) can be seen as beneficial, as the existence of many possible solutions reproducing the desired plasma boundary within a given tolerance allows some flexibility. Given this freedom inherent to the coil design process, desirable properties of coils, as introduced in Section 13.3, can be taken into account in formulating an optimization problem for the numerical approximation of coils.

In order to find approximate solutions that minimize the error in the integral equation (13.14), the additional desired coil properties are introduced under the form of a regularization term in the hope of defining a well-posed discrete problem. Given a current, the total objective function, usually denoted by χ^2, is commonly defined as

$$\chi^2\left(\boldsymbol{J}^{\text{coil}}\right) = \chi_B^2\left(\boldsymbol{J}^{\text{coil}}\right) + \lambda\chi_{\text{coil}}^2\left(\boldsymbol{J}^{\text{coil}}\right), \tag{13.31}$$

including a contribution for equilibrium properties, χ_B^2, and one for engineering properties of coils, χ_{coil}^2.

The primary goal, accounted for by the first term, is to find a current consistent with the desired equilibrium. While other equilibrium properties can also be taken into account, the standard objective function simply targets the normal field error. More precisely, given $\boldsymbol{B}^{\text{plasma}}(\boldsymbol{r})$ on the plasma boundary $\partial\Omega$, the total field depending on the current $\boldsymbol{J}^{\text{coil}}$ is defined as

$$\boldsymbol{B}\left[\boldsymbol{J}^{\text{coil}}\right](\boldsymbol{r}) = \boldsymbol{B}^{\text{plasma}}(\boldsymbol{r}) + \frac{\mu_0}{4\pi}\int_{\Omega_c}\frac{\boldsymbol{J}^{\text{coil}}(\boldsymbol{r}')\times(\boldsymbol{r}-\boldsymbol{r}')}{|\boldsymbol{r}-\boldsymbol{r}'|^3}\,d\boldsymbol{r}'.$$

Then, the normal field error at the plasma boundary can be expressed as

$$\chi_B^2\left(\boldsymbol{J}^{\text{coil}}\right) = \int_{\partial\Omega}\left(\boldsymbol{B}\left[\boldsymbol{J}^{\text{coil}}\right](\boldsymbol{r})\cdot\hat{\boldsymbol{n}}(\boldsymbol{r})\right)^2 d^2r, \tag{13.32}$$

where the domain of integration is the plasma boundary $\partial\Omega$, even though the value of the total field there depends on the values of the current supported away from this plasma boundary.

The specific expression of objectives for the additional desired coil properties in χ_{coils}^2 depends on further assumptions on the support of the current $\boldsymbol{J}^{\text{coil}}$. Thus, we will discuss separately the specifics of these regularization terms for each of the two models for current support: the toroidal surface and the set of curves.

13.4.4 ▪ Winding surface model

The first stellarator coil optimization tools were based on a winding surface approximation. Rather than seeking a current supported in a volume Ω_c, as in (13.14), the support of the unknown current is assumed to be restricted to a given surface called the winding surface. Furthermore, the current must be tangent to this surface. Leveraging the periodicity along the genus one winding surface, as well as the divergence-free condition, leads to a considerably simplified optimization problem. The individual coil shapes that are to be built in the experiment are obtained later as a postprocessing step. Compared to the individual coils, this winding surface approximation is often thought of as a limit of a very large number of individual coils.

As the coil optimization objective (13.31) is a function of the coil current $\boldsymbol{J}^{\text{coil}}$, it is then natural to leverage hypotheses on this current, namely its surface support and its divergence-free property, in order to define convenient minimization variables.

In terms of a mathematical model, a genus one surface S_{coil} will support an unknown surface current $\boldsymbol{K}$. The surface S_{coil} is assumed to be given, parameterized by a poloidal angle θ and toroidal angle ζ, and the plasma boundary $\partial\Omega$ is nested inside S_{coil}. This is illustrated in Figure 13.4. The corresponding 3D current $\boldsymbol{J}_K$ supported by and tangent to S_{coil} is then expressed as

$$\boldsymbol{J}_K(\boldsymbol{r}) = \begin{cases} \boldsymbol{K}(\theta(\boldsymbol{r}),\zeta(\boldsymbol{r})), & \boldsymbol{r}\in S_{\text{coil}},\\ 0 & \text{otherwise,}\end{cases}$$

where $\hat{\boldsymbol{n}}\cdot\boldsymbol{K} = 0$ on the surface. Moreover, while a smooth current density is divergence-free given Ampère's law, the equivalent condition for a current density supported on a surface is the

vanishing of the surface divergence, $\nabla_{S_{\text{coil}}} \cdot \boldsymbol{K} = 0$. The derivation of this condition can be found in Appendix C.3, using the local coordinate system $\left(b, \widetilde{\theta}, \widetilde{\zeta}\right)$ introduced in Appendix C.1. Given the definition of the surface divergence, this can be stated equivalently as

$$\frac{1}{\sqrt{g}}\left[\frac{\partial\left(\sqrt{g}\boldsymbol{K}\cdot\nabla\theta\right)}{\partial\theta}+\frac{\partial\left(\sqrt{g}\boldsymbol{K}\cdot\nabla\zeta\right)}{\partial\zeta}\right]=0.$$

Remark 13.1. *The previous equation is of the form* (6.1)*. Considering the coordinates* (θ,ζ) *as well as* $F_1 = \sqrt{g}\boldsymbol{K}\cdot\nabla\theta$ *and* $F_2 = \sqrt{g}\boldsymbol{K}\cdot\nabla\zeta$*, we can thus apply the results discussed in Section* 6.1.

According to Remark 13.1, for the surface divergence–free field $\boldsymbol{K}$, there exists one function Φ_{p} periodic in (θ,ζ) and two constants, G and I, satisfying, for

$$\Phi(\theta,\zeta) = \Phi_{\text{p}}(\theta,\zeta) + \frac{G\theta}{2\pi} + \frac{I\zeta}{2\pi}, \tag{13.33}$$

the following relations:

$$\begin{cases} \boldsymbol{K}\cdot\nabla\theta = \dfrac{1}{\sqrt{g}}\dfrac{\partial\Phi}{\partial\zeta}, \\ \boldsymbol{K}\cdot\nabla\zeta = -\dfrac{1}{\sqrt{g}}\dfrac{\partial\Phi}{\partial\theta}. \end{cases}$$

Remark 13.2. *It follows that the vector field* $\boldsymbol{K}$ *can then be expressed in terms of the current potential* Φ *as*

$$\boldsymbol{K} = \hat{\boldsymbol{n}}\times\nabla\Phi. \tag{13.34}$$

As a result of (13.34)*,* $\boldsymbol{K}\cdot\nabla\Phi = 0$*, or current streamlines flow along contours of the current potential. Thus, in postprocessing the winding surface current, filamentary coils can be chosen conveniently as a subset of contours of the current potential.*

As a consequence, the nonperiodic contributions to Φ can then be related to the current on the surface. Indeed, on the one hand,

$$\begin{aligned}\int_{S_{\text{coil}}}(\boldsymbol{K}\cdot\nabla\zeta)(\boldsymbol{r})\,d^2r &= \int_0^{2\pi}\int_0^{2\pi}\sqrt{g}(\theta,\zeta)\boldsymbol{K}(\theta,\zeta)\cdot\nabla\zeta\big(\boldsymbol{R}(0,\theta,\zeta)\big)\,d\theta d\zeta \\ &= -\int_0^{2\pi}\int_0^{2\pi}\frac{\partial\Phi(\theta,\zeta)}{\partial\theta}\,d\theta d\zeta \\ &= -\int_0^{2\pi}\int_0^{2\pi}\left(\frac{\partial\Phi_{\text{p}}(\theta,\zeta)}{\partial\theta}+\frac{G}{2\pi}\right)d\theta d\zeta \\ &= -2\pi G \text{ by periodicity of } \Phi_{\text{p}},\end{aligned}$$

and on the other hand

$$\begin{aligned}\int_{S_{\text{coil}}}(\boldsymbol{K}\cdot\nabla\theta)(\boldsymbol{r})\,d^2r &= \int_0^{2\pi}\int_0^{2\pi}\sqrt{g}(\theta,\zeta)\boldsymbol{K}(\theta,\zeta)\cdot\nabla\theta(\boldsymbol{R}(0,\theta,\zeta))\,d\theta d\zeta \\ &= \int_0^{2\pi}\int_0^{2\pi}\left(\frac{\partial\Phi(\theta,\zeta)}{\partial\zeta}\right)d\theta d\zeta \\ &= \int_0^{2\pi}\int_0^{2\pi}\frac{\partial\Phi_{\text{p}}(\theta,\zeta)}{\partial\zeta}+\frac{I}{2\pi}\,d\theta d\zeta \\ &= 2\pi I \text{ by periodicity of } \Phi_{\text{p}}.\end{aligned}$$

In other words, G is the net current linking the winding surface toroidally, and I is the net current linking the winding surface poloidally:

$$\begin{cases} 2\pi G = -\displaystyle\int_{S_{\text{coil}}} (\boldsymbol{K}\cdot\nabla\zeta)(\boldsymbol{r})\, d^2r, \\ 2\pi I = \displaystyle\int_{S_{\text{coil}}} (\boldsymbol{K}\cdot\nabla\theta)(\boldsymbol{r})\, d^2r. \end{cases} \tag{13.35}$$

Yet these two constants relate to the coils and the magnetic field in different ways.

- The constant I can be derived from known properties of the target equilibrium as follows. Consider the outer plasma surface, $\partial\Omega$, parameterized by two angles, θ_p and ζ_p. The integral form of Ampère's law applied to any surface S_P enclosed by a curve at constant θ_p on $\partial\Omega$, by ∂S_P, as represented in Figure 9.2, reads

$$\oint_{\partial S_P} \boldsymbol{B}(\boldsymbol{R}(0,\theta_p,\zeta_p))\cdot\frac{\partial\boldsymbol{R}(0,\theta_p,\zeta_p)}{\partial\zeta_p}\, d\zeta_p = \mu_0\int_{S_P}(\boldsymbol{J}\cdot\hat{\boldsymbol{n}})(\boldsymbol{r})\, d^2r,$$

  where $\boldsymbol{J}$ is the total current, including both the plasma current and the external current supported on S_{coil}. While the left-hand side is fixed by the desired equilibrium, since the domain of integration lies on the plasma boundary, the right-hand side only has contributions due to the current potential since the domain of integration lies outside the plasma boundary. Therefore, Ampère's law can be rewritten as

$$\oint_{\partial S_P} \boldsymbol{B}(\boldsymbol{R}(0,\theta_p,\zeta_p))\cdot\frac{\partial\boldsymbol{R}(0,\theta_p,\zeta_p)}{\partial\zeta_p}\, d\zeta_p = \mu_0\int_{S_P}(\boldsymbol{J}_K\cdot\hat{\boldsymbol{n}})(\boldsymbol{r})\, d^2r. \tag{13.36}$$

  The right-hand side can now be expressed in terms of the current potential. Indeed, using the dual relations between covariant and contravariant basis vectors from Table 5.1, for a tangential surface vector field, we see that

$$\begin{aligned} &\mu_0\int_{S_P}(\boldsymbol{J}_K\cdot\hat{\boldsymbol{n}})(\boldsymbol{r})\, d^2r \\ &= \mu_0\int_{b_-}^{b_+}\int_0^{2\pi}\left[\frac{\boldsymbol{J}_K\cdot\nabla\widetilde{\theta}}{|\nabla\widetilde{\theta}|}\right](\boldsymbol{R}(0,\theta_p,\zeta_p))\left|\frac{\partial\boldsymbol{R}}{\partial\widetilde{\zeta}}\times\frac{\partial\boldsymbol{R}}{\partial b}\right|(0,\theta_p,\zeta_p)\, d\widetilde{\zeta}db. \end{aligned}$$

  We will use the dual relation

$$\nabla\widetilde{\theta} = \frac{1}{\sqrt{g}}\left(\frac{\partial\boldsymbol{R}}{\partial b}\times\frac{\partial\boldsymbol{R}}{\partial\widetilde{\zeta}}\right),$$

  combined with the fact that the Jacobian in the coordinate system $\left(b,\widetilde{\theta},\widetilde{\zeta}\right)$ is expressed in terms of covariant vectors as $\sqrt{g} = \partial\boldsymbol{R}/\partial\widetilde{\zeta}\times\partial\boldsymbol{R}/\partial\widetilde{\theta}\cdot\partial\boldsymbol{R}/\partial b$, where $\partial\boldsymbol{R}/\partial b|_{S_P} = \hat{\boldsymbol{n}}$ so that $|\sqrt{g}| = |\partial\boldsymbol{R}/\partial\widetilde{\zeta}\times\partial\boldsymbol{R}/\partial\widetilde{\theta}|$. Moreover, as a reminder, the coordinate system is such that $\widetilde{\theta}|_{S_{\text{coil}}} = \theta$, $\widetilde{\zeta}|_{S_{\text{coil}}} = \zeta$, while $\partial\boldsymbol{R}/\partial\widetilde{\theta}|_{S_{\text{coil}}} = \partial\boldsymbol{R}/\partial\theta$, $\partial\boldsymbol{R}/\partial\widetilde{\zeta}|_{S_{\text{coil}}} = \partial\boldsymbol{R}/\partial\zeta$, and $\nabla\widetilde{\theta}|_{S_{\text{coil}}} = \nabla\theta$. Hence we get

$$\begin{aligned} &\mu_0\int_{S_P}(\boldsymbol{J}_K\cdot\hat{\boldsymbol{n}})(\boldsymbol{r})\, d^2r \\ &= \mu_0\int_0^{2\pi}\boldsymbol{K}(\theta_p,\zeta_p)\cdot[\nabla\theta]\left(\boldsymbol{R}(0,\theta_p,\zeta_p)\right)\left|\frac{\partial\boldsymbol{R}}{\partial\theta}\times\frac{\partial\boldsymbol{R}}{\partial\zeta}\right|(0,\theta_p,\zeta_p)\, d\zeta. \end{aligned}$$

Finally, according to (13.35), the right-hand side in (13.36) can be related to the constant I as follows:

$$\mu_0 \int_{S_P} (\boldsymbol{J}_K \cdot \hat{\boldsymbol{n}})(\boldsymbol{r})\, d^2 r = \mu_0 I.$$

Although, according to (13.35), I is defined in terms of an integral over both θ and ζ, it can equivalently be expressed in terms of an integral over only ζ since only periodicity with respect to ζ is exploited. So, the constant can be computed from the desired equilibrium as

$$I = \frac{1}{\mu_0} \oint_{\partial S_P} \boldsymbol{B}\big(\boldsymbol{R}(0, \theta_p, \zeta_p)\big) \cdot \frac{\partial \boldsymbol{R}(0, \theta_p, \zeta_p)}{\partial \zeta_p}\, d\zeta_p. \tag{13.37}$$

- Similarly, the integral form of Ampère's law applied to a surface S_T enclosed by a curve at constant ζ_p on $\partial\Omega$, ∂S_T, as represented in Figure 9.1, reads

$$\oint_{S_T} \boldsymbol{B}\big(\boldsymbol{R}(0, \theta_p, \zeta_p)\big) \cdot \frac{\partial \boldsymbol{R}(0, \theta_p, \zeta_p)}{\partial \theta_p}\, d\theta_p = \mu_0 \int_{S_T} (\boldsymbol{J}_K \cdot \hat{\boldsymbol{n}})(\boldsymbol{r})\, d^2 r.$$

However, the current density on the right-hand side has no contribution from the currents on the winding surface, as it is an integral over a toroidal cross-section of the plasma. As a consequence, this identity is not related to G, and therefore, unlike I, the constant G is not fixed by the equilibrium. By contrast, we can choose the value of G regarding the desired properties of the coils, in particular regarding their topology. For instance, as discussed in Remark 13.2, a set of streamlines of the current density, or contours of the current potential, can be chosen to provide the coils. In order to ensure that these streamlines are closed with a given helicity on average, we can assume that the ratio G/I takes a given rational value. In this case, consider any closed streamline C_{Φ_0} corresponding to a particular value of the current potential, Φ_0, and parameterized by $(\theta_0(l), \zeta_0(l))$, where l is a coordinate that measures length along the streamline. Along the surface S_{coil}, the numbers of poloidal and toroidal turns of the streamline are

$$\begin{cases} M(\Phi_0) = \dfrac{1}{2\pi} \displaystyle\oint_{C_{\Phi_0}} \frac{d\theta_0(\ell)}{d\ell}\, d\ell, \\ N(\Phi_0) = \dfrac{1}{2\pi} \displaystyle\oint_{C_{\Phi_0}} \frac{d\zeta_0(\ell)}{d\ell}\, d\ell. \end{cases}$$

Moreover, by definition of a streamline, the derivatives along the streamline are

$$\begin{cases} \dfrac{d\theta_0(\ell)}{d\ell} = \left[\dfrac{\boldsymbol{K}}{|\boldsymbol{K}|}\right]\big(\theta_0(\ell), \zeta_0(\ell)\big) \cdot [\nabla\theta]\big(\boldsymbol{R}(0, \theta_0(\ell), \zeta_0(\ell))\big), \\ \dfrac{d\zeta_0(\ell)}{d\ell} = \left[\dfrac{\boldsymbol{K}}{|\boldsymbol{K}|}\right]\big(\theta_0(\ell), \zeta_0(\ell)\big) \cdot [\nabla\zeta]\big(\boldsymbol{R}(0, \theta_0(\ell), \zeta_0(\ell))\big). \end{cases}$$

Averaging over all possible streamlines by integrating over Φ gives

$$\begin{cases} \int M(\Phi)\, d\Phi = \dfrac{1}{2\pi} \displaystyle\int \oint_{C_\Phi} \left[\dfrac{\boldsymbol{K}}{|\boldsymbol{K}|}\right]\big(\theta_0(\ell), \zeta_0(\ell)\big) \cdot [\nabla\theta]\big(\boldsymbol{R}(0, \theta_0(\ell), \zeta_0(\ell))\big)\, d\ell d\Phi, \\ \int N(\Phi)\, d\Phi = \dfrac{1}{2\pi} \displaystyle\int \oint_{C_\Phi} \left[\dfrac{\boldsymbol{K}}{|\boldsymbol{K}|}\right]\big(\theta_0(\ell), \zeta_0(\ell)\big) \cdot [\nabla\zeta]\big(\boldsymbol{R}(0, \theta_0(\ell), \zeta_0(\ell))\big)\, d\ell d\Phi. \end{cases}$$

Since

$$d\ell d\Phi = d\theta d\zeta |\boldsymbol{K}| \left| \frac{\partial \boldsymbol{R}}{\partial \theta} \times \frac{\partial \boldsymbol{R}}{\partial \zeta} \right|,$$

this yields

$$\begin{cases} \int M(\Phi)\, d\Phi = \dfrac{1}{2\pi} \displaystyle\int_{S_{\text{coil}}} (\boldsymbol{J}_K \cdot \nabla\theta)(\boldsymbol{r})\, d^2 r, \\ \int N(\Phi)\, d\Phi = \dfrac{1}{2\pi} \displaystyle\int_{S_{\text{coil}}} (\boldsymbol{J}_K \cdot \nabla\zeta)(\boldsymbol{r})\, d^2 r. \end{cases}$$

Using (13.35), we then conclude that $\int M(\Phi)\, d\Phi = I$ and $\int N(\Phi)\, d\Phi = -G$. In this way, G quantifies the average winding of streamlines of the current density in the toroidal direction, while I quantifies the average winding of the streamlines in the poloidal direction. In particular, the ratio of I/G is analogous to the rotational transform (7.3).

If coils are chosen as streamlines of the current density, following Remark 13.2, the value of G restricts the topology of the coil set. If one desires modular coils, linking the plasma poloidally but not toroidally, then $G = 0$ is chosen. If one desires helical coils, linking the plasma both poloidally and toroidally, then G is chosen based on the desired relative number of toroidal turns of the coils. Saddle coils, linking the plasma neither toroidally nor poloidally, might also be of interest. However, such coils, if they are streamlines of the current density, would correspond to $I = 0$ and $G = 0$. Therefore, such a coil set alone cannot be consistent with the equilibrium according to (13.37). Nevertheless, this condition can be satisfied with the addition of currents linking the plasma poloidally.

The last of the three terms contributing to (13.33) is the periodic function Φ_{p}. If the plasma boundary is assumed to be stellarator symmetric as in (13.11), the current density must also be stellarator symmetric, and $\boldsymbol{K}$ must be even with respect to θ and ζ. Hence, leveraging its periodicity, it can be represented as a sine Fourier series:

$$\Phi_{\text{p}}(\theta, \zeta) = \sum_{(m,n)\in\mathcal{D}} \Phi_{m,n} \sin(m\theta - n\zeta),$$

where $\mathcal{D} := (\mathbb{N}\times\mathbb{Z}) \cup (\{0\}\times\mathbb{N})$. The Fourier harmonics are then natural parameters to minimize a certain objective function of the current as introduced in (13.31). So the set of parameters

$$\{\Phi_{m,n} \in \mathbb{R}, (m,n) \in \mathcal{D}\}$$

uniquely defines the current density. In practice, a finite number of these modes are retained. Assuming that the maximum poloidal and toroidal mode numbers are fixed and denoted respectively by M and N, the set $\mathcal{D}_{M,N}$ of indices is defined as

$$\mathcal{D}_{M,N} := \{(m,n) \in \mathcal{D}, m \le M, n \le N\}.$$

The corresponding set of $2NM + M + N$ parameters

$$\mathcal{R}_{M,N} := \{\Phi_{m,n} \in \mathbb{R}, (m,n) \in \mathcal{D}_{M,N}\}$$

is the set of minimization variables for the coil optimization. If the current density is described for fixed maximum poloidal and toroidal mode numbers, respectively denoted M and N, by a set of $2MN + M + N$ coefficients $\mathcal{R}_{M,N}$, then $\boldsymbol{J}^{\text{coil}}(\mathcal{R}_{M,N})$ denotes the corresponding surface current for $\boldsymbol{K}$ defined by (13.34).

As a conclusion, under the winding surface assumption, a coil optimization problem can be summarized as follows:

1. Compute I from the field $\boldsymbol{B}$ according to (13.37).
2. Choose G according to the desired topology of the coils.
3. Solve

$$\min_{\mathcal{R}_{M,N}} \chi^2\left(\boldsymbol{J}^{\text{coil}}(\mathcal{R}_{M,N})\right) \text{ where } \chi^2\left(\boldsymbol{J}^{\text{coil}}\right) := \chi_B^2\left(\boldsymbol{J}^{\text{coil}}\right) + \lambda\chi_{\text{coil}}^2\left(\boldsymbol{J}^{\text{coil}}\right). \tag{13.38}$$

The first term is given by (13.32), while the regularization term is most often chosen such that (13.38) is a convex optimization problem. Under the winding surface assumption, the most common convex optimization problem is obtained by quantifying coil complexity as

$$\chi_K^2 = \int_{S_{\text{coil}}} |\boldsymbol{J}_K|^2(\boldsymbol{r})\, d^2r. \tag{13.39}$$

Larger values of $|\boldsymbol{J}_K|^2$ indicate that contours of the current potential are closer to each other, implying a smaller coil-coil distance. This feature is difficult to engineer and makes experimental access difficult as previously discussed in Section 13.3.

We can consider the formulation in (13.38) to be a form of Tikhonov regularization. As discussed in Section 13.4.2, there is a unique global minimum of χ^2 due to its strict convexity. Thus, for a given winding surface and target plasma boundary, the global minimum of χ^2 can be found efficiently by solving a single linear least-squares system for $\{\Phi_{m,n}\}$. According to Remark 13.2, once the current potential is obtained, a set of filamentary coils can be taken to be a set of the contours of the current potential. However, the winding surface assumption is very limiting. Indeed, certain coil topologies, such as interlinked coils, cannot be treated with this method, and effects due to the cross-sectional area of filamentary coils are not included. Nonetheless, the winding surface approach remains an important tool in the stellarator design community, as it can provide a reasonable initial guess for filamentary methods described in the following section.

The first implementation of this method was the NESCOIL code [213], that solves the problem without regularization such that $\lambda = 0$, or $\chi^2 = \chi_B^2$. In order to tackle ill-posedness, a truncated SVD approach was implemented during the NCSX design [242]. Tikhonov regularization was introduced with the REGCOIL code [175] by adding the second term (13.39) to (13.38). An example REGCOIL calculation for the NCSX equilibrium is shown in Figure 13.5.

The calculations described in this section have assumed a fixed winding surface. Often, this surface is taken to be a surface uniformly offset from $\partial\Omega$. However, the surface S_{coil} itself can be optimized [237] to improve the properties of the resulting coils. For example, such an optimization was performed during the design of the W7-X coils [96]. Table 13.2 summarizes common figures of merit to quantify the complexity of the current potential within winding surface optimization.

13.4.5 ▪ Filamentary model

Modern stellarator coil optimization tools are often based on filamentary coil optimization. Rather than seeking a current supported in a volume Ω_c, as in (13.14), or supported on a given winding surface, as in (13.38), the support of the unknown current is assumed to be restricted to a set of closed curves, whose shapes and positions are also degrees of freedom.

In terms of a mathematical model, a set of N unknown closed curves, $\{C_k\}_{1\leq k\leq N}$, will support the current, each curve supporting a scalar current I_k. Each C_k can be represented as a

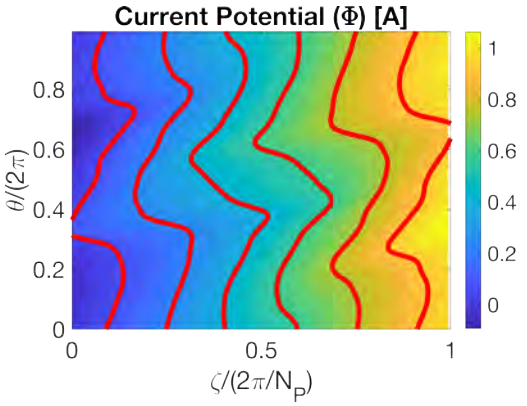

Figure 13.5*: The normalized current potential solution computed with REGCOIL in* (θ, ζ) *space. The fixed winding and plasma surfaces and the six contours corresponding to the coil shapes are respectively represented in three dimensions in Figures* 13.4a *and* 13.4b.

Table 13.2*: Properties of the continuous current,* $\boldsymbol{K}(\theta, \zeta)$*, on a winding surface,* S_{coil}*. Here* $\boldsymbol{R}_P(\theta_p, \zeta_p)$ *denotes the position on the fixed plasma boundary* $\partial\Omega$ *while* $\boldsymbol{R}_W(\theta, \zeta)$ *denotes the position on the winding surface. To define the curvature* κ*, a streamline of the current potential is expressed as a curve parameterized by the length,* $\boldsymbol{r}_C(\ell)$*, and* $\kappa(\ell) = |\boldsymbol{r}_C''(\ell)|$*. These metrics are described in* [175, 237, 60].

RMS current density	$\|\|\boldsymbol{K}\|\|_2 = \sqrt{\int_{S_{\text{coil}}} \|\boldsymbol{K}\|^2 \, d^2r / \int_{S_{\text{coil}}} d^2r}$
Maximum current density	$K_{\max} = \max_{\theta,\zeta} \|\boldsymbol{K}(\theta, \zeta)\|$
Harmonic content	$\mathcal{H} = \sum_{m,n} \Phi_{m,n}^2 (m^2 + n^2)$
Curvature	$f_\kappa = \int_{S_{\text{coil}}} \kappa^2 \|\boldsymbol{K}\|^2 \, d^2r$
Coil-plasma spacing	$\min_{\theta,\zeta,\theta_p,\zeta_p} \text{dist}\big(\boldsymbol{R}_P(\theta, \zeta), \boldsymbol{R}_W(\theta_p, \zeta_p)\big)$

parameterized curve, $\boldsymbol{R}_k$, under the form of a Fourier series:

$$\boldsymbol{R}_k(s) = \boldsymbol{R}_0^{k,c} + \sum_{m \in \mathbb{N}} \boldsymbol{R}_m^{k,c} \cos(ms) + \boldsymbol{R}_m^{k,s} \sin(ms).$$

Here $s \in [0, 2\pi)$ parameterizes the length along the curve. The Fourier harmonics are then natural parameters to minimize a certain objective function of the current as introduced in (13.31). So the set of parameters

$$\left\{ \boldsymbol{R}_0^{k,c}, (\boldsymbol{R}_m^{k,c}, \boldsymbol{R}_m^{k,s}) \in \mathbb{R}^2, m \in \mathbb{N}, 1 \le k \le N \right\}$$

together with the current values $\{I_k, 1 \le k \le N\}$ uniquely define the current. In practice, a finite number of Fourier modes are retained. Assuming that the maximum mode number is fixed, and denoted by M, the corresponding set of $2NM + 2N$ parameters

$$\mathcal{S}_{M,N} := \left\{ I_k, \boldsymbol{R}_0^{k,c}, (\boldsymbol{R}_m^{k,c}, \boldsymbol{R}_m^{k,s}) \in \mathbb{R}^2, 1 \le m \le M, 1 \le k \le N \right\}$$

Table 13.3*: Properties of a set of filamentary curves,* $\{C_k\}_{1\le k\le N}$*, parameterized by* $\boldsymbol{R}_k$ *as a function of the length along the curve* ℓ*. Here* $\boldsymbol{R}(\theta_p,\zeta_p)$ *denotes the position on the desired plasma boundary,* $\partial\Omega$*, parameterized by angles* (θ_p,ζ_p)*. These metrics are discussed in* [327, 60, 144].

Length	$L_k = \oint_{C_k} d\ell_k$
Curvature	$\kappa(\ell) = \lvert\boldsymbol{R}_k''(\ell)\rvert$
Torsion	$\tau_k(\ell) = \dfrac{\lvert\boldsymbol{R}_k'(\ell)\cdot\left(\boldsymbol{R}_k''(\ell)\times\boldsymbol{R}_k'''(\ell)\right)\rvert}{\lvert\boldsymbol{R}_k''(\ell)\rvert^2}$
Coil-coil separation	$\min_{i\neq j,\ell}\operatorname{dist}\left(\boldsymbol{R}_i(\ell),\boldsymbol{R}_j(\ell)\right)$
Coil-plasma separation	$\min_{k,\theta_p,\zeta_p,\ell}\operatorname{dist}\left(\boldsymbol{R}_k(\ell),\boldsymbol{R}(\theta_p,\zeta_p)\right)$

is the set of minimization variables for the coil optimization. If the current is described for fixed maximum mode number M, by a set of $2MN+2N$ coefficients $\mathcal{S}_{M,N}$, then $\boldsymbol{J}^{\text{coil}}$ denotes the corresponding current. In this context, a coil optimization problem can be expressed as follows:

$$\min_{\mathcal{S}_{M,N}} \chi^2\left(\boldsymbol{J}^{\text{coil}}(\mathcal{S}_{M,N})\right) \text{ where } \chi^2\left(\boldsymbol{J}^{\text{coil}}\right) := \chi_B^2\left(\boldsymbol{J}^{\text{coil}}\right) + \lambda\chi_{\text{coil}}^2\left(\boldsymbol{J}^{\text{coil}}\right).$$

In the context of filamentary methods, there are many choices for the objective function. It is common to include the coil length as a form of regularization. Other objectives include penalties on the curvature of coils, minimum distance between coils, and coil-plasma separation. Filamentary coil optimization software includes ONSET [58], COILOPT [278], FOCUS [327], and SIMSOPT [183]. Table 13.3 provides a summary of common metrics employed during filamentary coil optimization, motivated by the discussion in Section 13.3.

The choice of the number of coils, N, and the coil shape may be constrained by the N_{FP}-symmetry and stellarator symmetry described in Section 12.3. For example, if the coils link the plasma poloidally as in Figure 13.4b, then only half of one field period of coils needs to be determined, with the rest of the coil set obtained by applying rotations and translations. For this case, the number of degrees of freedom is reduced by $2N_{FP}$.

There are other possible choices for filamentary curve parameterization. For example, the set of filamentary coils can be modeled by a set of closed curves on a winding surface, the surface itself being allowed to evolve throughout the optimization [58, 278]. The winding surface could then be constrained to lie within two bounding toroidal surfaces.

While for the winding surface methods, the objective function can be chosen to lead to a convex optimization problem that can be solved with a linear least-squares method, the filamentary methods require the solution of a nonconvex, nonlinear optimization problem. Therefore, several local minima may exist, and the result of a configuration optimization will generally depend on the initial guess. In practice, the output of a winding surface calculation can, therefore, provide a reasonable initial solution for such nonlinear optimization methods. On the other hand, filamentary methods provide results that more closely approximate coils that can be constructed since the winding surface method is based on the assumption of a large number of coils. For this reason, filamentary methods are more amenable to the incorporation of engineering constraints. In addition, filamentary methods can also be used for coil topologies such as interlinked coils, which cannot be treated with the winding surface method.

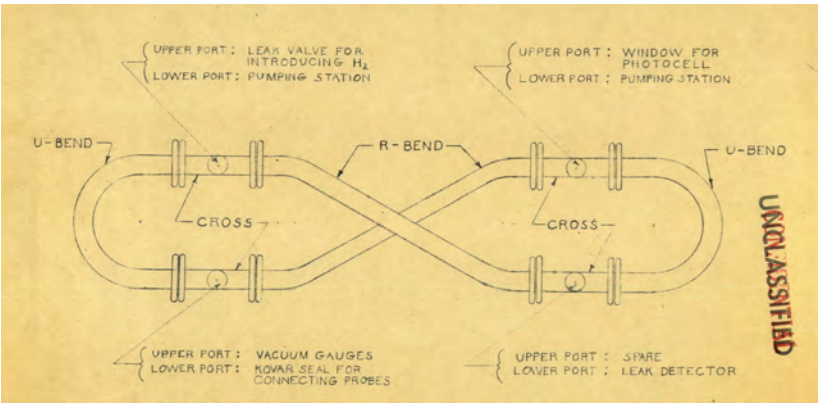

Figure 13.6*: A diagram of the Princeton Model A stellarator based on Lyman Spitzer's figure-eight design. Figure reproduced from* [305]. *Courtesy of the Department of Energy Office of Scientific and Technical Information.*

13.5 ▪ Examples of optimized configurations

Following this discussion on numerical methods and challenges associated with stellarator design, we provide a brief history of some optimized stellarators. While early stellarator experiments were not optimized, we also present an overview of these efforts to provide historical context in Section 13.5.1.

13.5.1 ▪ Early stellarator experiments

As discussed in Section 7.3, rotational transform can be produced with three physical mechanisms: by current in the plasma, twisting ellipticity of magnetic flux surfaces, and nonplanarity or torsion of the magnetic axis. The first stellarators, based on Lyman Spitzer's so-called figure-eight design [271], used torsion of the magnetic axis to produce rotational transform. Such a configuration is known as a heliac, a stellarator whose rotational transform is provided by a set of planar toroidal field coils arranged such that their centers follow a toroidal helix, producing a helical magnetic axis. The confinement was provided by a set of circular, planar toroidal field coils, and the plasma was contained in a twisted glass tube of circular cross-section. The corresponding geometry is illustrated in Figure 13.6. The figure-eight design was the basis for several early stellarator experiments at Princeton, in particular the Model A and B devices.

While the figure-eight design provided rotational transform, Spitzer discovered that stability properties could be improved by introducing magnetic shear, a nonzero derivative in the rotational transform, $\iota'(\psi)$. This shear was introduced experimentally in the Model C stellarator with helical coils, linking the plasma both poloidally and toroidally [275]. Such a configuration is known as a heliotron.[26] While the Model C team was able to experimentally demonstrate the existence of magnetic surfaces [265], the device was plagued by poor particle confinement [319]. These early stellarator experiments at Princeton operated until the late 1960s, when promising results from the Soviet T-3 tokamak became available, and it was decided that the Model C would be converted to a tokamak [245].

[26] Sometimes a distinction is made between a heliotron and a similar configuration known as a torsatron. We will instead use the term heliotron to refer to a stellarator with any helical coil.

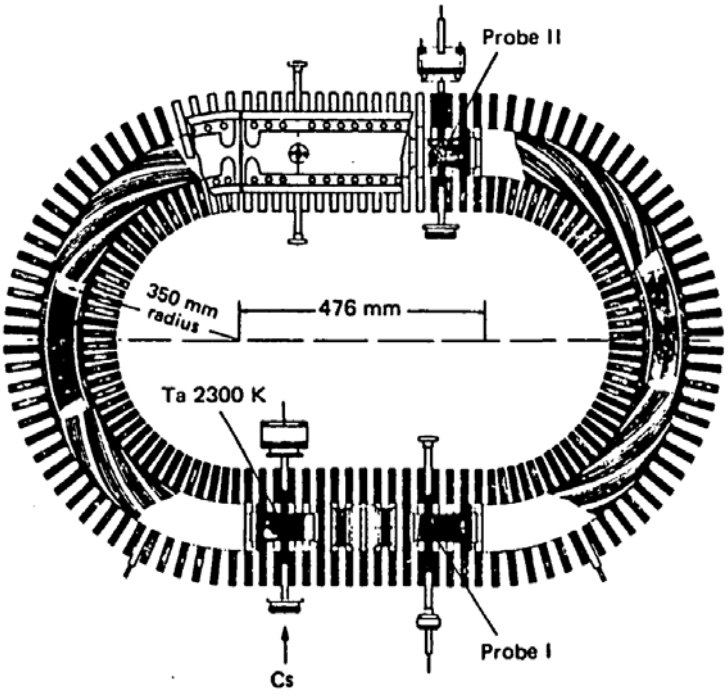

Figure 13.7*: A schematic diagram of the Wendelstein I (WI) experiment, with the racetrack design and helical coils of the Princeton Model C device. Reprinted with permission from IAEA. "Wendelstein stellarators", Nucl. Fusion* 25*, No.* 9*,* 1231 (1985)*, by G. Grieger et al.*

Meanwhile, the Wendelstein line of stellarators was active at IPP Garching, initially adopting designs similar to Princeton's Model C with the WI-A and WI-B devices. The corresponding geometry is illustrated in Figure 13.7. Experiments on WII-A, operating from 1968 to 1974, provided insight into the benefits of low magnetic shear and accurate construction of the coil system for avoiding magnetic islands [17]. The performance continued, however, to be limited by poor transport properties and low equilibrium beta limits due to the Shafranov shift [128], an outward shift of the magnetic axis.

13.5.2 ▪ Wendelstein 7-Advanced Stellarator (W7-AS)

The first experiment designed using optimization techniques was the Wendelstein 7-Advanced Stellarator (W7-AS). The principal objective of the design was the minimization of equilibrium Pfirsch–Schlüter currents discussed in Section 13.1.1; see [133]. As discussed in Section 13.1.2, this particular type of current gives rise to a Shafranov shift, hence limiting the maximum pressure at which good flux surfaces exist. Thus, a reduction of these parallel currents can increase the maximum achievable plasma beta.

In comparison with the unoptimized W7-A configuration, represented in Figure 13.8, W7-AS achieved a reduction of the parallel currents by about a factor of two. In addition to reducing the plasma current, the optimization resulted in reduced neoclassical transport in the higher collisionality plateau and Pfirsch–Schlüter regimes and improved guiding center confinement [128]. The magnetic field was produced by modular coils, linking the plasma poloidally, rather than helical coils, linking the plasma both poloidally and toroidally. This coil topology is represented in Figure 13.9. Modular coils are thought to make the careful design of the magnetic

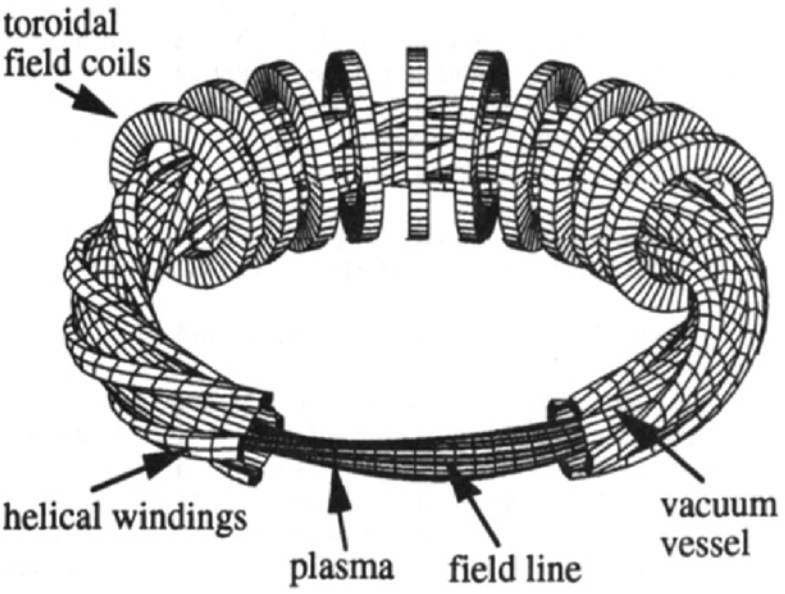

Figure 13.8*: The coil system of the Wendelstein* 7*-A stellarator, a classical stellarator whose confinement is provided by a set of helical and planar toroidal field coils. Figure reproduced from* [296]*. Stellarators and optimised stellarators, F. Wagner, Fusion Technology,* 33 (1998)*, pp.* 67–83*, reprinted by permission of Taylor & Francis Ltd.*

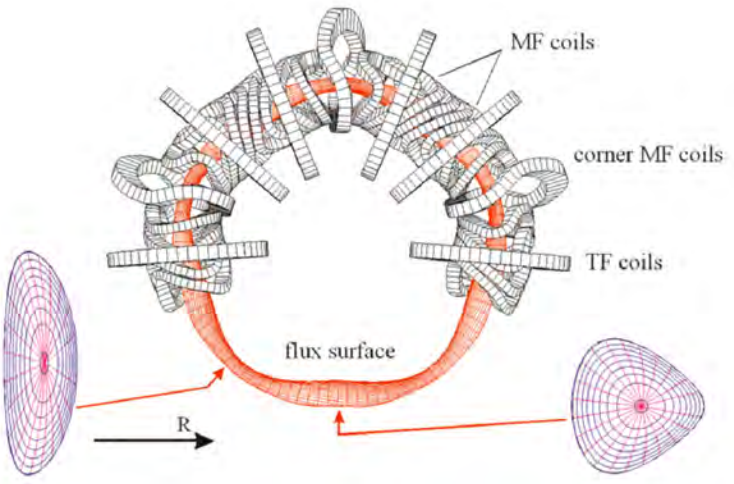

Figure 13.9*: The modular field coils, planar toroidal field coils, and flux surface of W7-AS. Figure reproduced from* [128]*. Used with permission of IOP Publishing, Ltd, from "Major results from the stellarator Wendelstein* 7*-AS," M. Hirsch, J. Baldzuhn, C. Beidler, R. Brakel, R. Burhenn, A. Dinklage, H. Ehmler, M. Endler, V. Erckmann, Y. Feng,* 50, 5, 2008*; permission conveyed through Copyright Clearance Center, Inc.*

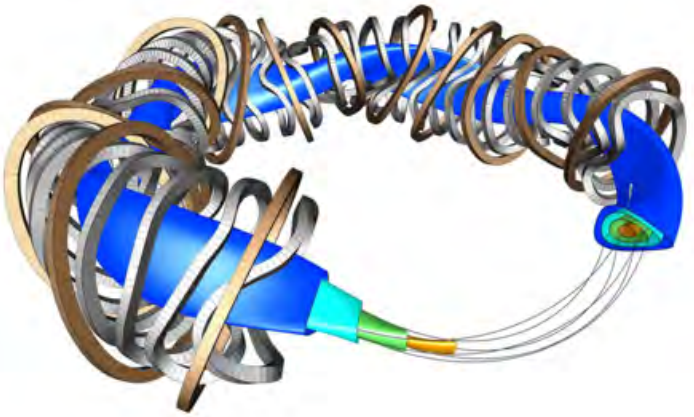

Figure 13.10*: Modular field coils (silver), toroidal field coils (bronze), and magnetic surfaces of the W7-X stellarator. Figure reproduced from* [283]*. T. Sunn Pedersen, A. Dinklage, Y. Turkin, R. Wolf, S. Bozhenkov, J. Geiger, G. Fuchert, H.-S. Bosch, K. Rahbarnia, H. Thomsen, et al., "Key results from the first plasma operation phase and outlook for future performance in Wendelstein 7-X," Physics of Plasmas,* 24 (2017), 055503*, distributed under CC BY* 4.0 *DEED License (*`https://creativecommons.org/licenses/by/4.0/`*).*

field more tractable and reduce electromagnetic forces between interlinked coils that were present in early stellarator devices. The coils of W7-AS were designed using a current potential method similar to that described in Section 13.4.4, with the desired plasma configuration defined by an analytic solution of Laplace's equation, known as Dommaschk potentials [57]. W7-AS, operating from 1988 to 2002, demonstrated the success of the stellarator optimization technique, including experimental verification of a reduction of neoclassical transport in higher collisionality regimes and improved stability properties [133]. The W7-AS experiment was able to demonstrate that modular coils could provide a large volume of good magnetic surfaces, with a few islands that are sufficiently small to not inhibit confinement properties.

13.5.3 ▪ Wendelstein 7-X (W7-X)

The resounding scientific success of W7-AS served as validation of the fixed-boundary optimization technique, wherein plasma properties are first optimized with the requisite coils subsequently determined. Experimental verification of neoclassical theory was also performed on W7-AS [69, 29], providing confidence in optimization of the bootstrap current and neoclassical transport for the later design of W7-X. There were also significant theoretical developments after the design of W7-AS, in particular, the discovery of quasisymmetry by Boozer in 1983 [22]. Soon after, in Garching, Nührenberg and Zille demonstrated that quasisymmetric configurations could be obtained through equilibrium optimization [232]. The W7-X configuration was designed using these equilibrium optimization techniques to achieve additional objectives: nested magnetic surfaces, fast-particle confinement, reduced parallel currents, minimal neoclassical transport at low collisionality, and MHD stability up to an average beta of 5% [13]. The resulting configuration was quasi-isodynamic, a quasiomnigeneous magnetic field with poloidally closed contours of the magnetic field strength [230, 119].

As can be seen in Figure 13.10, the device's coils are geometrically complex, with significant nonplanarity. The construction of W7-X took more than 10 years, and the project faced numerous challenges associated with quality assurance and limitations in engineering capacity, resulting in

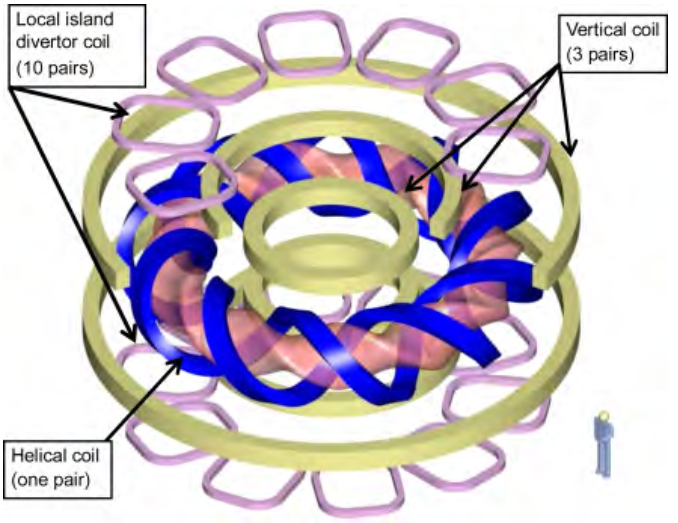

Figure 13.11*: The plasma (pink) and coils of the LHD. Figure reproduced from* [158]*. Reprinted from Magnetic Fusion Energy, O. Kaneko,* 15 *- Large helical device,* 469–491*,* 2016*, with permission from Elsevier.*

delays and significant project recovery efforts. These issues have been attributed to insufficient design tolerances and very strict margins and clearances, which considerably impacted project delivery [159]. Due to tight tolerances, the construction of the 50 modular coils alone took 10^6 man-hours [26]. Nonetheless, W7-X was ultimately completed successfully, and the first experimental campaign began in 2015.

Experiments from the initial campaigns of W7-X have demonstrated the success of the stellarator equilibrium optimization concept, confirming the desired magnetic geometry to within a tolerance of 10^{-5} [284]. Because of its neoclassical optimization, W7-X has been able to achieve record values of the fusion triple product for stellarators [308, 14]. The triple product parameter must be sufficiently large in order for the fusion reaction to be self-sustaining as described in Section 1.3.

13.5.4 ▪ Large Helical Device (LHD)

The success of the W7-A experiment and other early stellarators [281], demonstrating energy confinement comparable to some tokamak operating regimes, inspired physicists at the National Institute for Fusion Studies in Japan to probe the performance of stellarators at a larger size and higher plasma temperature. As opposed to W7-AS and W7-X, which were designed with modular coil systems, LHD was designed with a helical coil system. This coil type may provide certain advantages, including the presence of large magnetic shear at the edge, improving stability and equilibrium properties, as well as a simplified divertor system [315]. The design of LHD aimed to achieve $\beta = 5\%$, maximal confinement properties, and sufficient distance between coils and plasma to enable simple installation. Rather than performing equilibrium optimization, the winding of the helical coil was chosen based on simplified scaling relations of physics and engineering properties on coil parameters. These models were constructed from a database of simulations, empirical scalings based on experimental measurements, and theoretical scalings of confinement [315]. In particular, the device parameters were chosen to maximize the triple product as defined in Section 1.3. The resulting design is shown in Figure 13.11.

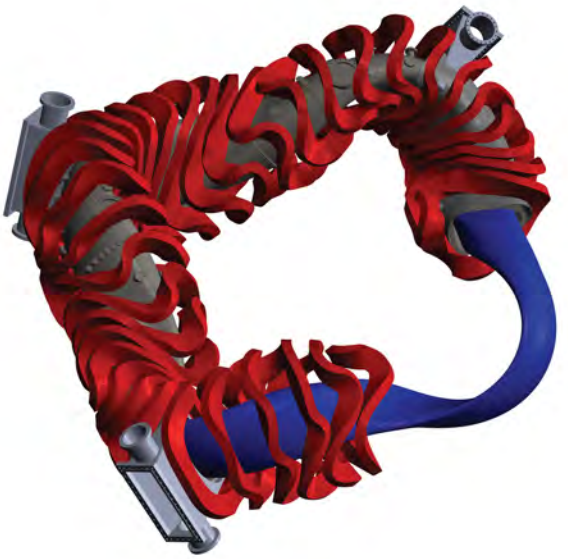

Figure 13.12*: Modular field coils (red), vacuum vessel with box ports (grey), and plasma (blue) of the HSX stellarator. Figure courtesy of the HSX Team. Distributed under CC BY* 4.0 *DEED License (*https://creativecommons.org/licenses/by/4.0/*).*

The LHD experiment enables great flexibility in the magnetic configuration space by adjusting the coil currents. The standard configuration features good MHD stability properties but relatively poor neoclassical confinement properties. Another configuration is also available with an inward shift of the magnetic axis. In this inward-shifted configuration, the MHD stability properties are predicted to deteriorate, but the neoclassical diffusion is reduced by about a factor of 10 [219]. Therefore, although LHD was not designed based on equilibrium optimization studies as W7-AS and W7-X were, the inward-shifted configuration is sometimes considered to be an optimized configuration, and improved energetic particle confinement [220] and energy confinement [313] have been confirmed in comparison with the standard configuration.

13.5.5 ▪ Helically Symmetric eXperiment (HSX)

The Helically Symmetric Experiment (HSX) was the first experimental validation of the quasisymmetry concept. The design of the device was based on the equilibrium optimization concept pioneered by Garching scientists [230]. The magnetic equilibrium was designed to have quasihelical symmetry, Mercier stability, and low magnetic shear [5] using the equilibrium optimization tools developed by the Wendelstein team [4]. The coils were then designed using a current potential method, as described in Section 13.4.4. The resulting design is shown in Figure 13.12. HSX has demonstrated a reduction of electron heat transport [37] and a reduction of flow damping in the symmetry direction [86], both of which are predicted to occur in quasisymmetric devices.

13.5.6 ▪ National Compact Stellarator eXperiment (NCSX)

Following the completion of the construction of the HSX, a team based at the Princeton Plasma Physics Laboratory (PPPL) began the design of a quasiaxisymmetric stellarator, the National Compact Stellarator eXperiment (NCSX). NCSX was designed using the fixed-boundary

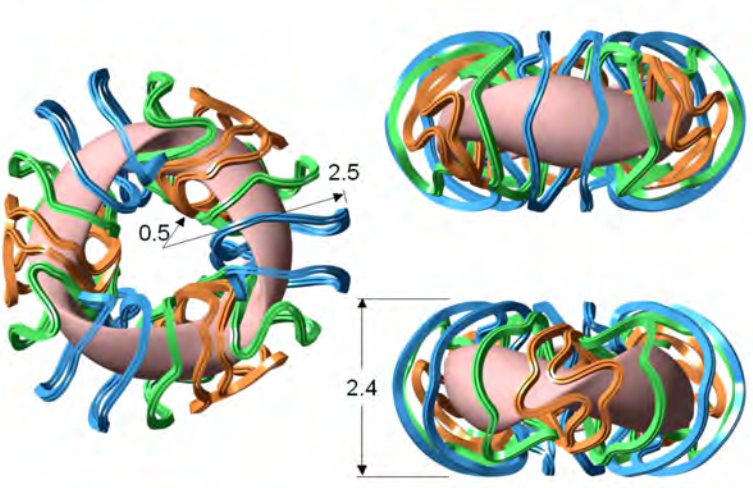

Figure 13.13*: The NCSX modular coils were obtained through integrated coil-plasma optimization. Figure reproduced from* [146]*. Reprinted with permission from the International Atomic Energy Agency. Strickler, D.J. "Integrated Plasma and Coil Optimization for Compact Stellarators," Fusion Energy Conference (Proc.* 19*th Int. Conf. Lyon,* 2002*, Paper No. CN-*94*/FT/P*2-06*), IAEA, Vienna* (2003)*.*

equilibrium optimization technique to achieve several physics objectives: demonstration of MHD stability at $\beta = 4.5\%$, a monotonically increasing ι profile predicted to reduce island widths and provide stabilizing properties [317], good flux surface quality, and good confinement properties provided by a quasiaxisymmetric magnetic field. The STELLOPT code [274, 249] was developed for the design of the NCSX equilibrium. The coils were then designed using the COILOPT code [278], modeling the currents as filamentary lines discussed in Section 13.4.5. In the final stages of the NCSX design, the coils and plasma were optimized simultaneously in a single-stage approach [142, 146]. This enabled the NCSX team to obtain a set of coils, represented in Figure 13.13, simultaneously meeting the physics objectives and coil engineering requirements, such as increased coil-coil spacing, increased coil-plasma spacing, sufficient access for neutral beams, and a sufficiently large curvature radius.

The construction of NCSX began in 2004. Like W7-X, the NCSX project faced significant implementation challenges due to the complexity of the device design. The inability to meet the stringent tolerances led to a redesign of critical components after construction of the device was already underway. The revisions resulted in a 50% increase in the projected final cost and a four-year delay in expected completion. It ultimately resulted in the cancellation of the project by the funding body in 2008 [63]. An analysis of the project indicated that the majority of the cost growth arose due to the tight tolerances required on the modular coil assembly [280], as calculations of the sensitivity of the magnetic island width indicated that an engineering tolerance of ≈ 1.5 mm on coil positions was required [32]. Lessons learned from both the W7-X and NCSX projects emphasize the importance of coil optimization accounting for practical constraints, most importantly including reasonably achievable tolerances and clearances.

13.5.7 ▪ Summary of major stellarator experiments

In Table 13.4, we provide a summary of major stellarator experiments, indicating the rough categorization of each experiment. Here heliotron indicates a device whose confinement is provided by a helically wound coil. A heliac is a stellarator for which rotational transform is provided by a

Table 13.4*: A summary (as of* 2023*) of some major stellarator devices* [19]*, approximately in chronological order. Here N_P is the number of field periods defined in Section* 12.3.1*, R is the average major radius, a is the average minor radius, and B is the maximum magnetic field strength. All of the above devices were constructed and conducted experiments except for NCSX, whose construction was terminated before its completion. *IL refers to interlocking.*

Device	Location	Type	N_P	R [m]	a [m]	B [T]	Status
Heliotron E [297]	Kyoto	heliotron	19	2.2	0.2	1.9	1980–1997
ATF [289]	Oak Ridge	heliotron	12	2.1	0.27	2	1988–1994
W7-AS [128]	Garching	optimized	5	2.0	0.18	3	1988–2002
CHS [228]	Nagoya/Toki	heliotron	8	1.0	0.2	2	1989–2006
H1 [100]	Canberra	heliac	3	1.0	0.2	0.5	1992–2017
TJ-II [126]	Madrid	heliac	4	1.5	0.2	1	1998–running
LHD [147]	Toki	heliotron	10	3.9	0.6	3	1998–running
HSX [3]	Madison	QH, optimized	4	1.2	0.15	1.4	1999–running
Heliotron J [261]	Kyoto	heliotron	4	1.2	0.2	1.5	2000–running
CNT [30]	Columbia	IL*, optimized	2	0.30	0.15	0.2	2004–2017
CTH [107]	Auburn	heliotron	2	0.75	0.29	0.7	2007–running
NCSX [322]	Princeton	QA, optimized	3	1.4	0.33	1.7	terminated
W7-X [310, 308]	Greifswald	optimized	5	5.5	0.53	3	2015–running
CFQS [148]	Chengdu	QA, optimized	2	1	0.25	1	under construction

helical magnetic axis produced by circular toroidal field coils centered around a helical axis. The confinement of CNT is provided by two coils that are linked together, denoted by an interlocking type stellarator, while QH indicates quasihelical symmetry, QA indicates quasiaxisymmetry, and optimized indicates a device that was designed using equilibrium optimization techniques.

Chapter 14
Further topics in stellarator design

The goal of the material presented in previous chapters was to provide an understanding of the stellarator concept, the necessity of optimization, and the principles of stellarator design. Beyond this material, there are many aspects of stellarator theory and design that have not been covered in this book. This chapter provide brief highlights about some of these additional topics, presented in alphabetical order.

14.1 ▪ Advances in numerical optimization

The design of modern stellarators requires numerical optimization tools; thus, further incorporation of modern optimization techniques can improve the navigation of the stellarator design space. Traditionally, stellarator optimization has largely proceeded with methods based on finite-difference approximations of the gradient. Choosing the finite-difference step size to limit the effect of the corresponding error is challenging in practice. Furthermore, the finite-difference calculation requires many function evaluations, significantly augmenting the computational time [64].

An alternative approach is the application of adjoint methods [237, 235, 88], with analytic gradient information computed efficiently by solving a supplementary set of differential equations. Gradient information can also be obtained through automatic differentiation tools, automatically computing the derivative of an arbitrary function defined by a computer program. This approach has been applied to the optimization of coil shapes [208] and fixed-boundary optimization for quasisymmetry [65].

Another example of the incorporation of modern optimization tools is the application of stochastic techniques for the design of stellarator coils. Rather than optimize a single set of stellarator coils, it is possible to instead optimize a distribution of possible stellarator coils, accounting for possible deviations of the design variables due to manufacturing or positioning errors. In this case, one can optimize the expected value of an objective function by performing a sample average over the distribution. Stochastic techniques can improve the robustness of the optimum by avoiding small local minima. In this way, the solutions have reduced risk of performance degradation due to errors. This technique has proven effective for the optimization of coil shapes with increased tolerances [199, 198, 299].

14.2 ▪ Direct construction of equilibria

The MHD equilibrium equations may not have analytic solutions in general. In order to make analytical progress, additional assumptions are typically necessary, such as the assumption of a

domain close to the magnetic axis. However, when such solutions can be found, direct construction techniques provide intuition about the relationship between physical quantities of interest, such as quasisymmetry, and geometric parameters, such as the magnetic axis shape.

As an alternative to optimizing the plasma boundary or a set of coils to obtain an omnigeneous or quasisymmetric equilibrium, a configuration can be constructed directly by obtaining analytical solutions to the MHD equilibrium equations upon an asymptotic expansion. For example, one approach is to perform a power series expansion of the equilibrium magnetic field equations near the magnetic axis as introduced in Section 11.2. In particular, this approach has been used to construct quasisymmetric [185, 186, 176, 155] and quasiomnigeneous [241] configurations near the magnetic axis. This method is several orders of magnitude more computationally efficient than the equilibrium optimization approach. Similar approaches are based on an asymptotic expansion in the distance from axisymmetry [240, 239] or in the distance from a magnetic surface [112]. Given that the expressions for the equilibrium field can be evaluated efficiently from closed-form solutions, direct construction techniques have also been used within the context of numerical optimization of the magnetic field. Specifically, they can provide good initial guesses for numerical optimization, or optimization can be carried out in the space of constructed solutions [154, 179].

14.3 ▪ Engineering metrics for coil design

Given that coil complexity can be a large driver of cost in stellarator devices [280], engineering criteria have been further incorporated into the coil design process. As was mentioned in Section 13.4, electromagnetic coils have traditionally been optimized with simplifying assumptions by approximating them as a sheet current or filamentary lines of current. More realistic modeling of coils has been performed with codes that take into account their cross-sectional build [266]. This requires optimization over not only the curve defining the center of the winding pack but also the orientation of the rectangular winding pack with respect to a fixed axis. In addition to modeling of the finite-build structure within optimization codes, constraints related to new magnet technology have been implemented. High-temperature superconducting (HTS) magnets enable access to high magnetic field strengths at higher temperatures. This reduces the cost and engineering complexity of cooling the conductor in comparison to low-temperature superconductors. Since confinement scales very strongly with the magnetic field strength in a magnetic confinement device, HTS enables access to improved performance in a more compact device. While the application of HTS is attractive for confinement in a stellarator, there are additional complexities introduced in building nonplanar HTS magnets due to anisotropic strains on the conductor. Techniques have been developed to optimize HTS coil parameters for reduced strain [238], and HTS cables have been wound into a nonplanar shape similar to the HSX modular coil shape [253].

14.4 ▪ Integrated coil design

As described in Section 13.4, stellarator design has traditionally decoupled coil optimization from optimization of the MHD equilibrium. However, such a decoupling may result in an equilibrium that can only be produced with overly complex coils. As the cost of constructing a stellarator experiment is closely related to coil complexity, it is important to consider how to couple coil design with equilibrium optimization. There are several approaches to address this issue.

One option is to directly optimize coils based on free-boundary solutions of the MHD equilibrium equations, eliminating the need to design coils as a second step. For example, this approach

was used in the final stages of the NCSX design [142, 146]. The direct optimization approach is somewhat more challenging for several reasons. Free-boundary equilibrium calculations tend to be more expensive than fixed-boundary calculations, as they require iterations between an equilibrium solution and vacuum field calculations. This iterative scheme will not always converge in practice, hence the historical use of the more robust fixed-boundary method. It has also been suggested that fixed-boundary optimization may yield better equilibrium properties, as the model assumes the existence of at least one magnetic surface.

An alternative approach is to perform fixed-boundary equilibrium optimization in tandem with the optimization of a set of coils to be consistent with the fixed-boundary [144, 153]. In a vacuum magnetic field, the equilibrium calculation can be eliminated entirely since the field is known from the Biot–Savart law. In this case, the properties of the magnetic field can be inferred from postprocessing of the field, such as by evaluating approximate magnetic surfaces [88].

14.5 ▪ Nonlinear MHD stability

As discussed in Section 13.1.6, if an equilibrium is unstable to macroscopic MHD modes, the plasma can undergo large-scale changes, potentially degrading confinement and damaging device components.

Historically, criteria for linear MHD stability in stellarator optimization have been based on reduced models localized to individual flux surfaces under the assumption of the existence of continuously nested flux surfaces discussed in Remark 4.4. For example, two common criteria are the magnetic well criterion and the Mercier criterion mentioned in Section 13.1.6. The corresponding reduced models involve local curvature and pressure gradients on individual flux surfaces that can drive or stabilize some MHD instabilities.

However, potentially important effects associated with nonlinearity or resistivity are not described in these reduced models. It has been suggested that targeting linear, ideal MHD stability in the optimization of quasiaxisymmetric configurations leads to coils with undesirable characteristics [72]. Moreover, as highlighted in Section 13.1.6, experimental evidence from LHD suggests that stellarators may be able to operate above linear stability thresholds without significantly degrading performance [162, 303]. Consequently, optimizing for nonlinear MHD stability is an important area of work [82]. Computational advances have enabled tools capable of modeling the nonlinear MHD time evolution of strongly shaped stellarator plasmas [325, 227, 268], allowing testing and continuing development of strategies to directly optimize for nonlinear MHD stability [12, 78].

14.6 ▪ Permanent magnets

There have been efforts to design permanent magnets rather than electromagnetic coils to confine stellarator plasmas. While toroidal field coils are necessary to provide the required toroidal flux, permanent magnets can provide the required shaping field and reduce the toroidal field coil complexity. Numerical simulations indicate that permanent magnets can be combined with simple planar toroidal field coils to confine stellarator equilibria. In comparison to nonplanar modular coil systems, permanent magnet solutions can also improve experimental access to the plasma chamber [326]. Several numerical methods have been developed to optimize the distribution and orientation of permanent magnets: some of these are based on a current potential solution [118, 328], while others require nonlinear optimization techniques [326, 102]. The concept of permanent magnet stellarators has been explored in both design studies [103] and experiments. MUSE, a small permanent magnetic quasiaxisymmetric stellarator, has been designed at the Princeton Plasma Physics Laboratory, and construction began in 2022 [246]. For the target

equilibrium, MUSE demonstrated that permanent magnets can produce improved neoclassical optimization of the field compared to nonplanar modular coils. In contrast to electromagnetic coils, however, it is more difficult to tune the magnetic field produced by permanent magnets. Consequently, different approaches for reducing magnetic field error may be necessary [258].

14.7 ▪ Theoretical understanding of quasisymmetry

While several decades have passed since the discovery of quasisymmetry [22], there continues to be activity in the theoretical understanding of quasisymmetry. This includes a reformulation of the conditions required for quasisymmetry without assumptions of ideal MHD equilibrium [35, 256] and the derivation of a Grad–Shafranov equation for quasisymmetric magnetic fields [35]. There remain open problems in this area. For example, the near-axis expansion of quasisymmetric MHD equilibria results in an overdetermined system of equations at sufficiently high order [81]. However, if MHD force balance is not enforced, it is possible to obtain quasisymmetric solutions to all orders [257]. Some results suggest that exact quasisymmetry cannot be achieved globally, but only on a single flux surface [81, 240, 262]. While numerical optimization results indicate that quasisymmetric MHD equilibria exist to a very high precision [184], it remains to be seen from fundamental theory if it is possible to circumvent the overdetermined nature of exact quasisymmetry with MHD force balance.

14.8 ▪ Turbulent transport

The transport of particles and heat in magnetically confined plasmas arises due to several mechanisms. Often, the two most important mechanisms are neoclassical transport, describing guiding center trajectories and collisions, and turbulent transport, caused by small-scale fluctuations of electric and magnetic fields described by gyrokinetic theory.

Experiments such as W7-X and HSX have demonstrated the ability to reduce neoclassical transport, arising due to unconfined trajectories and collisions, with equilibrium optimization methods. In fact, experiments on W7-X indicate that with neoclassical transport effectively reduced with optimization, turbulence is the dominant transport mechanism [83]. Thus, an important aspect of the design of stellarators is the optimization of the magnetic field to reduce turbulent transport.

While stellarators have historically been designed for stability with respect to large-scale MHD modes, optimization for microstability is much more challenging due to the computational expense of running nonlinear gyrokinetic simulations. There have been efforts to construct proxy functions that accurately capture the turbulent transport properties of stellarator configurations [254, 203], such as reducing the overlap between bad curvature and trapping regions [312, 85] or increasing nonlinear energy transfer between unstable and damped modes [115]. Properties of the parallel adiabatic invariant $J_{\|}$ can be targeted to improve microstability. For example, maximum-J configurations, for which $J_{\|}$ is a monotonic decreasing function of flux, have stabilizing effects on trapped-particle modes [1]. Some aspects of turbulence optimization have been verified experimentally. As an example, W7-X is a maximum-J configuration. As a result, W7-X has demonstrated improved performance in experiments with a large density gradient, for which the resulting microturbulence is dominated by trapped-particle modes [188].

Appendices

Appendix A
Brief review of Maxwell's equations for electric and magnetic fields

We discuss Maxwell's equations that model the electric and magnetic fields, respectively denoted $\boldsymbol{E}$ and $\boldsymbol{B}$. In this appendix, the plasma density ρ and current density $\boldsymbol{J}$ are considered to be prescribed by another model, and the electromagnetic fields consistent with these sources are the unknowns in the equations. The full set of Maxwell's equations is presented in Section A.1. In the following sections, we will discuss several limits of Maxwell's equations: the electrostatic limit in Section A.2.1, the magnetostatic limit in Section A.2.2, and the vacuum limit in Section A.3. Here, we consider Maxwell's equations in differential form, assuming the fields are smooth.

A.1 ▪ Electromagnetics

Maxwell's equations describe how the electric and magnetic fields, $\boldsymbol{E}$ and $\boldsymbol{B}$, propagate and interact together, as well as with currents and charges. Maxwell's equations refer to the following four equations.

Gauss's law is

$$\nabla \cdot \boldsymbol{E} = \frac{\rho}{\epsilon_0}, \tag{A.1}$$

Ampère's law is

$$\nabla \times \boldsymbol{B} = \mu_0 \boldsymbol{J} + \frac{1}{c^2}\frac{\partial \boldsymbol{E}}{\partial t}, \tag{A.2}$$

Faraday's law is

$$\nabla \times \boldsymbol{E} = -\frac{\partial \boldsymbol{B}}{\partial t}, \tag{A.3}$$

and magnetic fields must be divergence-free,

$$\nabla \cdot \boldsymbol{B} = 0. \tag{A.4}$$

Here $\mu_0 = 1.256 \times 10^{-6}$ NA^{-2} is the permeability of free space, $\epsilon_0 = 8.854 \times 10^{-12}$ Fm^{-1} is the permittivity of free space, and $c = 3 \times 10^8$ ms^{-1} is the speed of light in vacuum. This set of PDEs describes the response of the electric and magnetic fields to charge density ρ and current density $\boldsymbol{J}$ as functions of time and space. Under further assumptions on time scales of interest, Maxwell's equations can be reduced, as we will see in the following sections.

Often, the electric and magnetic fields are expressed in terms of scalar and vector potentials.

- As $\boldsymbol{B}$ is divergence-free, according to (A.4), it can always be written in terms of a vector potential $\boldsymbol{A}$,

$$\boldsymbol{B} = \nabla \times \boldsymbol{A}. \tag{A.5}$$

  We note that there is some nonuniqueness in the choice of the vector potential, as the gradient of any scalar function can be added to $\boldsymbol{A}$ without altering the magnetic field. In the physics literature, this nonuniqueness is referred to as gauge freedom.

- Inserting (A.5) into Faraday's law (A.3), $\boldsymbol{E}$ can be written as $-\partial \boldsymbol{A}/\partial t$ with the addition of a curl-free vector field,

$$\boldsymbol{E} = -\nabla \Phi - \frac{\partial \boldsymbol{A}}{\partial t}. \tag{A.6}$$

  Often Φ is referred to as the scalar potential.

Remark A.1. *The vector potential can be made unique using an appropriate choice of gauge, depending on the application of interest. One common choice is the Coulomb gauge defined by* $\nabla \cdot \boldsymbol{A} = 0$*. As we will see, the vector potential sometimes appears explicitly in physical quantities of interest, for instance, Sections* 7.2 *and* 11.4*, making it important to consider the impact of the choice of gauge.*

A.2 ▪ Static limit

A static system refers to a system in which all quantities are assumed to be time-independent. In the static case, $\partial/\partial t = 0$, the equations satisfied by $\boldsymbol{E}$ and $\boldsymbol{B}$ decouple. The set of equations separately satisfied by the electric and magnetic fields, in this case, are referred to as electrostatics and magnetostatics, respectively.

A.2.1 ▪ Electrostatics

The electrostatics model describes a static electric field. Under the static assumption, the electric field satisfies $\nabla \times \boldsymbol{E} = 0$. If, moreover, $\boldsymbol{E}$ is assumed to be continuously differentiable on a simply connected domain, then the electric field can be written in terms of only a scalar potential as

$$\boldsymbol{E} = -\nabla \Phi.$$

From Gauss's law (A.1) the electrostatic potential satisfies Poisson's equation,

$$\Delta \Phi = -\frac{\rho}{\epsilon_0}.$$

Gauss's law can be written in an equivalent integral form by integrating over a generic volume Ω,

$$\text{for all volume } \Omega \subset \mathbb{R}^3, \int_{\partial\Omega} \boldsymbol{E} \cdot \hat{\boldsymbol{n}}\, d^2 r = \frac{1}{\epsilon_0} \int_{\Omega} \rho\, d^3 r,$$

where $\hat{\boldsymbol{n}}$ is the outward unit vector normal to the boundary $\partial\Omega$ of the volume Ω.

A.2.2 ▪ Magnetostatics

The magnetostatics model describes a static magnetic field. Under the static assumption, Ampère's law becomes

$$\nabla \times \boldsymbol{B} = \mu_0 \boldsymbol{J}. \tag{A.7}$$

Remark A.2. *If fields $\boldsymbol{B}$ and $\boldsymbol{J}$ satisfy this equation, then necessarily $\nabla \cdot \boldsymbol{J} = 0$.*

Under the magnetostatic assumption, Ampère's law can be written in an equivalent integral form,

$$\text{for all surface } S \subset \mathbb{R}^3, \oint_{\partial S} \boldsymbol{B} \cdot d\boldsymbol{l} = \mu_0 \int_S \boldsymbol{J} \cdot \hat{\boldsymbol{n}}\, d^2 r, \tag{A.8}$$

where for an open surface, the line integral is taken along a closed curve forming the boundary of the surface S and $d\boldsymbol{l}$ is oriented counterclockwise with respect to the orientation induced by the normal $\hat{\boldsymbol{n}}$, while for a closed surface, the left-hand side is zero. Another integral form that is consistent with the magnetostatic equations is the Biot–Savart law,

$$\boldsymbol{B}(\boldsymbol{r}) = \frac{\mu_0}{4\pi} \int_{\mathbb{R}^3} \frac{\boldsymbol{J}(\boldsymbol{r}') \times (\boldsymbol{r} - \boldsymbol{r}')}{|\boldsymbol{r} - \boldsymbol{r}'|^3}\, d^3 r'. \tag{A.9}$$

This can be seen as an application of a Green's function approach to (A.7). For example, in a magnetic confinement fusion device, the integral can be taken throughout the plasma volume and along the electromagnetic coils.

Remark A.3. *Often, the displacement current term, $\partial \boldsymbol{E}/\partial t$ in* (A.2)*, can be neglected if the typical velocities of a system, v, are nonrelativistic so that $v/c \ll 1$. This is the assumption that the model does not include light waves, associated with very short time scales. Therefore, Ampère's law in the form* (A.7) *may still be applicable even if the system is not completely static.*

A.3 ▪ Vacuum magnetic fields

The term vacuum magnetic field is used to describe the magnetic field in a region Ω_{vac} without currents under the magnetostatics assumptions. In magnetic confinement fusion, this could be the region outside the plasma, not including the electromagnetic coils. In this case, we have $\nabla \times \boldsymbol{B} = 0$, so a scalar potential, Φ_B, can be used to describe the magnetic field,

$$\boldsymbol{B} = \nabla \Phi_B \text{ in } \Omega_{\text{vac}}. \tag{A.10}$$

The magnetic field must also satisfy the divergence-free condition (A.4), so the scalar potential must satisfy Laplace's equation,

$$\Delta \Phi_B = 0 \text{ in } \Omega_{\text{vac}}. \tag{A.11}$$

The solution of this equation in a toroidal domain, combined with adequate boundary conditions, will be discussed in Section 11.6.

Instead of solving Laplace's equation, the magnetic field in a vacuum region denoted Ω_{vac} can also be determined using the Biot–Savart law (A.9), integrating over all currents outside of the vacuum region,

$$\forall \boldsymbol{r} \in \Omega_{\text{vac}},\ \boldsymbol{B}(\boldsymbol{r}) = \frac{\mu_0}{4\pi} \int_{\mathbb{R}^3 \setminus \Omega_{\text{vac}}} \frac{\boldsymbol{J}(\boldsymbol{r}') \times (\boldsymbol{r} - \boldsymbol{r}')}{|\boldsymbol{r} - \boldsymbol{r}'|^3}\, d^3 r'.$$

A.4 ▪ Summary

Here, we described Maxwell's equations in the presence of some charge density ρ and current density $\boldsymbol{J}$. A realistic model would include coupling to a set of equations modeling the evolution of the charge and current density. Under various sets of hypotheses, Maxwell's equations can be reduced to simpler models. Common reduced models are gathered in Table A.1. For each reduced model, the table provides the hypotheses (Hyp.), the PDE model, a different formulation of the model, and the model data. Computational domains, as well as boundary conditions, are addressed in Section 11.6.

Table A.1: *Summary of Maxwell's equations under several hypotheses of interest for stellarator design.*

	Maxwell	Electrostatics	Magnetostatics	Vacuum fields
Hyp.		$\partial \boldsymbol{E}/\partial t = 0$ $\partial \boldsymbol{B}/\partial t = 0$	$\partial \boldsymbol{E}/\partial t = 0$ $\partial \boldsymbol{B}/\partial t = 0$	$\partial \boldsymbol{E}/\partial t = 0$ $\partial \boldsymbol{B}/\partial t = 0$ $\boldsymbol{J} = 0$ in Ω_{vac}
PDE model	$\nabla \cdot \boldsymbol{E} = \frac{\rho}{\epsilon_0}$ $\nabla \times \boldsymbol{B} = \mu_0 \boldsymbol{J} + \frac{1}{c^2}\frac{\partial \boldsymbol{E}}{\partial t}$ $\nabla \times \boldsymbol{E} = -\frac{\partial \boldsymbol{B}}{\partial t}$ $\nabla \cdot \boldsymbol{B} = 0$	$\nabla \cdot \boldsymbol{E} = \frac{\rho}{\epsilon_0}$ $\nabla \times \boldsymbol{E} = 0$	$\nabla \times \boldsymbol{B} = \mu_0 \boldsymbol{J}$ $\nabla \cdot \boldsymbol{B} = 0$	$\nabla \times \boldsymbol{B} = 0$ in Ω_{vac} $\nabla \cdot \boldsymbol{B} = 0$ in Ω_{vac}
Model $\Leftrightarrow$		$\boldsymbol{E} = -\nabla \Phi$ $\Delta \Phi = -\frac{\rho}{\epsilon_0}$	$\boldsymbol{B}(\boldsymbol{r}) = \frac{\mu_0}{4\pi} \times$ $\int_{\mathbb{R}^3} \frac{\boldsymbol{J}(\boldsymbol{r}') \times (\boldsymbol{r} - \boldsymbol{r}')}{\lvert \boldsymbol{r} - \boldsymbol{r}' \rvert^3} d^3 r'$	$\boldsymbol{B}(\boldsymbol{r}) = \frac{\mu_0}{4\pi} \times$ $\int_{\mathbb{R}^3 \setminus \Omega_{\text{vac}}} \frac{\boldsymbol{J}(\boldsymbol{r}') \times (\boldsymbol{r} - \boldsymbol{r}')}{\lvert \boldsymbol{r} - \boldsymbol{r}' \rvert^3} d^3 r'$ $\Leftrightarrow \begin{cases} \boldsymbol{B} = \nabla \Phi_B & \text{in } \Omega_{\text{vac}} \\ \Delta \Phi_B = 0 \end{cases}$
Given	$\boldsymbol{J}, \rho$	ρ	$\boldsymbol{J}$	$\boldsymbol{J}$ outside of Ω_{vac}

Appendix B
Brief review of classical mechanics for charged particle motion

Classical mechanics refers to the study of phenomena occurring at velocities much smaller than the speed of light and at length scales much larger than the atomic size. Here, we briefly review classical mechanics concepts necessary to describe charged particle motion in plasmas.

We begin in Section B.1 with Newton's law, taking the form of a set of ODEs. We will then show that these ODEs can be obtained from two variational principles involving the Lagrangian and Hamiltonian functionals, respectively in Sections B.2 and B.3. An alternative Lagrangian framework, known as the phase-space Lagrangian, is summarized in Section B.4.

B.1 ▪ Newton's law

Newton's law is a set of ODEs describing a relationship between the acceleration of an object and the net force $\boldsymbol{F}$ acting on this object. In dimension $N \in \mathbb{N}$, if the force depends on the position and the velocity of the object and the object is of mass m, then Newton's law can be expressed as an equation for the trajectory of a particle, $\boldsymbol{q}_T$ as a function of t, as

$$m\frac{d^2\boldsymbol{q}_T(t)}{dt^2} = \boldsymbol{F}\left(\boldsymbol{q}_T(t), \frac{d\boldsymbol{q}_T(t)}{dt}, t\right), \tag{B.1}$$

where the first-order derivative of $\boldsymbol{q}_T$ is the velocity and its second-order derivative is the acceleration. In words, Newton's law simply states that the force is equal to the acceleration of a particle multiplied by its mass. While some physical situations may introduce nonsmoothness in the dynamics, such as in collisions between particles, in the context of our discussion of classical mechanics, we assume smooth trajectories.

A foundational example is the study of single-particle motion in given electric and magnetic fields, respectively denoted $\boldsymbol{E}$ and $\boldsymbol{B}$. In this context, we take $N = 3$. The force acting on the particle depends on the particle charge q, on the position $\boldsymbol{q}$, on time t through $\boldsymbol{B}$ and $\boldsymbol{E}$, and explicitly on the velocity $\dot{\boldsymbol{q}}$. It is called the Lorentz force and is defined, for given vector fields $\boldsymbol{B}$ and $\boldsymbol{E}$ given as functions from $\mathbb{R}^3 \times \mathbb{R}$ to $\mathbb{R}^3$, as follows:

$$\boldsymbol{F}(\boldsymbol{q}, \dot{\boldsymbol{q}}, t) = q(\dot{\boldsymbol{q}} \times \boldsymbol{B}(\boldsymbol{q}, t) + \boldsymbol{E}(\boldsymbol{q}, t)). \tag{B.2}$$

For some simple enough vector fields $\boldsymbol{B}$ and $\boldsymbol{E}$, Newton's law can be solved explicitly to obtain

the trajectory of a particle, $\boldsymbol{q}_T$ as a function of t, given initial conditions at some time t_{init}:

$$\begin{cases} \boldsymbol{q}_T(t_{\text{init}}) = \boldsymbol{q}_{\text{init}}, \\ \dfrac{d\boldsymbol{q}_T(t_{\text{init}})}{dt} = \dot{\boldsymbol{q}}_{\text{init}}, \end{cases}$$

for given constants $(\boldsymbol{q}_{\text{init}}, \dot{\boldsymbol{q}}_{\text{init}})$.

In Section 4.1, we study trajectories within a uniform, straight magnetic field using the ODEs defined by (B.1)–(B.2).

B.2 ▪ Lagrangian formulation

The Lagrangian formulation is an equivalent formulation relying on a variational approach: the trajectories of a system minimize the so-called action of this system. This is known as the principle of stationary or least action. The action is defined in terms of a functional called the Lagrangian in a variational formalism. The Lagrangian is a real-valued functional describing the energies of the system, potential energy, and kinetic energy, rather than the forces. For further reading on Lagrangian mechanics, consider [293] and Chapter 2 in [90].

An important relation exists between the Newtonian and Lagrangian approaches: it can be shown that trajectories that are stationary points of the action correspond to those that satisfy Newton's law. Yet, calculations may be simplified when manipulating the scalar Lagrangian as opposed to the vector equations of motion like (B.1). Moreover, the Lagrangian formalism provides insight into certain conserved quantities.

B.2.1 ▪ Euler–Lagrange equations

To describe a physical system, in dimension $N \in \mathbb{N}$, the Lagrangian L may depend on the position, $\boldsymbol{q} \in \mathbb{R}^N$, the velocity, $\dot{\boldsymbol{q}} \in \mathbb{R}^N$, and time $t \in \mathbb{R}$. It is crucial that $\boldsymbol{q}$ and $\dot{\boldsymbol{q}}$ are independent variables in the definition of the Lagrangian, although the Lagrangian can be evaluated along trajectories, $\boldsymbol{q}_T : \mathbb{R} \to \mathbb{R}^N$ parameterized by t. Along these curves, the velocity is $d\boldsymbol{q}_T(t)/dt$. These variables are also referred to as the generalized coordinate, $\boldsymbol{q}$, and generalized momentum, $\dot{\boldsymbol{q}}$, of the system. If the Lagrangian L describes a given system, the definition of the action integral, referring to the action of this system during a time interval $[t_{\text{init}}, t_{\text{final}}]$ along a curve, is

$$\forall \boldsymbol{q}_T : \mathbb{R} \to \mathbb{R}^N, \quad S[\boldsymbol{q}_T] := \int_{t_{\text{init}}}^{t_{\text{final}}} L\left(\boldsymbol{q}_T(t), \frac{d\boldsymbol{q}_T(t)}{dt}, t\right) dt. \tag{B.3}$$

For compactness, the velocity is often denoted $\dot{\boldsymbol{q}}_T$, but it is important to keep in mind that this always means $\dot{\boldsymbol{q}}_T = d\boldsymbol{q}_T(t)/dt$. Since the trajectories of a system minimize this action integral, they are the stationary points.

In order to identify the stationary points of S, we then compute the first variation of S with respect to $\boldsymbol{q}_T$, keeping the endpoints of the curve fixed. Hence we consider a perturbation to the curve, denoted $\delta\boldsymbol{q}_T$, defining a vector field, together with the initial and final conditions $\delta\boldsymbol{q}_T(t_{\text{init}}) = 0$ and $\delta\boldsymbol{q}_T(t_{\text{final}}) = 0$. The resulting perturbation of S is then

$$\begin{aligned} &\delta S[\boldsymbol{q}_T; \delta\boldsymbol{q}_T] \\ &= \int_{t_{\text{init}}}^{t_{\text{final}}} \left(\frac{\partial L(\boldsymbol{q}_T(t), \dot{\boldsymbol{q}}_T(t), t)}{\partial \boldsymbol{q}} \cdot \delta\boldsymbol{q}_T(t) + \frac{\partial L(\boldsymbol{q}_T(t), \dot{\boldsymbol{q}}_T(t), t)}{\partial \dot{\boldsymbol{q}}} \cdot \delta\dot{\boldsymbol{q}}_T(t) \right) dt, \end{aligned}$$

where $\delta\dot{\boldsymbol{q}}_T(t) = d(\delta\boldsymbol{q}_T(t))/dt$, and $\partial L/\partial \boldsymbol{q}$ and $\partial L/\partial \dot{\boldsymbol{q}}$ respectively denote vectors of dimension N whose jth entries are the derivative with respect to the jth component of $\boldsymbol{q}$ and $\dot{\boldsymbol{q}}$. The

second term on the right-hand side can be integrated by parts, then thanks to the initial and final conditions for $\delta \boldsymbol{q}_T$, it yields

$$\delta S[\boldsymbol{q}_T; \delta \boldsymbol{q}_T] = \int_{t_{\text{init}}}^{t_{\text{final}}} \left(\frac{\partial L(\boldsymbol{q}_T(t), \dot{\boldsymbol{q}}_T(t), t)}{\partial \boldsymbol{q}} - \frac{d}{dt} \left(\frac{\partial L(\boldsymbol{q}_T(t), \dot{\boldsymbol{q}}_T(t), t)}{\partial \dot{\boldsymbol{q}}} \right) \right) \cdot \delta \boldsymbol{q}_T(t)\, dt.$$

In order for a curve $\boldsymbol{q}_T$ to be a stationary point of the action S, it is necessary for the perturbed action $\delta S[\boldsymbol{q}_T; \delta \boldsymbol{q}_T]$ to vanish for all $\delta \boldsymbol{q}_T$; thus, the integrand above must vanish for all perturbation $\delta \boldsymbol{q}_T$. This condition on the curve reads

$$\frac{d}{dt} \left(\frac{\partial L(\boldsymbol{q}_T(t), \dot{\boldsymbol{q}}_T(t), t)}{\partial \dot{\boldsymbol{q}}} \right) = \frac{\partial L(\boldsymbol{q}_T(t), \dot{\boldsymbol{q}}_T(t), t)}{\partial \boldsymbol{q}}. \tag{B.4}$$

Any curve $\boldsymbol{q}_T$ satisfying this equation is then called a trajectory and parameterizes the motion of a particle in the physical system described by the Lagrangian L. Along any trajectory, the particle's position and velocity are related through $\dot{\boldsymbol{q}}_T(t) = d\boldsymbol{q}_T(t)/dt$.

B.2.2 ▪ Properties of Lagrangian systems

In this formalism, an important relation exists between continuous symmetry and conserved quantities, referring to quantities that remain constant along any trajectory. The former refers to the invariance of a system under a continuous transformation. For example, the system is independent of a position coordinate, and the corresponding Lagrangian is then independent of this coordinate. The latter refers to quantities that are constant along each trajectory of the system. From the Euler–Lagrange equations, it is straightforward to see that if the Lagrangian is independent of a coordinate, denoted q_j, then the derivative of the Lagrangian with respect to the conjugate component of the velocity, namely $\dot{q}_j$, is a constant of the motion. Indeed, along a trajectory, $\boldsymbol{q}_T : \mathbb{R} \to \mathbb{R}^N$, we have

$$\frac{d}{dt} \left(\frac{\partial L(\boldsymbol{q}_T(t), \dot{\boldsymbol{q}}_T(t), t)}{\partial \dot{\boldsymbol{q}}_j} \right) = 0.$$

Such components can be called ignorable coordinates. The existence of an ignorable coordinate, therefore, implies the existence of a conserved quantity, as long as it is not a trivial quantity. As a result, an adequate choice of symmetries expressed in an adequate coordinate system then implies the existence of conserved quantities. This result is generalized by Noether's theorem [90] introduced in Remark 7.2.

B.2.3 ▪ Charged particle motion

We now consider charged particle motion in given electromagnetic fields and will illustrate how the Euler–Lagrange equations for the Lagrangian described below indeed correspond to Newton's law (B.1). Here, we restrict our attention to the 3D case, $N = 3$. In this context, subscripts j on vector fields indicate Cartesian components. To proceed, consider the standard expressions of the given electric and magnetic fields, $\boldsymbol{B}$ and $\boldsymbol{E}$, in terms of vector and scalar potentials:

$$\forall (\boldsymbol{q}, t) \in \mathbb{R}^3 \times \mathbb{R}, \begin{cases} \boldsymbol{B}(\boldsymbol{q}, t) = \nabla \times \boldsymbol{A}(\boldsymbol{q}, t), \\ \boldsymbol{E}(\boldsymbol{q}, t) = -\nabla \Phi(\boldsymbol{q}, t) - \dfrac{\partial \boldsymbol{A}(\boldsymbol{q}, t)}{\partial t}. \end{cases} \tag{B.5}$$

Then, to describe the motion of a particle of charge q and mass m in these fields, consider the Lagrangian defined by

$$\forall (\boldsymbol{q}, \dot{\boldsymbol{q}}, t) \in \mathbb{R}^3 \times \mathbb{R}^3 \times \mathbb{R}, L(\boldsymbol{q}, \dot{\boldsymbol{q}}, t) = \frac{m|\dot{\boldsymbol{q}}|^2}{2} + q\big(\boldsymbol{A}(\boldsymbol{q}, t) \cdot \dot{\boldsymbol{q}} - \Phi(\boldsymbol{q}, t)\big). \tag{B.6}$$

Directly from the definition of the Lagrangian, we obtain

$$\forall (\boldsymbol{q}, \dot{\boldsymbol{q}}, t) \in \mathbb{R}^3 \times \mathbb{R}^3 \times \mathbb{R}, \begin{cases} \dfrac{\partial L(\boldsymbol{q}, \dot{\boldsymbol{q}}, t)}{\partial \boldsymbol{q}} = q \left(\dfrac{\partial \big(\boldsymbol{A}(\boldsymbol{q}, t) \cdot \dot{\boldsymbol{q}} \big)}{\partial \boldsymbol{q}} - \dfrac{\partial \Phi(\boldsymbol{q}, t)}{\partial \boldsymbol{q}} \right), \\ \dfrac{\partial L(\boldsymbol{q}, \dot{\boldsymbol{q}}, t)}{\partial \dot{\boldsymbol{q}}} = m \dot{\boldsymbol{q}} + q \boldsymbol{A}(\boldsymbol{q}, t). \end{cases}$$

For the sake of compactness, we will now use the notation $\nabla = \partial / \partial \boldsymbol{q}$. In order to express explicitly all terms above, we use the subscript j to refer to the jth component of a vector and get

$$\begin{aligned} \nabla \big(\boldsymbol{A}(\boldsymbol{q}, t) \cdot \dot{\boldsymbol{q}} \big) &= \nabla \left(\sum_{j=1}^{3} A_j(\boldsymbol{q}, t) \dot{q}_j \right) \\ &= \sum_{j=1}^{3} \big(\nabla A_j(\boldsymbol{q}, t) \big) \dot{q}_j. \end{aligned}$$

Besides, along a trajectory, $\boldsymbol{q}_T : \mathbb{R} \to \mathbb{R}^3$, we have

$$\begin{aligned} \frac{d}{dt} \left(\frac{\partial L(\boldsymbol{q}_T(t), \dot{\boldsymbol{q}}_T(t), t)}{\partial \dot{\boldsymbol{q}}} \right) &= \frac{d}{dt} \left(m \dot{\boldsymbol{q}}_T(t) + q \boldsymbol{A}(\boldsymbol{q}_T(t), t) \right) \\ &= m \frac{d^2 \boldsymbol{q}_T(t)}{dt^2} + q \left(\sum_{j=1}^{3} \frac{\partial \boldsymbol{A}(\boldsymbol{q}_T(t), t)}{\partial q_j} \big(\dot{\boldsymbol{q}}_T(t) \big)_j + \frac{\partial \boldsymbol{A}(\boldsymbol{q}_T(t), t)}{\partial t} \right). \end{aligned}$$

Finally, it is straightforward to verify that

$$\forall (\boldsymbol{q}, \dot{\boldsymbol{q}}, t) \in \mathbb{R}^3 \times \mathbb{R}^3 \times \mathbb{R}, \sum_{j=1}^{3} \big(\nabla A_j(\boldsymbol{q}, t) \big) \dot{q}_j - \sum_{j=1}^{3} \frac{\partial \boldsymbol{A}(\boldsymbol{q}, t)}{\partial q_j} \dot{q}_j = \dot{\boldsymbol{q}} \times \big(\nabla \times \boldsymbol{A}(\boldsymbol{q}, t) \big).$$

As a consequence, the Euler–Lagrange equations read

$$m \frac{d^2 \boldsymbol{q}_T(t)}{dt^2} = q \dot{\boldsymbol{q}}_T(t) \times \big(\nabla \times \boldsymbol{A}(\boldsymbol{q}_T(t), t) \big) - q \nabla \Phi(\boldsymbol{q}_T(t), t) - q \frac{\partial \boldsymbol{A}(\boldsymbol{q}_T(t), t)}{\partial t}.$$

Recognizing the expressions for the electromagnetic fields in terms of vector and scalar potentials (B.5), we identify the familiar Lorentz force (B.2):

$$m \frac{d^2 \boldsymbol{q}_T(t)}{dt^2} = q \dot{\boldsymbol{q}}_T(t) \times \boldsymbol{B}(\boldsymbol{q}_T(t), t) + q \boldsymbol{E}(\boldsymbol{q}_T(t), t). \tag{B.7}$$

As expected, we conclude that the Euler–Lagrange equations for the Lagrangian (B.6) reduce to Newton's law (B.1) with the Lorentz force (B.2). This demonstrates that (B.6) is indeed the correct Lagrangian to describe single-particle motion in electromagnetic fields.

The Lagrangian approach will provide several advantages as we consider reduced models in the limit of a strong magnetic field in Section 4.2. In Sections 4.3.1 and 4.3.2, we will leverage the Lagrangian formalism to obtain conserved quantities.

B.3 ▪ Hamiltonian formulation

The Hamiltonian formulation also relies on a variational approach and is introduced as a reformulation of the Lagrangian formulation. Rather than treating the position $\boldsymbol{q}$ and velocity $\dot{\boldsymbol{q}}$ as

independent coordinates, in the Hamiltonian formalism, we take as independent coordinates the position, denoted $\boldsymbol{q}$, and the canonical momentum, denoted $\boldsymbol{p}$. The Hamiltonian H is a scalar-valued functional defined in terms of the Lagrangian. Calculations may also be simplified when manipulating the scalar Hamiltonian as opposed to the vector equations of motion. Moreover, the Hamiltonian formalism provides insight into certain geometric aspects of trajectories. For further reading on Hamiltonian mechanics, consider [292] and Chapter 8 of [90].

B.3.1 ▪ Hamilton's equations

Given a system described by a Lagrangian L, the Hamiltonian formulation can be introduced as follows. To describe the physical system characterized by L, in dimension $N \in \mathbb{N}$, the Hamiltonian H may depend on the position, $\boldsymbol{q} \in \mathbb{R}^N$, the canonical momentum, $\boldsymbol{p} \in \mathbb{R}^N$, and time $t \in \mathbb{R}$. These variables are also referred to, respectively, as the canonical coordinates and canonical momenta, and the space $\{(\boldsymbol{q}, \boldsymbol{p}) \in \mathbb{R}^N \times \mathbb{R}^N\}$ is then referred to as the phase space. Their relation to the position and velocity, respectively $\boldsymbol{q} \in \mathbb{R}^N$ and $\dot{\boldsymbol{q}} \in \mathbb{R}^N$, can be defined as a mapping from the Lagrangian coordinates $(\boldsymbol{q}, \dot{\boldsymbol{q}})$ to the Hamiltonian coordinates $(\boldsymbol{q}, \boldsymbol{p})$ at any given t:

$$\begin{cases} \boldsymbol{q} = \boldsymbol{q}, \\ \boldsymbol{p} = \dfrac{\partial L(\boldsymbol{q}, \dot{\boldsymbol{q}}, t)}{\partial \dot{\boldsymbol{q}}}, \end{cases} \tag{B.8}$$

where $\partial/\partial\dot{\boldsymbol{q}}$ are vectors of dimension N whose jth entries are the derivative with respect to the jth component of $\dot{\boldsymbol{q}}$. We will similarly write $\partial/\partial\boldsymbol{q}$ and $\partial/\partial\boldsymbol{p}$. The second relation is assumed to be invertible with respect to $\dot{\boldsymbol{q}}$ so that it can be expressed as a function of the position and momentum: $\dot{\boldsymbol{q}}(\boldsymbol{q}, \boldsymbol{p})$. The Hamiltonian is then defined as

$$H(\boldsymbol{q}, \boldsymbol{p}, t) = \boldsymbol{p} \cdot \dot{\boldsymbol{q}}(\boldsymbol{q}, \boldsymbol{p}) - L(\boldsymbol{q}, \dot{\boldsymbol{q}}(\boldsymbol{q}, \boldsymbol{p}), t). \tag{B.9}$$

It is beyond the scope of this book, but L and H are Legendre transforms of each other.

To describe the system, each conjugate pair (q_i, p_i) corresponds to one degree of freedom of the system. Hence, N is referred to as the number of degrees of freedom or the dimension of the system. An autonomous Hamiltonian system refers to a system defined by a Hamiltonian H independent of the time variable, that is, $\partial H/\partial t = 0$, while a nonautonomous Hamiltonian system refers to a system defined by a Hamiltonian H depending explicitly on time. In the literature, the dimension of an N-dimensional nonautonomous Hamiltonian system is said to be $N + \frac{1}{2}$. This is a way to distinguish between the time degree of freedom and the other degrees of freedom.

We will now apply the action integral, defined in terms of the Lagrangian (B.3), to the Hamiltonian, defined in terms of the Lagrangian through (B.9). By finding stationary points of the action integral, we will obtain equations of motion, known as Hamilton's equations. We will show the equivalence between the Euler–Lagrange equations and Hamilton's equation for the case of particle motion in electromagnetic fields in Section B.3.3.

The definition of the action integral, referring to the action of the system during a time interval $[t_{\text{init}}, t_{\text{final}}]$ along any phase-space curve $(\boldsymbol{q}_T, \boldsymbol{p}_T) : \mathbb{R} \to \mathbb{R}^N \times \mathbb{R}^N$ is then given by

$$\mathcal{W}[\boldsymbol{q}_T, \boldsymbol{p}_T] := \int_{t_{\text{init}}}^{t_{\text{final}}} \left(\boldsymbol{p}_T(t) \cdot \frac{d\boldsymbol{q}_T(t)}{dt} - H\big(\boldsymbol{q}_T(t), \boldsymbol{p}_T(t), t\big) \right) dt. \tag{B.10}$$

We will again consistently write $(\boldsymbol{q}, \boldsymbol{p})$ to denote the independent variables of the Hamiltonian, as opposed to $(\boldsymbol{q}_T, \boldsymbol{p}_T) : \mathbb{R} \to \mathbb{R}^N \times \mathbb{R}^N$ to denote a curve in phase space parameterized by time t.

In order to define the stationary points of $\mathcal{W}$, we then compute the first variation of $\mathcal{W}$ with respect to $(\boldsymbol{q}_T, \boldsymbol{p}_T)$, keeping the endpoints of the curve fixed. Hence we consider a perturbation of the curve, denoted $(\delta\boldsymbol{q}_T, \delta\boldsymbol{p}_T)$, defining a vector field in phase space, together with the initial and final conditions $\delta\boldsymbol{p}_T(t_{\text{init}}) = 0$, $\delta\boldsymbol{q}_T(t_{\text{init}}) = 0$, $\delta\boldsymbol{p}_T(t_{\text{final}}) = 0$, and $\delta\boldsymbol{q}_T(t_{\text{final}}) = 0$. The resulting perturbation of $\mathcal{W}$ is then

$$\begin{aligned}\delta\mathcal{W}[\boldsymbol{q}_T, \boldsymbol{p}_T; \delta\boldsymbol{q}_T, \delta\boldsymbol{p}_T] \\ = \int_{t_{\text{init}}}^{t_{\text{final}}} \Bigg(\delta\boldsymbol{p}_T(t) \cdot \frac{d\boldsymbol{q}_T(t)}{dt} + \boldsymbol{p}_T(t) \cdot \frac{d\delta\boldsymbol{q}_T(t)}{dt} - \frac{\partial H\big(\boldsymbol{q}_T(t), \boldsymbol{p}_T(t), t\big)}{\partial \boldsymbol{q}} \cdot \delta\boldsymbol{q}_T(t) \\ - \frac{\partial H\big(\boldsymbol{q}_T(t), \boldsymbol{p}_T(t), t\big)}{\partial \boldsymbol{p}} \cdot \delta\boldsymbol{p}_T(t) \Bigg)\, dt.\end{aligned}$$

Upon integration by parts with respect to t, we obtain

$$\begin{aligned}\delta\mathcal{W}[\boldsymbol{q}_T, \boldsymbol{p}_T; \delta\boldsymbol{q}_T, \delta\boldsymbol{p}_T] \\ = \int_{t_{\text{init}}}^{t_{\text{final}}} \Bigg(\delta\boldsymbol{p}_T(t) \cdot \frac{d\boldsymbol{q}_T(t)}{dt} - \frac{d\boldsymbol{p}_T(t)}{dt} \cdot \delta\boldsymbol{q}_T(t) - \frac{\partial H\big(\boldsymbol{q}_T(t), \boldsymbol{p}_T(t), t\big)}{\partial \boldsymbol{q}} \cdot \delta\boldsymbol{q}_T(t) \\ - \frac{\partial H\big(\boldsymbol{q}_T(t), \boldsymbol{p}_T(t), t\big)}{\partial \boldsymbol{p}} \cdot \delta\boldsymbol{p}_T(t) \Bigg)\, dt.\end{aligned}$$

In order for a curve $(\boldsymbol{q}_T, \boldsymbol{p}_T) : \mathbb{R} \to \mathbb{R}^N \times \mathbb{R}^N$ to be a stationary point of the action $\mathcal{W}$, it is necessary for the perturbed action $\delta\mathcal{W}[\boldsymbol{q}_T, \boldsymbol{p}_T; \delta\boldsymbol{q}_T, \delta\boldsymbol{p}_T]$ to vanish for all perturbations. Thus, the integrand above must vanish for all perturbations $(\delta\boldsymbol{q}_T, \delta\boldsymbol{p}_T)$. This condition is called Hamilton's equations, namely

$$\begin{cases} \dfrac{d\boldsymbol{q}_T(t)}{dt} = \dfrac{\partial H\big(\boldsymbol{q}_T(t), \boldsymbol{p}_T(t), t\big)}{\partial \boldsymbol{p}}, \\ \dfrac{d\boldsymbol{p}_T(t)}{dt} = -\dfrac{\partial H\big(\boldsymbol{q}_T(t), \boldsymbol{p}_T(t), t\big)}{\partial \boldsymbol{q}}. \end{cases} \tag{B.11}$$

Any curve $(\boldsymbol{q}_T, \boldsymbol{p}_T)$ satisfying these equations is then called a trajectory and parameterizes the motion of a particle in the phase-space system described by the Hamiltonian H, or equivalently by the Lagrangian L related to H through (B.9).

While the Euler–Lagrange equations provide N second-order ODEs, Hamilton's equations provide a set of $2N$ first-order ODEs. For some problems, it is more natural to work in the Hamiltonian formalism than the Lagrangian formalism, as for example in Section 10.1.

B.3.2 ▪ Properties of Hamiltonian systems

Autonomous Hamiltonians H have a particular property: H is a constant of the motion. In order to show this, first consider the total time derivative of a general Hamiltonian along the trajectory $(\boldsymbol{q}_T, \boldsymbol{p}_T) : \mathbb{R} \to \mathbb{R}^N \times \mathbb{R}^N$ is given by

$$\begin{aligned}&\frac{dH\big(\boldsymbol{q}_T(t), \boldsymbol{p}_T(t), t\big)}{dt} \\ &= \frac{\partial H\big(\boldsymbol{q}_T(t), \boldsymbol{p}_T(t), t\big)}{\partial t} + \frac{\partial H\big(\boldsymbol{q}_T(t), \boldsymbol{p}_T(t), t\big)}{\partial \boldsymbol{q}} \cdot \frac{d\boldsymbol{q}_T(t)}{dt} + \frac{\partial H\big(\boldsymbol{q}_T(t), \boldsymbol{p}_T(t), t\big)}{\partial \boldsymbol{p}} \cdot \frac{d\boldsymbol{p}_T(t)}{dt}.\end{aligned}$$

Hence, according to (B.11), this gives

$$\frac{dH\big(\boldsymbol{q}_T(t),\boldsymbol{p}_T(t),t\big)}{dt} = \frac{\partial H\big(\boldsymbol{q}_T(t),\boldsymbol{p}_T(t),t\big)}{\partial t}. \tag{B.12}$$

As a direct consequence, if H is autonomous, then H is a constant of the motion, also referred to as a conserved quantity: it is conserved along any trajectory. In many physical systems, H corresponds to total energy. Thus, a physical system that can be described by an autonomous Hamiltonian conserves energy.

More generally, in this formalism, there exists a close relationship between the geometry of trajectories and conserved quantities. The theoretical derivation of this relationship is beyond the scope of this book but described in [7], for example. It relies on the geometry, in phase space, of level sets of any conserved quantity, together with the fact that any trajectory is necessarily confined to such a level set. Here, we simply cite some fundamental consequences.

As a first illustration, for $N = 1$, a 1D system having one constant of motion, the surfaces in the 2D phase space defined by level sets of the constant of motion can be shown to have the topology of circles. Thus, any trajectory is confined to lie on one of these circles. Such a system is said to be integrable.

In higher dimensions, the formal definition of integrability relies on the notion of independent conserved quantities. In order to state the definition itself, we first introduce the notion of Poisson brackets. This notion is necessary to, in turn, introduce independent conserved quantities.

Consider any scalar function I of ($\boldsymbol{q}$,$\boldsymbol{p}$,t). Along any trajectory $(\boldsymbol{q}_T, \boldsymbol{p}_T) : \mathbb{R} \to \mathbb{R}^N \times \mathbb{R}^N$, the total time derivative of I is given by

$$\begin{aligned}\frac{d[I(\boldsymbol{q}_T(t),\boldsymbol{p}_T(t),t)]}{dt} = \sum_{i=1}^{N} \Bigg(&\frac{\partial I(\boldsymbol{q}_T(t),\boldsymbol{p}_T(t),t)}{\partial q_i} \frac{d\left(\boldsymbol{q}_T(t)\right)_i}{dt} \\ &+ \frac{\partial I(\boldsymbol{q}_T(t),\boldsymbol{p}_T(t),t)}{\partial p_i} \frac{d\left(\boldsymbol{p}_T(t)\right)_i}{dt} \Bigg) + \frac{\partial I(\boldsymbol{q}_T(t),\boldsymbol{p}_T(t),t)}{\partial t},\end{aligned} \tag{B.13}$$

where $d\boldsymbol{q}_T(t)/dt$ and $d\boldsymbol{p}_T(t)/dt$ are the total time derivatives. According to Hamilton's equations (B.11), this can be rewritten as

$$\begin{aligned}\frac{d[I(\boldsymbol{q}_T(t),\boldsymbol{p}_T(t),t)]}{dt} = \sum_{i=1}^{N} \Bigg(&\frac{\partial I(\boldsymbol{q}_T(t),\boldsymbol{p}_T(t),t)}{\partial q_i} \frac{\partial H(\boldsymbol{q}_T(t),\boldsymbol{p}_T(t),t)}{\partial p_i} \\ &- \frac{\partial I(\boldsymbol{q}_T(t),\boldsymbol{p}_T(t),t)}{\partial p_i} \frac{\partial H(\boldsymbol{q}_T(t),\boldsymbol{p}_T(t),t)}{\partial q_i} \Bigg) + \frac{\partial I(\boldsymbol{q}_T(t),\boldsymbol{p}_T(t),t)}{\partial t}.\end{aligned}$$

The terms involving products of derivatives of I and derivatives of H can then naturally be expressed more compactly thanks to the definition of the Poisson bracket. The Poisson bracket $\{.,.\}$ with respect to the variables $(\boldsymbol{q}, \boldsymbol{p})$ is defined for two functions f and g, while other variables are treated as parameters, as

$$\{f, g\} = \sum_{i=1}^{N} \left(\frac{\partial f}{\partial q_i} \frac{\partial g}{\partial p_i} - \frac{\partial f}{\partial p_i} \frac{\partial g}{\partial q_i} \right). \tag{B.14}$$

The Poisson bracket satisfies several algebraic properties, discussed in detail in [164]. Then along any trajectory $(\boldsymbol{q}_T, \boldsymbol{p}_T) : \mathbb{R} \to \mathbb{R}^N \times \mathbb{R}^N$, the total time derivative of any function I is

given by

$$\frac{d[I(\boldsymbol{q}_T(t),\boldsymbol{p}_T(t),t)]}{dt} = \{I,H\}(\boldsymbol{q}_T(t),\boldsymbol{p}_T(t),t) + \frac{\partial I(\boldsymbol{q}_T(t),\boldsymbol{p}_T(t),t)}{\partial t}.$$

The function I is said to be a constant of the motion, or equivalently a conserved quantity, if $dI(\boldsymbol{q}_T(t),\boldsymbol{p}_T(t),t)/dt = 0$ along any trajectory $(\boldsymbol{q}_T,\boldsymbol{p}_T) : \mathbb{R} \to \mathbb{R}^N \times \mathbb{R}^N$. A set of n constants of motion, $\{I_i, \forall i \text{ from 1 to } n\}$, are said to be independent, or in involution, if the following condition is satisfied:

$$\{I_i, I_j\} = 0, \ \ \forall i,j \text{ from 1 to } n, \text{ with } i \neq j.$$

An N-dimensional autonomous Hamiltonian system is integrable if and only if there exist N independent constants of the motion. A nonautonomous Hamiltonian system can be equivalently expressed as an $N+1$-dimensional autonomous Hamiltonian system [6, 195], and its integrability is equivalent to the integrability of this higher-dimensional autonomous system. Thus, an N-dimensional nonautonomous Hamiltonian system is integrable if and only if there exist $N+1$ independent constants of the motion in the $N+1$-dimensional phase space.

We will denote by $M \subset \mathbb{R}^N \times \mathbb{R}^N$ the set of all trajectory points in phase space, also defined as $\{(\boldsymbol{q}_T(t),\boldsymbol{p}_T(t)), \text{ for all } t, \text{ for all trajectories } (\boldsymbol{q}_T,\boldsymbol{p}_T) : \mathbb{R} \to \mathbb{R}^N \times \mathbb{R}^N\}$. Any point on a trajectory of an integrable system lies in phase space at the intersection of N hypersurfaces, each one being a level set of one of the independent conserved quantities. The intersection of these N level sets is itself an N-dimensional hypersurface in $\mathbb{R}^N \times \mathbb{R}^N$. The trajectory is then confined to such hypersurfaces, and M can only be a union of subsets of hypersurfaces. Integrable systems are said to exhibit regular motion. It can be shown that the hypersurfaces supporting trajectories are higher-dimensional analogues of a torus, known as N-tori, under the assumption that M is compact and connected [7]. Thus, they are often referred to as invariant tori. These invariant tori foliate the phase space: they continuously fill the volume of M. In contrast, if a system is not integrable, trajectories are not confined to hypersurfaces. They may exhibit irregular or ergodic motion, meaning they may eventually fill out a volume of phase space.

In practice, finding conserved quantities to determine if a system is integrable may be challenging, but an example of the Hamilton–Jacobi method presented in Section 10.2 is one way to do so.

B.3.3 ▪ Charged particle motion

We turn again to the study of charged particle motion in electromagnetic fields, here restricting our attention to the 3D case, $N = 3$. In this context, subscripts j on vector fields indicate Cartesian components. We will show that the Hamiltonian and Lagrangian variational principles lead to the same equations of motion as those produced by Newton's law. Consider, as in the previous section, the standard expression of the given electric and magnetic fields, $\boldsymbol{B}$ and $\boldsymbol{E}$, in terms of vector and scalar potentials:

$$\forall (\boldsymbol{q},t) \in \mathbb{R}^3 \times \mathbb{R}, \begin{cases} \boldsymbol{B}(\boldsymbol{q},t) = \nabla \times \boldsymbol{A}(\boldsymbol{q},t), \\ \boldsymbol{E}(\boldsymbol{q},t) = -\nabla \Phi(\boldsymbol{q},t) - \dfrac{\partial \boldsymbol{A}(\boldsymbol{q},t)}{\partial t}. \end{cases}$$

Given the Lagrangian (B.6) and according to the change of coordinates (B.8), the canonical momentum can be expressed as

$$\boldsymbol{p} = m\dot{\boldsymbol{q}} + q\boldsymbol{A}(\boldsymbol{q},t). \tag{B.15}$$

As assumed in the general case, this relation can be inverted with respect to $\dot{\boldsymbol{q}}$, in order to obtain $\dot{\boldsymbol{q}} = (\boldsymbol{p} - q\boldsymbol{A}(\boldsymbol{q},t))/m$. So in this case, starting from the definition (B.9), the Hamiltonian can be written as

$$\begin{aligned} H(\boldsymbol{q},\boldsymbol{p},t) &= \frac{|\boldsymbol{p} - q\boldsymbol{A}(\boldsymbol{q},t)|^2}{2m} + q\Phi(\boldsymbol{q},t) \\ &= \frac{1}{2m}\sum_{j=1}^{3}(p_j - qA_j(\boldsymbol{q},t))^2 + q\Phi(\boldsymbol{q},t). \end{aligned} \tag{B.16}$$

As a consequence, the partial derivatives of the Hamiltonian are given by

$$\begin{cases} \dfrac{\partial H(\boldsymbol{q},\boldsymbol{p},t)}{\partial \boldsymbol{p}} = \dfrac{1}{m}\big(\boldsymbol{p} - q\boldsymbol{A}(\boldsymbol{q},t)\big), \\ \dfrac{\partial H(\boldsymbol{q},\boldsymbol{p},t)}{\partial \boldsymbol{q}} = -\dfrac{q}{m}\displaystyle\sum_{j=1}^{3}\dfrac{\partial A_j(\boldsymbol{q},t)}{\partial \boldsymbol{q}}\big(p_j - qA_j(\boldsymbol{q},t)\big) + q\dfrac{\partial \Phi(\boldsymbol{q},t)}{\partial \boldsymbol{q}}. \end{cases}$$

We will then use the notation $\nabla = \partial/\partial\boldsymbol{q}$. As a result, here Hamilton's equations read

$$\begin{cases} \dfrac{d\boldsymbol{q}_T(t)}{dt} = \dfrac{\boldsymbol{p}_T(t) - q\boldsymbol{A}\big(\boldsymbol{q}_T(t),t\big)}{m}, \\ \dfrac{d\boldsymbol{p}_T(t)}{dt} = \dfrac{q}{m}\displaystyle\sum_{j=1}^{3}\nabla A_j(\boldsymbol{q}_T(t),t)\big(\boldsymbol{p}_T(t) - q\boldsymbol{A}(\boldsymbol{q}_T(t),t)\big)_j - q\nabla\Phi(\boldsymbol{q}_T(t),t). \end{cases} \tag{B.17}$$

In order to obtain an equation describing trajectories in physical space, we are seeking for the second derivative of $\boldsymbol{q}_T$ an expression independent of $\boldsymbol{p}_T$. To proceed, we will make use of the fact that along a trajectory, $\boldsymbol{p}_T(t) - q\boldsymbol{A}(\boldsymbol{q}_T(t),t) = m d\boldsymbol{q}_T(t)/dt$, according to the change of coordinates (B.8). We first take the derivative of the first equation:

$$m\frac{d^2\boldsymbol{q}_T(t)}{dt^2} = \frac{d\boldsymbol{p}_T(t)}{dt} - q\sum_{j=1}^{3}\frac{\partial \boldsymbol{A}\big(\boldsymbol{q}_T(t),t\big)}{\partial q_j}\left(\frac{d\boldsymbol{q}_T(t)}{dt}\right)_j - q\frac{\partial \boldsymbol{A}\big(\boldsymbol{q}_T(t),t\big)}{\partial t}.$$

Next, by identifying in the right-hand side the $d\boldsymbol{q}_T(t)/dt$ term, we rewrite the second equation as

$$\frac{d\boldsymbol{p}_T(t)}{dt} = q\sum_{j=1}^{3}\nabla A_j(\boldsymbol{q}_T(t),t)\left(\frac{d\boldsymbol{q}_T(t)}{dt}\right)_j - q\nabla\Phi(\boldsymbol{q}_T(t),t).$$

Combining the last two equations, we can now get rid of all the $\boldsymbol{p}_T$ terms,

$$\begin{aligned} m\frac{d^2\boldsymbol{q}_T(t)}{dt^2} = q\sum_{j=1}^{3}\nabla A_j(\boldsymbol{q}_T(t),t)\left(\frac{d\boldsymbol{q}_T(t)}{dt}\right)_j - q\nabla\Phi(\boldsymbol{q}_T(t),t) \\ - q\sum_{j=1}^{3}\frac{\partial \boldsymbol{A}\big(\boldsymbol{q}_T(t),t\big)}{\partial q_j}\left(\frac{d\boldsymbol{q}_T(t)}{dt}\right)_j - q\frac{\partial \boldsymbol{A}\big(\boldsymbol{q}_T(t),t\big)}{\partial t}, \end{aligned}$$

or equivalently

$$\begin{aligned} m\frac{d^2\boldsymbol{q}_T(t)}{dt^2} = q\sum_{j=1}^{3}\left(\nabla A_j(\boldsymbol{q}_T(t),t) - \frac{\partial \boldsymbol{A}\big(\boldsymbol{q}_T(t),t\big)}{\partial q_j}\right)\left(\frac{d\boldsymbol{q}_T(t)}{dt}\right)_j \\ - q\left(\nabla\Phi(\boldsymbol{q}_T(t),t) + \frac{\partial \boldsymbol{A}\big(\boldsymbol{q}_T(t),t\big)}{\partial t}\right). \end{aligned}$$

The last step consists in noting that

$$\sum_{j=1}^{3}\left(\nabla A_j(\boldsymbol{q}_T(t),t)-\frac{\partial \boldsymbol{A}\big(\boldsymbol{q}_T(t),t\big)}{\partial q_j}\right)\left(\frac{d\boldsymbol{q}_T(t)}{dt}\right)_j=\frac{d\boldsymbol{q}_T(t)}{dt}\times\big(\nabla\times\boldsymbol{A}(\boldsymbol{q}_T(t),t)\big).$$

As a consequence, here Hamilton's equations read

$$m\frac{d^2\boldsymbol{q}_T(t)}{dt^2}=q\frac{d\boldsymbol{q}_T(t)}{dt}\times(\nabla\times\boldsymbol{A}(\boldsymbol{q}_T(t),t))-q\nabla\Phi(\boldsymbol{q}_T(t),t)-q\frac{\partial\boldsymbol{A}(\boldsymbol{q}_T(t),t)}{\partial t}.$$

Recognizing the expressions for the electromagnetic fields in terms of vector and scalar potentials, we identify the familiar Lorentz force (B.2):

$$m\frac{d^2\boldsymbol{q}_T(t)}{dt^2}=q\frac{d\boldsymbol{q}_T(t)}{dt}\times\boldsymbol{B}(\boldsymbol{q}_T(t),t)+q\boldsymbol{E}(\boldsymbol{q}_T(t),t).$$

As expected, we conclude that Hamilton's equations for the Hamiltonian (B.16) reduce to Newton's law (B.1) with the Lorentz force (B.2), and equivalently to the corresponding Euler–Lagrange equations (B.7).

The Hamiltonian approach will be leveraged in the study of equilibrium magnetic fields in Chapter 10, in particular in relation to the geometry of magnetic field lines.

B.4 ▪ The phase-space Lagrangian

Given the relation between the Lagrangian and the Hamiltonian (B.9), we can express the Lagrangian as

$$L(\boldsymbol{q},\dot{\boldsymbol{q}},t)=\boldsymbol{p}(\boldsymbol{q},\dot{\boldsymbol{q}})\cdot\dot{\boldsymbol{q}}-H(\boldsymbol{q},\boldsymbol{p}(\boldsymbol{q},\dot{\boldsymbol{q}}),t),$$

where $\boldsymbol{p}$ is given by the relation between Lagrangian and Hamiltonian coordinates (B.8). While the Lagrangian is typically defined as a function of only time, the position, and its derivative, we can also define a function of the phase-space variables,

$$L_{\text{ph}}(\boldsymbol{q},\dot{\boldsymbol{q}},\boldsymbol{p},\dot{\boldsymbol{p}},t)=\boldsymbol{p}\cdot\dot{\boldsymbol{q}}-H(\boldsymbol{q},\boldsymbol{p},t),\tag{B.18}$$

referred to as the phase-space Lagrangian [173]. As we will see in Section 4.2, it is sometimes more convenient to study motion in this expanded phase space, providing more freedom in coordinate transformations.

B.4.1 ▪ Euler–Lagrange equations

Unlike for Sections B.2 and B.3, here we do not use an action integral to derive equations of motion. Instead, we leverage the Euler–Lagrange equations (B.4) and Hamilton's equations (B.11).

We now study the implications of the Euler–Lagrange equations (B.4) on the phase-space Lagrangian. To do so, we use the chain rule to evaluate the partial derivatives of L:

$$\begin{cases}\dfrac{\partial L(\boldsymbol{q},\dot{\boldsymbol{q}},t)}{\partial\boldsymbol{q}}=-\dfrac{\partial H(\boldsymbol{q},\boldsymbol{p},t)}{\partial\boldsymbol{q}}+\displaystyle\sum_{j=1}^{N}\frac{\partial\boldsymbol{p}(\boldsymbol{q},\dot{\boldsymbol{q}})}{\partial q_j}\left(\dot{q}_j-\frac{\partial H(\boldsymbol{q},\boldsymbol{p},t)}{\partial p_j}\right),\\ \dfrac{\partial L(\boldsymbol{q},\dot{\boldsymbol{q}},t)}{\partial\dot{\boldsymbol{q}}}=\boldsymbol{p}+\displaystyle\sum_{j=1}^{N}\frac{\partial\boldsymbol{p}(\boldsymbol{q},\dot{\boldsymbol{q}})}{\partial\dot{q}_j}\left(\dot{q}_j-\frac{\partial H(\boldsymbol{q},\boldsymbol{p},t)}{\partial p_j}\right).\end{cases}\tag{B.19}$$

We similarly compute the partial derivatives of L_{ph}:

$$\begin{cases} \dfrac{\partial L_{\text{ph}}(\boldsymbol{q},\dot{\boldsymbol{q}},\boldsymbol{p},\dot{\boldsymbol{p}},t)}{\partial \boldsymbol{q}} = -\dfrac{\partial H(\boldsymbol{q},\boldsymbol{p},t)}{\partial \boldsymbol{q}}, \\ \dfrac{\partial L_{\text{ph}}(\boldsymbol{q},\dot{\boldsymbol{q}},\boldsymbol{p},\dot{\boldsymbol{p}},t)}{\partial \dot{\boldsymbol{q}}} = \boldsymbol{p}. \end{cases} \tag{B.20}$$

If $(\boldsymbol{q}_T, \boldsymbol{p}_T)$ are such that the pair is a phase-space trajectory, satisfying Hamilton's equations (B.11), and $\boldsymbol{q}_T$ is a trajectory, satisfying the Euler–Lagrange equations (B.4), then evaluating (B.19) along the phase-space trajectory $(\boldsymbol{q}_T(t), \boldsymbol{p}_T(t))$ yields

$$\begin{cases} \dfrac{\partial L(\boldsymbol{q}_T(t),\dot{\boldsymbol{q}}_T(t),t)}{\partial \boldsymbol{q}} = -\dfrac{\partial H(\boldsymbol{q}_T(t),\boldsymbol{p}_T(t),t)}{\partial \boldsymbol{q}}, \\ \dfrac{\partial L(\boldsymbol{q}_T(t),\dot{\boldsymbol{q}}_T(t),t)}{\partial \dot{\boldsymbol{q}}} = \boldsymbol{p}_T(t), \end{cases} \tag{B.21}$$

and similarly evaluating (B.20) along the same phase-space trajectory $(\boldsymbol{q}_T, \boldsymbol{p}_T)$ yields

$$\begin{cases} \dfrac{\partial L_{\text{ph}}(\boldsymbol{q}_T(t),\dot{\boldsymbol{q}}_T(t),\boldsymbol{p}_T(t),\dot{\boldsymbol{p}}_T(t),t)}{\partial \boldsymbol{q}} = -\dfrac{\partial H(\boldsymbol{q}_T(t),\boldsymbol{p}_T(t),t)}{\partial \boldsymbol{q}}, \\ \dfrac{\partial L_{\text{ph}}(\boldsymbol{q}_T(t),\dot{\boldsymbol{q}}_T(t),\boldsymbol{p}_T(t),\dot{\boldsymbol{p}}_T(t),t)}{\partial \dot{\boldsymbol{q}}} = \boldsymbol{p}_T(t). \end{cases} \tag{B.22}$$

Comparing the right-hand side of (B.21) and (B.22), it is then clear that

$$\begin{cases} \dfrac{\partial L(\boldsymbol{q}_T(t),\dot{\boldsymbol{q}}_T(t),t)}{\partial \boldsymbol{q}} = \dfrac{\partial L_{\text{ph}}(\boldsymbol{q}_T(t),\dot{\boldsymbol{q}}_T(t),\boldsymbol{p}_T(t),\dot{\boldsymbol{p}}_T(t),t)}{\partial \boldsymbol{q}}, \\ \dfrac{\partial L(\boldsymbol{q}_T(t),\dot{\boldsymbol{q}}_T(t),t)}{\partial \dot{\boldsymbol{q}}} = \dfrac{\partial L_{\text{ph}}(\boldsymbol{q}_T(t),\dot{\boldsymbol{q}}_T(t),\boldsymbol{p}_T(t),\dot{\boldsymbol{p}}_T(t),t)}{\partial \dot{\boldsymbol{q}}}. \end{cases} \tag{B.23}$$

In words, the partial derivatives of L evaluated along a trajectory $\boldsymbol{q}_T$, satisfying the Euler–Lagrange equations (B.4), are equal to the partial derivatives of L_{ph} evaluated along the corresponding phase-space trajectory $(\boldsymbol{q}_T, \boldsymbol{p}_T)$. Therefore, the Euler–Lagrange equations for the standard Lagrangian (B.4) can be written in exactly the same form in terms of the phase-space Lagrangian L_{ph} using (B.23):

$$\frac{d}{dt}\left[\frac{\partial L_{\text{ph}}(\boldsymbol{q}_T(t),\dot{\boldsymbol{q}}_T(t),\boldsymbol{p}_T(t),\dot{\boldsymbol{p}}_T(t),t)}{\partial \dot{\boldsymbol{q}}}\right] = \frac{\partial L_{\text{ph}}(\boldsymbol{q}_T(t),\dot{\boldsymbol{q}}_T(t),\boldsymbol{p}_T(t),\dot{\boldsymbol{p}}_T(t),t)}{\partial \boldsymbol{q}}. \tag{B.24}$$

We also would like to derive a relation between the derivatives of L_{ph} with respect to $\boldsymbol{p}$ and $\dot{\boldsymbol{p}}$ in the same Euler–Lagrange form as (B.4). We then compute, from the definition of L_{ph} (B.18), its partial derivatives with respect to the canonical momentum,

$$\begin{cases} \dfrac{\partial L_{\text{ph}}(\boldsymbol{q},\dot{\boldsymbol{q}},\boldsymbol{p},\dot{\boldsymbol{p}},t)}{\partial \dot{\boldsymbol{p}}} = 0, \\ \dfrac{\partial L_{\text{ph}}(\boldsymbol{q},\dot{\boldsymbol{q}},\boldsymbol{p},\dot{\boldsymbol{p}},t)}{\partial \boldsymbol{p}} = \dot{\boldsymbol{q}} - \dfrac{\partial H(\boldsymbol{q},\boldsymbol{p},t)}{\partial \boldsymbol{p}}. \end{cases}$$

As a result, if $(\boldsymbol{q}_T, \boldsymbol{p}_T)$ are such that the pair is a phase-space trajectory, satisfying Hamilton's equations (B.11), and $\boldsymbol{q}_T$ is a trajectory, satisfying the Euler–Lagrange equations (B.4), then

$$\frac{\partial L_{\text{ph}}(\boldsymbol{q}_T(t),\dot{\boldsymbol{q}}_T(t),\boldsymbol{p}_T(t),\dot{\boldsymbol{p}}_T(t),t)}{\partial \boldsymbol{p}} = 0.$$

In particular, along such trajectories, the following equation holds:

$$\frac{d}{dt}\left[\frac{\partial L_{\text{ph}}(\boldsymbol{q}_T(t),\dot{\boldsymbol{q}}_T(t),\boldsymbol{p}_T(t),\dot{\boldsymbol{p}}_T(t),t)}{\partial \dot{\boldsymbol{p}}}\right] = \frac{\partial L_{\text{ph}}(\boldsymbol{q}_T(t),\dot{\boldsymbol{q}}_T(t),\boldsymbol{p}_T(t),\dot{\boldsymbol{p}}_T(t),t)}{\partial \boldsymbol{p}}.$$

This has the same form as the Euler–Lagrange equation (B.4).

As a summary, equations for the derivatives with respect to position and canonical momentum can be written in the standard Euler–Lagrange form:

$$\begin{cases} \dfrac{d}{dt}\left[\dfrac{\partial L_{\text{ph}}(\boldsymbol{q}_T(t),\dot{\boldsymbol{q}}_T(t),\boldsymbol{p}_T(t),\dot{\boldsymbol{p}}_T(t),t)}{\partial \dot{\boldsymbol{q}}}\right] = \dfrac{\partial L_{\text{ph}}(\boldsymbol{q}_T(t),\dot{\boldsymbol{q}}_T(t),\boldsymbol{p}_T(t),\dot{\boldsymbol{p}}_T(t),t)}{\partial \boldsymbol{q}}, \\ \dfrac{d}{dt}\left[\dfrac{\partial L_{\text{ph}}(\boldsymbol{q}_T(t),\dot{\boldsymbol{q}}_T(t),\boldsymbol{p}_T(t),\dot{\boldsymbol{p}}_T(t),t)}{\partial \dot{\boldsymbol{p}}}\right] = \dfrac{\partial L_{\text{ph}}(\boldsymbol{q}_T(t),\dot{\boldsymbol{q}}_T(t),\boldsymbol{p}_T(t),\dot{\boldsymbol{p}}_T(t),t)}{\partial \boldsymbol{p}}. \end{cases} \tag{B.25}$$

We will refer to these as the combined Euler–Lagrange equations for the phase-space Lagrangian. An important property of the phase-space Lagrangian is the preservation of the form of the Euler–Lagrange equations (B.25) under coordinate transformations for $\boldsymbol{q}$ and $\boldsymbol{p}$ [90]. This property will be used in Section 4.2 to study guiding center motion.

B.4.2 ▪ Charged particle motion

We turn one more time to the study of charged particle motion in magnetic fields. Again, here we restrict our attention to the 3D case, $N = 3$, with subscripts j on vector fields indicating Cartesian components. We use the general Hamiltonian for charged particle motion as introduced in Section B.3 to obtain the phase-space Lagrangian,

$$L_{\text{ph}}(\boldsymbol{q},\dot{\boldsymbol{q}},\boldsymbol{p},\dot{\boldsymbol{p}},t) = \boldsymbol{p}\cdot\dot{\boldsymbol{q}} - \frac{|\boldsymbol{p}-q\boldsymbol{A}(\boldsymbol{q},t)|^2}{2m} - q\Phi(\boldsymbol{q},t), \tag{B.26}$$

or equivalently

$$L_{\text{ph}}(\boldsymbol{q},\dot{\boldsymbol{q}},\boldsymbol{p},\dot{\boldsymbol{p}},t) = \sum_{j=1}^{3} p_j\dot{q}_j - \frac{1}{2m}\sum_{j=1}^{3}(p_j - qA_j(\boldsymbol{q},t))^2 - q\Phi(\boldsymbol{q},t).$$

To derive the equations of motion, we compute the partial derivatives of L_{ph}:

$$\begin{cases} \dfrac{\partial L_{\text{ph}}}{\partial \boldsymbol{q}} = \dfrac{q}{m}\displaystyle\sum_{j=1}^{3}(p_j - qA_j(\boldsymbol{q},t))\frac{\partial A_j(\boldsymbol{q},t)}{\partial \boldsymbol{q}} - q\frac{\partial \Phi(\boldsymbol{q},t)}{\partial \boldsymbol{q}}, \\ \dfrac{\partial L_{\text{ph}}}{\partial \dot{\boldsymbol{q}}} = \boldsymbol{p}, \\ \dfrac{\partial L_{\text{ph}}}{\partial \boldsymbol{p}} = \dot{\boldsymbol{q}} - \dfrac{\boldsymbol{p}-q\boldsymbol{A}(\boldsymbol{q},t)}{m}, \\ \dfrac{\partial L_{\text{ph}}}{\partial \dot{\boldsymbol{p}}} = 0, \end{cases}$$

and apply the Euler–Lagrange equations (B.25) along a phase-space trajectory $(\boldsymbol{q}_T, \boldsymbol{p}_T)$:

$$\begin{cases} \dfrac{d\boldsymbol{p}_T(t)}{dt} = \dfrac{q}{m}\displaystyle\sum_{j=1}^{3}(\boldsymbol{p}_T(t) - q\boldsymbol{A}(\boldsymbol{q}_T(t),t))_j \nabla A_j(\boldsymbol{q}_T(t),t) - q\nabla\Phi(\boldsymbol{q}_T(t),t), \\ 0 = \dfrac{d\boldsymbol{q}_T(t)}{dt} - \dfrac{\boldsymbol{p}_T(t) - q\boldsymbol{A}(\boldsymbol{q}_T(t),t)}{m}, \end{cases}$$

where we use the notation $\nabla = \partial/\partial \boldsymbol{q}$. These are the same equations of motion as those obtained from Hamilton's equations applied to the charged particle Hamiltonian (B.17).

B.5 ▪ Summary

We now summarize the Newtonian, Lagrangian, Hamiltonian, and phase-space Lagrangian approaches to classical mechanics in the Tables B.1–B.4.

Table B.1*: Summary of the Newtonian framework for classical mechanics. The equations of motion, unknown quantities, and given quantities are provided along with the form of the force for charged particle motion. Further details can be found in Section* B.1.

Equations of motion	$m\ddot{\boldsymbol{q}}_T(t) = \boldsymbol{F}\left(\boldsymbol{q}_T(t), \dot{\boldsymbol{q}}_T(t), t\right)$
Unknowns	$\boldsymbol{q}_T$
Given	m, $\boldsymbol{F}$
Charged particle	$\boldsymbol{F}(\boldsymbol{q}, \dot{\boldsymbol{q}}, t) = q\left(\dot{\boldsymbol{q}} \times \boldsymbol{B}(\boldsymbol{q}, t) + \boldsymbol{E}(\boldsymbol{q}, t)\right)$

Table B.2*: Summary of the Lagrangian framework for classical mechanics. The equations of motion, unknown quantities, and given quantities are provided along with the form of the Lagrangian for charged particle motion. Further details can be found in Section* B.2*.*

Equations of motion	$\dfrac{d}{dt}\left(\dfrac{\partial L\left(\boldsymbol{q}_T(t), \dot{\boldsymbol{q}}_T(t), t\right)}{\partial \dot{\boldsymbol{q}}}\right) = \dfrac{\partial L(\boldsymbol{q}_T(t), \dot{\boldsymbol{q}}_T(t), t)}{\partial \boldsymbol{q}}$
Unknowns	$\boldsymbol{q}_T$
Given	$L(\boldsymbol{q}, \dot{\boldsymbol{q}}, t)$
Charged particle	$L(\boldsymbol{q}, \dot{\boldsymbol{q}}, t) = \dfrac{m\lvert\dot{\boldsymbol{q}}\rvert^2}{2} + q\left(\boldsymbol{A}(\boldsymbol{q}, t) \cdot \dot{\boldsymbol{q}} - \Phi(\boldsymbol{q}, t)\right)$

Table B.3*: Summary of the Hamiltonian framework for classical mechanics. The equations of motion, unknown quantities, and given quantities are provided along with the form of the Hamiltonian for charged particle motion. Further details can be found in Section* B.3.

Equations of motion	$\dot{\boldsymbol{q}}_T(t) = \dfrac{\partial H(\boldsymbol{q}_T(t), \boldsymbol{p}_T(t), t)}{\partial \boldsymbol{p}}$ $\dot{\boldsymbol{p}}_T(t) = -\dfrac{\partial H(\boldsymbol{q}_T(t), \boldsymbol{p}_T(t), t)}{\partial \boldsymbol{q}}$
Unknowns	$\boldsymbol{q}_T, \boldsymbol{p}_T$
Given	$H(\boldsymbol{q}, \boldsymbol{p}, t)$
Charged particle	$H(\boldsymbol{q}, \boldsymbol{p}, t) = \dfrac{m\lvert \boldsymbol{p} - q\boldsymbol{A}\,(\boldsymbol{q}, t)\,\rvert^2}{2} + q\Phi(\boldsymbol{q}, t)$

Table B.4*: Summary of the phase-space Lagrangian framework for classical mechanics. The equations of motion, unknown quantities, and given quantities are provided along with the form of the phase-space Lagrangian for charged particle motion. Further details can be found in Section* B.4.

Equations of motion	$\dfrac{d}{dt}\left(\dfrac{\partial L_{\text{ph}}\,(\boldsymbol{q}_T(t), \dot{\boldsymbol{q}}_T(t), \boldsymbol{p}_T(t), \dot{\boldsymbol{p}}_T(t), t)}{\partial \dot{\boldsymbol{q}}}\right) = \dfrac{\partial L_{\text{ph}}(\boldsymbol{q}_T(t), \dot{\boldsymbol{q}}_T(t), \boldsymbol{p}_T(t), \dot{\boldsymbol{p}}_T(t), t)}{\partial \boldsymbol{q}}$ $\dfrac{d}{dt}\left(\dfrac{\partial L_{\text{ph}}\,(\boldsymbol{q}_T(t), \dot{\boldsymbol{q}}_T(t), \boldsymbol{p}_T(t), \dot{\boldsymbol{p}}_T(t), t)}{\partial \dot{\boldsymbol{p}}}\right) = \dfrac{\partial L_{\text{ph}}(\boldsymbol{q}_T(t), \dot{\boldsymbol{q}}_T(t), \boldsymbol{p}_T(t), \dot{\boldsymbol{p}}_T(t), t)}{\partial \boldsymbol{p}}$
Unknowns	$\boldsymbol{q}_T, \boldsymbol{p}_T$
Given	$L_{\text{ph}}(\boldsymbol{q}_T(t), \dot{\boldsymbol{q}}_T(t), \boldsymbol{p}_T(t), \dot{\boldsymbol{p}}_T(t), t)$
Charged particle	$L(\boldsymbol{q}, \dot{\boldsymbol{q}}, \boldsymbol{p}, \dot{\boldsymbol{p}}, t) = \boldsymbol{p} \cdot \dot{\boldsymbol{q}} - \dfrac{\lvert \boldsymbol{p} - q\boldsymbol{A}(\boldsymbol{q}, t)\rvert^2}{2m} - q\Phi(\boldsymbol{q}, t)$

Appendix C

Fields in the neighborhood of a surface current

In this appendix, we explore the properties of surface currents, also referred to as current sheets, in terms of the current density and divergence-free magnetic field related by Ampère's law. We assume that a current density is supported on a smooth surface denoted S_K: the surface S_K is assumed to be toroidal[27] and the current density $\boldsymbol{J}_K$ is supported on and tangent to S_K. As $\boldsymbol{J}_K$ is supported on S_K, we express it as

$$\boldsymbol{J}_K(\boldsymbol{r}) = \begin{cases} \boldsymbol{K}(\boldsymbol{r}) & \forall \boldsymbol{r} \in S_K, \\ 0 & \text{otherwise}, \end{cases} \tag{C.1}$$

where $\boldsymbol{K}$ is a function defined from S_K to $\mathbb{R}^3$. According to the discussion presented in Section 5.1, equivalently $\boldsymbol{K}$ can be seen as a function of two coordinates on the surface. This will, in particular, be the case in the expression of the surface divergence in Section C.3.

Without loss of generality, the unit normal denoted $\hat{\boldsymbol{n}}(\boldsymbol{r})$ to any surface is assumed to point in the outward direction if the surface is closed, while it is arbitrarily assumed to point to the same side of the surface for all $\boldsymbol{r}$ on the surface if the surface is open.

As $\boldsymbol{J}_K$ is not smooth but assumed to be integrable, the magnetic field $\boldsymbol{B}$ arising due to Ampère's law is also assumed to be integrable. Moreover, the magnetic field is assumed to be bounded. The divergence-free condition satisfied by $\boldsymbol{J}_K$ and $\boldsymbol{B}$ can be expressed under its integral form rather than its differential form,

$$\int_S \boldsymbol{B}(\boldsymbol{r}) \cdot \hat{\boldsymbol{n}}(\boldsymbol{r})\, d^2 r = 0 \quad \text{for any closed surface } S \in \mathbb{R}^3, \tag{C.2}$$

and Ampère's law,

$$\frac{\int_{\partial S} \boldsymbol{B}(\boldsymbol{r}) \cdot d\boldsymbol{l}(\boldsymbol{r})}{\mu_0} = \int_S \boldsymbol{J}_K(\boldsymbol{r}) \cdot \hat{\boldsymbol{n}}(\boldsymbol{r})\, d^2 r \quad \text{for any surface } S \in \mathbb{R}^3, \tag{C.3}$$

where ∂S is the boundary of the surface if the surface is open, while it is the empty set if the surface is closed. Hence, for any closed surface, the left-hand side of the above vanishes. As a

[27] However, the arguments in this appendix hold for any smooth surface without a boundary.

result, for any closed surface S the current density $\boldsymbol{J}_K$ satisfies the condition

$$\int_S \boldsymbol{J}_K(\boldsymbol{r}) \cdot \hat{\boldsymbol{n}}(\boldsymbol{r})\, d^2r = 0 \quad \text{for any closed surface } \in \mathbb{R}^3. \tag{C.4}$$

We will consider the case in which the surface is closed in order to derive the divergence-free condition for both the magnetic field and current density under its surface divergence formulation. We will then consider the case in which the surface S is open to compute the relation between $\boldsymbol{K}$ and $\boldsymbol{B}$ in the neighborhood of the current sheet.

C.1 ▪ Local coordinate system

As we are interested in the context of currents supported on toroidal surfaces S_K, we will construct a local toroidal coordinate system to describe the neighborhood of S_K. This coordinate system will be used to parameterize various open and closed surfaces S in the following sections. For more on the geometry of surfaces, we refer to [298].

Starting from the volume V_K enclosed by a surface S_K, we define the signed distance function to the surface, $b : \mathbb{R}^3 \to \mathbb{R}$, defined by

$$b(\boldsymbol{r}) := \begin{cases} \text{dist}(\boldsymbol{r}, S_K), & \boldsymbol{r} \in \mathbb{R}^3 \setminus \overline{V}_K, \\ 0, & \boldsymbol{r} \in S_K, \\ -\text{dist}(\boldsymbol{r}, S_K), & \boldsymbol{r} \in V_K, \end{cases}$$

where $\text{dist}(\boldsymbol{r}, S_K)$ is the minimum distance from $\boldsymbol{r}$ to any point on S_K. An important property of the signed distance function is that its gradient restricted to the surface S_K is the unit normal on the surface:

$$\nabla b(\boldsymbol{r}) = \hat{\boldsymbol{n}}(\boldsymbol{r}) \; \forall \boldsymbol{r} \in S_K. \tag{C.5}$$

Therefore, ∇b is an extension of the normal vector in a neighborhood of S_K, and b will be the first coordinate of the local toroidal coordinate system. Recall that the $b = 0$ surface is the toroidal surface S_K. Then, in a sufficiently small neighborhood of S_K, level sets of b will be nested toroidal surfaces.

The other two coordinates will be defined starting from a surface parameterization. The position on S_K is parameterized as $\boldsymbol{R}_s(\theta, \zeta)$, assuming that the parameterization is well-defined; therefore,

$$g_{S_K}\left(\boldsymbol{R}_s(\theta,\zeta)\right) = \left| \frac{\partial \boldsymbol{R}_s(\theta,\zeta)}{\partial \theta} \times \frac{\partial \boldsymbol{R}_s(\theta,\zeta)}{\partial \zeta} \right|^2 \neq 0,$$

where $\sqrt{g_{S_K}}$ is the area element on S_K. Using the projection from $\mathbb{R}^3$ onto the surface S_K along the ∇b direction, namely any point $\boldsymbol{r} \in \mathbb{R}^3$ is projected to $\boldsymbol{r} - b(\boldsymbol{r})\nabla b(\boldsymbol{r})$, we also define extensions $(\widetilde{\theta}, \widetilde{\zeta})$ of the angles (θ, ζ) away from S_K, for all $\boldsymbol{r}$ such that $\nabla b(\boldsymbol{r})$:

$$\begin{cases} \widetilde{\theta}(\boldsymbol{r}) = \theta(\boldsymbol{r} - b(\boldsymbol{r})\nabla b(\boldsymbol{r})), \\ \widetilde{\zeta}(\boldsymbol{r}) = \zeta(\boldsymbol{r} - b(\boldsymbol{r})\nabla b(\boldsymbol{r})). \end{cases} \tag{C.6}$$

The triplet $\left(b, \widetilde{\theta}, \widetilde{\zeta}\right)$ is defined in a neighborhood of S_K. In order to determine if it indeed forms a local coordinate system, the next goal is to prove that the quantity $\nabla b \times \nabla\widetilde{\theta} \cdot \nabla\widetilde{\zeta}$ is not zero in a neighborhood of the surface S_K. To do so, since this quantity is continuous in a

neighborhood of the surface, it is sufficient to prove that it is nonzero on the surface itself. This will now be performed by relating $\nabla b \times \nabla\widetilde{\theta} \cdot \nabla\widetilde{\zeta}$ to a corresponding surface quantity.

Given the definition of the extensions (C.6), we note that $\nabla b \cdot \nabla\widetilde{\theta}|_{S_K} = \nabla b \cdot \nabla\widetilde{\zeta}|_{S_K} = 0$, since $\widetilde{\theta}$ and $\widetilde{\zeta}$ are constant along the ∇b direction. Hence according to (C.5) $\nabla\widetilde{\theta}|_{S_K}$ and $\nabla\widetilde{\zeta}|_{S_K}$ are tangential to S_K. We can then leverage properties of the surface gradient to relate $\nabla\widetilde{\theta}$ and $\nabla\widetilde{\zeta}$ to the surface gradients of θ and ζ.

The surface gradient of a function f defined on a surface S_K can be defined in terms of its smooth extension $\widetilde{f}$ in a neighborhood of S_K as the projection of the 3D gradient of $\widetilde{f}$ onto the surface:

$$\nabla_{S_K} f = \left[\nabla\widetilde{f} - \left(\hat{\boldsymbol{n}} \cdot \nabla\widetilde{f}\right)\hat{\boldsymbol{n}}\right]\Big|_{S_K}. \tag{C.7}$$

In the literature, the surface gradient operator is often written as ∇_Γ if Γ is the surface. Note that the surface gradient is defined in terms of an extension but is independent of the choice of extension. Then the surface gradient of the quantity f can be expressed thanks to a surface parameterization $\boldsymbol{R}_s(\theta,\zeta)$, in terms of f_c defined by $f_c(\theta,\zeta) = f\left(\boldsymbol{R}_s(\theta,\zeta)\right)$, as follows:

$$\begin{aligned}\nabla_{S_K} f\left(\boldsymbol{R}_s(\theta,\zeta)\right) = {} & \frac{g_{\zeta\zeta}}{g_{S_K}}\left(\boldsymbol{R}_s(\theta,\zeta)\right)\frac{\partial f_c(\theta,\zeta)}{\partial\theta}\frac{\partial \boldsymbol{R}_s(\theta,\zeta)}{\partial\theta} \\ & - \frac{g_{\theta\zeta}}{g_{S_K}}\left(\boldsymbol{R}_s(\theta,\zeta)\right)\left(\frac{\partial f_c(\theta,\zeta)}{\partial\theta}\frac{\partial \boldsymbol{R}_s(\theta,\zeta)}{\partial\zeta} + \frac{\partial f_c(\theta,\zeta)}{\partial\zeta}\frac{\partial \boldsymbol{R}_s(\theta,\zeta)}{\partial\theta}\right) \\ & + \frac{g_{\theta\theta}}{g_{S_K}}\left(\boldsymbol{R}_s(\theta,\zeta)\right)\frac{\partial f_c(\theta,\zeta)}{\partial\zeta}\frac{\partial \boldsymbol{R}_s(\theta,\zeta)}{\partial\zeta},\end{aligned} \tag{C.8}$$

where $g_{ij}\left(\boldsymbol{R}_s(\theta,\zeta)\right) = [\partial\boldsymbol{R}_s/\partial x^i \cdot \partial\boldsymbol{R}_s/\partial x^j](\theta,\zeta)$ with $x^i, x^j \in \{\theta,\zeta\}$ defining the entries of the surface metric tensor, and satisfy $g_{s_K} = g_{\theta\theta}g_{\zeta\zeta} - (g_{\theta\zeta})^2$. According to the discussion presented in Section 5.1, we will now use a single symbol, for any function f, to refer to either f_c or f. For instance, some symbol g_{ij} may refer both to a function of the coordinates (θ,ζ) and to a function of the position $\boldsymbol{r}$. Further details on the tangential gradient can be found in Chapter 4 of [298]. Since $\nabla\widetilde{\theta}|_{S_K}$ and $\nabla\widetilde{\zeta}|_{S_K}$ are tangential to S_K, then the projection operator does not modify these vectors. Therefore $\nabla_{S_K}\theta = \nabla\widetilde{\theta}|_{S_K}$ and $\nabla_{S_K}\zeta = \nabla\widetilde{\zeta}|_{S_K}$.

This leads to a convenient expression of $\nabla b \times \nabla\widetilde{\theta} \cdot \nabla\widetilde{\zeta}$ in terms of $\nabla_{S_K}\widetilde{\theta}$ and $\nabla_{S_K}\widetilde{\zeta}$ valid on the surface S_K:

$$\forall \boldsymbol{r} \in S_K, \left[\nabla b \times \nabla\widetilde{\theta} \cdot \nabla\widetilde{\zeta}\right](\boldsymbol{r}) = [\hat{\boldsymbol{n}} \times \nabla_{S_K}\theta \cdot \nabla_{S_K}\zeta](\boldsymbol{r}).$$

Moreover, according to the definition (C.8), the surface gradients are

$$\begin{cases} \nabla_{S_K}\theta\left(\boldsymbol{R}_s(\theta,\zeta)\right) = \dfrac{g_{\zeta\zeta}}{g_{S_K}}\left(\boldsymbol{R}_s(\theta,\zeta)\right)\dfrac{\partial \boldsymbol{R}_s(\theta,\zeta)}{\partial\theta} - \dfrac{g_{\theta\zeta}}{g_{S_K}}\left(\boldsymbol{R}_s(\theta,\zeta)\right)\dfrac{\partial \boldsymbol{R}_s(\theta,\zeta)}{\partial\zeta}, \\ \nabla_{S_K}\zeta\left(\boldsymbol{R}_s(\theta,\zeta)\right) = \dfrac{g_{\theta\theta}}{g_{S_K}}\left(\boldsymbol{R}_s(\theta,\zeta)\right)\dfrac{\partial \boldsymbol{R}_s(\theta,\zeta)}{\partial\zeta} - \dfrac{g_{\theta\zeta}}{g_{S_K}}\left(\boldsymbol{R}_s(\theta,\zeta)\right)\dfrac{\partial \boldsymbol{R}_s(\theta,\zeta)}{\partial\theta}. \end{cases}$$

As a result for all $\boldsymbol{r} = \boldsymbol{R}_s(\theta,\zeta) \in S_K$

$$\left[\nabla b \times \nabla\widetilde{\theta} \cdot \nabla\widetilde{\zeta}\right]\left(\boldsymbol{R}_s(\theta,\zeta)\right) = \frac{1}{g_{S_k}\left(\boldsymbol{R}_s(\theta,\zeta)\right)}\left(\frac{\partial \boldsymbol{R}_s(\theta,\zeta)}{\partial\theta} \times \frac{\partial \boldsymbol{R}_s(\theta,\zeta)}{\partial\zeta}\right) \cdot \hat{\boldsymbol{n}}(\theta,\zeta). \tag{C.9}$$

Besides, since $\partial \boldsymbol{R}_s/\partial\theta$ and $\partial \boldsymbol{R}_s/\partial\zeta$ are both tangential vector fields at any point of the surface S_K, then $\partial \boldsymbol{R}_s/\partial\theta \times \partial \boldsymbol{R}_s/\partial\zeta \propto \hat{\boldsymbol{n}}$. They are also not aligned since the parameterization of the surface is well-defined, so $\partial \boldsymbol{R}_s/\partial\theta \times \partial \boldsymbol{R}_s/\partial\zeta \neq 0$. Hence, $\nabla b \times \nabla\widetilde{\theta} \cdot \nabla\widetilde{\zeta} \neq 0$ at any point on the surface. To conclude, as expected, the triplet $(b, \widetilde{\theta}, \widetilde{\zeta})$ defines a coordinate system in the neighborhood $\mathcal{N}$ of S_K.

As a result, the surface S_K itself is parameterized by $\boldsymbol{R}_s$ defining the position on S_K as a function of (θ, ζ). The neighborhood $\mathcal{N}$ of the surface can then be parameterized by a volume parameterization $\boldsymbol{R}_{\mathcal{N}}$, an extension of $\boldsymbol{R}_s$ defining the position in $\mathcal{N}$ as a function of $(b, \widetilde{\theta}, \widetilde{\zeta})$, so that at any point $\boldsymbol{R}_{\mathcal{N}}(0, \theta, \zeta) = \boldsymbol{R}_s(\theta, \zeta)$ on the surface S_K the surface Jacobian and the volume Jacobian are related by

$$\sqrt{g}\left(\boldsymbol{R}_{\mathcal{N}}(0, \theta, \zeta)\right) = \sqrt{g_{S_K}}\left(\boldsymbol{R}_s(\theta, \zeta)\right). \tag{C.10}$$

C.2 ▪ Normal magnetic field continuity

We will now consider the behavior of the normal magnetic field along the smooth toroidal surface S_K supporting the current sheet.[28] In particular, around any point $\boldsymbol{r}_0$ on the surface, we will use the local coordinate system defined in the previous section to build a small volume intersecting S_K. Taking the limit as this volume becomes small, we evaluate the integral form of the divergence-free condition (C.2) over the surface bounding this volume. Doing so, we show that although the current density is not smooth, the normal magnetic field is continuous across S_K. In this section, it is convenient to write all functions as functions of the position $\boldsymbol{r}$.

Around any point $\boldsymbol{r}_0 = \boldsymbol{R}_{\mathcal{N}}(0, \theta_0, \zeta_0) \in S_K$, we consider a specific closed volume V_0, so $\boldsymbol{r}_0 \in V_0$. Precisely, there exist $\Delta_b > 0$, $\Delta_\theta > 0$, and $\Delta_\zeta > 0$ such that the volume intersecting S_K,

$$V_0 = \left\{ \left(b, \widetilde{\theta}, \widetilde{\zeta}\right) \in \mathbb{R}^3; |b| \leq \Delta_b, \left|\theta_0 - \widetilde{\theta}\right| \leq \Delta_\theta, \left|\zeta_0 - \widetilde{\zeta}\right| \leq \Delta_\zeta \right\}, \tag{C.11}$$

is included in $\mathcal{N}$: $V_0 \subset \mathcal{N}$. The surface S, defining the boundary of V_0, is the union of six faces that can be defined explicitly as

$$\begin{cases} \left\{ \boldsymbol{R}_{\mathcal{N}}\left(-\Delta_b, \widetilde{\theta}, \widetilde{\zeta}\right) \in \mathbb{R}^3; \left|\theta_0 - \widetilde{\theta}\right| \leq \Delta_\theta, \left|\zeta_0 - \widetilde{\zeta}\right| \leq \Delta_\zeta \right\}, \\ \left\{ \boldsymbol{R}_{\mathcal{N}}\left(+\Delta_b, \widetilde{\theta}, \widetilde{\zeta}\right) \in \mathbb{R}^3; \left|\theta_0 - \widetilde{\theta}\right| \leq \Delta_\theta, \left|\zeta_0 - \widetilde{\zeta}\right| \leq \Delta_\zeta \right\}, \\ \left\{ \boldsymbol{R}_{\mathcal{N}}\left(b, \theta_0 - \Delta_\theta, \widetilde{\zeta}\right) \in \mathbb{R}^3; |b| \leq \Delta_b, \left|\zeta_0 - \widetilde{\zeta}\right| \leq \Delta_\zeta \right\}, \\ \left\{ \boldsymbol{R}_{\mathcal{N}}\left(b, \theta_0 + \Delta_\theta, \widetilde{\zeta}\right) \in \mathbb{R}^3; |b| \leq \Delta_b, \left|\zeta_0 - \widetilde{\zeta}\right| \leq \Delta_\zeta \right\}, \\ \left\{ \boldsymbol{R}_{\mathcal{N}}\left(b, \widetilde{\theta}, \zeta_0 - \Delta_\zeta\right) \in \mathbb{R}^3; |b| \leq \Delta_b, \left|\theta_0 - \widetilde{\theta}\right| \leq \Delta_\theta \right\}, \\ \left\{ \boldsymbol{R}_{\mathcal{N}}\left(b, \widetilde{\theta}, \zeta_0 + \Delta_\zeta\right) \in \mathbb{R}^3; |b| \leq \Delta_b, \left|\theta_0 - \widetilde{\theta}\right| \leq \Delta_\theta \right\}. \end{cases} \tag{C.12}$$

The curve $\mathcal{C}$ defines the intersection of S with S_K: $\mathcal{C} = S \cap S_K$. In the $\left(b, \widetilde{\theta}, \widetilde{\zeta}\right)$ coordinate system, V_0 is a cube centered at $\boldsymbol{r}_0$, and its boundary S as well as $\mathcal{C}$ are represented in Figure C.1. The point $(0, \theta_0, \zeta_0)$ lies at the center of V_0 and at the center of the subset of S_K bounded by $\mathcal{C}$.

[28] Again, the following arguments hold for any smooth surface without boundaries

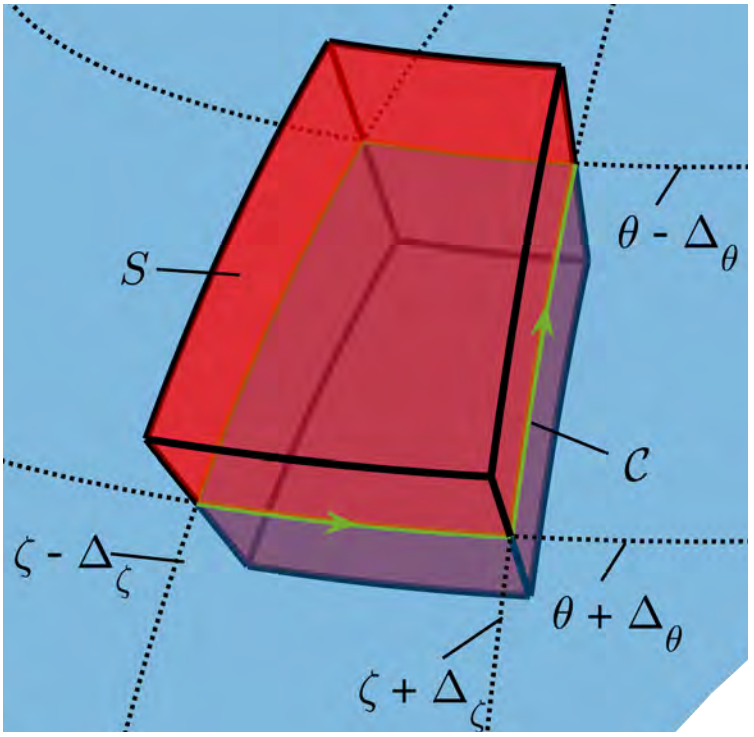

Figure C.1*: Given a surface S_K, represented in blue, and a point $\boldsymbol{r}_0$ on the surface S_K defined as $\boldsymbol{r}_0 = \boldsymbol{R}_{\mathcal{N}}(0, \theta_0, \zeta_0) \in S_K$ and parameters $\Delta_b > 0$, $\Delta_\theta > 0$ and $\Delta_\zeta > 0$, we consider the volume V_0 defined by $\left\{\boldsymbol{R}_{\mathcal{N}}\left(b, \widetilde{\theta}, \widetilde{\zeta}\right) \in \mathbb{R}^3; |b| \leq \Delta_b, \left|\theta_0 - \widetilde{\theta}\right| \leq \Delta_\theta, \left|\zeta_0 - \widetilde{\zeta}\right| \leq \Delta_\zeta\right\}$. The boundary of V_0, denoted S and defined explicitly in* (C.12)*, is represented in red. The intersection of S with the surface S_K is the curve $\mathcal{C}$, represented in green. Both S and $\mathcal{C}$ are used to evaluate the integral form of the divergence-free condition* (C.2) *and Ampère's law* (C.3)*.*

We now compute the integral appearing in the divergence-free condition (C.2) over this surface S as follows:

$$\begin{aligned}
\int_S [\boldsymbol{B}\cdot\hat{\boldsymbol{n}}](\boldsymbol{r})\, d^2r = &\int_{\theta_0-\Delta_\theta}^{\theta_0+\Delta_\theta}\int_{\zeta_0-\Delta_\zeta}^{\zeta_0+\Delta_\zeta} [\sqrt{g}\boldsymbol{B}\cdot\nabla b]\left(\boldsymbol{R}_{\mathcal{N}}\left(\Delta_b, \widetilde{\theta}, \widetilde{\zeta}\right)\right) d\widetilde{\zeta}d\widetilde{\theta} \\
&- \int_{\theta_0-\Delta_\theta}^{\theta_0+\Delta_\theta}\int_{\zeta_0-\Delta_\zeta}^{\zeta_0+\Delta_\zeta} [\sqrt{g}\boldsymbol{B}\cdot\nabla b]\left(\boldsymbol{R}_{\mathcal{N}}\left(-\Delta_b, \widetilde{\theta}, \widetilde{\zeta}\right)\right) d\widetilde{\zeta}d\widetilde{\theta} \\
&+ \int_{-\Delta_b}^{+\Delta_b}\int_{\zeta_0-\Delta_\zeta}^{\zeta_0+\Delta_\zeta} \left[\sqrt{g}\boldsymbol{B}\cdot\nabla\widetilde{\theta}\right]\left(\boldsymbol{R}_{\mathcal{N}}\left(b, \theta_0+\Delta_\theta, \widetilde{\zeta}\right)\right) d\widetilde{\zeta}db \\
&- \int_{-\Delta_b}^{+\Delta_b}\int_{\zeta_0-\Delta_\zeta}^{\zeta_0+\Delta_\zeta} \left[\sqrt{g}\boldsymbol{B}\cdot\nabla\widetilde{\theta}\right]\left(\boldsymbol{R}_{\mathcal{N}}\left(b, \theta_0-\Delta_\theta, \widetilde{\zeta}\right)\right) d\widetilde{\zeta}db \\
&+ \int_{-\Delta_b}^{+\Delta_b}\int_{\theta_0-\Delta_\theta}^{\theta_0+\Delta_\theta} \left[\sqrt{g}\boldsymbol{B}\cdot\nabla\widetilde{\zeta}\right]\left(\boldsymbol{R}_{\mathcal{N}}\left(b, \widetilde{\theta}, \zeta_0+\Delta_\zeta\right)\right) d\widetilde{\theta}db \\
&- \int_{-\Delta_b}^{+\Delta_b}\int_{\theta_0-\Delta_\theta}^{\theta_0+\Delta_\theta} \left[\sqrt{g}\boldsymbol{B}\cdot\nabla\widetilde{\zeta}\right]\left(\boldsymbol{R}_{\mathcal{N}}\left(b, \widetilde{\theta}, \zeta_0-\Delta_\zeta\right)\right) d\widetilde{\theta}db. \qquad \text{(C.13)}
\end{aligned}$$

The left-hand side is equal to zero from the divergence-free condition (C.2) because S is closed. On the right-hand side, we now are interested in the limit of the volume V_0 reducing to the single point $\boldsymbol{r}_0$. We first turn to the limit $\Delta_b \to 0$.

- The first two integrals of the right-hand side in (C.13) are defined at fixed $b = \pm\Delta_b$, so in the limit they converge respectively to

$$\lim_{\Delta_b \to 0} \pm \int_{\theta_0-\Delta_\theta}^{\theta_0+\Delta_\theta} \int_{\zeta_0-\Delta_\zeta}^{\zeta_0+\Delta_\zeta} [\boldsymbol{B} \cdot \nabla b \sqrt{g}] \left(\boldsymbol{R}_{\mathcal{N}} \left(\pm\Delta_b, \widetilde{\theta}, \widetilde{\zeta} \right) \right) d\widetilde{\zeta} d\widetilde{\theta}.$$

- Since the last four integrals of the right-hand side in (C.13) are, in particular, integrated with respect to b from $-\Delta_b$ to Δ_b and the integrands are integrable, then these four integrals converge to zero in the limit $\Delta_b \to 0$.

Hence taking the limit $\Delta_b \to 0$ in (C.13) we obtain for all $\Delta_\theta > 0$ and all $\Delta_\zeta > 0$

$$\begin{aligned} \lim_{\Delta_b \to 0} \int_{\theta_0-\Delta_\theta}^{\theta_0+\Delta_\theta} \int_{\zeta_0-\Delta_\zeta}^{\zeta_0+\Delta_\zeta} [\boldsymbol{B} \cdot \nabla b \sqrt{g}] \left(\boldsymbol{R}_{\mathcal{N}} \left(\Delta_b, \widetilde{\theta}, \widetilde{\zeta} \right) \right) d\widetilde{\zeta} d\widetilde{\theta} \\ = \lim_{\Delta_b \to 0} \int_{\theta_0-\Delta_\theta}^{\theta_0+\Delta_\theta} \int_{\zeta_0-\Delta_\zeta}^{\zeta_0+\Delta_\zeta} [\boldsymbol{B} \cdot \nabla b \sqrt{g}] \left(\boldsymbol{R}_{\mathcal{N}} \left(-\Delta_b, \widetilde{\theta}, \widetilde{\zeta} \right) \right) d\widetilde{\zeta} d\widetilde{\theta}. \end{aligned}$$

We can then turn to the limit $\Delta_\theta \to 0$, $\Delta_\zeta \to 0$ to obtain

$$\begin{aligned} \lim_{\Delta_b \to 0} \lim_{\Delta_\theta \to 0} \lim_{\Delta_\zeta \to 0} \int_{\theta_0-\Delta_\theta}^{\theta_0+\Delta_\theta} \int_{\zeta_0-\Delta_\zeta}^{\zeta_0+\Delta_\zeta} [\boldsymbol{B} \cdot \nabla b \sqrt{g}] \left(\boldsymbol{R}_{\mathcal{N}} \left(\Delta_b, \widetilde{\theta}, \widetilde{\zeta} \right) \right) d\widetilde{\zeta} d\widetilde{\theta} \\ = \lim_{\Delta_b \to 0} \lim_{\Delta_\theta \to 0} \lim_{\Delta_\zeta \to 0} \int_{\theta_0-\Delta_\theta}^{\theta_0+\Delta_\theta} \int_{\zeta_0-\Delta_\zeta}^{\zeta_0+\Delta_\zeta} [\boldsymbol{B} \cdot \nabla b \sqrt{g}] \left(\boldsymbol{R}_{\mathcal{N}} \left(-\Delta_b, \widetilde{\theta}, \widetilde{\zeta} \right) \right) d\widetilde{\zeta} d\widetilde{\theta}. \end{aligned}$$

Because the magnetic field is assumed to be bounded, then the integrands are bounded. Therefore, since $\nabla b|_{S_K} = \hat{\boldsymbol{n}}$, we obtain that the limits of the normal component of the field at the point $\boldsymbol{r}_0 = \boldsymbol{R}_{\mathcal{N}}(0, \theta_0, \zeta_0)$ approached from the two sides of the surface are equal.

In conclusion, at any point of the current sheet S_K, the normal component of the field, $\boldsymbol{B} \cdot \hat{\boldsymbol{n}}$, is continuous across S_K. In the literature, this is sometimes written as

$$[\![\boldsymbol{B}]\!]_{S_K} \cdot \hat{\boldsymbol{n}} = 0,$$

where $[\![...]\!]_{S_K}$ represents the jump across the surface S_K.

C.3 ▪ Divergence-free condition

For a smooth magnetic field $\boldsymbol{B}$ and current density $\boldsymbol{J}$, we can use the differential form of Ampère's law

$$\frac{\nabla \times \boldsymbol{B}}{\mu_0} = \boldsymbol{J}$$

to conclude that $\nabla \cdot \boldsymbol{J} = 0$. Here, we derive a similar condition for a current density supported on a surface. In this section, it is again convenient to write all functions as functions of the position $\boldsymbol{r}$.

The divergence of any integrable vector field $\boldsymbol{F}$ at a point $\boldsymbol{r}$ can be defined as the limit of the ratio between the flux of $\boldsymbol{F}$ through the boundary of any closed volume $V(\boldsymbol{r})$ enclosing $\boldsymbol{r}$ to the area of $\partial V(\boldsymbol{r})$, as V shrinks to zero at $\boldsymbol{r}$:

$$\left[\nabla \cdot \boldsymbol{F}\right](\boldsymbol{r}) := \lim_{V(\boldsymbol{r})\to 0} \frac{\displaystyle\int_{\partial V(\boldsymbol{r})} \boldsymbol{F}(\boldsymbol{r}') \cdot \hat{\boldsymbol{n}}(\boldsymbol{r}')\, d^2 r'}{\displaystyle\int_{\partial V(\boldsymbol{r})} d^2 r'}. \tag{C.14}$$

It can be shown that the limit is independent of how the volume goes to zero for both smooth and nonsmooth vector fields. In the case of a smooth vector field, the divergence can equivalently be defined in nonorthogonal coordinates as in Table 5.1. However, that formula does not apply to a vector field supported on a surface, as such a field is not differentiable. We now return to the surface S_K parameterized by two angles (θ, ζ) and the tangential vector field supported on S_K, expressed as $\boldsymbol{J}_K$ defined in terms of a function $\boldsymbol{K}$ of two variables in (C.1). Assuming that $\boldsymbol{K}$ is continuously differentiable along the surface, we will now derive the differential formula defining the surface divergence operator, denoted $(\nabla_{S_K} \cdot)$.

The differential definition of the surface divergence will be obtained from the definition of the divergence (C.14), for a particular choice of volume previously defined in (C.11), taking the limit $V_0 \to 0$. The boundary of V_0 introduced in (C.12) is the surface S. Then, integrating the flux of any vector field $\boldsymbol{F}$ over this surface S, we can easily see that

$$\begin{aligned}
\int_S \left[\boldsymbol{F}\cdot\hat{\boldsymbol{n}}\right](\boldsymbol{r})\, d^2 r = &\int_{\theta_0-\Delta_\theta}^{\theta_0+\Delta_\theta}\int_{\zeta_0-\Delta_\zeta}^{\zeta_0+\Delta_\zeta} \left[\boldsymbol{F}\cdot\nabla b\sqrt{g}\right]\left(\boldsymbol{R}_{\mathcal{N}}\left(b,\widetilde{\theta},\widetilde{\zeta}\right)\right) d\widetilde{\zeta} d\widetilde{\theta}\Big|_{b=-\Delta_b}^{b=+\Delta_b} \\
&+ \int_{-\Delta_b}^{+\Delta_b}\int_{\zeta_0-\Delta_\zeta}^{\zeta_0+\Delta_\zeta} \left[\boldsymbol{F}\cdot\nabla\widetilde{\theta}\sqrt{g}\right]\left(\boldsymbol{R}_{\mathcal{N}}\left(b,\widetilde{\theta},\widetilde{\zeta}\right)\right) d\widetilde{\zeta} db\Big|_{\widetilde{\theta}=\theta_0-\Delta_\theta}^{\widetilde{\theta}=\theta_0+\Delta_\theta} \\
&+ \int_{-\Delta_b}^{+\Delta_b}\int_{\theta_0-\Delta_\theta}^{\theta_0+\Delta_\theta} \left[\boldsymbol{F}\cdot\nabla\widetilde{\zeta}\sqrt{g}\right]\left(\boldsymbol{R}_{\mathcal{N}}\left(b,\widetilde{\theta},\widetilde{\zeta}\right)\right) d\widetilde{\theta} db\Big|_{\widetilde{\zeta}=\zeta_0-\Delta_\zeta}^{\widetilde{\zeta}=\zeta_0+\Delta_\zeta},
\end{aligned} \tag{C.15}$$

where the Jacobian in the coordinate system $(b, \widetilde{\theta}, \widetilde{\zeta})$ is expressed in terms of contravariant vectors as $\sqrt{g}^{-1} = \nabla b \times \nabla\widetilde{\theta} \cdot \nabla\widetilde{\zeta}$. In the particular case of the vector field $\boldsymbol{J}_K$ supported on S_K, as expressed in (C.1), it is clear that $\boldsymbol{J}_K\left(\boldsymbol{R}_{\mathcal{N}}\left(\pm\Delta_b, \widetilde{\theta}, \widetilde{\zeta}\right)\right) = 0$, and that more generally $\boldsymbol{J}_K\left(\boldsymbol{R}_{\mathcal{N}}\left(b, \widetilde{\theta}, \widetilde{\zeta}\right)\right) = 0$ unless $b = 0$. Hence the contribution to $\int_S \left[\boldsymbol{J}_K \cdot \hat{\boldsymbol{n}}\right](\boldsymbol{r})\, d^2 r$ from the first term on the right-hand side of (C.15) vanishes while the last two contributions on the right-hand side reduce to line integrals

$$\begin{aligned}
\int_S \left[\boldsymbol{J}_K\cdot\hat{\boldsymbol{n}}\right](\boldsymbol{r})\, d^2 r &= \int_{\zeta_0-\Delta_\zeta}^{\zeta_0+\Delta_\zeta} \left[\sqrt{g_{S_K}}\boldsymbol{K}\cdot\nabla_{S_K}\theta\right](\boldsymbol{R}_s(\theta,\zeta))\, d\zeta\Big|_{\theta=\theta_0-\Delta_\theta}^{\theta=\theta_0+\Delta_\theta} \\
&\quad + \int_{\theta_0-\Delta_\theta}^{\theta_0+\Delta_\theta} \left[\sqrt{g_{S_K}}\boldsymbol{K}\cdot\nabla_{S_K}\zeta\right](\boldsymbol{R}_s(\theta,\zeta))\, d\theta\Big|_{\zeta=\zeta_0-\Delta_\zeta}^{\zeta=\zeta_0+\Delta_\zeta} \\
&= \int_{\theta_0-\Delta_\theta}^{\theta_0+\Delta_\theta}\int_{\zeta_0-\Delta_\zeta}^{\zeta_0+\Delta_\zeta} \left[\frac{\partial\left(\left[\sqrt{g_{S_K}}\boldsymbol{K}\cdot\nabla_{S_K}\theta\right](\boldsymbol{R}_s(\theta,\zeta))\right)}{\partial\theta}\right. \\
&\qquad \left. + \frac{\partial\left(\left[\sqrt{g_{S_K}}\boldsymbol{K}\cdot\nabla_{S_K}\zeta\right](\boldsymbol{R}_s(\theta,\zeta))\right)}{\partial\zeta}\right] d\zeta d\theta,
\end{aligned}$$

which follows from (C.1), (C.7), and (C.10). Now, in order to evaluate (C.14), we take the ratio with the surface area and take the limit when $\Delta_\theta \to 0$ and $\Delta_\zeta \to 0$:

$$\lim_{\Delta_\zeta\to 0,\Delta_\theta\to 0} \frac{\int_S \left[\boldsymbol{J}_K\cdot\hat{\boldsymbol{n}}\right](\boldsymbol{r})\,d^2r}{\int_S d^2r} = \lim_{\Delta_\zeta\to 0,\Delta_\theta\to 0} \frac{1}{\int_{\theta_0-\Delta_\theta}^{\theta_0+\Delta_\theta}\int_{\zeta_0-\Delta_\zeta}^{\zeta_0+\Delta_\zeta} \sqrt{g_{S_K}}\left(\boldsymbol{R}_s(\theta,\zeta)\right)\,d\zeta d\theta}$$
$$\times \int_{\theta_0-\Delta_\theta}^{\theta_0+\Delta_\theta}\int_{\zeta_0-\Delta_\zeta}^{\zeta_0+\Delta_\zeta} \left[\frac{\partial\left(\left[\sqrt{g_{S_K}}\boldsymbol{K}\cdot\nabla_{S_K}\theta\right](\boldsymbol{R}_s(\theta,\zeta))\right)}{\partial\theta} + \frac{\partial\left(\left[\sqrt{g_{S_K}}\boldsymbol{K}\cdot\nabla_{S_K}\zeta\right](\boldsymbol{R}_s(\theta,\zeta))\right)}{\partial\zeta}\right] d\zeta d\theta.$$

Since $\boldsymbol{K}$ was assumed to have continuous derivatives, then the numerator's integrand is bounded. The denominator's integrand is bounded and bounded away from zero. Therefore, as a result, the limit is the ratio

$$\frac{1}{\sqrt{g_{S_K}}\left(\boldsymbol{R}_s(\theta,\zeta)\right)}\left(\frac{\partial\left(\left[\sqrt{g_{S_K}}\boldsymbol{K}\cdot\nabla_{S_K}\theta\right](\boldsymbol{R}_s(\theta,\zeta))\right)}{\partial\theta} + \frac{\partial\left(\left[\sqrt{g_{S_K}}\boldsymbol{K}\cdot\nabla_{S_K}\zeta\right](\boldsymbol{R}_s(\theta,\zeta))\right)}{\partial\zeta}\right)$$

evaluated at the point $\boldsymbol{R}_s(\theta_0,\zeta_0)$. This holds at any point of the current sheet S_K. According to the discussion presented in Section 5.1, the quantities involved in this equation can equivalently be considered as functions of two coordinates on the surface rather than functions of $\boldsymbol{r}\in S_K$.

In conclusion, the surface divergence of $\boldsymbol{K}$, as a function of two coordinates on the surface, is defined as

$$\nabla_{S_K}\cdot\boldsymbol{K} := \frac{1}{\sqrt{g_{S_K}}}\left[\frac{\partial\left(\sqrt{g_{S_K}}\boldsymbol{K}\cdot\nabla_{S_K}\theta\right)}{\partial\theta} + \frac{\partial\left(\sqrt{g_{S_K}}\boldsymbol{K}\cdot\nabla_{S_K}\zeta\right)}{\partial\zeta}\right].$$

See Chapter 4 of [298] for more on the surface divergence.

The zero-divergence condition for a current supported on the surface S_K can finally be expressed in a differential form by

$$\nabla_{S_K}\cdot\boldsymbol{K} = 0.$$

This is similar to the zero-divergence condition of the magnetic field in flux coordinates (9.1) since $\boldsymbol{B}$ is a tangential vector field on magnetic surfaces. See [8] for more details.

C.4 ▪ Tangential field discontinuity

Any magnetic field satisfying Ampère's law for a given current supported on a surface has a discontinuity across this surface. Here, we will leverage the coordinate system $\left(b,\widetilde{\theta},\widetilde{\zeta}\right)$ defined in the neighborhood $\mathcal{N}$ of S_K to express this tangential discontinuity in terms of the surface current. To do so, we apply the integral form of Ampère's law (C.3) to an open surface S defined around a point $\boldsymbol{r}_0 = \boldsymbol{R}_{\mathcal{N}}(0,\theta_0,\zeta_0)\in S_K$ by

$$\left\{\boldsymbol{R}_{\mathcal{N}}\left(b,\theta_0,\widetilde{\zeta}\right); |b|\le\Delta_b, \left|\zeta_0-\widetilde{\zeta}\right|\le\Delta_\zeta\right\}$$

for $\Delta_b>0$ and $\Delta_\zeta>0$. This is illustrated in Figure C.2.

In this section, it is sometimes more convenient to write functions as functions of the coordinates rather than functions of the position. In particular, as discussed in Section 5.1, the covariant basis vectors will always be written as functions of the coordinates $\left(b,\widetilde{\theta},\widetilde{\zeta}\right)$.

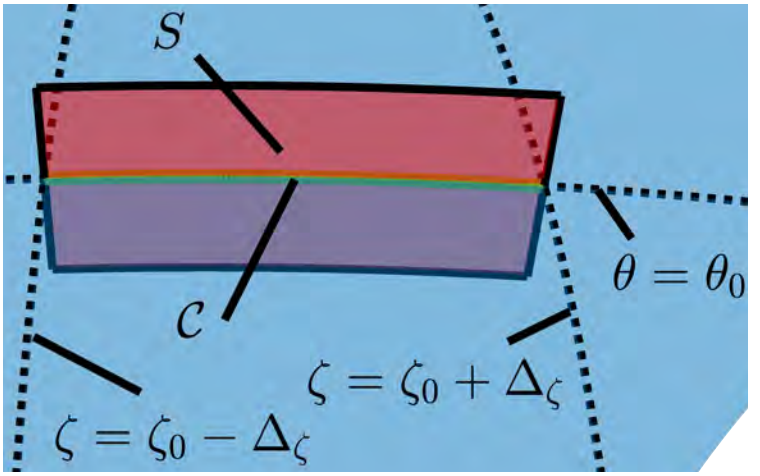

Figure C.2*: Given a surface S_K, represented in blue, a point $\boldsymbol{r}_0$ on the surface S_K defined as $\boldsymbol{r}_0 = \boldsymbol{R}_{\mathcal{N}}(0, \theta_0, \zeta_0) \in S_K$, and parameters $\Delta_b > 0$ and $\Delta_\zeta > 0$, we consider the surface S, represented in red, defined by $\left\{ \boldsymbol{R}_{\mathcal{N}}\left(b, \theta_0, \widetilde{\zeta}\right); |b| \leq \Delta_b, \left|\zeta_0 - \widetilde{\zeta}\right| \leq \Delta_\zeta \right\}$. The intersection of S with the surface S_K is the curve $\mathcal{C}$, represented in green. Both S and $\mathcal{C}$ are used to evaluate the integral form Ampère's law* (C.3) *to obtain the relation between the current density and the tangential discontinuity of the magnetic field across S_K.*

Integrating any vector field $\boldsymbol{F}$ over this surface S leads to

$$\int_S \left[\boldsymbol{F} \cdot \hat{\boldsymbol{n}}\right](\boldsymbol{r})\, d^2r = \int_{-\Delta_b}^{\Delta_b} \int_{\zeta_0-\Delta_\zeta}^{\zeta_0+\Delta_\zeta} \left[\sqrt{g}\boldsymbol{F} \cdot \nabla\widetilde{\theta}\right] \left(\boldsymbol{R}_{\mathcal{N}}\left(b, \theta_0, \widetilde{\zeta}\right)\right) d\widetilde{\zeta} db.$$

In the particular case of the vector field $\boldsymbol{J}_K$ supported on S_K, as expressed in (C.1), it is clear that $\boldsymbol{J}_K(b, \widetilde{\theta}, \widetilde{\zeta}) = 0$ unless $b = 0$. Hence, according to (C.7) and (C.10), the above reduces to a line integral on S_K:

$$\int_S (\boldsymbol{J}_K \cdot \hat{\boldsymbol{n}})(\boldsymbol{r})\, d^2r = \int_{\zeta_0-\Delta_\zeta}^{\zeta_0+\Delta_\zeta} \left[\sqrt{g_{S_K}}\boldsymbol{K} \cdot \nabla_{S_K}\theta\right] \left(\boldsymbol{R}_s\left(\theta_0, \zeta\right)\right) d\zeta.$$

We now focus on the left-hand side of the integral form of Ampère's law (C.3). Integrating any bounded vector field $\boldsymbol{F}$ over the boundary of this surface leads to

$$\begin{aligned}
\int_{\partial S} \boldsymbol{F}(\boldsymbol{r}) \cdot d\boldsymbol{l}(\boldsymbol{r}) = &\int_{\zeta_0-\Delta_\zeta}^{\zeta_0+\Delta_\zeta} \boldsymbol{F}\left(\boldsymbol{R}_{\mathcal{N}}\left(-\Delta b, \theta_0, \widetilde{\zeta}\right)\right) \cdot \frac{\partial \boldsymbol{R}_{\mathcal{N}}\left(-\Delta b, \theta_0, \widetilde{\zeta}\right)}{\partial \widetilde{\zeta}}\, d\widetilde{\zeta} \\
&- \int_{\zeta_0-\Delta_\zeta}^{\zeta_0+\Delta_\zeta} \boldsymbol{F}\left(\boldsymbol{R}_{\mathcal{N}}\left(\Delta b, \theta_0, \widetilde{\zeta}\right)\right) \cdot \frac{\partial \boldsymbol{R}_{\mathcal{N}}\left(\Delta b, \theta_0, \widetilde{\zeta}\right)}{\partial \widetilde{\zeta}}\, d\widetilde{\zeta} \\
&+ \int_{-\Delta b}^{+\Delta b} \boldsymbol{F}\left(\boldsymbol{R}_{\mathcal{N}}\left(b, \theta_0, \zeta_0 + \Delta\zeta\right)\right) \cdot \frac{\partial \boldsymbol{R}_{\mathcal{N}}\left(b, \theta_0, \zeta_0 + \Delta\zeta\right)}{\partial b}\, db \\
&- \int_{-\Delta b}^{+\Delta b} \boldsymbol{F}\left(\boldsymbol{R}_{\mathcal{N}}\left(b, \theta_0, \zeta_0 - \Delta\zeta\right)\right) \cdot \frac{\partial \boldsymbol{R}_{\mathcal{N}}\left(b, \theta_0, \zeta_0 - \Delta\zeta\right)}{\partial b}\, db.
\end{aligned}$$

Let us turn to the limit $\Delta b \to 0$. Since the integrands are bounded, in the limit, the last two terms on the right-hand side vanish, while the first two terms reduce to the integral of the limit. Hence, we obtain

$$\lim_{\Delta b \to 0} \int_{\partial S} \boldsymbol{F}(\boldsymbol{r}) \cdot d\boldsymbol{l}(\boldsymbol{r}) = -\int_{\zeta_0-\Delta\zeta}^{\zeta_0+\Delta\zeta} [\![\boldsymbol{F}]\!]_{S_K} \left(\boldsymbol{R}_{\mathcal{N}}\left(0, \widetilde{\theta}_0, \widetilde{\zeta}\right)\right) \cdot \frac{\partial \boldsymbol{R}_{\mathcal{N}}\left(0, \widetilde{\theta}_0, \widetilde{\zeta}\right)}{\partial \widetilde{\zeta}}\, d\widetilde{\zeta},$$

where again $[\![...]\!]_{S_K}$ represents the jump across the surface S_K in the normal direction. The integral form of Ampère's law then reads

$$-\frac{1}{\mu_0}\int_{\zeta_0-\Delta\zeta}^{\zeta_0+\Delta\zeta} [\![\boldsymbol{B}]\!]_{S_K} \left(\boldsymbol{R}_{\mathcal{N}}(0,\theta_0,\zeta)\right) \cdot \frac{\partial \boldsymbol{R}_s(\theta_0,\zeta)}{\partial \zeta}\, d\zeta = \int_{\zeta_0-\Delta\zeta}^{\zeta_0+\Delta\zeta} \left[\sqrt{g_{S_K}} \boldsymbol{K} \cdot \nabla_{S_K}\theta\right] \left(\boldsymbol{R}_s\left(\theta_0,\zeta\right)\right) d\zeta.$$

We can now take the limit $\Delta\zeta \to 0$ on both sides to obtain the relation

$$-\frac{1}{\mu_0} [\![\boldsymbol{B}]\!]_{S_K} \left(\boldsymbol{R}_{\mathcal{N}}(0,\theta_0,\zeta_0)\right) \cdot \frac{\partial \boldsymbol{R}_s(\theta_0,\zeta_0)}{\partial \zeta} = \left[\sqrt{g_{S_K}} \boldsymbol{K} \cdot \nabla_{S_K}\theta\right] \left(\boldsymbol{R}_s\left(\theta_0,\zeta_0\right)\right).$$

This holds for any point $\boldsymbol{r}_0 = \boldsymbol{R}_s(\theta_0,\zeta_0)$ on S_K. Recalling dual relations between covariant and contravariant bases, the fact that $\nabla\widetilde{\theta}|S_K = \nabla_{S_K}\theta$, and (C.10), we get

$$\frac{\partial \boldsymbol{R}_s}{\partial \zeta} = \left.\frac{\partial \boldsymbol{R}_{\mathcal{N}}}{\partial \widetilde{\zeta}}\right|_{S_K} = \sqrt{g}\nabla b \times \nabla\widetilde{\theta}\Big|_{S_K} = \sqrt{g_{S_K}}\hat{\boldsymbol{n}} \times \nabla_{S_K}\theta,$$

so we can conclude that

$$\forall \boldsymbol{r} \in S_K, \left[\boldsymbol{K} \cdot \nabla_{S_K}\theta\right](\boldsymbol{r}) = \mu_0^{-1}\left[\hat{\boldsymbol{n}} \times [\![\boldsymbol{B}]\!]_{S_K} \cdot \nabla_{S_K}\theta\right](\boldsymbol{r}). \tag{C.16}$$

A similar analysis for an open surface is given by

$$\left\{\boldsymbol{R}_{\mathcal{N}}\left(b, \widetilde{\theta}, \zeta_0\right); |b| \le \Delta_b, \left|\theta_0 - \widetilde{\theta}\right| \le \Delta_\theta\right\}$$

for $\Delta_\theta > 0$ leads to the conclusion that

$$\forall \boldsymbol{r} \in S_K, \left[\boldsymbol{K} \cdot \nabla_{S_K}\zeta\right](\boldsymbol{r}) = \mu_0^{-1}\left[\hat{\boldsymbol{n}} \times [\![\boldsymbol{B}]\!]_{S_K} \cdot \nabla_{S_K}\zeta\right](\boldsymbol{r}). \tag{C.17}$$

Since $\boldsymbol{K} \cdot \hat{\boldsymbol{n}} = 0$, we can summarize (C.16) and (C.17) as

$$\boldsymbol{K} = \mu_0^{-1}\hat{\boldsymbol{n}} \times [\![\boldsymbol{B}]\!]_{S_K}.$$

This expression, as expected, relates the discontinuity in the tangential magnetic field to the tangential current density.

Appendix D

Solutions to the Hahm–Kulsrud–Taylor model

The Hahm–Kulsrud–Taylor model provides a simple equilibrium for analyzing the impact of a perturbation on a rational surface. The assumptions of the model are described in Section 10.3.4. This appendix simply contains the details of the computations involved in constructing and analyzing a family of equilibria.

In Section D.1, in order to construct approximate solutions to the problem (10.33) for $\boldsymbol{B}$, namely

$$\begin{cases} \nabla \times ((\nabla \times \boldsymbol{B}) \times \boldsymbol{B}) = 0 & \text{in } \Omega_{\mathrm{d}}, \\ \nabla \cdot \boldsymbol{B} = 0 & \text{in } \Omega_{\mathrm{d}}, \\ \boldsymbol{B} \cdot \hat{\boldsymbol{n}} = 0 & \text{on } \Gamma_{\mathrm{d}}, \end{cases} \tag{D.1}$$

we construct solutions for the corresponding flux ψ defined through (10.35), namely

$$\boldsymbol{B}(x, y) = B_T \hat{\boldsymbol{z}} + \hat{\boldsymbol{z}} \times \nabla \psi(x, y),$$

by proposing a zeroth-order term ψ_0 and solving a reformulated BVP for the first-order term ψ_1. This will result in a closed formula for a first-order approximation of ψ.

Section D.2 focuses on two particular solutions for ψ of physical interest and studies in detail all their critical points to provide a full description of the topology of constant ψ surfaces.

For the sake of clarity, we recall here some details about the model described in Section 10.3.4. The function ψ of (x, y) satisfies

$$\begin{cases} B_x(x, y) = -\dfrac{\partial \psi(x, y)}{\partial y}, \\ B_y(x, y) = \dfrac{\partial \psi(x, y)}{\partial x}. \end{cases} \tag{D.2}$$

As a perturbation series with respect to d, the first terms of the function ψ are

$$\psi(x, y) = \psi_0(x) + \mathrm{d}\psi_1(x, y) + \mathcal{O}\left(\mathrm{d}^2\right), \tag{D.3}$$

and similarly, the first terms of the magnetic field are

$$\boldsymbol{B}(x, y) = \boldsymbol{B}_0(x, y) + \mathrm{d}\boldsymbol{B}_1(x, y) + \mathcal{O}\left(\mathrm{d}^2\right). \tag{D.4}$$

These satisfy, respectively,

$$\boldsymbol{B}_0 = B_T \hat{\boldsymbol{z}} + \hat{\boldsymbol{z}} \times \nabla \psi_0(x) \tag{D.5}$$

and

$$\boldsymbol{B}_1 = \hat{\boldsymbol{z}} \times \nabla \psi_1(x, y). \tag{D.6}$$

D.1 ▪ Constructing a family of solutions

Let us start with the choice of ψ_0. Since $\psi_0(x)$ is independent of y, the corresponding field $\boldsymbol{B}_0$ given by (D.5) trivially satisfies the governing PDE and the divergence condition in (D.1). Moreover, since ψ_0 only depends on x, then $\boldsymbol{B}_0 \cdot \hat{\boldsymbol{x}} = 0$ everywhere, thus the reference equilibrium has continuously nested magnetic surfaces. Since surfaces of constant x are magnetic surfaces, the boundary condition in (D.1) is trivially satisfied by $\boldsymbol{B}_0$ on the reference domain. Hence, a reference field $\boldsymbol{B}_0$ given by (D.5) for any ψ_0 depending only on x automatically satisfies the whole boundary value problem (D.1).

We now motivate a specific choice for $\psi_0(x)$, in relation to the rotational transform, defined here as $\iota(x) = \boldsymbol{B}_0(x) \cdot \hat{\boldsymbol{y}} / \boldsymbol{B}_0(x) \cdot \hat{\boldsymbol{z}}$. From the discussion of the magnetic differential equation under the assumption of continuously nested flux surfaces discussed in Remark 4.4, the δ-function and $1/x$ terms in the general Fourier solution (10.30) arise for mode numbers $(m, n) \in \mathbb{Z}^2 \backslash \{(0,0)\}$ such that $m\iota - n = 0$. Since here the problem is independent of z, then only Fourier harmonics with $n = 0$ are present in the solution, and the mode numbers satisfying the above condition correspond to $m \neq 0$ when $\iota = 0$. As the reference equilibrium $\boldsymbol{B}_0$ is independent of y, only the $(0,0)$ mode is present, so there is no δ-function or $1/x$ contribution to the solution. However, when a perturbation to the boundary is applied, introducing $m \neq 0$ harmonics, then a rotational transform profile that passes through zero allows for δ-function or $1/x$ terms in the perturbed solution. Specifically, we choose

$$\psi_0(x) = \frac{B_0 x^2}{2a} \tag{D.7}$$

such that $\boldsymbol{B}_0 \cdot \hat{\boldsymbol{z}} = B_T$, $\boldsymbol{B}_0 \cdot \hat{\boldsymbol{y}} = B_0 x / a$, and $\iota = B_0 x / (a B_T)$. Indeed, in this case, ι passes through zero at $x = 0$. Note that this choice satisfies the assumed reflection symmetry property that $\psi_0(-x) = \psi_0(x)$.

Let us then derive a PDE governing ψ_1. In order to derive an equation for ψ_1, the expansion of the magnetic field (D.4) can be substituted into the PDE in (D.1). The vector identity $\nabla \times (\boldsymbol{A} \times \boldsymbol{B}) = \boldsymbol{A}(\nabla \cdot \boldsymbol{B}) - \boldsymbol{B}(\nabla \cdot \boldsymbol{A}) + (\boldsymbol{B} \cdot \nabla)\boldsymbol{A} - (\boldsymbol{A} \cdot \nabla)\boldsymbol{B}$ is used to simplify the expressions. Using the relations between $\boldsymbol{B}_0 / \boldsymbol{B}_1$ and ψ_0 / ψ_1 given in (D.5) and (D.6), respectively, it is clear that both $\nabla \times \boldsymbol{B}_0$ and $\nabla \times \boldsymbol{B}_1$ are in the $\hat{\boldsymbol{z}}$ direction. So it follows that $((\nabla \times \boldsymbol{B}_1) \cdot \nabla)\boldsymbol{B}_0 = 0$ and $((\nabla \times \boldsymbol{B}_0) \cdot \nabla)\boldsymbol{B}_1 = 0$, while $(\boldsymbol{B}_1 \cdot \nabla)(\nabla \times \boldsymbol{B}_0) = 0$ since $\nabla \times \boldsymbol{B}_0$ is a constant. Hence the governing equation in (D.1) to $\mathcal{O}(\mathrm{d})$ reads

$$(\boldsymbol{B}_0 \cdot \nabla)(\nabla \times \boldsymbol{B}_1) = 0.$$

In terms of the ψ_1, this is equivalent to

$$\psi_0'(x) \frac{\partial}{\partial y}(\Delta \psi_1(x, y)) = 0,$$

and as explained earlier, it is sufficient to restrict this study to the upper-half domain Ω_0^+. Moreover, as $\psi_0'(x) > 0$ in Ω_0^+, the equation of interest reads

$$\frac{\partial}{\partial y}(\Delta \psi_1(x, y)) = 0 \text{ on } \Omega_0^+. \tag{D.8}$$

Let us now consider the boundary condition for ψ_1 on Ω_δ^+. As the problem is independent of z, since $\boldsymbol{B} \cdot \nabla \psi = 0$ by (D.2), the boundary condition for the magnetic field $\boldsymbol{B}$, namely $\boldsymbol{B} \cdot \hat{\boldsymbol{n}} = 0$ (D.1), is equivalent to ψ being constant along the boundary Γ_{d}^+. We choose this constant such that the flux at the boundary is preserved by the perturbation, $\psi(x_{+\mathrm{d}}(y), y) = \psi_0(a)$ for all

$y \in [0, 2\pi)$, thus preserving the integrated poloidal field in the domain. At $\mathcal{O}(\mathrm{d})$, the flux along the boundary Γ_{d}^{+} can be Taylor expanded with respect to $\mathrm{d} \ll 1$,

$$\psi(x_{+\mathrm{d}}(y), y) = \psi(a, y) - \mathrm{d}a \left.\frac{\partial \psi(x, y)}{\partial x}\right|_{x=a} \cos(ky) + \mathcal{O}(\mathrm{d}^2).$$

Now substituting in the right-hand side the expansion for ψ (D.3), while applying the boundary condition $\psi(x_{+\mathrm{d}}(y), y) = \psi_0(a)$ to the left-hand side, we obtain

$$\psi_0(a) = \psi_0(a) + \mathrm{d}\psi_1(a, y) - \mathrm{d}a\psi_0'(a)\cos(ky) + \mathcal{O}(\mathrm{d}^2).$$

At $\mathcal{O}(\mathrm{d})$, because $\psi_0'(a) = B_0$, we find

$$\psi_1(a, y) = aB_0 \cos(ky). \tag{D.9}$$

Note that this condition is imposed on the reference boundary since $x = a$. By construction, imposing this condition for ψ_1 on the reference boundary ensures that the boundary condition in (D.1) for $\boldsymbol{B}_1$ on the perturbed boundary is satisfied to $\mathcal{O}(\mathrm{d})$.

Let us now turn to the solution of the BVP for ψ_1. Combined, the equation (D.8) and boundary condition (D.9) form a boundary value problem for ψ_1 that we consider on the upper-half domain Ω_0^+ according to the symmetry assumption:

$$\frac{\partial}{\partial y}\Delta\psi_1(x, y) = 0 \text{ on } \Omega_0^+, \tag{D.10a}$$

$$\psi_1(a, y) = aB_0 \cos(ky) \text{ on } \Gamma_0^+, \tag{D.10b}$$

where as a reminder, k was introduced in the perturbation of the domain boundary. This problem does not have a unique solution, and we will now construct a family of solutions depending on a parameter.

Since $\psi_1(x, y)$ is 2π-periodic with respect to y on Ω_0^+ and the boundary condition is even with respect to y, we choose to expand $\psi_1(x, y)$ as a cosine Fourier series in y:

$$\psi_1(x, y) = \Psi^0(x) + \sum_{l=1}^{\infty} \Psi^l(x)\cos(ly). \tag{D.11}$$

Plugging the Fourier expansion (D.11) into the equation (D.10a) yields

$$\sum_{l=1}^{\infty} l\left[\frac{d^2\Psi^l(x)}{dx^2} - l^2\Psi^l(x)\right]\sin(ly) = 0. \tag{D.12}$$

The function $\Psi^0(x)$ is unconstrained by (D.10), and for simplicity, we choose to set it to zero and focus on the $l \neq 0$ terms. In order to satisfy the governing equation (D.12), each mode $l \neq 0$ must have the form $\Psi^l(x) = a_l \cosh(lx) + b_l \sinh(lx)$ for some constants $a_l = \Psi^l(0)$ and b_l. Then (D.10b) can be satisfied by retaining only the $l = k$ mode of (D.11), and the corresponding solution to the BVP (D.10) reads

$$\begin{aligned}\psi_1(x, y) &= \big(\Psi^k(0)\cosh(kx) + b_k \sinh(kx)\big)\cos(ky)\\ \text{with } aB_0 &= \Psi^k(0)\cosh(ka) + b_k \sinh(ka).\end{aligned}$$

Hence, we obtain a parameterized family of solutions through the value of $\Psi^k(0)$:

$$\psi_1(x, y) = \left(\Psi^k(0)\cosh(kx) + \frac{aB_0 - \Psi^k(0)\cosh(ka)}{\sinh(ka)}\sinh(kx)\right)\cos(ky). \tag{D.13}$$

As a summary, together (D.7) and (D.13) yield an approximate solution for ψ given the parameters B_0, k, a, and d defined on the domain Ω_0^+ by

$$\psi(x,y) = \frac{B_0}{2a}x^2 + \mathrm{d}\left(\Psi^k(0)\cosh(kx) + (aB_0 - \Psi^k(0)\cosh(ka))\frac{\sinh(kx)}{\sinh(ka)}\right)\cos(ky).$$

The solution on the full domain Ω_0 is then constructed by symmetry: for all x in Ω_0^+, we define $\psi(-x,y) = \psi(x,y)$.

D.2 ▪ Critical points for two particular solutions

We are interested here in the function ψ defined for real parameters B_0, a, k, d, and $\Psi^k(0)$ on $\mathbb{R}^2$ by

$$\begin{cases} \forall x \geq 0, \\ \psi(x,y) = \dfrac{B_0}{2a}x^2 + \mathrm{d}\left(\Psi^k(0)\cosh(kx) + (aB_0 - \Psi^k(0)\cosh(ka))\dfrac{\sinh(kx)}{\sinh(ka)}\right)\cos(ky), \\ \forall x < 0, \psi(x,y) = \psi(-x,y). \end{cases} \tag{D.14}$$

Considering B_0, a, and k fixed, we now study the critical points of the function in two particular cases corresponding to $\Psi^k(0)$ equal to 0 or $aB_0/\cosh(ka)$. We classify the critical points as local minima, maxima, and saddle points, which has implications for the topology of the level sets of $\psi(x,y)$ of interest in Section 10.3.4.

Since the function ψ is smooth for $x > 0$, then for all $x > 0$ the first- and second-order derivatives read

$$\begin{cases} \dfrac{\partial\psi(x,y)}{\partial x} = \dfrac{B_0 x}{a} + \mathrm{d}k\left(\Psi^k(0)\sinh(kx) + (aB_0 - \Psi^k(0)\cosh(ka))\dfrac{\cosh(kx)}{\sinh(ka)}\right)\cos(ky), \\ \dfrac{\partial\psi(x,y)}{\partial y} = -\mathrm{d}k\left(\Psi^k(0)\cosh(kx) + (aB_0 - \Psi^k(0)\cosh(ka))\dfrac{\sinh(kx)}{\sinh(ka)}\right)\sin(ky), \\ \dfrac{\partial^2\psi(x,y)}{\partial x^2} = \dfrac{B_0}{a} + \mathrm{d}k^2\left(\Psi^k(0)\cosh(kx) + (aB_0 - \Psi^k(0)\cosh(ka))\dfrac{\sinh(kx)}{\sinh(ka)}\right)\cos(ky), \\ \dfrac{\partial^2\psi(x,y)}{\partial x\partial y} = -\mathrm{d}k^2\left(\Psi^k(0)\sinh(kx) + (aB_0 - \Psi^k(0)\cosh(ka))\dfrac{\cosh(kx)}{\sinh(ka)}\right)\sin(ky), \\ \dfrac{\partial^2\psi(x,y)}{\partial y^2} = -\mathrm{d}k^2\left(\Psi^k(0)\cosh(kx) + (aB_0 - \Psi^k(0)\cosh(ka))\dfrac{\sinh(kx)}{\sinh(ka)}\right)\cos(ky). \end{cases}$$

D.2.1 ▪ Nonsmooth case

We treat here the case $\Psi^k(0) = 0$, for which the corresponding magnetic field exhibits a flux surface and a current sheet on the $x = 0$ axis. In this case, for $x \geq 0$ we have

$$\psi(x,y) = \frac{B_0}{2a}x^2 + \mathrm{d}aB_0\frac{\sinh(kx)}{\sinh(ka)}\cos(ky),$$

and, thanks to the symmetry property, we will first study ψ for $x \geq 0$ and then interpret these properties on the full domain.

- We first identify critical points based on the following formulas for $x > 0$:

$$\begin{cases} \dfrac{\partial\psi(x,y)}{\partial x} = \dfrac{B_0 x}{a} + \mathrm{d}kaB_0\dfrac{\cosh(kx)}{\sinh(ka)}\cos(ky), \\ \dfrac{\partial\psi(x,y)}{\partial y} = -\mathrm{d}kaB_0\dfrac{\sinh(kx)}{\sinh(ka)}\sin(ky). \end{cases}$$

1. Starting with the y derivative, we obtain

$$\frac{\partial \psi(x,y)}{\partial y} = 0 \Leftrightarrow \sin ky = 0 \Leftrightarrow ky = 0[\pi].$$

Hence, a necessary condition for any point (x, y) to be critical is $ky = 0[\pi]$.

2. We consider next the x derivative, and it depends on y only through the factor $\cos ky$. Under the necessary condition $ky = 0[\pi]$, two separate cases arise, corresponding respectively to $\cos ky = 1$ and $\cos ky = -1$.

   (a) If y_N is such that $ky_N = 0[2\pi]$ then $\cos ky_N = 1$, hence

$$\frac{\partial \psi(x,y_N)}{\partial x} = \frac{B_0 x}{a} + \mathrm{d}kaB_0 \frac{\cosh(kx)}{\sinh(ka)} > 0,$$

   therefore (x, y_N) cannot be a critical point.

   (b) If y_S is such that $ky_S = \pi[2\pi]$ then $\cos ky_S = -1$, hence

$$\frac{\partial \psi(x,y_S)}{\partial x} = \frac{B_0 x}{a} - \mathrm{d}kaB_0 \frac{\cosh(kx)}{\sinh(ka)}.$$

   So, the existence of a critical point depends on the parameters a, d, k: the existence of a critical point is equivalent to the existence of x_S such that

$$\frac{\sinh(ka)}{\mathrm{d}ka^2} x_S = \cosh(kx_S). \tag{D.15}$$

   Values of $\sinh(ka)/(\mathrm{d}ka^2)$ such that there exists such an x_S correspond to slopes of straight lines going through the origin intersecting the curve of the function f defined by $f(x) = \cosh(kx)$. The situation is illustrated in Figure D.1, and the existence of x_S depends on the value of $\sinh(ka)/(\mathrm{d}ka^2)$ compared to the slope of the only tangent to the curve of f that goes through the origin. First, we identify the single point x_L such that the tangent to the curve of f at x_L is a straight line going through the origin. At any point $x_0 > 0$ the tangent to the curve of the function f defined by $f(x) = \cosh kx$ has the following equation:

$$y = f(x_0) + f'(x_0)(x - x_0) \Leftrightarrow y = \cosh kx_0 + k \sinh kx_0 (x - x_0).$$

   Since the limit case x_L is the value of x_0 for which the tangent goes through the origin, then x_L must satisfy

$$0 = \cosh kx_L + k \sinh kx_L (0 - x_L) \Leftrightarrow kx_L = \frac{1}{\tanh(kx_L)}.$$

   As illustrated in Figure D.2, the function g defined by $g(x) = 1/\tanh x$ has a single positive fixed point x_F, approximately equal to 1.1997, independently of any parameter. Hence there exists a single x_L, namely $x_L = x_F/k$, such that $kx_L = 1/\tanh(kx_L)$, and the possible cases for the existence of critical points depend on comparing the values of $\sinh ka/(\mathrm{d}k^2a^2)$ with $\sinh kx_L$. So, defining

$$L := \frac{\sinh(ka)}{k^2 a^2 \sinh(kx_L)},$$

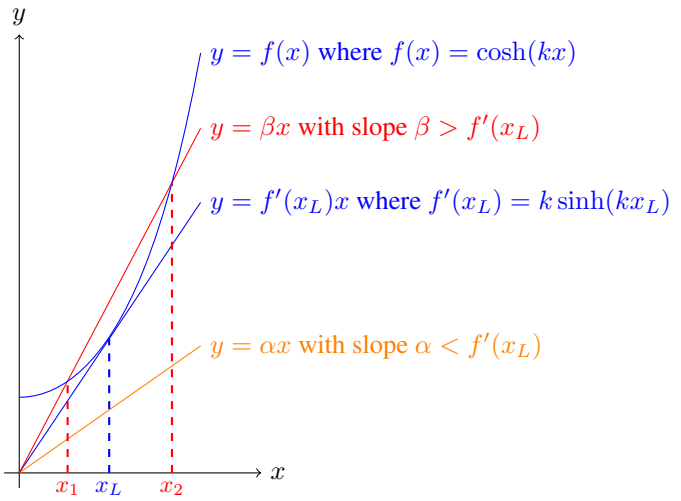

Figure D.1*: Illustration of the question of the existence of a solution to the equation* (D.15) *for* $x > 0$*. We consider the function* f *defined by* $f(x) = \cosh(kx)$ *and any straight line going through the origin. A single point* x_L *exists such that the tangent to the curve of* f *at* x_L *is a straight line going through the origin. For any other straight line going through the origin, there are two alternatives: if its slope is smaller than* $f'(x_L)$*, then the line does not intersect the curve of* f*, while if the slope is larger than* $f'(x_L)$ *then the line intersects the curve of* f *at two points* $(x_1, f(x_1))$ *and* $(x_2, f(x_2))$ *with* $x_1 < x_L < x_2$*. These alternatives are illustrated respectively by the yellow line with slope* $\alpha < f'(x_L)$ *and the red line with slope* $\beta > f'(x_L)$*.*

the cases are as follows:

- if a, d, k are such that $\sinh(ka)/(\mathrm{d}k^2a^2) < \sinh kx_L \Leftrightarrow L < \mathrm{d}$ then there is no critical point;
- if a, d, k are such that $\sinh(ka)/(\mathrm{d}k^2a^2) = \sinh kx_L \Leftrightarrow L = \mathrm{d}$ then there is one critical point for each given value of y_S;
- if a, d, k are such that $\sinh(ka)/(\mathrm{d}k^2a^2) > \sinh kx_L \Leftrightarrow L > \mathrm{d}$ then for each given value of y_S there are two critical points (x_S, y_S) for the two solutions $x_S = x_1$ and $x_S = x_2$ to the nonlinear equation (D.15) with $x_1 < x_L < x_2$.

As a result, critical points (x_S, y_S) with $ky_S = \pi[2\pi]$ may exist depending on the parameters: there are two sets of critical points for $\mathrm{d} < L$ with $x_S = x_1$ and $x_S = x_2$, there is one set of critical points for $\mathrm{d} = L$ with $x_S = x_L$, or there are no critical points for $\mathrm{d} > L$. As a reminder, for the physical interpretation, we are only interested in the regime $\mathrm{d} \ll 1$, so we will only search for extrema in the case $\mathrm{d} < L$.

- We then identify extrema via the second derivative test in the case $\mathrm{d} < L$, based on the following formulas for $x > 0$:

$$\begin{cases} \dfrac{\partial^2\psi(x,y)}{\partial x^2} = \dfrac{B_0}{a} + \mathrm{d}k^2aB_0\dfrac{\sinh(kx)}{\sinh(ka)}\cos(ky), \\ \dfrac{\partial^2\psi(x,y)}{\partial x\partial y} = -\mathrm{d}k^2aB_0\dfrac{\cosh(kx)}{\sinh(ka)}\sin(ky), \\ \dfrac{\partial^2\psi(x,y)}{\partial y^2} = -\mathrm{d}k^2aB_0\dfrac{\sinh(kx)}{\sinh(ka)}\cos(ky). \end{cases}$$

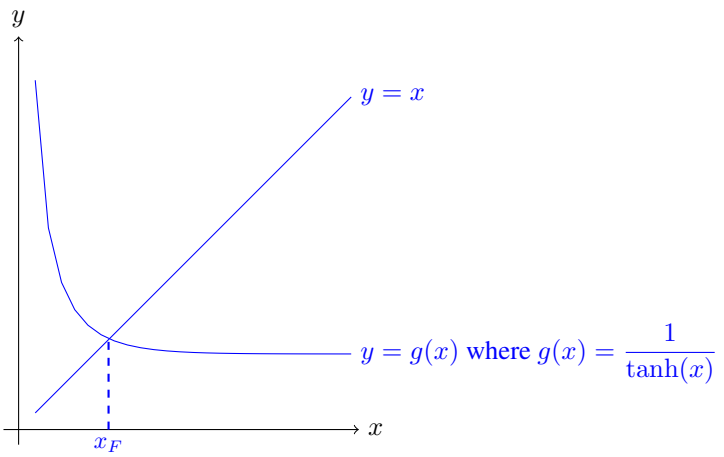

Figure D.2*: Unique fixed point x_F of the function g defined by $g(x) = 1/\tanh x$ for $x > 0$.*

Note that since $ky_S = \pi[2\pi]$, we have for any $x > 0$

$$\begin{cases} \dfrac{\partial^2\psi(x, y_S)}{\partial x \partial y} = 0 \text{ since } ky_S = \pi[2\pi], \\ \dfrac{\partial^2\psi(x, y_S)}{\partial y^2} = \mathrm{d}k^2 a B_0 \dfrac{\sinh(kx)}{\sinh(ka)} > 0. \end{cases}$$

Since we focus on the case $\mathrm{d} < L$, the two sets of critical points to study are (x_1, y_S) and (x_2, y_S) for any y_S satisfying $ky_S = \pi[2\pi]$, remembering that $x_1 < x_L < x_2$.

– Considering any point (x_1, y_S), we get

$$\frac{\partial^2\psi(x_1, y_S)}{\partial x^2} = \frac{B_0}{a}\left(1 - \mathrm{d}k^2a^2\frac{\sinh(kx_1)}{\sinh(ka)}\right).$$

So $\partial^2\psi(x_1, y_S)/\partial x^2 > 0$ because $\sinh(kx_1) < \sinh(kx_L) < \sinh(ka)/(dk^2a^2)$. Therefore, the second derivative test shows that any point (x_1, y_S) is a local minimum of ψ.

– Considering any point (x_2, y_S), we get

$$\frac{\partial^2\psi(x_2, y_S)}{\partial x^2} = \frac{B_0}{a}\left(1 - \mathrm{d}k^2a^2\frac{\sinh(kx_2)}{\sinh(ka)}\right).$$

So $\partial^2\psi(x_1, y_S)/\partial x^2 < 0$ because the function $x \mapsto \partial^2\psi(x, y_S)/\partial x^2$ is decreasing, it is equal to 0 at x_L, and $x_2 > x_L$. Therefore, the second derivative test shows that any point (x_2, y_S) is not an extremum of ψ but a saddle point.

As a result, in the case $\mathrm{d} < L$, given the two solutions x_1 and x_2 to the nonlinear equation (D.15), illustrated in Figure D.1 for reference, the critical points of ψ can be described as follows. Local minima exist at any points (x_1, y_S) with $ky_S = \pi[2\pi]$, while any points (x_2, y_S) with $ky_S = \pi[2\pi]$ are saddle points.

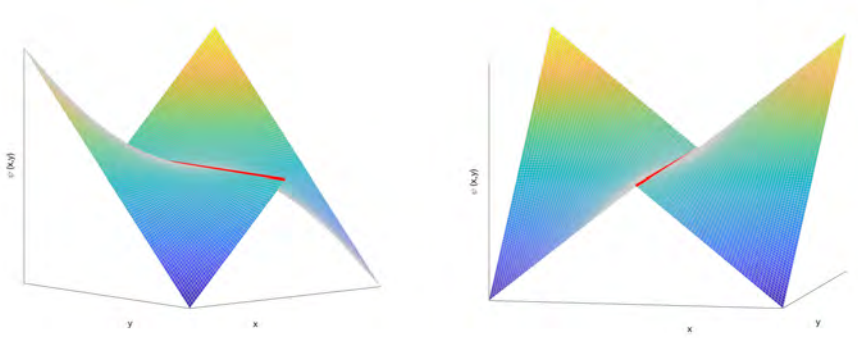

Figure D.3*: Graph of the function ψ in the case $\Psi^k(0) = 0$ in the neighborhood of points $(0, y)$ with $ky = \pi/2[\pi]$. The $x = 0$ axis is highlighted in red, and the two views illustrate the nonsmooth saddle point surface.*

- We now identify local extrema along the $x = 0$ axis. By symmetry, we have

$$\begin{cases} \lim\limits_{x\to 0, x>0} \dfrac{\partial\psi(x,y)}{\partial x} = \mathrm{d}kaB_0 \dfrac{1}{\sinh(ka)}\cos(ky), \\ \lim\limits_{x\to 0, x<0} \dfrac{\partial\psi(x,y)}{\partial x} = -\lim\limits_{x\to 0, x>0} \dfrac{\partial\psi(x,y)}{\partial x}, \end{cases}$$

  while the function $y \mapsto \psi(0, y)$ is constant. Hence (i) for all y such that $ky \neq \pi/2[\pi]$ then $(0, y)$ is a local maximum or minimum but is not isolated (not a strict extrema), (ii) for all y such that $ky = \pi/2[\pi]$ then $(0, y)$ is not a local extremum, as illustrated in Figure D.3.

As a conclusion, if the parameters are such that $\mathrm{d} < \sinh(ka)/(k^2a^2 \sinh kx_L)$ then the function defined in (D.14), on the period $\mathbb{R} \times [0, 2\pi/k]$, and similarly on any other period, has two minima at $(\pm x_1, \pi/k)$, two smooth saddle points $(\pm x_2, \pi/k)$, two nonsmooth saddle points $(0, \pi/(2k))$ and $(0, \pi/(2k)+\pi)$, as well as local minima along $\{0\} \times (\pi/(2k), \pi/(2k)+\pi)$, and maxima along $\{0\} \times (0, \pi/(2k))$ and $\{0\} \times (\pi/(2k)+\pi, 2\pi/k)$. This is illustrated in Figure D.4, where by convention, the function is represented in the y-x plane in order to have the radius-like variable in the vertical direction.

D.2.2 ▪ Smooth case

We treat here the case $\Psi^k(0) = aB_0/\cosh(ka)$, for which the function ψ is smooth and can be defined for all x as

$$\psi(x, y) = \frac{B_0}{2a}x^2 + \mathrm{d}\Psi^k(0)\cosh(kx)\cos(ky).$$

- We first identify critical points, based on the following formulas:

$$\begin{cases} \dfrac{\partial\psi(x,y)}{\partial x} = \dfrac{B_0 x}{a} + \mathrm{d}kaB_0 \dfrac{\sinh(kx)}{\cosh(ka)}\cos(ky), \\ \dfrac{\partial\psi(x,y)}{\partial y} = -\mathrm{d}kaB_0 \dfrac{\cosh(kx)}{\cosh(ka)}\sin(ky). \end{cases}$$

  1. Starting with the y derivative, we obtain

$$\frac{\partial\psi(x,y)}{\partial y} = 0 \Leftrightarrow \sin ky = 0 \Leftrightarrow ky = 0[\pi].$$

  Hence, a necessary condition for any point (x, y) to be critical is $ky = 0[\pi]$.

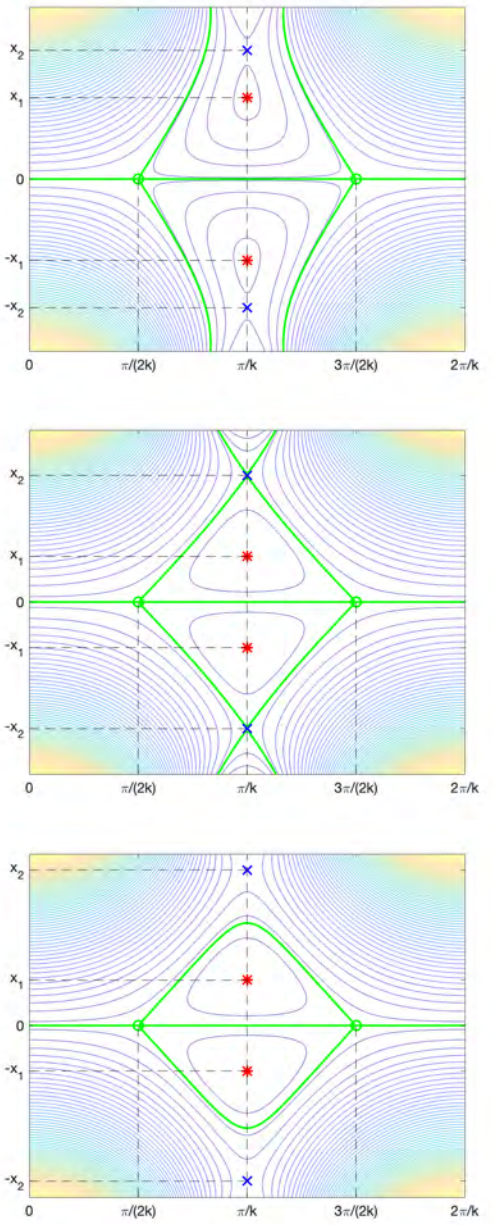

Figure D.4*: Level sets of the function ψ over one period in the y-x plane for $\Psi^k(0) = 0$ with $B_0 = 1$, $a = 1$, for three values of $d < \sinh(ka)/(k^2a^2 \sinh kx_L)$: $d = 0.75$ (top, for which if $k = 1$ $x_1 \approx 0.9450$ and $x_2 \approx 1.4964$), $d = 0.6$ (bottom, for which if $k = 1$ $x_1 \approx 0.6078$ and $x_2 \approx 2.0847$), as well as the intermediate case $d \approx 0.6491$ (middle, if $ka = 1$). The level set of level zero is highlighted in the thick green line. The function has minima at points $(\pm x_1, \pi/k)$, represented with red stars, smooth saddle points at points $(\pm x_2, \pi/k)$, represented with blue crosses, and nonsmooth saddle points at points $(0, \pi/(2k))$ and $(0, 3\pi/(2k))$, represented with green circles.*

2. We consider next the x derivative, and it depends on y only through the factor $\cos ky$. Under the necessary condition $ky = 0[\pi]$, two separate cases arise, corresponding respectively to $\cos ky = 1$ and $\cos ky = -1$.
   (a) If y_N is such that $ky_N = 0[2\pi]$ then $\cos ky_N = 1$, hence
   $$\frac{\partial \psi(x, y_N)}{\partial x} = \frac{B_0 x}{a} + \mathrm{d}kaB_0 \frac{\sinh(kx)}{\cosh(ka)},$$
   which is positive for $x > 0$, negative for $x < 0$, while
   $$\frac{\partial \psi(x, y_N)}{\partial x} = 0 \Leftrightarrow x = 0.$$
   Therefore, there is one critical point for each given value of y_N, namely $(0, y_N)$.
   (b) If y_S is such that $ky_S = \pi[2\pi]$ then $\cos ky_S = -1$, hence
   $$\frac{\partial \psi(x, y_S)}{\partial x} = \frac{B_0 x}{a} - \mathrm{d}kaB_0 \frac{\sinh(kx)}{\cosh(ka)}.$$
   So the existence of a critical point depends on the parameters a, d, k: the existence of a critical point is equivalent to the existence of x_S such that
   $$\frac{\cosh(ka)}{\mathrm{d}ka^2} x_S = \sinh(kx_S). \tag{D.16}$$
   Again values of $\cosh(ka)/(\mathrm{d}ka^2)$ such that there exists such an x_S correspond to slopes of straight lines going through the origin intersecting the curve of the function f defined by $f(x) = \sinh(kx)$. The situation is illustrated in Figure D.5, and the number of values x_S depends on the value of the ratio $\cosh(ka)/(\mathrm{d}ka^2)$ compared to the slope of the only tangent to the curve of f that goes through the origin, namely $f'(0) = k$. The possible cases depend on comparing the values of $\cosh(ka)/(\mathrm{d}ka^2)$ and k. So, defining
   $$L_N := \frac{\cosh ka}{k^2 a^2},$$
   the cases are as follows:
   – if a, d, k are such that $\cosh(ka)/(\mathrm{d}k^2a^2) \leq 1 \Leftrightarrow L_N \leq \mathrm{d}$ then there is a single critical point for each given value of y_S, namely $(0, y_S)$;
   – if a, d, k are such that $\cosh(ka)/(\mathrm{d}k^2a^2) > 1 \Leftrightarrow L_N > \mathrm{d}$ then there are three critical points for each given value of y_S, namely (x_S, y_S), $(-x_S, y_S)$ and $(0, y_S)$.

   As a result, there is one set of critical points of the form $(0, y_N)$ with $ky_N = 0[2\pi]$, while the number of critical points (x_S, y_S) with $ky_S = \pi[2\pi]$ depends on the parameters: there is one set of critical points for $\mathrm{d} \geq L_N$ while there are three sets of critical points for $\mathrm{d} < L_N$. Again here, as a reminder, for the physical interpretation, we are only interested in the regime $\mathrm{d} \ll 1$, so we will only search for extrema in the case $\mathrm{d} < L_N$.

- We then identify extrema via the second derivative test in the case $\mathrm{d} < L_N$, based on the following formulas:
$$\begin{cases} \dfrac{\partial^2 \psi(x, y)}{\partial x^2} = \dfrac{B_0}{a} + \mathrm{d}k^2 aB_0 \dfrac{\cosh(kx)}{\cosh(ka)} \cos(ky), \\ \dfrac{\partial^2 \psi(x, y)}{\partial x \partial y} = -\mathrm{d}k^2 aB_0 \dfrac{\sinh(kx)}{\cosh(ka)} \sin(ky), \\ \dfrac{\partial^2 \psi(x, y)}{\partial y^2} = -\mathrm{d}k^2 aB_0 \dfrac{\cosh(kx)}{\cosh(ka)} \cos(ky). \end{cases}$$

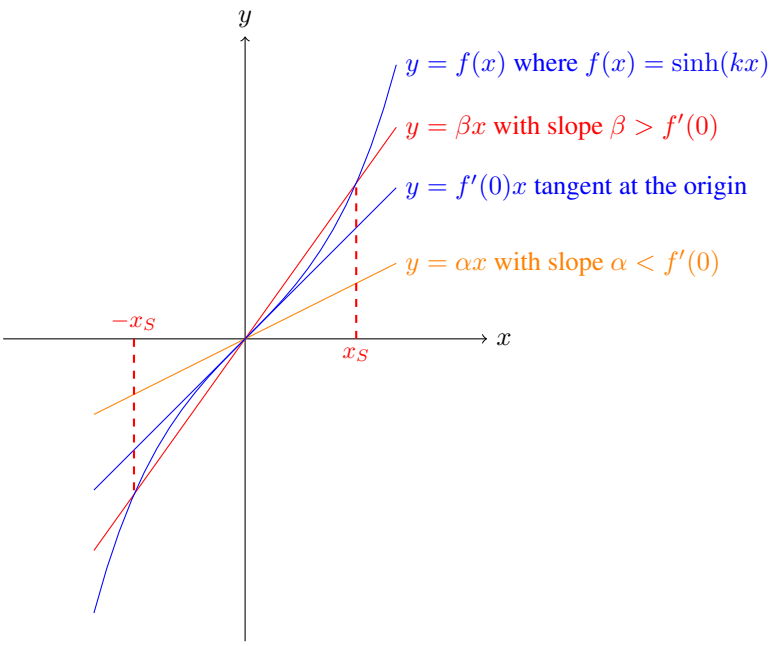

Figure D.5*: Illustration of the solution(s) to the equation* (D.16) *for* x *in* $\mathbb{R}$*. We consider the function* f *defined by* $f(x) = \sinh(kx)$ *and any straight line going through the origin. For any straight line going through the origin, there are two alternatives: if its slope is at most equal to* $f'(0) = k$*, then the line intersects the curve of* f *only at the origin, while if the slope is larger than* $f'(0) = k$*, then the line intersects the curve of* f *at three different points,* $(x_S, f(x_S))$*,* $(-x_S, -f(x_S))$*, and at the origin. These alternatives are illustrated respectively by the yellow line with slope* $\alpha < f'(0)$ *and the red line with slope* $\beta > f'(0)$*.*

Note that, since $ky_N = 0[2\pi]$, we have

$$\begin{cases} \dfrac{\partial^2\psi(0,y_N)}{\partial x^2} = \dfrac{B_0}{a} + \dfrac{\mathrm{d}k^2 aB_0}{\cosh(ka)} > 0, \\ \dfrac{\partial^2\psi(0,y_N)}{\partial x\partial y} = 0, \\ \dfrac{\partial^2\psi(0,y_N)}{\partial y^2} = -\dfrac{\mathrm{d}k^2 aB_0}{\cosh(ka)} < 0. \end{cases}$$

Therefore, the second derivative test shows that any point $(0, y_N)$ is a saddle point. Moreover note that, since $ky_S = \pi[2\pi]$, we have

$$\begin{cases} \dfrac{\partial^2\psi(x,y_S)}{\partial x^2} = \dfrac{B_0}{a}\left(1 - \mathrm{d}k^2a^2\dfrac{\cosh(kx)}{\cosh(ka)}\right), \\ \dfrac{\partial^2\psi(x,y_S)}{\partial x\partial y} = 0, \\ \dfrac{\partial^2\psi(x,y_S)}{\partial y^2} = \mathrm{d}k^2 aB_0\dfrac{\cosh(kx)}{\cosh(ka)}. \end{cases}$$

Since we focus on the case $\mathrm{d} < L_N$, the critical points to study are $(0, y_S)$, (x_S, y_S), and $(-x_S, y_S)$.

1. Considering any point $(0, y_S)$, we get

$$\begin{cases} \dfrac{\partial^2 \psi(0,y_S)}{\partial x^2} = \dfrac{B_0}{a}\left(1 - \dfrac{\mathrm{d}k^2a^2}{\cosh(ka)}\right) > 0 \text{ since } \mathrm{d} < L_N, \\ \dfrac{\partial^2 \psi(0,y_S)}{\partial y^2} = \dfrac{\mathrm{d}k^2 a B_0}{\cosh(ka)} > 0. \end{cases}$$

   Hence, the second derivative test shows that any critical point $(0, y_S)$ is a minimum.

2. Considering any point (x_S, y_S), then $\partial^2\psi(x, y_S)/\partial y^2 > 0$. Moreover, remembering that $\cosh(ka)/(\mathrm{d}ka^2)x_S = \sinh(kx_S)$, and since $\tanh(kx_S) \neq 0$ we can write

$$\frac{\partial^2 \psi(x_S,y_S)}{\partial x^2} = \frac{B_0}{a\tanh(kx_S)}\big(\tanh(kx_S) - kx_S\big).$$

   So $\partial^2\psi(x_S, y_S)/\partial x^2 < 0$ since on the one hand $B_0/(a\tanh(kx_S)) > 0$ and on the other hand the function $x \mapsto \tanh(kx) - kx$ is decreasing, it is equal to 0 at $x = 0$, and $x_S > 0$. Hence, the second derivative test shows that any critical point (x_S, y_S) is a saddle point.

3. By symmetry any critical point $(-x_S, y_S)$ is also a saddle point.

As a result, in the case $\mathrm{d} < L_N$, given the positive solution x_S to the nonlinear equation (D.16), illustrated in Figure D.5 for reference, the critical points of ψ can be described as follows. Local minima exist at any point $(0, y_S)$ with $ky_S = \pi[2\pi]$, while any point $(\pm x_S, y_S)$ with $ky_S = \pi[2\pi]$ is a saddle point. Moreover, there is one set of saddle points of the form $(0, y_N)$ with $ky_N = 0[2\pi]$,

In conclusion, if the parameters are such that $\mathrm{d} < \cosh ka/(k^2a^2)$ then the function defined in (D.14), on the period $\mathbb{R} \times [0, 2\pi/k]$, and similarly on any other period, has a minimum at $(0, \pi/k)$ and saddle points at $(0, 0)$ (and by periodicity at $(0, 2\pi/k)$) and at $(\pm x_S, \pi/k)$. This is illustrated in Figure D.6, where by convention, the function is represented in the y-x plane in order to have the radius-like variable in the vertical direction.

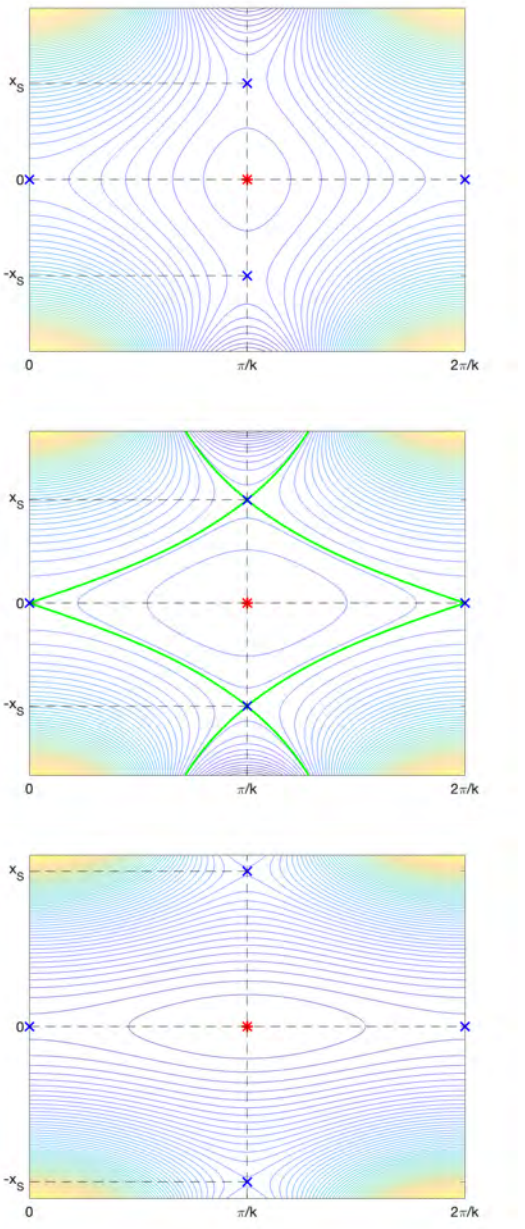

Figure D.6*: Level sets of the function* ψ *for* $\Psi^k(0) = aB_0/\cosh(ka)$ *over one period in the* y*-*x *plane with* $B_0 = 1$*,* $a = 1$*, and* $d = 1$ *(top, for which* $x_S \approx 1.6823$ *if* $k = 1$*),* $d = 0.3$ *(bottom, for which* $x_S \approx 3.6174$ *if* $k = 1$*), as well as the intermediate case* $d \approx 0.6778$ *(middle, if* $ka = 1$*). In the intermediate case, the level set separating closed from open level sets is highlighted in the thick green line. The function has a minimum at* $(0, \pi/k)$*, represented with a red star, and saddle points at* $(0, 0)$*,* $(0, 2\pi/k)$*, and* $(\pm x_S, \pi/k)$*, represented with blue crosses.*

Bibliography

[1] J. A. Alcusón, P. Xanthopoulos, G. G. Plunk, P. Helander, F. Wilms, Y. Turkin, A. Von Stechow, and O. Grulke, *Suppression of electrostatic micro-instabilities in maximum-J stellarators*, Plasma Physics and Controlled Fusion, 62 (2020), 035005. (Cited on p. 218)

[2] K. Aleynikova, S. R. Hudson, P. Helander, A. Kumar, J. Geiger, M. Hirsch, J. Loizu, C. Nührenberg, K. Rahbarnia, Z. Qu, Y. Gao, H. Thomsen, Y. Turkin, M. Zanini, and the W7-X Team, *Model for current drive induced crash cycles in W7-X*, Nuclear Fusion, 61 (2021), 126040. (Cited on p. 151)

[3] A. F. Almagri, D. T. Anderson, F. S. B. Anderson, P. H. Probert, J. L. Shohet, and J. N. Talmadge, *A helically symmetric stellarator (HSX)*, IEEE Transactions on Plasma Science, 27 (1999), pp. 114–115. (Cited on p. 214)

[4] D. Anderson, *Personal communication*, 2019. (Cited on p. 212)

[5] F. S. B. Anderson, A. F. Almagri, D. T. Anderson, P. G. Matthews, J. N. Talmadge, and J. L. Shohet, *The Helically Symmetric Experiment (HSX): Goals, design and status*, Fusion Technology, 27 (1995), pp. 273–277. (Cited on pp. 163, 212)

[6] R. M. Angelo, E. I. Duzzioni, and A. D. Ribeiro, *Integrability in time-dependent systems with one degree of freedom*, Journal of Physics A: Mathematical and Theoretical, 45 (2012), 055101. (Cited on p. 234)

[7] V. I. Arnold, *Proof of a theorem of AN Kolmogorov on the invariance of quasi-periodic motions under small perturbations of the Hamiltonian*, Collected Works: Representations of Functions, Celestial Mechanics and KAM Theory, 1957–1965, Springer, 2009, pp. 267–294. (Cited on pp. 119, 233, 234)

[8] H. F. Arnoldus, *Conservation of charge at an interface*, Optics Communications, 265 (2006), pp. 52–59. (Cited on p. 248)

[9] A. Bader, M. Drevlak, D. T. Anderson, B. J. Faber, C. C. Hegna, K. M. Likin, J. C. Schmitt, and J. N. Talmadge, *Stellarator equilibria with reactor relevant energetic particle losses*, Journal of Plasma Physics, 85 (2019), 905850508. (Cited on p. 182)

[10] A. Baillod, J. Loizu, J. P. Graves, and M. Landreman, *Stellarator optimization for nested magnetic surfaces at finite β and toroidal current*, Physics of Plasmas, 29 (2022). (Cited on p. 179)

[11] F. BAUER, *The Beta Equilibrium, Stability, and Transport Codes: Applications of the Design of Stellarators*, Elsevier, 1987. (Cited on p. 184)

[12] F. BAUER, O. BETANCOURT, AND P. GARABEDIAN, *Magnetohydrodynamic Equilibrium and Stability of Stellarators*, Springer Science & Business Media, 1984. (Cited on pp. 59, 217)

[13] C. BEIDLER, G. GRIEGER, F. HERRNEGGER, E. HARMEYER, J. KISSLINGER, W. LOTZ, H. MAASSBERG, ET AL., *Physics and engineering design for Wendelstein* VII-*X*, Fusion Technology, 17 (1990), pp. 148–168. (Cited on pp. 187, 210)

[14] C. D. BEIDLER, H. M. SMITH, A. ALONSO, T. ANDREEVA, J. BALDZUHN, M. N. A. BEURSKENS, M. BORCHARDT, ET AL., *Demonstration of reduced neoclassical energy transport in Wendelstein* 7-*X*, Nature, 596 (2021), pp. 221–226. (Cited on p. 211)

[15] M. A BERGER, *Introduction to magnetic helicity*, Plasma Physics and Controlled Fusion, 41 (1999), pp. B167–B175. (Cited on p. 153)

[16] M. A. BERGER AND G. B. FIELD, *The topological properties of magnetic helicity*, Journal of Fluid Mechanics, 147 (1984), pp. 133–148. (Cited on p. 153)

[17] INTERNATIONAL ATOMIC ENERGY AGENCY, *Plasma Physics and Controlled Nuclear Fusion Research* - 1968 (*Proceedings of an International Conference, Novosibirsk*, 1968), Proceedings Series, IAEA, Vienna, 1969. (Cited on p. 208)

[18] A. BHATTACHARJEE, T. HAYASHI, C. C. HEGNA, N. NAKAJIMA, AND T. SATO, *Theory of pressure-induced islands and self-healing in three-dimensional toroidal magnetohydrodynamic equilibria*, Physics of Plasmas, 2 (1995), pp. 883–888. (Cited on p. 178)

[19] R. BILATO AND R. KLEIBER, *IPP Summer University for Plasma Physics, September 17-21, 2012, Garching*, in IPP Summer University for Plasma Physics and Fusion Research, Max-Planck-Institut für Plasmaphysik, 2012. (Cited on p. 214)

[20] A. S. BISHOP, *Project Sherwood - The US Program in Controlled Fusion*, Addison-Wesley Publishing Company, Inc., 1958. Digitized version of report available at `https://babel.hathitrust.org/cgi/pt?id=uc1.$b113483&seq=7`. (Cited on p. 5)

[21] A. H. BOOZER, *Evaluation of the structure of ergodic fields*, The Physics of Fluids, 26 (1983), pp. 1288–1291. (Cited on pp. 109, 180)

[22] ——, *Transport and isomorphic equilibria*, The Physics of Fluids, 26 (1983), pp. 496–499. (Cited on pp. 210, 218)

[23] ——, *Quasi-helical symmetry in stellarators*, Plasma Physics and Controlled Fusion, 37 (1995), pp. A103–A117. (Cited on p. 160)

[24] ——, *Non-axisymmetric magnetic fields and toroidal plasma confinement*, Nuclear Fusion, 55 (2015), 025001. (Cited on p. 106)

[25] A. H BOOZER AND N. POMPHREY, *Current density and plasma displacement near perturbed rational surfaces*, Physics of Plasmas, 17 (2010), 110707. (Cited on p. 132)

[26] H.-S. BOSCH, R. BRAKEL, T. BRAEUER, V. BYKOV, P. VAN EETEN, J.-H. FEIST, F. FÜLLENBACH, ET AL., *Final integration, commissioning and start of the Wendelstein* 7-*X stellarator operation*, Nuclear Fusion, 57 (2017), 116015. (Cited on p. 211)

[27] S. BOYD, S. P. BOYD, AND L. VANDENBERGHE, *Convex Optimization*, Cambridge University Press, 2004. (Cited on p. 197)

[28] S. I. BRAGINSKII, *Transport processes in a plasma*, Reviews of Plasma Physics, 1 (1965), p. 205. (Cited on p. 136)

[29] R. BRAKEL, M. ANTON, J. BALDZUHN, R. BURHENN, V. ERCKMANN, S. FIEDLER, J. GEIGER, ET AL., *Confinement in W7-AS and the role of radial electric field and magnetic shear*, Plasma Physics and Controlled Fusion, 39 (1997), pp. B273–B286. (Cited on p. 210)

[30] P. W. BRENNER AND T. SUNN PEDERSEN, *Pure electron plasmas confined for* 90 *ms in a stellarator without electron sources or internal objects*, Physics of Plasmas, 19 (2012), 050701. (Cited on p. 214)

[31] R. P. BRENT, *Algorithms for Minimization Without Derivatives*, Courier Corporation, 2013. (Cited on p. 186)

[32] A. BROOKS AND W. REIERSEN, *Coil tolerance impact on plasma surface quality for NCSX*, in 20th IEEE/NPSS Symposium on Fusion Engineering, IEEE, 2003, pp. 553–556. (Cited on p. 213)

[33] O. P. BRUNO AND P. LAURENCE, *Existence of three-dimensional toroidal MHD equilibria with nonconstant pressure*, Communications on Pure and Applied Mathematics, 49 (1996), pp. 717–764. (Cited on pp. 84, 156)

[34] J. W. BURBY, N. KALLINIKOS, AND R. S. MACKAY, *Generalized Grad–Shafranov equation for non-axisymmetric MHD equilibria*, Physics of Plasmas, 27 (2020). (Cited on p. 86)

[35] ——, *Some mathematics for quasi-symmetry*, Journal of Mathematical Physics, 61 (2020), 093503. (Cited on pp. 161, 218)

[36] K. BURNS AND M. GIDEA, *Differential Geometry and Topology: With a View to Dynamical Systems*, CRC Press, 2005. (Cited on p. 34)

[37] J. M. CANIK, D. T. ANDERSON, F. S. B. ANDERSON, C. CLARK, K. M. LIKIN, J. N. TALMADGE, AND K. ZHAI, *Reduced particle and heat transport with quasisymmetry in the Helically Symmetric Experiment*, Physics of Plasmas, 14 (2007), 056107. (Cited on p. 212)

[38] J. R CARY AND A. J. BRIZARD, *Hamiltonian theory of guiding-center motion*, Reviews of Modern Physics, 81 (2009), pp. 693–738. (Cited on p. 24)

[39] J. R. CARY AND R. G. LITTLEJOHN, *Noncanonical Hamiltonian mechanics and its application to magnetic field line flow*, Annals of Physics, 151 (1983), pp. 1–34. (Cited on p. 109)

[40] J. R. CARY AND S. G. SHASHARINA, *Helical plasma confinement devices with good confinement properties*, Physical Review Letters, 78 (1997), pp. 674–677. (Cited on p. 170)

[41] ——, *Omnigenity and quasihelicity in helical plasma confinement systems*, Physics of Plasmas, 4 (1997), pp. 3323–3333. (Cited on pp. 169, 170, 180)

[42] F. Castejón, A. Gómez-Iglesias, M. A. Vega-Rodríguez, J. A. Jiménez, J. L. Velasco, and J. A. Romero, *Stellarator optimization under several criteria using metaheuristics*, Plasma Physics and Controlled Fusion, 55 (2012), 014003. (Cited on p. 183)

[43] S. Chapman and T. G. Cowling, *The Mathematical Theory of Non-uniform Gases: An Account of the Kinetic Theory of Viscosity, Thermal Conduction and Diffusion in Gases*, Cambridge University Press, 1990. (Cited on pp. 6, 134, 136)

[44] F. F. Chen, *Introduction to Plasma Physics and Controlled Fusion*, vol. 1, Springer, 1984. (Cited on pp. 2, 80)

[45] D. Colton and R. Kress, *Integral Equation Methods in Scattering Theory*, Classics in Applied Mathematics 72, SIAM, 2013. (Cited on p. 191)

[46] L. Comisso, M. Lingam, Y.-M. Huang, and A. Bhattacharjee, *General theory of the plasmoid instability*, Physics of Plasmas, 23 (2016), 100702. (Cited on p. 127)

[47] P. Constantin, T. D. Drivas, and D. Ginsberg, *On quasisymmetric plasma equilibria sustained by small force*, Journal of Plasma Physics, 87 (2021), 905870111. (Cited on p. 84)

[48] O. Czarny and G. Huysmans, *Bézier surfaces and finite elements for MHD simulations*, Journal of Computational Physics, 227 (2008), pp. 7423–7445. (Cited on p. 137)

[49] D. Palumbo, *Some considerations on closed configurations of magnetohydrostatic equilibrium*, Il Nuovo Cimento B (1965-1970), 53 (1968), pp. 507–511. (Cited on p. 167)

[50] D. del Castillo-Negrete, J. M. Greene, and P. J. Morrison, *Area preserving nontwist maps: Periodic orbits and transition to chaos*, Physica D: Nonlinear Phenomena, 91 (1996), pp. 1–23. (Cited on p. 119)

[51] R. L. Dewar, A. Bhattacharjee, R. M. Kulsrud, and A. M. Wright, *Plasmoid solutions of the Hahm–Kulsrud–Taylor equilibrium model*, Physics of Plasmas, 20 (2013), 082103. (Cited on p. 128)

[52] R. L. Dewar and S. R. Hudson, *Stellarator symmetry*, Physica D: Nonlinear Phenomena, 112 (1998), pp. 275–280. (Cited on p. 171)

[53] R. L. Dewar, S. R. Hudson, A. Bhattacharjee, and Z. Yoshida, *Multi-region relaxed magnetohydrodynamics in plasmas with slowly changing boundaries- Resonant response of a plasma slab*, Physics of Plasmas, 24 (2017), 042507. (Cited on p. 132)

[54] R. L. Dewar, Z. Yoshida, A. Bhattacharjee, and S. R. Hudson, *Variational formulation of relaxed and multi-region relaxed magnetohydrodynamics*, Journal of Plasma Physics, 81 (2015). (Cited on pp. 154, 185)

[55] W. D. D'haeseleer, W. N. G. Hitchon, J. D. Callen, and J. L. Shohet, *Flux Coordinates and Magnetic Field Structure: A Guide to a Fundamental Tool of Plasma Theory*, Springer, 1991. (Cited on pp. 39, 41, 44, 48, 52, 97, 100, 102, 168)

[56] M. P. do Carmo, *Riemannian Geometry*, Birkhäuser Boston, 1992. (Cited on p. 41)

[57] W. Dommaschk, *Representations for vacuum potentials in stellarators*, Computer Physics Communications, 40 (1986), pp. 203–218. (Cited on p. 210)

[58] M. DREVLAK, *Automated optimization of stellarator coils*, Fusion Technology, 33 (1998), pp. 106–117. (Cited on p. 206)

[59] ——, *Thermal load on the W7-X vessel from NBI losses*, in 36th EPS Conference on Plasma Physics, European Physical Society, 2009. (Cited on p. 182)

[60] M. DREVLAK, C. D. BEIDLER, J. GEIGER, P. HELANDER, AND Y. TURKIN, *Optimisation of stellarator equilibria with ROSE*, Nuclear Fusion, 59 (2018), 016010. (Cited on pp. 182, 186, 205, 206)

[61] M. DREVLAK, F. BROCHARD, P. HELANDER, J. KISSLINGER, M. MIKHAILOV, C. NÜHRENBERG, J. NÜHRENBERG, AND Y. TURKIN, *ESTELL: A Quasi-toroidally symmetric stellarator*, Contributions to Plasma Physics, 53 (2013), pp. 459–468. (Cited on p. 163)

[62] M. DREVLAK, J. GEIGER, P. HELANDER, AND Y. TURKIN, *Fast particle confinement with optimized coil currents in the W7-X stellarator*, Nuclear Fusion, 54 (2014), 073002. (Cited on pp. 180, 182)

[63] L. E. DUDEK, J. H. CHRZANOWSKI, P. J. HEITZENROEDER, S. RAFTOPOULOS, M. E. VIOLA, G. H. NEILSON, D. REJ, M. J. COLE, P. GORANSON, AND K. FREUDENBERG, *Status of the NCSX construction*, Fusion Engineering and Design, 84 (2009), pp. 351–354. (Cited on p. 213)

[64] D. W. DUDT, R. CONLIN, D. PANICI, AND E. KOLEMEN, *The DESC stellarator code suite Part 3: Quasi-symmetry optimization*, Journal of Plasma Physics, 89 (2023), 955890201. (Cited on pp. 186, 215)

[65] D. W. DUDT, A. G. GOODMAN, R. CONLIN, D. PANICI, AND E. KOLEMEN, *Magnetic fields with general omnigenity*, Journal of Plasma Physics, 90 (2024), 905900120. (Cited on pp. 180, 215)

[66] D. W. DUDT AND E. KOLEMEN, *DESC: A stellarator equilibrium solver*, Physics of Plasmas, 27 (2020). (Cited on pp. 142, 184)

[67] E. ELBARMI, W. SENGUPTA, AND H. WEITZNER, *Charged particle dynamics near an X-point of a non-symmetric magnetic field with closed field lines*, Journal of Plasma Physics, 86 (2020), 905860209. (Cited on pp. 161, 169)

[68] K. ELSASSER, *Magnetic field line flow as a Hamiltonian problem*, Plasma Physics and Controlled Fusion, 28 (1986), pp. 1743–1752. (Cited on p. 109)

[69] V. ERCKMANN AND U. GASPARINO, *Electron cyclotron resonance heating and current drive in toroidal fusion plasmas*, Plasma Physics and Controlled Fusion, 36 (1994), pp. 1869–1962. (Cited on p. 210)

[70] L. C. EVANS, *Partial Differential Equations*, 2nd ed., American Mathematical Society, 2010. (Cited on p. 54)

[71] T. E. EVANS, *Resonant magnetic perturbations of edge-plasmas in toroidal confinement devices*, Plasma Physics and Controlled Fusion, 57 (2015), 123001. (Cited on p. 75)

[72] Z. FENG, D. A. GATES, S. A. LAZERSON, M. LANDREMAN, N. POMPHREY, AND G. FU, *Optimization of quasi-axisymmetric stellarators with varied elongation*, Physics of Plasmas, 27 (2020). (Cited on p. 217)

[73] T. L. FERRELL, *Hamilton-Jacobi perturbation theory*, American Journal of Physics, 39 (1971), pp. 622–627. (Cited on p. 115)

[74] R. FITZPATRICK, *Helical temperature perturbations associated with tearing modes in tokamak plasmas*, Physics of Plasmas, 2 (1995), pp. 825–838. (Cited on pp. 34, 179)

[75] J. P. FREIDBERG, *Plasma Physics and Fusion Energy*, Cambridge University Press, 2008. (Cited on pp. 4, 5, 31, 33, 183)

[76] ——, *Ideal MHD*, Cambridge University Press, 2014. (Cited on pp. 80, 83, 84, 86, 136, 139)

[77] P. R. GARABEDIAN, *A method of canonical coordinates for flow computations*, Communications on Pure and Applied Mathematics, 23 (1970), pp. 313–327. (Cited on p. 185)

[78] ——, *Three-dimensional codes to design stellarators*, Physics of Plasmas, 9 (2002), pp. 137–149. (Cited on p. 217)

[79] ——, *Three-dimensional stellarator codes*, Proceedings of the National Academy of Sciences, 99 (2002), pp. 10257–10259. (Cited on pp. 142, 184)

[80] ——, *Three-dimensional analysis of tokamaks and stellarators*, Proceedings of the National Academy of Sciences, 105 (2008), pp. 13716–13719. (Cited on p. 185)

[81] D. A. GARREN AND A. H. BOOZER, *Existence of quasihelically symmetric stellarators*, Physics of Fluids B: Plasma Physics, 3 (1991), pp. 2822–2834. (Cited on pp. 149, 218)

[82] D. A. GATES, D. ANDERSON, S. ANDERSON, M. ZARNSTORFF, D. A. SPONG, H. WEITZNER, G. H. NEILSON, ET AL., *Stellarator research opportunities: A report of the national stellarator coordinating committee*, Journal of Fusion Energy, 37 (2018), pp. 51–94. (Cited on p. 217)

[83] B. GEIGER, T. WEGNER, C. D. BEIDLER, R. BURHENN, B. BUTTENSCHÖN, R. DUX, A. LANGENBERG, ET AL., *Observation of anomalous impurity transport during low-density experiments in W7-X with laser blow-off injections of iron*, Nuclear Fusion, 59 (2019), 046009. (Cited on p. 218)

[84] J. GEIGER, C. D. BEIDLER, M. DREVLAK, H. MAASSBERG, C. NÜHRENBERG, Y. SUZUKI, AND Y. TURKIN, *Effects of net currents on the magnetic configuration of W7-X*, Contributions to Plasma Physics, 50 (2010), pp. 770–774. (Cited on p. 178)

[85] M. J. GERARD, B. GEIGER, M. J. PUESCHEL, A. BADER, C. C. HEGNA, B. J. FABER, P. W. TERRY, S. T. A. KUMAR, AND J. C. SCHMITT, *Optimizing the HSX stellarator for microinstability by coil-current adjustments*, Nuclear Fusion, 63 (2023), 056004. (Cited on p. 218)

[86] S. P. GERHARDT, J. N. TALMADGE, J. M. CANIK, AND D. T. ANDERSON, *Measurements and modeling of plasma flow damping in the Helically Symmetric eXperiment*, Physics of Plasmas, 12 (2005), 056116. (Cited on p. 212)

[87] A. GIBSON AND JET TEAM, *Deuterium–tritium plasmas in the Joint European Torus (JET): Behavior and implications*, Physics of Plasmas, 5 (1998), pp. 1839–1847. (Cited on p. 5)

[88] A. GIULIANI, F. WECHSUNG, G. STADLER, A. CERFON, AND M. LANDREMAN, *Direct computation of magnetic surfaces in Boozer coordinates and coil optimization for quasisymmetry*, Journal of Plasma Physics, 88 (2022), 905880401. (Cited on pp. 176, 215, 217)

[89] J. P. GOEDBLOED AND S. POEDTS, *Principles of Magnetohydrodynamics: With Applications to Laboratory and Astrophysical Plasmas*, Cambridge University Press, 2004. (Cited on pp. 80, 82)

[90] H. GOLDSTEIN, C. POOLE, AND J. SAFKO, *Classical Mechanics*, Addison-Wesley, 2002. (Cited on pp. 13, 28, 70, 109, 110, 115, 228, 229, 231, 238)

[91] R. J. GOLDSTON AND P. H. RUTHERFORD, *Introduction to Plasma Physics*, CRC Press, 1995. (Cited on p. 1)

[92] A. G. GOODMAN, K. C. MATA, S. A. HENNEBERG, R. JORGE, M. LANDREMAN, G. G. PLUNK, H. M. SMITH, R. J. J. MACKENBACH, C. D. BEIDLER, AND P. HELANDER, *Constructing precisely quasi-isodynamic magnetic fields*, Journal of Plasma Physics, 89 (2023), 905890504. (Cited on p. 180)

[93] H. GRAD, *Toroidal containment of a plasma*, The Physics of Fluids, 10 (1967), pp. 137–154. (Cited on p. 125)

[94] J. M. GREENE, *A brief review of magnetic wells*, Comments on Plasma Physics and Controlled Fusion, 17 (1997), pp. 389–402. (Cited on p. 183)

[95] G. GRIEGER, C. BEIDLER, AND E. HARMEYER, *Physics studies for helical-axis advanced stellarators*, in Plasma Physics and Controlled Nuclear Fusion Research, vol. 2, IAEA, 1988. (Cited on p. 170)

[96] G. GRIEGER, W. LOTZ, P. MERKEL, J. NÜHRENBERG, J. SAPPER, E. STRUMBERGER, H. WOBIG, ET AL., *Physics optimization of stellarators*, Physics of Fluids B: Plasma Physics, 4 (1992), pp. 2081–2091. (Cited on pp. 170, 178, 204)

[97] J. HADAMARD, *Le probleme de Cauchy et les équations aux dérivées partielles linéaires hyperboliques*, vol. 220, J. Gabay, 1932. (Cited on p. 190)

[98] T. S. HAHM AND R. M. KULSRUD, *Forced magnetic reconnection*, The Physics of Fluids, 28 (1985), pp. 2412–2418. (Cited on pp. 127, 128)

[99] L. S. HALL AND B. MCNAMARA, *Three-dimensional equilibrium of the anisotropic, finite-pressure guiding-center plasma: Theory of the magnetic plasma*, The Physics of Fluids, 18 (1975), pp. 552–565. (Cited on p. 169)

[100] S. M. HAMBERGER, B. D. BLACKWELL, L. E. SHARP, AND D. B. SHENTON, *H*-1 *design and construction*, Fusion Technology, 17 (1990), pp. 123–130. (Cited on p. 214)

[101] G. W. HAMMETT, *Gyrokinetic theory and simulation of experiments*, in APS Meeting of the Division of Plasma Physics, 2007. (Cited on p. 38)

[102] K. C. HAMMOND, C. ZHU, T. BROWN, K. CORRIGAN, D. A. GATES, AND M. SIBILIA, *Geometric concepts for stellarator permanent magnet arrays*, Nuclear Fusion, 60 (2020), 106010. (Cited on p. 217)

[103] K. C. Hammond, C. Zhu, K. Corrigan, D. A. Gates, R. Lown, R. Mercurio, T. M. Qian, and M. C. Zarnstorff, *Design of an arrangement of cubic magnets for a quasi-axisymmetric stellarator experiment*, Nuclear Fusion, 62 (2022), 126065. (Cited on p. 217)

[104] P. C. Hansen, *Rank-Deficient and Discrete Ill-Posed Problems: Numerical Aspects of Linear Inversion*, Mathematical Modeling and Computation 4, SIAM, 1998. (Cited on p. 191)

[105] J. D. Hanson and J. R. Cary, *Elimination of stochasticity in stellarators*, in Hamiltonian Dynamical Systems, CRC Press, 2020, pp. 688–690. (Cited on p. 179)

[106] K. Harafuji, T. Hayashi, and T. Sato, *Computational study of three-dimensional magnetohydrodynamic equilibria in toroidal helical systems*, Journal of Computational Physics, 81 (1989), pp. 169–192. (Cited on p. 150)

[107] G. J. Hartwell, S. F. Knowlton, J. D. Hanson, D. A. Ennis, and D. A. Maurer, *Design, construction, and operation of the Compact Toroidal Hybrid*, Fusion Science and Technology, 72 (2017), pp. 76–90. (Cited on p. 214)

[108] R. J. Hawryluk, *Results from D–T experiments on TFTR and implications for achieving an ignited plasma*, Philosophical Transactions of the Royal Society of London. Series A: Mathematical, Physical and Engineering Sciences, 357 (1999), pp. 443–469. (Cited on p. 5)

[109] R. D. Hazeltine, *The Framework of Plasma Physics*, CRC Press, 2018. (Cited on p. 23)

[110] R. D. Hazeltine and J. D. Meiss, *Plasma Confinement*, Courier Corporation, 2003. (Cited on pp. 6, 33)

[111] C. He and Z. Xin, *On the regularity of weak solutions to the magnetohydrodynamic equations*, Journal of Differential Equations, 213 (2005), pp. 235–254. (Cited on p. 134)

[112] C. C. Hegna, *Local three-dimensional magnetostatic equilibria*, Physics of Plasmas, 7 (2000), pp. 3921–3928. (Cited on p. 216)

[113] C. C. Hegna and A. Bhattacharjee, *Islands in three-dimensional steady flows*, Journal of Fluid Mechanics, 227 (1991), pp. 527–542. (Cited on p. 156)

[114] C. C. Hegna and N. Nakajima, *On the stability of Mercier and ballooning modes in stellarator configurations*, Physics of Plasmas, 5 (1998), pp. 1336–1344. (Cited on p. 183)

[115] C. C. Hegna, P. W. Terry, and B. J. Faber, *Theory of ITG turbulent saturation in stellarators: Identifying mechanisms to reduce turbulent transport*, Physics of Plasmas, 25 (2018), 022511. (Cited on p. 218)

[116] P. Helander, *Theory of plasma confinement in non-axisymmetric magnetic field*, Reports of Progress in Physics, 77 (2014), 087001. (Cited on pp. 73, 97, 100, 102, 109, 124, 142, 149, 160, 163, 168, 176, 177, 179, 180, 182)

[117] P. Helander, C. D. Beidler, T. M. Bird, M. Drevlak, Y. Feng, R. Hatzky, F. Jenko, et al., *Stellarator and tokamak plasmas: A comparison*, Plasma Physics and Controlled Fusion, 54 (2012), 124009. (Cited on p. 181)

[118] P. Helander, M. Drevlak, M. Zarnstorff, and S. C. Cowley, *Stellarators with permanent magnets*, Physical Review Letters, 124 (2020), 095001. (Cited on p. 217)

[119] P. Helander and J. Nührenberg, *Bootstrap current and neoclassical transport in quasi-isodynamic stellarators*, Plasma Physics and Controlled Fusion, 51 (2009), 055004. (Cited on pp. 178, 210)

[120] P. Helander and D. J. Sigmar, *Collisional Transport in Magnetized Plasmas*, vol. 4, Cambridge University Press, 2005. (Cited on pp. 21, 33, 34, 71, 86, 182)

[121] P. Helander and A. N. Simakov, *Intrinsic ambipolarity and rotation in stellarators*, Physical Review Letters, 101 (2008), 145003. (Cited on pp. 163, 180)

[122] S. A. Henneberg, M. Drevlak, and P. Helander, *Improving fast-particle confinement in quasi-axisymmetric stellarator optimization*, Plasma Physics and Controlled Fusion, 62 (2019), 014023. (Cited on p. 182)

[123] S. A. Henneberg, M. Drevlak, C. Nührenberg, C. D. Beidler, Y. Turkin, J. Loizu, and P. Helander, *Properties of a new quasi-axisymmetric configuration*, Nuclear Fusion, 59 (2019), 026014. (Cited on pp. 163, 183)

[124] J. G. Heywood, *Auxiliary flux and pressure conditions for Navier-Stokes problems*, in Approximation Methods for Navier-Stokes Problems, R. Rautmann, ed., Springer, 1980, pp. 223–234. (Cited on p. 154)

[125] J. G. Heywood, R. Rannacher, and S. Turek, *Artificial boundaries and flux and pressure conditions for the incompressible Navier–Stokes equations*, International Journal for Numerical Methods in Fluids, 22 (1996), pp. 325–352. (Cited on p. 154)

[126] C. Hidalgo, C. Alejaldre, A. Alonso, J. Alonso, L. Almoguera, F. de Aragón, E. Ascasíbar, et al., *Overview of TJ-II experiments*, Nuclear Fusion, 45 (2005), pp. S266–S275. (Cited on p. 214)

[127] E. G. Highcock, N. R. Mandell, M. Barnes, and W. Dorland, *Optimisation of confinement in a fusion reactor using a nonlinear turbulence model*, Journal of Plasma Physics, 84 (2018). (Cited on p. 175)

[128] M. Hirsch, J. Baldzuhn, C. Beidler, R. Brakel, R. Burhenn, A. Dinklage, H. Ehmler, et al., *Major results from the stellarator Wendelstein 7-AS*, Plasma Physics and Controlled Fusion, 50 (2008), 053001. (Cited on pp. 208, 209, 214)

[129] S. P. Hirshman, W. I. Van Rij, and P. Merkel, *Three-dimensional free boundary calculations using a spectral Green's function method*, Computer Physics Communications, 43 (1986), pp. 143–155. (Cited on pp. 142, 143)

[130] S. P. Hirshman, R. Sanchez, and C. R. Cook, *SIESTA: A scalable iterative equilibrium solver for toroidal applications*, Physics of Plasmas, 18 (2011), 062504. (Cited on p. 150)

[131] S. P. Hirshman, D. A. Spong, J. C. Whitson, B. Nelson, D. B. Batchelor, J. F. Lyon, R. Sanchez, et al., *Physics of compact stellarators*, Physics of Plasmas, 6 (1999), pp. 1858–1864. (Cited on pp. 178, 185)

[132] S. P. HIRSHMAN AND J. C. WHITSON, *Steepest descent moment method for three-dimensional magnetohydrodynamic equilibria*, The Physics of Fluids, 26 (1983), pp. 3553–3568. (Cited on pp. 142, 184)

[133] J. V. HOFMANN, J. BALDZUHN, R. BRAKEL, Y. FENG, S. FIEDLER, J. GEIGER, P. GRIGULL, ET AL., *Stellarator optimization studies in W7-AS*, Plasma Physics and Controlled Fusion, 38 (1996), pp. A193–A211. (Cited on pp. 208, 210)

[134] M. J. HOLE, S. R. HUDSON, AND R. L. DEWAR, *Stepped pressure profile equilibria in cylindrical plasmas via partial Taylor relaxation*, Journal of Plasma Physics, 72 (2006), pp. 1167–1171. (Cited on pp. 154, 185)

[135] R. J. HOSKING AND R. L. DEWAR, *Fundamental Fluid Mechanics and Magnetohydrodynamics*, Springer, 2016. (Cited on p. 136)

[136] Y.-M. HUANG, Y. ZHOU, J. LOIZU, S. HUDSON, AND A. BHATTACHARJEE, *Structure of pressure-gradient-driven current singularity in ideal magnetohydrodynamic equilibrium*, Plasma Physics and Controlled Fusion, 65 (2023), 034008. (Cited on p. 125)

[137] J. D. HUBA, *NRL Plasma Formulary*, Technical report, Naval Research Laboratory, 2006. (Cited on pp. xiii, 6, 11, 26)

[138] S. R HUDSON, *A regularized approach for solving magnetic differential equations and a revised iterative equilibrium algorithm*, Physics of Plasmas, 17 (2010), 114501. (Cited on p. 150)

[139] S. R. HUDSON, R. L. DEWAR, G. DENNIS, M. J. HOLE, M. MCGANN, G. VON NESSI, AND S. LAZERSON, *Computation of multi-region relaxed magnetohydrodynamic equilibria*, Physics of Plasmas, 19 (2012), 112502. (Cited on p. 185)

[140] S. R. HUDSON, R. L. DEWAR, M. J. HOLE, AND M. MCGANN, *Non-axisymmetric, multi-region relaxed magnetohydrodynamic equilibrium solutions*, Plasma Physics and Controlled Fusion, 54 (2011), 014005. (Cited on pp. 154, 155)

[141] S. R. HUDSON AND B. F. KRAUS, *Three-dimensional magnetohydrodynamic equilibria with continuous magnetic fields*, Journal of Plasma Physics, 83 (2017), 715830403. (Cited on p. 126)

[142] S. R. HUDSON, D. A. MONTICELLO, A. H. REIMAN, A. H. BOOZER, D. J. STRICKLER, S. P. HIRSHMAN, AND M. C. ZARNSTORFF, *Eliminating islands in high-pressure free-boundary stellarator magnetohydrodynamic equilibrium solutions*, Physical Review Letters, 89 (2002), 275003. (Cited on pp. 179, 213, 217)

[143] S. R. HUDSON AND N. NAKAJIMA, *Pressure, chaotic magnetic fields, and magnetohydrodynamic equilibria*, Physics of Plasmas, 17 (2010), 052511. (Cited on p. 137)

[144] S. R. HUDSON, C. ZHU, D. PFEFFERLÉ, AND L. GUNDERSON, *Differentiating the shape of stellarator coils with respect to the plasma boundary*, Physics Letters A, 382 (2018), pp. 2732–2737. (Cited on pp. 206, 217)

[145] S. HYSING, S. TUREK, D. KUZMIN, N. PAROLINI, E. BURMAN, S. GANESAN, AND L. TOBISKA, *Quantitative benchmark computations of two-dimensional bubble dynamics*, International Journal for Numerical Methods in Fluids, 60 (2009), pp. 1259–1288. (Cited on p. 154)

[146] D. J. STRICKLER ET AL., eds., *Integrated plasma and coil optimization for compact stellarators*, in 19th International Atomic Energy Agency (IAEA) Fusion Energy Conference (FEC) proceedings, 2002. (Cited on pp. 213, 217)

[147] A. IIYOSHI, A. KOMORI, A. EJIRI, M. EMOTO, H. FUNABA, M. GOTO, K. IDA, ET AL., *Overview of the Large Helical Device project*, Nuclear Fusion, 39 (1999), pp. 1245–1256. (Cited on p. 214)

[148] M. ISOBE, A. SHIMIZU, H. LIU, H. LIU, G. XIONG, D. YIN, K. OGAWA, ET AL., *Current status of NIFS-SWJTU joint project for quasi-axisymmetric stellarator CFQS*, Plasma and Fusion Research, 14 (2019), 3402074. (Cited on p. 214)

[149] ITER, *What Will ITER Do?* ITER, `https://www.iter.org/sci/Goals`. Accessed: 2019-08-14. (Cited on p. 5)

[150] J. D. JACKSON, *Classical Electrodynamics*, 2nd ed., Wiley, 1975. (Cited on p. 11)

[151] S. JARDIN, *Computational Methods in Plasma Physics*, CRC Press, 2010. (Cited on pp. 86, 142)

[152] S. C. JARDIN, J. BRESLAU, AND N. FERRARO, *A high-order implicit finite element method for integrating the two-fluid magnetohydrodynamic equations in two dimensions*, Journal of Computational Physics, 226 (2007), pp. 2146–2174. (Cited on p. 137)

[153] R. JORGE, A. G. GOODMAN, M. LANDREMAN, J. RODRIGUES, AND F. WECHSUNG, *Single-stage stellarator optimization: Combining coils with fixed boundary equilibria*, Plasma Physics and Controlled Fusion, (2023). (Cited on pp. 176, 217)

[154] R. JORGE, G. G. PLUNK, M. DREVLAK, M. LANDREMAN, J.-F. LOBSIEN, K. C. MATA, AND P. HELANDER, *A single-field-period quasi-isodynamic stellarator*, Journal of Plasma Physics, 88 (2022), 175880504. (Cited on pp. 180, 216)

[155] R. JORGE, W. SENGUPTA, AND M. LANDREMAN, *Construction of quasisymmetric stellarators using a direct coordinate approach*, Nuclear Fusion, 60 (2020), 076021, doi: 10.1088/1741-4326/ab90ca. (Cited on pp. 146, 216)

[156] ——, *Near-axis expansion of stellarator equilibrium at arbitrary order in the distance to the axis*, Journal of Plasma Physics, 86 (2020), 905860106. doi:10.1017/S0022377820000033. (Cited on pp. 145, 149)

[157] J. V. JOSÉ AND E. J. SALETAN, *Classical Dynamics: A Contemporary Approach*, Cambridge University Press, 1998. (Cited on p. 13)

[158] O KANEKO, *Large Helical Device*, in Magnetic Fusion Energy, Elsevier, 2016, pp. 469–491. (Cited on p. 211)

[159] T. KLINGER, C. BAYLARD, C.D. BEIDLER, J. BOSCARY, H.S. BOSCH, A. DINKLAGE, D. HARTMANN, P. HELANDER, H. MASSBERG, A. PEACOCK, T. SUNN PEDERSEN, T. RUMMEL, F. SCHAUER, L. WEGENER, AND R. WOLF, *Towards assembly completion and preparation of experimental campaigns of Wendelstein 7-X in the perspective of a path to a stellarator fusion power plant*, Fusion Engineering and Design, 88 (2013), pp. 461–465. (Cited on pp. 187, 211)

[160] A. N. KOLMOGOROV, *On conservation of conditionally periodic motions for a small change in Hamilton's function*, in Proceedings of the USSR Academy of Sciences, vol. 98, 1954, pp. 527–530. (Cited on p. 119)

[161] A. KOMORI, T. MORISAKI, T. MUTOH, S. SAKAKIBARA, Y. TAKEIRI, R. KUMAZAWA, S. KUBO, ET AL., *Overview of progress in LHD experiments*, Fusion Science and Technology, 50 (2006), pp. 136–145. (Cited on p. 7)

[162] A. KOMORI, N. OHYABU, H. YAMADA, O. KANEKO, K. KAWAHATA, K. IDA, Y. NAKAMURA, ET AL., *Recent results from the Large Helical Device*, Plasma Physics and Controlled Fusion, 45 (2003), pp. 671–686. (Cited on p. 217)

[163] M. G. KONG, G. KROESEN, G. MORFILL, T. NOSENKO, T. SHIMIZU, J. VAN DIJK, AND J. L. ZIMMERMANN, *Plasma medicine: an introductory review*, New Journal of Physics, 11 (2009), 115012. (Cited on p. 3)

[164] V. V. KOZLOV, *Integrability and non-integrability in Hamiltonian mechanics*, Russian Mathematical Surveys, 38 (1983), pp. 3–67. (Cited on pp. 59, 109, 115, 233)

[165] N. A. KRALL AND A. W. TRIVELPIECE, *Principles of Plasma Physics*, McGraw-Hill, 1973. (Cited on p. 6)

[166] B. F. KRAUS AND S. R. HUDSON, *Theory and discretization of ideal magnetohydrodynamic equilibria with fractal pressure profiles*, Physics of Plasmas, 24 (2017), 092519. (Cited on p. 125)

[167] R. KRESS, *On constant-alpha force-free fields in a torus*, Journal of Engineering Mathematics, 20 (1986), pp. 323–344. (Cited on p. 151)

[168] ——, *Linear Integral Equations*, Applied and Mathematical Sciences 82, Springer, 1989. (Cited on pp. 191, 192, 195)

[169] J. A. KROMMES AND A. H. REIMAN, *Plasma equilibrium in a magnetic field with stochastic regions*, Physics of Plasmas, 16 (2009), 072308. (Cited on p. 150)

[170] M. D. KRUSKAL AND R. M. KULSRUD, *Equilibrium of a magnetically confined plasma in a toroid*, The Physics of Fluids, 1 (1958), pp. 265–274. (Cited on pp. 53, 140, 142)

[171] L. P. KU AND A. H. BOOZER, *New classes of quasi-helically symmetric stellarators*, Nuclear Fusion, 51 (2010), 013004. (Cited on pp. 163, 196)

[172] L. P. KU, P. R. GARABEDIAN, J. LYON, A. TURNBULL, A. GROSSMAN, T. K. MAU, M. ZARNSTORFF, AND ARIES TEAM, *Physics design for ARIES-CS*, Fusion Science and Technology, 54 (2008), pp. 673–693. (Cited on pp. 181, 188)

[173] L. D. LANDAU AND E. M. LIFSHITZ, *Landau and Lifshitz Course of Theoretical Physics, Mechanics, Volume* 1, Elsevier, 1976. (Cited on p. 236)

[174] M. LANDREMAN, *Electric Fields and Transport in Optimized Stellarators*, PhD thesis, Massachusetts Institute of Technology, 2011. (Cited on p. 163)

[175] ——, *An improved current potential method for fast computation of stellarator coil shapes*, Nuclear Fusion, 57 (2017), 046003. (Cited on pp. 204, 205)

[176] M. LANDREMAN, *Optimized quasisymmetric stellarators are consistent with the Garren–Boozer construction*, Plasma Physics and Controlled Fusion, 61 (2019), 075001. (Cited on pp. 149, 216)

[177] ——, *Quasisymmetry: A Hidden Symmetry of Magnetic Fields*, University of Maryland, 2019, https://terpconnect.umd.edu/~mattland/assets/notes/Introduction_to_quasisymmetry.pdf. (Cited on p. 163)

[178] ——, *Figures of merit for stellarators near the magnetic axis*, Journal of Plasma Physics, 87 (2021), 905870112. (Cited on p. 149)

[179] ——, *Mapping the space of quasisymmetric stellarators using optimized near-axis expansion*, Journal of Plasma Physics, 88 (2022), 905880616. (Cited on p. 216)

[180] M. LANDREMAN AND A. H. BOOZER, *Efficient magnetic fields for supporting toroidal plasmas*, Physics of Plasmas, 23 (2016), 032506. (Cited on p. 196)

[181] M. LANDREMAN, S. BULLER, AND M. DREVLAK, *Optimization of quasi-symmetric stellarators with self-consistent bootstrap current and energetic particle confinement*, Physics of Plasmas, 29 (2022). (Cited on pp. 178, 182, 185)

[182] M. LANDREMAN AND P. J. CATTO, *Omnigenity as generalized quasisymmetry*, Physics of Plasmas, 19 (2012), 056103. (Cited on p. 170)

[183] M. LANDREMAN, B. MEDASANI, F. WECHSUNG, A. GIULIANI, R. JORGE, AND C. ZHU, *SIMSOPT: A flexible framework for stellarator optimization*, Journal of Open Source Software, 6 (2021), pp. 3525–3531. (Cited on pp. 186, 206)

[184] M. LANDREMAN AND E. PAUL, *Magnetic fields with precise quasisymmetry for plasma confinement*, Physical Review Letters, 128 (2022), 035001. (Cited on pp. 180, 182, 218)

[185] M. LANDREMAN AND W. SENGUPTA, *Direct construction of optimized stellarator shapes. Part* 1. *Theory in cylindrical coordinates*, Journal of Plasma Physics, 84 (2018). (Cited on pp. 149, 216)

[186] M. LANDREMAN, W. SENGUPTA, AND G. G. PLUNK, *Direct construction of optimized stellarator shapes. Part* 2. *Numerical quasisymmetric solutions*, Journal of Plasma Physics, 85 (2019). (Cited on pp. 149, 171, 216)

[187] M. LANDREMAN, H. M. SMITH, A. MOLLÉN, AND P. HELANDER, *Comparison of particle trajectories and collision operators for collisional transport in nonaxisymmetric plasmas*, Physics of Plasmas, 21 (2014), 042503. (Cited on p. 100)

[188] H. P. LAQUA, J. BALDZUHN, H. BRAUNE, S. BOZHENKOV, K. BRUNNER, M. HIRSCH, U. HOEFEL, ET AL., *High-performance ECRH at W7-X: Experience and perspectives*, Nuclear Fusion, 61 (2021), 106005. (Cited on p. 218)

[189] A. LARIOS AND E. S. TITI, *On the higher-order global regularity of the inviscid Voigt-regularization of three-dimensional hydrodynamic models*, Discrete & Continuous Dynamical Systems - B, 14 (2010), pp. 603–627. (Cited on p. 134)

[190] J. D. LAWSON, *Some criteria for a power producing thermonuclear reactor*, Proceedings of the Physical Society. Section B, 70 (1957), pp. 6–10. (Cited on p. 5)

[191] P.D. LAX, *Functional Analysis*, Pure and Applied Mathematics, Wiley, 2002. (Cited on p. 192)

[192] S. A. LAZERSON, J. LOIZU, S. HIRSHMAN, AND S. R. HUDSON, *Verification of the ideal magnetohydrodynamic response at rational surfaces in the VMEC code*, Physics of Plasmas, 23 (2016), 012507. (Cited on pp. 126, 127)

[193] D. K. LEE, J. H. HARRIS, AND G. S. LEE, *Magnetic island widths due to field perturbations in toroidal stellarators*, Nuclear Fusion, 30 (1990), pp. 2177–2184. (Cited on p. 179)

[194] I. LEVCHENKO, S. XU, G. TEEL, D. MARIOTTI, M. L. R. WALKER, AND M. KEIDAR, *Recent progress and perspectives of space electric propulsion systems based on smart nanomaterials*, Nature Communications, 9 (2018), pp. 879–898. (Cited on p. 3)

[195] A. J. LICHTENBERG AND M. A. LIEBERMAN, *Regular and Stochastic Motion*, Applied Mathematical Sciences 38, Springer Science & Business Media, 2013. (Cited on pp. 115, 119, 179, 234)

[196] M. A. LIEBERMAN AND A. J. LICHTENBERG, *Principles of Plasma Discharges and Materials Processing*, vol. 2, Wiley Online Library, 2005. (Cited on p. 3)

[197] R. G. LITTLEJOHN, *Variational principles of guiding centre motion*, Journal of Plasma Physics, 29 (1983), pp. 111–125. (Cited on pp. 21, 71)

[198] J.-F. LOBSIEN, M. DREVLAK, T. KRUGER, S. LAZERSON, C. ZHU, AND T. SUNN PEDERSEN, *Improved performance of stellarator coil design optimization*, Journal of Plasma Physics, 86 (2020), 815860202. (Cited on p. 215)

[199] J.-F. LOBSIEN, M. DREVLAK, T. SUNN PEDERSEN, AND THE W7-X TEAM, *Stellarator coil optimization towards higher engineering tolerances*, Nuclear Fusion, 58 (2018), 106013. (Cited on p. 215)

[200] J. LOIZU, S. HUDSON, A. BHATTACHARJEE, AND P. HELANDER, *Magnetic islands and singular currents at rational surfaces in three-dimensional magnetohydrodynamic equilibria*, Physics of Plasmas, 22 (2015), 022501. (Cited on pp. 126, 127)

[201] J. LOIZU, S. R. HUDSON, A. BHATTACHARJEE, S. LAZERSON, AND P. HELANDER, *Existence of three-dimensional ideal-magnetohydrodynamic equilibria with current sheets*, Physics of Plasmas, 22 (2015). (Cited on p. 126)

[202] J. LOIZU, S. R. HUDSON, C. NÜHRENBERG, J. GEIGER, AND P. HELANDER, *Equilibrium β-limits in classical stellarators*, Journal of Plasma Physics, 83 (2017), 715830601. (Cited on p. 179)

[203] R. J. J. MACKENBACH, J. H. E. PROLL, AND P. HELANDER, *Available energy of trapped electrons and its relation to turbulent transport*, Physical Review Letters, 128 (2022), 175001. (Cited on p. 218)

[204] D. MALHOTRA, A. CERFON, L.-M. IMBERT-GÉRARD, AND M. O'NEIL, *Taylor states in stellarators: A fast high-order boundary integral solver*, Journal of Computational Physics, 397 (2019), 108791. (Cited on p. 154)

[205] Max Planck Institute for Plasma Physics, *Concept planning: The initial planning for Wendelstein 7-X was aimed at finding the optimum magnetic field*, `https://www.ipp.mpg.de/2815232/konzeptentwicklung`. Accessed: 2018-10-04. (Cited on p. 77)

[206] ——, *Tokamak*. `http://www.ipp.mpg.de/14869/tokamak`, 2018. Accessed: 2018-10-04. (Cited on p. 76)

[207] K. McCormick, P. Grigull, R. Burhenn, R. Brakel, H. Ehmler, Y. Feng, F. Gadelmeier, et al., *New advanced operational regime on the W7-AS stellarator*, Physical Review Letters, 89 (2002), 015001. (Cited on p. 7)

[208] N. McGreivy, S. R. Hudson, and C. Zhu, *Optimized finite-build stellarator coils using automatic differentiation*, Nuclear Fusion, 61 (2021), 026020. (Cited on p. 215)

[209] M. McMillan and S. A. Lazerson, *BEAMS3D neutral beam injection model*, Plasma Physics and Controlled Fusion, 56 (2014), 095019. (Cited on p. 182)

[210] C. Mercier, *Equilibrium and stability of a toroidal magnetohydrodynamic system in the neighbourhood of a magnetic axis*, Nuclear Fusion, 4 (1964), pp. 213–226. (Cited on pp. 73, 143, 149)

[211] C. Mercier and H. Luc, *The MHD approach to the problem of plasma confinement in closed magnetic configurations*, Lectures in Plasma Physics, Commission of the European Communities, Luxembourg, 1974. (Cited on p. 183)

[212] P. Merkel, *An integral equation technique for the exterior and interior Neumann problem in toroidal regions*, Journal of Computational Physics, 66 (1986), pp. 83–98. (Cited on p. 156)

[213] ——, *Solution of stellarator boundary value problems with external currents*, Nuclear Fusion, 27 (1987), pp. 867–871. (Cited on p. 204)

[214] M. I. Mikhailov, J. Nührenberg, and R. Zille, *Elimination of current sheets at resonances in three-dimensional toroidal ideal-magnetohydrodynamic equilibria*, Nuclear Fusion, 59 (2019), 066002. (Cited on pp. 126, 127)

[215] H. K. Moffatt, *Magnetostatic equilibria and analogous Euler flows of arbitrarily complex topology. Part* 1. *Fundamentals*, Journal of Fluid Mechanics, 159 (1985), pp. 359–378. (Cited on p. 156)

[216] J. J. Moré, *The Levenberg-Marquardt Algorithm: Implementation and Theory*, in Numerical Analysis, Springer, 1978, pp. 105–116. (Cited on p. 186)

[217] P. J. Morrison, *Hamiltonian description of the ideal fluid*, Reviews of Modern Physics, 70 (1998), pp. 467–521. (Cited on pp. 109, 119)

[218] J. K. Moser, *On invariant curves of area-preserving mapping of an annulus*, Matematika, 6 (1962), pp. 51–68. (Cited on p. 119)

[219] S. Murakami, A. Wakasa, H. Maassberg, C. D. Beidler, H. Yamada, K. Y. Watanabe, and LHD Experimental Group, *Neoclassical transport optimization of LHD*, Nuclear Fusion, 42 (2002), pp. L19–L22. (Cited on p. 212)

[220] S. Murakami, H. Yamada, M. Sasao, M. Isobe, T. Ozaki, T. Saida, P. Goncharov, et al., *Effect of neoclassical transport optimization on energetic ion confinement in LHD*, Fusion Science and Technology, 46 (2004), pp. 241–247. (Cited on p. 212)

[221] H. E. MYNICK, *Transport optimization in stellarators*, Physics of Plasmas, 13 (2006), 058102. (Cited on p. 182)

[222] H. E. MYNICK, N. POMPHREY, AND S. ETHIER, *Exploration of stellarator configuration space with global search methods*, Physics of Plasmas, 9 (2002), pp. 869–876. (Cited on p. 186)

[223] F. NAJMABADI, A. R. RAFFRAY, S. I. ABDEL-KHALIK, L. BROMBERG, L. CROSATTI, L. EL-GUEBALY, P. R. GARABEDIAN, ET AL., *The ARIES-CS compact stellarator fusion power plant*, Fusion Science and Technology, 54 (2008), pp. 655–672. (Cited on pp. 163, 188)

[224] V. V. NEMOV, S. V. KASILOV, W. KERNBICHLER, AND M. F. HEYN, *Evaluation of $1/\nu$ neoclassical transport in stellarators*, Physics of Plasmas, 6 (1999), pp. 4622–4632. (Cited on pp. 100, 181)

[225] V. V. NEMOV, S. V. KASILOV, W. KERNBICHLER, AND G. O. LEITOLD, *Poloidal motion of trapped particle orbits in real-space coordinates*, Physics of Plasmas, 15 (2008), 052501. (Cited on p. 182)

[226] D. R. NICHOLSON, *Introduction to Plasma Theory*, Wiley, 1983. (Cited on pp. 6, 33, 80)

[227] N. NIKULSIN, R. RAMASAMY, M. HOELZL, F. HINDENLANG, E. STRUMBERGER, K. LACKNER, S. GÜNTER, AND THE JOREK TEAM, *JOREK3D: An extension of the JOREK nonlinear MHD code to stellarators*, Physics of Plasmas, 29 (2022), 063901. (Cited on p. 217)

[228] K. NISHIMURA, K. MATSUOKA, M. FUJIWARA, K. YAMAZAKI, J. TODOROKI, T. KAMIMURA, T. AMANO, ET AL., *Compact Helical System physics and engineering design*, Fusion Technology, 17 (1990), pp. 86–100. (Cited on p. 214)

[229] M. NOCENTE, V. KIPTILY, M. TARDOCCHI, P. J. BONOFIGLO, T. CRACIUNESCU, A. D. MOLIN, E. DE LA LUNA, ET AL., *Fusion product measurements by nuclear diagnostics in the Joint European Torus deuterium–tritium 2 campaign*, Review of Scientific Instruments, 93 (2022), 093520. (Cited on p. 5)

[230] J. NÜHRENBERG, *Development of quasi-isodynamic stellarators*, Plasma Physics and Controlled Fusion, 52 (2010), 124003. (Cited on pp. 210, 212)

[231] J NÜHRENBERG AND R ZILLE, *Equilibrium and stability of low shear-stellarators*, in Proceedings of the Workshop on Theory of Fusion Plasmas, 1987. (Cited on p. 179)

[232] J. NÜHRENBERG AND R. ZILLE, *Quasi-helically symmetric toroidal stellarators*, Physics Letters A, 129 (1988), pp. 113–117. (Cited on pp. 160, 163, 184, 186, 210)

[233] M. O'NEIL AND A. J. CERFON, *An integral equation-based numerical solver for Taylor states in toroidal geometries*, Journal of Computational Physics, 359 (2018), pp. 263–282. (Cited on p. 185)

[234] K. E. PARSOPOULOS AND M. N. VRAHATIS, *Recent approaches to global optimization problems through particle swarm optimization*, Natural Computing, 1 (2002), pp. 235–306. (Cited on p. 186)

[235] E. J. Paul, I. G. Abel, M. Landreman, and W. Dorland, *An adjoint method for neoclassical stellarator optimization*, Journal of Plasma Physics, 85 (2019). (Cited on p. 215)

[236] E. J. Paul, T. Antonsen, M. Landreman, and W. A. Cooper, *Adjoint approach to calculating shape gradients for three-dimensional magnetic confinement equilibria. Part 2. Applications*, Journal of Plasma Physics, 86 (2020), 905860103. (Cited on p. 181)

[237] E. J. Paul, M. Landreman, A. Bader, and W. Dorland, *An adjoint method for gradient-based optimization of stellarator coil shapes*, Nuclear Fusion, 58 (2018), 076015. (Cited on pp. 204, 205, 215)

[238] C. Paz-Soldan, *Non-planar coil winding angle optimization for compatibility with non-insulated high-temperature superconducting magnets*, Journal of Plasma Physics, 86 (2020), 815860501. (Cited on p. 216)

[239] G. G. Plunk, *Perturbing an axisymmetric magnetic equilibrium to obtain a quasi-axisymmetric stellarator*, Journal of Plasma Physics, 86 (2020), 905860409. (Cited on p. 216)

[240] G. G. Plunk and P. Helander, *Quasi-axisymmetric magnetic fields: Weakly non-axisymmetric case in a vacuum*, Journal of Plasma Physics, 84 (2018), 905840205. doi:10.1017/S0022377818000259. (Cited on pp. 216, 218)

[241] G. G. Plunk, M. Landreman, and P. Helander, *Direct construction of optimized stellarator shapes. Part 3. Omnigenity near the magnetic axis*, Journal of Plasma Physics, 85 (2019), 905850602. doi:10.1017/S002237781900062X. (Cited on pp. 170, 216)

[242] N. Pomphrey, L. Berry, A. Boozer, A. Brooks, R. E. Hatcher, S. P. Hirshman, L.-P. Ku, et al., *Innovations in compact stellarator coil design*, Nuclear Fusion, 41 (2001), pp. 339–347. (Cited on pp. 196, 204)

[243] C. Pozrikidis, *Boundary Integral and Singularity Methods for Linearized Viscous Flow*, Cambridge Texts in Applied Mathematics, Cambridge University Press, 1992. (Cited on p. 191)

[244] E. Priest and T. Forbes, *Magnetic Reconnection: MHD Theory and Applications*, Cambridge University Press, 2000. (Cited on p. 133)

[245] Princeton Plasma Physics Laboratory, *Timeline*, `https://www.pppl.gov/timeline`. Accessed: 2019-03-01. (Cited on p. 207)

[246] T. Qian, M. Zarnstorff, D. Bishop, A. Chamblis, A. Dominguez, C. Pagano, D. Patch, and C. Zhu, *Simpler optimized stellarators using permanent magnets*, Nuclear Fusion, 62 (2022), 084001. (Cited on pp. 163, 217)

[247] A. B. Rechester and T. H. Stix, *Magnetic braiding due to weak asymmetry*, Physical Review Letters, 36 (1976), pp. 587–591. (Cited on p. 179)

[248] L. E. Reichl, *The Transition to Chaos*, Springer, 1992. (Cited on p. 119)

[249] A. Reiman, G. Fu, S. Hirshman, L. Ku, D. Monticello, H. Mynick, M. Redi, et al., *Physics design of a high-quasi-axisymmetric stellarator*, Plasma Physics and Controlled Fusion, 41 (1999), pp. B273–B283. (Cited on p. 213)

[250] A. Reiman and H. Greenside, *Calculation of three-dimensional MHD equilibria with islands and stochastic regions*, Computer Physics Communications, 43 (1986), pp. 157–167. (Cited on pp. 138, 149)

[251] A. Reiman, M. C. Zarnstorff, D. Monticello, A. Weller, J. Geiger, and the W7-AS Team, *Pressure-induced breaking of equilibrium flux surfaces in the W7-AS stellarator*, Nuclear Fusion, 47 (2007), pp. 572–578. (Cited on pp. 136, 150)

[252] D. J. Rej and R. L. Strykowsky, *Project closeout report: National Compact Stellarator Experiment (NCSX)*, Technical report, Princeton Plasma Physics Laboratory, 2009. (Cited on p. 187)

[253] N. Riva, R. S. Granetz, R. Vieira, A. Hubbard, A. T. Pfeiffer, P. Harris, C. Chamberlain, et al., *Development of the first non-planar REBCO stellarator coil using VIPER cable*, Superconductor Science and Technology, 36 (2023), 105001. (Cited on p. 216)

[254] G. T. Roberg-Clark, P. Xanthopoulos, and G. G. Plunk, *Reduction of electrostatic turbulence in a quasi-helically symmetric stellarator via critical gradient optimization*, Journal of Plasma Physics, 90 (2024), 175900301. (Cited on p. 218)

[255] E. Rodriguez and A. Bhattacharjee, *Solving the problem of overdetermination of quasisymmetric equilibrium solutions by near-axis expansions.* I. *Generalized force balance*, Physics of Plasmas, 28 (2021), 012508. (Cited on p. 98)

[256] E. Rodriguez, P. Helander, and A. Bhattacharjee, *Necessary and sufficient conditions for quasisymmetry*, Physics of Plasmas, 27 (2020), 062501. (Cited on p. 218)

[257] E. Rodríguez, W. Sengupta, and A. Bhattacharjee, *Weakly quasisymmetric near-axis solutions to all orders*, Physics of Plasmas, 29 (2022). (Cited on p. 218)

[258] A. Rutkowski, K. Hammond, C. Zhu, D. Gates, and A. Chambliss, *A novel scheme for error field correction in permanent magnet stellarators*, Nuclear Fusion, 63 (2023), 026027. (Cited on p. 218)

[259] S. Sakakibara, K. Y. Watanabe, Y. Suzuki, Y. Narushima, S. Ohdachi, N. Nakajima, F. Watanabe, et al., *MHD study of the reactor-relevant high-beta regime in the Large Helical Device*, Plasma Physics and Controlled Fusion, 50 (2008), 124014. (Cited on pp. 136, 179, 183)

[260] R. Sanchez, M. Y. Isaev, S. P. Hirshman, W. A. Cooper, G. Y. Fu, J. A. Jimenez, L. P. Ku, et al., *Ideal MHD stability calculations for compact stellarators*, Computer Physics Communications, 141 (2001), pp. 55–65. (Cited on p. 183)

[261] F. Sano, T. Obiki, M. Wakatani, K. Kondo, and T. Mizuuchi, *Experimental program of Heliotron J*, J. Plasma and Fusion Res. Ser., 3 (2000), pp. 26–30. (Cited on p. 214)

[262] W. Sengupta, E. J. Paul, Harold Weitzner, and A. Bhattacharjee, *Vacuum magnetic fields with exact quasisymmetry near a flux surface. Part* 1. *Solutions near an axisymmetric surface*, Journal of Plasma Physics, 87 (2021), 905870205. (Cited on p. 218)

[263] K.-C. Shaing, E. C. Crume, Jr., J. S. Tolliver, S. P. Hirshman, and W. I. Van Rij, *Bootstrap current and parallel viscosity in the low collisionality regime in toroidal plasmas*, Physics of Fluids B: Plasma Physics, 1 (1989), pp. 148–152. (Cited on p. 178)

[264] A. Shimizu, H. Liu, M. Isobe, S. Okamura, S. Nishimura, C. Suzuki, Y. Xu, et al., *Configuration property of the Chinese first quasi-axisymmetric stellarator*, Plasma and Fusion Research, 13 (2018), 3403123. (Cited on p. 163)

[265] R. M. Sinclair, J. C. Hosea, and G. V. Sheffield, *Magnetic surface mappings by storage of phase-stabilized low-energy electron beams*, Applied Physics Letters, 17 (1970), pp. 92–95. (Cited on p. 207)

[266] L. Singh, T. G. Kruger, A. Bader, C. Zhu, S. R. Hudson, and D. T. Anderson, *Optimization of finite-build stellarator coils*, Journal of Plasma Physics, 86 (2020), 905860404. (Cited on p. 216)

[267] L. S. Solovèv and V. D. Shafranov, *Plasma confinement in closed magnetic systems*, in Reviews of Plasma Physics, Springer, 1970, pp. 1–247. (Cited on p. 149)

[268] C. Sovinec and B. Cornille, *Initial results of NIMSTELL, the stellarator variant of NIMROD*, in APS Division of Plasma Physics Meeting Abstracts, vol. 2021, 2021. (Cited on p. 217)

[269] C. R. Sovinec, A. H. Glasser, T. A. Gianakon, D. C. Barnes, R. A. Nebel, S. E. Kruger, S. J. Plimpton, A. Tarditi, M. S. Chu, and the NIMROD Team, *Nonlinear magnetohydrodynamics with high-order finite elements*, Journal of Computational Physics, 195 (2004), pp. 355–386. (Cited on p. 137)

[270] L. Spitzer, Jr., *The stellarator concept*, The Physics of Fluids, 1 (1958), pp. 253–264. (Cited on p. 76)

[271] L. Spitzer, Jr., and R. Härm, *Transport phenomena in a completely ionized gas*, Physical Review, 89 (1953), pp. 977–981. (Cited on pp. 134, 207)

[272] D. A. Spong and J. H. Harris, *New QP / QI symmetric stellarator configurations*, Plasma and Fusion Research, 5 (2010), S2039. (Cited on p. 179)

[273] D. A. Spong, S. P. Hirshman, L. A. Berry, J. F. Lyon, R. H. Fowler, D. J. Strickler, M. J. Cole, et al., *Physics issues of compact drift optimized stellarators*, Nuclear Fusion, 41 (2001), pp. 711–716. (Cited on p. 186)

[274] D. A. Spong, S. P. Hirshman, J. C. Whitson, D. B. Batchelor, B. A. Carreras, V. E. Lynch, and J. A. Rome, *J* optimization of small aspect ratio stellarator/tokamak hybrid devices*, Physics of Plasmas, 5 (1998), pp. 1752–1758. (Cited on pp. 180, 186, 213)

[275] T. H. Stix, *Highlights in early stellarator research at Princeton*, Journal of Plasma and Fusion Research Series, 1 (1998), pp. 3–8. (Cited on p. 207)

[276] R. Storn and K. Price, *Differential evolution–A simple and efficient heuristic for global optimization over continuous spaces*, Journal of Global Optimization, 11 (1997), pp. 341–359. (Cited on p. 186)

[277] B. STRATTON, A. BROOKS, T. BROWN, D. JOHNSON, G. LABIK, E. LAZARUS, N. POMPHREY, S. RAFTOPOULOS, AND M. ZARNSTORFF, *External magnetic diagnostics for the National Compact Stellarator Experiment*, Review of Scientific Instruments, 77 (2006), 10e314. (Cited on p. 187)

[278] D. J. STRICKLER, L. A. BERRY, AND S. P. HIRSHMAN, *Designing coils for compact stellarators*, Fusion Science and Technology, 41 (2002), pp. 107–115. (Cited on pp. 206, 213)

[279] D. J. STRICKLER, S. P. HIRSHMAN, D. A. SPONG, M. J. COLE, J. F. LYON, B. E. NELSON, D. E. WILLIAMSON, AND A. S. WARE, *Development of a robust quasi-poloidal compact stellarator*, Fusion Science and Technology, 45 (2004), pp. 15–26. (Cited on pp. 163, 185)

[280] R.L STRYKOWSKY, T. BROWN, J. CHRZANOWSKI, M. COLE, P. HEITZENROEDER, G. H. NEILSON, D. REJ, AND M. VIOL, *Engineering cost & schedule lessons learned on NCSX*, in 23rd IEEE/NPSS Symposium on Fusion Engineering, IEEE, 2009, pp. 1–4. (Cited on pp. 213, 216)

[281] S. SUDO, Y. TAKEIRI, H. ZUSHI, F. SANO, K. ITOH, K. KONDO, AND A. IIYOSHI, *Scalings of energy confinement and density limit in stellarator/heliotron devices*, Nuclear Fusion, 30 (1990), pp. 11–21. (Cited on p. 211)

[282] L. E. SUGIYAMA, W. PARK, H. R. STRAUSS, S. R. HUDSON, D. STUTMAN, AND X.-Z. TANG, *Studies of spherical tori, stellarators and anisotropic pressure with the M3D code*, Nuclear Fusion, 41 (2001), pp. 739–746. (Cited on p. 137)

[283] T. SUNN PEDERSEN, A. DINKLAGE, Y. TURKIN, R. WOLF, S. BOZHENKOV, J. GEIGER, G. FUCHERT, ET AL., *Key results from the first plasma operation phase and outlook for future performance in Wendelstein 7-X*, Physics of Plasmas, 24 (2017), 055503. (Cited on pp. 7, 210)

[284] T. SUNN PEDERSEN, M. OTTE, S. LAZERSON, P. HELANDER, S. BOZHENKOV, C. BIEDERMANN, T. KLINGER, R. C. WOLF, H.-S. BOSCH, AND THE WENDELSTEIN 7-X TEAM, *Confirmation of the topology of the Wendelstein 7-X magnetic field to better than* 1:100,000, Nature Communications, 7 (2016), 13493. (Cited on p. 211)

[285] Y. SUZUKI, K. IDA, K. KAMIYA, M. YOSHINUMA, S. SAKAKIBARA, K. Y. WATANABE, H. YAMADA, AND THE LHD EXPERIMENT GROUP, *3D plasma response to the magnetic field structure in the Large Helical Device*, Nuclear Fusion, 53 (2013), 073045. (Cited on p. 136)

[286] Y. SUZUKI, N. NAKAJIMA, K. WATANABE, Y. NAKAMURA, AND T. HAYASHI, *Development and application of HINT2 to helical system plasmas*, Nuclear Fusion, 46 (2006), pp. L19–L24. (Cited on pp. 138, 150)

[287] Y. SUZUKI, K. WATANABE, H. FUNABA, S. SAKAKIBARA, N. NAKAJIMA, N. OHYABU, AND THE LHD EXPERIMENT GROUP, *Effects of the stochasticity on transport properties in high-β LHD*, Plasma and Fusion Research, 4 (2009), pp. 036-1–036-6. (Cited on pp. 136, 137)

[288] J. B. TAYLOR, *Equilibrium and stability of plasma in arbitrary mirror fields*, Physics of Fluids, 7 (1964), pp. 767–773. (Cited on p. 21)

[289] P. B. THOMPSON AND THE ATF TEAM, *The Advanced Toroidal Facility (ATF)*, Fusion Technology, 8 (1985), pp. 450–455. (Cited on p. 214)

[290] A. N. TIKHONOV, *On the solution of ill-posed problems and the method of regularization*, in Proceedings of the USSR Academy of Sciences, vol. 151, Russian Academy of Sciences, 1963, pp. 501–504. (Cited on p. 196)

[291] Y. TODO, N. NAKAJIMA, M. SATO, AND H. MIURA, *Simulation study of ballooning modes in the large helical device*, Plasma and Fusion Research, 5 (2010), pp. 2062-2–2062-4. (Cited on p. 137)

[292] D. TONG, *The Hamiltonian Formalism*. http://www.damtp.cam.ac.uk/user/tong/dynamics/four.pdf, 2015. Accessed: 2018-03-05. (Cited on p. 231)

[293] ——, *The Lagrangian Formalism*. http://www.damtp.cam.ac.uk/user/tong/dynamics/two.pdf, 2015. Accessed: 2018-03-05. (Cited on pp. 13, 228)

[294] S. TUREK, O. MIERKA, AND K. BÄUMLER, *Numerical benchmarking for 3D multiphase flow: New results for a rising bubble*, in Numerical Mathematics and Advanced Applications ENUMATH 2017, F. A. Radu, K. Kumar, I. Berre, J. M. Nordbotten, and I. S. Pop, eds., Springer, 2019, pp. 593–601. (Cited on p. 154)

[295] J. L. VELASCO, I. CALVO, S. MULAS, E. SÁNCHEZ, F. I. PARRA, A. CAPPA, AND THE W7-X TEAM, *A model for the fast evaluation of prompt losses of energetic ions in stellarators*, Nuclear Fusion, 61 (2021), 116059. (Cited on p. 182)

[296] F. WAGNER, *Stellarators and optimised stellarators*, Fusion Technology, 33 (1998), pp. 67–83. (Cited on pp. 177, 209)

[297] M. WAKATANI AND S. SUDO, *Overview of Heliotron E results*, Plasma Physics and Controlled Fusion, 38 (1996), pp. 937–988. (Cited on p. 214)

[298] S. W. WALKER, *The Shapes of Things: A Practical Guide to Differential Geometry and the Shape Derivative*, Advances in Design and Control 28, SIAM, 2015. (Cited on pp. 82, 242, 243, 248)

[299] F. WECHSUNG, A. GIULIANI, M. LANDREMAN, A. CERFON, AND G. STADLER, *Single-stage gradient-based stellarator coil design: Stochastic optimization*, Nuclear Fusion, 62 (2022), 076034. (Cited on p. 215)

[300] H. WEITZNER, *Ideal magnetohydrodynamic equilibrium in a non-symmetric topological torus*, Physics of Plasmas, 21 (2014), 022515. (Cited on p. 126)

[301] ——, *Expansions of non-symmetric toroidal magnetohydrodynamic equilibria*, Physics of Plasmas, 23 (2016), 062512. (Cited on p. 126)

[302] H. WEITZNER AND W. SENGUPTA, *Exact non-symmetric closed line vacuum magnetic fields in a topological torus*, Physics of Plasmas, 27 (2020), 022509. (Cited on p. 126)

[303] A. WELLER, S. SAKAKIBARA, K. Y. WATANABE, K. TOI, J. GEIGER, M. C. ZARNSTORFF, S. R. HUDSON, ET AL., *Significance of MHD effects in stellarator confinement*, Fusion Science and Technology, 50 (2006), pp. 158–170. (Cited on pp. 183, 217)

[304] J. WESSON AND D. J. CAMPBELL, *Tokamaks*, International Series of Monographs on Physics 149, Oxford University Press, 2011. (Cited on pp. 5, 75)

[305] C. H. WILLIS, *Design and Construction of Model A Stellarator*, Technical report, NJ Project Matterhorn, Princeton University, 1953. (Cited on p. 207)

[306] G. M. WING, *A Primer on Integral Equations of the First Kind: The Problem of Deconvolution and Unfolding*, Other Titles in Applied Mathematics 27, SIAM, 1991. (Cited on p. 191)

[307] H. WOBIG, *Theory of advanced stellarators*, Plasma Physics and Controlled Fusion, 41 (1999), pp. A159–A173. (Cited on p. 177)

[308] R. C. WOLF, A. ALONSO, S. ÄKÄSLOMPOLO, J. BALDZUHN, M. BEURSKENS, C. D. BEIDLER, C. BIEDERMANN, ET AL., *Performance of Wendelstein 7-X stellarator plasmas during the first divertor operation phase*, Physics of Plasmas, 26 (2019), 082504. (Cited on pp. 211, 214)

[309] J. WU, *Bounds and new approaches for the 3D MHD equations*, Journal of Nonlinear Science, 12 (2002), pp. 395–413. (Cited on p. 134)

[310] G. A. WURDEN, C. BIEDERMANN, F. EFFENBERG, M. JAKUBOWSKI, H. NIEMANN, L. STEPHEY, S. BOZHENKOV, ET AL., *Limiter observations during W7-X first plasmas*, Nuclear Fusion, 57 (2017), 056036. (Cited on p. 214)

[311] S. E. WURZEL AND S. C. HSU, *Progress toward fusion energy breakeven and gain as measured against the Lawson criterion*, Physics of Plasmas, 29 (2022), 062103. (Cited on p. 5)

[312] P. XANTHOPOULOS, H. E. MYNICK, P. HELANDER, Y. TURKIN, G. G. PLUNK, F. JENKO, T. GÖRLER, D. TOLD, T. BIRD, AND J. H. E. PROLL, *Controlling turbulence in present and future stellarators*, Physical Review Letters, 113 (2014), 155001. (Cited on p. 218)

[313] H. YAMADA, K. Y. WATANABE, K. YAMAZAKI, S. MURAKAMI, S. SAKAKIBARA, K. NARIHARA, K. TANAKA, ET AL., *Energy confinement and thermal transport characteristics of net current free plasmas in the Large Helical Device*, Nuclear Fusion, 41 (2001), pp. 901–908. (Cited on p. 212)

[314] M. YAMADA, R. KULSRUD, AND H. JI, *Magnetic reconnection*, Reviews of Modern Physics, 82 (2010), pp. 603–664. (Cited on p. 133)

[315] K. YAMAZAKI, O. MOTOJIMA, AND M. ASAO, *Design scalings and optimization for the superconducting Large Helical Device*, Fusion Technology, 21 (1992), pp. 147–160. (Cited on p. 211)

[316] J.-C. YOCCOZ, *An Introduction to Small Divisors Problems*, Springer, 1992, pp. 659–679. (Cited on p. 59)

[317] M. YOKOYAMA, K. ITOH, S. OKAMURA, K. MATSUOKA, AND S.-I. ITOH, *Maximum-J capability in a quasiaxisymmetric stellarator*, Physical Review E, 64 (2001), 015401. (Cited on p. 213)

[318] M. YOKOYAMA, Y. NAKAMURA, AND M. WAKATANI, *An optimized helical axis stellarator with modulated l=1 helical coil*, Journal of Plasma and Fusion Research, 73 (1997), pp. 723–731. (Cited on p. 183)

[319] S. YOSHIKAWA AND T. H. STIX, *Experiments on the Model C stellarator*, Nuclear Fusion, 25 (1985), pp. 1275–1279. (Cited on p. 207)

[320] D. YUAN AND X. ZHANG, *An overview of numerical methods for the first kind Fredholm integral equation*, SN Applied Sciences, 1 (2019). (Cited on p. 195)

[321] L. E. ZAKHAROV, *Implementation of Hamada principle in calculations of nested* 3*-D equilibria*, Journal of Plasma Physics, 81 (2015). (Cited on p. 126)

[322] M. C. ZARNSTORFF, L. A. BERRY, A. BROOKS, E. FREDRICKSON, G. Y. FU, S. HIRSHMAN, S. HUDSON, ET AL., *Physics of the compact advanced stellarator NCSX*, Plasma Physics and Controlled Fusion, 43 (2001), pp. A237–A249. (Cited on pp. 35, 36, 163, 181, 190, 214)

[323] M. C. ZARNSTORFF, A. WELLER, J. GEIGER, E. FREDRICKSON, S. HUDSON, J. P. KNAUER, A. REIMAN, ET AL., 20*th IAEA Fusion Energy Conference*, Technical report, EX/3-4 (IAEA, Vilamoura, 2004), 2004. (Cited on p. 136)

[324] Y. ZHOU, *Regularity criteria for the generalized viscous MHD equations*, Annales de l'IHP Analyse non linéaire, 24 (2007), pp. 491–505. (Cited on p. 134)

[325] Y. ZHOU, N.M. FERRARO, S.C. JARDIN, AND H.R. STRAUSS, *Approach to nonlinear magnetohydrodynamic simulations in stellarator geometry*, Nuclear Fusion, 61 (2021), 086015. (Cited on p. 217)

[326] C. ZHU, K. HAMMOND, T. G BROWN, D. A GATES, M. C ZARNSTORFF, K. CORRIGAN, M. SIBILIA, AND E. FEIBUSH, *Topology optimization of permanent magnets for stellarators*, Nuclear Fusion, 60 (2020), 106002, doi:10.1088/1741-4326/aba453. (Cited on p. 217)

[327] C. ZHU, S. R. HUDSON, Y. SONG, AND Y. WAN, *New method to design stellarator coils without the winding surface*, Nuclear Fusion, 58 (2018), 016008. (Cited on p. 206)

[328] C. ZHU, M. ZARNSTORFF, D. GATES, AND A. BROOKS, *Designing stellarators using perpendicular permanent magnets*, Nuclear Fusion, 60 (2020), 076016. (Cited on p. 217)

[329] E. G. ZWEIBEL AND M. YAMADA, *Perspectives on magnetic reconnection*, Proceedings of the Royal Society A: Mathematical, Physical and Engineering Sciences, 472 (2016), 20160479. (Cited on p. 127)

[330] A. B. ZYLSTRA, A. L. KRITCHER, O. A. HURRICANE, D. A. CALLAHAN, J. E. RALPH, D. T. CASEY, A. PAK, ET AL., *Experimental achievement and signatures of ignition at the National Ignition Facility*, Physical Review E, 106 (2022), 025202. (Cited on p. 4)

Index

An Introduction to Stellarators: From Magnetic Fields to Symmetries and Optimization – Imbert-Gérard et al (9781611978216)

This self-contained book is the first to provide readers with an introduction to the mathematical foundations of stellarator design and modeling. It covers the fundamental theoretical building blocks of modeling magnetic fields, some of the associated challenges, and the main concepts behind optimization for the design of stellarators. The book is divided into two parts, with Part I providing a general introduction to the stellarator concept and Part II describing mathematical models and numerical methods commonly used in stellarator design.

In this book, the authors

- derive, present, and discuss relevant models;
- use equations and figures to demonstrate the main ideas;
- include references to other relevant introductory material; and
- carefully select language that is close to the plasma physics literature, while providing enough details to be accessible to a reader without previous background in this field.

Audience

An Introduction to Stellarators is intended for mathematicians, physicists, and engineers interested in learning about stellarators. Readers are expected to have a basic knowledge of classical physics, partial differential equations, and variational calculus, but prior knowledge of plasma physics is not required.

About the Authors

Lise-Marie Imbert-Gérard is an associate professor in the Department of Mathematics at the University of Arizona. Her research focuses on models, analysis, and numerical methods for wave propagation in inhomogeneous media. She works on applications in plasma physics for waves in magnetized plasmas and aeroacoustics for noise propagation around planes. She has received a Cathleen Morawetz fellowship from the Courant Institute, a Leslie Fox Prize from the Institute of Mathematics and its Applications (UK), as well as a Department of Energy Early Career Research Award. She was also selected as a 2023 Kavli fellow by the National Academy of Sciences.

Elizabeth J. Paul is an assistant professor at Columbia Engineering, Columbia University. In 2021, she received the Marshall N. Rosenbluth Award from the American Physical Society in recognition of her doctoral work, and in 2023 she received the DOE Early Career Research Award. Prior to joining Columbia University, Dr. Paul was a Presidential Postdoctoral Research Fellow at Princeton University. She uses theoretical and computational methods to study the magnetic confinement of plasmas for fusion energy sciences. Her research integrates applied mathematical techniques to improve the design of stellarator configurations through numerical optimization. She studies the rich behavior present in three-dimensional magnetic confinement devices, including the nonlinear dynamics of fast particle populations.

Adelle M. Wright is an assistant professor in the Department of Nuclear Engineering and Engineering Physics at the University of Wisconsin-Madison. Prior to joining the faculty at UW-Madison, Dr. Wright was a staff research physicist in the Princeton Plasma Physics Laboratory's Theory Department and has held positions at the Australian Academy of Science, where she specialized in managing international scientific engagement. Her research combines high performance scientific computing, multiscale physics modeling, and applied mathematics to understand and predict the macroscopic properties of magnetically confined plasmas.

For more information about SIAM books, journals, conferences, memberships, or activities, contact:

siam

Society for Industrial and Applied Mathematics
3600 Market Street, 6th Floor
Philadelphia, PA 19104-2688 USA
+1-215-382-9800
siam@siam.org • *www.siam.org*

ISBN: 978-1-61197-821-6

OT202